Etude expérimentale et numérique du comportement dynamique de composites aéronautiques sous choc laser. Optimisation du test d'adhérence par ondes de choc sur les assemblages composites collés

Romain Ecault

▶ **To cite this version:**

Romain Ecault. Etude expérimentale et numérique du comportement dynamique de composites aéronautiques sous choc laser. Optimisation du test d'adhérence par ondes de choc sur les assemblages composites collés. Autre. ISAE-ENSMA Ecole Nationale Supérieure de Mécanique et d'Aérotechique - Poitiers, 2013. Français. NNT : 2013ESMA0031 . tel-01242721

HAL Id: tel-01242721
https://theses.hal.science/tel-01242721

Submitted on 14 Dec 2015

HAL is a multi-disciplinary open access archive for the deposit and dissemination of scientific research documents, whether they are published or not. The documents may come from teaching and research institutions in France or abroad, or from public or private research centers.

L'archive ouverte pluridisciplinaire **HAL**, est destinée au dépôt et à la diffusion de documents scientifiques de niveau recherche, publiés ou non, émanant des établissements d'enseignement et de recherche français ou étrangers, des laboratoires publics ou privés.

THESE

pour l'obtention du Grade de
DOCTEUR DE L'ECOLE NATIONALE SUPERIEURE DE MECANIQUE ET D'AEROTECHNIQUE
(Diplôme National - Arrêté du 7 août 2006)

Ecole Doctorale :
Sciences et Ingénierie en Matériaux, Mécanique, Energétique et Aéronautique

Secteur de Recherche : Mécanique des Matériaux

Présentée par :

Romain ECAULT

****

Experimental and numerical investigations on the dynamic behaviour of aeronautic composites under laser shock - Optimization of a shock wave adhesion test for bonded composites

Etude expérimentale et numérique du comportement dynamique de composites aéronautiques sous choc laser – Optimisation du test d'adhérence par ondes de choc sur des assemblages composites collés

Version finale
****

Directeurs de Thèse : Michel BOUSTIE, Fabienne TOUCHARD, Laurent BERTHE

****
Soutenue le 13 décembre 2013
devant la Commission d'Examen

****

JURY

Pr. I. Iordanoff	ENSAM Paristech-Bordeaux, Directeur général adjoint de la Recherche et de l'Innovation, Arts et Métiers
Dr D. Vanderhaegen,	Chef du Dpt. Physique Théorique et Appliquée, CEA-BIII
Dr A. Johnston	Senior Researcher at NRC Institute for Aerospace Research, Ottawa, Canada
Dr C. Bockenheimer	Airbus Toulouse, Head of 'Testing, Surface, Standardisation', A350 Materials & Processes
Dr R. Fabbro	Directeur de Recherches CNRS-PIMM, ENSAM Paristech,
Dr F. Touchard	Chargée de Recherches CNRS-PPRIME, ISAE-ENSMA,
Dr L. Berthe	Directeur de Recherches CNRS-PIMM, ENSAM Paristech,
Dr M. Boustie	Directeur de Recherches CNRS-PPRIME, ISAE-ENSMA.

REMERCIEMENTS

Trois ans de Thèse, c'est parfois très long, mais finalement très court quand je regarde tout ce que j'ai eu l'opportunité de vivre et de réaliser. Ces trois ans de thèse, c'est avant tout de très belles rencontres, de grands moments de vie, et beaucoup de travail qui en font une expérience humaine et professionnelle riche et unique. Bien sûr, cette belle aventure n'aurait pas été la même sans toutes les personnes qui m'ont entouré et soutenu. Je tiens à les remercier très sincèrement au travers de ces quelques paragraphes, car sans eux je ne serais certainement pas le même aujourd'hui. Ils sont très nombreux, alors j'espère que je n'oublierai personne… Si jamais c'était le cas, vous avez le droit de vous plaindre, et je verrai ce que je peux faire !

Je tiens tout d'abord à remercier ceux qui m'ont suivi au quotidien, et qui ont énormément compté pour moi pendant trois ans, à savoir mes trois directeurs de Thèse, **Michel Boustie**, **Fabienne Touchard** et **Laurent Berthe**. Je m'estime très chanceux et je suis très fier de les avoir eu tous les trois comme encadrants, à un tel point que c'est la seule chose que je ne changerais absolument pas si je devais remettre ça. Je trouve qu'on a formé une très belle équipe, et nos nombreux échanges, toujours dans la bonne humeur, vont clairement me manquer. Chacun à leur manière, ils m'ont apporté différentes choses pour lesquelles je ne les remercierai jamais assez. Je ne peux évidemment pas réduire ça à un ou deux traits de caractère tant ce sont des scientifiques complets, mais je retiendrai surtout ton côté humain et ton excellent relationnel Michel, ta sagesse et ton recul Fabienne, ta capacité de travail et ta motivation positive Laurent. Je souhaite à tous les petits jeunes un aussi bon et aussi sympa encadrement que le mien.

Avant de me lancer dans les nombreux remerciements à nos partenaires et amis, je tiens à remercier sincèrement les membres de mon Jury de thèse pour la pertinence de leurs questions et de leurs remarques, ainsi que pour la qualité de leurs interventions. Ce jury était composé, pour ses membres extérieurs, de : **Dr. Rémy Fabbro**, **Dr. Ivan Iordanoff**, **Dr. Daniel Vanderhaegen**, **Dr. Andrew Johnston**, **Dr. Clemens Bockenheimer**, **M. Hubert Voillaume**, et **Dr. Dorothea Stuebing**. Mention spéciale aux deux rapporteurs, **Dr. Vanderhaegen** et **Dr. Iordanoff**, à qui j'ai donné beaucoup de travail en leur demandant de lire 300 pages en langue de Shakespeare (ou avoisinant). En guise de remerciement, et parce qu'ils me l'ont demandé, je mets un petit dessin juste là.

J'aimerais ensuite remercier l'ensemble de nos partenaires, industriels, académiques et un mix des deux, qui ont largement contribué à la bonne conduite de mes travaux. Certains proviennent des collaborations établies avec mon équipe de Recherche, d'autres se sont révélés au cours de ces trois ans. Comme j'aime bien le travail en équipe, je trouve là aussi qu'on a formé de très belles équipes, et que travailler dans ce contexte a été très stimulant et enrichissant.

- Comment ne pas commencer par **Bastien Ehrhart** avec qui j'ai échangé quasi-quotidiennement pendant 3 ans, et toujours avec un réel plaisir (ci-dessus, hommage à un certain L.B.). C'est une très belle rencontre, et ça a été tellement facile de travailler ensemble qu'il faudrait que ce soit toujours comme ça. Merci donc pour tous ces bons moments, au travail bien sûr, mais après aussi, en France et à l'étranger (sacré moment Gdansk ! entre autre). Dans la foulée, j'en profite pour remercier également **Clemens Bockenheimer** pour son soutien indéfectible à notre équipe, sa bonne humeur et ses talents de DJ… Les équipes d'EADS Innovations Works (Airbus Group Innovations, quand j'écris ces lignes) ont également collaboré à ces travaux. Je tiens en particulier à remercier **Hubert Voillaume** et **Benjamin Campagne** pour leur disponibilité, et leur aide dans l'utilisation des techniques ultrasonores. C'était très sympa de travailler et d'échanger avec vous, et j'espère pouvoir continuer à le faire !
- Tant que je suis sur les partenaires rencontrés dans le cadre du projet ENCOMB, I would like to welcome this opportunity to thank **all the ENCOMB partners** I have been working with during three years. I cannot name all of you; I will forget somebody for sure. I think that the success of ENCOMB project is mainly due to the good atmosphere we were working in. I really enjoyed working with all of you, exchanging on the different scientific subjects and not only. From my point of view, it is what Scientific Research should look like everywhere, results from one team helping others, sharing information, and progressing toward a common goal. Thank you very much for all the good times spent altogether, I will never forget these moments and try to do my best to keep in touch. I wish you the best for the years to come, starting with great collaborations.

- C'est le moment de remercier **l'équipe de choc** élargie ! ou la fameuse **« Bousteam »** comme j'aime la nommer, et je pense que vous m'accorderez cette fantaisie amis des chocs. Là encore, de très bons moments, de très riches échanges scientifiques et humains, et des collaborateurs fidèles sur qui on peut compter à tout instant. Ce que j'ai dit au-dessus en anglais vaut pour vous également. Par votre aide et votre soutien à nos travaux expérimentaux, vous avez contribué à de beaux résultats, et je vous en remercie très sincèrement. Dans le désordre : Merci à **Patrick**

Mercier et **Jacky Benier** pour les sondes VH ainsi que pour de nombreuses et passionnantes discussions. **Patrick**, merci aussi pour ce petit coup de main mémorable un matin de novembre de retour de Singapour et sans téléphone… Merci à **Arnaud Sollier** et **Emilien Lescoute** pour leur soutien sur les manips LULI, et leur force motrice même à 3h du matin sur ELFIE ! Merci à **Michel Arrigoni** pour nous avoir ouvert les portes de l'ENSTA Bretagne à plusieurs reprises pour de superbes manips, pour m'avoir fait découvrir les ravioles du Dauphiné (ça a changé ma vie) et pour ce souvenir frissonnant d'un câble sous pression volant… Merci également aux bordelais **Frédéric Malaise** et **David Hebert** pour nos nombreux échanges (à Seattle entre autres David) toujours intellectuellement savoureux. Enfin, merci aux **Titidoctorants** !!! J'aurais plein de choses à vous dire Messieurs, mais finalement je crois que ce n'est pas la peine car on se comprend bien et ce n'est pas un hasard qu'on se soit retrouvés dans la même équipe. Alors il y a les « vieux » avec qui c'est toujours un plaisir d'échanger, **Damien Laporte, Emilien Lescoute, Serge Guetta** (ou 007…ta tadam tam, tadam tada tam…) et **Jean-Paul Cuqlelandais**, à qui je dois un peu (p = 0.39) cette aventure, rappelons-nous en. Et puis les plus jeunes, **Pierre-Antoine Frugier**, **Gabriel Prudhomme, Damien Courapied** et Mister **Gabriel Seisson** [1]. **Matthieu Lecouvez**, je te mets également dans cette catégorie car ton état d'esprit est homogène. Je ne peux pas énumérer tous ces bons moments en manip, après ou avant, car ils sont trop nombreux, mais merci pour tout ça. Mention spécial aux Forum ILP, à Seattle, à Pommery etc… Je dois faire cas à part de mon **Didier Loison**, qui bien sûr a contribué à tout ce que je viens de citer, mais qui en plus m'a supporté comme co-bureau pendant 3 ans, et croyez-moi ce n'est pas facile, d'autant plus que je parle tout seul… Merci Didier pour ta présence, ton soutien et pour avoir toujours été prêt à m'aider quelle que soit l'heure ou les circonstances (Merci d'avoir conduit aussi ^^)

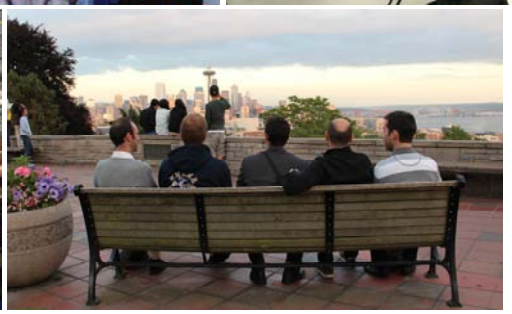

- Je termine cette longue liste en remerciant **Ekaterina Mazanchenko**, qui a dû supporter mes fautes de français et mes expressions pas possible en plein apprentissage du français… ça a dû être dur ; mais aussi les stagiaires que j'ai eu la chance de co-encadrer pendant ces trois ans et qui ont contribué à ces résultats, par ordre chronologique : **Hélène Sapardanis, Raquel Martinez, Nacim Laimeche,** et **Nereida Salas**. Je ne t'oublie pas **Marion Trombini**, même si je n'étais pas encore là, car il faut savoir reconnaître les bonnes idées ;)

- D'une manière plus large, je souhaite remercier les **équipes du LULI**, en particulier des sources **LULI 2000** et **ELFIE**, pour leur gentillesse et leur accueil. Et puis désolé d'avoir mis plein de petits bouts d'époxy dans les enceintes à vide…
- Merci également à **David Assous**, et la Société IDIL, pour leur aide sur les manips.
- Merci à **Julien Lacambre**, de la société Alyotech, pour son aide apportée sur la modélisation numérique sous LS-DYNA.

J'en viens maintenant aux équipes locales au sein du laboratoire et de l'ENSMA qui ont apporté leur pierre à l'édifice. Là encore, je vais essayer de n'oublier personne, mais la tâche est ardue. C'est plus ou moins dans le désordre.

- Je tiens d'abord à remercier l'équipe locale qui s'est impliquée dans le projet ENCOMB au sein du laboratoire, et en particulier **Laurence Chocinski** avec qui c'est toujours un plaisir de travailler. Bon, on a pas mal galéré avec nos petits bouts d'époxy, mais c'est aussi ça la recherche, et ça montre que trouver des choses qui ne marchent pas comme on veut, et bien c'est aussi trouver !
- Merci à **Jacques Baillargeat** pour son soutien et son appui sur les installations laser du laboratoire. Heureusement qu'on a notre star de télé toujours présent pour placer un miroir, polariser un faisceau, ou aligner des têtes (Jacques, on tire !)
- Merci à l'ensemble des ingénieurs d'étude de l'axe, en particulier **Anne-Laure Gorge**, **David Mellier**, **Guillaume Benoit**, **Médéric Morisset** (bon courage pour ton genou), **Florence Hamon**, **Mickael Gueguen**, pour leur appui. Je remercie aussi **les ingénieurs du PIMM**, qui m'ont également aidé lors de mes venues. Merci à **Noël Brunetière** pour ses bons conseils sur l'utilisation du microscope confocal. Merci à **Gérald Sailly** et à **Hervé Doreau** pour leur aide.
- Je remercie également tous les personnels administratifs qui ont dû me supporter pendant 3 ans, et il y a eu du boulot. Côté laboratoire, merci à **Eliane Bonneau**, **Francine Bayle**, **Marie-Cannelle Cossin**, **Jocelyne Bardeau** et surtout à **Brigitte Vigner** pour son aide et sa bonne humeur permanente malgré mes missions à répétition (alors Brigitte, en fait je dois partir à Toulouse mercredi, puis Paris jeudi et je prends l'avion vendredi pour Kuala Lumpur, et finalement Singapour… comment on fait ? ^^). Je tiens aussi à remercier **les équipes de l'ENSMA** qui eux me connaissent depuis un peu plus longtemps. Je m'appuie sur **Audrey Veron** (que j'ai aussi pas mal embêtée), **Corinne Dutault**, **Lydie Guérin** pour remercier l'ensemble du personnel. Je ne peux pas ne pas remercier **Olivier Geay** pour ces 6 années de beaux projets et d'échanges toujours sympas. Merci à lui aussi !
- Merci à l'ensemble des doctorants, à la fois **la fine équipe du BDD**, et aussi **les doctorants de l'axe et de l'ENSMA** pour tous ces bons moments et ces conversations parfois passionnées (parfois moins, et c'est bien aussi !). J'ai une pensée pour **Florian Riebel**, qui a sa thèse dans nos cœurs.
- Merci aux quelques permanents (pas encore cités !) avec qui j'ai toujours pris du plaisir dans les discussions : **Catherine Gardin**, **Damien Halm**, **Séverine Boyer**, **Frédéric Pons**. J'espère pouvoir continuer à le faire ! Enfin merci au **super couloir**, qui se reconnaitra !!
- Merci à **mes élèves** pour ces bons moments passés en TD et en projet ;)

Je termine en remerciant celles et ceux qui ont toujours été là pour moi, depuis longtemps et depuis un peu moins aussi. Leur soutien, direct ou indirect, a forcément compté pendant ces années, et m'a permis d'en arriver là aujourd'hui.

- J'ai une pensée pour les enseignants que j'ai croisé au cours de ma scolarité, qui ont tous une part de « responsabilité ». Je remercie en particulier **Laurent Lepetit**, pour tout ce qu'il a su me transmettre (à son insu ?) et pour m'avoir fait découvrir cet état d'esprit ovale qui m'accompagnera toute ma vie.
- Merci aux amis d'ici, **Didier Loison**, **Clara Moriconi**, **Julien Jaravel**, **Leatitia et Dédé** (qui ont quitté le labo trop vite), **Pierre Belleoud**, **Florent Germain**, **Aurélien Helstroffer**, **Benjamin Tressou**, **Luc Doremus**, et j'en oublie surement.
- Il y a aussi les amis un peu plus loin qui ont connu et qui connaissent la même aventure que moi, ma Bibie **Anais Farrugia** (around the world en ce moment), **Julien Nicoloso**, **Antoine Hurmane** ; et puis les amis qui ne seront jamais docteurs (ah AH !) : **Tristan Bartalini**, **Maxime Marchand** bien sûr, **Mylène Loubatière**, **Vivien H. et sa moitié**, **Claire H.**, **Julie M**., et puis tous **les autres** dont la belle **famille ENSMA**.
- Mes derniers mots vont à **ma famille** et à **mes parents** qui m'ont toujours soutenu tout au long de ces années, et ce malgré parfois mes sauts d'humeur. Sans votre aide, la route aurait été bien plus tortueuse. J'en profite pour féliciter **ma petite sœur** pour son récent diplôme d'école de commerce, je suis très fier de toi. Merci également à mes beaux-parents pour leur soutien. Enfin, merci à **ma ptite femme Sarah**, pour à peu près tout, pendant ces 3 ans. J'ai conscience que ça a été très dur pour toi, et je te remercie du fond du cœur pour ton amour, ta présence, ton soutien et ton dadi humour malgré ça. C'est fini, je ne recommence pas, promis ;)

PS : Si vous trouvez ces remerciements longs, dites-vous qu'ils ne représentent que 1.3% du manuscrit…

PSS : Si vous trouvez des fautes d'orthographe, rassurez-vous, la suite est en anglais !

[1] G. Seisson, 2013. « *The bear is always in the wood* », published in *Ma Thèse, cette grande aventure !*, Natures, 233-333, 2013

INTRODUCTION
CHAPTER 1: CONTEXT AND BIBLIOGRAPHY

Introduction **14**

Part 1: Weak bond issue and NDT techniques in Aeronautics **14**

1 Weak bond industrial context **14**

2 ENCOMB European project **16**

2.1 Need for new NDT techniques 16
2.2 ENCOMB Industrial challenges and studied cases 17

3 Techniques developed for weak bonds detection **19**

3.1 Common NDT Techniques 20
3.2 Weak bonds in the literature 21
3.3 Why a need for LASAT (LASer Adhesion Test) 22

Part 2: LASAT technique: principle, history and state of art **23**

1 Principle and description of the LASAT technique **23**

1.1 About LASER shocks 23
1.2 Application to material and LASAT principle 25

2 LASAT history and overview **29**

2.1 Early years and LASAT for coated systems 29
2.2 LASAT for composite applications 33
2.2.1 Laser Bond Inspection 33
2.2.2 SATAC project 36

3 Our scientific approach **38**

Part 3: Bibliography on epoxy and composite under shocks **40**

1 About composite materials **40**

1.1 Generalities, GFRP and CFRP 40
1.2 Dynamic loading and damage in composite materials 41
1.2.1 Low velocity impact 42
1.2.2 High strain rate and very high strain rate 43
1.2.3 Laser irradiation, laser shock and related phenomena 45
1.2.4 Strain rate effects on CFRP mechanical properties 46

2 Epoxy resins under dynamic loading **46**

3 About bonded composite materials **48**

3.1 State of the art 48
3.1.1 Adhesion models 48
3.1.2 Characterization of adhesive bonding 49

3.2 About ENCOMB bonded composite 50
3.2.1 Elaboration of bonded composite 50
3.2.2 How to evaluate the degradation of adhesive bonds 51
3.2.3 Release agent scenario 52
3.2.4 Moisture scenario 54
Conclusions 55
REFERENCES 55

CHAPTER 2: EXPERIMENTAL TOOLS FOR INVESTIGATING THE COMPOSITE AND BONDED COMPOSITE UNDER DYNAMIC LOADING

Introduction 70
1 Experimental shock sources 70
1.1 1.1 Presentation of PPRIME 25 laser source 71
1.2 Research sources 73
1.3 Plate impact experiments 74
1.4 Summary 75
2 Time resolved measurements 75
2.1 Velocity Interferometer System for Any Reflector (VISAR) 75
2.2 The Photonic Doppler Velocimetry (PDV) technique 79
2.3 Transverse observations 80
2.4 Table of the experimental configurations 83
3 Used post-mortem techniques 85
3.1 Cross section micrographies 85
3.2 X-Ray radiography 86
3.3 Interferometric confocal microscopy 87
3.4 Ultrasounds and laser ultrasounds 88
3.5 Microstructure characterization by DSC 90
4 Summary on the used techniques 91
REFERENCES 92

CHAPTER 3: BEHAVIOR AND TRANSFORMATION UNDER LASER SHOCK DYNAMIC LOADING OF EACH ELEMENTARY COMPONENT OF BONDED COMPOSITE MATERIALS

Introduction 96
Part 1: Epoxy resins 96
1 Samples description 96
1.1 1.1. Transparent epoxy sample 96

1.2 FM300 material 97

2 Time resolved observation of the shock wave propagation and associated phenomena into an epoxy .98

2.1 Nanosecond scale experiments (LULI2000 source) 98
2.2 Femtosecond scale experiments (ELFIE) 103

3 Characterization of FM300 bond 109

Part 2: Composites 110

1 Sample description 110

2 Post – mortem description of the damage resulting from the laser shock loading on T800/M21 CFRP materials 113

2.1 Thin cross-ply T800/M21 CFRP 113
2.2 Thick cross-ply T800/M21 CFRP investigations 118

3 Comparison of different unidirectional CFRP responses to laser shocks – damage tolerance 125

3.1 Laser shocks and goal study 125
3.2 Post mortem observations 126
3.3 Toward the use of dimensionless number for composite sample classifications 130
3.4 Differences in the spallation behavior of unidirectional CFRP 132

4 Time resolved analysis of CFRP response to shock loading 134

4.1 Time resolved measurements of thin unidirectional T800/M21 samples 135
4.2 Time resolved measurements of thick unidirectional T800/M21 samples 138
4.3 Reproducibility 140
4.4 Time resolved measurement of crossed ply composite dynamic response 142

Part 3: Material property modifications under laser shock loading: mechanical, thermal and chemical modifications 143

1 Mechanical modification under repeated laser shocks under damage threshold 143

2 Residual stresses in shocked epoxy resins 146

3 Chemical or microstructural modification under laser shock loading 149

3.1 DSC analysis 149
3.2 Highlighting of a possible microstructural modification on epoxy resins 153

Conclusions and synthesis 155

References 157

CHAPTER 4: NUMERICAL MODELING AND EXPERIMENTAL VALIDATION

Introduction 160

Part 1: Literature overview and presentation of the numerical tools 160

1 Different finite element codes 160

2 2. Shock and damage modeling on composite materials (literature overview) 161

2.1 Quasi static loading and interlaminar strength 161

2.2 Low velocity impacts 162
2.3 A few words about buckling 164
2.4 Modeling High Velocity Impacts on composites 165
2.5 Epoxy resins modeling 167
2.6 What to keep in mind for laser shocks 167

3 Numerical tools selected and developed 168

4 Preliminary step: Calibration of the pressure profiles 169

Part 2: Modeling of the epoxy behavior under laser shocks 171

1 Simulation of the shock wave propagation into an epoxy 171

1.1 Model and parameters 171
1.2 Mapping of the shock wave propagation by simulation 172
1.3 Mapping of the shear stresses 174

2 Modeling FM300 behavior 176

2.1 Modeling choice 176
2.2 Comparison experiment/simulation 176

Part 3: Composites: understanding the model to obtain a correct description of the dynamic behavior 177

1 Composite model presentation 177

2 Parametric studies on the composite models 181

2.1 Pressure load parametric study 182
2.2 Influence of the interface stiffness 183
2.3 Anisotropic effect on the back face velocity 184
2.4 Analysis of the shock propagation along X, Y and Z directions 187
2.5 Parametric study on the material elastic parameters 189
2.6 Parametric study on sample thickness 192
2.7 A few words about thick composite model 192

3 From experiments to numerical modeling validation, results and discussions 195

3.1 Numerical simulations validation procedure on thin unidirectional T800/M21 composite 195
3.2 Validation on other thin unidirectional T800/M21 experiments 200
3.3 Numerical simulation of 3 mm thick T800/M21 experiments 202
3.4 Numerical simulation of T700/M21 cross-ply composite 204

Conclusions & Synthesis 206

References 209

CHAPTER 5: CHARACTERIZATION OF THE BONDED COMPOSITE DYNAMIC BEHAVIOR UNDER LASER SHOCK - DEVELOPMENT OF THE LASER SHOCK WAVE ADHESION TEST

Introduction 212

Part 1: Description of the bonded samples and experimental procedure 212

1 Bonded samples and weak bonds 212

2 Experimental procedure 217

Part 2: Laser shock on symmetrical bonded composite: damage investigations, discrimination of weak bonds, and optimization issue 218

1 Laser shocks 218

2 Laser shock induced damage investigations on reference bonded samples 219

3 Laser shock induced damage investigations on weak bonds 222

4 Synthesis and discussion about LASAT discrimination potential 227

4.1 Discrimination of weak bonds 227
4.2 Synthesis 229

Part 3: Laser shock on ENCOMB scenarios to qualify the mechanical adhesion of the bond under different contamination degrees 231

1 Laser shocks 231

2 About laser induced damage in non-symmetrical bonded composite 232

2.1 Laser shock induced damage in Reference sample 232
2.2 Laser shock induced damage in release agent contaminated samples 233
2.3 Laser shock induced damage in moisture contaminated samples 233
2.4 Comparison between release agent contaminant and moisture contamination 235

3 Determination of the debonding and damage thresholds by use of post-mortem analysis 236

3.1 Composite damage threshold for the reference sample 236
3.2 Damage thresholds for the release agent contaminated sample 239
3.3 Damage thresholds for the moisture contaminated samples ..... 245 **Erreur ! Signet non défini.**

Part 4: Bonded composite modeling 249

1 Time resolved experimental measurements 249

2 Bonded composite modeling, and low intensity validation 251

3 Numerical simulation at low intensity and results discussion 251

4 Numerical simulation at mid intensity and in case of spallation 256

Conclusions & synthesis 258

References 259

CHAPTER 6: LASAT CURRENT CAPABILITIES, NUMERICAL OPTIMIZATION AND ASSOCIATED EXPERIMENTAL DEMONSTRATION

Introduction 262

Part 1: Current LASAT possibilities 262

1 Repeated loading on bonded targets 262

2 Current LASAT possibilities for the considered assemblies 265

Part 2: Tunable focus diameter 268

1 Principle of the optimization by tunable focus diameter 269

2 Non-symmetrical bonded assembly: loading on the thick composite face 271

3 Non-symmetrical bonded assembly: loading on the thin composite face 274

Part 3: Tunable pulse duration 276

1 Principle of the optimization by tunable pulse duration 276

2 Numerical optimization by tunable pulse duration 278

2.1 On non-symmetrical bonded assembly 278
2.2 On symmetrical bonded composite assembly 282

3 Experimental validation of the numerical optimization by plate impacts experiments 285

3.1 Plate impacts and VH measurements 286
3.2 On really weak bonds (LE) 288
3.3 On reference ES1 289

Part 4: Double shock approach 290

1 Double shock on the assembly front face solution 290

1.1 Principle of the optimization by the front face double shock 290
1.2 Double shock on the front face, numerical approach 291

2 The symmetrical laser shock 293

2.1 Principle of the optimization by symmetrical laser shock 294
2.2 Symmetrical laser shock on bonded composite, numerical optimization and experimental validation 295
2.2.1 Non-symmetrical T700/M21 bonded samples 295
2.2.2 Symmetrical T800/M21 bonded samples 296
2.3 Experimental validation of symmetrical laser shock on bonded composite 297
2.3.1 On ENCOMB ES1 & ES2 298
2.3.2 On weak bonds 299

Conclusions & synthesis 300

CONCLUSIONS AND PERSPECTIVES (P.303)

APPENDIX A - ENCOMB PROJECT AND ENCOMB TECHNIQUES (P. 311)

APPENDIX B - DMA ANALYSIS OF SHOCKED COMPOSITE (P. 323)

APPENDIX C - CALIBRATION OF THE PRESSURE PROFILE (P. 327)

APPENDIX D - SAMPLE SET 2 LASER SHOCK PARAMETERS (P. 335)

APPENDIX E – RESUME DES CHAPITRES EN FRANÇAIS (P. 337)

INTRODUCTION

©Ecault, 2013

During this PhD, experimental and numerical investigations have been performed in order to develop an optimized laser shock adhesion test for aeronautic bonded composites. It is related to a strong industrial need, and linked to important scientific and technologic challenges in the use of composite material in aeronautics.

Indeed, the excellent performance of A380, or the announced success of A350, both Airbus Company last airplanes, are partially due to the use of composite materials. Their low density and high mechanical performances are well adapted to the aircraft manufacturer policy of consumption reduction, which is also meeting the current environmental challenges. In case of the A350, the part of composite in the aircraft structure is up to 52%. Nevertheless, one of the main show-stoppers of the CFRP (Carbon Fiber Reinforced Polymer) material expansion in the aeronautical structure remains the assembly problems. The current assembly techniques are not well adapted to the use of CFRP and result in extra costs, longer production time, and less efficient structures. Adhesive bonding process could be the next technology because it has many advantages, in terms of stress distribution, structure design, manufacturing costs… The potential gain could be up to 12% of the total weight of the aircraft structure, which is quite important for aeronautics. The design regarding primary adhesive CFRP structures is not fully deployed yet, because nondestructive proof cannot be made of the adhesive bond mechanical strength. That is why many works are currently conducted in order to certify or to evaluate the mechanical quality of bonded composites. These works mainly address to the detection of weak bonds which are the most dangerous, because not detectable by conventional non destructive techniques (NDT). In this work, a laser shock wave adhesion test (LASAT) is developed to deal with this industrial issue. This technique enables the generation of high tensile stresses within the material tested, which can open or not the interface to be tested depending on its strength. The central question developed in these investigations is the optimization of the technique for a wide adaptation of the test to different bonded composites.
This work has been conducted in the frame of ENCOMB (Extended Nondestructive testing for COMposite Bonds, www.encomb.eu) European Project, started in November 2010. It aims to the development of ENDT (Extended Non Destructive Techniques) to enable the quantification of bonding process quality. The technique developed in this work is one of them. 14 different industrial and academic European partners are gathered within ENCOMB. From the industrial point of view, the project is leaded by Airbus (Bremen, Germany), whereas the scientific coordination is steered by the Fraunhofer Institute IFAM (Bremen, Germany).

The LASAT technique has already been investigated to test the bond quality of metallic and ceramic coatings on various substrates. More recently, some other works demonstrated the interest of the technique for bonded metals and composites. Despite the experimental investigations made, it appears that some relevant data for developing an optimized technique are missing. The dynamic behavior under laser shock loading of CFRP composite material and consequently of bonded CFRP remains not well known. The physics is quite complex, and requires both deep experimental and numerical investigations. Some fundamental questions can be raised, such as the anisotropy influence on the material response, the laser shock induced damage quantification, or the microstructural modification under laser shock. The technique optimization is also an important

aspect of this work, divided in two key points: i) the control of damage position and level in the bonded composite target, ii) The numerical modeling of laser shock loading on composite material for its behavior understanding and stress distribution quantification. Therefore, a progressive investigation approach has been established in this work. This approach corresponds to the route of this manuscript.

In the **1st chapter** of this manuscript, elements are given on the industrial context and the scientific frame of this study. ENCOMB project and the studied cases are presented. State-of-art on the different techniques currently developed to deal with weak bond issue is given before focusing on the LASAT technique. The recent activities on bonded composites are detailed to lighten what is currently missing to enable the development of an optimized test. Finally, the known elements concerning the mechanical shock propagation and related phenomenon in CFRP are given.

The **2nd chapter** presents all the experimental devices used in this work, through collaborations which contributed to the experimental work. Shock loadings were induced either by high power laser irradiation or plate impacts. For that, several shock sources used in this work are described. In order to monitor the shock experiments, time resolved techniques have been used and are also presented. Finally, the post-mortem techniques available to study the residual state of the shocked composite materials and bonded assemblies are described in the way they were used in this work.

In the **3rd chapter**, experimental results on each constituent of CFRP material are presented, namely: epoxy resins, FM300 adhesive bond materials, CFRP of different thicknesses and lay-up. The aim is to gather enough experimental data to enable a better understanding of the shock response of these different materials in the perspective of their combination. Both time resolved and post-mortem techniques have been used to respectively quantify the composite dynamic response and the laser shock induced damage. The last part gives some elements about the material properties or microstructural modifications which could occur under laser shock loading.

The **4th chapter** presents the results obtained by numerical modeling of laser shock on epoxy resins and CFRP composites. It is a key point for the development of an optimized laser shock wave adhesion test. First, a literature review on existing shock modeling in composite materials is presented. The second part focuses on the numerical modeling of epoxy resins, and FM300 adhesive bond material, in constant comparison with the different experimental results presented in Chapter 3. Finally, the numerical simulations of the laser shock on composite material are presented. Different parametric studies are performed to reach a better understanding of the target geometry, material model parameters, and laser parameters effects on the shock propagation. Model validation from results on thin and thick unidirectional or cross-ply composites, are then presented.

The two previous chapters have set the basis of the experimental and numerical investigations on the bonded composites under laser shock loading, which are presented in the **5th chapter**. The first part gives some elements on the bonded material tested in this work. Experimental results obtained on these assemblies are then presented. The laser shock induced damage is investigated for all the samples, and the damage thresholds are particularly studied in comparison with the classic mechanical testing. The correlation with the contamination degree of weak bonds is aimed. Finally, the laser shock propagation in bonded composites is numerically investigated. The comparison of numerical simulations with experimental data gathered leads to a validation of the proposed modeling and to a deep thorough knowledge of the behavior of bonded assemblies under shock.

In the **6th and last chapter** of this document, the LASAT capabilities in the current laser configurations are first discussed. It shows that some types of bonded assemblies can already be controlled by the current LASAT technique. For the ones which cannot, different optimization solutions are presented by acting on the shock loading configuration: tunable shock loading diameter, tunable pulse duration, front face double shocks and symmetrical laser shock. The key point is to drive a dynamic tensile loading as close as possible to the bond line, and therefore avoiding breaking the composite during the test.

This work is concluded in two steps. The first one focuses on scientific results, and the second one is oriented on the industrial readiness of the technique.

CHAPTER 1: CONTEXT AND BIBLIOGRAPHY

Introduction **14**

Part 1: Weak bond issue and NDT techniques in Aeronautics **14**

1 Weak bond industrial context **14**

2 ENCOMB European project **16**

2.1 Need for new NDT techniques 16
2.2 ENCOMB Industrial challenges and studied cases 17

3 Techniques developed for weak bonds detection **19**

3.1 Common NDT Techniques 20
3.2 Weak bonds in the literature 21
3.3 Why a need for LASAT (LASer Adhesion Test) 22

Part 2: LASAT technique: principle, history and state of art **23**

1 Principle and description of the LASAT technique **23**

1.1 About LASER shocks 23
1.2 Application to material and LASAT principle 25

2 LASAT history and overview **29**

2.1 Early years and LASAT for coated systems 29
2.2 LASAT for composite applications 33
2.2.1 Laser Bond Inspection 33
2.2.2 SATAC project 36

3 Our scientific approach **38**

Part 3: Bibliography on epoxy and composite under shocks **40**

1 About composite materials **40**

1.1 Generalities, GFRP and CFRP 40
1.2 Dynamic loading and damage in composite materials 41
1.2.1 Low velocity impact 42
1.2.2 High strain rate and very high strain rate 43
1.2.3 Laser irradiation, laser shock and related phenomena 45
1.2.4 Strain rate effects on CFRP mechanical properties 45

2 Epoxy resins under dynamic loading **46**

3 About bonded composite materials **48**

3.1 State of the art 48
3.1.1 Adhesion models 48
3.1.2 Characterization of adhesive bonding 49
3.2 About ENCOMB bonded composite 50
3.2.1 Elaboration of bonded composite 50
3.2.2 How to evaluate the degradation of adhesive bonds 51
3.2.3 Release agent scenario 52
3.2.4 Moisture scenario 54

Conclusions **55**

References **55**

Introduction

In this chapter, the first part explains the industrial context of this study. The weak bond issue is introduced and discussed as a first step. Then, the ENCOMB (Extended Non-destructive testing for COMposite Bonds) European Project is presented. The two complementary directions chosen for investigation will be justified: control of adherent surfaces before bonding, and control of the bond mechanical quality after bonding. The different techniques currently developed to deal with weak bond issue are presented and compared.

The laser shock wave adhesion test technique (LASAT) developed during this work is presented in the second part of this chapter. The principle of the technique based on the shock wave theory is first explained, as well as its specificities in case of composite material tests. Then, the history of the technique development is given to reach its state of art with the latest work related to the laser shock wave adhesion test. The recent activities on bonded composites are more detailed to lighten what is currently missing to enable the development of an optimized test. Thanks to these elements, our scientific approach is finally presented.

In the third part, the elements needed for the comprehension and the development of the laser shock technique are described. In accordance with the scientific approach followed in this work, elements on the epoxy resins behaviour under shock are first given. Then, the composite materials are described in detail. Focus is made on several aspects useful for the development of the laser shock wave adhesion test for bonded composites: damage, deformation, low and high velocity impacts, strain rate effects, NDT (Non Destructive Testing), shocks and laser irradiation. Finally, some elements on adhesive bonding are given. Especially, the failure mechanisms, the strength testing techniques, and the weak bond issue are described in detail to highlight what can be improved using the laser shock wave adhesion test.

Part 1: Weak bond issue and NDT techniques in Aeronautics

1 Weak bond industrial context

Composite materials are now widely used in aeronautic industries, as shown by the choices of the two major companies, namely Airbus and Boeing, for their last generations of aircraft. In this high technology field in which any pound counts, the composite materials have a real interest.

Figure 1.1 Picture of the first public flight of the new Airbus A350 XWB taken at Le Salon du Bourget, June 21st 2013 – made of 52% of composite materials.

Their low density and high mechanical performances are well adapted to the aircraft manufacturer policy of consumption reduction, which is also meeting the current environmental challenges. These last years, the use of composite material in the aircraft structures has considerably increased, especially the CFRP (Carbon Fiber Reinforced Polymer) which have in addition good fatigue and damage behaviors. Speaking of Airbus Company, the A380 is the first major step in the use of this kind of material in the aircraft structure. Many parts have been designed in composite: the tail and tailfin, the non-pressurized fuselage, the sealed bulkhead part which is probably one of the biggest parts made of CFRP worldwide, etc... Even the critical structures such as the main wing box were chosen to be partly in composite material. In case of the main wing box, 50% was produced using CFRP, which saved 1500 kg compared to the former aluminum design. This is also the case for the A400M Airbus military aircraft. This trend has been increased with the last Airbus aircraft, the A350 XWB, which had his first successful public flight on June 21st, at Salon du Bourget, Paris (see Figure 1.1). The part of composite in the aircraft structure is up to 52% for this plane, and now including the hybrid fuselage (CFRP), the wings, the whole tail, engine pylons, the ventral fairing…[1]. Its competitor, the Boeing 787 (Dreamliner) has been developed according to the same arguments, and is made of 50% of composite materials (see Figure 1.2). All these examples prove that CFRP has become essential for the aeronautic industries, and that the gain is quite important, but some progress can still be made.

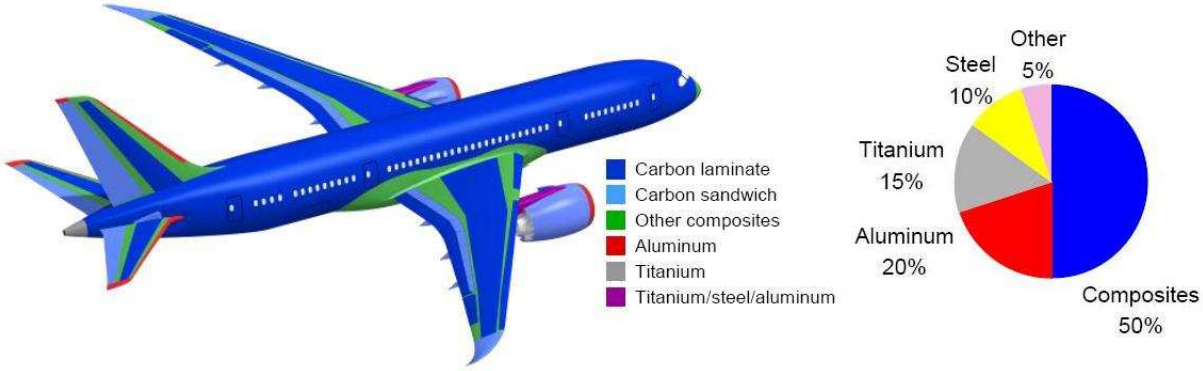

Figure 1.2 Repartition and proportion of composite materials used in the last released Boeing aircraft, Boeing 787, Dreamliner [2]

Indeed, one of the main show stoppers of the CFRP material expansion in the aeronautical structure remains the assembly problems. Of course, switching to composite material parts have enabled the production of bigger and complex parts, as well as the conception of smarter structures [1], but the assembly of the different structure components remains to be achieved in any case, so far using fasteners and rivets. This assembly technique requires the CFRP material to be drilled. Drilling in composite material is expensive and time costing for several reasons. It requires specific expensive diamond head tools, because of the composite stiffness. The process can also easily damage the composite part due to the low transverse resistance of these materials. Several studies have shown that the drilling process can induce strong damage in CFRP materials such as delamination, fiber breakage or transverse cracking along the drilled hole [3-5]. Even if some techniques are currently developed to reduce the induced damage [6], residual behavior after drilling is decreased and this leads to the over-sizing of structural part thickness to take into account the machining damage in many cases. The gain made by using low density materials is thus reduced by the use of over-sized plates. Moreover, aluminum rivet cannot be used to avoid oxidation. Titanium should be used for its chemically neutral properties as well as to conserve the mechanical strength, which has also an important cost.

Therefore, adhesive bonding process could be a solution because it has many advantages. Instead of drilling and riveting, an adhesion film can directly be used to bond two parts. No hole has to be created, which reduces the operating and machining costs, and also suppresses all the stress concentration due to this change of geometry. The mechanical performances are enhanced and no more over-sizing is needed to obtain the correct behavior of the bonded assembly since the bonding process is non-destructive for the composite part. Moreover, titanium rivets would not be useful anymore which would considerably reduce the assembly cost, as well as the global weight of the structure. In some cases, adhesive bonding is already used in flying structures, like on the A380's tail, and for repair applications. Adhesive bonding is well adapted to repairs, in particular, where a CFRP part is added to reinforce a degraded part after an in-service impact [7]. Nevertheless, adhesive bonding is not fully deployed on primary aeronautic structures so far, because non-destructive proof cannot be made of the adhesive bond mechanical properties [7-8]. This main issue, lasting for 20 years, is the key enabler to the extension of bonded composite to the whole aeronautic structure. The potential gain could be up to 12% of the total weight of the aircraft structure, which is quite important for aeronautic. That is why many works are currently conducted in order to certify the bonding mechanical quality of bonded composites. These works mainly address to the detection of weak bonds which are the most dangerous for three reasons. These reasons are also the characteristics commonly used to define a weak bond:

i. Weak bonds cannot be discriminated from correct ones by using a conventional NDT (Non Destructive Testing) method, already used to inspect defects in composite part such as ultrasounds for example.

ii. The bonding strength of the assembly is below 20% of the nominal strength. In case of an adhesion close to 0, meaning perfect contact but no adhesion, the term kissing bond is usually used in the literature (zero thickness void).

iii. The failure of the bonded composite should be fully adhesive, meaning that the composite part should not be broken while testing the bonded composite until failure.

The main issue is to be able to measure the strength of the adhesive layer, as well as the cohesive properties of the adhesive joints [9-10]. That is the global aim of ENCOMB project, described in next section, in which this work takes place.

2 ENCOMB European project

2.1 Need for new NDT techniques

ENCOMB (Extended Nondestructive testing for COMposite Bonds, www.encomb.eu) Project has been started in November 2010 and will end in April 2014. Its long term objective is to enable the reduction of aircraft consumption by lightening the plane structures. The solution chosen for that is to increase the use of adhesively-bonded composites on primary structures as previously explained. In order to do that, the integrity of the whole structure should be well known and quantified. This relies on three main fields: the knowledge of in-service loadings, the control and detection of defects and the quantification of bonds mechanical properties as shown in Figure 1.3 [11].

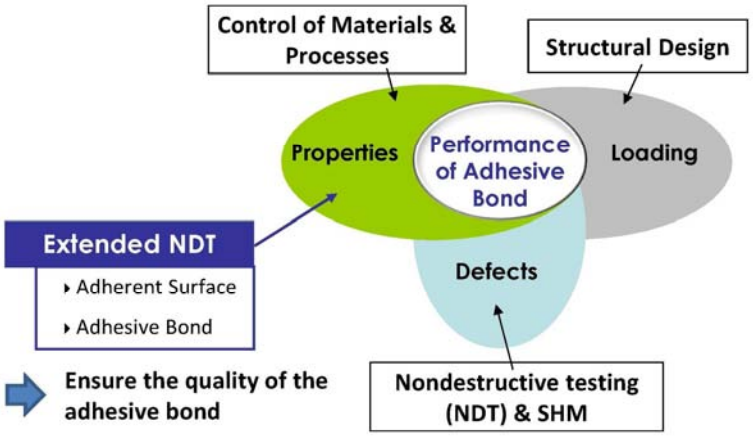

Figure 1.3 Fields of matter for the characterization of the adhesive bond performance, from S. Markus [11]

The knowledge of the loading is a bit beside the purpose discussed here. Of course, the bonded composite structures have to be correctly designed in order to support these different loadings. This part mainly relies on the aircraft manufacturer experiences and will not be detailed here. Nevertheless, these considerations have been taken into account for the production of the sample used and investigated in this work. The chosen thickness of the bonded assemblies is indeed representative of wing skins or fuselage parts. The objective of ENCOMB project is to develop a method which would give information on the bond mechanical properties in a non-destructive way. Different techniques which would enable to solve that are investigated in the frame of ENCOMB project, and have been named ENDT, for Extended Non Destructive Testing. They are divided in two main categories. The first one concerns the contaminant detection prior to bonding, when the second one is related to the adhesive bond properties (see in Figure 1.3). In other words, the problem of weak bonds is investigated from two different points of view in the frame of ENCOMB project:

- ENDT are developed to detect a contamination (release agent, moisture…) prior to bonding on composite and thus to avoid the weak bond risk.
- ENDT are developed to detect contaminants after bonding, to characterize and quantify the adhesion of bonded composite. The discrimination of weak bonds from correct bonds is aimed.

2.2 ENCOMB Industrial challenges and studied cases

14 different European partners are gathered within ENCOMB. From the industrial point of view, the project is leaded by Airbus (Bremen, Germany), whereas the scientific coordination is steered by the Fraunhofer Institute IFAM (Bremen, Germany). The project organization is detailed in Appendix A. The involved partners as well as the project Work Package (WP) organization are presented there. This work is particularly connected with two WP: The WP3, which is focused on the composite contamination before bonding; and the WP4, which deals with the mechanical characterization of weak bonds and investigations post-bonding. The test scenarios are formulated by Airbus, on the basis of the industrial issues faced by the company. They are shortly described in this section [12-13]. Five main critical scenarios have been identified by Airbus. The first two of them are related to in lifetime issues, the others are linked to manufacturing issues [14-15]:

- **Hydraulic fluids (Skydrol)/Water (WP3)**: This application scenario concerns the repair application (patching). In case of an in-service impact on composite panel, composite patches are used to reinforce the weakened structures. Depending on the structure to repair, some part can be close to the hydraulic fluid network which may leak. Thus, some hydraulic fluid can be present on the panel to repair. The hydraulic fluid commonly used (Skydrol) is made with phosphate, and coupled with water, it can produce phosphoric acid which can contaminate the composite. The same kind of contamination can also occur with Kerosene, even if it is less known. If so, the patch bonding process will be modified, and the repair less efficient. To avoid this risk, an ENDT should be found to certify the absence of Skydrol on composite panels.

- **Heat damage on CFRP panels (WP3)**: This application is also a repair application. Like the composite panels can be contaminated by hydraulic fluid leakage, they can also be subjected to heat exposition and heat damage. Especially, the fuselage close to the engine outlet is particularly exposed. Thermal damage can also be due to lightning strike, even if in this case a mechanical load is also applied. These thermal loads can chemically modify the CFRP panels, especially the epoxy content, which can also have an influence on the patch bonding quality. These modifications cannot be detected using ultrasounds, which are currently used only for the detection of severe induced damage such as delamination.

- **Release Agent (silicon-based) contamination (WP3 & WP4):** One step of the composite panel manufacturing is the molding process. To remove the cured parts from the molds, a silicon-based release agent solution is used. After the molding process, the amount of silicon remaining on the composite panel can reach between 5 to 20 at.% [16-17]. This contamination strongly influences the adhesion, between two composites, or with a paint layer… Of course, methods exist to clean the composite panel prior to bonding. Two pre-treatment processes are qualified to remove Si contamination: Wet abrading with Fixil (manually with cleaning agent) and Laser/Plasma activation of surface for adhesive bonding. Nevertheless, the cleaning step has to be controlled to be sure that no more silicon is present on the composite surfaces. This is currently performed by the Water Break Test (WBT), which is efficient to detect silicon, but complicated for big parts and based on human observation. That is why techniques are developed in WP3 to enable the detection and the quantification of silicon amount on composite surfaces. Release agent contamination is also investigated in WP4. Indeed, release agent is a good candidate to investigate weak bonds for the quoted reasons. Moreover, if the contamination is missed for any reason by the previous steps, an ENDT should be used to control that the bonding strength is correct. In the frame of WP4, the correlation between the concentration of release agent contaminant and the mechanical performance is expected.

- **Moisture uptake in CFRP (WP3 & WP4)**: Moisture uptake should be avoided because it can lower the adhesion of two contaminated panels. That is why storage procedures are applied to preserve the composite from water. Nevertheless, composite panels go through different processes using large amount of water during the whole manufacturing process, such as the WBT. They can absorb water during transportation from one place to another. Currently, an autoclave procedure is systematically applied for the part on which a doubt has been formulated. This procedure has an important cost, and cannot be applied to every composite part, especially in case of large parts. Therefore, monitoring the composite surfaces to detect the presence of water is an important challenge. Moreover, the moisture scenario is also

investigated in the WP4. The unexpected presence of water can deeply modify the bonding process by increasing the porosity in bonds especially. Like for release agent, weak bonds can also be produced using composite contaminated with moisture.

- **Poorly cured adhesive in bonded CFRP (WP4):** This last scenario deals with both manufacturing issue and repair issue. In case of manufacturing, the bonds are cured using autoclave. The temperature and pressure are monitored during the process, but if one of the parameter shows an anomaly, there is currently no way to control the final curing state of the bond. The bond curing state has a direct influence on its adhesive properties. A correlation between the curing state and the adhesive strength is aimed.

To sum up, ENDT are needed to evaluate the composite surface quality in case of several scenarios: Skydrol contamination, heat damage, release agent and moisture contaminations. This is done in frame of WP3. On the other hand, ENDT should be developed to evaluate the bonding strength in case of release agent and moisture contamination or poor curing state. This is the objective of WP4. In these cases, correlations between the concentration of the contaminant or the curing degree and the mechanical performance are expected. In addition to these test scenarios, Airbus has also provided requirements to guide the ENDT technique developments [12-13]. Meeting all these requirements is hypothetic, but it gives a perspective for the aeronautical technique development in the year to come. It also shows how the technique will be used in industry. There are common specifications, shortly described below, and specific requirements which deal with in-service or manufacturing applications.

- Simple handling and use,
- Quick data evaluation (including both measuring and post calculation time) – 1m²/10min,
- Universal target application (Different CFRP geometries, curvatures),
- Clear diagnostics (bond/surface ok or bond/surface not ok),
- Detection capability (discriminate different levels of contamination),
- Variable inspection range,
- Low cost,
- Long Lifetime (10 years for hardware, and easy to find consumables).

Facing these requirements, and the previously described test scenarios, each ENCOMB partners develop his/their techniques to improve the knowledge on adhesive bonding. It is possible that several techniques could do the job, alone or in addition with another technique. Project leaders clearly let all the possibilities available, and are looking forward to a better comprehension of adhesive bonding and weak bond issue, as well as to the Non Destructive Testing of composite bonds feasibility. These points are discussed in the following sections.

3 Techniques developed for weak bonds detection

In this section, the common NDT techniques for the damage and defects detection in composite materials are first described from a literature overview. Indeed, these techniques have been investigated since the beginning of composite material use in the industry. Some techniques have reached a high development state, and provide a good basis to start with for bond investigations. Therefore, the second step is to see how these conventional NDT techniques are adapted to the control of adhesive bonds. Especially, some research works focus on the detection of defects in adhesive bonds thanks to these common NDT techniques. Then, some investigations conducted on

the weak bond issue will be described. The production of weak bond is a first point, and the adaptation of common NDT techniques to the weak bond issue is a second point. Some techniques are also developed specifically for this particular case. Finally, the need for LASAT technique developed in this work is justified from this different technique overview and the ENCOMB project context.

3.1 Common NDT Techniques

The composite material itself is already well characterized, and the scope of techniques which enable the detection of defects or damage in composite material is wide: ultrasounds inspections and laser ultrasound, X-Ray imaging, Microtomograhy, Lamb waves or vibration methods, Infrared thermography, etc… Ultrasound inspection is probably the Non Destructive Test the most used in aeronautic industries. Ultrasounds are really adapted to the delamination or sizable voids detection. They can be used with contact probes (or rolling probes) for small part analysis, or in water pool for faster inspection of bigger parts. Recently, the development of laser ultrasounds has enabled the control of big and complex parts without water coupling and contactless. Such lasers have increased the scanning capacities of the technique and simplified the process. EADS Innovation Works has been working for several years on this technique, and developed two ultrasounds laser: LUIS and LUCIE which are giving promising results [18-20]. X-Ray imaging is also used in aeronautic industry despite the care to take with this technique [21]. Once again, this imaging technique is useful to quantify the size of delamination. Currently, the development of Microtomography pushes forward the use of X-Ray for the damage detection. This NDT technique has a better spatial resolution than the classic X-Ray imaging and can detect smaller defects such as pore or voids. The current investigations are aimed to reduce the scanning time of the method, increase the frequency of measurement, and allow bigger part scanning [22-23]. Infrared thermography and active thermography is also an important field of investigation for the defect detection in composite panel. They are contactless and enable the scanning of big part in one acquisition. The spatial resolution of these techniques is also a key point because it depends on the IR camera resolution, which is the main development point [24-26]. Finally, vibrations methods rely on the surface wave propagation to detect defects. These methods are developed for sizable plates and need an excitation device as well as a recording system (Laser 3D scanning) [27-30]. All these techniques are still under development to detect smaller and smaller defects, as for example nonlinear ultrasounds. Globally, they are well adapted to the detection of delamination between composite plies, defects due to manufacturing, as long as it is a sizable discontinuity. It is generally harder to detect small damage in the axis of observation like cracks.

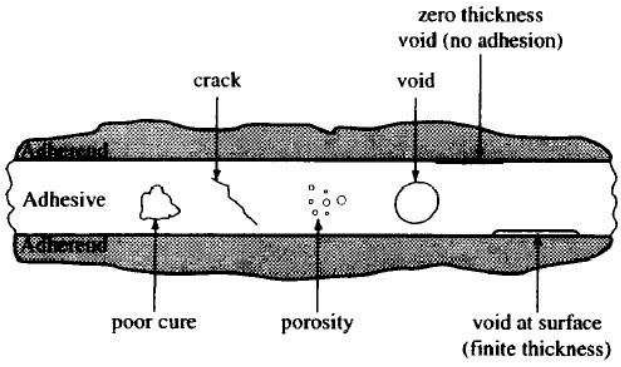

Figure 1.4 Main defects which could be found in an adhesive layer between two composite parts as shown by R. D. Adams and B. W. Drinkwater [31]

Similarly, the defect detections in a bond can be performed using the same techniques [9-10], [31] (see the different defect types in Figure 1.4). Recently, Microtomography has enabled to investigate the porosity in bonds for example. Ultrasounds can also be used to control the presence of large defects in the bondline or obvious debonding. In order to get more data on the bond state (small porosity, cracking), the ultrasounds have to be more precisely analyzed using post-treatment in the signal. In some cases, a shift in amplitude or in frequency could indicate the presence of small defects [32]. Nevertheless, it is hard to control the presence of defects in a bondline due to the size of what is sought as well as the complex geometry of the layered composite material. Thus, what is more commonly investigated when it comes to defect or damage in bonded composite is structure health monitoring (SHM) also called smart materials. Indeed, without speaking about the weak bond issue, even small defects in a bond can have a strong influence on the bonding strength [32]. Another way of seeing the defects is to prevent the damage propagation by monitoring the bonded composite structures. This can be done using several techniques currently investigated. They aim is to monitor the stress history in the material during its lifetime. Periodic controls can enable to check that the material response still corresponds to what was expected. One technique uses the electro-mechanical impedance of the bonded structure, which can vary depending on the stress level in the layered structure, and damage growth in the worst cases. Piezoelectric sensors are then implemented in the composite layers to monitor this hypothetic change [33-36]. The other main way of monitoring the stresses in the composites is to use fiber grating sensors. It requires glass fibers to be impregnated while curing the bond line, but then, a strain in the bond will induce a modification of the refractive index of the fibers. That way, a strain and the corresponding stresses can be monitored [37-39]. New techniques are using carbon nanotubes (CNT) mixed with the bond epoxy to enable a current circulation. The bond is monitored as an electrical resistance, and any change can traduce a particular loading [40].

Despite the numerous research works carried out in the past, no technique can be clearly identified as the solution to discriminate weak bonds. NDT techniques such as ultrasounds, radiography, thermography, lamb waves, vibration methods, etc… are well adapted to the detection of defects in composites. The thermal or mechanical impedance mismatch is much more important in this case than in a weak bond case, which leaves these methods less adapted and less sensitive to weak bonds [31]. That is why new investigation fields appeared to developed Extended Non Destructive Testing (or Extended NDT) to adapt or create method to detect weak bond and quantifying the bonding strength of adhesively-bonded composites [11], [14-15].

3.2 Weak bonds in the literature

In the literature, few works address to the weak bond issue. The relative novelty of this aeronautic questioning and the complexity of the problem could be reasons for that. The term itself of weak bond as defined here is even more recent than the first investigations on the subject. Some works dealing with weak bonds are in fact using this term to describe bond with defects. In this case, the NDT techniques presented in the previous section such as ultrasounds or thermography could be efficient [41-42]. In other studies, the weak adhesion issue is considered using Teflon film to lower the adhesion [43]. A film is inserted during the manufacturing process of the structure to test (stringer – skin composite in this case). Of course, the presence of Teflon is considerably reducing the adhesion, but it is also changing the structure geometry and its mechanical impedance. This way, an ultrasonic guided wave inspection can detect the problem [43]. Ultrasounds are probably more sensitive to the presence of a Teflon film than to the low adhesion characteristic. This is interesting

but a bit far from the industrial matter and not the purpose here. Some other research teams are taking the problem from the other side. Instead of looking for weak bonds, they develop techniques to ensure of the composite surface quality. For example, I. Jölly et al. have studied the influence of the surface preparation on the bonding strength. They used several pre-treatment methods such as sanding, grit blasting or physico-chemical treatments [44]. Another team has investigated the plasma treatment of CFRP to enhance the bonding quality, even if this technique could have some limitations in case of large parts. They showed that the plasma treatment could have a positive influence on the bonding [45]. Speaking of weak bonds detection as defined here, some literature reviews on the existing techniques to deal with adhesive structures and weak bonds can be found [46-48]. Some works on the surface contaminant detection have been also recently reported [49]. Mainly, the ultrasounds based techniques have been investigated the most for the weak bond detection even if some works are addressing to thermography methods. The reason is probably their adaptability to the industrial context, and their wide use in the aeronautical sector. Thus, wave propagation seems interesting, as also shown by the work of S. Yang et al. [46]. They have looked at the adhesion quality by monitoring the damping and the vibration frequencies of bonded composite materials. Thanks to that, some differences were highlighted in the adhesion quality between bonded composites which had different surface preparations (sanded/ unsanded). The sanding of surfaces can remove contaminants, but also changes the surface roughness. It is this surface geometrical change which has been probably detected. Recent works have shown new approaches to investigate weak bonds, in case of bonding repair using shear [50] or strength evaluation using digital image correlation [51]. Nevertheless, in these cases the tests are destructive.

3.3 Why a need for LASAT (LASer Adhesion Test)

The techniques found in the literature and described in the previous sections, both for composite material and bonded composite, are relative to the detection of defect and the corresponding damage growth. None of them, as presented, enable the mechanical properties of the bonded material evaluation, as well as the cohesive properties of the adhesive or adherent surfaces quantification. Classical mechanical tests can of course be used to provide quantitative information on the bond state, but these methods are fully destructive, which is annoying for the part certification. Therefore, with common NDT techniques, no measurement of the mechanical strength can be made, and it is impossible to be sure of the bond strength.

Back to ENCOMB, the different techniques developed in the project to deal with weak bonds are described in details in Appendix A. Note that some of the techniques developed by ENCOMB partners could be complementary to our investigations. A synthesis made on each technique state of the art is presented in Appendix A. The more promising results are presented and commented. This synthesis gives an overview of what is currently done to face the weak bond issue, in the frame of ENCOMB project. Instead of presenting the techniques per work package, the developed methods are sorted out by major families. Note that a selection has been made to describe only the techniques which are already giving some promising results. When a technique is used by several partners, the most advanced is presented. Details are given in Appendix A, but a short summary is made in the next paragraph in order to position our investigations

For the contamination detection, it seems clear that several techniques enable the detection of contaminants. The most efficient for that are probably FTIR (Agilent), OSEE (IFAM) and E-nose (ENEA), which have enabled so far the detection of each contaminants listed by Airbus. The different contamination degrees have even been discriminated in some cases. The other techniques presented

have also some interest. Indeed, they often have a better sensitivity to one or two contaminants only, but could enable faster evaluation of surfaces. It is the case of AWT (IFAM) or Laser Scanning Vibrometry (IMP PAN). The hard point remains for all the technique to establish a correlation between the measurement and the effective contaminant (or degradation) concentration on the CFRP surface. In case of bonded composite, the conclusions are slightly different. First, it seems to be harder to detect a contaminant or a low curing inside the material. This can be easily understood since no direct access to the contaminant is possible. So the detection methods should be indirect, and pass through the bonded composite. So far, EMI (IMP PAN) and ultrasound frequency analysis (EADS Cassidian) seem to be the only two techniques to enable the detection of two contamination scenario at least. EMI has also the advantage to be close to health monitoring applications, and is really interesting for future applications, but cannot be used as a production control device. Anyway, the detection of contaminant is an important task partly fulfilled by the presented techniques but one question remains the quantification of the mechanical strength of the contaminated bonds. The correlations between the contamination degree and the mechanical performances are hard to get. This is probably due to the fact that none of the technique presented is actually loading the bonded material to test. That is probably the main difference with the technique developed during this work and discussed in this document: LASAT (LASer shock Adhesion Test). As it is explained in the next section, the laser shock technique for adhesion test is generated high tensile stresses inside the bonded composite, which is loading the material. The level of stress can be evaluated thanks to time resolved measurement and numerical modeling. In the work presented, these stresses have been used to try to discriminate low mechanical strength bonds from correct quality bonds. So the issue is more the detection of the contaminant effects on the bonding strength than the detection of the contaminant itself. The question of correlation between these measurements, the contamination degrees and the conventional mechanical test is the major interest.

Part 2: LASAT technique: principle, history and state of art

1 Principle and description of the LASAT technique

1.1 About LASER shocks

There are many different ways to produce a shock, from the biggest scale - it is to say the natural geophysical and astrophysical impacts - to the smallest such as atomic fission or femtosecond lasers [52]. In Material Sciences, different kinds of experimental shock sources can be used: Hopkinson bar [53], explosive loads [54], plate impacts by gas gun [55] and high power nanoseconds laser sources [56]. The shocks induced by laser are the most recent, and are now widely used in the Material research laboratories as well as in high technology industries for some applications. At a first look, high power laser sources are composed of two main parts. The first one is the laser cavity whose characteristics determine the laser pulse properties, especially the pulse duration and the wavelength (see in Figure 1.5). The pulse shaped by the cavity is then amplified by one or several amplifiers which increase the pulse energy. After the amplifiers, the laser pulse is up to several joules, and the beam has several centimeter diameters. The commercial sources go from a few joules to 50 J (Thalès, Quantel, Continuum…) but research sources can be even more powerful: LULI (1000J), Laser Mega Joule (LMJ), National Ignition Facility (NIF)…In order to tune this energy level, optical density can be used on the beam path, and mirrors are generally used to take off a small part of the beam energy to measure it (see in Figure 1.5). Then, this high power beam can be focused on a target by using a convex lens, which is considerably increasing the beam intensity. Indeed, the laser

intensity I (GW/cm²) is calculated using the beam energy E (J), the pulse duration Δt (ns) and the focal surface S (cm²) as defined in equation 1.1. Some research teams are also using the fluence F (J/cm²) as defined in equation 1.2 to quantify the laser irradiation. These are important parameters, because they are directly linked to the induced pressure in the material irradiated.

$$I\left(GW/cm^2\right)=\frac{E\left(J\right)}{S\left(cm^2\right)\times\Delta t\left(ns\right)} \quad \text{where} \begin{cases} \text{I: laser Intensity} \\ \text{E : laser energy} \\ \text{S : irradiated surface} \\ \Delta\text{t : laser pulse duration} \end{cases} \tag{1.1}$$

$$F\left(J/cm^2\right)=\frac{E\left(J\right)}{S\left(cm^2\right)} \quad \text{where} \begin{cases} \text{F : Fluence} \\ \text{E : laser energy} \\ \text{S : irradiated surface} \end{cases} \tag{1.2}$$

The laser interaction with the matter is responsible for the high pressure load. Indeed, when the laser irradiation is reaching the target surface, its first few micrometers are immediately transformed into intense plasma which expands rapidly against the surface. It is this plasma expansion release which is creating by reaction a shock wave into the material, whose pressure can cover a range from MPa to GPa. Indeed, the laser matter interaction is a complex phenomenon which deeply influences the laser irradiation induced pressure [57-63]. Three parameters at least are of major influence: the wavelength, the pulse duration, and the confinement medium. If the plasma can release easily, the resulting pressure will be lower than when the plasma is confined by a confinement layer for example. Of course, the irradiated material plays also a role. Several research teams have worked on the laser/matter interaction in order to find a correlation between the laser intensity and the induced pressure. It has been shown that the relations were not the same in air or vacuum interaction [57-59] and with a confinement [60-63]. Especially, water confinement is interesting. Water has a good transparency to the laser wavelength commonly used (532 nm, 1063 nm) and enables to increase the pressure unless the laser intensity is below the confinement breakdown threshold (typically a few GW/cm^2). It has an influence on the pressure pulse width, which becomes 2 to 3 times longer than the laser pulse width. The peak release shape is also extended (see in Figure 1.5) [60-63].

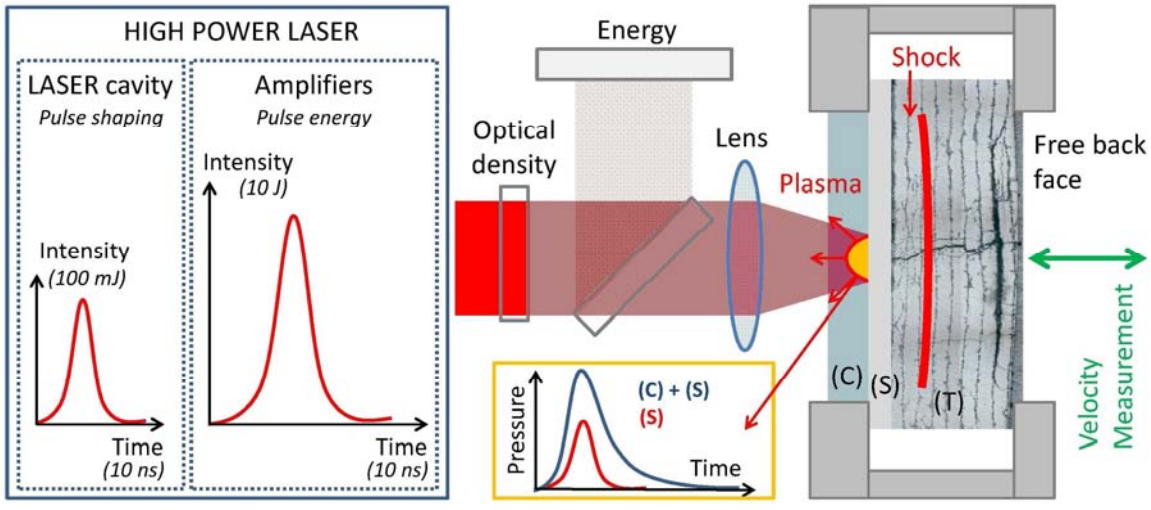

Figure 1.5 Principle of laser shock generation on composite target (T), presented with a confinement layer (C), and a sacrificial layer (S)

1.2 Application to material and LASAT principle

Speaking of the laser shock industrial applications, the Laser Shock Peening (LSP) is probably one of the most well-known [64]. It uses laser induced shocks to create residual stresses resulting in material's hardening. This is used to increase the fatigue lifetime by delaying the crack propagation or corrosion effects. This process is now commonly used for turbine disks, nuclear power plants [64-67] or medical applications [68]. In case of LASer Adhesion Test, the whole wave propagation pattern is interesting because laser induced shock can also generate dynamic tensile stresses. According to shock wave theory, the shock propagates through the material thickness depending on the material property. The matter is compressed from state (0) to state (1) at a given pressure P1 (see in Figure 1.6). The shock impedance Z defined in equation 1.3 is often used to compare the shock response of material. It depends on the material density ρ and the shock velocity D. This velocity is defined as the addition of the sound velocity in the material c_0 with a term depending on the particle velocity u and an experimental parameter s different for each material (see equation 1.4)

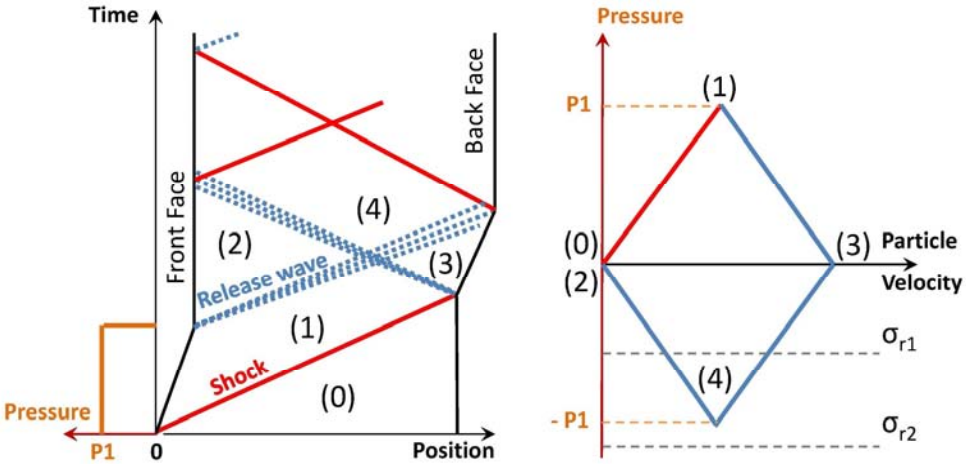

Figure 1.6 Schematic 1D Time/position diagram explaining the principle of shock induced dynamic tensile loading (shock in solid red line, release in dashed blue lines) – Associated Pressure versus Particle velocity diagram (Hugoniot) giving the pressure states considering no attenuation. Two failure stress limits (σ_{r1} and σ_{r2}) are added to show the spallation phenomenon origin.

$$Z = \rho \cdot D \quad \text{where} \quad \begin{cases} \text{Z : shock impedance} \\ \rho \text{ : material volumic density} \\ \text{D : shock velocity} \end{cases} \tag{1.3}$$

$$D = C_0 + s \cdot U \quad \textit{where} \quad \begin{cases} \text{D : shock velocity} \\ C_0 \text{ : material sound velocity} \\ \text{s : Experimental parameter} \\ \text{U : particle velocity} \end{cases} \tag{1.4}$$

When a shock is reaching a zero impedance frontier, like a free surface, it is thus reflected into a release wave propagating backward. Meanwhile, the material front face is unloaded at the end of the pressure pulse which is also generating a release wave propagating from the front face to the back face. Regarding the pressure, this release wave reduces the pressure from state (1) to state (2), which is also state (0) in this case. Depending on the material impedance and thickness, these two

release waves can intersect inside the material thickness. The resulting state (4) of this release crossing is a negative pressure. In a 1D approach, considering no attenuation, the negative pressure is thus equal to – P1. In any case, the negative pressure level is directly correlated to the input pressure, itself linked to the laser irradiation energy. The irradiated target is thus under dynamic tensile loading, whose strain rate is close to 10^7 s^{-1} for nanoseconds laser. Two different cases can now be considered. Firstly, if the failure stress is above in absolute value than the tensile stresses generated by the shock wave propagation, then no mechanical damage will occur. The waves continue to propagate in the whole target thickness (see σ_{r2} in Figure 1.6, and Time/position diagram in Figure 1.7). A signature of that is the back face velocity schematically represented in Figure 1.7 in case of a simple pulse with attenuation. This type of signal can be measured by using for example a time resolved diagnostic based on optical interferometry called VISAR (Velocity Interferometer System for Any Reflector). These two peaks correspond respectively to the first and to the second shock breaking out. The period t_3-t_1 corresponds to one shock going backward and forward. This period depends on the material acoustic impedance. In the second case, it can be possible that the tensile stresses resulting from the wave propagations exceed the strength of the material. In this case, the tensile stresses lead to the spallation of the target, creating voids inside the matter (see in Figure 1.8, the Time/position diagram) [69]. This phenomenon can also be clearly identified by looking to the back face velocity. From the opening point, the waves travelling in the spall have a much smaller period (see in Figure 1.8). Moreover, the wave propagating backward in the target has no more influence on the back face velocity signal. The back face velocity study is thus quite interesting for the spallation and damage investigations [70-71].

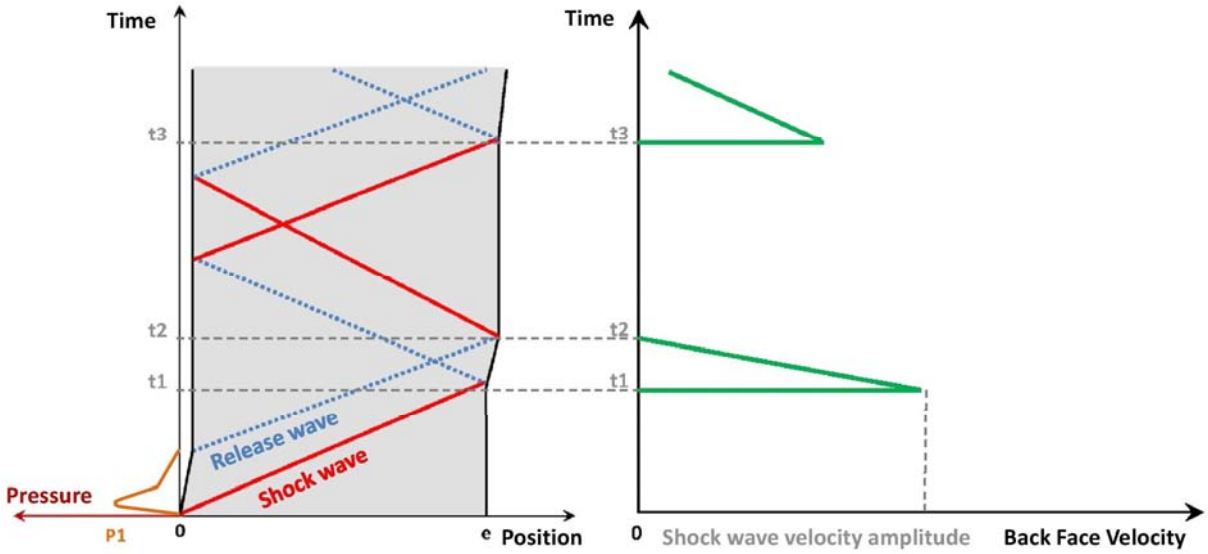

Figure 1.7 Schematic 1D Time/position diagram in case of no spallation (shock in solid red line, release in dashed blue lines) – Associated back face velocity versus time schematic graph showing no induced damage as proved by the period t_3 - t_1

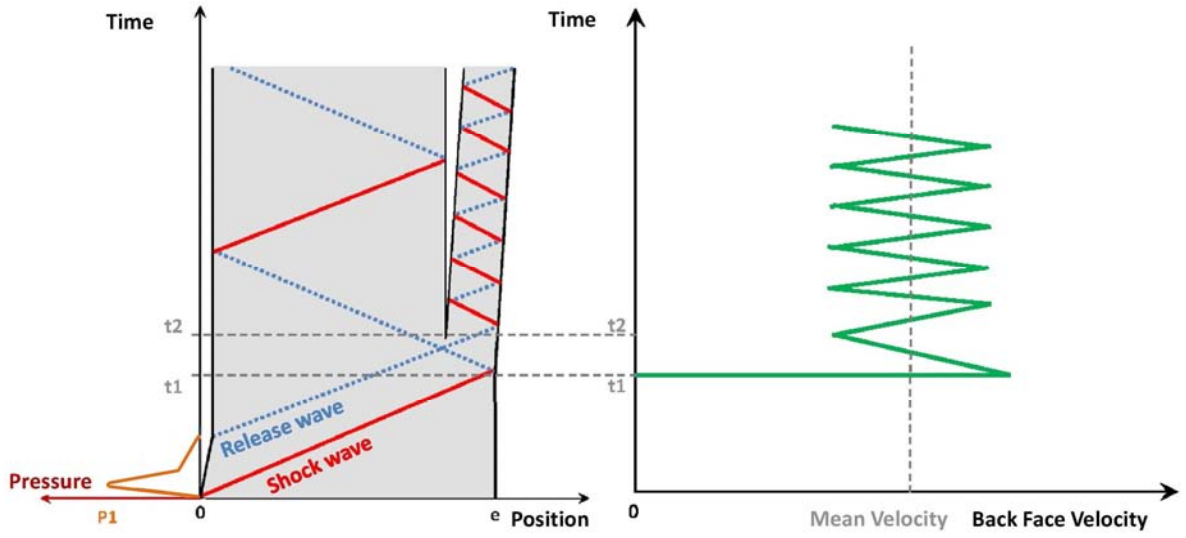

Figure 1.8 Schematic 1D Time/position diagram in case of spallation (shock in solid red line, release in dashed blue lines) – Associated back face velocity versus time schematic graph showing a change in the velocity profile traducing the spallation

In case of LASAT, the tensile stresses are aimed to be localized close to the interface to test. Thus, the pressure pulse width is an important parameter because it is the one to influence the position of the tensile stress maximum. In Figure 1.9, two time/position diagrams are presented. The first one a) represents the case of a non-optimized laser shock on a three layer system to test. The pulse width is too short and locates the crossing of release wave in the last layer (C). Moreover, the stresses generated by the input pressure load P1 are not high enough for the tension propagating backward from the crossing point to be high enough to open the interface. The diagram in Figure 1.9 b) represents an ideal case. The pulse width is longer than in the previous case, which enables the crossing to occur right at the interface. Moreover, the input pressure has been increased. The level of induced stresses is high enough to exceed the interface damage threshold. The interface is opened.

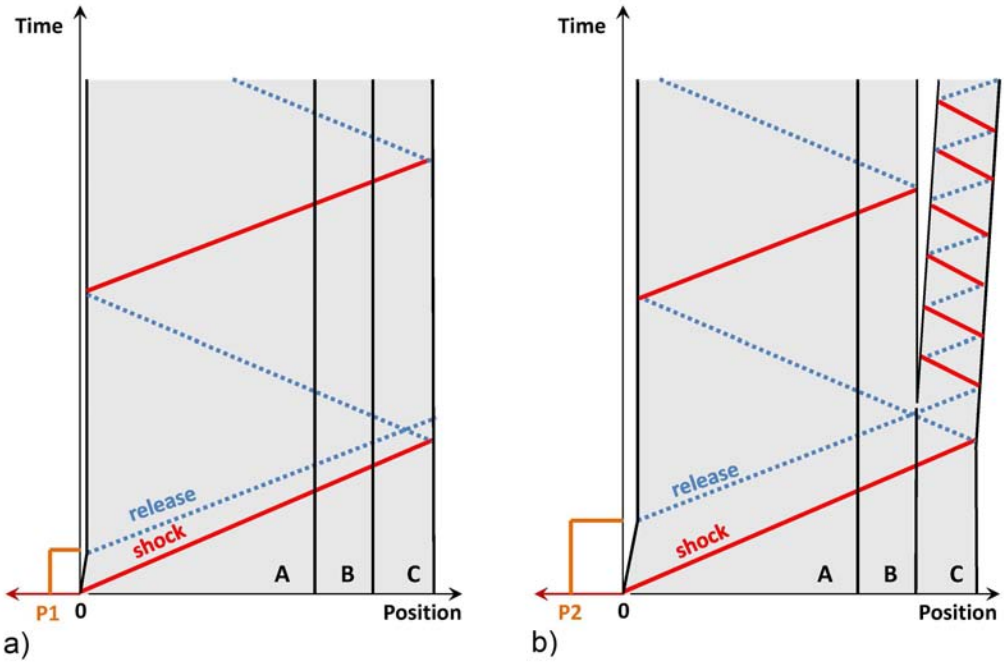

Figure 1.9 a) Schematic 1D Time/position diagram in case of not correctly configured shock on a three-layer target – No interfacial debonding obtained b) Schematic 1D Time/position diagram in case of a well configured shock on a three-layer target – Strength adhesion test of the B-C interface (Impedance mismatch neglected)

The approach presented in Figure 1.9 was quite simple to explain the LASAT principle in the case of a three-layer material. In reality, the wave propagation is more complex between the layers because of the impedance mismatch possibility. Indeed, among these three layers, one of them could be softer than the two others. It is the case when two metals are glued together for example. The three layers can be three completely different materials. In these cases, the acoustic impedances of the materials are not the same, which leads to a transmission/ reflection phenomenon when the shock wave reaches an interface. This is explained in Figure 1.10 and 1.11 on two-layer target materials A and B. A shock is initiated in material A at time = 0. Two cases can be considered:

- $Z_A > Z_B$ (Figure 1.10): means that the material A acoustic impedance is higher than the material B acoustic impedance. It also means the Hugoniot curve of material A (in green) is above the one of material B (in purple) as shown in Figure 1.10. Therefore, when the shock is reaching the interface A-B, it is reflected backward into a release wave, and transmitted as a shock wave into material B. The pressure state (2) is a compressed state lower than the initial compressed state (1) resulting from the shock loading. It can be calculated from the initial state thanks to an impedance ratio. Note that this case is the generalized case presented in Figure 1.6. Indeed, the free surface in air or vacuum can be considered as a zero impedance material layer.

- $Z_A < Z_B$ (Figure 1.11): means that the material A acoustic impedance is lower than the material B acoustic impedance. In this case, the Hugoniot curve of the first material layer is under the Hugoniot curve of the second one. Therefore, when the shock reaches the A-B interface, it is reflected backward into a shock wave inside the first material. A shock is also transmitted into the second material. The pressure state (2) is this time higher than the pressure state (1), which means that the first layer receives more pressure than what it has been initially input (see in Figure 1.11). This phenomenon can be used to enhance pressure on a given material in position B.

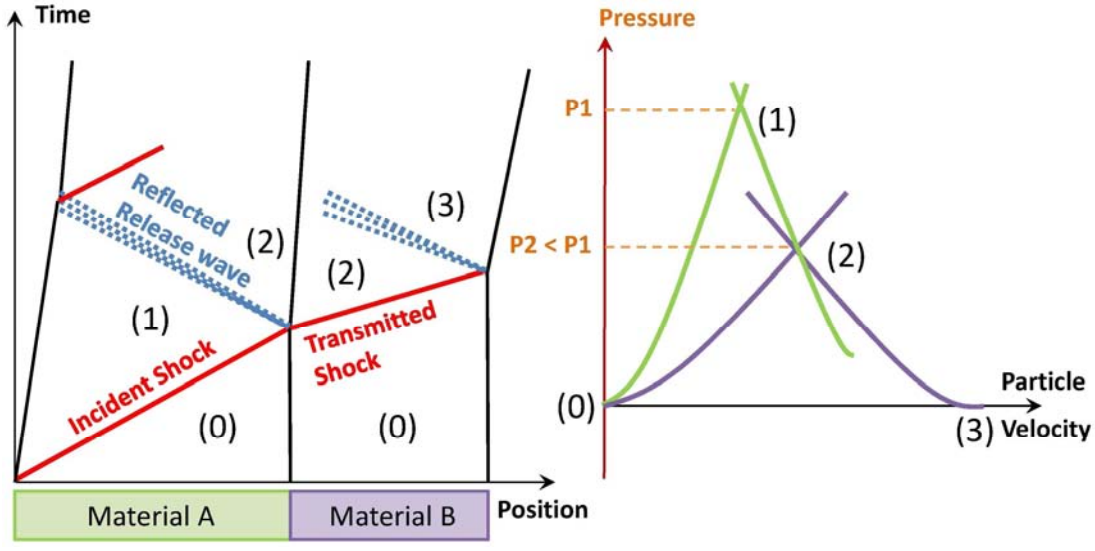

Figure 1.10 Schematic 1D Time/position diagram in case of two layer target whose first material has a bigger mechanical impedance Z_A than the second material impedance Z_B (shock in solid red line, release in dashed blue lines) – Associated Pressure versus time schematic graph (Hugoniot)

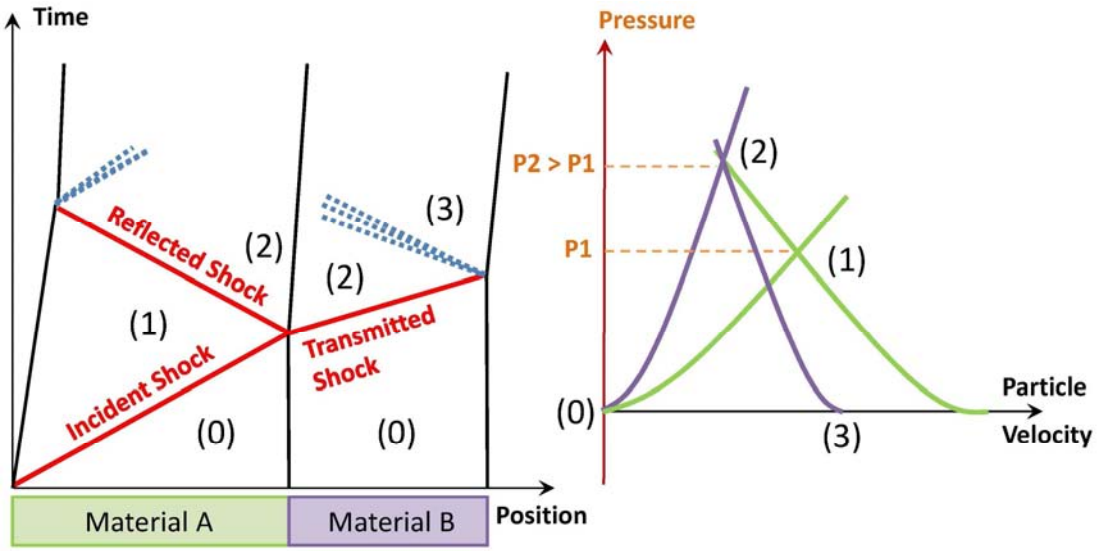

Figure 1.11 Schematic 1D Time/position diagram in case of two layer target whose first material has a smaller mechanical impedance Z_A than the second material impedance Z_B (shock in solid red line, release in dashed blue lines) – Associated Pressure versus time schematic graph (Hugoniot)

Note that the phenomenon described in Figure 1.10 can also be at the origin of tensile loading in the first layer material. If the pulse is short enough, a crossing between the unloading release propagating forward and the reflected release wave can create tension. In the next section, the application of LASAT to industrial cases will be described. Some details about the techniques development are given before reaching the LASAT application to composites.

2 LASAT history and overview

2.1 Early years and LASAT for coated systems

The measurement of adhesion bond strength by high power laser is 30 years old. It has been first developed for film adhesion test by J. L. Vossen in the late 70's [72]. The technique was investigated by V. Gupta, who obtained patent on the method for measuring the interface tensile strength [73-74]. The first investigation made on the technique were clearly addressing to the adhesion test of thin samples, thin films, thin layers. There are several reasons for that. First, the laser induced shock wave is less softened in a thin target, which enables higher level stress generation. The thin film or thin coated systems are particularly well adapted to test by laser shock. Indeed, short pulses (8ns - 20ns) create a maximum of tensile stresses close to the sample back face, between 10 to 200 µm deep. This corresponds to the thickness of the layers to test. In the years 2000's, several PhD works addressed jointly the adhesion test of coated systems, thermal barrier and thin films: C. Bolis [75], M. Arrigoni [76], and S. Barradas [77]. They did the demonstration of the test efficiency on several different systems by experiments and numerical modeling. For example, C. Bolis studied the adhesion of pure copper and electrolytic-deposited nickel (see in Figure 1.12) [78]. Experimental investigations and microscopy observations were used to determine the damage threshold to laser shocks of the system (see Figure 1.12 a, b). Then, the hydrodynamic code SHYLAC was used to calculate the corresponding pressure and the equivalent stresses in order to evaluate the adhesion strength (see in Figure 1.12 c).

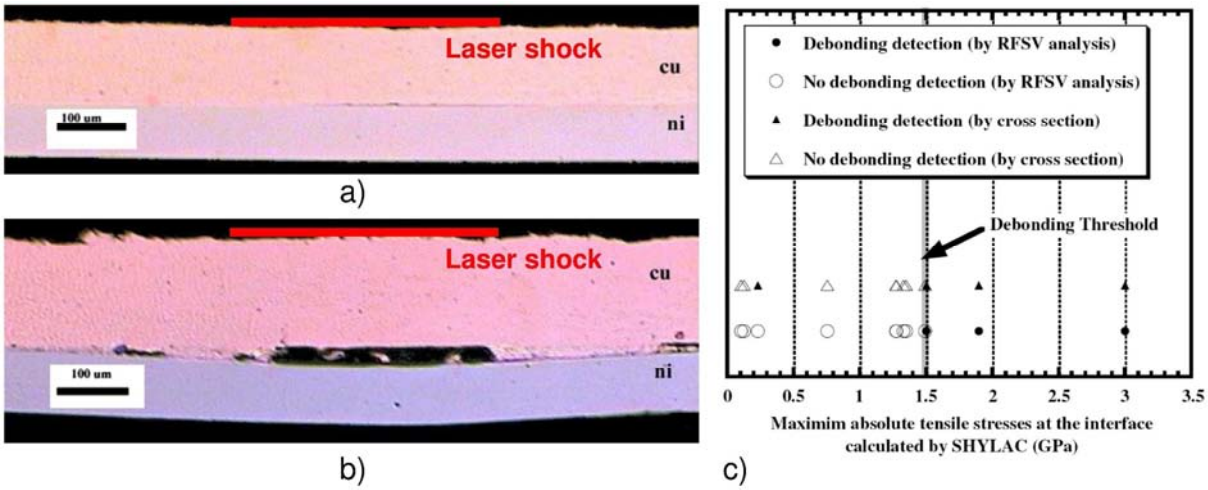

Figure 1.12 Work from C. Bolis [78]: Adhesion test of coated system: pure copper and electrolytic-deposited nickel – Experimental and numerical determination of the debonding threshold
***a)** Cu-Ni coated system unharmed after laser shock (79 GW/cm²) **b)** Cu-Ni coated system fractured after laser shock (370 GW/cm²) **c)** Determination of the interface damage threshold represented in pressure (calculation SHYLAC)*

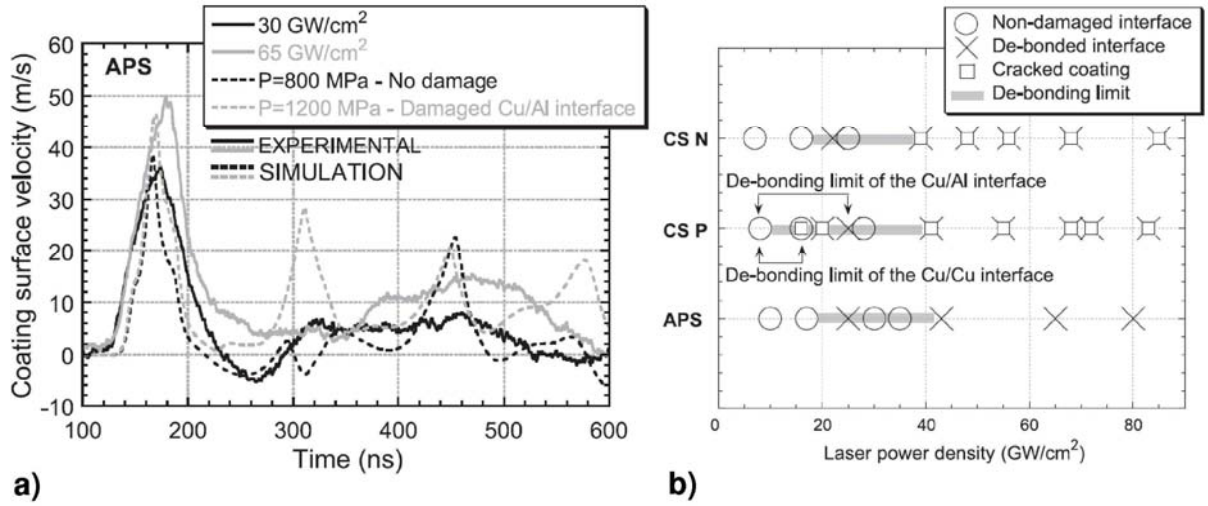

Figure 1.13 Work from S. Barradas [77]: Adhesion test of cold-sprayed copper coating of aluminum – Experimental and numerical determination of the debonding threshold
a) Experimental determination of the damage threshold by using back face velocity analysis and the corresponding numerical modeling b) Synthesis chart of different coated system damage thresholds expressed in laser intensity (GW/cm²)

At the same time, S. Barradas investigated the damage threshold of cold-sprayed system [77]. Laser shock experiments were also used to determine this threshold. Back face velocity measurements were also used to investigate the coated system dynamic response and to enable the numerical modeling like in the previous work (see in Figure 1.13 a). Several coated systems were tested and an interesting representation of the damage threshold was used to compare the targets between each other (see in Figure 1.13 b). All the thresholds were plotted on the same chart, and both unharmed and debonded shocked targets were represented. This way, the damage threshold can be directly compared versus the laser intensity, and an idea of the uncertainties is given. Another study focuses on the comparison between the laser shock adhesion test and more conventional adhesion test. This is an important point because the laser shock method strain rate is very different from other method. In his work, M. Arrigoni compared laser shock test with bulge and blister tests [79]. In spite of some differences due to the test nature, the results were shown to be consistent. Therefore, the

laser shock adhesion test experiments, reinforced with the numerical modeling, is an adhesion test in itself, consistent with other methods but which can be distinguished by its high strain rate and localized load, as well as its contactless characteristic.

During several years, the investigations on the LASAT technique were mainly done on thin metal systems or metal/ceramic coating, generally of two layers [80]. Even if the technology is now well understood, some studies are currently deeper investigating deeper the technique. New material diagnostics enable to have a better knowledge of the coated system microstructure. G. Rolland et al. have used this knowledge to obtain better numerical modeling of the tested material. It helped to a better description of the coated system damage under shock loading [81]. Nevertheless, the use of LASAT technique can be wider than that [82]. As an example, D. Laporte recently investigated the dynamic response of aluminum/epoxy three layer targets in order to evaluate the adhesion between these materials [83-85].

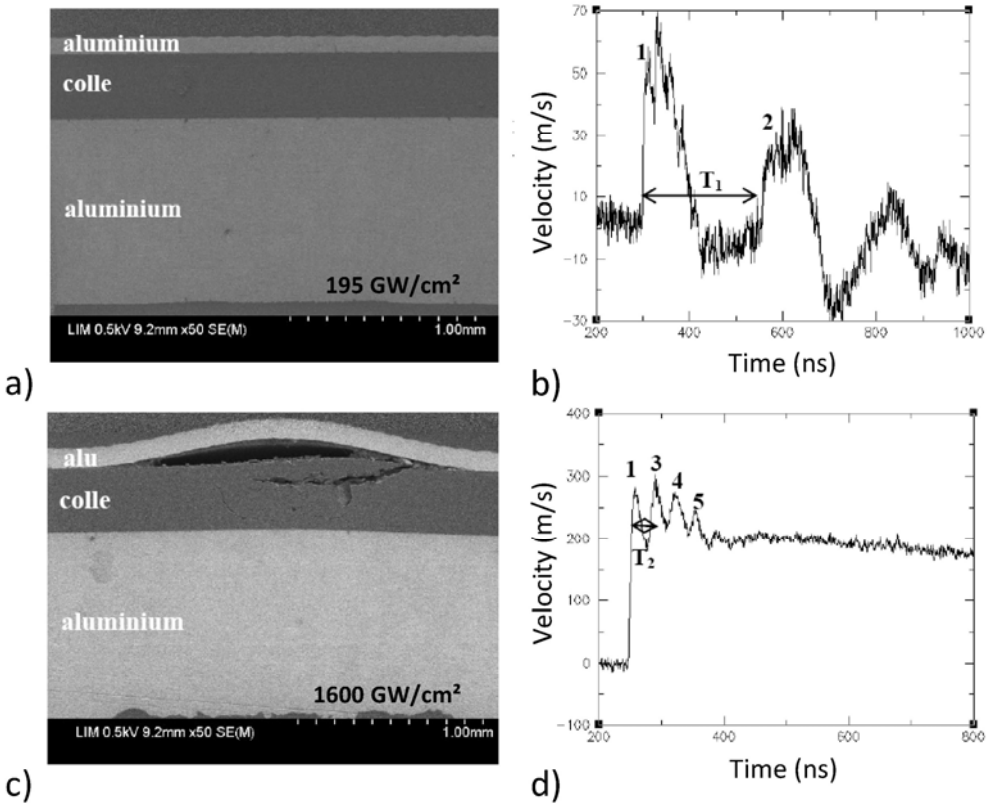

Figure 1.14 Work from D. Laporte [84]: Adhesion test of aluminum/epoxy three layer composite – Experimental determination of the debonding threshold
a) Post-mortem observation of an aluminum/epoxy sample after laser shock (195 GW/cm²) – No observable damage b) Corresponding back face velocity signal measured by VISAR in which no period change can be noticed c) Post-mortem observation of an aluminum/epoxy sample after laser shock (1600 GW/cm²) – Obvious debonding d) Corresponding back face velocity signal measured by VISAR clearly indicating the interface fracture and last layer spallation

This was a challenging step since the samples were globally thicker than in case of coated systems. D. Laporte used the same scientific approach than the one used in the previous presented studies. The debonding threshold of aluminum/epoxy system was investigated using high power laser shock and both post-mortem analysis and time resolved diagnosis (VISAR). One of his main results is reported in Figure 1.14. A given aluminum/epoxy three-layer target was tested using laser shocks. On the first sample presented in Figure 1.14 a) and b), the 195 GW/cm² laser shock produced on the three-layer material was not high enough to open the interface. The unharmed interface can be observed on the

micrograph presented in Figure 1.14 a), but it can also be observed on the back face velocity signal. As explained previously, the long period between two peaks which can be observed on the signal represents two shocks breaking out, the second occurring after the shock going backward and forward. The second sample presented in Figure 1.14 c) and d) was exactly the same, but was shocked using a 1600 GW/cm² laser irradiation. This time, the shock amplitude was high enough to create tensile stresses exceeding the interface strength. Thus, the interface broke out, which can be observed on the sample micrography after shock (see in Figure 1.14 c). The back face velocity signal recorded during the laser shock experiment is characteristic of a spallation process and describes well the ongoing damage (see in Figure 1.14 d). By looking to the post-mortem micrography, it appears that the last layer did not spall completely, but on the VISAR recording time this layer acts as if it is going to spall completely.

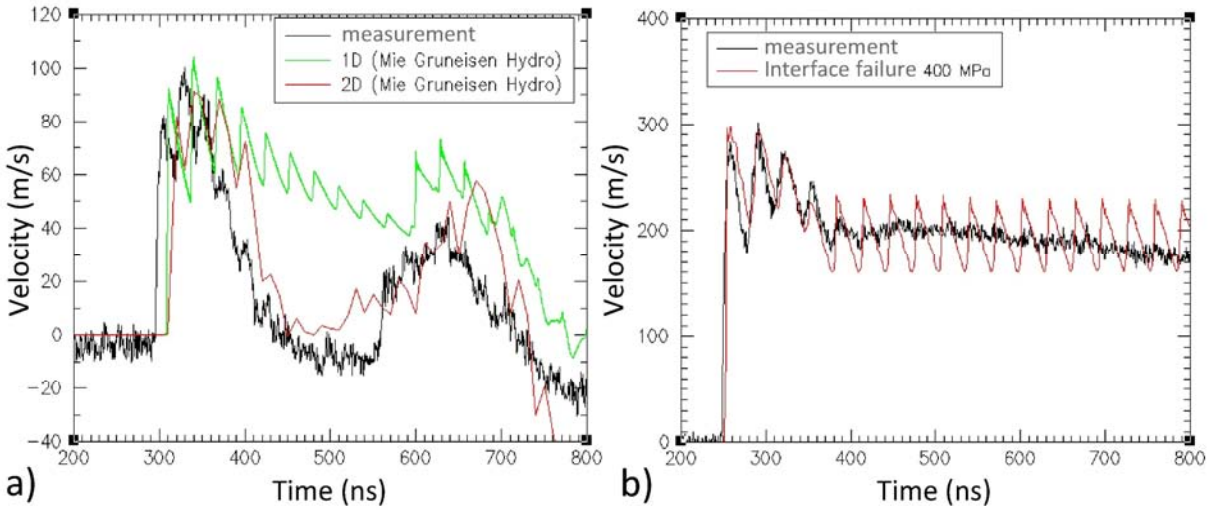

Figure 1.15 Work from D. Laporte [84]: Adhesion test of aluminum/epoxy three-layer composite – Numerical modeling of the Figure 1.14 experiments for the bonding strength evaluation
a) Fitting of the laser shock experiments by use of different models in case of no damage b) Fitting of the laser experiments in case of damage – determination of the interface strength

Numerical modeling is also an important part of D. Laporte work. Indeed, the first step was to correctly describe the experimental signal in order to obtain a reliable model. To this aim, several models were developed and used (see in Figure 1.15 a). D. Laporte showed that a 2D model should be used for a correct modeling of the material response under laser shock loading. Once the behavior understood and correctly modeled, the damage parameters have been adjusted to reproduce the damage opening obtained during the experiments (see in Figure 1.15 b). This modeling enables the interface damage threshold evaluation around 400 MPa. The second step was to investigate deeper the complex wave propagation in this three-layer system. Indeed, the epoxy shock impedance is quite different from the aluminum one. Therefore, the transmission/reflection at the interfaces is really not negligible. D. Laporte used time/position representation to understand the phenomena. The question of the technique optimization, taking into account the wave propagation pattern, is raised.

These last results have demonstrated the LASAT feasibility on three layer thick sample. Based on previous studies on thermal barrier and coated system, several studies show the interest of using the back face velocity measurement to identify an unharmed sample from a fractured interface. This could be applied to composite, and to the weak bond detection. Back to ENCOMB project, a technique to discriminate weak bonds is sought, with the special condition to be non-destructive.

With LASAT, controlled tensile stresses can theoretically be generated at the bond/composite interface. Then, if this interface is correctly bonded, the stresses should not exceed the debonding threshold, but if it is not, the tension would be high enough for the debonding to occur. Thus, the LASAT technique can be non-destructive for good bonds, but destructive for weak ones like a proof test. According to previous work, a time resolved discrimination between debonding or not could be done using a back face velocity measurement. All the question is now: How to adapt the LASer Adhesion Test to bonded composite materials? This point is discussed in the following sections.

2.2 LASAT for composite applications

LASAT technique has always been closely connected to the industry since the first pattern of V. Gupta in 1995 [74]. As explained, the industrial interest for the technique is indeed quite important, since it is answering an issue like none other method. More recently, other patterns have also demonstrated that the technology could represent a commercial interest. This is the case for the test of thermal barrier patterned by Mines de Paris and SNECMA (France). This also proves that there is still room for improvement. So far, no universal technique is available to test any kind of system. That is why LSP Technology has succeeded to pattern the laser shock adhesion for composite [86] and the associated diagnostic they are using for the test [87]. The investigations on composite material are more recent, and may be even more connected to industry for the objectives in stake. Their technique and the use of it are described in the following section.

2.2.1 Laser Bond Inspection

R. Bossi et al., for Boeing Company, is one of the first to publish scientific research on laser shock adhesion test applied to composite material in 2002 [88]. Over 10 years, R. Bossi et al. presented in different scientific papers the work conducted at Boeing Phantom Work for the weak bond issue detection [88-94]. These studies have been done in collaboration with LSP Technologies which develops laser sources, generally for LSP process but here for Laser Bond Inspection (LBI). During their technique development, some elements evolved such as diagnoses, as well as the laser sources. The description given in the next paragraphs focuses on the latest experimental configuration and latest results on the basis of published work [88-94].

Speaking about the laser source, LSP Technology and Boeing use longer laser pulse than the one used in coated system applications. The pulse width presented in their work is generally close to 200 ns [82]. This has two consequences. Firstly, the laser pulse is better adapted to thick composite target because it avoids a strong attenuation phenomenon. Then, it considerably reduces the intensity of the laser irradiation. This effect is accentuated by the fact that large focal laser spots are used (generally around one centimeter). In their work, a strong bond is defined if it can sustain from 15 J/cm² to 30 J/cm² laser shock (see in Figure 1.16). This averagely corresponds from 0.08 GW/cm² to 0.16 GW/cm², which is much lower than the intensity used by D. Laporte and older studies. Therefore, even if water confinement is also used in this application, the pressure is really different from the one to use on metal. Composites behave differently and seem to be much weaker than metal assembly. While speaking about the laser pulse, it has to be noticed that in the work presented, a black tape is generally used as a sacrificial layer on the composite target in addition to water confinement. It is difficult to know how this non-conventional material reacts to laser irradiation. Therefore the pressure pulse characterization seems complicated and no explanation has been found on that subject.

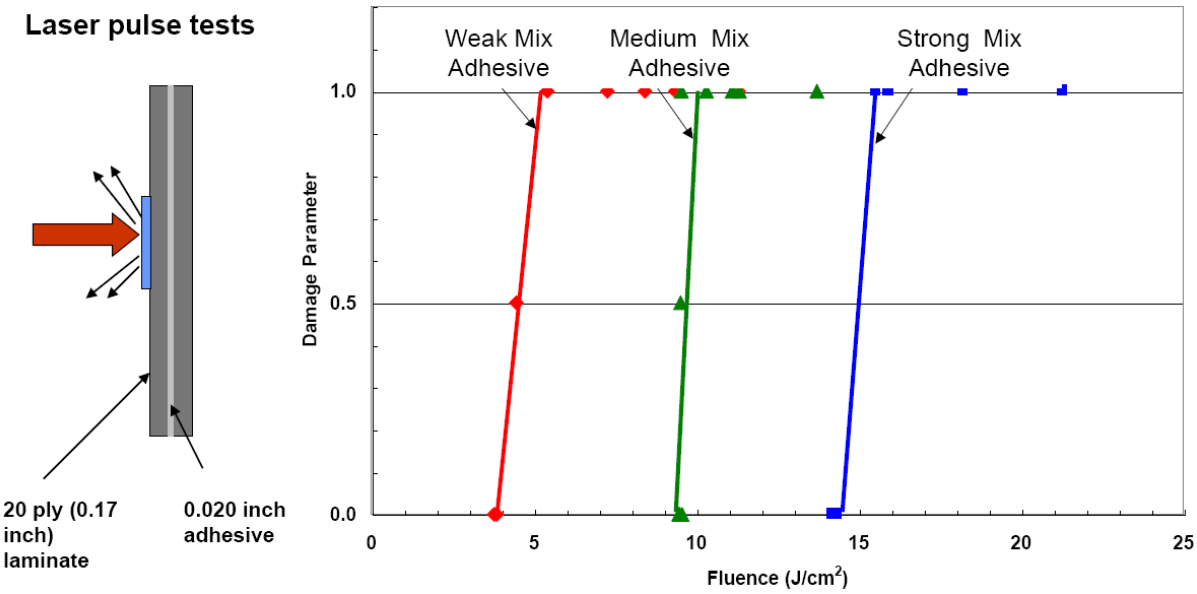

Figure 1.16 from R. Bossi [91] Laser bond inspection damage representation chosen by Boeing to investigate the weak bond issue

In the work of R. Bossi et al., some elements on the damage representation are also given. About the induced damage detection firstly, R. Bossi et al. present several diagnostics. It seems that both VISAR (Velocity Interferometer System for Any Reflector) and EMAT (ElectroMagnetic Acoustic Transducer) are used to measure the back face velocity. In this case, the back face velocity seems to be used only for understanding the dynamic response of the bonded composite and enables numerical modeling. No damage interpretation is made on these measurements. Nevertheless, in the most recent works, EMAT is presented as a means to monitor the damage induced by the laser shock [87]. It is mounted on the front face to record the sample front face velocity, but it is not used as a time resolved diagnosis of damage. Indeed, three shocks are in fact necessary to evaluate the bond strength. A first shock is produced at really low energy level, just to generate wave propagation in the target. The EMAT signal recorded is the signature of an unharmed sample. Then the second shock is performed at the energy expected to damage a weak bond and not a good one. The EMAT signal is recorded but not directly used. Finally, a third shock similar to the first one is produced on the same spot. If this third signal is identical to the first one, then no damage occurred during the second shock. In the case where the signals are different, it means that the target has been modified by the second shock. This technique is really interesting on its principle, but can practically be discussed. Indeed, the EMAT probe is composed of a rectangular aluminum sticker glued to the composite target. The movement of the surface in a magnetic field induces current in the aluminum sticker by Laplace force, which can be correlated to a velocity. Anyway, this layer addition complicates the wave propagation contrary to VISAR which is a non-intrusive method. Thus, some amplitude differences could occur between the three shocks due to the measurement device in itself. Careful analysis of the signal should be done to establish the correct diagnosis.

Thanks to these measurements, the damage induced by laser shock wave propagation is quantified by a damage parameter equal to 0.5 or 0 or 1. “0” means that no damage was observed, “1” means that damage has been clearly evidenced. As it can be sometime hard to decide especially because of the uncertainties mentioned, the damage parameter “0.5” has been added to represent the half-fractured, half-unharmed composite target (see in Figure 1.16). This parameter represents in fact the

debonding threshold. These damage parameters are plotted versus the laser irradiation fluence which enables the damage threshold identification by a jump from 0 to 1 (see in Figure 1.16 and 1.17). On the charts, different material qualities can also be compared this way. Note that in these studies, only the bondline damage is considered, because the hypothesis of no damage in the composite is made. Indeed, it is assumed that the composite is much stronger than the bond interface. The long pulse width and large focal spot are other arguments. Nevertheless, the question of composite damage could be raised. There is no clear evidence that the EMAT diagnosis could discriminate an interface debonding from a composite delamination. With the fluence in stake, there is no reason for the composite to break as it will be discussed later, but in any case, the description of the damage given here is not adequate enough to fully understand it. In spite these questionings, R. Bossi et al. have provided several experimental studies on different bonded composite systems which prove that the test can be efficient under some conditions. Interesting results are reported in Figure 1.17 [93]. The first one presented in Figure 1.17, a) was an investigation conducted to evaluate the bonding strength of composite material in regards of their surface preparation. It has been shown that the progress made in the composite surface preparation have leaded to a better bonding strength.

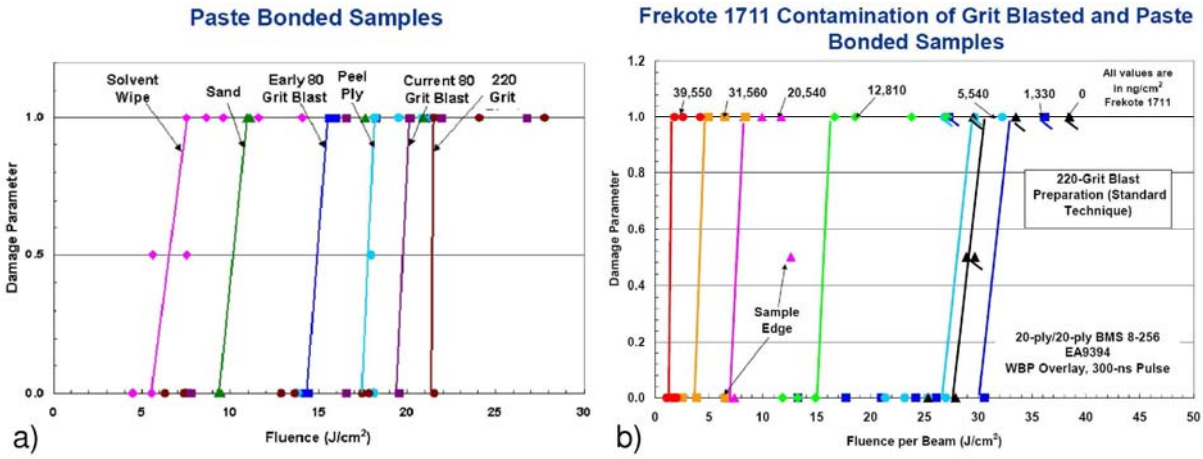

Figure 1.17 from R. Bossi [93] Laser bond inspection investigations at Boeing on bonded composite material a) Laser bond test on differently prepared bonded panels to show the improvement in time of the surface preparation b) Laser bond inspection of weak bonds using frekote contamination of composite panels

Another experimental study presented in Figure 1.17, b) is closer from the weak bond application. Indeed, R. Bossi et al. also investigated frekote contaminated bonds. They succeed to show some differences in the debonding threshold of the bonded composite. One more time, this experimental investigation proves the efficiency of the test under some particular conditions. Nevertheless, several elements are missing. As previously explained, there is no clear localization of the damage in the thickness of the material. Optical micrography of the shocked samples would have given more information. The chosen damage parameter prevents from a clear understanding of the composite material behavior under laser shock. Moreover, the numerical modeling of the phenomenon has not been deeply investigated. Some shocks on aluminum samples were performed with time resolved diagnostic to have an idea of the induced stresses by numerical modeling. Nevertheless, the behavior of composite material could be really different from the aluminum because of its anisotropy for example. What has been evaluated on aluminum cannot be easily transposed to composite target. The shock on composite material has not been modeled which rises one more time the question of the technique optimization.

Figure 1.18 from R. Bossi [93]: Laser bond inspection at Boeing a) Picture of a Boeing fellow in charge of the laser bond inspection testing a composite part b) Picture of the commercial Laser Bond Inspection unit (LBI) developed by LSP Technology

Finally, some information about the LSP Technology LBI unit can be found on their internet website [95]. As it can be seen in Figure 1.18 b), the system seems easily transportable to be moved from one site to another. A scanning head which integrates EMAT and water confinement has been developed for a faster use of LBI (see in Figure 1.18, a). The following characteristics are given:

- Pulse energy: 10J – 50J
- Wavelength : 1054 nm
- Pulse width: 100 – 300ns
- Pulse repetition rate = 1/8 Hz

This laser source is really interesting. Its characteristics, especially the pulse width and the energy ranges, enable the source to be efficient for several different composite systems. So far, it adaptability to different assemblies has been tested only experimentally by several parameter studies. In other words, this source could be really efficient for a given bonded composite structure, but oversized for some other composite structures. In this work, a method is proposed to optimize the test and take the best of each laser source.

2.2.2 SATAC project

Recently, M. Perton [96-99] and E. Gay [100-103] also investigated the laser shock adhesion test applied to bonded composite materials. They were part of a French-Canadian research project named SATAC (Shock Adhesion Test for Adhesively Bonded Composites) built in collaboration between several French and Canadian laboratories [100-103]. In both works, an effort was made to understand the dynamic behavior of CFRP composites and bonded composites under laser shock loading. E. Gay used several diagnostics such as microcopy observation, time resolved transverse visualization, and time resolved back face velocity measurements [103]. Numerical models were also developed to understand the phenomena, especially the complex back face velocity signals. ABAQUS, SHYLAC (hydrodynamic code) where used, but the hard point to get was the influence of anisotropy in the signal description [102]. M. Perton et al. has also performed laser shocks on composites and bonded composites [97]. Like in the E. Gay PhD, the materials investigated were: 4 plies CFRP, 8 plies CFRP and the respectively bonded structures. The Canadian team performed laser interaction with black tape, like in the work of R. Bossi. The numerical modeling was performed using LS-DYNA

software to simulate the back face velocity signals obtained on composite but also to get the induced pressure profile. For that, the back face velocity signal of the tape itself was measured and compared to numerical modeling results although the model used for the black tape is not very clear. This could add an uncertainty on the pressure load. A pressure pulse of averagely 100 ns was deduced. M. Perton et al. succeed to obtain several back face velocity measurements of composite and bonded composite loaded with laser shock. The shape and the signal amplitude give some clues about the composite behavior under dynamic loading. In particular, the damage thresholds of both composite target and bonded composite target have been evaluated thanks to back face velocity signal measurements. These signals are quite complex to explain though, because of the anisotropy of the samples tested (several orientations). The used isotropic models seem to enable a correct fitting of the experiments in the presented cases [97] but could be too limited for the understanding of the complex phenomenon on all the composite targets, and for any pulse duration.

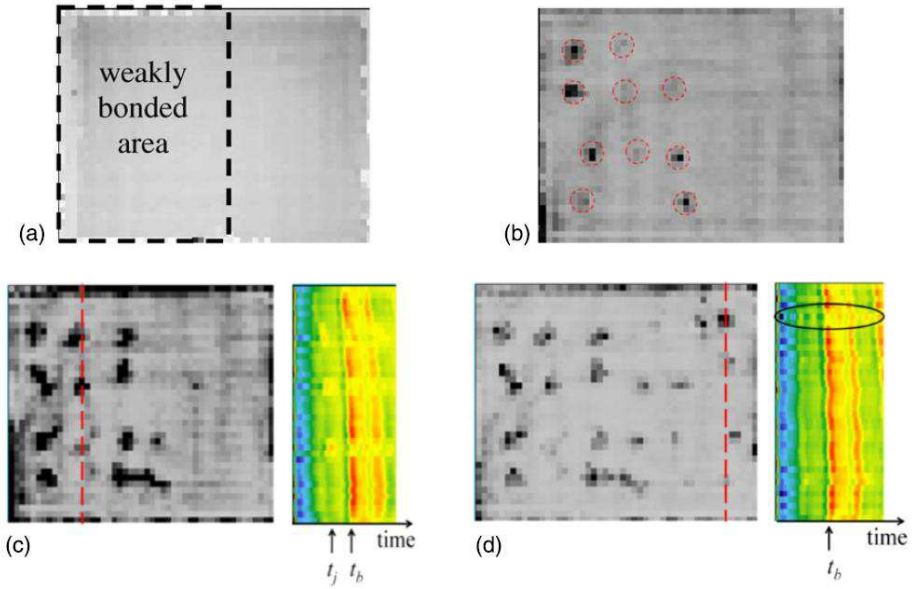

Figure 1.19 Work from M. Perton [97]: Use of laser ultrasound C-scan for the control of bonded composite panel before and after laser shock adhesion test a) C-scan of a bonded composite before laser shocks b) C-scan after laser shock showing the shocks which induced damage (600 mJ) c) 1000 mJ d) 1200 mJ, where the rupture of composite itself can be observed

M. Perton et al. also used laser ultrasound to control the presence of damage created by laser shock as shown in Figure 1.19 [97]. This approach is quite interesting because a C-scan can reveal the damage under the shocked zone. In Figure 1.19 a) and b), the bonded composite panel C-scans are compared between the initial state and after shock state (E = 600 mJ). The debonded areas can be observed on the C-Scan presented. Moreover, the ultrasounds have also revealed damage inside the composite layer of the bonded structure. Indeed, higher intensity laser shock were performed on the non-weak zone (see Figure 1.19 a, c and d). By increasing the laser intensity up to 1.20 GW/cm² (1200 mJ), good quality bond has been opened. In addition, damage in the back face composite has also been created by the laser shock, as revealed by the C-scan. Regarding these results, two remarks can be made. Firstly, the ultrasounds in general seem adapted to the detection of laser induced damage in the composite targets. Secondly, when the bond becomes stronger, the composite itself can be fractured by the laser shock wave propagation. This rises one more time the question of the technique optimization discussed in the next section.

3 Our scientific approach

Despite the numerous experimental investigations made, it appears that the dynamic behavior of CFRP composite material and consequently of bonded CFRP remain not well known. The phenomenon is quite complex, and requires both deep experimental and numerical investigations. Some fundamental questions can be raised.

- How the anisotropy of composite material influences the wave propagation, the composite dynamic response in itself, and the damage growth under laser shock loadings?
- How to correctly measure and quantify the damage resulting from laser shock wave propagation, in composite and bonded composite?
- Below the damage threshold, is there any mechanical or chemical modification of the composite structure which could prefigure a fatigue phenomenon due to repeated tests on the same structure?

Moreover, it can be noticed that results on laser adhesion test for composite were published with short pulses (M. Perton, E. Gay) but also that long pulses can and should be used according to R. Bossi. It can be interesting to see if there is a link between the different kinds of pulse and if there is one pulse more adapted than the other for a given configuration. In other words, that is the question of the technique optimization which is raised here. Several related questions can also come with it:

- How to be sure that the laser shock wave propagation will not fracture the composite itself? In other words, How to be sure that the dynamic tension is correctly located and with the correct level of stresses for the damage to occur only in the bond, and not in the composite?
- Is it still possible to do a non-destructive testing of composite bonds when the bondline interface strength is getting closer to the composite inter-laminate strength? This was not a problem on metals.
- Is it possible to adapt the laser shock adhesion test to any kind of CFRP composite target, meaning any kind of lay-up, structure or thickness, and if so, what kind of tool can be used to adapt the technique?

All these questions are related to two key points: i) the control of damage position and level in the bonded composite target, ii) The numerical modeling of laser shock loading on composite material for its behavior understanding and the technique optimization. Therefore, a progressive investigation approach has been established in this work. It is described in Figure 1.20. At first, it is essential to characterize the dynamic behavior under laser shock loading of the elements constituting the bonded CFRP. Thus, a part of this work has been dedicated to experimental investigation of both epoxy and CFRP composite under laser shock. Epoxy resins have been chosen because it is the main constituent of the bond, and because their acoustic and shock properties are close to the composite one, in the transverse direction. Different CFRP composites should be investigated, from the most simple which means unidirectional composite, to more complex such as crossed plies CFRP. The idea is to use post-mortem analysis and time resolved measurements to understand the dynamic behavior of these elementary constituents. The quantification of the damage or other related phenomenon is also one of the objectives. Thanks to the experimental results, the next step is to

establish a reliable numerical model describing the shock response of the CFRP. Simulations could be used to have a better understanding of composite behavior under laser shock. The model is also an important part of the numerical tool for optimization developed in this work. Before that, the third step is the experimental study of the bonded composite behavior under laser shock. Both correct and weak bonds should be investigated to understand the damage mechanisms and the global behavior. The debonding and damage threshold determination is aimed. Meanwhile, a numerical model of the bonded composite could be developed on the basis of the composite model to help the phenomena comprehension. This model can also be used in the last step of this investigation to study the optimization of the technique. Indeed, this model would be validated thank to the previous experimental steps, ensuring that the phenomenon description is correct. Therefore, it could be used to test different pressure pulses and composite configurations to evaluate the potential of each load to produce an optimized test. This numerical demonstration of optimization will finally be validated by the corresponding experiments. The approach described here is also the route of this manuscript.

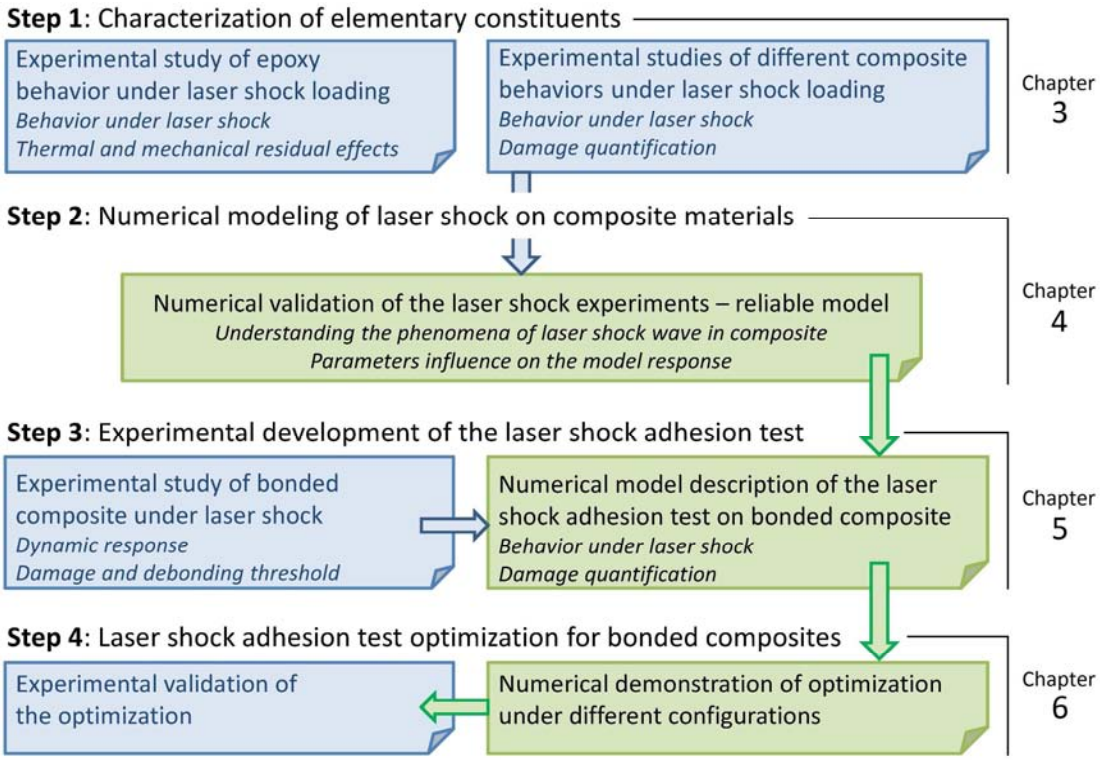

Figure 1.20 Sketch of the scientific approach applied in this work for the development of an optimized laser shock adhesion test (color code: blue = experiments, green = modeling)

Part 3: Bibliography on epoxy and composite under shocks

In this last part, some elements are given on the shock response of epoxy resins and composites regarding the previous studies conducted in the literature. Indeed, as it has been previously explained, the laser shock adhesion test deals with shock, and it is important to know what has been done on the subject. First, the composite materials are described. After a short presentation, we focus on laminates such as GFRP (Glass Fiber Reinforced Polymer) and CFRP (Carbon Fiber Reinforced Polymer) which are closer to the application presented here. Then, the epoxy resins are shortly presented as well as the bonded composite. Globally, the dynamic behavior of these materials is the point of interest regarding the previous given conclusions.

1 About composite materials

1.1 Generalities, GFRP and CFRP

As seen, composites are high performance materials mainly thanks to their low weight and good mechanical strength [104-106]. The universe of composite material is wide because as soon as two or several different materials are associated to combine their good properties, the term composite material can be used. Generally, they are made of two different parts:

- A strong part, also called reinforcement, occupying a small volume but which gives its strength to the composite material. Generally, they have one or several preferential loading directions in which they are stronger,
- A softer part, also called matrix, whose proportion depends on the applications and which has a lower mechanical resistance but enables the correct positioning of the reinforcement, and the stress transfer between fibers.

In aeronautics, CFRP (Carbon Fiber Reinforced Polymer) are the most widely used composite materials for numerous advantages related to this sector. GFRP (Glass Fiber Reinforced Polymer) are also used even if they are more common in the automotive industry. Indeed, glass fibers are generally less expensive than carbon fiber, but they are denser and they have a lower mechanical strength (see in Table 1.1). These composite materials are made of two major constituents: i) the fibers are the reinforcement, giving the mechanical strength to the material; ii) the resin is the matrix, protecting fibers and insuring the stress transfer. In Table 1.1, characteristics of fibers and common resins are given according to the literature. In the case studied here, we focus on carbon fibers and epoxy resin.

	Diameter (µm)	Density (kg/m^3)	Young Modulus (GPa)	Shear Modulus (GPa)	Yield stress (MPa)	Thermal Expansion (10-5 K-1)	Limit Temp. of use (°C)
Fibers							
Carbon	5 – 8	1800	235	18	4500	-0.1	500
Glass	4 – 25	2600	75	30	2500	0.5	650
Matrix							
Polyester		1200	4	1.4	80	8	200
Epoxy		1260	5.2	1.6	110	5	200
Polyamide		1360	2.5	0.8	100	5	80

Table 1.1 Compared properties of composite fibers reinforcement and associated organic matrix as found in the literature [107-108]

The unidirectional ply is the elementary component of the CFRP or GFRP composite laminates. Its cured mechanical characteristics are orthotropic, which means higher mechanical performance in the longitudinal direction, also called fiber direction, than in the two others orthogonal directions, called transverse directions. For example, the Young modulus of CFRP can be 20 times higher in the longitudinal direction than in the transverse directions. The same effect is present on the yield stresses in the different directions (more detailed in Appendix A). The ply in itself is never used in a mechanical structure, because it is really thin (between 120 µm to 250 µm). Thus, the solution is to use several unidirectional orthotropic plies to create thicker structure. All the plies can be stacked in the same direction – it gives an unidirectional composite, or plies can be placed with different orientations according to the load expected – it gives a cross-ply laminate. For that, the material is layered at the pre-impregnated state, to be cured at once. The pre-impregnated plies are in fact a ply with the correct amount of fibers already impregnated with raw epoxy. Indeed, the epoxy content of CFRP obtains its mechanical characteristics after its reticulation which requires an adapted thermo-mechanical curing cycle. Therefore, the plies are first placed as designed in a tool which gives their final shape, and a vacuum bag used to avoid porosity creation during the curing process (see Figure 1.21, a). The raw composite is then placed in an autoclave (the composite material oven) to follow a curing cycle which mainly depends on the epoxy characteristic. When the part is recovered from the autoclave, it has its final shape and mechanical characteristic. The final mechanical characteristic of the composite can be calculated by homogenization methods which are mainly based on the fiber volume ratio. Relations describe the link between the different elastic properties (see Appendix A for more details) [108], [109].

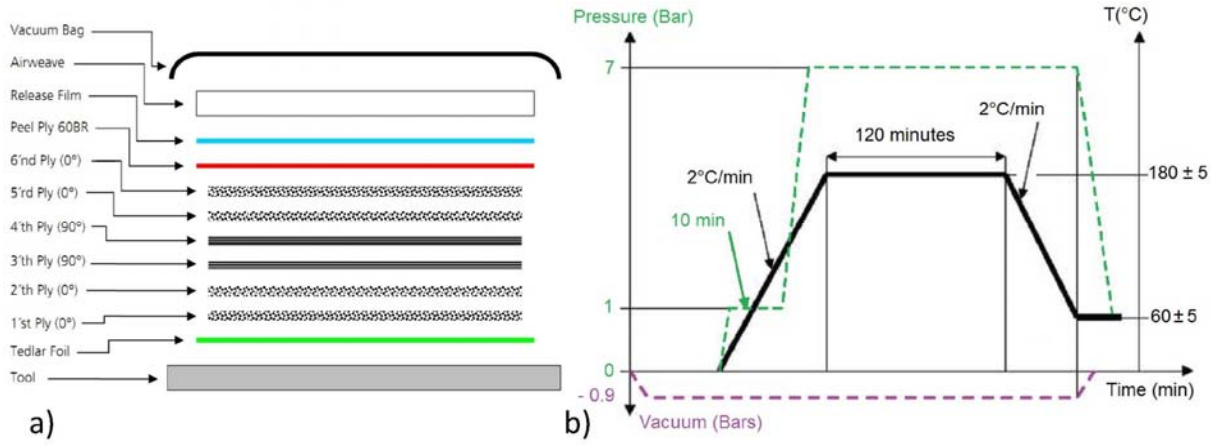

Figure 1.21 a) Sketch of a composite typical lay-up and the tool layers used for the curing cycle of composite material (Example taken from ENCOMB project) b) Curing cycle respected at EADS Cassidian for the curing of composite panels in autoclave in accordance with Hexcel recommendations [110]

The Figure 1.21 illustrates this process. An example of lay-up is given in Figure 1.21, a). This is the lay-up chosen in the frame of ENCOMB project [111]. The different process elements described in the previous paragraph are presents.

1.2 Dynamic loading and damage in composite materials

In the literature, we can find many experiments related to the dynamic behavior of composite material. Dynamic also means high strain rate, but depending on the experimental setup used, the strain rate can be completely different. In order to organize these works, a high strain rate classification can be used as presented in Figure 1.22 (inspired by K.T Ramesh work [112]).

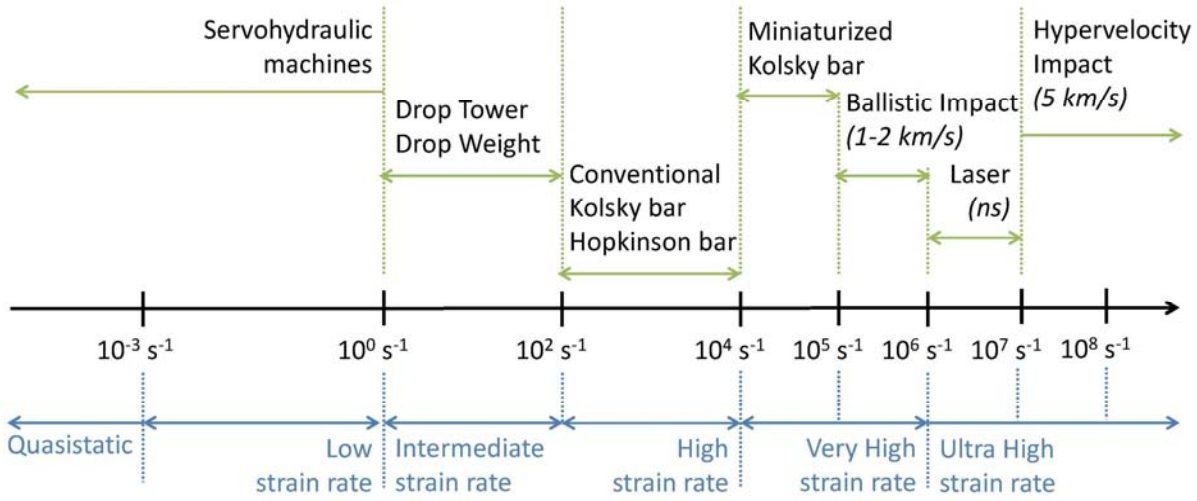

Figure 1.22 Classification of the experimental setup to investigate the dynamic response of material versus the strain rate load, inspired by K. T. Ramesh [112].

K. T. Ramesh also gave four main categories of experiments in which each experimental device quoted in Figure 1.22 can be used:

- High-strain-rate experiments, designed to measure the high-strain-rate properties of a material
- Wave-propagation experiments, to understand the characteristics of wave propagation within the material or structure
- Dynamic failure experiments, to understand the processes of dynamic failure and damage within a material or structure.
- Direct impact experiments, to investigate broad impact phenomena (cratering, vehicle crash experiments…).

The experimental dynamic investigations found in the literature about composite materials respect these four categories. A short overview is given in the following sections sorted by increasing strain rate. The laser shock experiments and other original studies are kept for the end. Note that there are generally two main interests of the work found in the literature. The first one concerns the investigations of the composite damage tolerance [113]; the second is the data base constitution for numerical model development. This second point will be developed in Chapter 4, Part 1.

1.2.1 Low velocity impact

Low velocity impacts are from different types. Concerning aeronautic, these impacts can be due to a tool falling on the composite structure during the manufacturing, or to a small collision on the airport. In the labs, these impacts are generally reproduced by using drop towers. In the literature, several works focus on the description and quantification of low velocity impact induced damage, even if these investigations have different goals [114-119]: the comparison of low velocity impact induced damage between CFRP with or without a thermal shield [114]; the effect of the stacking sequence on the damage propagation and extent trough the composite thickness [115-116]; the development of reliable numerical model for the damage growth description inside composite CFRP [117-119]. In order to describe the damage produced by the impacts, cross section microscopy observations and ultrasounds scanning are generally jointly used. The micrography observations enable the quantification of cracks, fiber/matrix decohesion, and location of delamination. On the

other hand, ultrasounds give the representation of the in-plane damage; it is to say the delamination extent in the composite ply plane. This last post-mortem analysis technique is quite useful when complex stacking sequence is investigated [115-116]. In all these works, the damage area is observed to be cone shaped in the CFRP thickness, the basis being on the opposite face to the shock loading face (see in Figure 1.23, a). This cone shaped damage area includes delaminations, cracks in the epoxy and between the matrix and the fiber even if they are less numerous. Depending on the shock intensity, it is to say the impacting head mass and its velocity, the depth of the damage in the composite thickness is more or less important. The cone frontiers visible on micrographies are generally resulting from shear, induced by the bending component of the impact loading. Speaking of delamination now, ultrasounds show that they follow the ply orientations forming elliptical average shapes which mainly depend on the stacking sequence (see in Figure 1.23, b). In case of a cross-ply composite, the delaminations are distributed in helix through the composite thickness [115-116]. Time resolved measurements are also performed during these experiments. Thanks to the low strain rate, force versus time or force versus displacement graphs can be obtained [120]. These data give a quantification of the mechanical resistance of the CFRP panels. Residual deformations are also observed in many cases, except in case of barely visible impacts [114]. The shape depends on the impacting head, but also on the material tested. This way, B. Vieille et al. compared the mechanical resistance of different composite panels subjected to the same impact load [121].

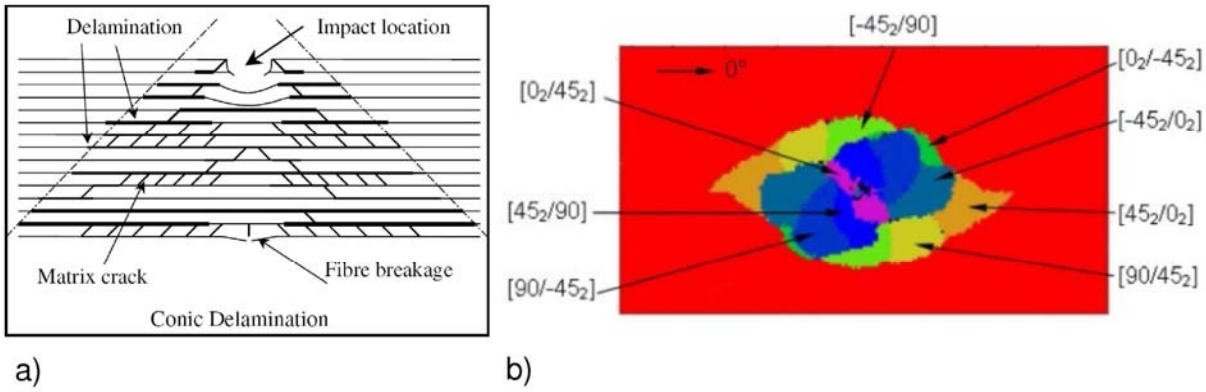

Figure 1.23 a) Description of the damage resulting from a low velocity impact through the CFRP thickness (from S. Petit work [114]), b) Orientation of the delamination measured by ultrasounds in a case of low velocity impact on a T2H/EH25 CFRP (from F. Lachaud work [118])

Using similar tools, studies focus on investigating the residual strength of impacted CFRP panels [114], [122-123]. The idea is to show that the composite panels have still a correct mechanical resistance in spite of a damage resulting from a low velocity impact. This is the case below the yield stress, but after, the failure is much earlier than on non-impacted panels. Note that other original works are also conducted on hybrid composite materials. One of them presents the investigation of a composite made of both GFRP and CFRP [124]. Another presents the interest of using polymer ring inside GFRP laminate to reduce the damage propagation after a low velocity impact load [125].

1.2.2 High strain rate and very high strain rate

In the previous section, the shock wave propagation, to understand as shock theory, was not the point of interest because it was not necessary to get a correct description of the damage growth. When it comes to high strain rates, and very high strain rates, the mechanics start to be different, and the shock theory is more commonly used. From the literature overview [126-139], plate impacts are generally used to investigate these strain rates, even if Hopkinson bars are also often used.

Several techniques are added to monitor the experiments such as: VISAR to monitor the back face velocity of the composite targets; High speed camera for imaging the damage formation, generally macroscopic damage; piezoelectric resistive gauges, inserted in targets set up on purpose and including composite in order to measure the strain, and consequently the stress induced by a shock propagation after impact [126-139]. Some investigations have been made on GFRP [126-128] and other are dedicated to the response of CFRP [129-139]. These investigations are mainly motivated by the military applications, but some works are dedicated to civilian applications. For example, ice stone impacts on composite panel are studied for aeronautics [129], and crash tests are performed for automotive applications [130]. Numerous studies are the one dedicated to perforation, cratering and ejecta under ballistic impacts [127], [131-134]. High speed cameras are generally used to observe these phenomena. The energy threshold for perforation is about 100 J for a CFRP laminate [132]. The cavities formed by the projectile as well as the cone shaped deformation developing on the back face during impact are analyzed. A research team has developed a 3D imaging in order to measure precisely this deformation and to compare it with numerical modeling [133]. Other works focus more on the shock wave theory [135-136]. By using strain measurements, they look to the Hugoniot curve of CFRP to compare the shock response of different CFRP. Spall strength can also be evaluated by using back face velocity measurements under plate impact. For example, the spall strength of GFRP under ballistic impact has been measured from 53 to 110 MPa, depending on the material used. Some differences have also been observed between normal shock loading, and normal shock combined with shear loading [128]. Finally, other works directly investigate the anisotropic response of the composite material [137-139]. In case of unidirectional composite (2D), the shock response has been compared between the fiber direction and the transverse direction. According to J.C.F Millett et al. and C. T. Key et al., the shock response in the transverse direction appears to be identical to the response of the polymer matrix alone. No elastic precursor has been observed on the velocity signal (see in Figure 1.24, b). Nevertheless, the shock response in the fiber direction seems completely different. The velocity is much higher, and the free surface velocity is divided in two parts. The first part is attributed to the elastic response of the fiber, in which the shock is travelling much faster. The second would be the bulk response of the matrix resin, arriving later (see in Figure 1.24, a). These differences are also visible on the Hugoniot curves according to C. S. Alexander [139], but are less and less important with the increase of pressure.

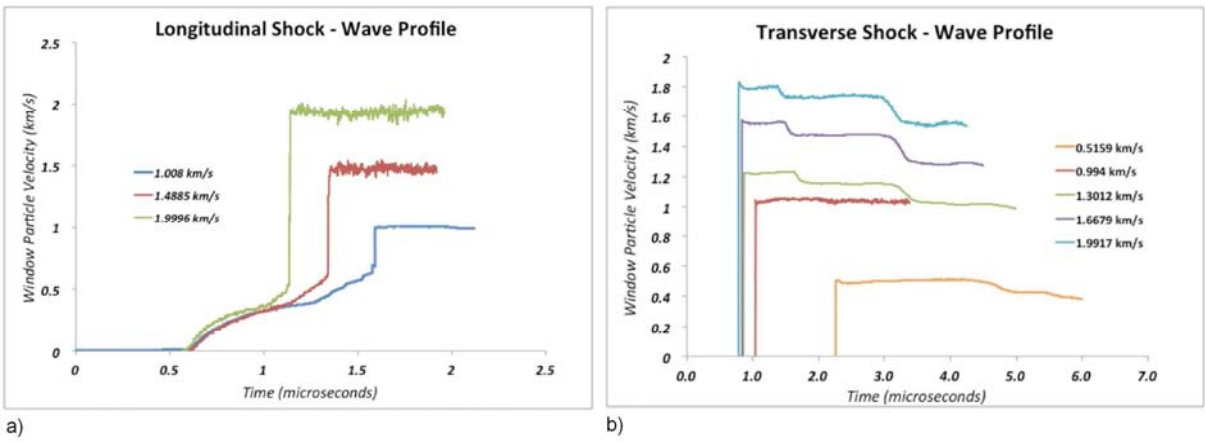

Figure 1.24 From C. T. Key work [138] Anisotropy effect on the CFRP unidirectional shock response observed by plate impact experiments and VISAR measurements a) Velocity profiles in the longitudinal direction, meaning the fiber are parallel to the shock propagation axis, b) Velocity profiles in the transverse direction, fibers are orthogonal to the shock propagation direction

Speaking of pressure load, other work describes the shock response as elastic if the pressure is below 1.3 GPa [126]. Anyway, the anisotropy of composite plays an important role in their dynamic response to very high strain rates.

1.2.3 Laser irradiation, laser shock and related phenomena

Except from the recent work of R. Bossi, M. Perton and E. Gay which have already been presented, really few studies are focused on laser shock and laser interaction on composite materials. Nevertheless, two industrial applications require a better understanding of the laser/composite interaction: the use of lasers for welding the composite materials [140] in one of them, the second is the laser cutting technique applied to composite materials [141]. For their development, several investigations have conducted to the evaluation of thermal degradation of composite material under laser irradiation as well as the thermo-mechanical effect of a laser irradiation [142]. The degradation of the CFRP mechanical properties and the modification of its vibration modes are also studied [143]. In these studies, long irradiation times are used, which is quite different from the laser shock case. Speaking of laser induced shock in composite, some studies can be mentioned. One of the earliest is probably the work from J. R. Triplett et al. High power laser were performed on CFRP target. The intensities used were really high, and widely above the damage threshold. The damage analysis was thus complicated [144]. Later, V. Gupta also published some work on the spall strength evaluation of composite material. Differences in the spallation threshold have been observed according to the composite ply direction [145]. This is in agreement with the work presented in the previous section. At the same time, another research team published a stress measurement in composite CFRP induced by laser shock. The laser intensity was about 1 GW/cm², and the induced pressure measured by PVDF gauges was about 0.25 GPa [146]. In any case, the literature is not deeply documented on laser shock induced damage in composite CFRP materials. Our work will contribute to a better knowledge of this point.

1.2.4 Strain rate effects on CFRP mechanical properties

In the previous sections, the experiments on composite materials to study their dynamic response were discussed, sorted out per strain rate; but it could be interesting to compare the different strain rate effects on a given material. Indeed, several studies have shown a strain rate effect on the elastic and failure characteristics of composite material. One of the first works dated from 1985, the authors compared the dynamic response of unidirectional T300/5208 composite thanks to quasi-static loading (10^{-2} s^{-1}) and Hopkinson Bars (10^{3} s^{-1}) [147]. Changes in the stress/strain curve have been noticed between the two cases, which means an increase in elastic modulus in both longitudinal and transverse directions. An increase in the ultimate strength of averagely 25 % has been observed in both cases, when the final strain seems not modified. These results have been confirmed by more recent work [148-149]. J. Fitoussi et al. developed a method to measure various strain rates in the intermediate range. A significant change in all the composite properties has been observed starting from 100 s^{-1} at least [148]. That is the reason why almost no difference is observed between quasi-static loading and low velocity impact. In that case, the residual indentation only has been shown more significant in the quasi-static test than in the dynamic one, but the absorbed energy and the damage morphology are equivalent for both tests [150] (see in Figure 1.25). The same reason can justify the absence of differences observed in the GIC energy of delamination in CFRP composite at 10 m/s [151-152]. In conclusion, a strain rate effect should be expected on composite shocked by laser irradiation.

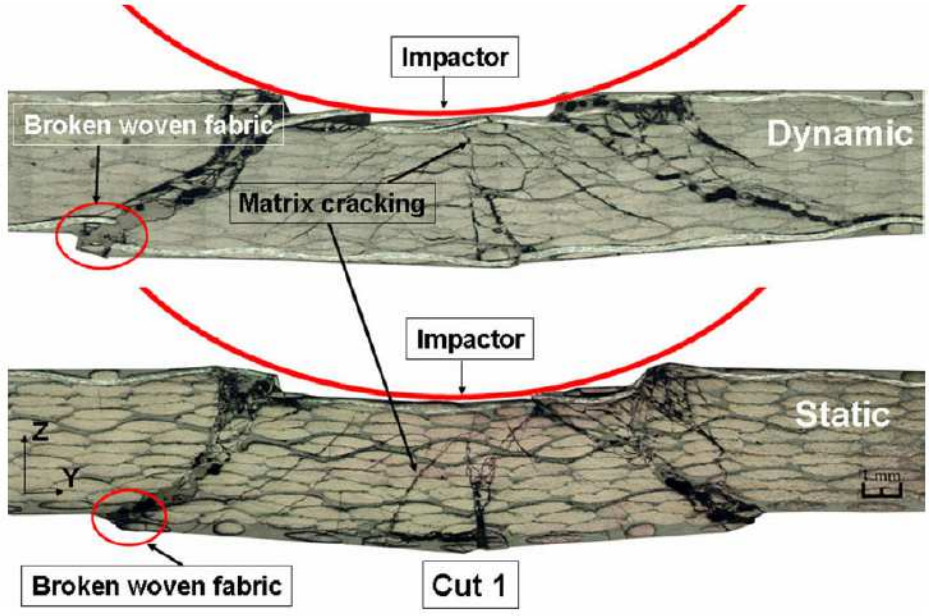

Figure 1.25 From E. A. Abdallah work [150] Comparison of damage between a quasi-static load and low velocity impact on a CFRP

2 Epoxy resins under dynamic loading

One of the major applications of thermoset polymers such as epoxy resin is their use as matrix material in the construction of a wide variety of modern fiber reinforced composite materials [104-106]. Indeed, there is an important requirement for such light-weight materials with high strength from the automotive (crashworthiness testing) and aerospace industries (foreign object damage, bird strike and blade containment), and also for military applications (armor materials). Nowadays, epoxy resins are also used in non-critical structural parts in aeronautics such as engine nacelle which are made of RTM6 resin. Concerning laser shock adhesion test, the shock is produced in order to load the sample in the transverse direction. As explained, this can create tension in the loading direction which could open or not the interface to test. In this case, the shock wave propagation characteristics in composite material are close to ones in the matrix content, meaning the epoxy in case of the studied CFRP (cf. previous section). Therefore, it could be interesting to have a look to the epoxy dynamic behaviour. Since its behavior is close to the composite one, epoxy can also be a good candidate to investigate thermal residual effect of the laser shock loading. Indeed, the absence of carbon fibers can enable an easier analysis by simplifying the tested material. Moreover, epoxy is the main constituent of the bond film used in the ENCOMB bonded composite sample, and as a part of it, its behaviour under dynamic loading should also be understood. Some elements addressing these three main points are given in the following paragraphs.

Over the past, a number of different researchers have investigated the dynamic response of epoxy resins, focusing mainly on the measurement of the Hugoniot curve [153-157], the evolution of strength with impact stress using both longitudinal and lateral pressure gauges [155-158], and the mechanical response at high strain rate in compression, tension and shear [159-162]. While different responses were apparent at low strain rates, similar Hugoniot relationships were found for all materials at higher pressure (representing similar high strain rate responses). The results of the lateral stress measurements indicated an increase in shear strength with impact stress and behind the shock, which was attributed to the visco-plastic nature of epoxy based resins. The various mechanical characterizations performed with different experimental apparatus in order to

investigate the response of epoxy resins at high strain rates show a substantial strain rate dependence of yield stress [163-165], initial modulus and strain to failure. The epoxy dynamic response seems also linked to the initial or constraint state before loading [166]. Another recent work should be mentioned. Indeed, a research team has recently developed a strain diagnostic using mechano-chemical sensor molecule adapted to reveal damage inside epoxy target. This specific sensor is in fact taking a particular color as a function of the pressure applied on these specific molecules. The sensor has been tested on Hopkinson bar in compression. Thanks to this device, residual stresses along the dynamic crack have been evidenced [167]. Except in D. Laporte work, the investigations of epoxy under laser shocks are rare.

When it comes to epoxy material, the temperature increase associated with the shock wave propagation is an important issue. Indeed, epoxy material can have different mechanical behaviors according to the temperature. For conventional polymers, there are mainly to states: a glassy and relatively brittle state, and a rubber-like state. The transition from one to the other is generally characterized by the glass temperature. This temperature can be defined using DSC (Differential Scanning Calorimetry) because it is linked to the jump of calorific capacity induced by the change of state. The glass transition temperature is also an indicator of the thermoset curing rate, and consequently of the material mechanical properties. The epoxy developed for composite materials are generally used in the glassy state, in order to have good mechanical resistance and low deformation rate. Therefore, the glass transition temperature should be as high as possible to extend the temperature of use limit. It is generally above 150°C. This is not the case of the polymers used for tires for example, which have to be in the rubber-like state for a better adhesion response with the ground. Anyway, the temperature increase associated with the shock propagation can thus locally modify the material. The evaluation of the temperature under shock state can be interesting on these materials, but is not an easy task. The most reliable data which can be obtained through the literature comes from thermodynamic modeling [168-170]. There are not many experimental options. Recent investigations aim the development of thin metal thermistor with high response time which could be well adapted to polymer [171], but the more common systems remain the pyrometric method. A Russian team has investigated the brightness temperature of shock-compressed EC141 NF epoxy resin [171]. They compared the wavelength emitted by the shocked sample to a reference one. Thanks to ballistic plate impacts (averagely 7 km/s), they succeed to study a range of pressure from 18 GPa to 40 GPa. The corresponding maximum temperatures observed behind the shock front are respectively in the range 940 K to 2100 K. The raise of temperature lasts during 0.5 µs, which correspond to the travel time of shock wave. Moreover, back face velocity measurement were performed with a VISAR. The back face was not let free, which means that the velocity measured is the particle velocity. On this profile, no change which could have indicated a chemical reaction was noticed under 22 GPa. The authors conclude that in spite the high temperature state, no chemical modifications are occurring during the shock state behind the shock front on the recorded period. This is good news for the work presented here, since the pressure and the load duration induce by laser shock are below these levels. Nevertheless, no information on the temperature state under high tensile stresses as those generated by laser shock propagation has been found. That is why this aspect will be evaluated in this work.

3 About bonded composite materials

3.1 State of the art

3.1.1 Adhesion models

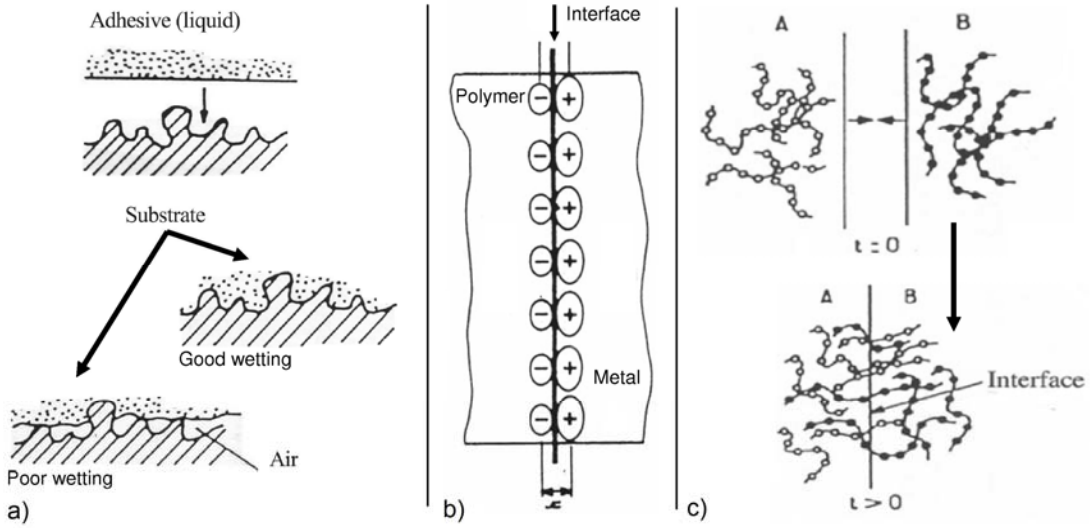

Figure 1.26 Adhesion mechanisms principle from G. Fourche [174], a) Sketch of the mechanical interlocking model in both good wetting and poor wetting cases, b) Sketch of the electrical model principle, c) Sketch of the diffusion model principle

The application of adhesive bonding to composite material is quite recent but the adhesion mechanisms are investigated since the 1930s. Recent progresses in chemistry have enabled a better understanding of the polymer/polymer adhesion, as well as polymer/metal adhesion. It also conducted to more powerful adhesive epoxy resins [173]. Adhesion is a really complex phenomenon, linking several domains of sciences. G. Fourche [174-175] described some important adhesion model in his review of 1995. Some elements are shortly given here (see also Figure 1.26, adapted from G. Fourche [174-175]):

- *Mechanical interlocking model* (see in Figure 1.26, a): In this model, adhesion is considered as the result of a mechanical interlocking between the substrate asperities and the liquid polymer adhesive before curing. Therefore, two parameters are important, the substrate roughness and the polymer wettability.

- *Electrical model* (see in Figure 1.26, b): This model is applied in the case of incompatible materials such as polymer and metal for example.

- *Diffusion model* (see in Figure 1.26, c): This model takes into account the diffusion of molecule species of the superficial layers. The interface becomes a region where molecules from the two materials in contact can be found. Of course, in that case, the two materials have to be chemically compatible

Speaking of bonded composites, the adhesive layer is generally an epoxy, identical or different according to the epoxy content of the CFRP. The mechanism in stake is thus the mechanical interlocking model and in some cases the diffusion model.

- *Model of weak boundary layers (Bikerman [176])*: In this model, the nature of the adhesive bond failure is raised. When the failure occurred right at the interface, without induced failure on the two layers in contact, the failure mode is called 'adhesive'. That is the case of weak bonds. On the opposite, when the failure propagates in the substrate, the failure is considered to be 'cohesive'. In the case of two materials bonding together by an adhesive layer, the bonding strength depends only on the bulk properties of the adhesive layer, whatever the adhesion mechanism is. Finally, the term mixed mode is used when the failure occurs in both substrate and adhesive layer.

3.1.2 Characterization of adhesive bonding

Even if the application of bonding technology is relatively new, bonding and adhesive have already been widely investigated, in the quasi-static range at least. Several techniques have been developed in order to characterize the bonded assembly mechanical characteristic as well as the adhesive mechanical characteristics. This is detailed in P. Cognard's review of 2005 [177]. These techniques are applied on specific samples, dimensioned for the test. The most common ones are single lap joints and double lap joints. They have been used to study the damage mechanisms in Composite/composite bonded joints in case of tensile loading in a first step. A. Roy et al. have worked on that subject [178]. They developed several techniques to characterize the mechanical resistance of single lap joint made of glass/polyester laminates. Colored dye impregnation, extensometry, optical observation, and photoelasticimetry were used to evaluate the strength, failure strain, etc. of these bonded samples.

The characterization of adhesive bonds, and bonded assemblies, has become an important subject these last years, especially for maritime applications [179-187]. Indeed, this industrial sector uses a lot of composite material, and is particularly interested in bonding because of the corrosion issues coming with metallic parts and fasteners. Therefore, many studies have been conducted to reach a better understanding and characterization of adhesive material, which is especially useful for design and numerical modeling. J. Y. Cognard et al. have developed an improved adhesive test method based on the ARCAN test [180]. This technique enables to load the investigated material with a tension/shear or compression/shear combination. They proposed the addition of a special part in beak shape to the ARCAN fixture in order to reduce the edges effects. It has been firstly used with metal substrate, in order to characterize only the adhesive material. J.Y. Cognard et al. principally worked with Redux 420 or Araldite epoxy resins. The modified ARCAN test enables to evaluate the adhesive fracture envelop in tension/shear and compression/shear. Similar results were obtained with different substrates [180-181]. The modified device has been used in other investigations still with metal substrates. P. Davies et al. demonstrated the influence of the bond thickness on the adhesive mechanical properties. They observed a strength and failure strain drop with the thickness increase in case of tensile loading (above 0.8 mm) [182]. C. Babulescu et al. investigated the temperature dependency of the adhesive characteristics [183] and D. Thevenet et al. worked on the fatigue properties of adhesive still with the same setup [184]. The environmental effects have also been investigated by M. Bordes et al. [185]. They use sea water in an aging procedure of the adhesive material. They showed that the adhesive failure changes with the material aging. Especially, they observed that after 3 months aging, the failure changes from cohesive to adhesive. Finally the ARCAN test was used on bonded composite materials and composite materials [186-187]. Their quasi-static response up to failure was studied as well as the bond strength in different configurations. Failure envelops have been determined in some cases.

In other application fields, some studies can be found on the concrete-to-concrete, concrete-to-metal, concrete-to-composite adhesion strength testing. The application of these materials being for structural design, no dynamic studies seem to have been performed. The goals of these studies are generally to evaluate the assembly system which has the best mechanical resistance to both tension and shear loading [188-190]. Closer to the aeronautical applications, some investigations are performed in order to evaluate the behavior and failure mechanism of composite-to-metals bonds. These materials have been a first alternative to the full metal structure at the beginning of composite use in aeronautics structures [191-195]. In some work, acoustic emission has been used to monitor the debonding behavior of several different assemblies under quasi-static loading [196-199]. Since the use of bonded composite material is quite new, in the aeronautic at least, really few studies address to the dynamic behavior of bonded composite. Nevertheless, some intermediate strain rates were tested by H. Al-Zubaidy et al. on metal/composite assemblies [193-195]. Small differences on bond strength, elastic response and so on were found between the dynamic and the quasi-static case, but there are not really sharp. Indeed, the tests were performed with drop tower, and the strain rate was not exceeding 100 s^{-1}. From what is known on composite, this result is not surprising. When it comes to bonded composites, some work can be found in the quasi-static range. To conclude, dynamic behavior studies are missing in the literature for bonded composite CFRP, but destructive methods exist to test the adhesive strength. The GIC test presented in the previous test is probably the most interesting to compare with laser shock adhesion test, knowing that some strain rate effect can occur. Indeed, in regard of strain rate effects, there is no reason why it should be different from composites to bonded composites. It is just a superposition principle.

3.2 About ENCOMB bonded composite

In this section, some complementary information is given about the ENCOMB sample tested in this work. The procedure to contaminate the bonds is explained, and the characterizations of the bonded samples are also given. This includes non-destructive testing after the bonding process and mechanical performance assessment by GIC testing. A general overview is given first, and then focus is made on two contamination scenarios: Release Agent and Moisture. Note that this work has been mainly conducted by IFAM, EADS Cassidian, and the University of Patras in the frame of ENCOMB project.

3.2.1 Elaboration of bonded composite

In aeronautics the bonding of CFRP can be achieved using two different processes. The first one is the one used in ENCOMB project and is named secondary bonding. In this process, the two CFRP to bond are cured separately. Then, the two panels are placed a second time in the autoclave with the adhesive layer in between in order to process with the curing cycle of the adhesive layer. In case of ENCOMB project, this adhesive layer is a FM300 adhesive film composed of an epoxy adherent and a polyester carrier [200]. An example of the curing process and a corresponding curing cycle is given in Figure 1.27 [111]. This curing cycle is in fact not really different from the curing cycle of an epoxy, since it is the same kind of material. The second bonding process used at Airbus is the co-bonding. In this case, one of the two panels to bond is cured separately, but the second one is cured simultaneously with the adhesive. In the industry, this process is more interesting because it removes one curing cycle over three, which enables to go faster.

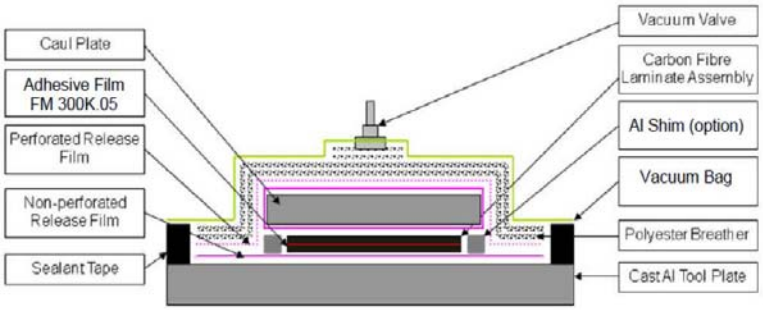

N°	Characteristic	Units	Requirements
			Example of curing cycle
1	Cure equipment	-	Autoclave
2	Heating rate	°C/min	2 ± 1
3	Cure temperature	°C	170 to 185
4	Cure time	min	90 ± 5
5	Bonding pressure	kPa	300 ± 100
6	Cooling rate	°C/min	2 ± 0.5
7	Vacuum pressure 1)	kPa	> 95

Figure 1.27 Example of bonding process as used in ENCOMB and corresponding curing cycle [111]

3.2.2 How to evaluate the degradation of adhesive bonds

In a first investigation, the different ways of weakening an adhesive bond have been studied [201]. This requires two main points: i) the development of contamination procedure in accordance with the airbus scenario, ii) the characterization of the effect induced by the contamination on the bonding strength. The first point was the task of IFAM and EADS Cassidian which developed procedure to contaminate, or at least degraded the surface quality before bonding. For that, several bonded composite were prepared by secondary bonding, but one of the two composite parts was "contaminated" before the bonding process using: release agent, Skydrol, moisture, thermal degradation, or uncured adhesive state. The second point was the work of University of Patras, which performed the GIC testing for the mechanical characterization of the bond [200]. GIC testing consists in loading the bonded composite in mode I (full tension) until the crack opening in or close to the bonding. In order to do that, a pre-cracking is located at the bond level thanks to the use of a Teflon film substituing the bond on the sample edge (see in Figure 1.28, a). The force versus the displacement is measured until the maximum, which corresponds to the failure initiation. Then, the crack propagates close to the bondline, which corresponds to a decrease in the force applied combined to an increase of the displacement (see in Figure 1.28, b). The area under the curve is then calculated to evaluate the failure energy dissipated during the test. This GIC energy, generally expressed in J/m², is the quantity used to evaluate the bond strength as well as to compare bonds between each other. In the work of D. N. Markatos, the GIC values of several weak bonds have been evaluated this way (see in Figure 1.29, a). It can be noticed by comparing these values that poor curing, release agent contamination and thermal degradation are really efficient to reduce the bond strength and thus create weak bonds. However, moisture and Skydrol contamination give higher GIC values, which are closer to the reference strength. According to the definition of weak bonds, the term cannot really be used here, but these bonds are cleary degraded. In addition, the bond failure profiles have been analyzed as shown in Figure 29, b. After the GIC test, the samples are recovered to be analyzed. Each sample is now in two parts since the bonded composite has been completely opened. An observation of the bond in the bond plane is thus possible on the two composites which constituted the assembly. This is the pictures presented in Figure 1.29, b, enabling the identification of the bond failure type. In this case, thermal degradation, poor curing, and release agent contamination leaded to adhesive failure, when the three other scenarios resulted in mixed mode failures.

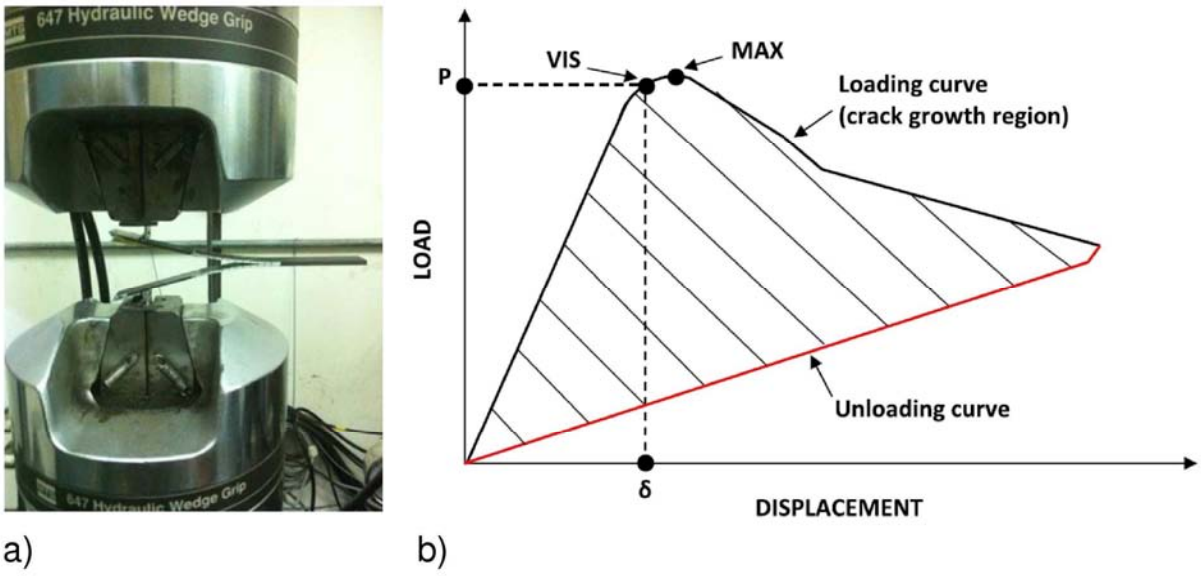

Figure 1.28 GIC testing of bonded composite by D. N. Markatos [201] a) Picture of the testing servohydraulic machine during a bonded composite test, b) Sketch of a typical GIC testing curve in which the failure energy can be evaluated.

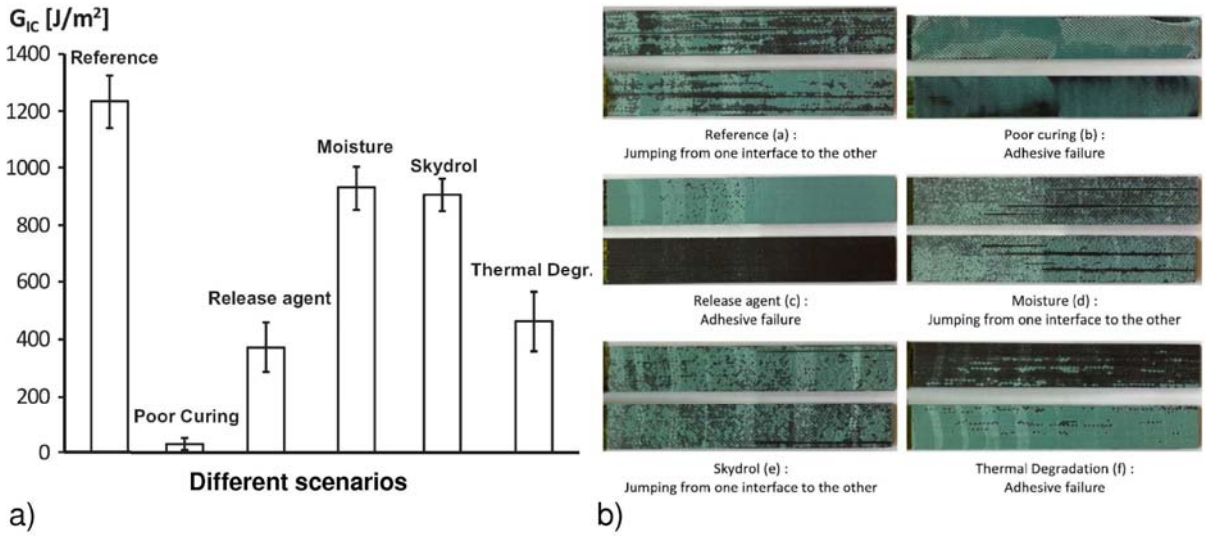

Figure 1.29 GIC results on weak bond investigation by D. N. Markatos [201] a) Comparison of the GIC values between the different scenarios, b) Pictures of the failure pattern over the different contamination scenarios

3.2.3 Release agent scenario

In this section, some more details are given on the release agent contamination scenario. Like in the previous case, this contamination is produced on only one of the two composite panels of the bonded composite. The procedure to contaminate the composite surface with a release agent based solution has been developed by IFAM. In order to produce different levels of contamination, different Frekote 700 NC (release agent) concentration solutions where used. A dip coating of the sample in the solution was used to create a small deposition of the solution molecule on the composite surface, especially Si. Then, the sample is dried during 30 min at ambient temperature and finally put in an oven at 60°C during one hour. The aim of this last step is to create a stable surface state by curing the contamination. After this, the quantity of contaminants is evaluated by using XPS analysis (X-Ray Photoelectron Spectroscopy) by IFAM. The silicon amount present on the composite surface increases with the degree of contamination (see in Table 1.2).

Samples	Av. Amount of Si (at%)	Sdt Dev. (at%)	Average GIC [J/m²]	Sdt Dev. [J/m²]	Rel. Sdt Dev (%)
UT	0	0	1072.7	132.8	12.8
RE-1	2.2	0.3	1062.7	119.0	10.9
RE-2	6.7	0.2	439.2	74.6	17.0
RE-3	8.4	0.8	60.8	23.1	38.0
RE-4	10.5	0.3	40.4	31.2	77.0

Table 1.2 Release agent contamination degrees, corresponding amount of Si measured on the composite surface and corresponding mechanical performance measured by GIC test [202] (work from IFAM for contamination values, and University of Patras for GIC values)

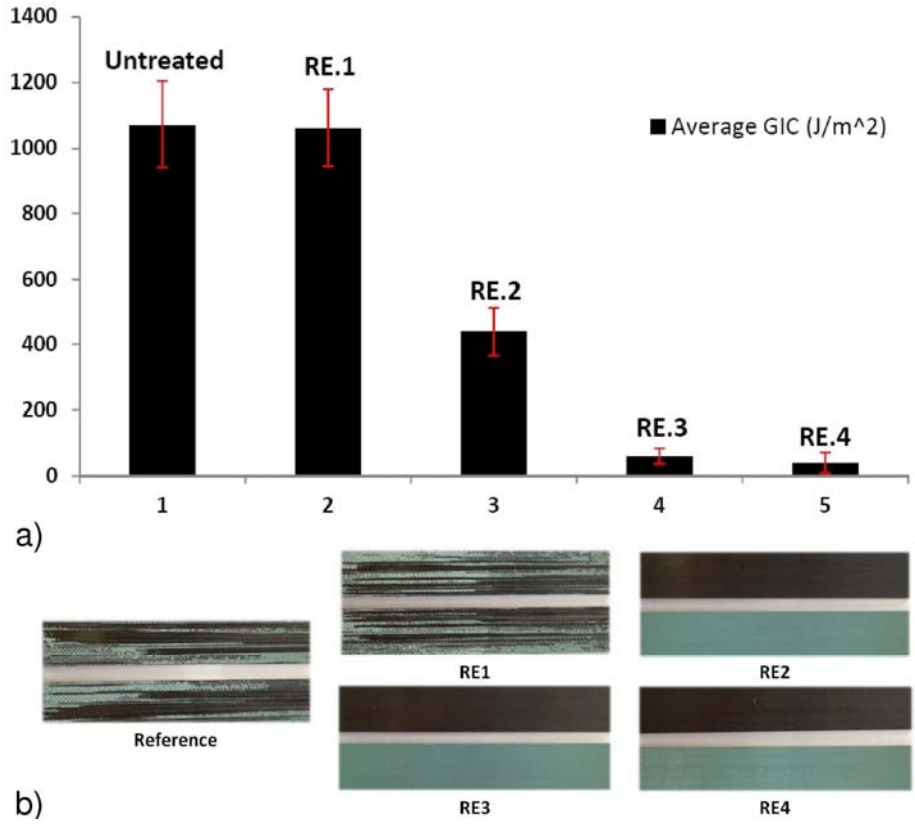

Figure 1.30 GIC results of release agent contaminations by D. N. Markatos [202] a) GIC failure energy showing a progressive loss of mechanical performance, b) Pictures of the failure pattern over the different release agent contamination degrees.

After this contamination characterization, the bonded composite is cured by secondary bonding. The bonded contaminated composites are then analyzed by conventional NDT technique. There is a double goal. The first objective is to evaluate if the bonding process run well. Ultrasounds are used by EADS Cassidian to detect voids, or obvious contaminated areas. The second objective is to see if the contamination can be detected. If it is the case, the bond produced will not be a weak bond, according to the definition of it. In case of release agent sample, no contamination has been noticed by ultrasounds, and no defect as well. Microtomography has been performed by EADS Cassidian and has highlighted the presence of pores on the panel edges, which is common. It has also shown some local small pores regions on the most contaminated sample. These defects were not numerous enough to be annoying. After the NDT control, the bonded composite are then tested by GIC to evaluate their mechanical performance by University of Patras. In case of release agent contamination, these performances are reported in Table 1.3 and Figure 1.30 [202]. It can be observed that the GIC tests reveal a progressive loss of mechanical performance with the increasing

degree of Si contamination. *Si* is responsible for the loss of mechanical performance. Nevertheless, the first contamination degree is close to the reference value in spite of the contamination used. This is confirmed by the mixed mode failure pattern observed after the test (see in Figure 1.30, b). The amount of Si deposed on the composite surface by the contamination process was probably too small to have an influence on the GIC test. Nevertheless, five different scenarios have successfully been created using release agent contamination.

3.2.4 Moisture scenario

In this section, a few elements about moisture contamination scenario are given. The idea developed is the same than in the previous section. Moisture in the composite contamination is used to try to reduce the mechanical properties of the bonded composites. Only one over the two composites panel of the bonded composite is contaminated. This time, the contamination is done using water diffusion in the composite panel by IFAM. Different salt saturated solutions using water at 70°C are used. Composite are placed in the solution, in an air-tight box during 40 days. The mass increased is monitored in order to evaluate the sample mass uptake, which gives the level of contamination reached by the process (see in Table 1.3).

Samples	Mass increase [wt%]	Relative humidity	Average GIC [J/m²]	Sdt Dev. [J/m²]	Rel. Sdt Dev (%)
UT	0	0	1072.72	132.8	12.8
MO-1	0.46 ± 0.01%	28.5	1129.95	182.0	16.6
MO-2	0.84 ± 0.05%	75.0	914.4	103.0	11.3
MO-3	1.19 ± 0.01%	99.0	795.3	98.4	12.4
MO-4	1.29 ± 0.01%	99.0	885.2	42.4	4.8

Table 1.3 Moisture contamination degrees, corresponding mass increase of the composite contaminated and corresponding mechanical performance measured by GIC test [202] (work from IFAM for the contamination degree, and University of Patras for the GIC values)

Then, the samples are bonded as usual and controlled using conventional NDT. The ultrasounds realized by EADS Cassidian revealed no defects, but the Microtomography showed important porosity in the bond layer, especially for the highest contamination (EADS Cassidian results). This phenomenon is not well understood yet, but is probably a direct effect of the contamination. During the bonding process, water can vaporize and create bubbles in the bondline. Anyway, the GIC tests have also been done [202] (see in Figure 1.31). This time, the correlation between the degree of contamination and the bond mechanical strength is not so clear. The first contamination degree does not seem to affect the bond strength. In addition, the bond failure has been observed to be all mixed, which indicates that the contamination did not have the same effect than in the case of release agent. Nevertheless, the last three contamination degrees are lower than the reference, which proves that the bond has been degraded any way.

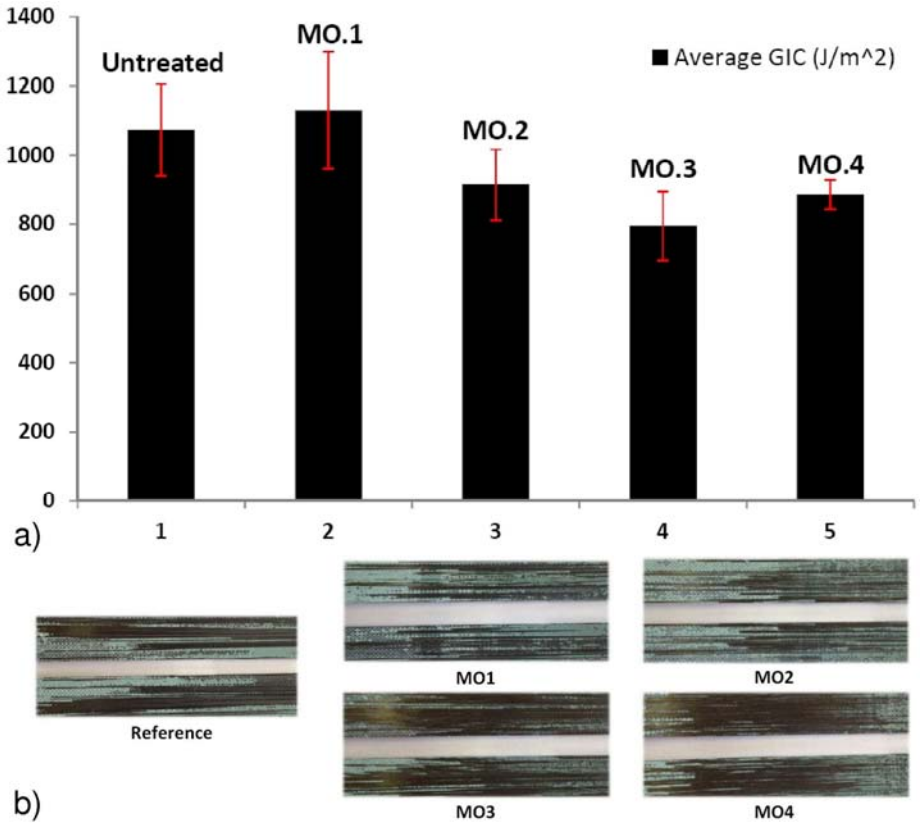

Figure 1.31 GIC results of moisture contaminations by D. N. Markatos [202] a) GIC failure energy showing no particular trend between the contamination and the mechanical performance, b) Pictures of the failure pattern over the different moisture contamination degrees.

Conclusions

Despite the numerous NDT techniques available in the aeronautic industry, no technique can be clearly identified to deal with the weak bond issue. According to previous investigations, it seems that LASAT technique (LASer shock Adhesion Test) could bring some solution. It is well adapted to the industrial context, and can provide a non-destructive proof of the mechanical bonded quality. Nevertheless, few studies about the response of CFRP to laser shock can be found. The understanding of this phenomenon is a key point for the technique development. The investigations conducted in this work aim to a better understanding of the phenomenon. Moreover, the developed technique will be tested on two industrial scenarios provided by Airbus in the frame of ENCOMB European project: Release Agent and Moisture. Thanks to ENCOMB partners, these two scenarios are well described by conventional characterization technique and mechanical testing, which would enable comparisons with the LASAT technique, and associated correlations.

References

[1] M. Thomas, Head of Composite Structure Department, Airbus, *Les Matériaux nouveaux dans le monde Aéronautique Airbus*, ENSMA Conference, February 14th, 2007, Poitiers, France.

[2] R. Bossi, Senior Technical Fellow, Boeing Research & Technology, *NDE Challenges for Composite Aircraft, A4A Conference*, NDT Forum, September 25th, 2012, Seattle, WA, USA.

[3] L-A. Généreux, M. Viens, G; Lebrun, *Comparison of Ultrasonic Testing and Infrared Thermography for the Detection of Machining Defects in Composite Materials*, presented at the 26th Annual Technical Conference of ASC, September 26th – 28th, 2011, Montreal, Quebec, Canada.

[4] S. Catché, R. Piquet, F. Lachaud, B. Castanié, A. Bénaben, *Interaction between surface texture after drilling and bearing behaviour of UD carbon/epoxy structures*, presented at the 17ème Journée Nationale des Composites (JNC 17), June, 2011, Poitiers, France.

[5] T. Miyake, T. Tanaka, M. Ftamura, *Evaluation of machining damage around drilled holes in CFRPs using micro-raman spectroscopy*, presented at the 15th European Conference on Composite Materials (ECCM15), June 24th – 28th, 2012, Venice, Italy.

[6] V. A. Phadnis, F. Makhdum, A. Roy, V. V. Silberschmidt, *Ultrasonically assisted drilling in CFRP composites*, presented at the 15th European Conference on Composite Materials (ECCM15), June 24th – 28th, 2012, Venice, Italy

[7] K. B. Katman, L. F. M. Da Silva, T. M. Young, *Bonded repair of composite aircraft structures: a review of scientific challenges and opportunities*, Progress in Aerospace Sciences, in press, 2013.

[8] T. Stöven, *Rivetless Aircraft Assembly - a dream or feasible concept,* presented to the European Conference on Materials and Structures in Aerospace (EUCOMAS) 2010, Berlin, Germany.

[9] R. D. Adams et P. Cawley*, A review of defect types and nondestructive testing techniques for composites and bonded joints*, NDT International, vol. 21, no. 4, p. 208-222, Août 1988

[10] Light GM, Kwun H. *Nondestructive Evaluation of Adhesive Bond Quality: State of the Art Review*. San Antonio, Texas: Nondestructive Testing Information Analysis Center San Antonio Tx; 1989. p. 1–10. Report No.: SwRI Project 17-7958-838.

[11] S. Markus, C. Tornow, S. Dieckhoff , M. Boustie, R. Ecault, L. Berthe, C. Bockenheimer *Extended Non-Destructive Testing of Composite Bonds*, presented at the SAE International Conference, 2011, Toulouse, France. Report No.: 2011-01-2514.

[12] ENCOMB (266226) Deliverable D1.1: *Report on applications scenarios, technology specifications, samples and test definition for preliminary testing*, 1st April, 2011

[13] ENCOMB (266226) Deliverable D1.2: *Report on technology specifications, samples and test definition for testing, development and adaptation of ENDT technologies*, 6th September, 2011

[14] B. Ehrhart, B. Valeske, R. Ecault, M. Boustie, L. Berthe, C. Bockenheimer, *Extented NDT for the quality assessment of adhesive bonded CFRP structures*, presented at the Smart Materials, Structures & NDT in Aerospace Conference, November 2th – 4th, 2011, Montreal, Quebec, Canada.

[15] C. Bockenheimer, *Novel Approaches to Non-Destructive CFRP Bond Quality Assessment*, presented at the SAE International Conference, 2011, Toulouse, France.

[16] ENCOMB (266226) Deliverable D2.1: *Set of samples and sample characterization (by reference methods for adherend surface and adhesive bond characterization and mechanical testing) for screening of ENDT methods*, 20th December, 2011

[17] ENCOMB (266226) Deliverable D2.2: Set of samples and report on sample characterization (by reference methods for adherend surface and adhesive bond characterization and mechanical teting) for testing of ENDT methods, 2nd May, 2012

[18] A. Blouin, B. Campagne, C. Neron, J-P. Monchalin, Detection of Skin Disbond in Honeycombs and coating detachment by laser tapping technique, presented at the 1st International Symposium on Laser Ultrasonics : Science, Technology and application, July 16-18 2008, Montreal, Canada, www.ndt.net

[19] A. Blouin, C. Néron, B. Campagne, J-P. Monchalin, Application of Laser-Ultrasonics and Laser-Tapping to Aerospace Composite Structures, presented at the 17th world conference on Nondestrcutive Testing, 25-28 Oct 2008, Shanghai, China, www.ndt.net

[20] B. Campagne, H. Voillaume, Development of Laser Ultrasonics: Application to Complex Shape Aeronatical Parts, presented at the 1st International Symposium on Laser Ultrasonics : Science, Technology and application, July 16-18 2008, Montreal, Canada, www.ndt.net

[21] G. Georgeson, T. Edwards, J. Engel, Boeing Research and Technology, X-Ray Backscatter Imaging for Aerospace Applications, 2010, http://www.nasa.gov/pdf/626353main_5-2_Georgeson.pdf

[22] S. Reisinger, A. Ennen, T. Wörlein, M. Schmitt, V. Voland, Quality control for X-Ray Systems – A tool chain for NDT applications, presented at the 4th International Symposium on NDT in Aerospace 2012, Augsburg, Germany

[23] M. Salamon, M. Firsching, M. Khabta, N. Uhlmann, Fast computed Tomography with sub Micron resolution for Investigation of Microstructures, presented at the 4th International Symposium on NDT in Aerospace 2012, Augsburg, Germany

[24] Y.Y. Hung, Y.S. Chen, S.P. Ng, L. Liu, Y.H. Huang, B.L. Luk, R.W.L. Ip, C.M.L. Wu, P.S. Chung, Review and comparison of shearography and active thermography for nondestructive evaluation, published in Materials Science and Engineering R 64 (2009) 73–112, 2009

[25] X. Han, L. D. Favro, R. L. Thomas, Sonic IR Imaging of delaminations and disbonds in composites, published in J. Phys. D: Appl. Phys. 44 (2011) 034013 (5pp) doi:10.1088/0022-3727/44/3/034013, 2011

[26] J. Tashan, R. Al-mahaidi, Investigation of the parameters that influence the accuracy of bond defect detection in CFRP bonded specimens using IR thermography, published in Composite Structures 94 (2012) 519–531, 2012

[27] Z. Su, Lin Ye , Ye Lu, Guided Lamb waves for identification of damage in composite structures: A review, published in Journal of Sound and Vibration 295 (2006) 753–780

[28] W. J. Staszewski, B. C. Lee, R. Traynor, Fatigue crack detection in metallic structures with Lamb waves and 3D laser vibrometry, published in Meas. Sci. Technol. 18 (2007) 727–739 doi:10.1088/0957-0233/18/3/024

[29] A. Z Ak, M. Radzienski, M. Krawczuk, W. Ostachowicz, Damage detection strategies based on propagation of guided elastic waves, published in Smart Mater. Struct. 21 (2012) 035024 (18pp), doi:10.1088/0964-1726/21/3/035024

[30] P. Malinowski, T. Wandowski, W. Ostachowicz, Guided waves for aircraft panel monitoring, published in Key Engineering Materials Vol. 558 (2013) pp 107-115, doi:10.4028/www.scientific.net/KEM.558.107

[31] R. D. Adams, B. W. Drinkwater, Nondestructive testing of adhesively-bonded joints, published in NDT & E International, Vol 30, No. 2, pp. 93-98, 1997.

[32] R.L. Vijaya Kumar, M.R. Bhat, C.R.L. Murthy, Some studies on evaluation of degradation in composite adhesive joints using ultrasonic techniques, published in Ultrasonics 53 (2013) 1150–1162, 2013

[33] J. Cheng, F. Taheri, A novel smart adhesively bonded joint system, published in Smart Mater. Struct. 14 (2005) 971–981 doi:10.1088/0964-1726/14/5/035, 2005

[34] R. Chadha, J. G. Bakuckas, JR., I. Y. Won, Y. Tian, K. Hunziker, K. M. Greene, C. Schlottman, J. Awerbuch, T-M Tan, *Monitoring Damage Growth in Adhesively Bonded Repairs*, presented at the 26th Annual Technical Conference of ASC, September 26th – 28th, 2011, Montreal, Quebec, Canada.

[35] Z. Hasan, A. Muliana, *Analysis and Contro of Smart Composite Laminates using Piezoelectric Materials*, presented at the 26th Annual Technical Conference of ASC, September 26th – 28th, 2011, Montreal, Quebec, Canada.

[36] S. Park, J-W. Kim, C. Lee, S-K. Park, Impedance-based wireless debonding condition monitoring of CFRP laminated concrete structures, NDT&E International 44 (2011) 232–238, 2011

[37] A.R. Sanderson, S.L. Ogin, T.F. Capell, A.D. Crocombe, M.R.L Gower, E.Barton, R.J. Lee, J.Hawker, *Monitoring the disbanding of CFRP plate-bonded reinforcement of a structural beam using a chirped FBG*

sensor, presented at the 15th European Conference on Composite Materials (ECCM15), June 24th – 28th, 2012, Venice, Italy.

[38] D. Li, Z. Zhou, J. Ou, Dynamic behavior monitoring and damage evaluation for arch bridge suspender using GFRP optical fiber Bragg grating sensors, published in Optics & Laser Technology 44 (2012) 1031–1038, 2012

[39] L. P. Canal, B. D. Manshadi, V. Michaud, J. Botsis, G. Violakis, H. G. Limberger, *Monitoring strain gradients in adhesive composite joints by embedded Fibre Bragg Grating sensors*, presented at the 6th International Conference on Composites Testing and Model Identification, 2013, Aalborg, Denmark

[40] R. Mactabi, I. D. Rosca, S. V. Hoa, *In-situ Health Monitoring of Adhesively Bonded Aluminum Joints Using Carbon Nanotubes*, presented at the 26th Annual Technical Conference of ASC, September 26th – 28th, 2011, Montreal, Quebec, Canada.

[41] Y. J. Chen, Y. W. Shi, X. P. Zhang, *Detection of weak bonding in friction welds by ultrasound*, published in Ultrasonics 36 (1998) 141 – 146, 1998

[42] M. Omar, M. Hassan, K. Donohue, K. Saito, R. Alloo, *Infrared thermography for inspecting the adhesion integrity of plastic welded joints*, published in NDT&E International 39 (2006) 1–7, 2006

[43] B. Ren, C. J. Lissenden, *Ultrasonic guided wave inspection of adhesive bonds between composite laminates*, published in International Journal of Adhesion & Adhesives 45 (2013) 59–68, 2013

[44] I. Jölly, M. Wolfahrt, A. Wolfberger, G. Pinter, W. Kern, J. Noisternig, *Study of mechanical and physico-chemical surface properties of composites and thier impact on bond strengths in repair technologies*, presented at the 15th European Conference on Composite Materials (ECCM15), June 24th – 28th, 2012, Venice, Italy

[45] R. J. Zaldivar, G. L. Steckel, J. P. Nokes, B. Morgan, H. I. Kim, *Atmospheric plasma treatment of fiber reinforced composites for adhesive bonding*, presented at the 15th European Conference on Composite Materials (ECCM15), June 24th – 28th, 2012, Venice, Italy

[46] S. Yang, L. Gu, R. F. Gibson*, Nondestructive detection of weak joints in adhesively bonded composite structures*, published in Composite Structures 51 (2001) 63-71, 2001

[47] R. L. Crane, G. Dillingham, *Composite bond inspection*, published in J Mater Sci (2008) 43:6682–6694, DOI 10.1007/s10853-008-2690-2, 2008

[48] B. Ehrhart, B. Valeske, C-E Muller, C. Bockenheimer, *Methods for the Quality Assessment of Adhesive Bonded CFRP Structures - A Resumé*, presented at the 2nd International Symposium on NDT in Aerospace 2010, November, 22nd – 24th, 2010, Hamburg, Germany

[49] G. Wachinger, T. Meer, S. Beer, G. Müller, A. Helwig, J. Bublitz, H. Hohmann, Ch. Thomas, *Detection of contaminants – a key aspect for composite adhesive repair bonding*, presented at the 15th European Conference on Composite Materials (ECCM15), June 24th – 28th, 2012, Venice, Italy

[50] A. Baker, D. Bitton, J. Wang, *Development of a proof test for through-life monitoring of bond integrity in adhesively bonded repairs to aircraft structure*, published in International Journal of Adhesion & Adhesives 36 (2012) 65–76, 2012

[51] R.L. VijayaKumar, M.R.Bhat, C.R.L.Murthy, *Evaluation of kissing bond in composite adhesive lap joints using digital image correlation: Preliminary studies*, International Journal of Adhesion & Adhesives 42 (2013) 60–68, 2013

[52] J-P. Cuq-Lelandais, *Etude du comportement dynamique de matériaux sous choc laser sub-picoseconde*, Thèse de l'ENSMA (Ecole Nationale Supérieure de Mécanique et d'Aérotechnique), Ecole doctorale SIMMEA, 2010

[53] B. A. Gama, S. L. Lopatnikov, J. W. Gillespie, *Hopkinson bar experimental technique: A critical review*, Appl. Mech. Rev., 57 (4) 223, 2004

[54] P. S. Bulson, *Explosive loading of engineering structures*, Edited by E&FN Spon – London, ISBN 0-419-16930-X, 1997

[55] R. Kinslow, *High Velocity Impact Phenomena*, Etided by New-York/ London: Acamdemic Press, ISBN 0-12408-950-X, 1971

[56] L. R. Veeser, J. C. Solem, *Studies of Laser-Driven Shock Waves in Aluminum*, Phys. Rev. Lett, 40 1391, 1978

[57] N.C. Anderholm, *Laser-generated pressure waves*, Bull American Physical Society. Vol. 13, 388-389, 1968

[58] J.A. Fox, *Effect of water and paint coatings on laser-irradiated targets*, Applied Physics Letters, Vol. 24, n°10, 461-464, 1974

[59] C.R. Phipps, *Impulse coupling to targets in vacuum by KrF, HF, and CO2 single pulse lasers*, Journal of Applied Physics, Vol. 64, n°3, 1083-1096, 1988

[60] R. Fabbro, J. Fournier, P. Ballard, D. Devaux, J. Virmont, *Physical study of laser produced plasma in confined geometry*, Journal of Applied Physics, Vol. 68, n°2,775-784 (1990).

[61] L. Berthe, R. Fabbro, P. Peyre, L. Tollier, E. Bartnicki, *Shock waves from a water confined laser-generated plasma,* Journal of Applied Physics, Vol. 82, n°6, 2826-2832, 1997

[62] L. Berthe, *Processus de claquage de milieux transparents sous irradiation laser. Application au choc laser en régime de confinement par eau*, Thèse de l'Université Paris XI, 1998

[63] A. Sollier, *Étude des plasmas générés par interaction laser-matière en régime confiné. Application au traitement des matériaux par choc laser*, Thèse de l'Université de Versailles Saint-Quentin- en -Yvelines (2002)

[64] A. Clauer, LSP Technology Inc. (USA*), Laser Shock Processing, Past, Present and Future*, presented at the 4th International Conference on Laser Peening and Related Phenomena, May 6th – 10th, 2013, Madrid, Spain

[65] D. Furfari, Airbus Operations GmbH (Germany), *LSP in Commercial Aeronautical Applications*, presented at the 4th International Conference on Laser Peening and Related Phenomena, May 6th – 10th, 2013, Madrid, Spain

[66] Y. Sano, Toshiba Corp (Japan*), Progress in Laser Peening Technology for Applications to Infrastructure and Energy system*, presented at the 4th International Conference on Laser Peening and Related Phenomena, May 6th – 10th, 2013, Madrid, Spain

[67] Y. Sano, Toshiba Corp (Japan), *Effects of Laser Peening on Steels for welded structures*, presented at the 4th International Conference on Laser Peening and Related Phenomena, May 6th – 10th, 2013, Madrid, Spain

[68] S. Mannava, University of Cincinnati (USA), *LSP in Biomedical Applications*, presented at the 4th International Conference on Laser Peening and Related Phenomena, May 6th – 10th, 2013, Madrid, Spain

[69] T. Antoun, L. Seaman, D. R. Curran et al., *Spall Fracture*, Edited by Springer-Verlag – New-York, ISBN 0-385-95500-3, 2002

[70] L. Tollier, R. Fabbro, E. Bartnicki, *Study of laser-driven spallation process by VISAR interferometry technique. I. Laser-shock characterization*, J. Appl. Phys., 83(3) 1224, 1998

[71] L. Tollier, R. Fabbro, E. Bartnicki, *Study of laser-driven spallation process by VISAR interferometry technique. II. Experiment and simulation of the spallation process*, J. Appl. Phys., 83(3) 1231, 1998

[72] J. L. Vossen, *Measurement of Film-Substrate Bond Strength by Laser Spallation, Adhesion Measurement of Thin Films, Thick Films, and Bulk Coatings, ASTM STP 640*, K.L Mittal, Ed., American Society for Testing and Materials, 1978, pp. 122-133.

[73] J. Yuan and V. Gupta, *Measurement of Interface Strength by the Modified Laser Spallation Technique*, Journal of Applied Physics, 74 (4), pp 2388-2410, 1993

[74] V. Gupta, System and method for measuring the interface tensile strength of planar interfaces, US PATENT No. 5 438 402, 1995

[75] C. Bolis, *Etude numérique et expérimentale de la séparation par chocs brefs d'interface de revêtement multi-couches. Application au test d'adhérence par chocs laser,* Thèse de l'Université de Poitiers, Ecole Doctorale Sciences pour l'Ingénieur, 2004

[76] M. Arrigoni, *Etude de l'influence des rugosités d'interface, de porosités, et de l'épaisseur d'échantillon sur la propagation des chocs dans des systèmes revêtus. Application au procédé LASAT (LASer Adherence Test)*, Thèse de l'Université de Poitiers, Ecole Doctorale Sciences pour l'Ingénieur, 2004

[77] S. Barradas, R. Molins, M. Jeandin, M. Arrigoni, M. Boustie, C. Bolis, L. Berthe, M. Ducos, *Application of laser shock adhesion testing to the study of the interlamellar strength and coating–substrate adhesion in cold-sprayed copper coating of aluminum*, published in Surface & Coatings Technology 197 (2005) 18– 27, 2005

[78] C. Bolis, L. Berthe, M. Boustie, M. Arrigoni, S. Barradas, M. Jeandin, *Physical approach of adhesion test using laser driven shock wave*, J. Phys. D: Appl. Phys., Vol. 40, No. 10, pp. 3155-3163, 2007

[79] M. Arrigoni, S. Barradas, M. Braccini, M. Dupeux, M. Jeandin, M. Boustie, C. Bolis, L. Berthe, *A comparative study of three adhesion tests (EN 582, similar to ASTM C633, LASAT (LASer Adhesion Test), and bulge and blister test) performed on plasma sprayed copper deposited on aluminium 2017 substrates*, J. Adhesion Sci. Technol., Vol. 20, No. 5, 2006, pp. 471–487, 2006

[80] L. Berthe, M. Arrigoni, M. Boustie, J. P. Cuq-Lelandais, C. Broussillou, G. Fabre, M. Jeandin, V. Guipont, M. Nivard, *State-of-the-art laser adhesion test (LASAT)*, published in Nondestructive Testing and Evaluation, DOI:10.1080/10589759.2011.573550, 2011

[81] G. Rolland, P. Sallamand, V. Guipont, M. Jeandin, E. Boller, C. Bourda, *Laser-induced damage in cold-sprayed composite coatings*, published in Surface & Coatings Technology 205 (2011) 4915–4927, 2011

[82] M. Boustie, L. Berthe, T de Resseguier and M. Arrigoni, *Laser Shock Waves: fundamentals and Applications*, presented at the 1st International Symposium on Laser Ultrasonics: Science, Technology and Applications, July 16-18, 2008 Montreal, Canada

[83] D. Laporte, F. Malaise, P.L. Hereil, E. Buzaud, J.M. Chevalier, *Response of bonded assembly under shock wave loading*, proceedings of the DYMAT, Bruxelles, 2009.

[84] D. Laporte, *Analyse de la réponse d'assemblages collés sous des solicitations en dynamique rapide. Essais et modélisations*, Thèse de l'ENSMA (Ecole Nationale Supérieure de Mécanique et d'Aérotechnique), Ecole doctorale SIMMEA, 2011

[85] D. Laporte, F. Malaise, M. Boustie, J-M. Chevalier, E. Buzaud, *Tensile strength of aluminum-epoxy resin composite structure under high strain rate conditions*, presented at the APS – SCCM Conference (Proceedings), June 26th – July 1st, 2011, Chicago, Illinois, USA.

[86] Bossi et al., *Bond strength measurement system using shock loads*, United States Patent Application publication, Pub No.: US 2003/0079552 A1, May 1st, 2003

[87] Toller, et al., *Apparatus and method for non-destructive testing*, United States Patent 8,156,811, April 17th, 2012

[88] R.H. Bossi, K. Housen, W. Shepherd, *Using shock loads to measure bonded joint strength*, Material evaluation, Vol. 60, pp.1333-1338, 2002.

[89] R. Bossi, K. Housen, C. Walters, *Laser Bond Inspection Device for Composites - has the Holy Grail been found?* NTIAC (Nondestructive Testing Information Analysis Center) Newsletter Volume 30, No. 2, June 2005

[90] R. Bossi, *NDE developments for composite structures*, Review of quantitative non-destructive evaluation Vol 25, 2006.

[91] R. Bossi, *Assessing the Quality Of Bonded Joints, Boeing Phantom Works*, Seattle Washington, ASIP San Antonio TX, November 28-30th 2006

[92] R. Bossi et al., *Laser Bond Testing*, Mater. Eval. 67, 2009, pp. 819–27.

[93] R. Bossi, Senior Technical Fellow, Boeing Research & Technology, Validating the strength of Adhesively bonded Joints, presented at the 2011 Aircraft Airworthiness & Sustainment Conference, April 18th – 21st, 2011, San Diego, CA, USA

[94] R. Bossi, Senior Technical Fellow, Boeing Research & Technology, *NDE Challenges for Composite Aircraft, A4A Conference*, NDT Forum, September 25th, 2012, Seattle, WA, USA.

[95] www.lsptechnologies.com/lbi-application-development.php

[96] M. Perton, Z. Gu, J-P. Monchalin, E Gay, L. Berthe, M. Boustie, M. Arrigoni, Laser shock waves for adhesive bon testing, Proceedings of International SAMPE conference, 2010.

[97] M. Perton, A. Blouin, J-P. Monchalin, Adhesive bond testing of carbon–epoxy composites by laser shockwave, J. Phys. D: Appl. Phys. 44 034012, 2010.

[98] M. Perton, A. Blouin, J-P. Monchalin, *Adhesive bond strength evaluation in composite materials by laser-generated high amplitude ultrasound*, presented at the 2nd International Symposiumon Laser-Ultrasonics - Science, Technology and Applications, Journal of Physics: Conference Series 278 (2011) 012044, doi:10.1088/1742-6596/278/1/012044, 2011

[99] Z. Gu, M. Perton, S. E. Kruger, A. Blouin, D. Lévesque, J-P. Monchalin, A. Johnston, M. Boustie, L. Berthe, M. Arrigoni, Laser Induced Shock Waves for Composites Adhesive Bond Testing, published in REVIEW OF PROGRESS IN QUANTITATIVE NONDESTRUCTIVE EVALUATION VOLUME 29, AIP Conference Proceedings, Volume 1211, pp. 295-302, 2010

[100] M. Arrigoni, S. E. Kruger, A. Blouin, D. Lévesque, B. Arsenault, J-P. Monchalin, M. Boustie, L. Berthe, *Adhesive Bond Testing By Laser Induced Shock Waves*, 17th World Conference on Nondestructive Testing, Shanghai, China, 25-28 Oct 2008

[101] M. Boustie, E. Gay, L. Berthe, M. Arrigoni, J. Radhakrishnan, T. de Résséguier, A.Blouin, J.P. Monchalin, S. Kruger, M. Perton, A. Johnston, R. Cole, E. Buzaud, *LAser Shock Adhesion Test (LASAT) of composite materials for aerospace industry*, 23rd Int. Conf. on Surface Modification Technologies (SMT23), 2 -5 Nov., Madras, India, T.S. Sudarshan et al. eds., 2009.

[102] E. Gay, *Comportement de composites sous choc induit par laser: Développement de l'essai d'adhérence par choc des assemblages de composites collés*, Thèse de l'Ecole Nationale Supérieure d'Arts et Métiers, Université Paris Tech, Ecole doctorale Sciences des Métiers de l'Ingénieur, 2011

[103] E. Gay, L. Berthe, M. Boustie, M. Arrigoni, P. Mercier, J. Bénier, *Experimental study of composite damage under laser shock*, presented at the 17ème Journée Nationale des Composites (JNC 17), June, 2011, Poitiers, France.

[104] S. K. Mazumdar, *Composites manufacturing – materials, product, and process engineering*, CRC Press, (2002).

[105] G. H. Staab, *Laminar composites*, Butterworth Heinemann (1999).

[106] S. T. Peters, *Handbook of composites*, Chapman and Hall (1998).

[107] E. Gay, *Comportement de composites sous choc induit par laser: Développement de l'essai d'adhérence par choc des assemblages de composites collés*, Thèse de l'Ecole Nationale Supérieure d'Arts et Métiers, Université Paris Tech, Ecole doctorale Sciences des Métiers de l'Ingénieur, 2011

[108] D. Gay, *Matériaux Composites*, 5ème édition, Ed. Hermès (2005)

[109] D. Roylance, Department of Materials Science and Engineering, MIT, Cambridge, MA 02139, 2000, http://ocw.mit.edu/courses/materials-science-and-engineering/3-11-mechanics-of-materials-fall-1999/modules/laminates.pdf

[110] http://www.hexcel.com/Resources/DataSheets/Prepreg-DataSheets/M21_global.pdf

[111] ENCOMB (266226) Deliverable D2.1: Set of samples and sample characterization (by reference methods for adherend surface and adhesive bond characterization and mechanical testing) for screening of ENDT methods, 20th December, 2011

[112] K. T. Ramesh, *Hight Strain Rates and Impact Experiments*, pusblished in Springer Handbook of Experimental Solid Mechanics, pages 929-960, 2008

[113] W.J. Cantwell, J. Morton, *The impact resistance of composite materials – a review*, published in Composites, volume 22, Issue 5, pages 347-362, 1991

[114] S. Petit, C. Bouvet, A. Bergerot, J-J. Barrau, *Impact and compression after impact experimental study of a composite laminate with a cork thermal shield*, published in Composites Science and Technology 67 (2007) 3286–3299, 2007

[115] C.S. Lopes, O. Seresta, Y. Coquet, Z. Gürdal, P.P. Camanho, B. Thuis, *Low-velocity impact damage on dispersed stacking sequence laminates. Part I: Experiments*, published in Composites Science and Technology 69 (2009) 926–936

[116] N. Hongkarnjanakul, C. Bouvet, S. Rivallant, *The effect of stacking sequence on the low-velocity impact response of composite laminate,* presented at the 15th European Conference on Composite Materials (ECCM15), June 24th – 28th, 2012, Venice, Italy

[117] C.S. Lopes, P.P. Camanho, Z. Gürdal, P. Maimí, E.V. González, *Low-velocity impact damage on dispersed stacking sequence laminates. Part II: Numerical simulations*, published in Composites Science and Technology 69 (2009) 937–947

[118] F. Lachaud, Ch. Espinosa, L. Michel, *Impact damage of carbone-epoxy laminates*, presented at the 17ème Journée Nationale des Composites (JNC 17), June, 2011, Poitiers, France.

[119] A. Faggiani, B.G. Falzon, *Predicting low-velocity impact damage on a stiffened composite panel*, published in Composites: Part A 41 (2010) 737–749, 2010

[120] C.K.L. Davies, S. Turner, K.H. Williamson, *Flexed plate impact testing of carbon fibre-reinforced polymer composites*, published in Composites, 1985

[121] B. Vieille, V. M. Casado, C. Bouvet, *Comparative study of the impact behavior and damage tolerance of woven carbon fiber reinforced thermoplastic – and thermosetting composites*, presented at the 15th European Conference on Composite Materials (ECCM15), June 24th – 28th, 2012, Venice, Italy

[122] L. Ballère, P. Viot, J.-L. Lataillade, L. Guillaumat, S. Cloutet, *Damage tolerance of impacted curved panels*, International Journal of Impact Engineering 36 (2009) 243–253

[123] Y. Zhang, M. Genest, D. Backman, A. Jonhston, A. Komus, M. Singh, *Impact and Compression after Impact Tests of a Carbon/Epoxy Composite*, presented at the 26th Annual Technical Conference of ASC, September 26th – 28th, 2011, Montreal, Quebec, Canada.

[124] M. Sayer, N. B. Bektas, O. Sayman, *An experimental investigation on the impact behavior of hybrid composite plates*, published in Composite Structures 92 (2010) 1256–1262, 2010

[125] M. Yasaee, I. P. Bond, R. S. Trask, *Novel compartmentalisation of low velocity Impact damage*, presented at the 26th Annual Technical Conference of ASC, September 26th – 28th, 2011, Montreal, Quebec, Canada

[126] D.P. Dandekar, C.A. Hall, L.C. Chhabildas, W.D. Reinhart, *Shock response of a glass-fiber-reinforced polymer composite*, published in Composite Structures 61 (2003) 51–59

[127] N.K. Naik, P. Shrirao, B.C.K. Reddy, *Ballistic impact behaviour of woven fabric composites: Parametric studies*, Materials Science and Engineering A 412 (2005) 104–116

[128] F. Yuan, L. Tsai, V. Prakash, A.M. Rajendran, D. P. Dandekar, *Spall strength of glass fiber reinforced polymer composites*, published in International Journal of Solids and Structures 44 (2007) 7731–7747

[129] J. Rhymer, H. Kim, *Critical force prediction of high velocity impact onto unidirectional carbon/epoxy composite panels*, presented at the 26th Annual Technical Conference of ASC, September 26th – 28th, 2011, Montreal, Quebec, Canada.

[130] M. Waimer, D. Kohlgrüber, D. Hachenberg, H. Voggenreiter, *Experimental study of CFRP components subjected to dynamic crash loads*, published in Composite Structures 105 (2013) 288–299

[131] P.J. Hazell, G. Kister, C. Stennett, P. Bourque, G. Cooper, *Normal and oblique penetration of woven CFRP laminates by a high velocity steel sphere*, published in Composites: Part A 39 (2008) 866–874

[132] P.J. Hazell, A. Cowie, G. Kister, C. Stennett, G.A. Cooper, *Penetration of a woven CFRP laminate by a high velocity steel sphere impacting at velocities of up to 1875 m/s*, published in International Journal of Impact Engineering 36 (2009) 1136–1142

[133] M. Yamada, Y. Tanabe, A. Yoshimura, T. Ogasawara, *Three-dimensional measurement of CFRP deformation during high-speed impact loading*, published in Nuclear Instruments and Methods in Physics Research A 646 (2011) 219–226

[134] M. Nishida, H. Kato, K. Hayashi, M. Higashide, *Ejecta Size Distribution Resulting from Hypervelocity Impact of Spherical Projectiles on CFRP Laminates*, published in the proceedings of The 12th Hypervelocity Impact Symposium, Procedia Engineering 58 (2013) 533 – 542

[135] Y. Tanabe, M. Aoki, *Stress and strain measurements in carbon-related materials impacted by a high-velocity steel sphere*, published in International Journal of Impact Engineering 28 (2003) 1045–1059

[136] P.J. Hazell, C. Stennett, G. Cooper, *The effect of specimen thickness on the shock propagation along the in-fibre direction of an aerospace-grade CFRP laminate*, published in Composites: Part A 40 (2009) 204–209

[137] J. C. F. Millett, N.K. Bourne, Y.J.E. Meziere, R. Vignjevic, A. Lukyanov, *The effect of orientation on the shock response of a carbon fibre–epoxy composite*, published in Composites Science and Technology 67 (2007) 3253–3260

[138] C. T. Key, S. C. Schumacher, *Anisotropic shock response of unidirectional composite materials*, presented at the 15th European Conference on Composite Materials (ECCM15), June 24th – 28th, 2012, Venice, Italy

[139] C. S. Alexander, *Dynamic response of a carbon fiber-epoxy composite subjected to planar impact*, presented at the 15th European Conference on Composite Materials (ECCM15), June 24th – 28th, 2012, Venice, Italy

[140] V.Wippo, P. Jaeschke, U. Stute, D. Kracht, H. Haferkamp, *The influence of carbon fibres in the temperature distribution during the laser transmission welding process*, presented at the 15th European Conference on Composite Materials (ECCM15), June 24th – 28th, 2012, Venice, Italy

[141] Y. Harada, T. Ito, T. Suzuki, M. Nishino, H. Niino, T. Teramoto, *Environmental effects on mechanical behavior of CFRP using laser cutting process*, presented at the 15th European Conference on Composite Materials (ECCM15), June 24th – 28th, 2012, Venice, Italy

[142] J. K. Chen, A. Perea, F. A. Allahdadi, *Laser effects on the dynamic response of laminated composites*, published in Composites Engineering, Vol. 5. No. 9. pp. 1135-l 147, 1995

[143] J. K. Chen, A. Perea, F. A. Allahdadi, *A study of laser/composite material interactions*, published in Composite Science and Technology 54 (1995) 35-44

[144] J. R. Triplett, G. A. Gurtman, *A study of composite material damage induced by laser-supported detonation waves*, published in Systems, science and softwre, 1976

[145] V. Gupta, A. S. Argon, *Measurement of the anisotropic strength and toughness of Pitch-55 carbon ribbons*, published in Journal of Material Science 27 (1992) 777-785.

[146] Z. Li, W. Zhu, J. Cheng, G. Zhou, *Measurements of laser induced shock waves in carbon epoxy composite*, published in Journal of materials science letters 15 (1996) 2122-2123

[147] C. Cazeneuve, J-C. Maille*, Etude du comportement de composites à fibre de carbone sous différentes vitesses de sollicitation*s, published in Journal de Physique, Colloque C5, supplgment au n08, Tome 46, aoOt 1985

[148] J. Fitoussi, F. Meraghni, Z. Jendli, G. Hug, D. Baptiste, *Experimental methodology for high strain-rates tensile behaviour analysis of polymer matrix composite*, published in Composites Science and Technology 65 (2005) 2174–2188

[149] T. Gomez-del Rio, E. Barbero, R. Zaera, C. Navarro, *Dynamic tensile behaviour at low temperature of CFRP using a split Hopkinson pressure bar*, publised in Composites Science and Technology 65 (2005) 61–71

[150] Elias Abi Abdallah, Christophe Bouvet, Samuel Rivallant, Bernhard Broll, Jean-Jacques Barrau, *Experimental analysis of damage creation and permanent indentation on highly oriented plates*, published in Composites Science and Technology 69 (2009) 1238–1245

[151] H. Koerber, J. Xavier, P.P. Camanho, *High strain rate characterisation of unidirectional carbon-epoxy IM7-8552 in transverse compression and in-plane shear using digital image correlation*, published in Mechanics of Materials 42 (2010) 1004–1019

[152] P. Robinson, C.A. McCarroll, S.T. Pinho, L.Iannucci, P.T. Curtis, *Design and evaluation of a high rate mode I translaminar fracture toughness test for composite laminates*, presented at the 15th European Conference on Composite Materials (ECCM15), June 24th – 28th, 2012, Venice, Italy

[153] D.E. Munson, R.P. May, *Dynamically Determined High-Pressure Compressibilities of Three Epoxy Resin Systems*, J. Appl. Phys. 43 (3), 962-971 (1972), http://dx.doi.org/10.1063/1.1661315

[154] W.J. Carter, S.P. Marsh, *Hugoniot equation of state of polymers*, LANL Report No. LA-13006-MS, 1995.

[155] N.R. Barnes, N.K. Bourne, J.C.F. Millett, *The Shock Hugoniot of an Epoxy Resin*, in Shock Compression of Condensed Matter-2001, AIP CP620, edited by M.D. Furnish, N.N. Thadhani, and Y. Horie, (AIP, 2002), pp.135-138.

[156] J. C. F. Millett, N.K. Bourne, N.R. Barnes, *The Behavior of an epoxy resin under one-dimensional shock loading,* published in J. Appl. Phys. 92 (11), 6590-9594 (2002).

[157] G.J Appleby-Thomas, P.J. Hazell, C. Stennett*, The variation in lateral and longitudinal stress gauge response within an RTM6 epoxy resin under one-dimensional shock loading*, published in J. Mat. Sci. 44 (22), 6187 (2009)

[158] N.K. Bourne, J.C.F. Millett, N.R. Barnes, I. Belcher, *The deviatoric response of an epoxy resin to one-dimensional shock loading*, published in Shock Compression of Condensed Matter-2001, AIP CP620, edited by M.D. Furnish, N.N. Thadhani, and Y. Horie, (AIP, 2002), pp.649-652.

[159] A. Gilat, R.K. Goldberg, G.D. Roberts, *High strain rate response of epoxy in tensile and shear loading*, published in J. Phys. IV France 110, 123 (2003).

[160] R. Gerlach, C.R Siviour, N. Petrinic, J. Wiegand, *Experimental characterization and constitutive modelling of RTM6 resin under impact loading*, published in Polymer 49, 2728-2737 (2008).

[161] N.K. Naik, R. Gadipatri, N.M. Thoram, V.R. Kanala, V. Ch, *Shear properties of epoxy under high strain rate loading*, published in Polymer Eng. Sci. 50,780 (2010).

[162] N.K. Naik, P.J. Shankar, V.R. Kanala, G. Ravikumar, J.R. Pothnis, H. Arya, *High strain rate mechanical behaviour of epoxy under compressive loading: Experimental and modelling studies*, published in Mat. Sci. Eng. A 528, 846 (2011)

[163] T. Jiao, R. Clifton, *Measurement of the response of an elastomer at pressures up to 9 GPa and strain rates of 105 to 106*, presented at the 18th International Conference of APS-SCCM, July 7th – 12th, 2013, Seattle, WA, USA

[164] A. Stickle, K.T. Ramesh, *Deformation response of rocky material for a range of stress states and strain rates*, presented at the 18th International Conference of APS-SCCM, July 7th – 12th, 2013, Seattle, WA, USA

[165] J. Wilgeroth, A. Khan, J. Balzer, *characterization of epoxy-based encapsulment*s, presented at the 18th International Conference of APS-SCCM, July 7th – 12th, 2013, Seattle, WA, USA

[166] J. R. Pothnis, G. Ravikumar, M. Joshi, K. Akella, S. Kumar, N.K. Naik, *High strain rate compressive behavior of epoxy LY 556: Radial constraint effect*, published in Materials Science and Engineering A 538 (2012) 210– 218

[167] J. Hooper, P. Smith, J. Hemmer, J. Read de alaniz, Brian Mason, J. Carney, *In situ polymer strain diagnostic using mechanochemical sensor molecules*, presented at the 18th International Conference of APS-SCCM, July 7th – 12th, 2013, Seattle, WA, USA

[168] P. V. Skripov, A. A. Starostin, and S. É. Puchinskis, *Heat Transfer and Thermal Fracture of Polymers in Pulsed Processes*, Doklady Physics, Vol. 45, No. 12, 2000, pp. 663–666, Translated from Doklady Akademii Nauk, Vol. 375, No. 5, 2000, pp. 615–618.

[169] K. V. Khishchenko, V. E. Fortov, I. V. Lomonosov, *Thermodynamic Properties and Physical–Chemical Transformations of Polymer Materials at High Temperatures and Pressures*, International Journal of Thermophysics, Vol. 23, No. 1, January 2002 (© 2002)

[170] B. E. Clements, *A continuum glassy polymer model applicable to dynamic loading* , J. Appl. Phys. 112, 083511 (2012); http://dx.doi.org/10.1063/1.4759015

[171] N. Taylor, D. Williamson, A. Jardine, *Thin film metal thermistors with microsecond time response for shock temperature measurement of polymer*, presented at the 18th International Conference of APS-SCCM, July 7th – 12th, 2013, Seattle, WA, USA

[172] S. A. Bordzilovskii, S. M. Karakhanov, K. V. Khishchenko, *Measurement of the Brightness Temperature of Shock-Compressed Epoxy Resin*, published in Combustion, Explosion, and Shock Waves, Vol. 49, No. 1, pp. 121–124, 2013, Original Russian Text S.A. Bordzilovskii, S.M. Karakhanov, K.V. Khishchenko

[173] J. Cognard, *Some recent progress in adhesion technology and science*, C. R. Chimie 9 (2006) 13–24

[174] G. Fourche, *An overview of the basic aspects of polymer adhesion, Part I: fundamentals*, published in Poly Eng Sci 1995; 35(12):957±67

[175] S. Yang, L. Gu, R. F. Gibson, *Nondestructive detection of weak joints in adhesively bonded composite structures*, published in Composite Structures 51 (2001) 63±71

[176] JJ. Bikerman, *The science of adhesive joints*, New York: Academic Press; 1961.

[177] P. Cognard, *Technical Characteristics and Testing Methods for Adhesives and Sealants*, Handbook of Adhesives and Sealants, 2005 Elsevier Ltd

[178] A. Roy, C. Mabru, J. L. Gacougnolle, P. Davies, *Damage Mechanisms in Composite/Composite Bonded Joints Under Static Tensile Loading*, published in Applied Composite Materials 4: 95–119, 1997

[179] P. Baur, A. Roy, P. Casari, D. Choqueuse, P. Davies, *Structural mechanical testing of a full-size adhesively bonded motorboat*, Proceedings of the Institution of Mechanical Engineers, Part M: Journal of Engineering for the Maritime Environment December 1, 2004 vol. 218 no. 4 259-265 doi: 10.1177/147509020421800405

[180] J.Y. Cognard, P. Davies, B. Gineste, L. Sohier, *Development of an improved adhesive test method for composite assembly design*, published in Composites Science and Technology 65 (2005) 359–368

[181] J.Y. Cognard, P. Davies, L. Sohier, R. Créac'hcadec, *A study of the non-linear behaviour of adhesively-bonded composite assemblies,* published in Composite Structures 76 (2006) 34–46

[182] P.Davies, L.Sohier, J.Y. Cognard, A.Bourmaud, D.Choqueuse, E.Rinnert, R.Créac'hcadec, *Influence of adhesive bondline thickness on joint strength*, International Journal of Adhesion & Adhesives 29 (2009) 724–736

[183] C. Badulescu, J.Y.Cognard, R.Créac'hcadec, P.Vedrine*, Analysis of the low temperature-dependent behaviour of a ductile adhesive under monotonic tensile/compression–shear loads*, International Journal of Adhesion & Adhesives 36(2012) 56–64

[184] D. Thevenet, R. Créac'hcadec, L.Sohier, J.Y.Cognard, *Experimental analysis of the behavior of adhesively bonded joints under tensile/compression–shear cyclic loadings*, International Journal of Adhesion & Adhesives 44 (2013) 15–25

[185] M. Bordes, P.Davies, J.-Y.Cognard, L.Sohier, V.Sauvant-Moynot, J.Galy, *Prediction of long term strength of adhesively bonded steel epoxy joints in sea water,* International Journal of Adhesion & Adhesives 29 (2009) 595–608

[186] J.Y. Cognard, L. Sohier, P. Davies, *A modified Arcan test to analyze the behavior of composites and their assemblies under out-of-plane loadings*, Composites: Part A 42 (2011) 111–121

[187] L. Sohier, J.Y. Cognard, P. Davies, *Analysis of the mechanical behaviour of adhesively bonded assemblies of composites under tensile–shear out-of-plane loads*, Composites: Part A 53 (2013) 65–74

[188] S. Austin, P. Robins, Y. Pan, *Shear bond testing of concrete repairs*, published in Cement and Concrete Research 29 (1999) 1067–1076

[189] S. Chataigner, J-F. Caron, K. Benzarti, M. Quiertant, C. Aubagnac, *Use of a single lap shear test to characterize composite-to-concrete or composite-to-steel bonded interfaces*, published in Construction and Building Materials 25 (2011) 468–478

[190] D. S. Santos, P. M.D. Santos, D. Dias-da-Costa, *Effect of surface preparation and bonding agent on the concrete-to-concrete interface strength*, published in Construction and Building Materials 37 (2012) 102–110

[191] G. Lawcock, L. Ye, Y-W. Mai, C-T. Sun, *the effect of adhesive bonding between aluminum and composite prepreg of the mechanical properties of carbon-fiber-reinforced metal polymer*, published in Composites Science and Technology 57 (1997) 35-45

[192] J-H. Kweon, J-W. Jung, T-H. Kim, J-H. Choi, D-H Kim, *Failure of carbon composite-to-aluminum joints with combined mechanical fastening and adhesive bonding*, published in Composite Structures 75 (2006) 192–198

[193] H. A. Al-Zubaidy, X-L. Zhao, R. Al-Mahaidi, *Dynamic bond strength between CFRP sheet and steel*, published in Composite Structures 94 (2012) 3258–3270

[194] H. Al-Zubaidy, R. Al-Mahaidi, X-L. Zhao, *Experimental investigation of bond characteristics between CFRP fabrics and steel plate joints under impact tensile loads*, published in Composite Structures 94 (2012) 510–518

[195] H. Al-Zubaidy, R. Al-Mahaidi, X-L. Zhao, *Mechanical characterisation of the dynamic tensile properties of CFRP sheet and adhesive at medium strain rates*, published in Composite Structures 96 (2013) 153–164.

[196] H-D. Yun, W-C. Choi, S-Y. Seo, *Acoustic emission activities and damage evaluation of reinforced concrete beams strengthened with CFRP sheets*, published in NDT&E International 43 (2010) 615–628, 2010

[197] M. Kempf, O. Skrabala, V. Altstädt, *Acoustic emission analysis for quantitative characterisation of the damage behaviour in fibre reinforced composites under static and dynamic loading*, presented at the 15th European Conference on Composite Materials (ECCM15), June 24th – 28th, 2012, Venice, Italy

[198] H. Zhang, D.Y. Li, *Determination of interfacial bonding strength using a cantilever bending method with in situ monitoring acoustic emission*, published in Surface and Coatings Technology 155 (2002) 190–194, 2002

[199] A.G. Magalhaesa, M.F.S.F. de Mourab, *Application of acoustic emission to study creep behaviour of composite bonded lap shear joints*, published in NDT&E International 38 (2005) 45–52, 2005

[200] Technical product information sheet, http://www.cemselectorguide.com/pdf/FM_300_081211.pdf

[201] D.N. Markatos, K.I. Tserpes, E. Rau, S. Markus, B. Ehrhart, Sp. Pantelakis, *The effects of manufacturing-induced and in-service related bonding quality reduction on the mode-I fracture toughness of composite bonded joints for aeronautical use*, published in Composites: Part B 45 (2013) 556–564

[202] D. N. Markatos, K. I. Tserpes, E. Rau, K. Brune, Sp. Pantelakis, *Degradation of Mode-I Fracture Toughness of CFRP Bonded Joints Due to Release Agent and Moisture Pre-Bond Contamination*, published in Journal of Adhesion, 2013

CHAPTER 2: EXPERIMENTAL TOOLS FOR INVESTIGATING THE COMPOSITE AND BONDED COMPOSITE UNDER DYNAMIC LOADING

Introduction **70**

1 Experimental shock sources **70**

1.1 1.1 Presentation of PPRIME 25 laser source 71
1.2 Research sources 73
1.3 Plate impact experiments 74
1.4 Summary 75

2 Time resolved measurements **75**

2.1 Velocity Interferometer System for Any Reflector (VISAR) 75
2.2 The Photonic Doppler Velocimetry (PDV) technique 79
2.3 Transverse observations 80
2.4 Table of the experimental configurations 83

3 Used post-mortem techniques **85**

3.1 Cross section micrographies 85
3.2 X-Ray radiography 86
3.3 Interferometric confocal microscopy 87
3.4 Ultrasounds and laser ultrasounds 88
3.5 Microstructure characterization by DSC 90

4 Summary on the used techniques **91**

References **92**

Introduction

In this chapter, the experimental devices used in this work are described, through collaborations which contributed to the experimental work. All the setups are sorted out in the way the experiments are performed for the shock investigations. The first step is to produce shocks. For that, shock sources should be used such as laser or plate impact. In the frame of ILP (Institut Laser Plasma, http://www.ilp.u-bordeaux1.fr), several laser sources are available. They all have different specificities which are described in the first section:

- LULI2000 and ELFIE laser source developed by the LULI laboratory (Laboratoire pour l'Utilisation des Laser Intenses, Polytechnique, Palaiseau), are research sources providing short pulses (respectively ns and fs) and high intensity levels.
- PPRIME laser source, more compact than the previous installation, this source is closer to industrial laser applications, and was the most used in this work.
- PIMM laser source (Laboratoire Procédés et Ingénierie en Mécanique et Matériaux, Art et Métiers, Paristech), operating a different set of laser parameters.
- Plate impact experiments by means of the gas gun available in ENSTA-Bretagne.

In order to monitor the shock experiments, time resolved techniques have been used and are also presented in a second time. They enable to monitor the shock experiments in order to measure the dynamic response of the material tested

- VISAR (Velocity Interferometer System for Any Reflector)
- PDV probe (Photonic Doppler Velocimetry), developed by the CEA-BIII
- Transverse visualization shadowgraphy also used thanks to the collaboration with CEA-BIII.

As a last step, the shocked samples can generally be recovered from the experimental shock chamber. Post-mortem techniques can be used to study the residual state of the shocked composite materials.

- Cross-section micrographies, X-Ray radiography, Interferometric confocal microscopy (ICM), Differential Scanning Calorimetry (DSC) and Dynamic Mechanical Analysis (DMA) available in PPRIME Institute
- Conventional ultrasounds and laser ultrasounds, developed by EADS Innovation Works (Suresnes and Technocampus EMC2, Nantes).

All these techniques were applied to study the damage resulting from the laser shock wave propagation as well as the corresponding residual deformations. The different post-mortem techniques provide complementary information helpful for correlating the damage to the irradiation intensity. At the chapter's end, a synthesis of all the diagnostics is given, showing the advantages and disadvantages of each technique.

1 Experimental shock sources

Laser sources are already available in the industry. These lasers are developed and sold by companies such as Quantel, Continumm, or Thalès and could easily be transferred to industry for applications such as Laser shock adhesion test. For example, this is the case of GAIA sources developed by Thalès, and currently through assembly-line production. The LSP Technology laser source already presented in the first Chapter is also in this category, even if it has been through development before that. In

this work, the laser settled in PIMM (Art et Métiers, Paris Tech), named Pimm-LASAT, has been used. This laser, developed and produced by Continumm can also be considered as an industrial source. Indeed, this laser is really compact, it fits in one room, fully equipped with different diagnosis setups and an automatic translation table is available, which enables to switch faster from one shock to the following. Moreover, it has been used for the previous development of the LASAT technique, for which it was really well adapted to coated system and thermal barrier. It delivers up to 1.5 J, in the 532 nm wavelength and with 10 ns pulse duration. Focus spots from 1 to 2 mm are generally used to reach intensities high enough to perform the test. These industrial lasers are the future of laser application to industry. A proof of that could be the recent acquisition of HEPHAISTOS source made by the PIMM, provided by Thalès, and which will push forward the development of industrial applications based on laser. Nevertheless, other sources are still necessary for the development of these technologies. These sources can be considered as research sources. When an industrial laser source is generally developed with specific parameters for specific applications, research sources enable to investigate different parameters in some cases may be more adapted to the technique developed. Especially in terms of energy and pulse duration, research sources can provide different ranges not available on commercial lasers and thus give more flexibility to development. This is the case of the laser source used in PPRIME (PPRIME 25) and developed by Quantel. This laser remains relatively compact, and could be considered as the frontier between the industry and the laboratory. It is presented in section 1.1. Other sources only dedicated to research should also be used for the same reasons. Each of these laser sources is unique and developed by laboratories for research application. In this category, there are of course the biggest laser sources such as LMJ (Laser Mega Joule) or NIF (National Ignition Facility) but also smaller ones such as the ones developed in LULI (Laboratoire pour l'Utilisation des Laser Intenses, Polytechnique, Palaiseau). In this laboratory, two laser sources named LULI2000 and ELFIE were used. These two lasers are presented in section 1.2. Finally, shock can also be produced using plate impacts (ENSTA Bretagne, Brest, France). The pressure load is different but the results for the target are similar. In this work, plate impact was used in order to demonstrate the optimization possibilities of the LASAT technique. Therefore, the experimental setup used in this work is also presented in section 1.3. In the last section 1.4, a summary of all these shock source characteristics is given.

1.1 1.1 Presentation of PPRIME 25 laser source

The laser source available in PPRIME Institut (PPRIME 25J) has been the most used source in this work and is presented in Figure 2.1. It delivers up to 20 J in a 1053 nm wavelength, and with average pulse duration of 30 ns, full width medium height of a Gaussian pulse. The focal diameter generally used on target is about 4 mm, which enable to load until 5 GW/cm². This intensity level prevent from using a vacuum chamber because it is far enough from the breakdown intensity in air. In order to drive significant shock pressure, a water confinement is also generally used [1-4]. This laser experimental facility is laid out in three parts, which correspond to three different rooms supervised by a command room. The first room is the command control. It is where the laser oscillator and amplifiers are turned on and off. The shot order is sent from here after the loading sequence (see in Figure 2.1, a). The laser itself is placed in a second room with the capacitors racks supplying the flash lamps (see in Figure 2.1, b). This laser was developed by Quantel 30 years ago. It is made of a laser cavity which generates a Gaussian pulse of 30 ns in average, measured by a high speed photodiode. It is then amplified by two linear amplifiers Φ12 and Φ25, classically made of flash lamps and laser rods. The beam reaches 20 J and has a 25 mm diameter. It goes out from the laser side, orthogonally to the amplifiers axis and leaves the room for the experimental room. There, the laser beam goes

first through an optical density rack. Densities placed on the beam path are calibrated and used to reduce the beam energy. In this way, different loads can be applied on the targets. After the rack, the laser beam is guided toward the target by two mirrors placed at 45° (see in Figure 2.1, c). The first mirror reflects in fact only 99 % of the beam, which enables to measure the beam energy on the first laser axis with a calibrated Gentek. A second photodiode is also placed here to trigger the scope and the diagnostic if need be. Finally, the beam is focalized on target after the second mirror using a convergent lens. Note a He-Ne small laser is placed in the optical path of the high power laser to perform the beam alignment.

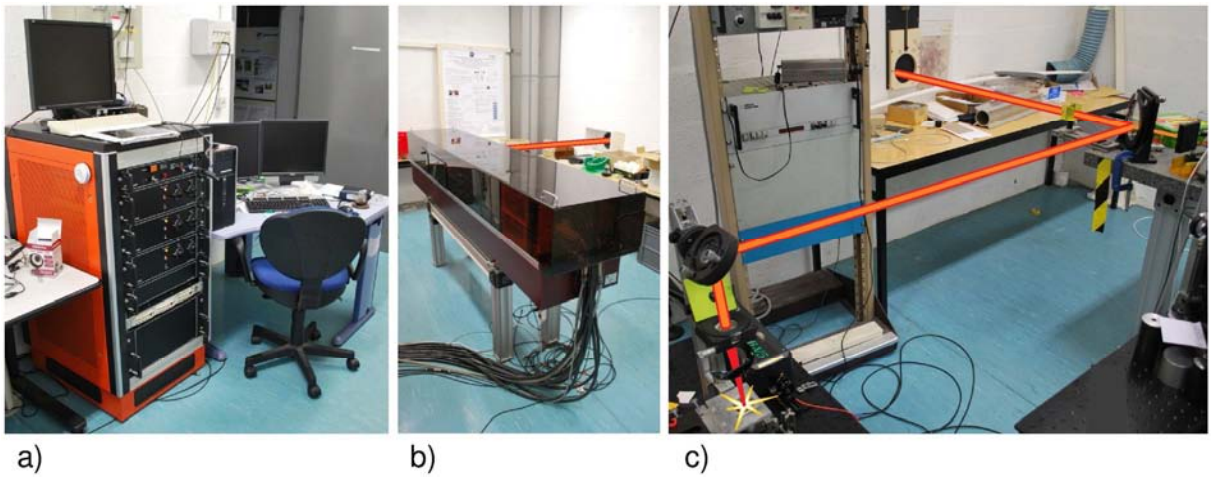

Figure 2.1 PPRIME 25J laser source, a) Command room, with the laser shot button, b) Laser room, where the laser itself is placed, c) Experimental room, where the laser is focalized to generate shocks

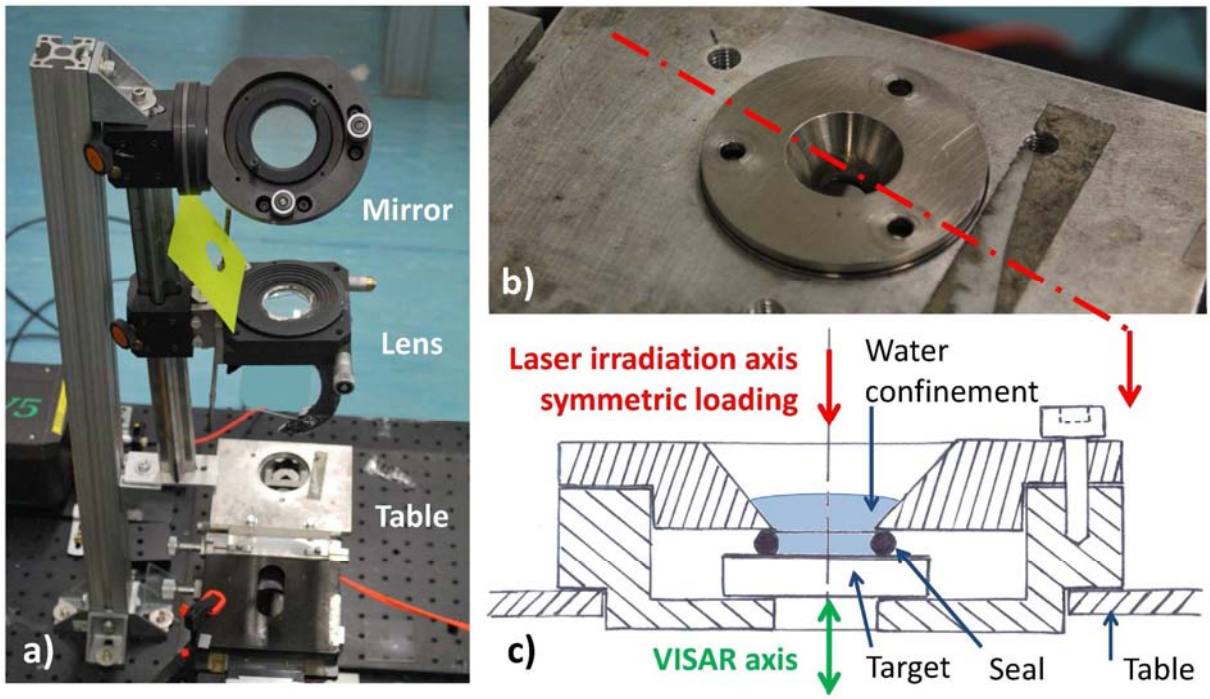

Figure 2.2 PPRIME 25J – close look to the on-target configuration, a) Focalization step by the convergent lens , b) Sample carrier aligned with the laser beam on a three axes translation table, c) Sketch of a target carrier cross section in VISAR experiment configuration

Since the powerful irradiation can be reflected once focalized on target, a small tilt angle of the beam axis was setup to avoid the beam going backward. After the lens, a protective glass was also added to prevent water from splashing on the critical optic parts (see in Figure 2.2, a). The target is generally placed in a target holder, mounted on a translation table (see in Figure 2.2, b). This table can move along the three axes, which enables to align the sample on the laser beam, and to adjust the focusing by moving up and down (see in Figure 2.2, a). The sample holder was designed for shock experiments especially (see in Figure 2.2, c). Indeed, the sample back face is let free to enable the shock wave reflection, and thus the tension loading. This back face hole, aligned with the front face hole, also enables the back face velocity measurement by VISAR. Water confinement can easily be added by using a seal as shown in Figure 2.2, c.

1.2 Research sources

Research sources are really different from the small industrial lasers. Indeed, when a few rooms are needed for these lasers, research sources require one or several buildings. The reason is of course the energy level which is much higher (1000 J for LULI2000) or the pulse duration which is much smaller (300 fs for ELFIE). The beam intensities are huge and require particular care. The number of optic to use is increased, the optics should be thicker, and it also requires the use of vacuum control lines. These facilities are run by several teams in charge of the different parts of the laser sources (optics, electronics, mechanics, fluids…). For giving an example, a picture of a LULI2000 vacuum experimental chamber is presented in Figure 2.3, a). It is quite challenging to enable the use of several diagnostics at the same time. Indeed, on this kind of facility, the operating rate is of one shot every (for LULI2000) or 20 minutes (for ELFIE). Therefore, each shock is monitored with as many diagnostics as possible. The beam lines of LULI2000 and the amplifiers of ELFIE source are also presented in Figure 2.3, b) and c) respectively. These sources are more and more equipped with self-automatic settings and controls, leading to complex command room (see in Figure 2.3, d). LULI2000 and ELFIE sources have different characteristics

- LULI2000: Two independent beams up to 1 kJ each are available. The wavelength used is 1053 nm, and the pulse duration is tunable between 0.6 ns and 5 ns (generally set to 3 ns in our case). The temporal profile is square. Laser beams can be dispatched in two experimental rooms can be supplied equipped with an experimental chamber.
- ELFIE: Three different beams can be provided in the short pulse range (femtosecond). The one used in this work can reach 10J, and is 300 fs wide. The wavelength is 1057 nm. The intensities in stake also require vacuum that is why the beam is delivered in a vacuum chamber, including the last compression stage of the facility.

In this work, these two lasers have been used especially for the investigation of shock propagation into epoxy targets. The reliability of these facilities, in addition to the used intensity levels were ones of the reasons for that.

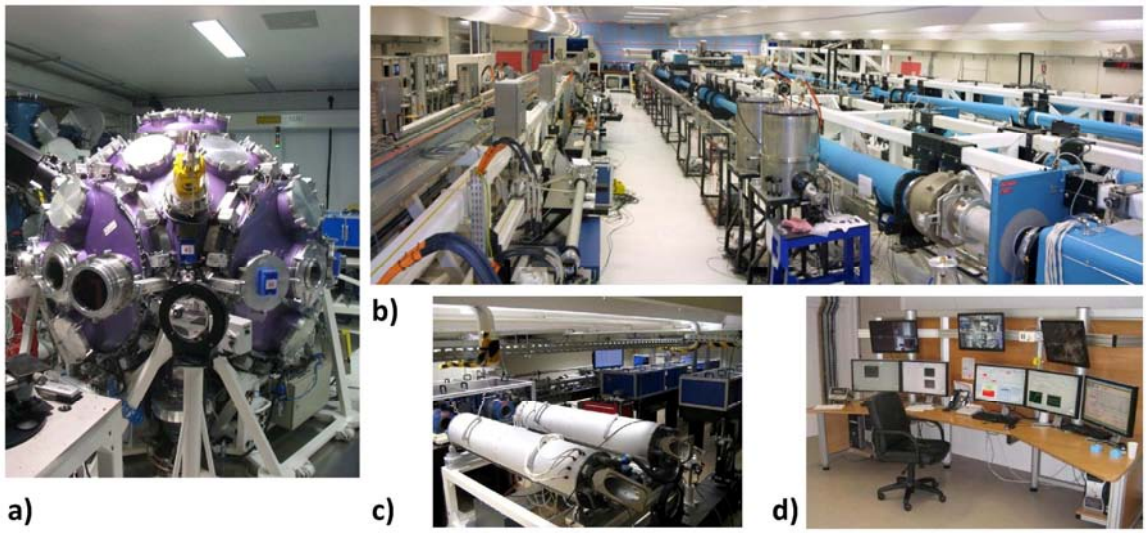

*Figure 2.3 LULI experimental sources [5], **a)** Picture of one of the LULI2000 laser source experimental chamber (MILKA), **b)** Picture of the laser hall of the LULI2000 laser source, **c)** Picture of ELFIE laser source amplifiers, **d)** Picture of ELFIE command control room*

1.3 Plate impact experiments

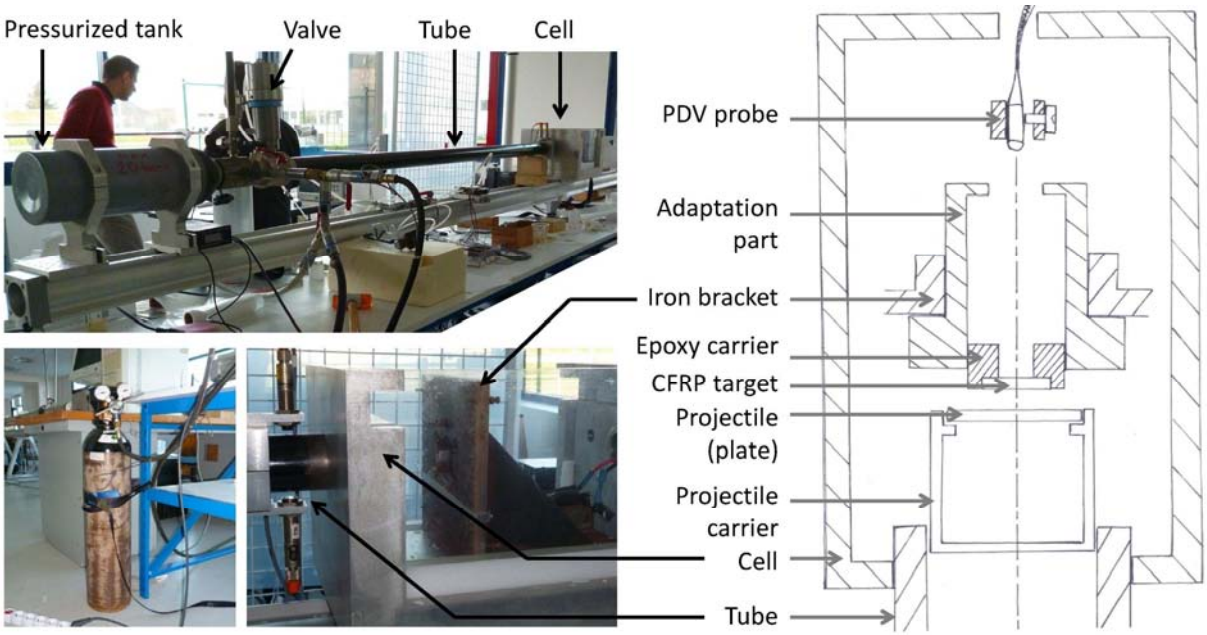

Figure 2.4 Experimental plate impact configuration - Picture of the gas gun used for the plate impact experiment on composite, and associated element such as pressure bottle and experimental cell (left), sketch of the cell experimental configuration (right)

Shocks can also be generated using plate impacts. In that case, the projectile nature and velocity determine the induced pressure on the Hugoniot curve. The faster the projectile, the higher the pressure. In this work, plate impacts were not used to study ballistic impact and perforation, but in a complementary range of durations longer than the laser shock ones. Therefore, a small gas gun can be used like the one set up in ENSTA Bretagne (see in Figure 2.4). This experimental device enables to send projectiles on target with a velocity up to 100 m/s. For that, a pressure bottle is used to fill a pressure tank up to 20 bars, which is then released in a tube by a valve, thus pushing the projectile. The projectile is composed of two parts: the projectile carrier made of delrin (averagely 15 g) and the plate whose mass can vary from 3 to 10 g, depending on the plate thickness (see in Figure 2.4). Note

that in this work, only aluminum has been used for the plate. The tube in which the projectile accelerates is 2 m long. At the end, two barrier photodiodes spaced by 71 mm are used to calculate the projectile velocity just before impact. The projectile then reaches the experimental cell, in which the target is locked. In order to adapt the already existing iron bracket, a part has been designed to hold the composite material. Each composite target is then placed in an epoxy carrier to be held in the adaptation part (see in Figure 2.4). This way, the coaxiality between the tube, the impact axis, the target and the back face velocity measurement set up behind the iron bracket is respected.

1.4 Summary

The shock sources presented in this first section are summarized up in Table 2.1 with their main characteristics. The diagnostics used on these experimental setups in this work are also given. These monitoring techniques are described in the next section.

			Main characteristics				Associated diagnostics
	Shock source	**Laboratories**	**Wavelengths**	**Pulse duration**	**Energy (J)**	**Repetition rate**	
LASER	LULI 200	LULI (Polytechnique, Palaiseau)	1053 nm	3 ns	1000 J	1 shot/ 60 min	VISAR, PDV, Transverse visualization
	ELFIE	LULI (Polytechnique, Palaiseau)	1057 nm	300 fs	0 - 10 J	1 shot/ 20 min	VISAR, PDV, Transverse visualization
	PPRIME 25J	PPRIME (Poitiers)	1053 nm	30 ns	0 - 20 J	1 shot/ 5 min	VISAR
	Pimm-LASAT	PIMM (Art et Métier Paris Tech, Paris)	532 nm	10 ns	0 - 1.5 J	10 shots/ s	VISAR
Plate impacts			**Pressure**	**Velocity**	**Kinetic energy**	**Repetition rate**	
	Gas gun	ENSTA Bretagne (Brest)	0 - 20 bar	0 - 100 m/s	~ 125 J	1 impact/ 20 min	VISAR, PDV, Transverse visualization

Table 2.1 Summary of the shock sources used in this work, with their main characteristics

2 Time resolved measurements

Three time resolved measurements techniques were used in this work. The first two deal with the back face velocity measurement. This experimental data is quite important for the shock wave propagation history understanding, and consequently for LASAT technique. The last one is used to observe the phenomenon in order to obtain more qualitative data, also important for the phenomena understanding.

2.1 Velocity Interferometer System for Any Reflector (VISAR)

As previously explained, the back face velocity measurement is probably one of the most important data to get during a shock experiment. Indeed, the particle velocity is connected to the stress history. Non-intrusive measurement of the back face history reflects the dynamic response of the material after shock propagation, including the signature of possible events occurring such as phase changes,

anisotropy effects or damage. Therefore, it enables to discriminate an unharmed sample from a spallation process during the shock experiment. In case of spallation, the measurement can give an idea of the tensile stress level which leads to damage. In order to obtain this data, VISAR (Velocity Interferometer System for Any Reflector) has been widely used in shock research. It is particularly interesting for its fast time response, well adapted to the shock experiments [6-8]. The velocity measurement is based on the Doppler Effect. Indeed, the wavelength emitted or reflected from a moving object depends on the object velocity. In the case presented here, the target to measure is irradiated with a continuous laser (Verdi, 5 W, λ_0 nm). The reflected light wavelength $\lambda(t)$ coming back from the sample back face depends on the sample velocity and is analyzed thanks to an optical interferometer. For that, the reflected signal is divided in two path, one being delayed from the other one, in order to produce Interferometric fringe correlated to the back face velocity .

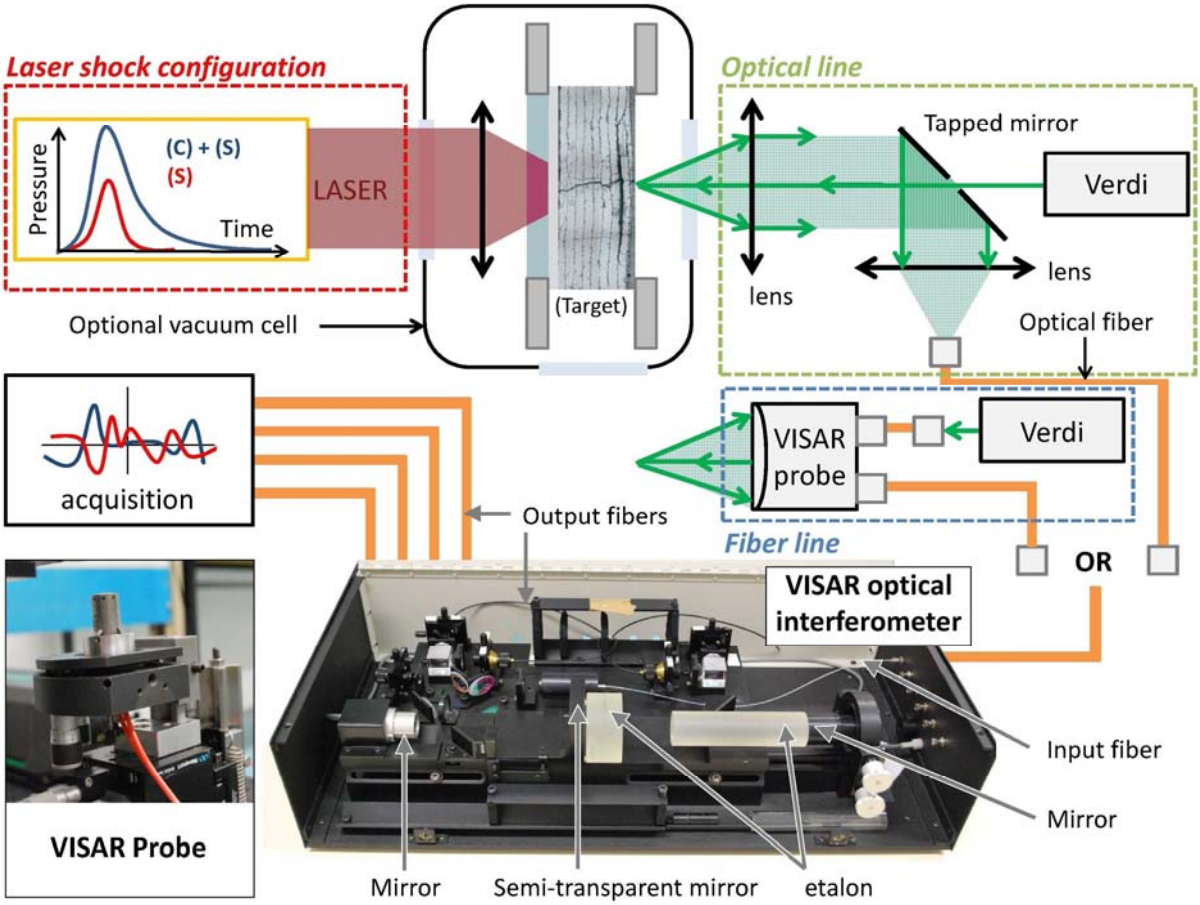

Figure 2.5 Sketch of the two VISAR practical setups: the optical line and the fiber line - Picture of the VALYN VISAR interferometer; and the barker probe used to irradiate the target and collect the reflected light

Practically, it exists two ways to set up what is named the optical part of the VISAR. It enables to irradiate the target and to collect the reflected light (see in Figure 2.5). The more commonly used is an auto-collimated optical line. The continuous laser irradiates the target through a drilled mirror. The reflected light is collected thanks to an achromatic lens which parallelizes the beam toward the drilled mirror. This mirror reflects the beam until another achromatic lens which focuses the light in a fiber connected to the optical interferometer. The second solution is to use a Barker probe [9]. This probe integrates in fact directly this optical arrangement in one small cylinder. The continuous laser is driven until the probe head by a fiber. The reflected light is directly collected by the lens present at the probe surface, and focused on a second fiber, this one being connected to the interferometer. This configuration is named the fiber line, or the probe line (see the probe picture in Figure 2.5). Both

systems have their own advantages. The Barker probe is easy to implement since no optics have to be adjusted, but it requires well reflecting surfaces because of the small diameter of the probe optic. Fully optical system requires less intensity, but the focus on the target is smaller. The adjustments are also longer and sometime more complex. These differences between the two systems are in fact directly linked to the VISAR use in case of composite materials. Indeed, VISAR experiments cannot be performed on composite materials the same way as on metals. The main reason is that composite materials have a strong absortivity to the Verdi wavelength, especially fiber carbon. Moreover, they are more sensitive than the metal to thermal loading coming along with the continuous laser irradiation. With metals, which reflect light, the Verdi can be used up to 2 W without any problem, when 0.5 W is already problematic for composite materials. These two issues are in contradiction. Indeed, to get rid of the low composite reflectivity, one could increase the Verdi intensity in order to have more reflected light. On the other hand, in order to avoid thermal degradation of the composite during the adjustments prior to the shot, and during the shoot, low Verdi intensity should be used. Note also that Verdi longitudinal mode instabilities were observed for intensities lower than 1 W. All these experimental issues were partially solved using two rules of thumb.

- Regarding the Verdi issue, the use of VISAR Barker probe helps a lot. First, the incident light is driven by a fiber instead of being directly sent on target by air. The fiber which is at least 2 m long can strongly reduce the Verdi intensity until the probe and thus the target. That way, the Verdi power can be set close to 1W to avoid instabilities as much as possible, and the target will not be irradiated with 1 W. Moreover, the Barker's probe focuses less the Verdi light than an optical lens, which make the focus spot wider on the target and thus reduces once again the input intensity.

- Considering the composite reflection issue, two preparation protocols were used. In each case, the composite back face should be polished. Indeed, due to the curing process of CFRP, the cured parts usually present a thin epoxy layer on each surface, with a strong roughness. It can be due to the drainage fabric or the peel-ply used. In any case, this is not helping for the composite reflectivity. Therefore, the samples are polished to remove this layer, and to reach the carbon fiber, which are much more reflecting once polished. Nevertheless, the polishing should not be too good. In that case a small back face deformation will lead to the reflected beam loss (mirror polishing). Finally, aluminum painting was used to enhance the global back face reflectivity. The amount of painting deposited on the target should be low enough to avoid the creation of an additional layer. An additional layer would be subjected to spallation. This technique was used especially for composite below the damage threshold. Above the damage threshold, the painting could be ejected, so a better polishing is applied, knowing that the signal will be lost sooner anyway.

After the post-treatment on the lissajou curve, and noise reduction of the signal, back face velocity curve can be obtained such as the ones presented in Figure 2.6. These two measurements have been chosen to show the difference between a shock inducing damage (spallation) and a shock leaving the sample unharmed. They have been obtained on T800/M21 CFRP targets (500 µm thick). In case of the red shock, no damage occurred. Indeed, first peak observable close to t = 200 ns corresponds to the shock wave breaking out. This leads to the back face acceleration until 100 m/s which correspond to the free surface velocity in this case. The velocity starts then to decrease, denoting the breaking-out of the release waves. 400 ns later, a second peak can be observed on the red curve, corresponding to the back and forth of the shock in 1 mm. The wave velocity is thus about 2500 m/s, which corresponds to the composite sound speed properties (see in Chapter 1). Consequently, this

back face velocity proves that the sample has not been fractured by the shock wave propagation because the waves can go through the whole composite thickness. On the contrary, the blue curve clearly indicates that the damage has occurred in the composite target in the second case. Indeed, the shock breaks out close to 200 ns. The pressure being higher, the free surface velocity is also more important (about 350 m/s). After the shock, the release also breaks out and then the velocity profile flattens to reach an asympthotic velocity. As explained in Chapter 1, this is a clear sign of spallation. According to shock theory, this signal can also be used to quantify the tensile rupture stresses using equation 2.1 and the measured ΔU (see in Figure 2.6).

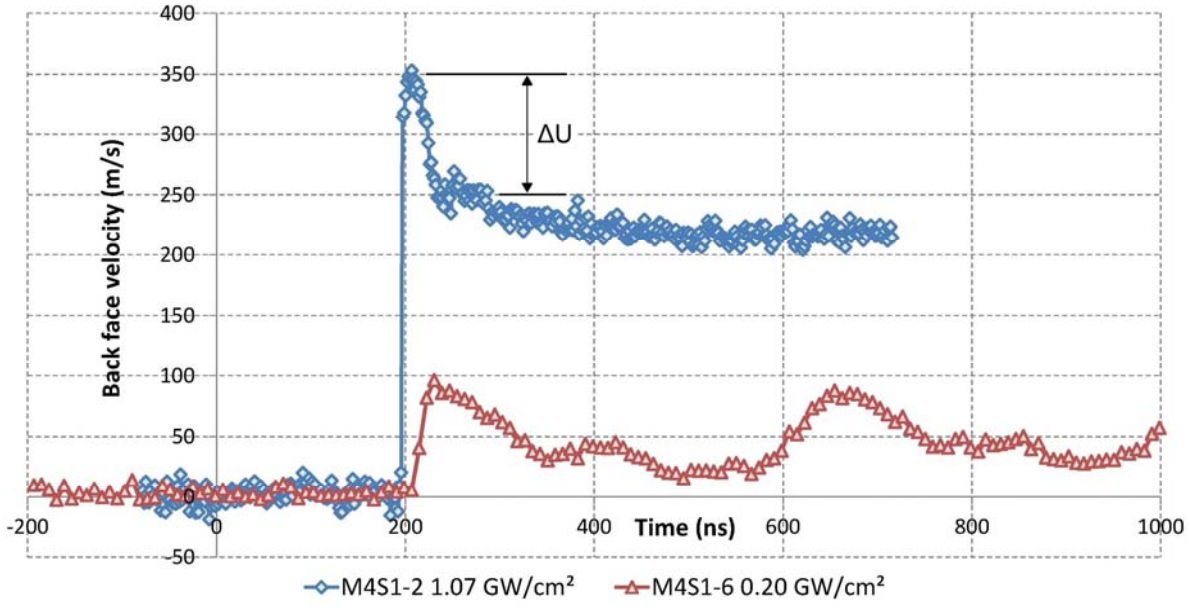

Figure 2.6 Examples of back face velocity measurements performed using Valyn VISAR on unidirectional T800/M21 CFRP targets, in case of spallation in blue curve (water confined laser shock, 1.07 GW/cm²) and without damage in red curve (same conditions, 0.20 GW/cm²)

$$\sigma_R = \frac{1}{2} \cdot \rho_0 \cdot c_0 \cdot \Delta U \qquad where \quad \begin{cases} \rho_0 : \text{initial density} \\ c_0 : \text{sound speed in the material} \end{cases} \tag{2.1}$$

The use of VISAR is thus very helpful to characterize the dynamic response of materials. Thanks to these measurements, it is interesting to evaluate damage threshold of the tested material by comparing the signal with and without damage.

2.2 The Photonic Doppler Velocimetry (PDV) technique

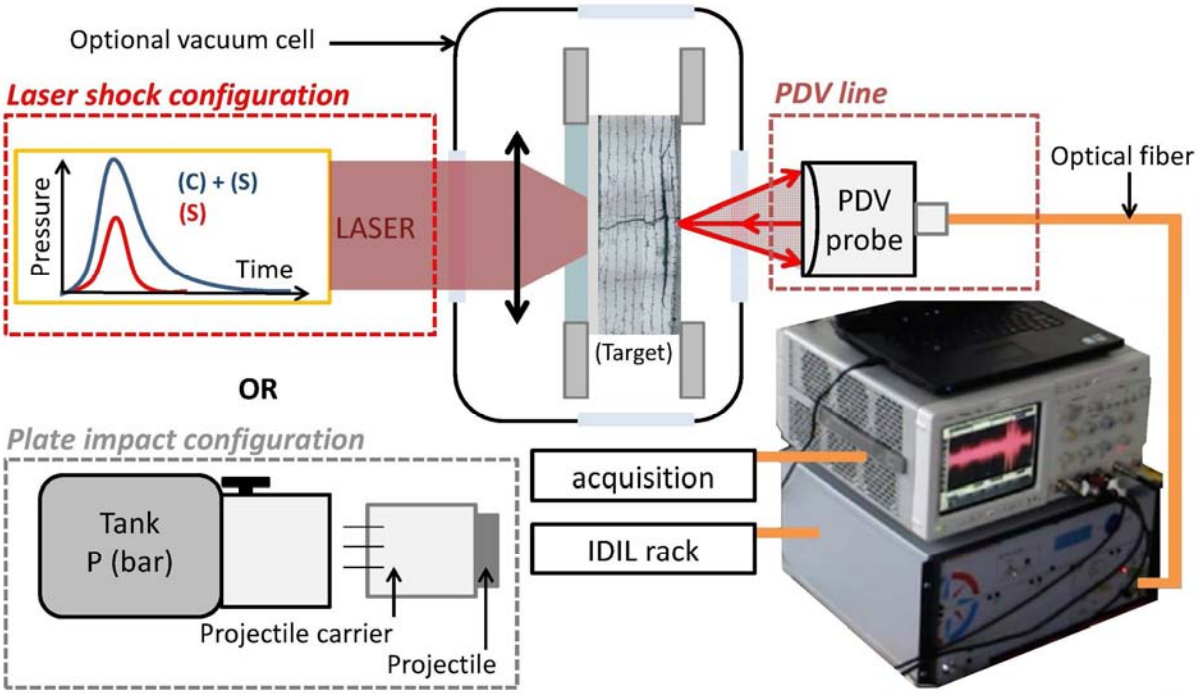

Figure 2.7 Sketch of the two PDV practical setups in laser shock or plate impact configurations

PDV probes are an alternative to VISAR when it comes to the back face velocity measurement (see in Figure 2.7). The main difference with the VISAR is that these probes enable the measurement of several different velocities by using a frequency analysis of the recorded signals. This is possible thanks to the use of wide bandwidth detectors (from 50 KHz to 12 GHz) coupled with high capacities oscilloscope (12 GHz, 50 Gpt/s). The system used in this work has been first developed by P. Mercier, J. Benier, and P.-A. Frugier from CEA (Arpajon, France), especially for shock applications [10-15]. The PhD of D. Loison recently demonstrated the interest of PDV probes in case of micro spallation and micro jetting processes [16]. The technology has been transferred to IDIL (www.idil.fr), a company in charge of its commercialization and its application to industry. In this work, the last PDV system release (IDIL rack 1550 nm) was tested in order to evaluate its efficiency for composite application. The system tested is presented in Figure 2.8. It is made of two lasers. The first one is used for the measurement. It is sent on the target through an optical fiber and a head probe including the focusing lens. The used wavelength is generally close to 1550 nm. Due to the target motion, the reflected wavelength is shifted until a frequency f_d (see in Figure 2.8). The reflected signal is sent back on a detector through another fiber. The detector also receives the measurement laser initial frequency f_m and the reference frequency f_r coming from the second laser (same wavelength range). Interferences are made with the signal coming from this reference laser contrary to the VISAR for which the interferences are made using only the reflected beam. Other systems use the f_m frequency, but by using this reference frequency f_r, the velocity measuring range can be wider in the limit of the detector bandwidth. A frequency analysis is then performed on the recorded signal. In that case, it is made by a software named VaHiné developed by P.-A. Frugier [13]. Since the velocities measured can change with the time, the frequency analysis has to be done on small parts along the whole frequency spectra in order to get this evolution. The software thus enables to change the discretization width as well as the sliding steps. These two parameters influence respectively the velocity uncertainties, and the temporal resolution. A compromise has often to be chosen. An example of calculation is given in Figure 2.8. The spectrogram presented in the Figure is the

calculated back face velocity extracted from the PDV data. It is a plate impact experiment on a 3 mm CFRP target. In that case, only one velocity has been measured and extracted by the software. Indeed, in this experiment, no debris was produced. Therefore, the PDV probe only measures the sample back face velocity. It can also be noticed that the signal is not starting from 0. This is due to the choice of the pivot frequency which gives a constant velocity on the spectrogram. It has to be marked to be taken into account when extracting the velocity.

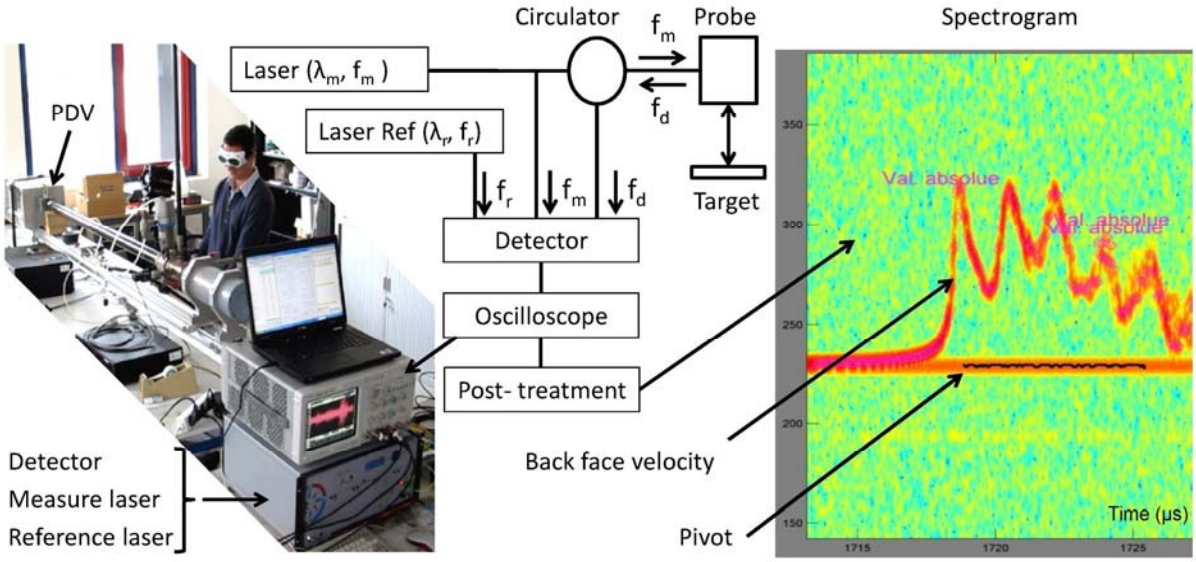

Figure 2.8 PDV technique explained in a few images (from left to right): practical setup on gaz gun applications, sketch of the technique principle, and spectrogram resulting from the frequency analysis on composite

From the literature, it can be concluded that PDV probes are particularly well adapted to shock investigations with high speed (km/s) and multi-velocity phenomenon [10-16]. From this point of view, the PDV probes are less adapted than VISAR for the laser shock on composite application as defined here. In particular, the small free surface velocities in the range [0-100 m/s] are harder to get with a high enough resolution. In the literature case, one of the PDV advantages is also the long recording time, but that becomes an inconvenient on thin targets because the temporal resolution is not high enough. Despite these small disadvantages, the use of PDV probe has also several advantages. First of all, it is a really compact system (see in Figure 2.8). The two lasers and the detector are in the same rack, directly connected to the oscilloscope. Only the probe, with its two fibers, has to be plug in. This is quite different from the VISAR setting up. The adjustments on target are also easier, simply because there are less things to adjust. Indeed, the interferences have not to be manually found as it is the case in VISAR, which saves time. The last point is specific to composite. Indeed, thanks to the wavelength used, the detector bandwidth and the spectral analysis, the light irradiation of the target is much less intense than in case of VISAR (200 mJ) for an equivalent reflection quality. Thus, the composite is not easily degraded as it is the case with the use of Verdi. All these advantages would open the way of an easier implementation of PDV rather than VISAR in an industrial environment.

2.3 Transverse observations

Two different transverse visualization systems were used in this work: the one on gas gun, and the one on laser installations. In both case, it is added on the loading axis orthogonal direction, which generally enables to be used jointly with back face velocity measurement. For this last technique, a flash lamp is placed on one side of the target and faces the camera set-up on the opposite side. For

plate impact experiments in the range [0 – 100 m/s], the phenomena are long enough (several milliseconds) to enable the use of only one camera and to record movies. The flash lamp can be turned on before the experiments. For that reasons, this diagnostic is not really complicated to set up. A spot light, diffused by a white plastic plate, provides enough light to enable observation by ombroscopy. The camera is triggered by the scope recording the photo diodes signals, and the impact timing. The data generated is generally used in order to control the projectile impact. As an example, three snapshot extracted from one recorded movie of a plate impact is given in Figure 2.9.

*Figure 2.9 Snapshot of a plate impact experiment, **a)** Projectile is leaving the gas gun tube, **b)** Impact has occurred, the projectile carrier crashes, **c)** After impact, the debris continue to fly in the experimental cell.*

For laser experiments, the phenomena are so fast that the high speed camera can only take one well-resolute picture (few microseconds). In order to have several images of the same laser experiment, several cameras have to be added. For that, the beam containing the images is divided using beam splitters (see in Figure 2.10). The flash lamp should also be really powerful, and is generally synchronized with the laser beam. Transverse visualization was used for two goals. The first one is the observation of thin composite target dynamic spallation for a comparative study. The second one is the investigation of shock propagation into epoxy targets. For this second application, two main configurations presented in Figure 2.10 were defined and used on both LULI2000 and ELFIE sources. They are both based on shadowgraphy principle and the first one is a classic configuration (see Figure 2.10) [16-17]. The shock wave propagation induces local physical properties changes in the material. These modifications lead to a variation of its optical properties [18-19]. In particular, when the density increases, the light is deflected. Therefore, the compression due to the shock is yielding by a contrast difference between the loaded and the unloaded zones. Consequently, the shock wave propagation observation is possible [20]. Epoxy samples present two polished edges perpendicular to the observation axis (see in Figure 2.10). Thus, one polished edge is placed in front of a high power flash lamp (Balcar Starflash 3) which provides white light (400 to 700 nm) during the laser experiment. The other one is let free to be observed with a camera acquisition system. The camera can take a picture of the sample while the laser shock is propagating within the sample. With the set-up used, the camera can picture phenomena happening inside the epoxy sample. In this case, the focus was made in the middle of each sample, and the exposure time was 3 ns. Three DICAM pro cameras are used on the same optical axis. The whole observation system (flash and cameras) is fully synchronized with the laser shock timing which is perfectly known. The three cameras can be delayed independently of each other to picture three different instants of the shock wave propagation.

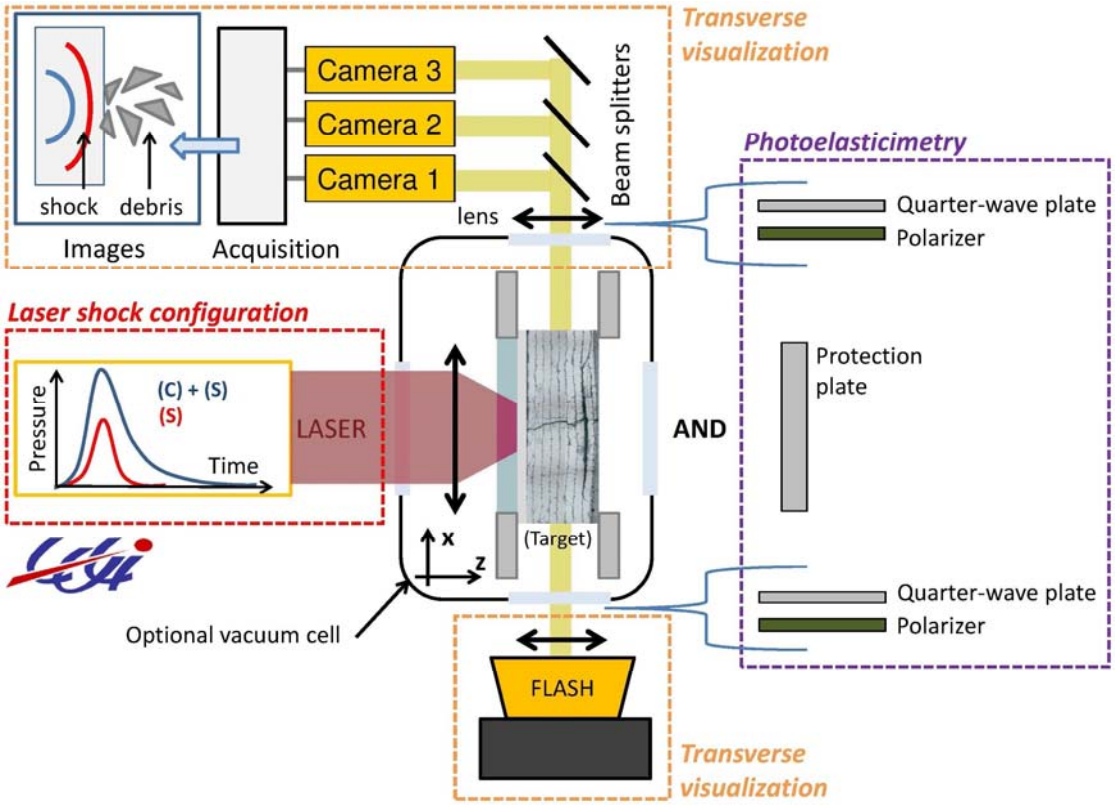

Figure 2.10 Configurations of the transverse visualizations: configuration for classical shadowgraphy observations and using crossed polarizers for photoelasticimetry shadowgraphy observations

The second configuration is just an adaptation of this classic configuration (see in Figure 2.10, b). Indeed, epoxies are bi-refringent material. Therefore, the use of a time resolved photo-elasticimetry technique can provide information on the stress relaxation during the shock wave propagation. This is quite interesting to understand the wave propagation phenomenon in these materials. For that, two circular polarisers are placed on each side of the vacuum experimental chamber (see in Figure 2.10, b). These polarisers are made of linear polarizer coupled with a quarter-wave plate. They have been chosen to visualize only the isochromatic fringes, which are a direct image of the stresses gradient [21-24]. They were oriented to perform the observations in both dark field (parallel polarizer) and clear field (orthogonal polarizer) with polychromatic and monochromatic light (0.542 ± 0,003 µm wavelengths). The sample is lightened on one side by the flash, and observed on the opposite side by the camera. In the monochromatic case and assuming that behaviour is elastic, the difference between main stresses σ_1 and σ_2 can be described by equation (2.2), where k is referring to the fringe order. Except for this parameter which depends on the observations, the other parameters are well known, and a calculation can be performed [21-24]. In the following numerical calculation, the photoelastic constant has been chosen equal to 55.10^{-12} Pa^{-1}.

$$\sigma_1 - \sigma_2 = \frac{k\lambda}{Ce} \quad with \quad \begin{cases} k : \text{fringe order} \\ \lambda : \text{filter wavelength} \\ C : \text{Photoelastic constant} \\ e : \text{thickness} \end{cases} \tag{2.2}$$

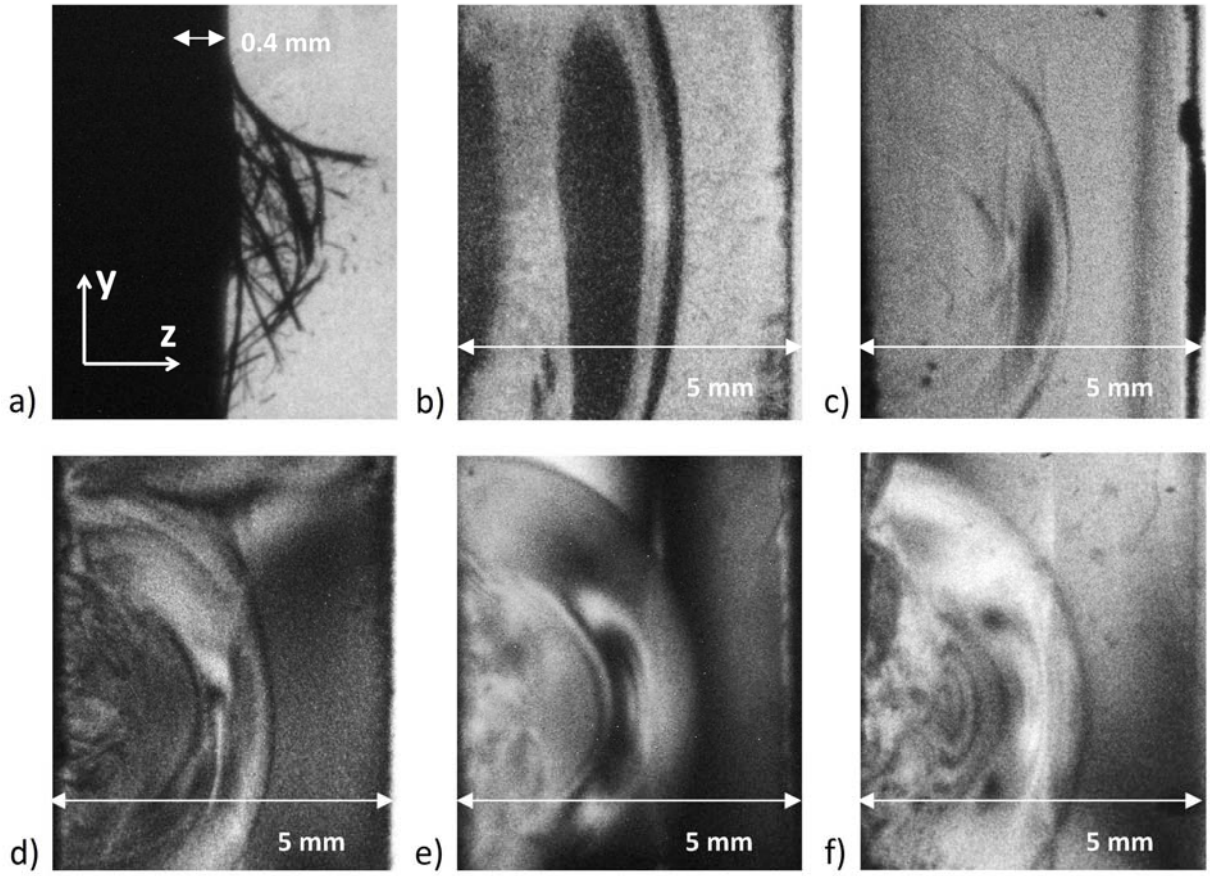

Figure 2.11 Snapshots obtained in each different transverse visualization configuration, ***a)*** *Observation of spallation process on a CFRP target (ELFIE, I = 0.30 PW/cm², t = 4µs),* ***b)*** *Observation of a shock wave propagation into an epoxy target by shadowgraphy (LULI2000, I = 3.15 TW/cm², t = 1µs),* ***c)*** *shock wave propagation into an epoxy target by shadowgraphy (ELFIE, I = 0.60 PW/cm², t = 1µs),* ***d)*** *shock wave propagation into an epoxy target by polarized shadowgraphy in clear field (ELFIE, I = 0.57 PW/cm², t = 1µs),* ***e)*** *shock wave propagation into an epoxy target by polarized shadowgraphy in dark field (ELFIE, I = 2.38 PW/cm², t = 1µs),* ***f)*** *shock wave propagation into an epoxy target by polarized shadowgraphy in monochromatic clear field (ELFIE, I = 2.56 PW/cm², t = 1µs)*

Finally, for two main transverse visualization experimental setups on the laser application, 6 different configurations were used. Snapshots are shown in Figure 2.11 to illustrate these different configurations. The Figures 2.11 a) b) and c) come from a classic ombroscopy configuration respectively for composite and epoxy investigations on both LULI2000 and ELFIE installations. The three other snapshots were taken under photoelasticimetry observation. The images d) and e are respectively from clear and dark field with polychromatic light. The last snapshot was obtained in monochromatic clear field.

2.4 Table of the experimental configurations

A short summary of the previous information is given here. For shock investigations, the central point is the material to test. On the front face of this material, pressure can be applied by laser irradiation. Depending on the laser source used, this target can be placed or not in a vacuum chamber. If no vacuum chamber is used, then a confinement layer is added to increase the induced pressure. In case of plate impact, no vacuum chamber is required but an experimental cell is generally set up to protect operators from debris. For the time resolved measurements, two axes are generally available. The first one is the loading axis direction, generally used for measuring the back face velocity. Two techniques based on optical interferometry can be used: PDV and VISAR, itself available

in optical line or fiber line. The second axis is the loading axis orthogonal direction, on which transverse visualization systems can be added. All the experimental configurations used in this work are synthesized in the Table 2.2. The configuration are named, and given with the used shock sources, diagnostic and investigation aims. In the following sections, the experimental configurations used will be referring to this table.

Experimental configuration names	**Shock source**	**Time resolved diagnostic**	**Time resolved diagnostic configuration**	**Related investigations**
Config-PPRIME-1	PPRIME 25	none		. Investigation of laser shock induce damage in CFRP . Damage threshold of CFRP . Damage threshold of bonded CFRP and weak bonds .Thermal effect of laser shock waves on CFRP and epoxies
Config-PPRIME-2	PPRIME 25	VISAR	VISAR fiber line (probe) (Verdi, 5W, 532 nm)	. Dynamic behaviour of CFRP under laser shocks . Dynamic behaviour of bonded CFRP under laser shock . Fatigue effects due to laser shock
Config-PPRIME-SYM	PPRIME 25	none		. Investigation of LASAT optimization by symmetrical shocks
Config-PIMM-1	Pimm-LASAT	none		. Residual back face deformation of unidirectional CFRP
Config-PIMM-2	Pimm-LASAT	VISAR	VISAR Optical line (Verdi, 5W, 532 nm)	. Dynamic behaviour of CFRP under laser shocks
Config-LULI-1	LULI2000	Transverse Visualization	Shadowgraphy	. Investigation of shock propagation in epoxies, . Investigation of thermo-mechanical laser effects on epoxies
Config-ELFIE-1	ELFIE	Transverse Visualization	Shadowgraphy	. Investigation of shock propagation in epoxies . Investigation of the dynamic spallation of CFRP
Config-ELFIE-2	ELFIE	Transverse Visualization	Shadowgraphy + Photoelasticimetry clear field	. Investigation of shock propagation and stress relaxation in epoxies
Config-ELFIE-3	ELFIE	Transverse Visualization	Shadowgraphy + Photoelasticimetry clear field (0.532 µm)	. Investigation of shock propagation and stress relaxation in epoxies
Config-ELFIE-4	ELFIE	Transverse Visualization	Shadowgraphy + Photoelasticimetry dark field	. Investigation of shock propagation and stress relaxation in epoxies
Config-ENSTA-1	Gas gun	none		. Investigation of LASAT optimization by tuneable pulse
Config-ENSTA-2	Gas gun	PDV + Transverse Visualization	IDIL rack (1550 nm), PDV probe + Shadowgraphy	. Dynamic behaviour of CFRP under plate impacts

Table 2.2 Summary of the experimental configurations used in this work

3 Used post-mortem techniques

In this section, the different post-mortem techniques used for the shocked composite analysis are presented. These analyses are performed after the laser shocks, contrary to time resolved measurements presented in the previous section. Each technique enables to get different information on the damage resulting from the shock wave propagation. The data obtained are generally complementary which is helpful for the understanding of the CFRP response to laser shock loading.

3.1 Cross section micrographies

Cross section micrography observation is probably one of the oldest techniques to investigate materials, but it is also one of the most important. Indeed, it enables to have a direct observation on the material state before or after a given loading without any intermediate steps (see in Figure 2.12). Therefore, the damage in the observation plane can be quantified. In case of CFRP composite, it is the case for delamination, matrix cracking, fiber/matrix de-cohesion… Nevertheless, no information in the other plane can be obtained using this technique, which is problematic in crossed ply composite. This observation technique has to be completed with other post-mortem diagnostics in order to get more data. Before observation, the shocked samples have to be prepared. The first step is to cut a cross section. This has always been done smoothly by using a diamond wire saw, in order to avoid creating more damage than the laser driven damage. The observation plane is always chosen to be orthogonal to the 0° fiber direction. This way, the delamination and especially the matrix cracking are easier to observe. In case of crossed-ply composite, the plane containing the greatest intersection number with a given orientation ply is always chosen (practically, it is 0° direction). Then, the cut samples are cold coated to be polished for observation. Finally, the samples are ready for observation. The composite cross section observations are performed using a Optical microscope, whose resolution is close to a few micrometers which is below the fiber dimensions (see in Figure 2.12, c).

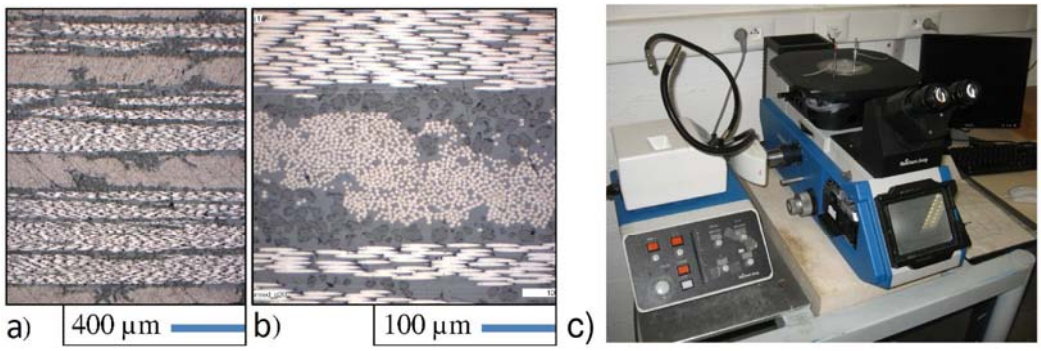

Figure 2.12 Cross section observation of a T800/M21 composite material made of 41 plies, ***a)*** *small magnification,* ***b)*** *bigger magnification: observation of ply,* ***c)*** *Picture of the MEF used for the observations*

Another microscopy technique was used to investigate the residual stresses in transparent materials (see in Figure 2.13, a). In this case, the light is provided from the objective opposite side (observation by transmission), contrary to the previous microscope (observation by reflection). Like for the time resolved technique, two circular polarizers are used and placed on each side of the epoxy target to enable the residual stress observation (see in Figure 2.13, b). In case of monochromatic observation, a 542 nm filter is placed before the microscope objective. In this case, the stress level can be calculated using the same equation 2.3 presented in the previous section.

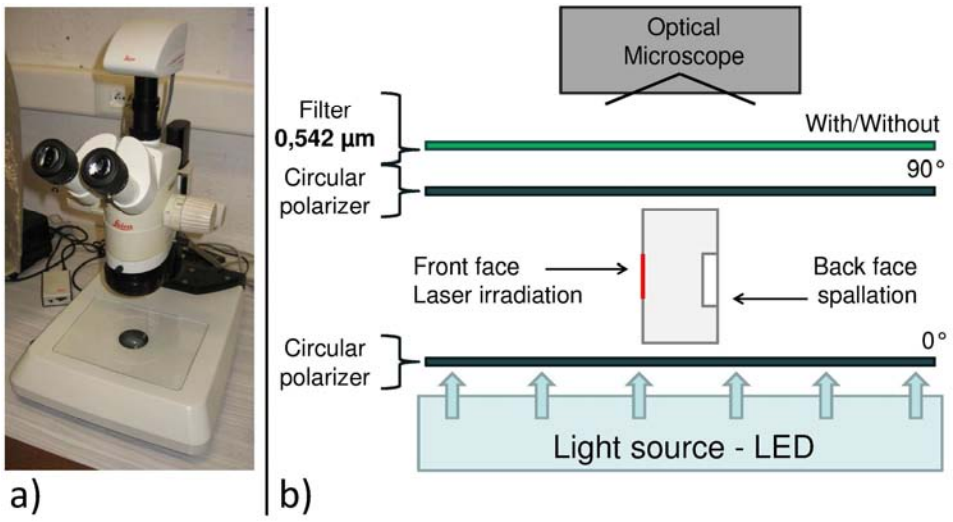

*Figure 2.13 Setup used for the post-mortem photoelasticimetry analysis of shocked epoxy targets for the residual stress investigations, **a)** Picture of the used microscope, **b)** Sketch of the layered structure set up using polarizers for the residual stresses observations*

3.2 X-Ray radiography

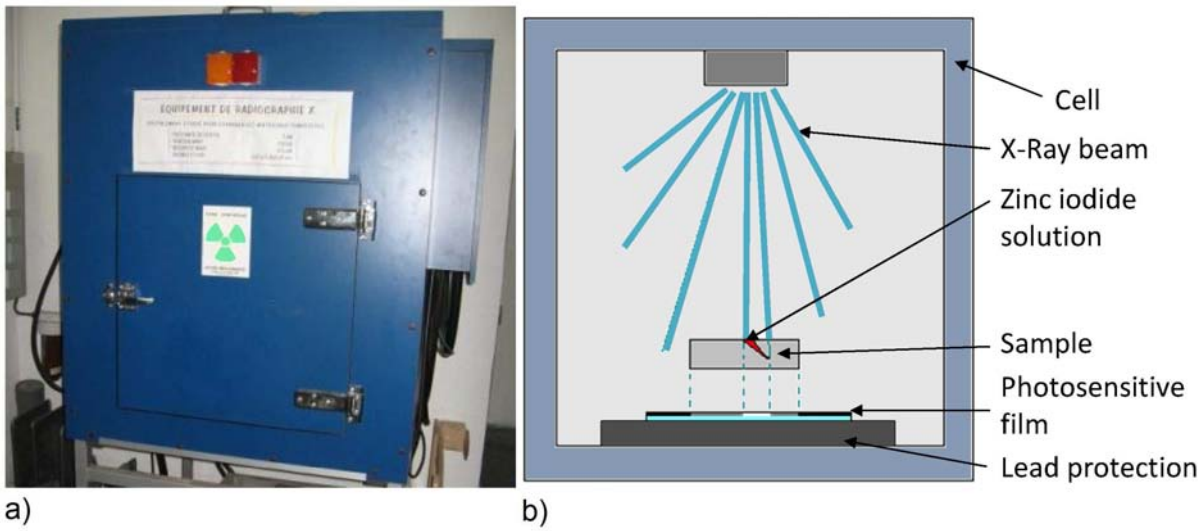

*Figure 2.14 X-Ray radiography setup **a)** Picture of the X-Ray cell **b)** Sketch of the X-Ray radiography principle as used for composite materials*

X-Ray radiography is one of the techniques which can be used on composite materials to get more information in order to complete microscopy observation. Indeed, like for rugby match broken leg observation, X-Ray radiography in materials science enables to observe what happened inside the material (see in Figure 2.14). In case of induced damage in CFRP composite, X-Ray radiography enables the delamination observation in the ply plan. For that, a specific Zinc Iodide solution is used to enhance the contrast between void or air and carbon/epoxy material to X-Ray. The solution is made to impregnate the composite target. Through matrix cracking which propagated until the sample edges or surfaces, the solution can reach all the free space created in the material. It is thus reducing these areas transparency to X-Ray compared to the unharmed areas. The X-Ray radiographies are taken thanks to a photosensitive film placed after the target in the X-Ray beam direction (see in Figure 2.14, b). The film is then recovered from the experimental cell and placed in a special scanner to get the image on a computer. This technique gives useful information but has

some disadvantages. Indeed, the different delaminations are all superposed on the image plane. The depth information is lost. Moreover, for the delamination to be observed, the solution has to be guided to them. If there is no crack breaking out from the sample, the inside damage will not be observed in any case. Finally, the use of Iodide solution is also polluting the sample, which can be annoying for further investigations.

3.3 Interferometric confocal microscopy

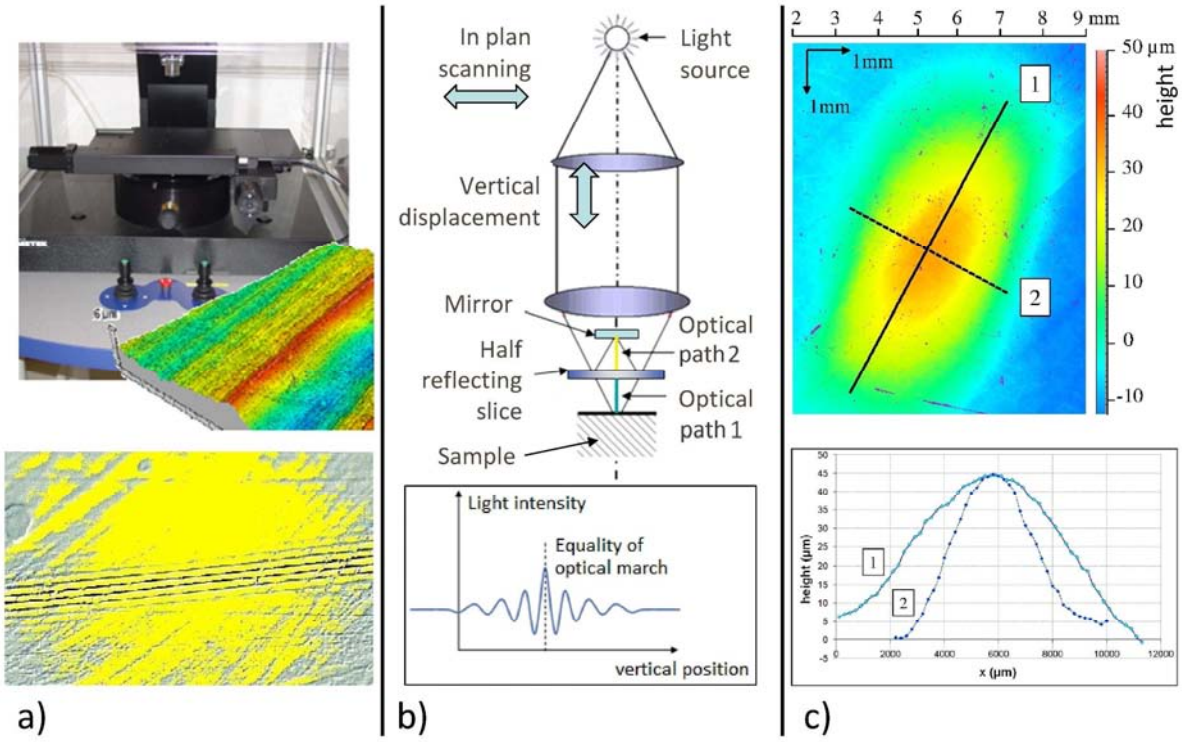

Figure 2.15 Interferometric confocal microscopy ***a)*** *Picture of the Talysurf confocal microscope with an example of Interferometric fringes focus on a material surface* ***b)*** *Sketch Interferometric confocal microscopy principle,* ***c)*** *Example of measurement on CFRP back face residual deformation by 3D display and 2D profiles*

Interferometric confocal microscopy is a recent technique which has been developed for roughness measurement. It enables the accurate quantification of surface geometries and deformations (see Figure 2.15, a). It is based on optical interferometry. The technique principle is explained in Figure 2.15, b. A mirror is placed in the microscope objective. The light going through the objective is partially reflected on a semi-transparent mirror toward this mirror. The distance between the mirror and the semi-transparent mirror being fixed, this beam forms the reference optical path (named optical path 2). Then, the light also reaches the sample surface to measure, where it is reflected toward the semi-transparent mirror (optical path 1). Thus, optical interferences are created on the slip board, whose maximum is reached when the optical paths are equal. At this position, height information can be recorded. In case of surface roughness measurement, the maximum of interferences is sought by vertically moving the objective for each pixel composing the surface. The system resolution and capacities depend on the objective used. For example, the highest magnification is × 50. In this case, the working distance is 3.4 mm. It means that for a flat surface, the interferences occur when the objective is placed 3.4 mm above the surface. The measurable surface is about 360 µm² and the resolution is close to 0.35 µm. The system can quantify height variation with a slope between 0 and 22°, and which are not exceeding 30 µm high. This objective is quite well adapted for roughness measurements. On the other hand, the smaller magnification is × 5. The

working distance is more important (9.4 mm). The surface which can be measured in one acquisition is about 9 mm² with a resolution between 1 and 2 µm. The slope above 2.5° will not be detected, but height variation under 250 µm can all be measured. This last objective is better adapted to composite target. Indeed, it can be used to precisely quantify the composite residual back face deformation resulting from the inside delamination induced by laser shock wave propagation. As it will be explained later, these deformations are generally several millimeters long. For that, several measurements have to be stitched using the post treatment tool of the Talysurf confocal microscope (see in Figure 2.15, c). In this case, the different scanned zones should admit a 20% area of recovery to be then merged. The example presented in Figure 2.15, c, measures 9mm × 12 mm, and is made thanks to 12 pictures. The color bar gives the height information. From this 3D measurement, 2D profiles can be extracted with the same resolution. The scanning time can be 2 min long as well as half an hour long depending on the surface to measure.

3.4 Ultrasounds and laser ultrasounds

The ultrasounds technique has been presented in the first chapter. It is one of the most common NDT techniques in the aeronautic industry for defect detection in composite materials. It is quite efficient to detect sizeable defect or damage. That is the reason why ultrasounds have been used in this work to measure the damage induced by laser shock wave propagation. There are mainly two methods for conventional ultrasound control. The first one is the transmission mode. In that case, an ultrasound emitter is placed on one side, and a receiver is placed on the other side. The input and received signals are both monitored, and when a difference is observed between these two signals, it means that something inside the sample changes the ultrasounds propagation. The defect can be detected. The second mode is the pulse echo technique. In this case, only one emitter/receiver is used. For that reason, this technique is more used in industry because it does not require having access to both sides of the part to test, contrary to the first method. This technique is described in Figure 2.16. The ultrasounds probes are generally made of piezoelectric sensors. The excitation frequencies are around 5 MHz. One piezoelectric element emits and receives the ultrasounds signal. The material response to one element is called an A-scan (see in Figure 2.16). It is characterized like every signal by several features such as amplitude, time of flight, frequency… For ultrasounds display, Amplitude (Amp.) and Time of flight (T.O.F) are the most used. In case of a structure without damage, the ultrasounds wave can propagate from the front face where the probe is placed, to the back face where it is reflected due to the acoustic impedance mismatch. On an A-scan, this is traduced by a front face peak and a back face peak marking the ultrasound reflection. The gap in between represents the ultrasound back and forth duration, meaning the T.O.F. If the tested material sound velocity is known, this gap can be displayed as a distance. In case of strong and large defects such as delamination for example, the ultrasounds propagation changes. The defect acts like a sample back face in term of impedance mismatch. It can create a partial or total reflection of the ultrasound waves toward the piezo probe. In this case, the timing and the amplitude of the second peak change, and the defect can be detected. Note that in case of a strong defect, the back face signal will be completely lost, but not for a small or partial defect. In this latter case, the ultrasounds can somehow succeed to pass through the material and reflect on the back face. The back wall echo amplitude will be reduced anyway. An A-scan thus represents the material response to the ultrasounds propagation along the propagation axis. When several A-scans are put together along a given axis, a B-scan is obtained (see in Figure 2.16). It can be named a D-scan depending on the plane chosen in the material. With the B-Scan, the 2D dimension of the defect on the observation plane can be evaluated. It can also be displayed in Amplitude or Time of Fligth. EADS Innovation Works

developed multi-element probes which enable to display directly B-scan (see picture in Figure 2.16). This kind of probe also enables to get a better resolution of the feature observed by adapting the emission/reception sequence between each piezoelectric element. It can be used with coupling agent or in a pool (see in Figure 2.16). Finally, C-scan can be used to obtain two dimensions defects in addition to their depth (see in Figure 2.16). A C-scan represents a juxtaposition of B-scan, which can also be seen as a 2D mapping of A-scans. Using a multi-element probe, a C-scan can be obtained just by a probe translation along one axis. The data gathered is then computed and post-treated using NDT Kit software. It gives access to each A-scan recorded, and enables B-scan and C-scan displays in Amplitude or Time of Flight. Speaking of CFRP, ultrasounds are well adapted to the detection of delamination. The defect parallel to the propagation axis such as matrix cracking can not really be detected, because of their size and orientation. The defect resolution is about 1 mm.

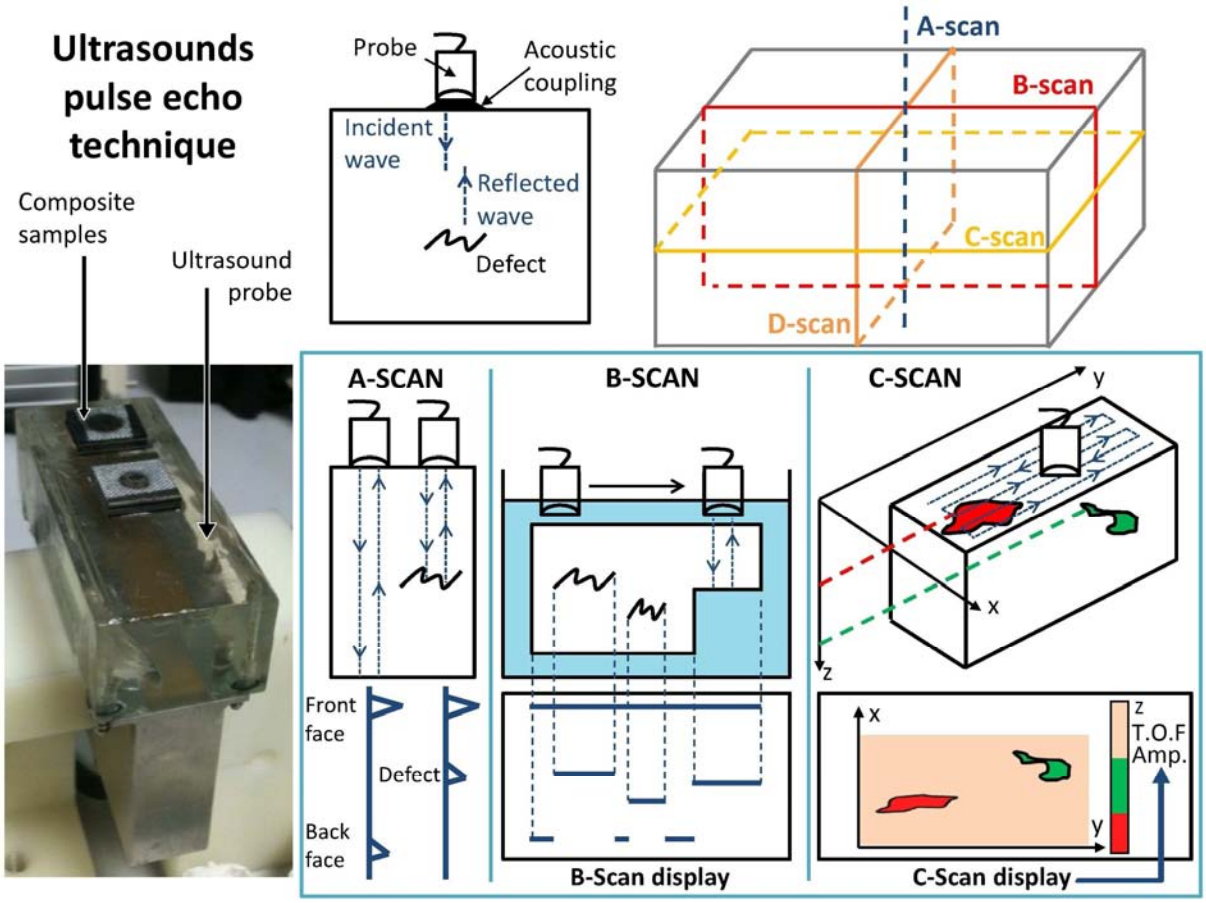

Figure 2.16 Different sketches explaining the pulse echo ultrasound technique, with the corresponding A-Scan, B-Scan and C- Scan displays for defect or damage detection

These last years, the control by ultrasounds has evolved toward laser ultrasounds technique [25]. This contact less technique is well adapted to complex geometry composite parts such as fuselage composite panels (see in Figure 2.17, b). It is thus complementary to conventional ultrasounds techniques. The principle is similar to conventional ultrasound technique. Instead of using a piezoelectric probe for the sample excitation, a laser is used. The laser irradiation induces a thermo elastic response of the material, in the ultrasound frequency range, which is monitored by a second laser (response analysis laser) using Doppler effect (see in Figure 2.17, c). The two laser spots can then be guided to control a whole surface. The step chosen between each irradiation defines the system resolution. EADS Innovation Works (Technocampus ECM², Nantes, France) developed two ultrasounds lasers [25]. The first one, named LUIS, demonstrated the technology (see in Figure 2.17,

a). For this system, the two laser beams are guided thanks to a mirror mounted on two axes. In case of LUCIE, the second system, the scanning head containing the two beam mirrors output has been mounted on a robotic arm (see in Figure 2.17, b). The two lasers are guided through the robotic system. This solution has considerably increased the number of geometries which can be scanned by laser ultrasound technique. Nevertheless, the technique weakness remains the spatial resolution of the scan which is lower than in case of conventional ultrasounds.

*Figure 2.17 Laser ultrasound technique, **a)** Picture of LUIS laser ultrasound setup from EADS IW, **b)** Picture of LUCIE laser ultrasound setup [26], **c)** Sketch of the laser ultrasound principle*

3.5 Microstructure characterization by DSC

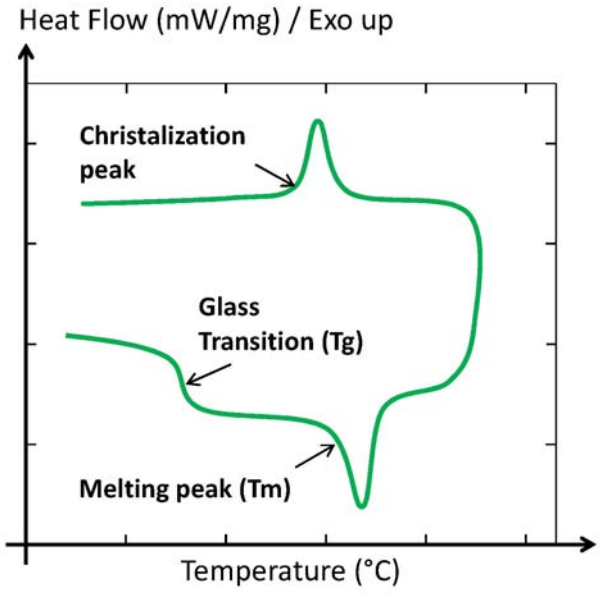

Figure 2.18 Sketch of a typical thermogram obtained by DSC (Differential Scanning Calorimetry)

The DSC (Differential Scanning Calorimetry) is a technique which can be used to characterize the microstructure of polymer materials. The DSC can evaluate the glass transition temperature of a polymer, and for semi-crystalline ones, the crystalline phase amount, the melting temperature and the crystallization temperature… It is based on the analysis of the thermal flux between a cell containing the material to test, and an empty reference cell both placed in a tight oven. The thermal

flux variation with time gives information about the material response to the applied thermal variation, which can be correlated to molecular changes such as glass transition. A schematic example of thermogram obtained by DSC on a semi-crystalline polymer material is given in Figure 2.18. One can see the capacity calorific jump corresponding to the glass transition. The glass temperature (Tg) can be evaluated thanks to this jump. At a higher temperature, the endothermic peak represents the melting (Tm) of the crystalline phase. After the heating up, one can see re-crystallization peak of the same phase.

4 Summary on the used techniques

In this final section, a summary on all the techniques necessary to investigate the behavior of composite material and thermoset material are summarize in Table 2.3. Both time-resolved techniques and post-mortem diagnostics are presented with associated measurement or analysis, their advantages and disadvantages.

To conclude, several shock sources have been used to investigate the dynamic behavior of composite material and bonded composite materials. This behavior have been studied thanks to several techniques, some of them being time resolved, the other being used after the shock. Each used technique has its own advantages and disadvantages, but provide unique data which is complementary to the information gathered thanks to the other techniques. The results obtained in this context are given and detailed in the following chapters.

Techniques	Measurement		Pro	Cons
Time resolved techniques				
VISAR 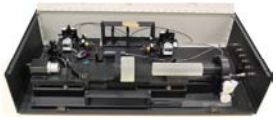	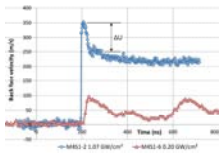	Back face velocity	. Measurement of the CFRP dynamic response . Contact less . good resolution	. Complex implementation of the interferometer . Need sample preparation
PDV	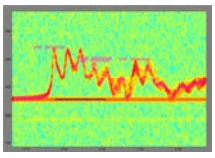	Back face velocity	. Measurement of the CFRP dynamic response . Easy to set up . multi velocities	. Lower temporal resolution for thin target for shock jump measurement
Transverse Visualization	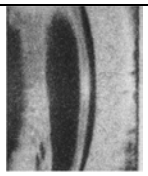	Shock phenomenon observation	. Direct observation of the phenomena . Shock mechanism identification	. Qualitative imaging due to the sample thickness

Post-mortem techniques				
Micrographies	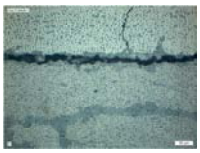	Damage observation and quantification	. Direct observation of the damage . identification of the damage	. Destroy the samples . Long preparation time
X-Ray Radiography	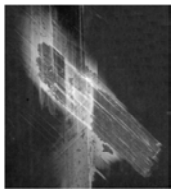	Damage observation	. Complete the observations made by microscopy . Visualization of delaminated area	. No information in the depth direction . Zinc iodide pollutes the samples
ICM 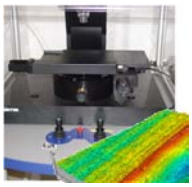	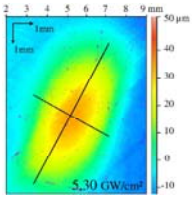	Residual deformation quantification	. Non Destructive technique . High resolution . Quantitative data on the back face residual state	. Need for a polished sample back face . Restricted to small deformation
Ultrasounds	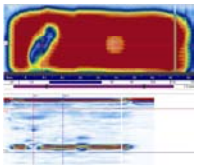	Delamination and debonding analysis	. Fast use . Can detect delamination as well as debonding . Industrial use	. Can not detect all the cracks . Cannot detect small defects . Could be long to acquire
Laser ultrasounds	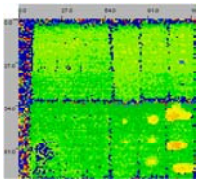	Delamination and debonding analysis	. Fast use . In line for industrial application . Complex geometry control	. Cannot detect all the cracks . Cannot detect small defects . Lower resolution than probes
DSC/DMA	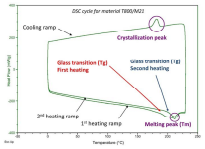	Thermo mechanical properties of composite targets	. Characterize the chemical state of the composite material	. Need for a small amount of matter from the material to analyze (destroy the sample)

Table 2.3 Summary of the experimental techniques used in this work

References

[1] R. Fabbro, J. Fournier, P. Ballard, D. Devaux, J. Virmont, *Physical study of laser produced plasma in confined geometry*, Journal of Applied Physics, Vol. 68, n°2,775-784 (1990).

[2] L. Berthe, R. Fabbro, P. Peyre, L. Tollier, E. Bartnicki, *Shock waves from a water confined laser-generated plasma,* Journal of Applied Physics, Vol. 82, n°6, 2826-2832, 1997

[3] L. Berthe, *Processus de claquage de milieux transparents sous irradiation laser. Application au choc laser en régime de confinement par eau*, Thèse de l'Université Paris XI, 1998

[4] A. Sollier, *Étude des plasmas générés par interaction laser-matière en régime confiné. Application au traitement des matériaux par choc laser*, Thèse de l'Université de Versailles Saint-Quentin- en -Yvelines (2002)

[5] http://www.luli.polytechnique.fr/accueil/les-installations/

[6] L.M. Baker, Laser Interferometry in Shock-wave Research, published in Experimental Mechanics, 1971, pages 209 – 215

[7] Daniel H. Dolan, *Foundations of VISAR analysis*, Sandia Report, SAND2006-1950, 2006

[8] J-P. Cuq-Lelandais, *Etude du comportement dynamique de matériaux sous choc laser sub-picoseconde*, Thèse de l'ENSMA (Ecole Nationale Supérieure de Mécanique et d'Aérotechnique), Ecole doctorale SIMMEA, 2010

[9] http://www.valynvisar.com/

[10] P.Mercier, J. Benier, A. Azzolina, J.M. Lagrange, D. Partouche, *Photonic Doppler velocimetry in shock physics experiments*, presented at Dymat 2006 : 8th International conference on mechanical and physical behaviour of materials under dynamic loading, Dijon, France, September 11st - 15th 2006

[11] P.Mercier, J. Benier, P.A. Frugier, G. Contencin, J. Veaux, S. Lauriot-Basseuil, M. Debruyne, *Heterodyne velocimetry and detonics experiments*, presented at the 28th International Congress on High-Speed Imaging and Photonics. Canberra, Australie, November 9-14th, 2008.

[12] P.Mercier, J. Benier, A. Sollier, M. Rabecle Glohaec, E. Lescoute, J.P. Cuq-Lelandais, E. Gay, T. De Resseguier, L. Berthe, M. Boustie, M. Nivard, A. Claverie, *Velocity Heterodyne measurements under high power laser shock into solids*, presented at APS Shock Physics. Nashville. USA June 29th – July 3rd, 2009

[13] P.A. Frugier, P. Mercier, J. Benier, E. Dubreuil, J. Veaux, *New Heterodyne Velocimetry and shock physics PDV and shock physics*. SPIE - Optics and photonics. San Diego. USA 2-6 august 2009.

[14] J. Benier, P. Mercier , E. Dubreuil, J. Veaux, P.A. Frugier, *New Heterodyne Velocimetry and shock physics*, presented at DYMAT 2009. Bruxelles. Belgique, September 7th – 11st 2009.

[15] P. Mercier, J. Benier, P.A. Frugier, M. Debruyne, B. Crouzet, *Nitromethane ignition observed with embedded PDV optical fibers*, presented to 8th International Conference "New models and hydrocodes for shock wave processes in condensed matter" PARIS, 24-28 may 2010.

[16] D. Loison*, Etude expérimentale et numérique du micro écaillage de cibles métalliques soumises à des chocs laser*, Thèse de l'ENSMA (Ecole Nationale Supérieure de Mécanique et d'Aérotechnique), Ecole doctorale SIMMEA, 2012

[17] E. Lescoute, Etude de la fragmentation dynamique de métaux sous choc laser, Thèse de l'ENSMA (Ecole Nationale Supérieure de Mécanique et d'Aérotechnique), Ecole doctorale SIMMEA, 2010

[18] R E. Setchell, *Refractive index of sapphire at 532 nm under shock compression and release*, J. Appl. Phys. 91, 2833 (2002)

[19] D. E. Fratanduono, J. H. Eggert, T. R. Boehly, M. A. Barrios, D. D. Meyerhofer & al., *Index of refraction of shock-released materials*, J. Appl. Phys. 110, 083509 (2011)

[20] Schlieren, *Shadowgraph techniques, visualizing phenomena in transparent media*, G.S. Settles, ISBN 3-540-66155-7, Springer Verlag Berlin Heidelberg New York

[21] M. M. Frocht, M. M. Leven, *Photoelasticity: the selected scientific papers of M. M. Frocht*, Pergamon press, 1969

[22] H. Aben, L. Ainola, J. Anton, *Integrated photoelasticity for nondestructive residual stress measurement in glass*, Optics and Lasers in engineering, Volume 33, Issue, January 2000, p 49-64

[23] H. Aben. *Integrated Photoelasticity*. McGraw-Hill, New York, 1979

[24] J. L. F. Freire, A. Voloshin, *Photoelasticity*, Experimental mechanics http://www.eolss.net/Sample-Chapters/C05/E6-194-05-00.pdf)

[25] B. Campagne, H. Voillaume, *Development of Laser Ultrasonics: Application to Complex Shape Aeronatical Parts*, presented at the 1st International Symposium on Laser Ultrasonics : Science, Technology and application, July 16-18 2008, Montreal, Canada, www.ndt.net

[26]http://www.humanoides.fr/wpcontent/uploads/2012/07/Humanoides_Blog_LUCIE_robot_inspection_a%C3%A9ronautique_composites.jpg

CHAPTER 3: BEHAVIOR AND TRANSFORMATION UNDER LASER SHOCK DYNAMIC LOADING OF EACH ELEMENTARY COMPONENT OF BONDED COMPOSITE MATERIALS

Introduction **96**

Part 1: Epoxy resins **96**

1 Samples description **96**

1.1 1.1. Transparent epoxy sample 96
1.2 FM300 material 97

2 Time resolved observation of the shock wave propagation and associated phenomena into an epoxy **98**

2.1 Nanosecond scale experiments (LULI2000 source) 98
2.2 Femtosecond scale experiments (ELFIE) 103

3 Characterization of FM300 bond **109**

Part 2: Composites **110**

1 Sample description **110**

2 Post – mortem description of the damage resulting from the laser shock loading on T800/M21 CFRP materials **113**

2.1 Thin cross-ply T800/M21 CFRP 113
2.2 Thick cross-ply T800/M21 CFRP investigations 118

3 Comparison of different unidirectional CFRP responses to laser shocks – damage tolerance **125**

3.1 Laser shocks and goal study 125
3.2 Post mortem observations 126
3.3 Toward the use of dimensionless number for composite sample classifications 130
3.4 Differences in the spallation behavior of unidirectional CFRP 132

4 Time resolved analysis of CFRP response to shock loading **134**

4.1 Time resolved measurements of thin unidirectional T800/M21 samples 135
4.2 Time resolved measurements of thick unidirectional T800/M21 samples 138
4.3 Reproducibility 140
4.4 Time resolved measurement of crossed ply composite dynamic response 142

Part 3: Material property modifications under laser shock loading: mechanical, thermal and chemical modifications **143**

1 Mechanical modification under repeated laser shocks under damage threshold **143**

2 Residual stresses in shocked epoxy resins **146**

3 Chemical or microstructural modification under laser shock loading **149**

3.1 DSC analysis 149
3.2 Highlighting of a possible microstructural modification on epoxy resins 153

Conclusions and synthesis **155**

References **157**

Introduction

In this chapter, the materials constituting CFRP composite and bonded CFRP materials are investigated. As it has been explained in the first chapter, the laser shock very high strain rate this loading is quite complex, especially on composite target due to their anisotropy characteristics. The shock front is not the same in the fiber direction and orthogonally to the fiber for example. Therefore, the laser shock propagation and effects in composite targets should be understood before starting to investigate bonded composite targets. The knowledge of epoxy behavior, major constituent of CFRP, is also a key issue for the overall understanding of the dynamic response of the bonded composite under shock. Indeed, previous studies have shown that the CFRP behavior under shocks in the orthogonal direction is similar to the one of epoxy (see in Chapter 1). The carbon could have been interesting to study in order to complete the data. Nevertheless, it is less important than the study of epoxy for the given goals. In this chapter, the shock propagation effects on the epoxy resin under laser shock loading is first presented. The use of transverse visualizations on the LULI laser sources has enabled to observe the shock phenomenon in these materials with an unreached time resolution so far. The FM300 adhesive film used for the bond is also investigated. The second part of this chapter deals with composite materials under laser shocks. Different types of materials have been used from the simplest to more complex ones. The laser shock phenomenon on CFRP has been investigated using both time resolved and post-mortem techniques to respectively quantify the composite dynamic response and the laser shock induced damage. The last part gives some elements about the material property modifications which could occur under laser shock loading. Especially, the question of thermo mechanical changes under laser shock is raised.

Part 1: Epoxy resins

The purpose of the investigations presented in this part is to characterize the dynamic behavior of epoxy materials under laser shock loading. As explained in the first chapter, very few studies were performed on that subject. We improved our knowledge of the behavior of epoxy resins under shock by two main investigations. The first one is the study of laser shock propagation on a classic epoxy material. Its transparency to white light was used to perform time-resolved transverse observations of the propagation and sub-sequent effects. It has been performed in two steps. The first one has been realized on LULI2000 laser source, with classic shadowgraphy observation. Then, ELFIE source was used, and photoelasticimetry imaging was set up to observe different mechanisms of the shock propagation phenomenon. The second investigation has been conducted on the FM300 film, made of epoxy and polyester fabric, which is the adhesive film chosen for ENCOMB bonded composites. As a constituent on the bonded composite, this material is shocked as the composites are during the LASAT test. Its response can influence the whole shock wave propagation pattern, especially in terms of transmission/reflection. Recording its dynamic response to laser shock provides a layout for the phenomenon understanding and particularly for numerical modeling validation.

1 Samples description

1.1 1.1. Transparent epoxy sample

For the first investigations, a classic polymer material was used (see its main characteristics in Table 3.1) [1-2]. It has been chosen for several reasons. Its mechanical properties are close from the M21 properties used in the composite investigated. Finally, it has a glass transition temperature high

enough to be representative of the epoxy resins used in CFRP and low enough to enable to highlight a possible thermo-mechanical effect of the laser shock loading (this point will be discussed in Part 3). Each square sample was about 10 mm per side and 5 mm thick. All the targets were cut from a bigger coupon using a diamond wire saw to avoid important cutting induced residual stresses. On two opposite edges, the samples were hand polished to obtain an excellent transparency which enabled the shock wave observation. Since epoxy is more or less transparent to the infra-red wavelengths laser source such as LULI or PPRIME sources, the samples were covered with an aluminum painting on their front faces to force the laser interaction with the matter and shock generation at the surface of the sample. In the following sections, the painted face is named 'the front face' (interaction with laser), the other face is called 'the back face', and the two polished edges through which the observation is possible are simply named 'the edges'.

ρ (g/cm^3)	E (GPa)	Poisson ratio ν	σ_r (MPa)	ε_r (%)	Thickness (mm)	T_g (°C)
1.14	3.09	0.35	29.7	0.02	5	120

Table 3.1 Epoxy sample properties as presented by M. Bertin [1-2]

After the sample preparation, the epoxy targets were controlled using the photoelasticimetry setup described in the Chapter 2. An example is given in both dark and clear field in Figure 3.1. No particular residual stresses schemes have been observed. Only large and dark fringes are observed on the monochromatic images, which correspond to the description of the zero order (meaning no stresses). It indicates that the two surfaces and the four edges are probably loaded with tiny stresses due to curing process and cutting procedure respectively. Considering the stress level induced by laser shock, the hypothesis of no residual stresses due to preparation procedure is made.

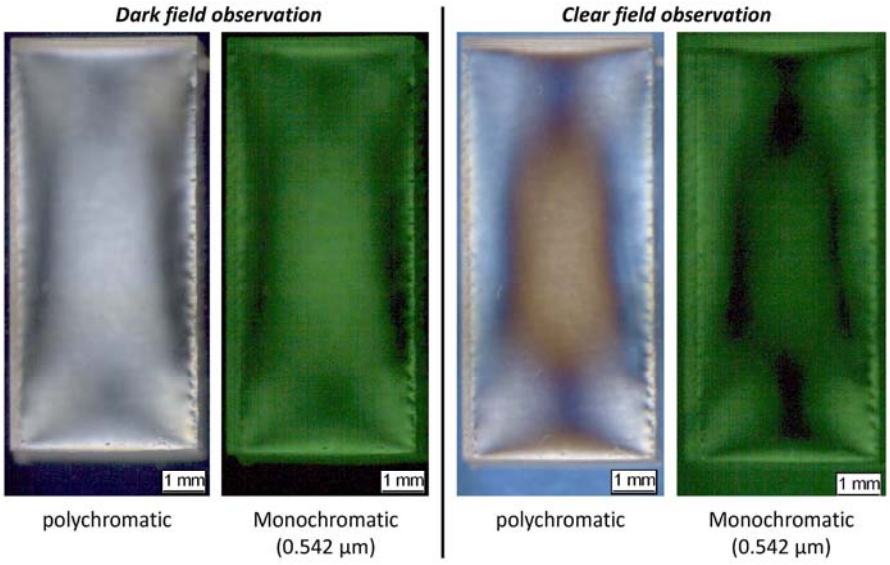

Figure 3.1 Observation by photoelasticimetry of the epoxy target initial state in both dark and clear fields using polychromatic light and monochromatic light (0.542 µm) for the stress observation

1.2 FM300 material

The FM300 adhesive film is made of two main components: an adhesive epoxy and a polyester fabric. Initially, one film is about 125 µm thick, and reaches between 100 and 120 µm once cured as a bond (see in Figure 3.2). The polyester strands forming the film reinforcement is meshed diamond-

shape as shown by the radiography realized on a bonded sample in Figure 3.2. The polyester fibers repartition in the strands can be really different in the same bondline. Indeed, the cross section micrography presented in Figure 3.2 shows three different fiber densities in the same bondline. Note that the real bond width as been truncated (white strips) to enable a better observation. This heterogeneity could have an influence on the local shock wave propagation and should be kept in mind. An FM300 sample was specially provided by Airbus for investigating this material dynamic response. For that, a 3 mm thick sample was created by superposing several adhesive films. The layered system was cured according to the Airbus standards presented in the first chapter, part 3.

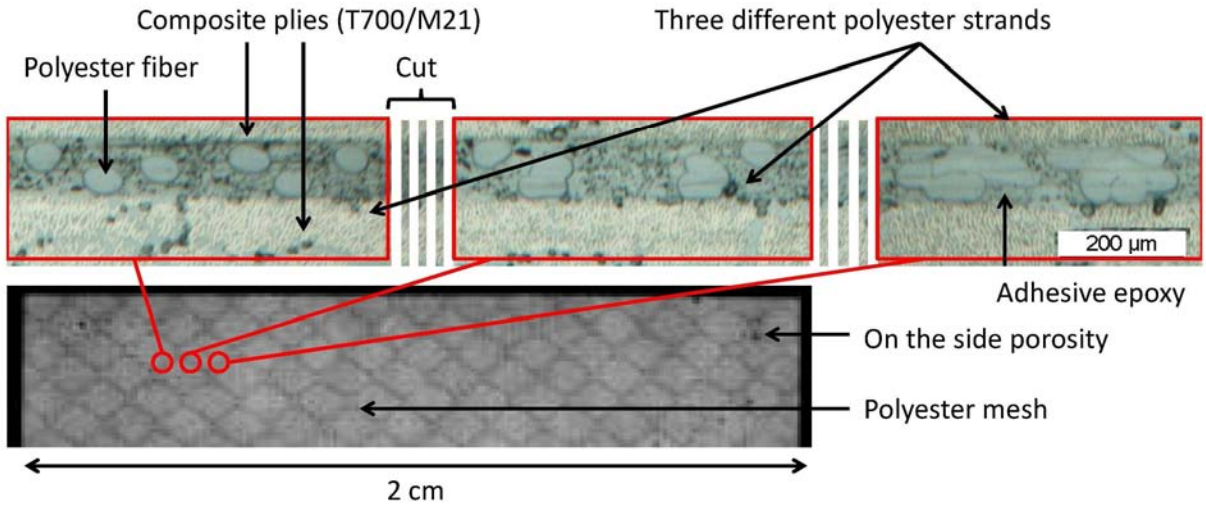

Figure 3.2 Observation of the FM300 adhesive film using both cross section observation (up) and X-ray radiography imaging (bottom) for its characterization

2 Time resolved observation of the shock wave propagation and associated phenomena into an epoxy

2.1 Nanosecond scale experiments (LULI2000 source)

Three different transparent epoxy samples, named Sep1.1, Sep1.2 and Sep1.3, were used to study the shock wave propagation in epoxy targets. The experimental configuration used for this study is Config-LULI-1 described in the 2nd chapter, Table 2.2. Thanks to the synchronized camera system, three pictures per shock were taken. Images were delayed one from each other according to the settings chosen for the cameras. In order to get more than three images to study the wave propagation, two laser shock were requested to be identical within the laser uncertainties (Sep1.2 and Sep1.3). Sample Sep1.1 was shocked on purpose with half-lower intensity, in order to study the loading amplitude influence on the wave propagation. The laser shock parameters used are given in Table 3.2: energy, pulse duration, focalized laser impact diameter (D_{foc}) and intensity. The uncertainties have been evaluated by considering the experimental setup and the diagnostic accuracy (see in Table 3.2. The pressure has been calculated using ESTHER software, [3-4]. The shock wave velocity measurement was performed on two samples shocked with different intensities. The small difference in the laser intensity between the two shots is not significant to deeply influence the pressure level induced inside the material, [5-6]. This point will be discussed in a second time. The phenomenon is first described according to theory (see in Figure 3.3) and thanks to the experimental observations (see in Figure 3.4). Then, the shock velocity measurement and reproducibility are discussed in Figures 3.5 and 3.6.

Target reference	Energy (J)	Laser pulse (ns)	Dfoc (mm)	Intensity (TW/cm²)	Calc. pressure (GPa)	Exp. shock velocity ($m.s^{-1}$)
Sep1-1	279 ± 5	3.12 ± 0.02	3 ± 0.1	1.26 ± 0.13	44 ± 4.4	2928 ± 50
Sep1-2	690 ± 5	3.10 ± 0.02	3 ± 0.1	3.15 ± 0.27	93.5 ± 7.5	3140 ± 60
Sep1-3	750 ± 5	3.12 ± 0.02	3± 0.1	3.40 ± 0.29	98.9 ± 7.9	not measured

Table 3.2 Laser shock parameters and measured velocities in epoxy resins

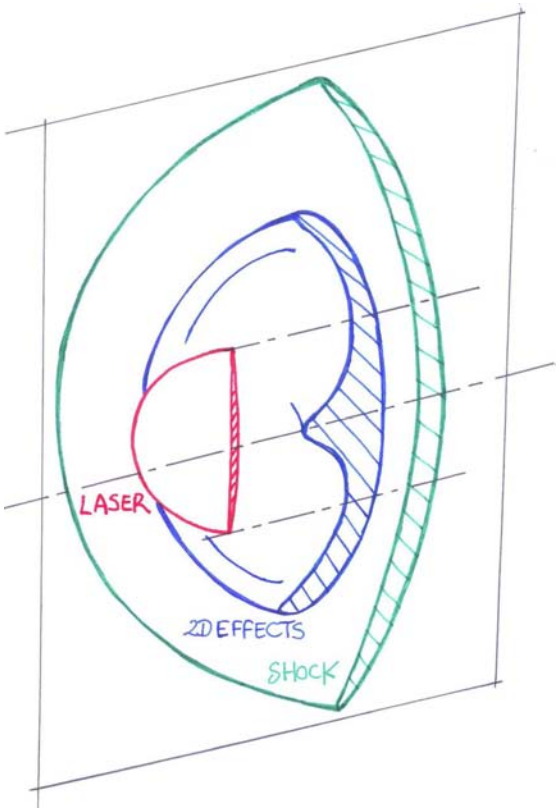

Figure 3.3 Cut and 3D sketch of the shock propagation according theory

A 3D theoretical representation of the phenomenon is given in Figure 3.3. Indeed, it has to be kept in mind during the snapshots analysis that the images are taken through the whole sample transverse thickness. Some phenomenon can be hidden. Experimentally, samples Sep1.2 and Sep1.3 were used to map the shock wave propagation history in an epoxy target and to describe the phenomenon. These two shocks realized under the same conditions enable to gather a sequence of 6 pictures thanks to the delays between each camera. The pictures are presented using the same scale in Figure 3.4. The shock wave setting up (at t = 0.5 µs) and propagation (t = 1µs and 1.5 µs) are shown by the first three images. Two main shapes can be observed in these snapshots. The thin curved black line, which is clearly visible at time 1 µs, is the shock wave. The material is compressed due to the pressure state which is leading to this darkness. Since the shock is really short, the pressure is released right after the loading, bringing back the material to its initial state. In the images, the shock wave is followed by a grey area, which is the colour also found in the unloaded areas. A sizeable black blur can also be observed behind the first two waves. This shape is traducing a tensile loading due to the geometry of the laser impact. This phenomenon is called edge effect, or 2D effects [8-9]. It relies on the fact that release waves are spherically propagating inside the target and from the edge of the impact area. These waves start to cross each other on the loading axis first, and then in a larger zone, creating tensile stresses. Compared to theory, the shape is slightly different from what

could be expected. Especially, the particular geometry of edges circular release waves should create a cone-shape 2D effect tension on the axisymmetric loading axis (as shown in Figure 3.3). Experimentally, this geometry is probably hidden by the 2D effect tension envelop curvature, being between this cone shape region and the cameras.

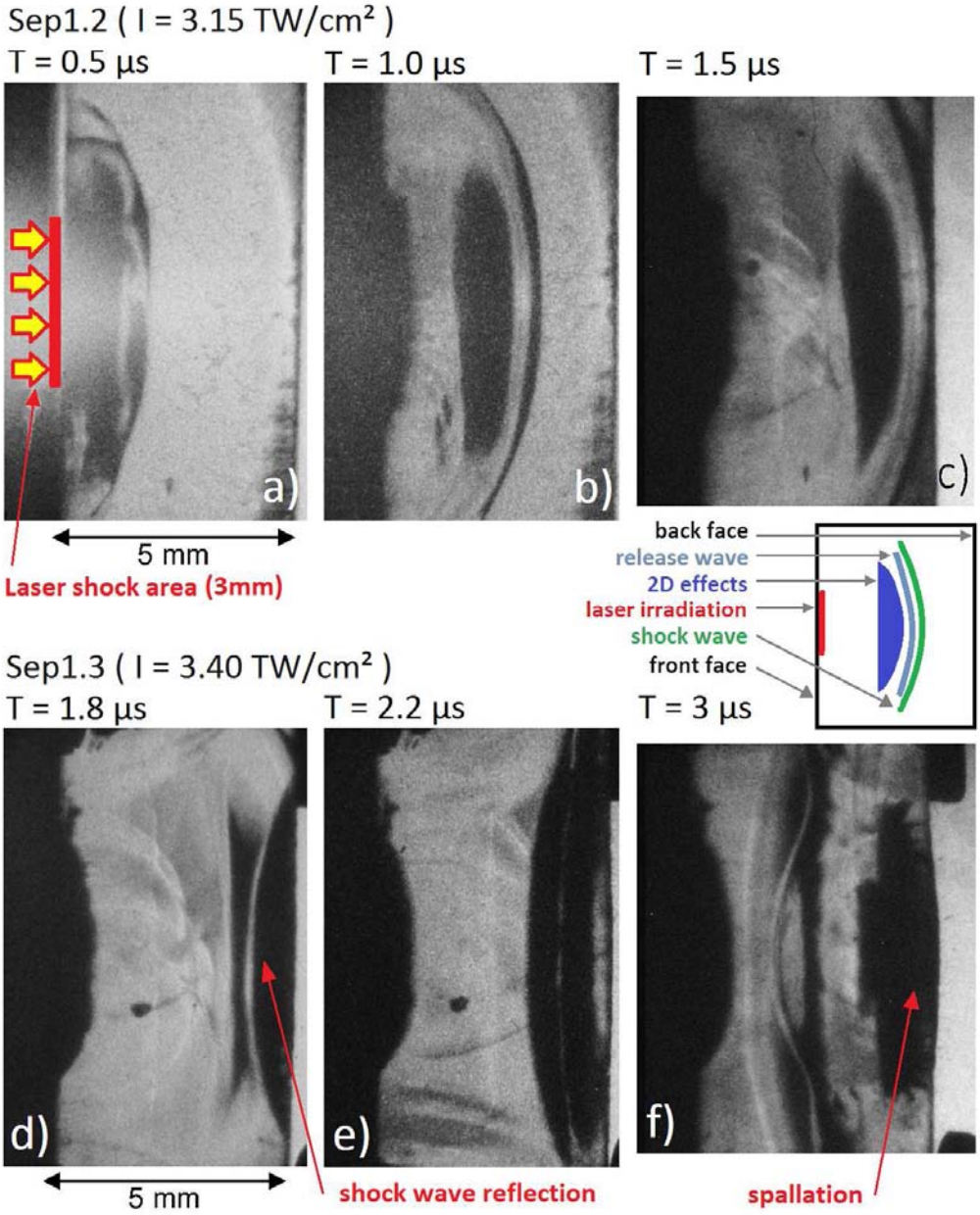

Figure 3.4 Laser shock wave propagation history obtained by shadowgraphy in epoxy resin:
3.4-a, Snapshot at t = 0.5 µs: setting up of the shock wave (from sample Sep1.2)
3.4-b, Snapshot at t = 1.0 µs: shock wave propagation with edge effect (from sample Sep1.2).
3.4-c, Snapshot at t = 1.5 µs: the shock wave is reaching the target back face (from sample Sep1.2).
3.4-d, Snapshot at t = 1.8 µs: reverberation of the shock at the free surface (from sample Sep1.3)
3.4-e, Snapshot at t = 2.2 µs: crossing of release waves inducing tensile stresses (from sample Sep1.3)
3.4-f, Snapshot at t = 3.0 µs: beginning of the spallation mechanism (from sample Sep1.3)

The second line of images in Figure 3.4 is relative to the shock wave reflection on the back face. Indeed, when a shock wave reaches a free surface, it is reflected into a release wave due to the absence of matter. This release wave can be observed on the snapshot taken at time 1.8 µs. It is the curved grey line, propagating backward from right to left, and crossing the incident tensile stresses

area (black blur). Behind this release wave, a dark area can be observed. This observation reveals one more time a tensile loading induced by the crossing of the incident release wave with the one propagating backward. So the back face is progressively loaded with tensile stresses, as it can be seen at time 2.2 µs. The last image shows the concerned wave propagation and the spallation phenomenon (3.3 µs). Indeed, the backward release wave approaches the front face. Behind, the material is under tension, especially in the darkest shape close to the back face. It is traducing intense tensile stresses which will lead to spallation a few µs later. The little deformation of the back face can show that the spallation has already started. Finally, these observations agree with the shock wave propagation and spallation phenomena described in the first chapter, part 2 and give for the first time a time resolved insight of the shock wave propagation inside the target.

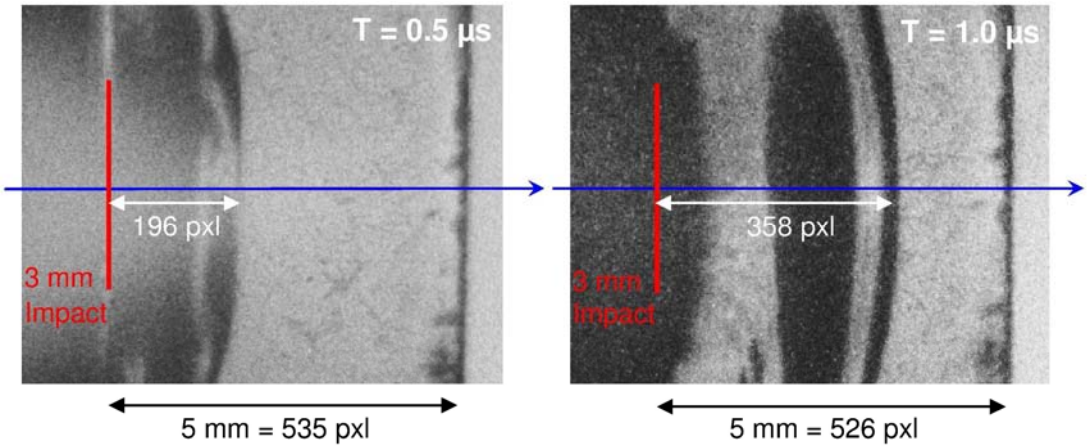

Figure 3.5 Snapshots treatment to calculate the experimental shock wave velocity in epoxy resin from the laser shock performed on sample Sep1.2 (3.15 TW/cm²)

The snapshots gathered during the laser shock experiments can also provide quantitative information. Indeed, by measuring on the images the shock wave displacement between two images, the shock wave velocity can be calculated (see the measurement principle on sample Sep1.2 in Figure 3.5). In case of Sep1.2 sample, the measurement has been made using the pictures taken at 0.5 µs and 1.0 µs. Then, equation (3.1) is used to evaluate the mean shock wave velocity D_{shock}. The method was the same for sample Sep1.1.

$$D_{shock} = \frac{\text{traveled distance}}{\text{time between two pictures}} = \frac{1.57\ mm}{500\ ns} = 3140\ m.s^{-1} \quad (3.1)$$

Thanks to the image quality, the accuracy on the travelled distance measurement is about ± 0.01 mm (1 pixel). Moreover, the snapshot instant is known at ± 3ns due to the camera exposure time, which leads to an uncertainty of ± 6ns on the time between two pictures. The shock velocity is measured in a frame of ± 60 m/s in case of sample Sep1.2. The shock wave velocities calculated are reported in Table 3.2. Moreover, the shock velocity is dependent on the shock wave pressure level as shown in equation (3.2), where ρ is the density, C_0 is the sound celerity, and u is the material velocity. Thus, a first approximation of the shock wave velocity D_{shock} can be given by equation (3.3) as explained in Chapter 1, part 2. It uses an experimental parameter s, even if recent works were performed to enhance the behaviour law. Especially, the sensitivity to strain rate and tested materials have been shown by D. Laporte [7].

$$\begin{cases} P = \rho \cdot c_0 \cdot u & (3.2) \\ D_{shock} = c_0 + s \cdot u & (3.3) \end{cases}$$

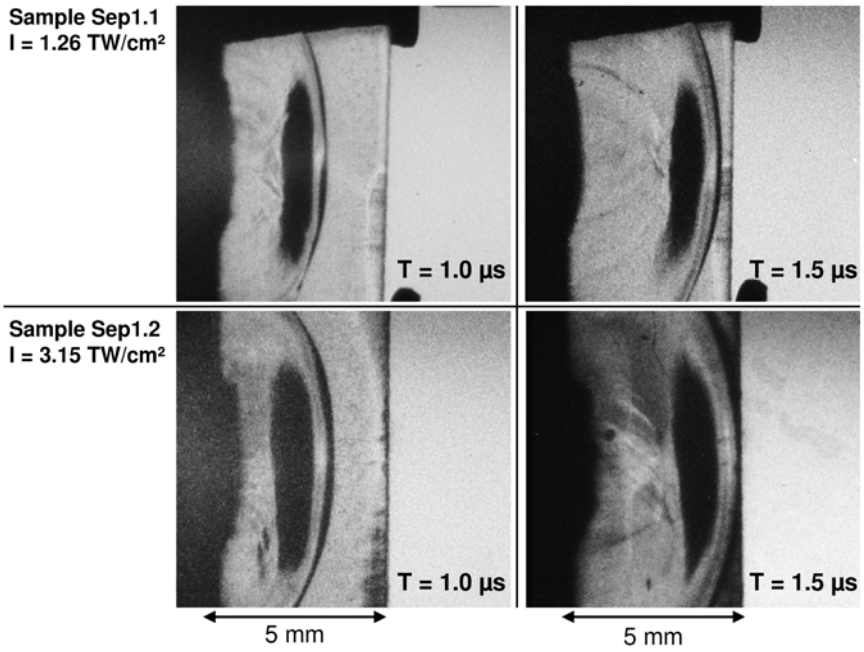

Figure 3.6, Snapshots of the laser shockwave propagation for two different samples of epoxy resin (Sep1.1 – 1.26 TW/cm² and Sep1.2 – 3.15 TW/cm²) at time t = 1µs after shock ant t = 1.5µs after shock:
3.6-a, Snapshot at t = 1.0 µs from sample Sep1.1 (1.26TW/cm²).
3.6-b, Snapshot at t = 1.5 µs from sample Sep1.1 (1.26TW/cm²).
3.6-c, Snapshot at t = 1.0 µs from sample Sep1.2 (3.15 TW/cm²).
3.6-d, Snapshot at t = 1.5 µs from sample Sep1.2 (3.15 TW/cm²).

Despite the laser intensity used in case of sample Sep1.2 (3.15 TW/cm²) was up to twice higher than in case of sample Sep1.1 (1.26 TW/cm²), the difference in the shock wave velocity measured remained relatively small: 6% (see in Table 3.2). Moreover, the phenomenon itself hardly changes from a shock produced at 3.15 TW/cm² to a shock produced at 1.26 TW/cm² as shown in Figure 3.6. Four different snapshots from Sep1.1 and Sep1.2 samples are presented in this Figure, with the same scale. At the same moment, the patterns are almost exactly the same for the two different laser intensities, meaning the different pressure loadings. This comparison proves the reliability of the developed methodology and the reproducibility from one sample to another. Therefore, it can be considered that for Sep1.2 and Sep1.3, the slight difference on the laser intensity (about 8%) will lead to the same shock wave propagation in the two samples. This observation ex-post demonstrates the use of these two samples for the analysis of the same phenomenon

These results can constitute a useful data base, complementary to free surface velocity measurements for comparison with results from numerical modelling. So far, the comparisons are mostly performed on back free surface velocity records or post-mortem inspection, providing information on the behaviour of the material only after the shock wave has fully crossed the sample. Many efforts are put in getting more experimental data during the first steps of shock wave propagation via difficult X-ray radiography diagnostics for non transparent materials [10]. Here we evidence for the first time the ability to get snapshots of laser shock wave propagation within transparent materials at chosen times before the shock breakout, after and even pictures of damage occurring upon reverberation. The experimental data gathered are helpful to characterize the wave

propagation history, and enable the shock velocity measurement, close to 3000 m/s, which is consistent with the literature. Note that the shock samples presented in this section have also been used to study the residual stresses inside the epoxy target. This point is discussed in the third part of this chapter.

2.2 Femtosecond scale experiments (ELFIE)

Ref LULI	Ref. Target	Energy (J)	Pulse (ps)	Dfoc (mm)	Intensity (PW/cm²)	Synchronisation (ns)	Fig nb	Color code
Shadowgraphy classic (Config-ELFIE-1)								
n°10	Sep1.5	6.62	0.35	2	0.602	500 – 1000 – 1500 - 2000		
n°12	Sep1.7	6.33	0.35	2	0.576	200 – 400 – 600 - 800	3.7	
n°13	Sep1.9	5.83	0.35	2	0.530	1000 – 1200 – 1800 -2200	3.7	
Photoelasticimetry clear field (Config-ELFIE-2)								
n°14	Sep1.13	6.37	0.35	2	0.579	200 – 400 – 500 - 600	3.7	
n°15	Sep1.12	6.35	0.35	2	0.577	800 – 1000 – 1200 - 1500	3.7-3.8	
n°16	Sep1.10	5.97	0.35	2	0.543	1800 – 2000 – 2200 -2500	3.7-3.8	
Photoelasticimetry dark field (Config-ELFIE-4)								
n°42	Sep2.1	6.54	0.35	1	2.38	100 – 600 – 800 - 1000	3.9	
n°43	Sep2.5	6.39	0.35	1	2.32	200 – 1200 – 1500 - 1800	3.9	
n°44	Sep2.6	5.75	0.35	1	2.09	400 – 2000 – 2200 - 2500		
Photoelasticimetry clear field monochromatic (Config-ELFIE-3)								
n°45	Sep1.6	7.03	0.35	1	2.56	400 – 600 – 800 - 1000	3.9	
n°46	Sep1.11	6.46	0.35	1	2.35	100 – 1200 – 1500 - 1800	3.9	
n°47	Sep1.14	7.03	0.35	1	2.56	200 – 2000 – 2200 - 2500		

Table 3.3 Laser shock parameters used for the ELFIE investigations on epoxy resin

In order to push further the laser shock investigation in epoxy materials, other experiments were conducted using ELFIE laser source. There are two main reasons for that. As shown by J.-P. Cuq Lelandais, the shortness of femtosecond shock prevent from macroscopic deformation and ease the sample recovery, in spite of the extreme pressure condition [4]. Complementary post-mortem analyses can be performed when it usually not the case for this pressure levels. ELFIE laser source also provide one shock every 20 minutes. Different photoelasticimetry configurations described in the 2nd chapter have been tried thanks to this repeatability rate. The ELFIE shock parameters are different. Indeed, the laser pulse duration is about 0.35 ps, which is much lower than the pulse duration of LULI2000 source. As a consequence, the loading strain rate is even higher as well as the laser intensity, and the corresponding induced pressure. The loaded characteristic dimension loaded is thus the molecule level [11]. Therefore, performing shock with this laser source also gives the opportunity of studying different phenomena such as relaxation and chemical modification [11]. The material used is the same than in the previous section, and the four ELFIE experimental configurations were used (see in Table 2.2). Note that in order to get more snapshots per shock, a fourth camera was used directly on the imaging axis to gather one more image per shock (see in Figure 2.10, chapter 2). Like in the previous investigation, several laser shocks were used to obtain a complete history of the shock propagation and reverberation within the sample. Therefore, three samples were shocked with the same laser parameters for each experimental configuration in order to get 12 images of the shock propagation. The laser shock parameters are given in Table 3.3, in which a color code is indicated for each sample. This color code is then used in the phenomenon descriptions in the Figures 3.7, 3.8 and 3.10. The reproducibility is fully assumed based on the previous experiments, and has been checked by calculating the shock velocity in each case. In this study, quantitative information was not especially expected. The idea was to observe the shock under different configurations in order to gather as much as possible information. The patterns resulting from the photoelasticimetry observations are quite complex and not fully understood so far.

In Figure 3.7, the same phenomenon observation is presented in two different configurations. In the first line, the images were taken using the shadowgraphy imaging (see previous section). The laser spot was smaller in that case, which leads to a faster 2D effects formation. Indeed, in Figure 3.7-a, a release network can be observed behind the shock formation. These waves can be attributed to 2D effects. 0.6 µs later, the shock front is settled and propagates through the epoxy target (see in Figure 3.7-b). It is followed by a release wave, and a tension region due to the 2D effects as it was the case on the previous LULI2000 observations. Nevertheless, the shock wave shape is slightly different in this case. Indeed, the deepest dark line corresponding to the shock front is much thinner than in the LULI2000 experiments. This is due to the pulse duration which is smaller on ELFIE laser source (0.35 ps) which leads to a thinner instantaneous loaded zone. For the same reason, the 2D effects tension region is also thinner. Indeed, when the release beams have crossed each other, the material is relaxed as it can be seen in Figure 3.7-b behind the 2D effects zone. The shorter the release beam, the smaller the 2D effects zone. The 2D effects geometry also changed, but this is due to the change of focal diameter. In case of a 2 mm diameter, the circular release waves coming from the irradiated spot cross earlier than in a 3 mm diameter case [9], [12]. In Figure 3.7-b, it can be observed that the zone influenced by the laser shock is approximately 1 mm wide. Finally, the last image presented is taken after the shock reverberation on the epoxy free surface. The black line corresponds to tension loading propagating backward into the epoxy material. The shock propagation described by these three images is thus similar to the one observed on the LULI2000 experiments.

The same shock propagation has then been observed using circular polarizers (Config-ELFIE-2). The observation has been made in clear field first, to have more light on the cameras, and better images. Three images are first presented in the second line of Figure 3.7. Note that the snapshots presented were taken exactly at the same time than the ones just described. Moreover, the laser intensities were really similar between the first observation by shadowgraphy and this second one by photoelasticimetry. Therefore, the first two images of each configuration are really close. The shock front has reached the same depth in both cases and the release wave can also be compared. In the shock front point of view, it can be concluded that the two phenomena are identical since it propagates with the same velocity and the same shape.

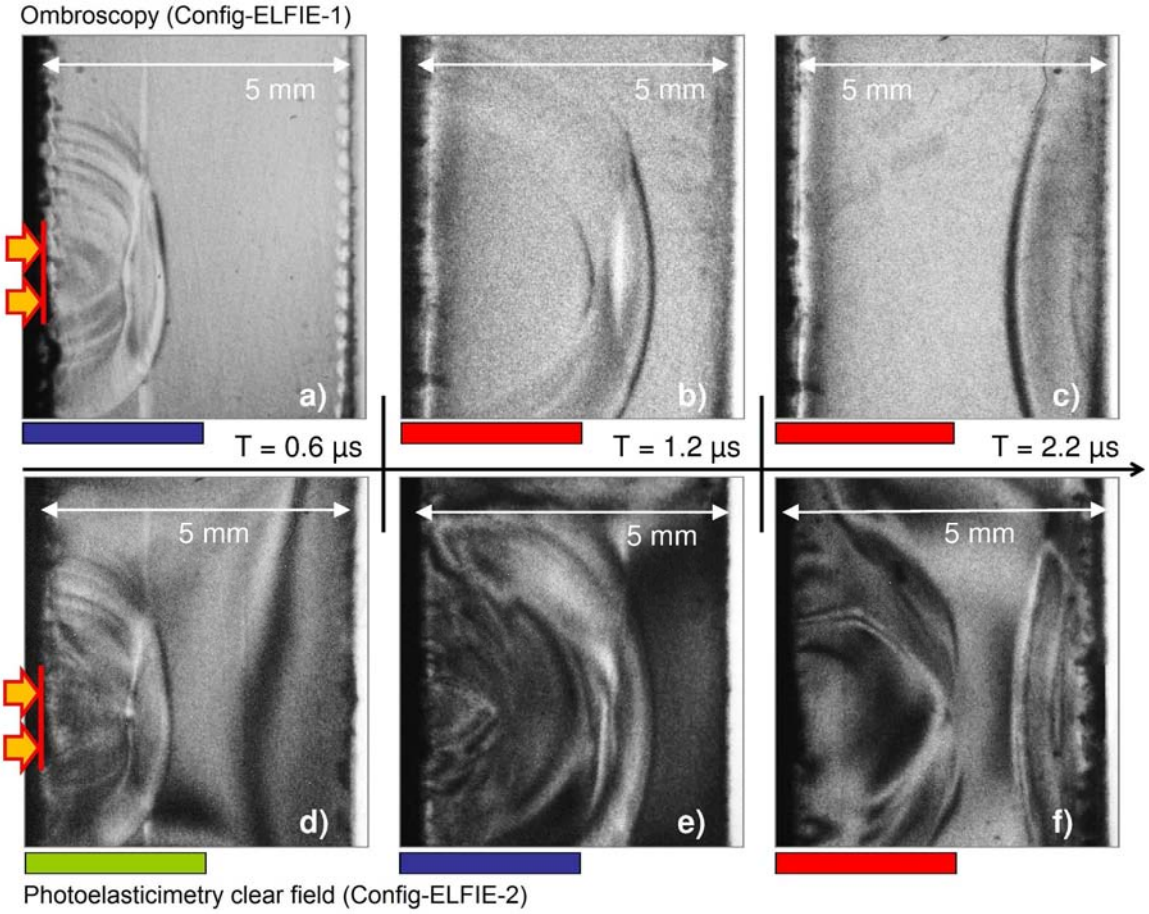

Figure 3.7 Comparison between a time resolved observation by shadowgraphy and by photoelasticimetry clear field shadowgraphy of a shock propagation into an epoxy target:
3.7-a, Snapshot at t = 0.6 µs: setting up of the shock wave by shadowgraphy (from sample Sep1.7)
3.7-b, Snapshot at t = 1.2 µs: shock wave propagation with 2D edge effect by shadowgraphy (from Sep1.9).
3.7-c, Snapshot at t = 2.2 µs: after shock reflection and release crossing by shadowgraphy (from Sep1.9).
3.7-d, Snapshot at t = 0.6 µs: setting up of the shock wave by photoelasticimetry (from Sep1.13)
3.7-e, Snapshot at t = 1.2 µs: shock wave propagation with 2D edge effect by photoelasticimetry (from Sep1.12)
3.7-f, Snapshot at t = 2.2 µs: after shock reflection and release crossing by photoelasticimetry (from Sep1.10).

Nevertheless, the use of polarizers enables the observation of patterns which have not been seen on the first observation. As explained in the 2nd chapter, the pattern observed can be correlated to stresses. It is the case on the first snapshot presented in Figure 3.7-d. A black fringe can be observed deeper from the shock front position. This is probably the 0 order. The fringe traduces the fact that the right part of the epoxy target is not yet loaded because the shock front is still behind. For proof, it can be compared to Figure 3.1. The following snapshot shows surprising patterns. Indeed, when nothing was observed in the first configuration behind the 2D effects tension zone, the polarizers

reveal a complex pattern is this area which should not be loaded. The organization is not clear, but it is axisymmetrical, and centered on the laser loading axis. This phenomenon is clearly coupled with the laser shock propagation, but different from the phenomenon as previously explained. It is probably due to the material and could traduce an equilibrium effect. From the front face, a diamond shape starts to grow still centered on the laser loading axis. On the last snapshot presented in Figure 3.7-d, this diamond shape has spread in the material thickness to reach the middle of the sample. No direct interpretation of the fringe can be done here, since the light used was not monochromatic. But this observation clearly indicates that something is happening inside the material, and results in stresses.

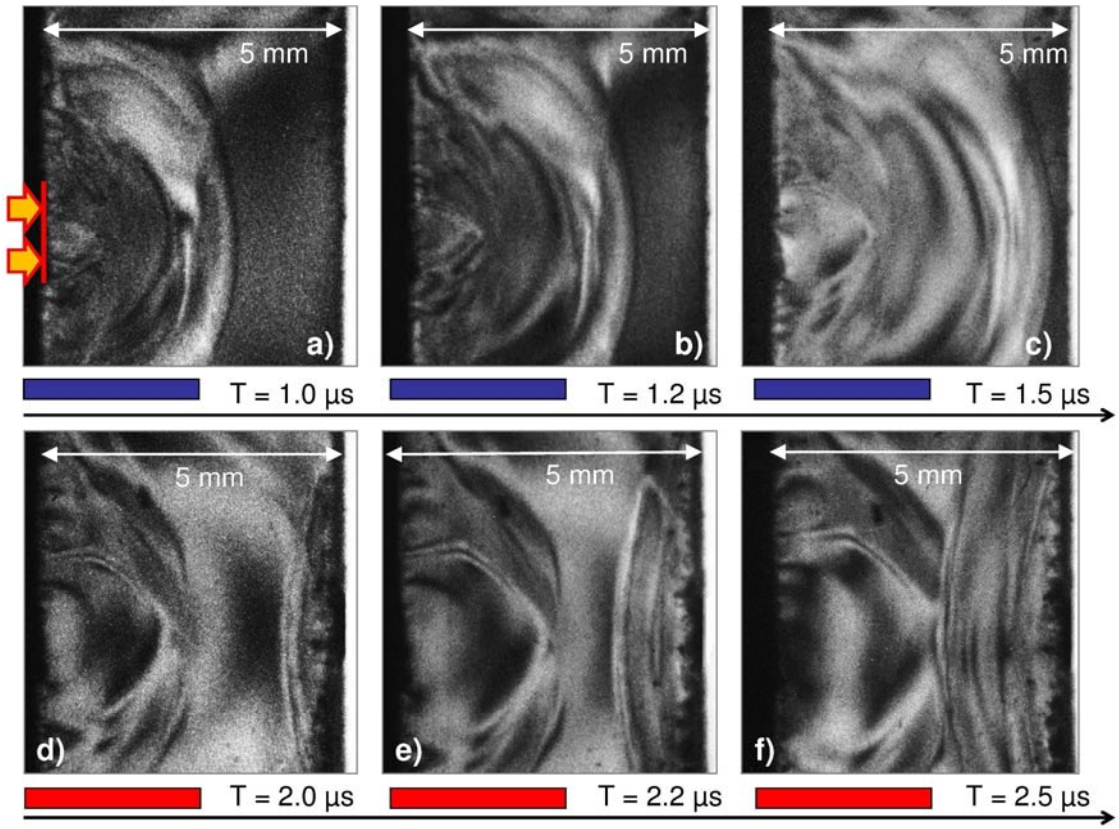

Figure 3.8 Observation of the shock wave propagation into an epoxy target using Config-ELFIE-2 (Photoelasticimetry clear field) – Highlighting of a second coupled phenomenon
3.8-a, Snapshot at t = 1.0 µs (from sample Sep1.12)
3.8-b, Snapshot at t = 1.2 µs (from sample Sep1.12)
3.8-c, Snapshot at t = 1.5 µs (from sample Sep1.12)
3.8-d, Snapshot at t = 2.0 µs (from sample Sep1.10)
3.8-e, Snapshot at t = 2.2 µs (from sample Sep1.10)
3.8-f, Snapshot at t = 2.5 µs (from sample Sep1.12)

In order to evaluate at least the difference of velocity between the shock wave propagation as known and this second coupled phenomenon, the whole sequence taken in Config-ELFIE-2 has been used. In Figure 3.8, the last 6 snapshots of the sequence are presented. Both phenomena evolution can be observed from t = 1.0 µs to t = 2.5 µs after laser. In these images, it appears that the shock front goes much faster than the second coupled phenomenon. The shock has traveled through the whole epoxy thickness and has been reflected when the secondary phenomenon hardly reaches the middle of the samples. These images were used to evaluate the two propagations velocities by using the method described in Figure 3.5. For that, the shock front has been followed on the six images, as well as the diamond shape tip located on the loading axis. Since the velocities can change with time

due to the pressure modification, the velocities has been evaluated between each images. The results are presented in Figure 3.9. As shown, the first three propagation velocities were used to calculate an average propagation velocity of each phenomenon. The last velocity range has been excluded on purpose because it is after the shock reverberation. The shock front propagates at 2800 m/s when the second coupled phenomenon propagates at 1300 m/s. This is quite different, and far from the measurement uncertainties. By comparing the propagation velocity level, it can be guessed that the second phenomenon is not a shock wave or an acoustic wave because it is too slow. Consequently, it seems to be correlated to the epoxy material mechanical response to laser shock loading. Nevertheless, it is hard to say if it is a visco-elastic or plastic effect, a mechanical equilibrium phenomenon or a sign of microstructural modification induced by mechanical loading.

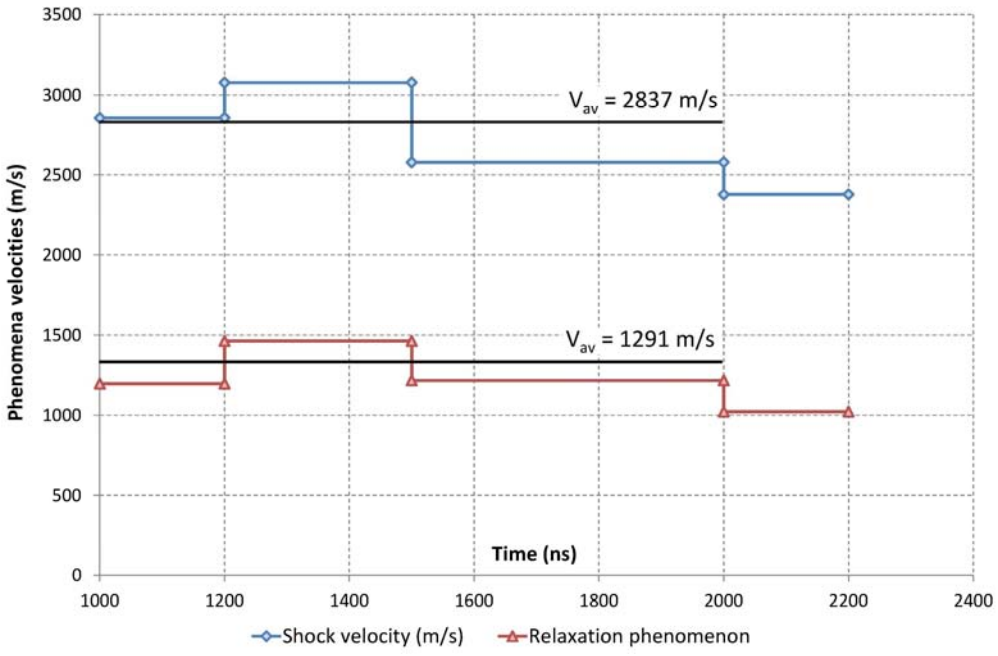

Figure 3.9 Comparison of the shock wave celerity and the second coupled phenomenon velocity on four successive time ranges in epoxy resin

Finally, the laser spot diameter was changed to evidence its influence on this second phenomenon. Indeed, according to the previous observations, it seems that what is seen is located in the shape formed after the release crossing, behind the 2D effects tension zone. It is thus possible for the phenomenon to be influenced by the 2D effects shape. This has been checked using Config-ELFIE-4 (dark field) and Config-ELFIE-3 (clear field monochromatic). One more time, the two configurations can be compared because the laser shock parameters were identical between the different shocks (see in Figure 3.10). It can also be noticed that the patterns observed in both configurations are identical, but just opposite in terms of contrast. Note that the monochromatic observation has been made in the clear field observation, because not enough light was obtained in case of monochromatic dark field. The first three snapshots presented in Figure 3.10, a, b and c, evidence that the phenomenon shape has changed. The diamond shape is no longer visible, and has been replaced by something more spherical (more visible in Figure 3.10, c). The monochromatic observations are particularly interesting in case of the snapshot taken at t = 1.0 µs and presented in Figure 3.10, e. Indeed, this is the only image in which a fringe network observation has been possible. They are circular, and reduce in direction of the front face. Their level could theoretically be evaluated. For that, the order 0 should be found, and that is not obvious on this image. Nevertheless, it seems clear that a stress gradient occurs behind the 2D effects zone in this case.

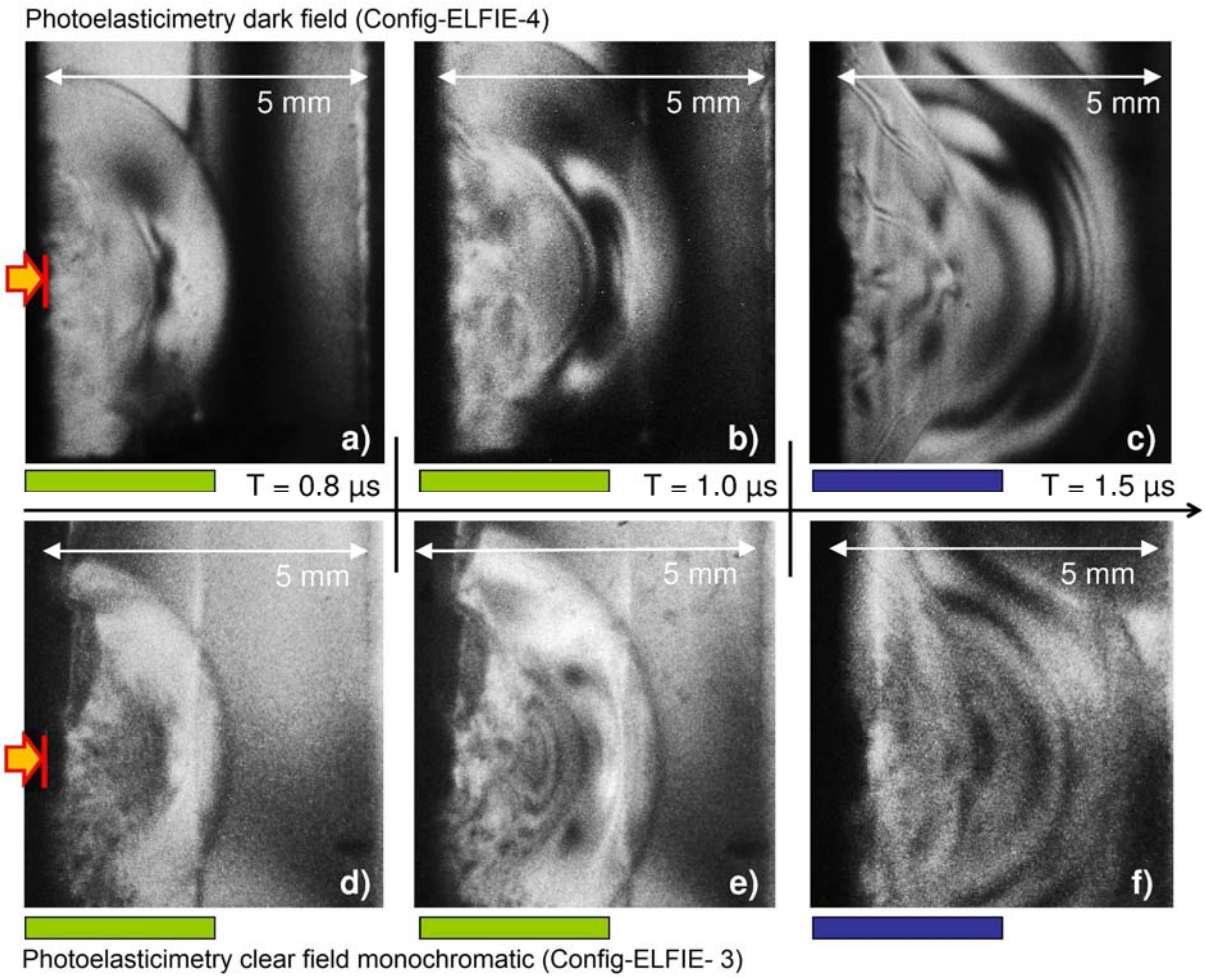

Figure 3.10 Compared observations of the shock wave propagation into an epoxy target in case of a smaller focal diameter by two different configurations – Observation of a fringe organization behind the shock
3.10-a, Snapshot at t = 0.8 µs, using Config-ELFIE-4 (from sample Sep2.1)
3.10-b, Snapshot at t = 1.0 µs, using Config-ELFIE-4 (from sample Sep2.1)
3.10-c, Snapshot at t = 1.5 µs, using Config-ELFIE-4 (from sample Sep2.5)
3.10-d, Snapshot at t = 0.8 µs, using Config-ELFIE-3 (from sample Sep1.6)
3.10-e, Snapshot at t = 1.0 µs, using Config-ELFIE-3 (from sample Sep1.6)
3.10-f, Snapshot at t = 1.5 µs, using Config-ELFIE-3 (from sample Sep1.11)

As a conclusion, it can be said that the time resolved observation of shock propagation in epoxy targets by use of photoelasticimety have considerably enhanced the phenomenon observation. It highlighted a second phenomenon coupled with the laser shock wave propagation. This phenomenon seems different from a shock or acoustic propagation. It could be thus attributed to the material mechanical response. Its exact nature is not fully understood yet, but can be from different types: visco-elastic, mechanical equilibrium, thermal diffusion, molecular changes… In any case, it is correlated to 2D effects, especially its shape which changes from one laser spot diameter to another. It is clear that more investigations should be performed to have a better understanding of the phenomenon. Numerical modeling could also help, even if it is harder in this case because of the pulse shortness and the need for 2D modeling (see chapter 4)

3 Characterization of FM300 bond

FM300 material has been tested especially for checking our ability to simulate laser shock wave propagation in this material using existing constitutive laws in numerical codes. Laser shocks were performed using the PPRIME 25 laser (Config-PPRIME-2), in water confinement configuration and with aluminum painting sacrificial layer on the front face. Two shocks are presented in this section. The laser shock parameters are given in Table 3.4. The first shot has been performed over the spallation threshold of the material as shown by the back face damage. It is presented in Figure 3.11

Ref Sample	Energy (J)	Pulse duration (ns)	Focus diameter (mm)	Intensity (GW/cm²)
FMS1-01	18.774	29.24	4	5.11
FMS1-06	4.023	24.54	4	1.30

Table 3.4 Laser shock parameters for the investigations made on FM300 sample

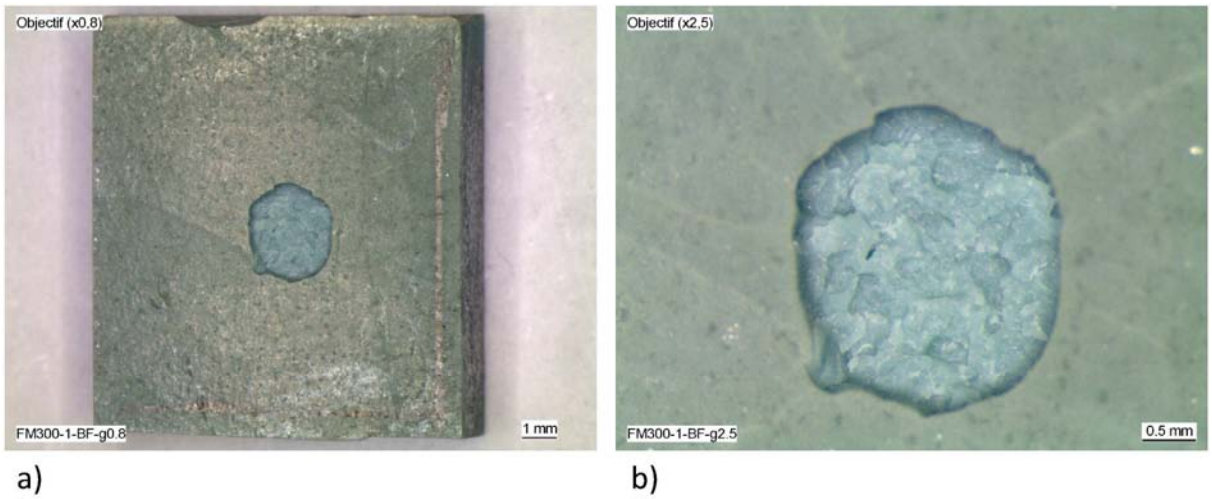

Figure 3.11 Optical micrography of a FM300 sample back face – Observation of the spallation, a) Observation of whole sample back (0.8 magnification), b) Observation of the spallation geometry with a higher magnification (2.5)

The spallation can be evidenced by looking to the sample back face, especially the crater left by the spall. In the micrographies presented in Figure 3.11, it can be observed that this crater is round shape. This means the damage growth has probably been isotropic, despiste the complex material arrangement due to polyester fabric. The diameter of the crater is about 2.5 mm, which is smaller than the initial focal diameter. This can be explained by the attenuation resulting from the propagation in thick targets.

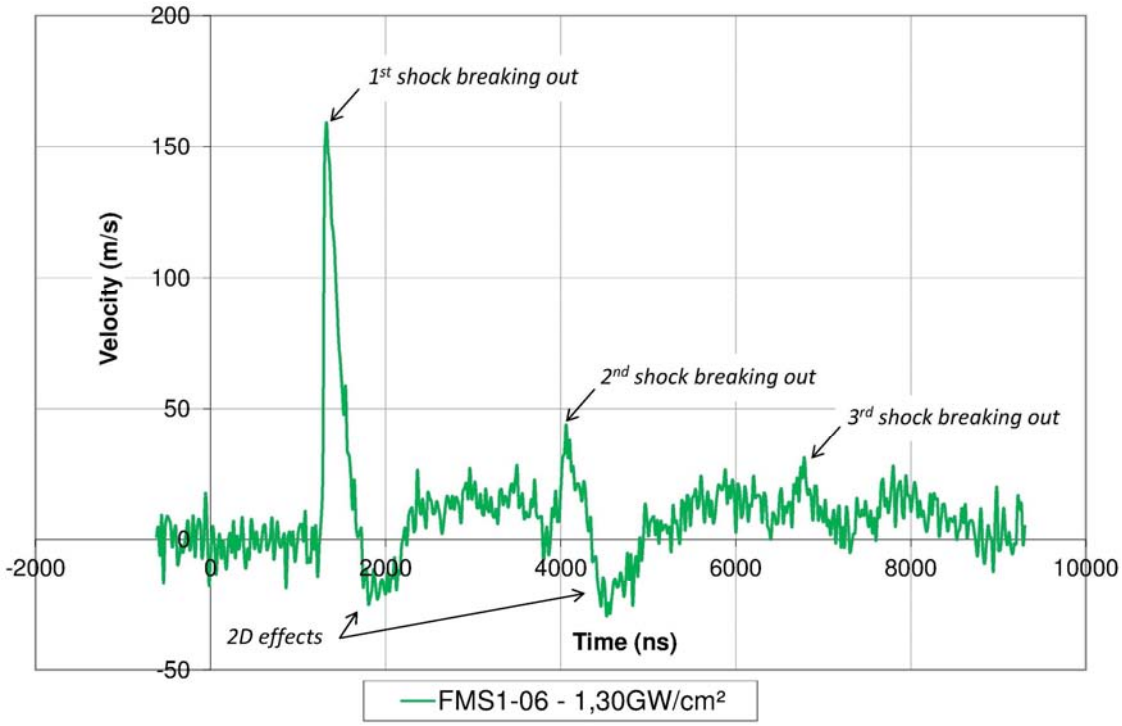

Figure 3.12 VISAR back face velocity measurement on FM300 material FMS1-06 sample (see in Table 3.4)

The time resolved measurements on FM300 samples were quite difficult. Indeed, the sample itself is green (see in Figure 3.11). To avoid the Verdi signal absorption by the target, a coating on the sample back should be used. A signal is presented in Figure 3.12. The 1.3 GW/cm² laser intensity leads to free surface velocity about 150 m/s. In the signal, three periodic shocks breaking out can be observed, which is synonymous of the absence of dynamic damage. Moreover, the attenuation is really strong. On the second shock breaking out, the free surface velocity has been reduced by 70 % compared to the first breaking out. This could be due to the presence of polyester fibers which can break the shock front by multiple transmission/reflection phenomena. The large thickness is also responsible for that as well as for the observation of 2D effects breaking out on the velocity signal. It corresponds to the two negative velocity peaks [8, 9], [12]. Finally, no particular anisotropic feature can be observed on the velocity signal (see in the following sections). This information, added to the isotropy damage growth, can lead to the conclusion than the FM300 sample behavior is isotropic. Intuitively, this seems normal by looking at the polyester fabric mesh (see in Figure 3.2). By extension, the behavior of one adhesive film will be assumed to be isotropic as well.

Part 2: Composites

1 Sample description

A T800/M21 (Hexcel) composite material has been used in this investigation. It has been provided by Airbus and is really close to the T700/M21 composite material used in the frame of ENCOMB project. This CFRP is well-known as a classic composite material for aeronautical applications, more specifically for structures which are prone to impacts. It is made of a non-conventional matrix, mixed from a thermoset epoxy resin and thermoplastic nodules whose mechanical behaviour should enhance the global composite shock resistance. On the tested samples, the matrix composition has been checked using DSC (Differential Scanning Calorimetry) characterization. The thermogram

presented in Figure 3.13 has been obtained using a classic thermic cycle, whose temperature ramp was equal to 5°C/min. On the first heating ramp, the actual glass transition temperature can be identified by the change in the signal curvature. The following endothermic peak traduces the melting of a thermoplastic content (M21 matrix contains thermoplastics). This is confirmed by the crystallization peak which can be observed on the cooling ramp. After the cooling cycle, a second heating ramp enables to measure the glass transition one more time. A shift between the first and the second evaluation gives some information about the initial curing state of the material tested. The shift between the two glass transition temperatures indicates that the material tested was not fully reticulated. The glass transition of the epoxy was evaluated around 194 °C and the thermoplastic phase melt has been identified from the endothermic melting peak close to 212 °C. Micrographs of a 6mm thick T800/M21 sample are presented in Figure 3.14, a, b and c with three different magnifications. This sample is made of 33 pre-impregnated plies assembled with different orientations [A] = $[45°/0°/0°/-45°/0°/0°/\ 45°/0°/0°/-45°/0°/-45°/0°/0°/45°/0°/0°_{0.5}]_S$ and cured by autoclave.

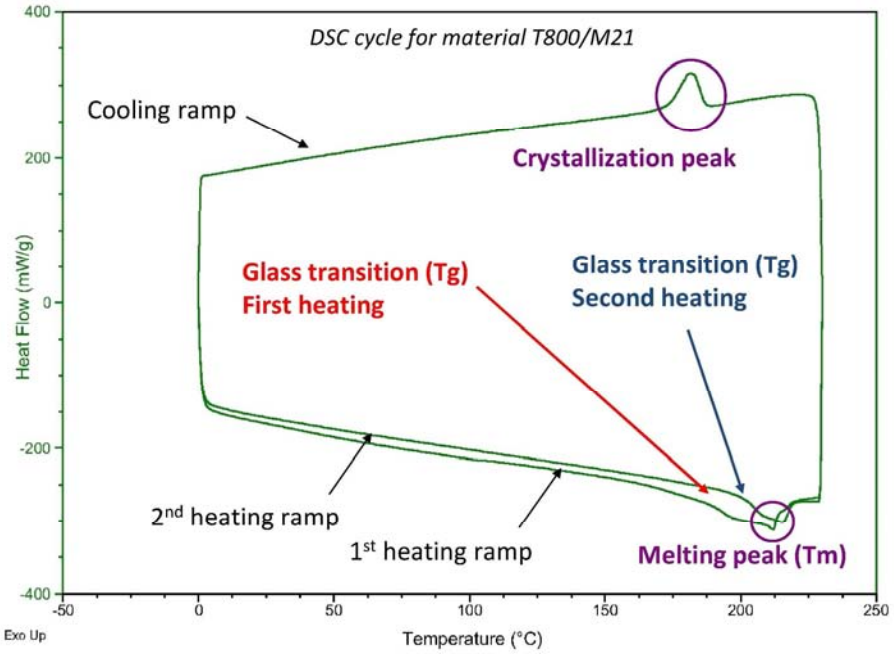

Figure 3.13 Thermogram obtained by DSC (Differential Scanning Calorimetry) on a T800/M21 composite material – Three cycle signal, 1st heating, cooling and 2nd heating

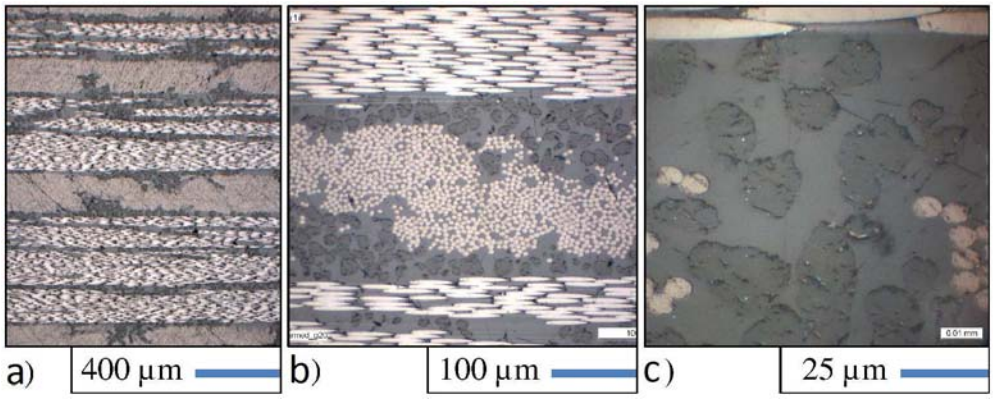

Figure 3.14 Optical micrographies (a, b, c) of a 6 mm thick T800/M21 sample with different magnifications – Observation of the ply constituents

In Figure 3.14, the thermoplastic nodules can be observed mostly between the plies as round dark grey shapes, but are sometimes present inside the plies, forming channels or veins (see Figure 3.14, a and b). Their approximated diameter has been evaluated in the range [10-20 µm] (see Figure 3.14, c). The pre-impregnated plies are about 180 µm, but the presence of the thermoplastic nodules induces a strong deviation of the ply thickness. This deviation could have an influence on the shock response of this material. Moreover, the presence of thermoplastic nodules could have an influence on the shock wave propagation because their shock impedance might be different from the epoxy one. This 6 mm thick T800/M21 material has provided samples tested in the laser shock induced damage studies. In case of thin composite investigation, the 6 mm thickness has been reduced to a smaller one by use of a circular diamond saw, and finished by polishing.

Unidirectional samples have also been used, especially for time resolved measurement. Indeed, simple lay-up structures were preferred to simplify the shock propagation pattern and enable a correct understanding of back face velocity signals. Different materials were used in order to compare their dynamic response (see in Figure 3.15, a, b, c). Especially, the effect of thermoplastic nodule on the crack propagation inside the material was aimed to be investigated. For that reason, a material without nodules has been used. It is the T300/914, used before T800/M21 in aeronautical structures, which has been chosen (see in Figure 3.15, c). The thicknesses of these samples were adjusted by polishing between 0.4 mm to 3 mm, depending on the conducted study.

Finally, the ENCOMB T700S/M21 composite material has been tested, especially to quantify its dynamic response under laser shock loading. This experimental data is quite important for numerical modeling. A micrography of this sample is presented in Figure 3.16. It can be noticed that this 1.5 mm composite is made of 6 pre-impregnated plies of M21/T700 oriented as follow [0°, 0°, 90°, 90°, 0°, 0°]. “M21” refers to the matrix (HexPly M21, Hexcel Composite) and T700 is the carbon fibers reference. On the micrography presented in Figure 3.16-a, the different ply orientations are visible. An even closer look is given in Figure 3.16-c, to enable the microscopic observation of the cured composite. Three components can be observed: i) the carbon fibers, with a fiber volume of averagely 60 %, ii) the epoxy content, particularly visible between the pre-impregnated plies, iii) Thermoplastic nodules between or in the plies forming veins or canals as previously explained.

A summary of the used samples, their geometry, and associated experimental campaign is given in table 3.5.

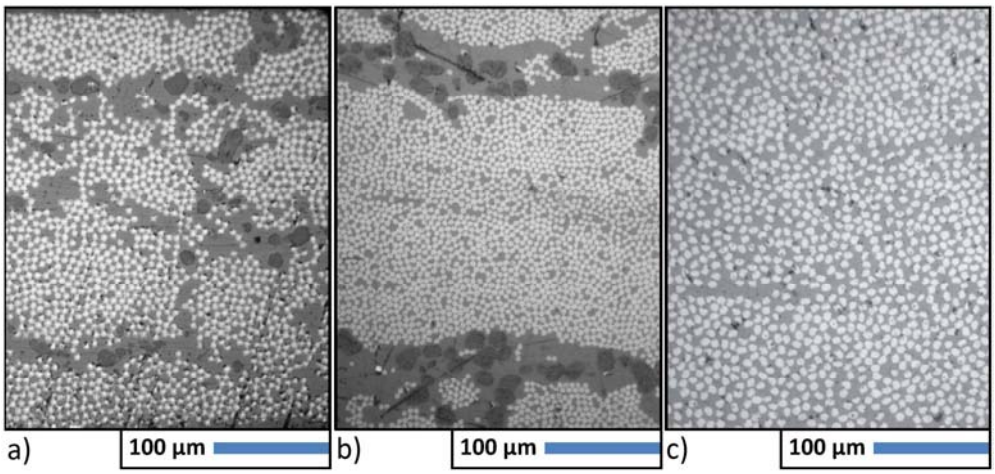

Figure 3.15 Optical micrographs of unidirectional sample used in this work: a) IM7/M21, b) T800/M21 and c) T300/914 – Observation of the ply constituents

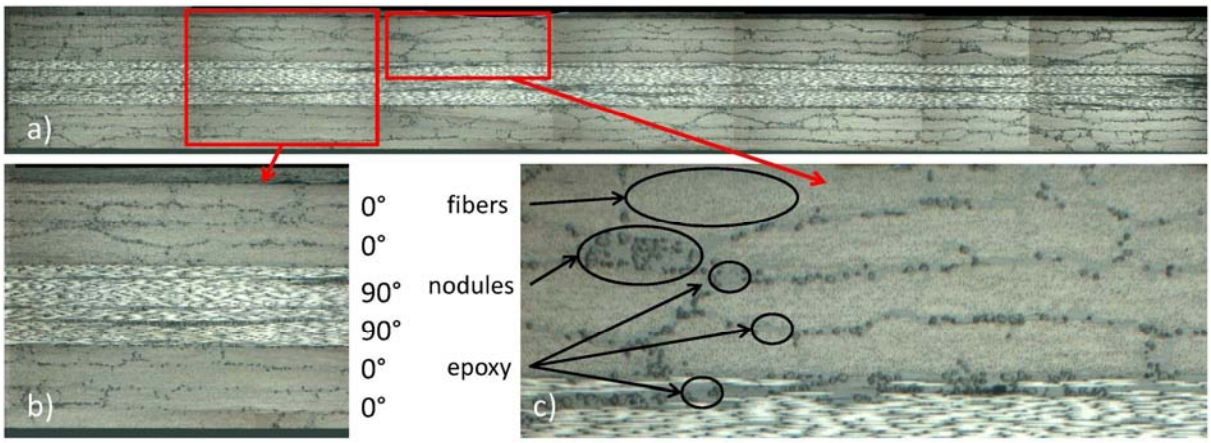

Figure 3.16 ***a)*** *Micrography of a CFRP composite of 1.5 mm thick,* ***b)*** *Observation of the whole thickness with plies orientation,* ***c)*** *Close look of the composition of T700S/M21 composite material, observation of fibers, epoxy and thermoplastic nodules*

Material	thickness (mm)	ply thickness (µm)	lay-up	Investigations	Used in section
T800/M21	1.5	250	[0°/0°/-45°/0°/0°/ 45°]	Induced damage	2.1
T800/M21	6.0	180	[A] 33 plies	Induced damage	2.2
T300/914	2.0	125	[0°]	Differences in damage tolerance	3.1, 3.2
T800/M21	2.0	250	[0°]		
IM7/M21	1.0	125	[0°]	Induced damage	3.3
IM7/M21	0.4	125	[0°]	Differences in spallation behavior	3.4
T300/914	0.4	125	[0°]		
T800/M21	0.5	250	[0°]	Dynamic response	4.1
T800/M21	3.0	250	[0°]	Dynamic response	4.2, 4.3
T700/M21	1.5	250	[0°/ 0°/ 90°/ 90°/ 0°/ 0°]	Dynamic response	4.4

Table 3.5 Summary on the CFRP composite samples used in this chapter: cross-ply composites for damage investigation (light blue), unidirectional model samples (mid blue), material for application (blue)

2 Post – mortem description of the damage resulting from the laser shock loading on T800/M21 CFRP materials

All the laser shocks presented in the two following sections have been performed in Institute PPRIME, in the Config-PPRIME-1 configuration, with water confinement and aluminum painting sacrificial layer. In section 2.3, the presented results have been obtained in Config-PIMM-1, using the same on-target configuration. The results are here divided in two categories which are thin CFRP and thick CFRP. These categories are in fact referring to the damage induced by the laser shock wave propagation, more than to the sample thickness even if the two are linked. Indeed, in case of a thin sample (compared to the laser spot), a full spallation of the sample can be observed, which did not occurred in case of a thick sample because of the shock wave decay increasing with sample's thickness.

2.1 Thin cross-ply T800/M21 CFRP

Results obtained on 1.5 mm T800/M21 composite samples are presented in this section (see in Table 3.5). These samples were shocked with four different laser energy levels on their front face. The samples have been cut perpendicularly to the 0° fiber direction, and cold coated in an Epofix resin to

be observed. Results show that the damage induced by the laser shock is cone-shaped through the thickness of the sample, with the cone basis on the back face (see in Figure 3.17). This observation is consistent with other scientific work and different impact loadings such as drop tower [13-16]. The same kind of damage can be observed for each laser shock. The position numbers given in the first column of Table 3.6 are referring to the corresponding damage in Figure 3.17. The laser spot diameter of 4 mm is also reported in this figure. Two main kinds of damage can be observed in a laser shocked composite sample. Transverse cracks in the matrix, through the ply thicknesses can be observed in Figure 3.17 and the most obvious damage is delamination between the plies, which can lead to ply ejection if the stresses level is high enough. The delaminations are initiated by the high tensile stresses generated by the propagation of the laser induced shock wave inside the composite. In these experiments, the high power laser irradiation of the composite sample results in a strong pressure load driven on a small spot (4mm diameter circle) compared to the size of the sample. Added to the target carrier effects, bending and shear loadings are induced, especially on the side of the impacted area. These high stresses lead to the apparition of transverse cracks perpendicularly to the ply plan inside the composite sample (see in Figure 3.17, references 1 & 5).

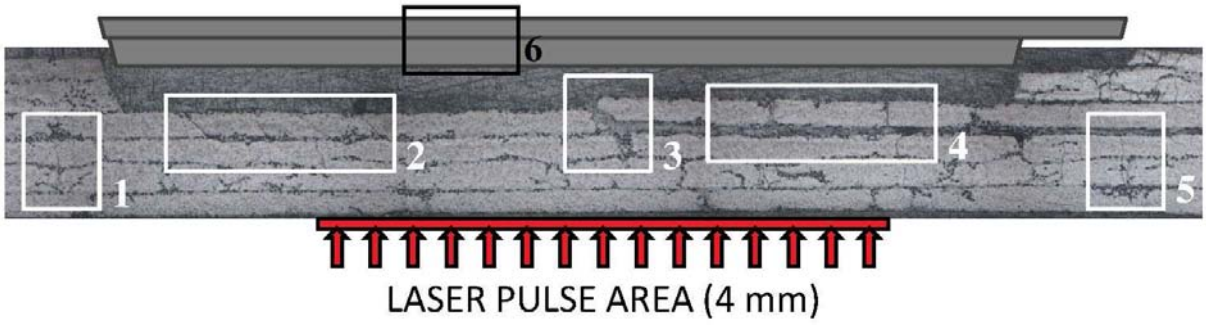

Figure 3.17 Shocked composite sample T800/M21 with reference numbers for damage analysis (Water confined laser pulse: I=5.30 GW/cm², Δt =30 ns, Dspot=4mm) – Optical micrography

Damage number	Short description of the observed damage
1 & 5	Transverse cracks through several plies close to a zone of high thermoplastic nodule concentration. Located on the edges of the loaded area
2	Local delamination with transverse cracks through the considered ply
3	Important damage with both ply failure and delamination, observed close to a zone of high thermoplastic nodule concentration
4	Two kinds of delamination: 1. Delamination with a ply ejection on the back face side. The delamination geometric profile can be observed. 2. Delamination without full ply ejection. Observation of the inter-ply after laser shock impact.
6	Ejected plies

Table 3.6 List of common laser induced damage observed in CFRP

An overview of the classic composite damage resulting from laser shock wave propagation is given in Figure 3.18. The observed zone is located under the impact loading area (reference number 2 in Table 3.6 and Figure 3.17). A ply delamination can clearly be identified, as well as transverse cracks inside the top ply. The cracks inside the ply have propagated between the fibers. According to other scientific works, these cracks through the plies are prior to the cracks leading to delamination. In the laser case treated in this paper, it can be assumed too as the high tensile stress area is propagating from the back face to the front face (from top to bottom in Figure 3.18). So the plies are loaded

before the inter-plies and can be damaged first. The plies that were just above the damaged one have been ejected during the laser shock test due to the high level of tensile stress (see in Figure 3.17 and 3.18). As the tensile loading level is progressively softened because of the energy dissipation resulting from the previous delaminations, the stresses were not strong enough to eject this ply but high enough to damage it.

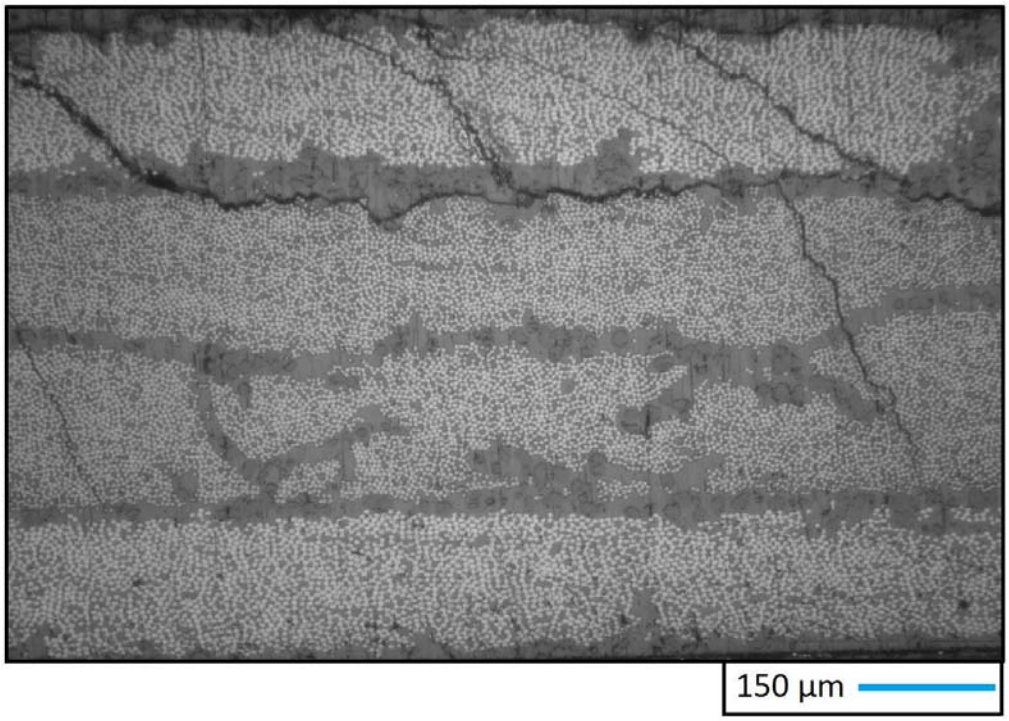

Figure 3.18 Close observation of damage resulting from laser shock waves propagation in cross-ply T800/M21 (Water confined laser pulse: I=5.30 GW/cm², Δt =30 ns, Dspot=4mm)

The crack profile leading to delamination can be linked to the presence of thermoplastic nodules inside the composite matrix M21. Indeed, the crack is following the ply surface geometry meanwhile it goes around the thermoplastic nodules. Moreover, cracks going through the nodules have never been observed on the many shocked samples analyzed. Two hypotheses can be made: the first one complies with the main goal of these nodules which is to enhance the shock resistance of composite material. Their presence makes the crack propagation harder because it increases the distance to cover before leading to delamination. The second one relies on the fact that adding nodules inside the matrix content can locally increase the stress concentration which can explain why the cracks are propagating around these thermoplastic nodules. In any case, the thermoplastic nodules seem to enhance the shock resistance of composite material. Their presence could slow down the crack propagation and thus prevent from an early delamination in case of high intensity impact. This hypothesis will be checked in section 3.

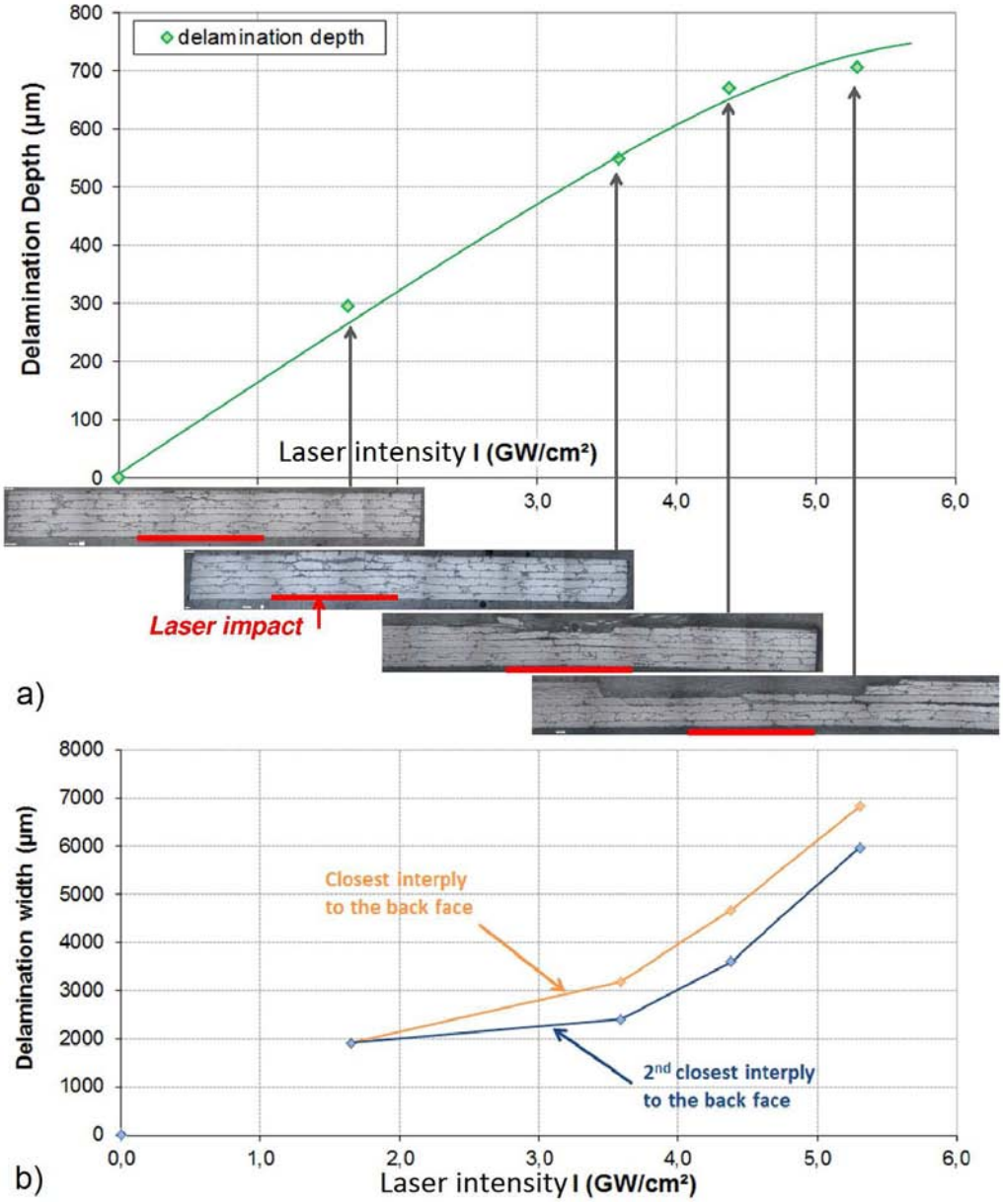

Figure 3.19 Correlation between the laser intensity and the damage depth (a), the delamination width (b) inside the composite target with the associated micrographies (Results obtained by optical inspection of four laser shocks on T800/M21 CFRP target, 1.5mm thick)

The observations performed have also highlighted the existing correlation between the laser intensity and the damage extent inside the composite targets. Different damage parameters can be observed thanks to optical micrographies (observations and results presented in Figure 3.19, 3.20 and 3.21) and linked to the laser shock parameters. In Figure 3.19-a, the damage depth is plotted against the laser intensity. The damage depth represents the existing distance between the sample back face and the furthest observed crack inside the composite. These measurements have been performed on four different micrographies of an impacted T800/M21 CFRP target also presented in Figure 3.19. It can be noticed that the delamination depth is increasing with the laser intensity. Indeed, the tensile stresses generated by the shock wave propagation are directly linked to the laser energy, meaning the laser intensity if both the focused diameter and the pulse duration remain constant. The stresses level is thus higher for higher energy pulse. In case of the lowest laser shock, the tensile stresses located close to the back face are just high enough to create a small delamination in the last inter-ply (see in Figure 3.19-a, first micrography). When the laser intensity is increased, the

highest stresses remain located close to the back face, but there is enough energy left propagating backward to delaminate a deepest inter-ply (see in Figure 3.19-a, second micrography and following ones). The same kind of correlation can be found between the laser intensity and the delamination width for a given inter-ply (see in Figure 3.19-b). For highest laser intensity loadings, the tensile stresses initiating the delamination are stronger. It facilitates the damage propagation and finally leads to a wider delamination. The same trend can be observed for several inter-plies. The delamination growth is shifted to higher intensity for the plies located deeper in the composite, which is consistent with the correlation between the laser intensity and the delamination depth.

In order to complete the previous comments, the ply delamination direction can be observed using X-Ray radiography. In Figure 3.20, the micrographies presented in Figure 3.19 are completed with the corresponding X-Ray radiographies, taken in the (x,y) composite plane. For the X-Ray images, the horizontal direction corresponds to the 0° direction. In case of the lowest intensity shock, the delamination and matrix cracking was observed between the two 0° last plies (see the first micrography in Figure 3.20). Consequently, the delamination propagated mainly in the 0° direction. Indeed, it can be observed in the Figure 3.20 first radiography that the delamination has an elliptical shape. It is contained in the laser shock spot area (marked in red), excepted in the 0° direction. The same observation can be made on the 3.59 GW/cm² laser shock. In this case, delamination occurred between the two 0° last plies, and between the 0° and the -45° direction because the energy was higher. Both delaminations propagated in the 0° direction. In case of the last shock presented in Figure 3.20, the delamination has gone deeper, because the laser intensity was even higher. In this laminate, they are both 45° and -45° plies which can be seen in the micrography. The 45° thin ply, remaining over the two 0° plies after polishing, is strongly delaminated as obviously shown on the radiography. It can also be observed that an additional delamination below the -45° ply has occurred compared to the previous sample. In that case, the delamination propagated in the -45° direction. The -45 ° delamination is also visible on the radiography, and thus corresponds to the description given.

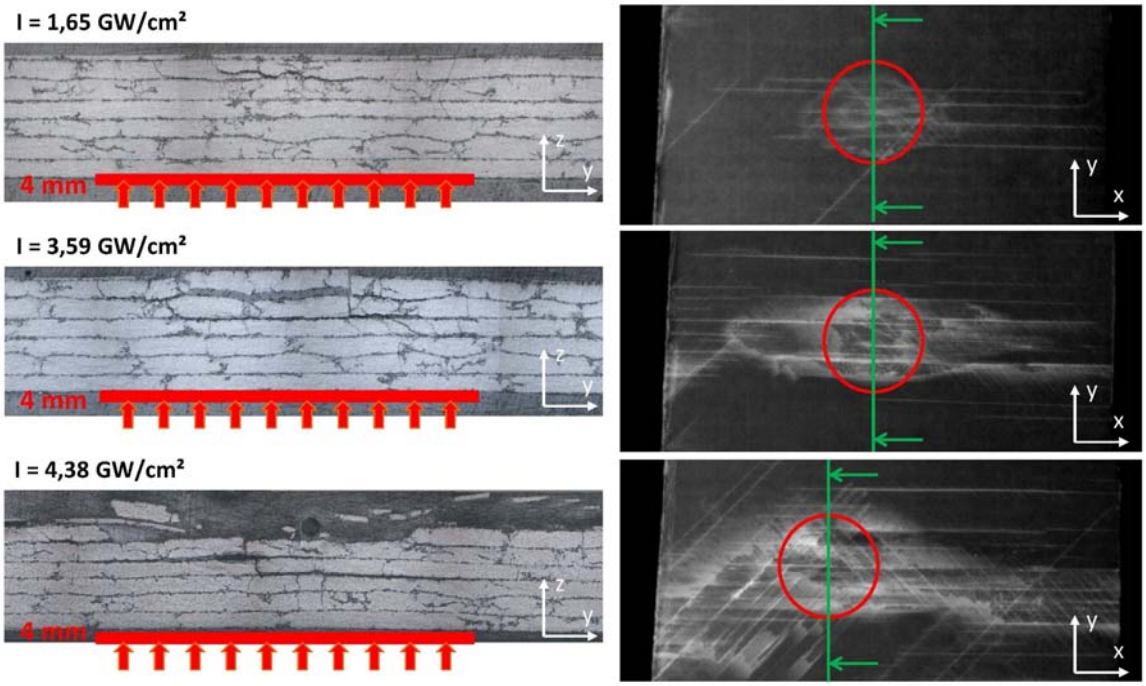

Figure 3.20, Additional information on the delamination propagation given by the X-Ray radiographies obtained in the T800/M21 composite plane – associated micrographies

The crack density evolution has also been studied (see in Figure 3.21). Using the micrographies presented in Figure 3.19-a, the number of transverse cracks inside all the plies was counted over a 10 mm length centered on the laser impact axis for each laser shocks. Consequently, cracks induced by the laser shock wave propagation and cracks resulting from the bending component of the loading are both taken into account (see Table 3.6 and Figure 3.17). The number of cracks was divided by the 10 mm length to obtain the crack density. As expected, it is increasing with the laser intensity. One more time, the highest laser intensity induces the highest level of damage which agrees with the previous observations. Finally, all the damage extent parameters seem to increase with the laser intensity. In this case of thin CFRP T800/M21 composite target, a clear correlation is established between the laser intensity irradiating the material and the resulting inside damage. Moreover, a quantification of this correlation has been obtained thanks to these original laser shock results on composite targets.

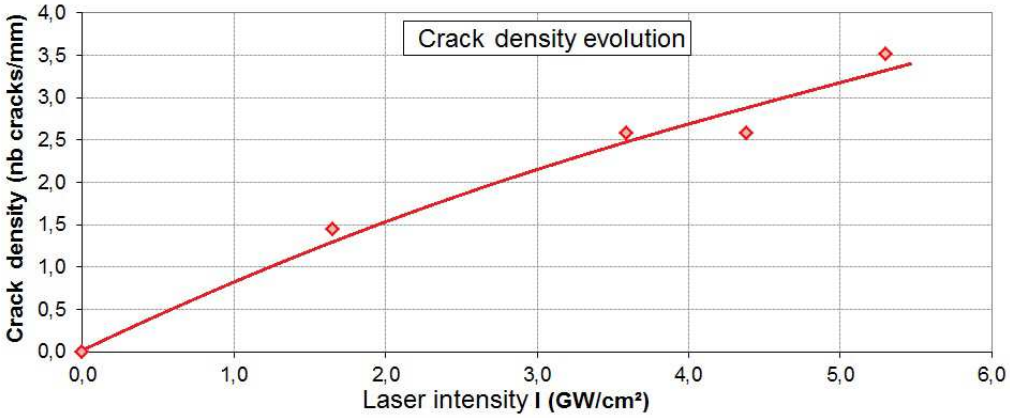

Figure 3.21, Correlation between the laser intensity and crack density inside the composite plies (Results obtained by optical inspection of the four T800/M21 targets)

2.2 Thick cross-ply T800/M21 CFRP investigations

Laser shocks were also performed on the 6 mm thick T800/M21 CFRP samples. Like for the previous samples, post-mortem analyses are performed in order to quantify delaminations and residual deformations. Four different laser pulse intensities (similar to the previous ones) have been applied. As this type of samples was much thicker than the previous ones, the damage induced by the shock waves propagation inside the material did not spall it completely (compared to the samples presented in Figure 3.17). Indeed, the laser shock wave amplitude is more decayed through the material thickness since there is a longer distance to cross before reaching the back face. In this case, the resulting damage is characterized by small blisters on the sample back face, which were measured using Interferometric confocal microscopy (ICM) and X-Ray radiography (see in Figure 3.22). ICM is based on optical interferometry to convert the flux intensity into height information. In the case presented here, several measurement areas have been needed in order to get the global blister shape. For each pixel located on the back face ply plan by an (x,y) coordinate, a height information is added. The measurement is obtained in the form of a matrix (x,y,z) and can be represented in the plan (x,y) using a color scale for the z coordinate as shown in Figure 3.22-a. In this example, an elliptical shape can be observed. The anisotropic characteristic of the delamination propagation is evidenced by this shape, in spite the axisymmetric loading, but directly linked with the 0° and 45° ply orientations. This observation can be confirmed by the X-Ray radiography measurement as shown by Figure 3.22, b and c.

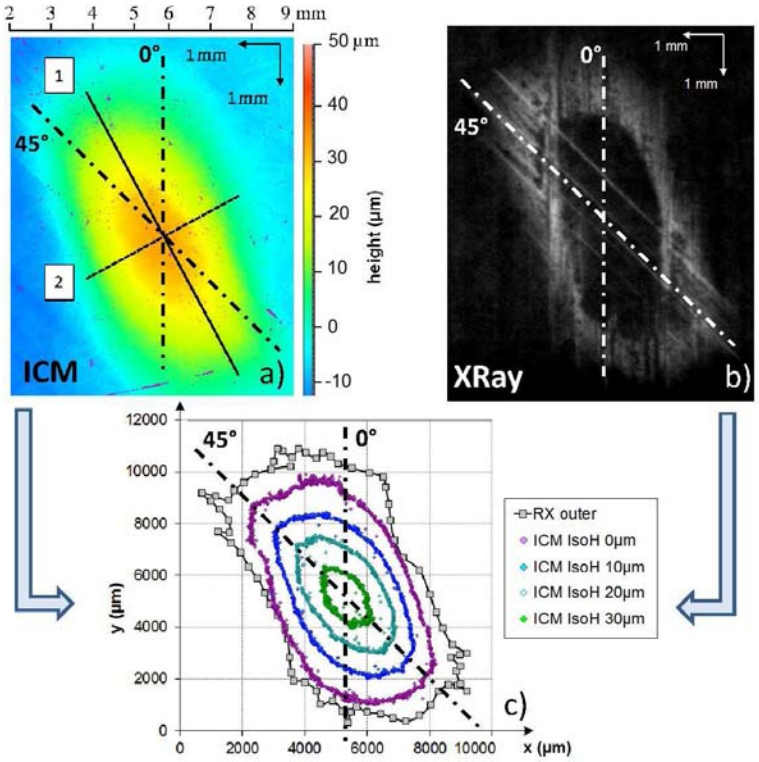

Figure 3.22, a) Interferometric confocal microscopy measurement of a back face deformation resulting from a laser shock on a 6mm thick T800/M21 composite sample, b) Corresponding X-Ray radiography of the same sample, c) Comparison between the radiography and the ICM measurements of the same back face deformation (Water confined laser pulse: I=5.30 GW/cm², Δt = 30 ns, Dspot=4mm)

The cross sections of the back face deformation are presented in Figure 3.23 and the corresponding ICM measurements are shown in Figure 3.24. These cross sections were performed perpendicularly to the 0° direction, and centered on the laser impacts. The two measurement techniques are consistent. Indeed, the delamination width observed in Figure 3.23 for each shock corresponds to the one which can be evaluated orthogonally to the 0° direction by taking the 0 µm isoheight ICM measurements. The comparisons of the different experimental values are given in Table 3.7.

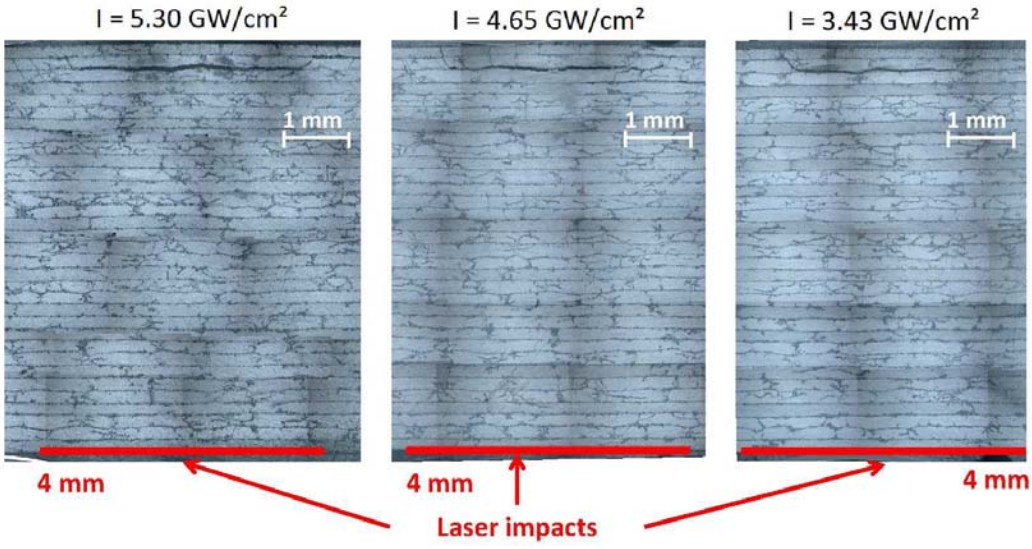

Figure 3.23, Cross section micrographies corresponding to the back face deformation of thick cross-ply T800/M21 samples, measured by ICM and analyzed in the following figures referred 3.24 (Water confined laser pulse: Δt =30 ns, Dspot=4mm)

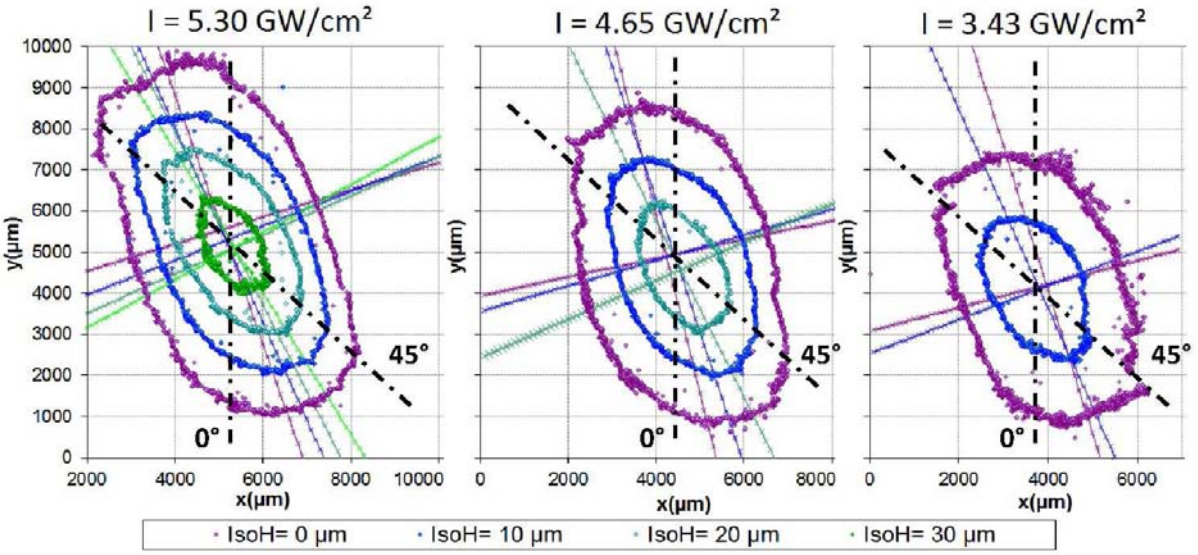

Figure 3.24, ICM post treated results for three different laser shock intensities. For different height levels, the (x,y) data highlighting the elliptical back face deformation and the associated major and minor axes calculated by statistical analysis are plotted (Water confined laser pulse: Δt =30 ns, Dspot=4mm)

	Delamination perpendicularly to the 0° direction		
I (GW/cm²)	**Micrographies**	**ICM**	**Deviation**
5.30	5095 µm	4713 µm	7.5 %
4.65	4240 µm	4384 µm	3.4 %
3.43	3680 µm	3719 µm	1.1 %

Table 3.7 Comparison of the delamination width in the 90° direction measured on micrographies and by ICM.

An accurate study of the ICM experimental results has been performed by using a statistical analysis, considering the experimental data as statistical series. First, it has been checked that the shape of isoheight is true ellipse. [x,y] data are extracted from the [x,y,z] obtained by ICM, for a given z, meaning a given height. The idea is to show that the correlation between the x and the y data, for all the given heights, is an ellipse. For that, the covariance matrix Σ whose expression is given in equation (3.4) is calculated. The Σ matrix is traducing the correlation between the x and the y data. The main directions of the statistical series x and y are thus given by the eigenvectors of the Σ matrix. For each [x,y] series, the eigenvectors can be calculated using equations (3.5), (3.6) and (3.7).

$$\Sigma = \begin{pmatrix} \sigma_x^{\,2} & R\sigma_x\sigma_y \\ R\sigma_x\sigma_y & \sigma_y^{\,2} \end{pmatrix} \quad with \quad \begin{cases} \sigma_x : \text{standard deviation of the x data} \\ \sigma_y : \text{standard deviation of the y data} \\ \text{R} : \text{Correlation coefficient} \end{cases} \tag{3.4}$$

First, the equation (3.5) is solved for each series to determine their eigenvalues noted λ_1 and λ_2. Once calculated, these eigenvalues can be used to determine the two eigenvectors named U and V of each statistical series using the equations (3.6) and (3.7).

$$Det(\Sigma - \Lambda I) = 0 \quad with \quad \begin{cases} \Lambda = [\lambda_1, \lambda_2] : \text{vector of eigenvalues} \\ I : \text{Identity matrix of dimension 2} \end{cases} \tag{3.5}$$

$$\begin{cases} \Sigma \cdot U = \lambda_1 \cdot U \\ \Sigma \cdot V = \lambda_2 \cdot V \end{cases} \quad with \quad \begin{cases} U : \text{eigenvector associated to } \lambda_1 \\ V : \text{eigenvector associated to } \lambda_2 \end{cases} \tag{3.6}$$
(3.7)

As explained previously, the two vectors U and V give the main directions for the statistical series [x,y]. It was checked that these vectors were orthogonal for each isoheight series of each laser shock, showing that it could correspond to an elliptical distribution. Then, the two main axes of the statistical [x,y] series can be deduced using the eigenvectors as director vectors. A point which is known to be on each axis has to be chosen to plot the axes. In this case, if the two main axes are respectively the minor and the major axes of the ellipse searched, they are passing by the ellipse center. This center point is obtained by calculating the average of all x data as first coordinate, and the average of all y data as second coordinate. All these axes are plotted with their isoheights statistical data [x,y] in Figure 3.24. It can be observed that the calculated axes are well corresponding to the major and minor axes of each [x,y] contour lines, and for each laser shock deformation. Finally, the axes got from the eigenvectors can be used to calculate theoretical semi-major and semi-minor axes. The intersection point between the axes and the [x,y] contour line is picked for each series and used to calculate the axes length. Then, the semi-major and semi-minor axes lengths, respectively noted α and β, are used to build the corresponding theoretical elliptical shape with the equation (3.8). For each x value, the corresponding y value is calculated with the parameters α and β using equation (3.8) for each series. The obtained ellipses are then rotated using a classic transformation given in equation (3.9), and translated in the (x,y) plan to be compared to the experimental isoheight data.

$$\frac{x^2}{\alpha^2} + \frac{y^2}{\beta^2} = 1 \quad with \quad \begin{cases} \alpha : \text{semi-major axis length} \\ \beta : \text{semi-minor axis length} \end{cases} \tag{3.8}$$

$$z \rightarrow z e^{i\theta} \tag{3.9}$$

$$S = \pi \cdot \alpha \cdot \beta \tag{3.10}$$

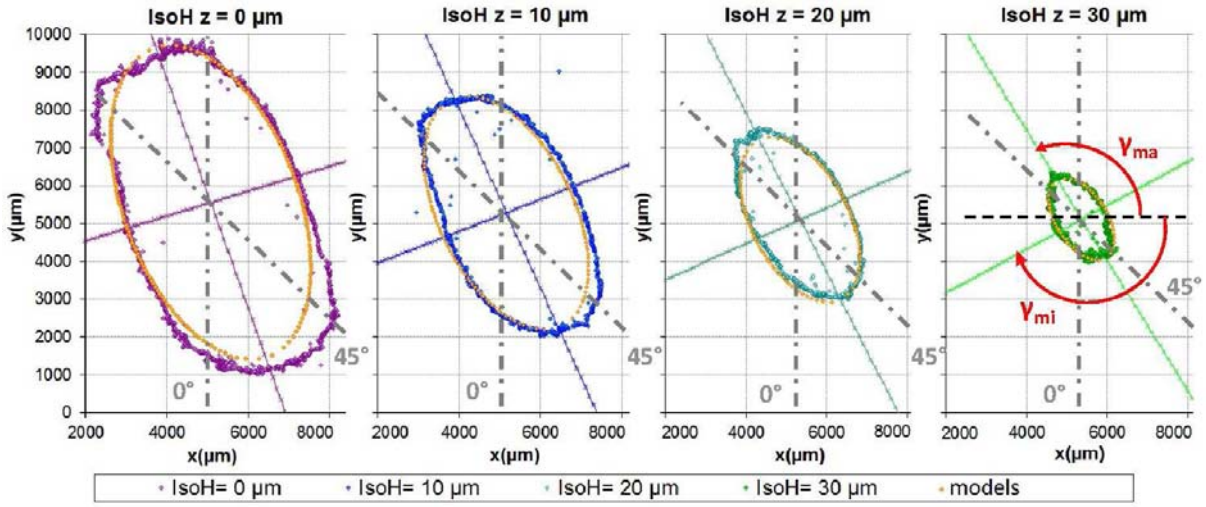

Figure 3.25, Comparison between the experimental isoheight lines and the theoretical elliptical shapes calculated using the experimental parameters of the statistical series, for four different isoheight levels measured by ICM on the highest shocked T800/M21 sample.
(Water confined laser pulse: I=5.30 GW/cm², _t =30 ns, Dspot=4mm)

Some comparisons are given in Figure 3.25 for four different isoheight levels measured by ICM on the shocked sample with the highest laser intensity level. The calculated ellipses are fitting quite well with the experimental contour lines. The agreement is even better for the high z values contour-lines, when a few differences can be observed at low height (see z = 0 µm chart in Figure 3.25). This is probably due to edge effects which are more significant closer to the back face normal height. Finally, the good agreement between calculation of the elliptical curves and experimental data enables some model analysis.

Three different studies are presented in Figure 3.26. The evolution of the semi-major and semi-minor axes lengths with the height level is first presented in Figure 3.26-a. It can be noticed that for each laser shock both parameters are decreasing when the height level of contour lines is decreasing. The evolutions are linear with a good correlation (see the correlation equations Figure 3.26-a). It gives precise quantitative data on the blister shape created at the sample back face by the laser shocks. Another interesting parameter is the damage area. It can be calculated using equation (3.10). The evolution of the damage surface area with the height level of the back face deformation is presented in Figure 3.26-b. Logically, it decreases with the altitude. Curves can be modeled by a quadratic equation as presented in Figure 3.26-b.

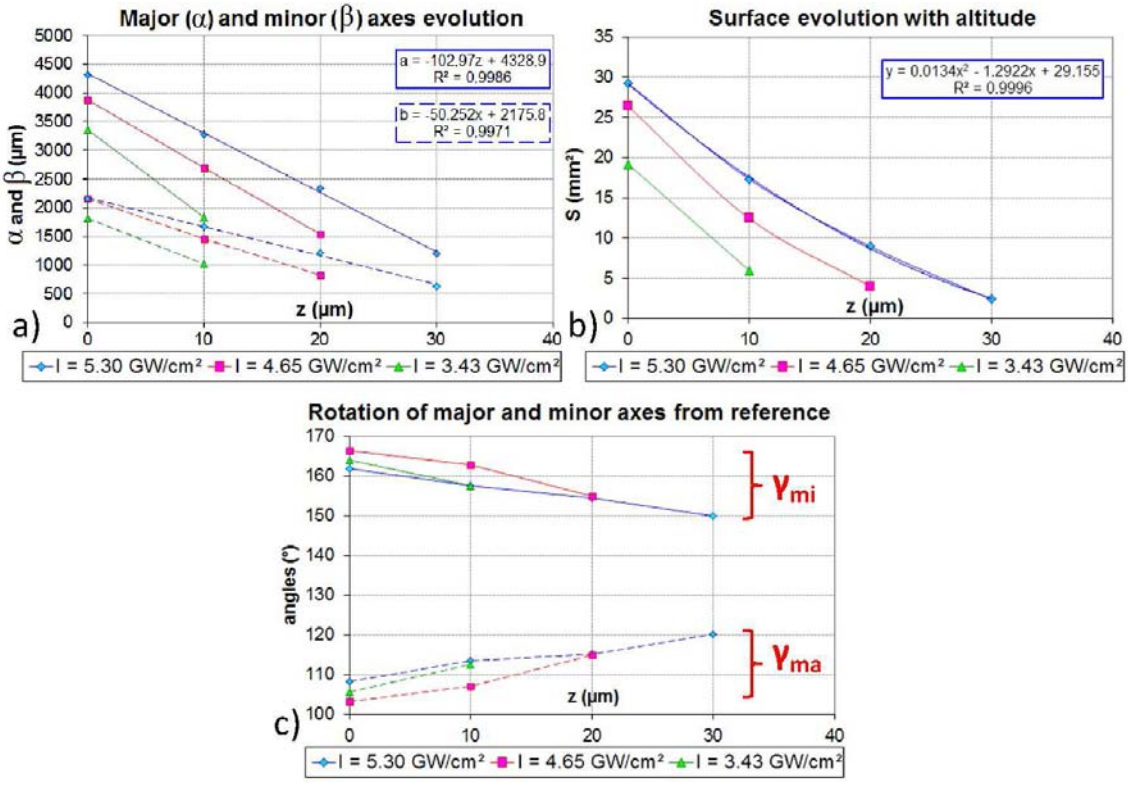

*Figure 3.26, Analysis of the back face blister on T800/M21 samples: **a)** Evolution of the semi-minor (dash line) and semi-major axes (plain line) lengths versus the height of the contour line with the associated correlations, for the different laser intensities, **b)** Evolution of the in-plane deformation surface defined by the contour line versus the height level of the contour line with the associated correlation, for the different laser intensities, **c)** Evolution of the angles between the major and minor axes and the horizontal axis versus the height of the contour line, for the different laser intensities*

Finally, the angles γ_{mi} and γ_{ma} to the horizontal axis of both minor and major axes respectively can be plotted as a function of the back face deformation height. These angles are defined in Figure 3.25, on the last chart. Their evolutions according to the height deformation for each laser shock are presented in Figure 3.26-c. A small rotation of the elliptical contour line of about 15 degrees can be

noticed on both axes. This rotation is probably traducing the history of the delamination propagation between the closest plies to the back face. As it can be seen in the Figure 3.23, the delamination occurred close to the back face between two 0° plies. The delamination propagated in the 0° direction, but the back face ply is in the +45° direction. This could explain why the deformation orientation at the top of ellipse is closest to the 0° direction than the deformation orientation at the bottom of the blister. Moreover, the bending component of the loading could also have an influence. Once delaminated, the plate bended is non-symmetrical, since it is only composed of two plies in the 0° and 45° directions. The buckling of this non-symmetrical plate can increase this unconventional characteristic of the delamination. Indeed, in this case of thick sample, it is possible that the stresses reaching the composite back face are probably just high enough to initiate delamination. The following damage propagation and back face deformation are probably mainly due to the detached plies buckling, more than in the case of thin composite targets. For that reason, this data would be very interesting to compare with numerical modeling.

This mathematical analysis can then be used to study the existing correlation between the composite back face deformation and the laser intensity. Indeed, by using the major and minor axes deduced from the statistical analysis, blister profiles were extracted from the ICM measurements, especially along these two axes of the elliptical shape (respectively referred 1 and 2 in Figure 3.22-a). A comparison between these two profiles is given in Figure 3.27, which allows quantifying the anisotropy of the back face deformation. These profiles can also be used to correlate the back face deformation with the laser intensity used to irradiate the composite target as shown in Figure 3.28. On this figure, the minor and major axes profiles were plotted for the three highest laser shock levels. The back face profile obtained with the lowest one was measured as a completely flat surface, and was not reported on these charts (see laser shock parameters in Table 3.8). Two experimental parameters can be gathered on each profile: the maximum height and the width at mid-height, both reported in Table 3.8. These parameters were used to fit models on the experimental profiles. Indeed, each experimental profile obtained from ICM can be fitted using Gaussian function as presented in Figure 3.28, characterized by A, b and c parameters. This kind of function was already used to fit experimental deformation in case of other types of loading on CFRP [17]. The three model parameters corresponding to the optimized fittings are given in Table 3.8. The “A” parameter is chosen to be equal to the maximum height measured experimentally, and “c” is adjusted to fit the waviness of the deformation profiles. “b” parameter is just used to adjust the position of the symmetrical axis of the model.

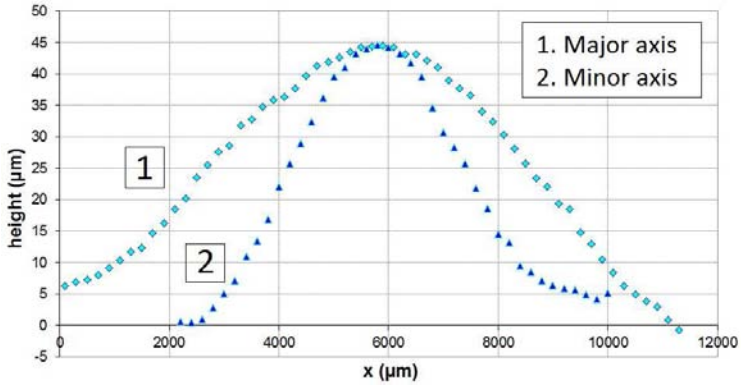

Figure 3.27, Comparison between the major and the minor axes of the elliptical back face deformation extracted from the Interferometric confocal microcopy for thick T800/M21 samples (Water confined laser pulse: I=5.30 GW/cm², Δt =30 ns, Dspot=4mm)

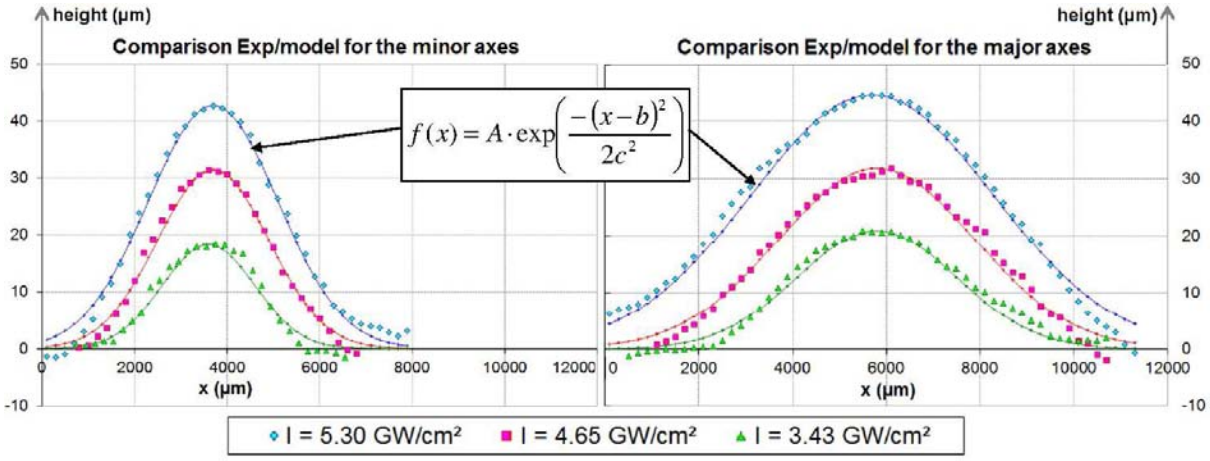

Figure 3.28, Comparison between the profiles along the major and the minor axes of the elliptical back face deformation for different laser intensities applied on T800/M21 laminates (Water confined laser pulse: Δt =30 ns, Dspot=4mm)

Major Axes	Experiments		Models		
I (GW/cm²)	**hmax (µm)=A**	**D(h/2) (µm)**	**A (µm)**	**b (µm)**	**c (µm)**
5.30	44.5	6500	44.5	5700	2600
4.65	31.8	5150	31.8	5800	2100
3.43	20.9	4325	20.9	5800	1700
1.83	0	0	0	0	0
Minor Axes	Experiments		Models		
I (GW/cm²)	**hmax (µm)=A**	**D(h/2) (µm)**	**A (µm)**	**b (µm)**	**c (µm)**
5.30	42.7	3475	42.7	3700	1400
4.65	31.4	2925	31.4	3700	1200
3.43	18.3	2600	18.3	2600	1000
1.83	0	0	0	0	0

Table 3.8 Experimental and model parameters for the back face deformation profiles on T800/M21 laminates

The “A” and “b” parameters can then be used to represent the existing correlation between the residual back face deformation and the laser intensity level. These correlations are presented in Figure 3.29. The damage represented by the maximum height and the waviness parameters grows with the laser intensity level. Moreover, the evolution linking the maximum height to the laser intensity seems to be linear with a good correlation (see in Figure 3.29). Thanks to these charts, it can be assumed that the damage threshold on the T800/M21 composite sample tested is close to 2 GW/cm². This is valid for a 6 mm thickness, and this specific lay-up. The determination of its exact position would require more laser shock experiments to refine the bottom of the curve and deduce precisely the behavior at low laser intensity. Cross section micrographies have also proved that the inside delamination sizes agree with the back face deformation height (see micrographies in Figure 3.23). The lowest shock showing no back face deformation was not delaminated either. The highest back face deformation corresponds to the longer delamination width and so on. These results show that there is a direct link between the inside delamination size and the back face blister height.

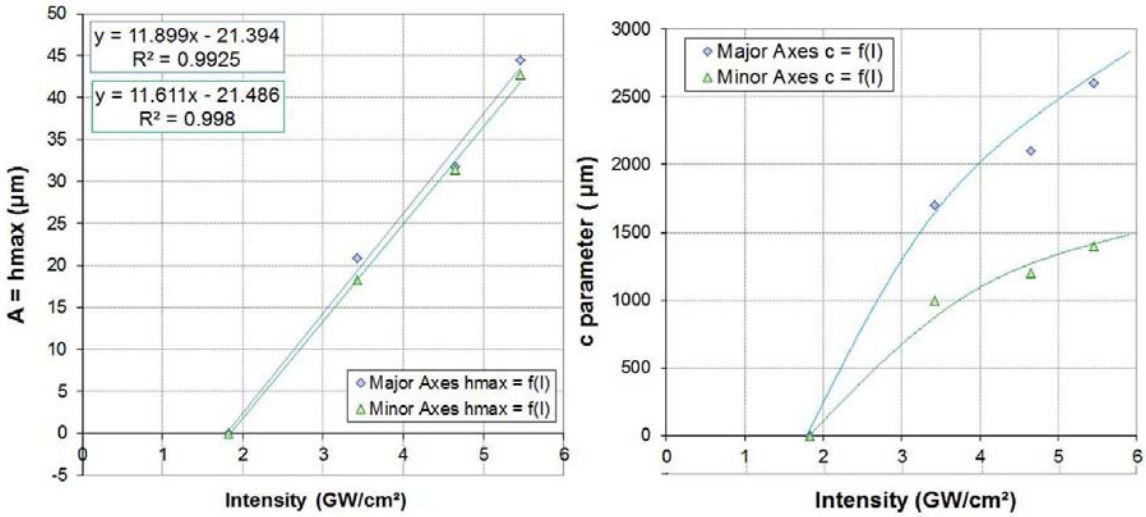

Figure 3.29, Correlations between the laser intensity and the main back face deformation parameters for thick cross-ply T800/M21 composite (Water confined laser pulse: Δt =30 ns, Dspot=4mm)

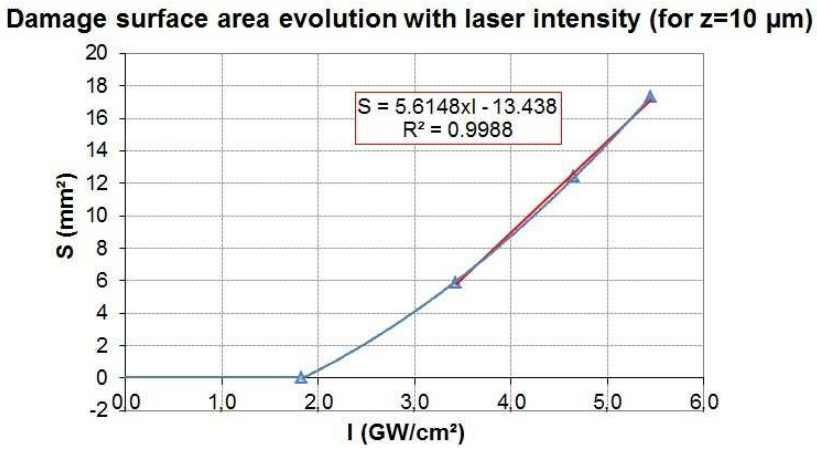

Figure 3.30, Evolution of the damage surface area for a given height (z = 10 µm) against the laser intensity, with the associated correlation for T800/M21 laminates - Damage threshold determination.

Finally, the calculated surface area can also be plotted against the laser intensity for a given height using α and β length (see equation 3.10). In the chart presented in Figure 3.30, the damage surface area at z = 10µm is plotted for different laser intensities. The global trend of the obtained curve is quadratic (see the correlation equations in Figure 3.30). Figure 3.30 also shows that this type of chart provides a good way for the damage threshold determination. These three last correlations between the composite damage features and the laser intensity allow the creation of charts to compare different composite materials dynamically loaded. As it has been evaluated in Figure 3.29, the damage threshold for the studied T800/M21 composite is confirmed to be around 2 GW/cm².

3 Comparison of different unidirectional CFRP responses to laser shocks – damage tolerance

3.1 Laser shocks and goal study

In this section, two aeronautical composite materials are compared. Based on the previous analyses, the idea is here to show that the laser shock technique can also be used to investigate CFRP composite damage tolerance. Meanwhile, the shock resistant effect of M21 matrix is investigated by

comparing the laser shock damage in a unidirectional T800/M21 material, and the one produced in a second composite, presenting a conventional matrix. This material is a unidirectional T300/914 CFRP. It is composed of several pre-impregnated plies of carbon fibers and epoxy matrix (approximately 150 µm thick). In order to quantify only the difference of the resin content, the two material lay-ups have been chosen to be identical (unidirectional) as well as the sample thickness (2 mm). In addition to the resin content, the plies thickness (250 µm in case of T800/M21) and the fibers are also different. Nevertheless, this is not a big issue since the literature proved that the dynamic response of CFRP in transverse direction is close to the one of the matrix content. Therefore, the shocks produced on samples from each material are comparable. For the same reason, the laser shocks performed on each material should be perfectly identical. The Config-PPRIME-1 was also used in this investigation, still in water confinement configuration, and with aluminum painting sacrificial layer. The laser shock parameters are given in Table 3.9. Four different shock levels were produced on each material, and are really close one from another on T800/M21 and T300/914 compared to the uncertainties values. The results are thus comparable. After the laser shocks, the samples were recovered from the experimental setup to be analyzed using with the three diagnostics used in the previous section: X-Ray radiography, Interferometric confocal microscopy, and optical microscopy.

Sample	Thickness (mm)	Energy (J)	Duration (ns)	Dfoc (mm)	Intensity (GW/cm²)
T300/914-1	2	7.22 ± 0.1	28.25 ± 0.2	4 ± 0.1	2.03 ± 0.1
T800/M21-1	2	7.22 ± 0.1	27.30 ± 0.2	4 ± 0.1	2.11 ± 0.1
T300/914-2	2	3.15 ± 0.1	28.27 ± 0.2	4 ± 0.1	0.89 ± 0.1
T800/M21-2	2	3.15 ± 0.1	28.40 ± 0.2	4 ± 0.1	0.88 ± 0.1
T300/914-3	2	1.68 ± 0.1	25.60 ± 0.2	4 ± 0.1	0.52 ± 0.05
T800/M21-3	2	1.68 ± 0.1	28.40 ± 0.2	4 ± 0.1	0.47 ± 0.05
T300/914-4	2	0.66 ± 0.1	27.60 ± 0.2	4 ± 0.1	0.19 ± 0.05
T800/M21-4	2	0.66 ± 0.1	27.37 ± 0.2	4 ± 0.1	0.19 ± 0.05

Table 3.9 Laser shock parameters used for T300/914 and T800/M21 composite samples

3.2 Post mortem observations

The X-ray radiographies of the two series are presented in Figure 3.31. The fiber direction is horizontal and the samples are ordered from left to right in the laser intensity level decreasing order. The main in (x,y) plane damage dimensions are revealed in white by the zinc iodide inserted using a specific solution beforehand. Compared to the previous results, it can be observed here that the delamination mainly propagated in the 0° direction for each series. For the highest intensity shocks, the damage in the 90° is not very larger than the laser spot area (marked by a red circle). Once again, a direct correlation can be made between the damage extent and the laser intensity for each material. Moreover, a large rupture in the fiber direction can be observed for both materials. The flexural component of the loading is responsible for that failure since unidirectional composites are quite weak in that direction. This effect should be enhanced by the small size of the sample. Differences between T300/914 and T800/M21 materials can be noticed in Figure 3.31. Even if both materials were not broken for the lowest intensity level, the T300/914 samples are globally more damaged than the T800/M21 samples for an equivalent laser shock. The delaminations seem wider, and the ruptures are more obvious on T300/914 samples. This could be confirmed by the optical micrographies presented in Figure 3.32.

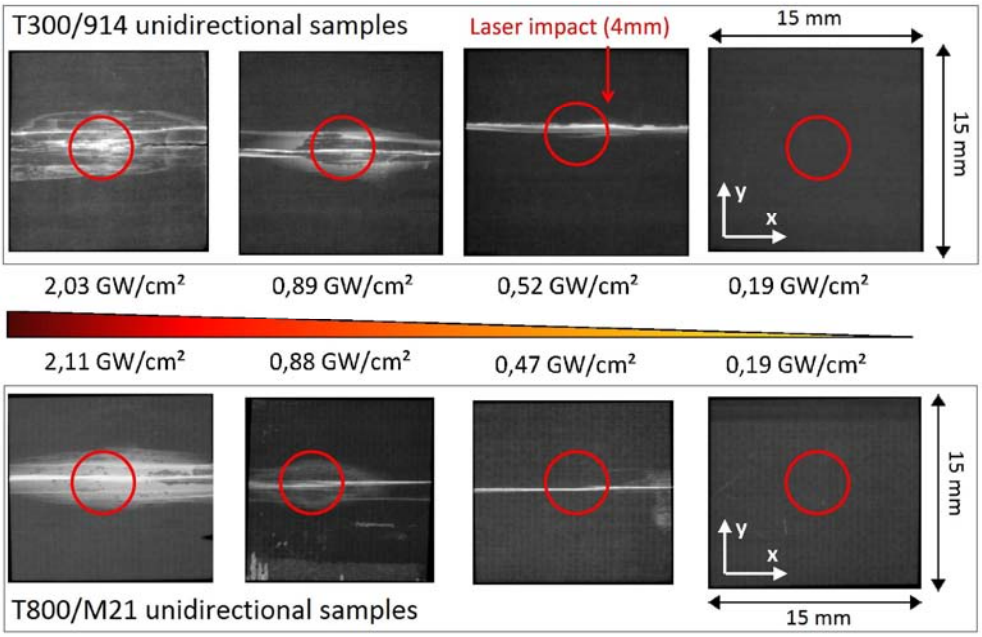

Figure 3.31, X-Ray radiographies of T300/914 and T800/M21 unidirectional composite samples – Four different laser shocks of various intensities were performed on each series

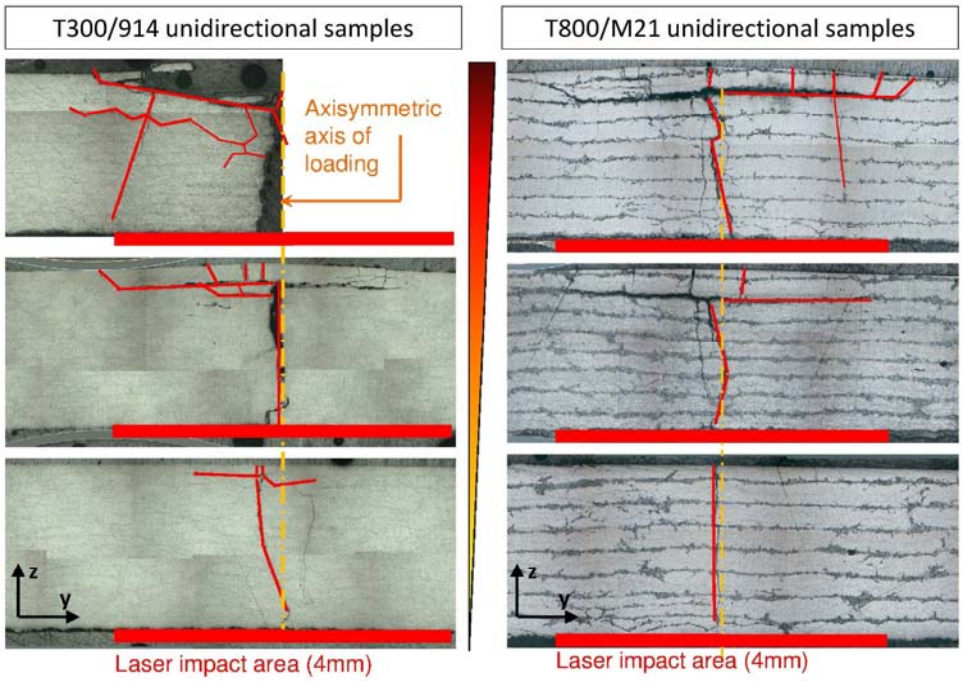

Figure 3.32, Comparison of the inside damage for two set of samples: T300/914 and T800/M21 – All the samples were shocked with various laser intensities (cf. Table 3.9)

Cross section observations perpendicularly to the fibers were made (see in Figure 3.32). For all the presented micrographies, the 4 mm diameter laser impact area is represented on the bottom of each sample; it is meaning the front face. They are separated in two by the axisymmetric axis of laser shock loading which is also defining the symmetric plan of the samples since they are all unidirectional. On one side only, the observed damage such as delaminations or cracks is highlighted by red lines. On both materials, the damage is located close to the back face, around 250 µm deep. This is due to the pulse duration of the laser source used as previously explained. This is consistent with the previous results. One more time, a direct correlation between the laser intensity level and

the damage extent can be observed. Long transverse cracks due to the flexural component of the loading can also be seen on the micrographies. They are more obvious for T300/914 samples than for T800/M21 samples, especially for the highest intensity values. In that loading case, the T300/914 sample was broken in two by the laser shock, when the T800/M21 sample was still in one part. But the laser irradiation is also responsible for the delamination which can be observed on almost all the micrographies. Delaminations and associated transverse cracks are due to the local tensile stresses induced by the laser shock wave propagation. In case of the highest intensity value, complete spallation has occurred for T300/914 material, and a few plies were ejected under impact. The corresponding T800/M21 sample is completely delaminated too, but all the plies remained on the sample (see the first two images in Figure 3.32). In case of the lowest intensity value, the T800/M21 is not delaminated, but the T300/914 is delaminated along a small length. The micrographies confirm the observations made by X-Ray radiography: T800/M21 material seems stronger face to laser shocks.

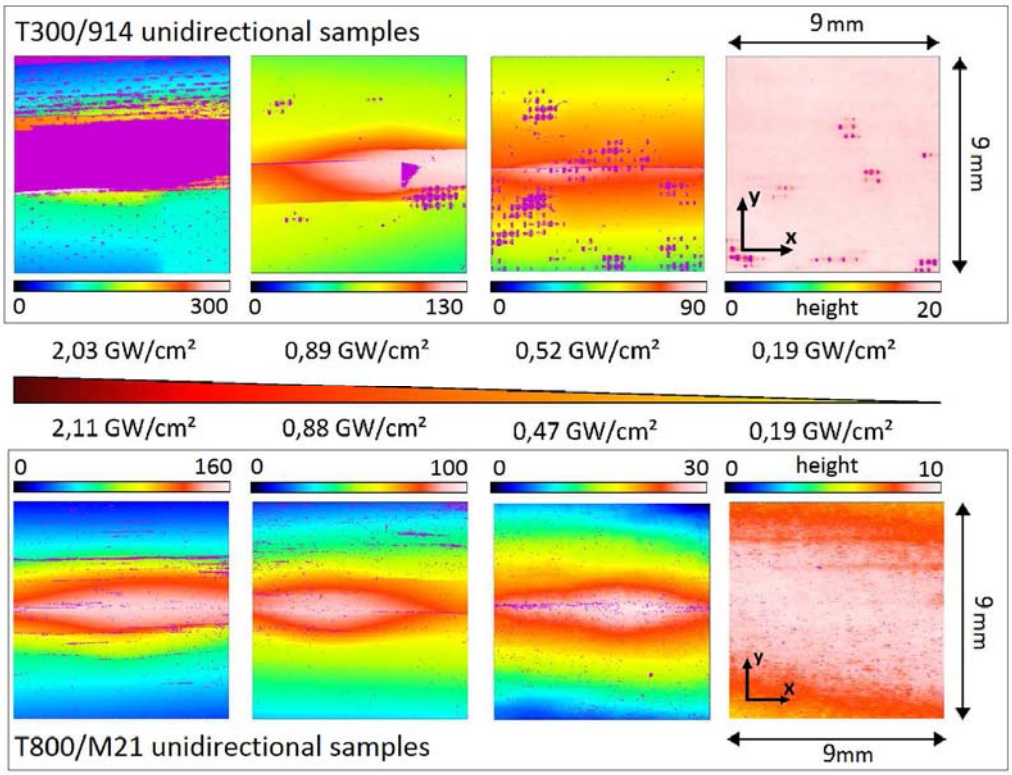

Figure 3.33, Interferometric confocal microscopy on T300/914 and T800/M21 unidirectional composite back face samples – The deformation amplitude in µm is given by the color scale.

Interferometric confocal microscopy can provide complementary information and has been used to quantify the difference in the residual deformation of each sample. The two series have been measured and compared using this technique (see in Figure 3.33). A zone of 9 mm per 9 mm is measured for each sample. The back face deformation amplitude is given in micrometers by the color scale. In case of the most destroyed T300/914 sample, the area where ejection occurred was not measured (too deep). These measurements and the other ones previously presented are consistent. However, it can be noticed that the elliptical shapes measured on these unidirectional samples are much more stretched out than in the case of more complex lay-up (see section 2). The laser parameters being very close to the one used in the previous study, it can be concluded that the material itself and its lay-up have a strong influence on the damage propagation and back face residual shape. The thickness has also a role to play. This point will be discussed in section 3.3. In

order to compare the two materials, profiles orthogonal to the fiber direction and centered on the observed elliptical shape were extracted (see in Figure 3.34). For the two materials, a correlation between the back face deformation and the laser intensity level can be made. As expected, when the laser intensity increases, the residual back face deformation is more important. In case of T300/914 samples, the spallation is also visible by the blank in the curve (see in Figure 3.34).

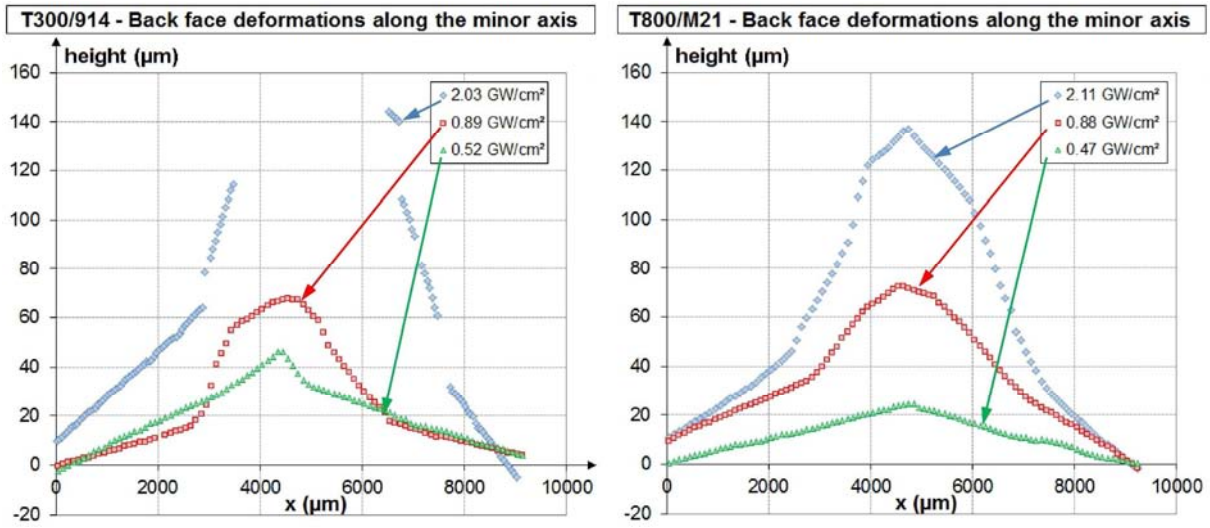

Figure 3.34, Residual back face deformation measurements by ICM for two sets of samples: T300/914 and T800/M21

Based on the work presented in the previous section, the maximum of residual back face deformation can be used to compare the different shocks. Except for the mid energy level, the residual back face deformations are more important in case of T300/914 samples. This observation can be summarized by plotting the maximum deformation height against the laser intensity values (see the graph in Figure 3.35). It enables to evidence a possible difference in damage threshold to the laser shock between the two composite materials used in this investigation even if more numerous shocks could be necessary to refine the damage threshold values. In addition to the cross section observations and to the X-Ray radiographies, this last analysis justifies the enhanced shock resistance of the T800/M21 compared to the T300/914 characteristic. Thus, the laser shock wave technique could be used as a way to compare the shock resistance of materials.

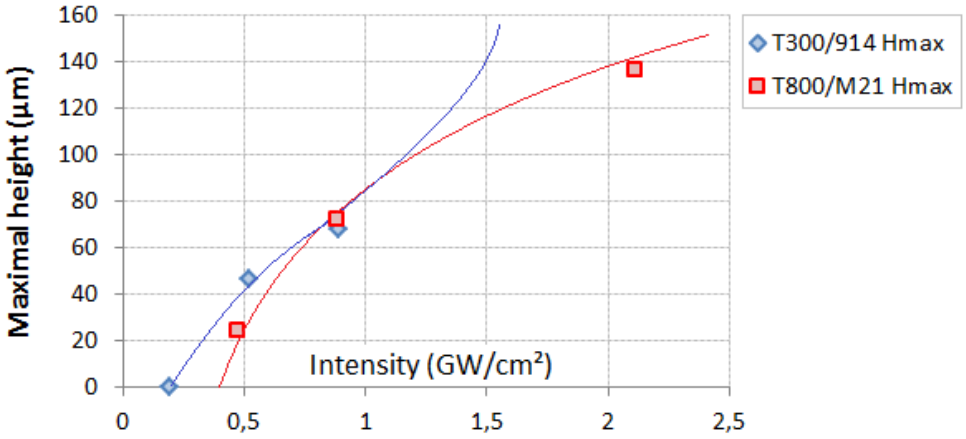

Figure 3.35, Comparison of the maximal back face deformation height between T300/914 and T800/M21 materials – Spallation occurs at the last intensity level for T300/914 samples

3.3 Toward the use of dimensionless number for composite sample classifications

From the Figure 3.33, it has been observed that the direction of the delamination, and consequently on the residual back face deformation can change from one material lay-up to another. This is quite normal, since it has been shown that it depends on the anisotropic characteristic of the material. Nevertheless, damage orientation and damage extent are two different things. From the observations made, it can be assumed that for a given CFRP, the three following parameters can play a role on the damage propagation, orientation and corresponding residual back face deformation: laser spot diameter, material thickness and material lay-up. Indeed, it has been shown in section 2 and 3 that in some directions the damage was not exceeding the laser spot area. This could be due to the fact that the damage initiation is everywhere the same under the impact loading area. The damage propagation is then a question of material response and only that. This could explain why some directions are preferred. The material thickness is also important because it has a consequence on the shock wave decay as well as on the influence of 2D effects on the spatial shock front attenuation. In other words, both focused diameter and sample thickness have an influence on the level of tensile stresses, and on their repartition in the (x,y) plane. Finally, the lay-up is important for the quoted reasons. It has a strong influence on the damage propagation and on the back face buckling after damage initiation. Starting from these observations, it can be wondered if one parameter would remain constant and would intrinsically characterize each CFRP samples, with its thickness and lay-up. This parameter could be the major axis length/ minor axis length ratio. Indeed, from the measurements presented in section 1.2 (Figures 3.22 – 3.29), it can be observed that this ratio remains constant regarding to the laser shock intensity (see in Figure 3.36, blue series).

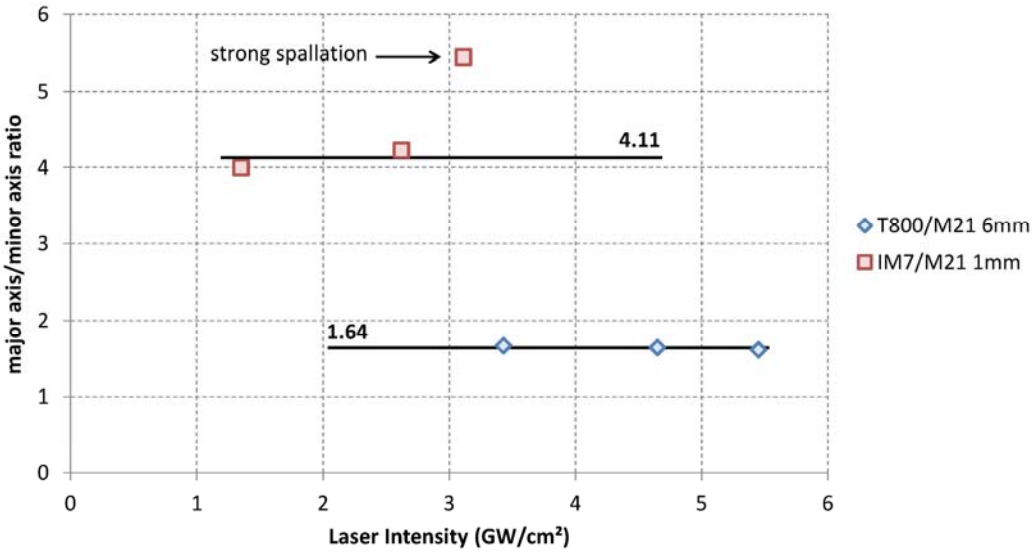

Figure 3.36, Graph representing the major axis length/ minor axis length ratio for two different shocked materials as a function of laser intensity

This observation has been checked using another series of laser shocks (see in Figure 3.36, red series). They have been performed on a 1 mm thick unidirectional IM7/M21 material, using Config-PIMM-1 configuration with water confinement and aluminum painting. The laser parameters are given in Table 3.10. The use of different laser parameters on a 1 mm thick sample enables to avoid complete spallation of the target, even if a few fibers are missing. The laser shock parameters have been chosen in order to enable a full quantification of the residual back face deformation. Indeed, this deformation should not be too wide compared to the sample size to be fully measured. This was

not the case of the samples presented in Figure 3.33 for example, because the samples were too small compared to the 0° delamination. The smaller pulse duration and the smaller focused diameter enable to produce shocks with the same laser intensity order. The ICM measurements of the 3 samples are presented in Figure 3.37. Once again, the correlation between the laser intensity and the residual back face deformation is respected (see in Figure 3.37 and Figure 3.38). The elliptical shapes evidenced on the ICM measurements are more stretched than the ones measured on the previous T800/M21 6 mm thick sample. The ratio between major and minor axes lengths is also much more important as shown in Figure 3.38 and summarized in Figure 3.36. It is about 4 and also more or less not dependant from the laser intensity as well. The highest shock is a bit different because it leads to a strong delamination (see on the right of the blister in Figure 3.38).

Samples	Thickness (µm)	Energy (J)	Pulse duration (ns)	Spot diameter (mm)	Intensity (GW/cm²)
S2-5 A2	1000	1.02	10.43	2	3.13
S2-5 C2	1000	0.85	10.32	2	2.63
S2-5 E2	1000	0.54	12.72	2	1.34

Table 3.10 Laser shock parameters used for unidirectional IM7/M21 composite samples

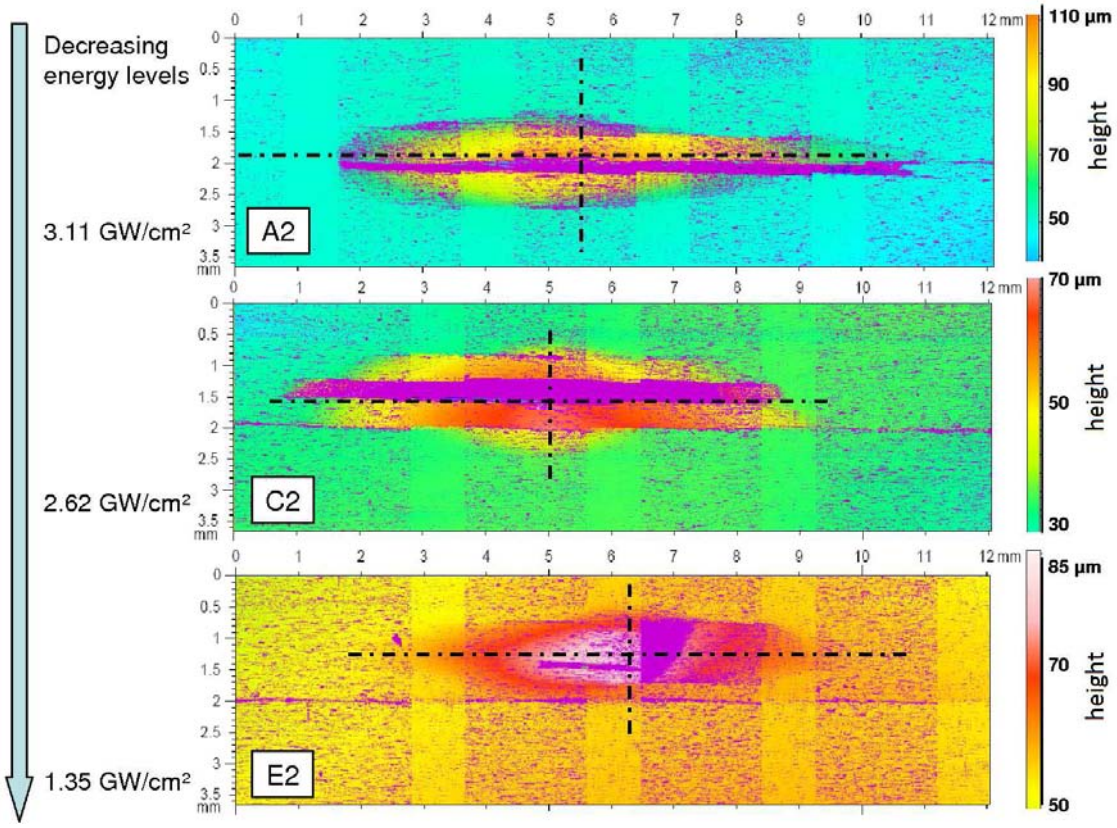

Figure 3.37, Residual back face deformations obtained by ICM in case of unidirectional IM7/M21 samples

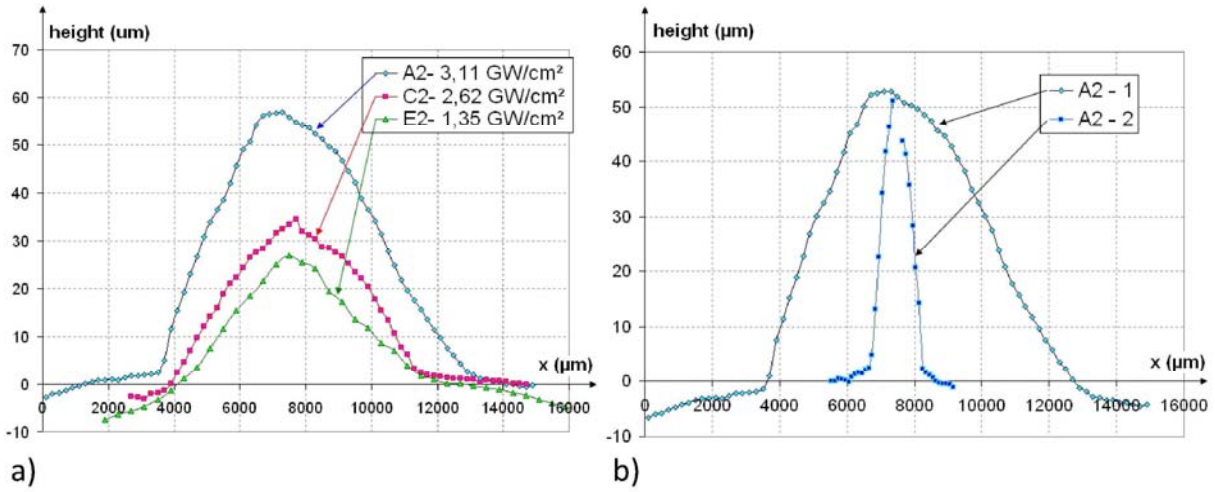

*Figure 3.38, Laser shocks on unidirectional IM7/M21 samples : **a)** Comparison of the back face deformations along the main damage axis for various laser pulse intensities – **b)** Back face deformation of sample S2-5, position A2, along X and Y axes*

Nevertheless, it is not possible to conclude that this major/minor axes ratio could represent an intrinsic damage parameter of each CFRP samples. So far, it has been proved that this ratio do not depend on the laser intensity for two different CFRP samples. Other investigations should be performed to prove the influence of the material thickness, the CFRP lay-up and the focused spot on the residual deformation. The first step would be to produce similar shock on two materials made of the same pre-impregnated plies and whose thicknesses are identical but with a different lay-up. Then, it should be re do on several CFRP sample.

3.4 Differences in the spallation behavior of unidirectional CFRP

Targets	Thickness (µm)	Energy (J)	Pulse duration (ps)	Dfoc (mm)	Intensity (PW/cm²)
IM7/M21	400	3.87	0.35	2	0.35
T300/914	400	3.33	0.35	2	0.3

Table 3.11 Laser shock parameters for the ELFIE dynamic response investigation

Keeping this idea of comparing two different CFRP material dynamic responses, time resolved observations were also used. The goal of the investigation presented in this section is to highlight differences in the CFRP damage growth, by observing what happens between the spallation induced failure and the corresponding damage until post mortem state. In other words, it is possible that the damage, especially the spallation, does not occur identically from one CFRP sample to another as shown in previous work [18]. For this study, laser shocks were performed in LULI (Polytechnique, Palaiseau). The experimental configuration used is the one presented in the chapter 2 and referred Config-ELFIE-1. Samples are placed in a vacuum chamber and aluminum painting was used for interaction. The shadowgraphy set-up was in this case scanning the sample back face in order to observe the dynamic spallation of the target and relative phenomena. Two different CFRP materials were used: T300/914 and IM7/M21, both unidirectional and 400µm thick. For the shock effects to be comparable, the target geometry and positioning in the vacuum chamber were the same. In Figure 3.39, the 0° direction is thus the vertical direction for both samples. For the same reason, the laser shocks performed on both materials were requested to be identical even if a small difference can be

noticed in Table 3.11 where the shock parameters are given. Finally, three images of spallation on each material have been recorded. The snapshots were taken at the same time.

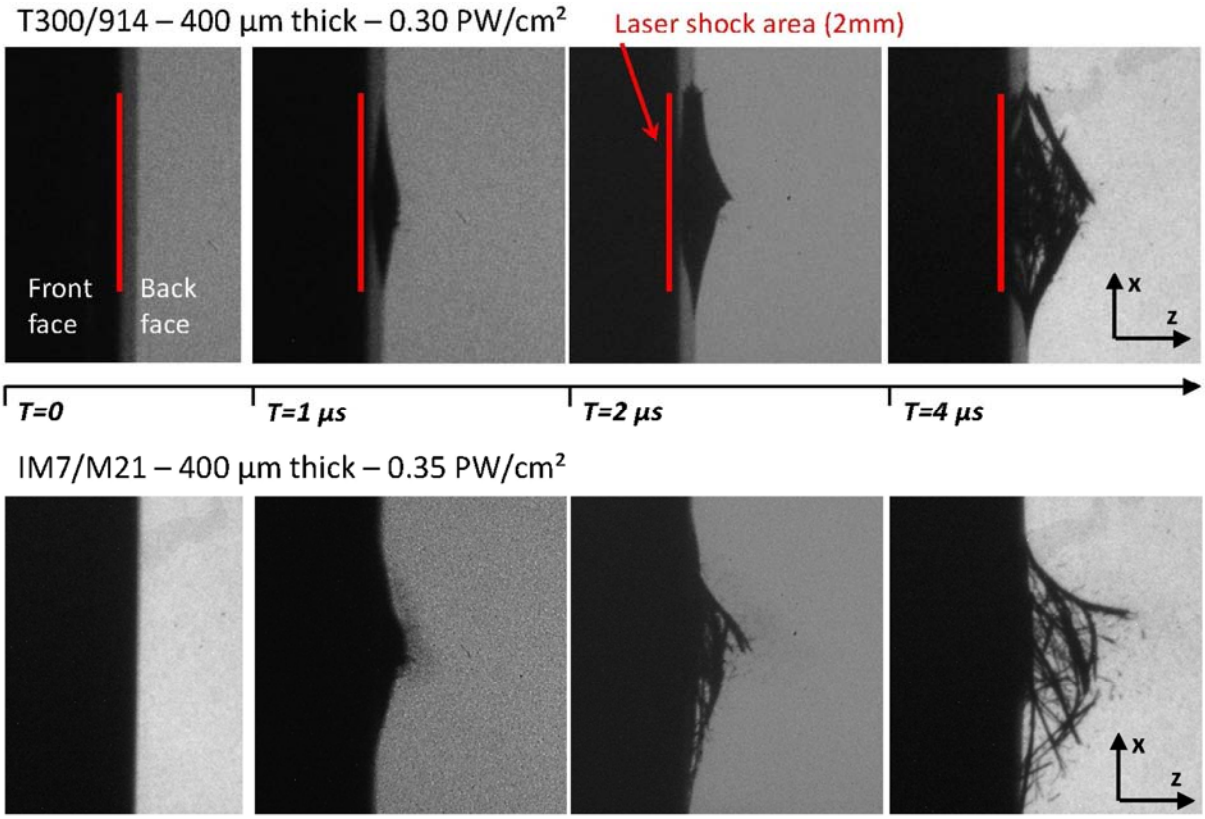

Figure 3.39, Compared time resolved observations at different instants for unidirectional composite materialsT300/914 (up) and IM7/M21 (down) – 400µm thick

The results are presented in Figure 3.39. The same phenomenon occurs on both materials. At time 0, the laser shock is produced on the sample front face. After one microsecond, a thin part of the material starts to grow due to the tensile stresses generated by the laser shock wave propagation. It results from spallation induced failure, which should have occurred about t = 100ns. It is a thin slice of material, meaning a few fibers still taken into the epoxy matrix like a thin composite ply. Indeed, the pulse duration used here is really short compared to the one used in the previous section. Here, the tensile stresses are really located close to the composite back faces. The early stages of the spallation occur within the ply thickness, over a few microns. That is why at time 2 µs, the first fiber breakages have already occurred as proved by the space between the two growing slopes on sample T300/914. It is more obvious on the IM7/M21 sample. Two microseconds later, a lot of small parts composed of a few fibers only start to separate from the sample. The ejection has started and the damage becomes significant. That was for the phenomenon in common, but some differences can be observed especially after t = 2 µs. Indeed, it can be noticed that the fiber spallation does not occur the same way on T300/914 material than on IM7/M21 material. The first one is triangular shaped, when the second one is more round shaped. Moreover, much more ejecta are visible in case of T300/914 material compared to the spallation of the IM7/M21 material. These observations could be explained by two differences: the different fiber mechanical properties and especially the different matrix of the composite. The quasi static properties are given in Table 3.12 (obtained from online datasheets). Of course, it is known from the literature that these mechanical properties are not the same at this strain rate, but it can be assumed that the shift will be the same for both materials. In any case, this is a good start for comparison. Indeed, the tensile strength and the ultimate elongation

at failure are more important in case of IM7 fibers (see in Table 3.12). This could explain why the IM7 does not break as much as T300 fibers where the strain is maximum. The round shape is a consequence of this non breaking compared to the triangular shape. The second parameter is the resin content difference. Indeed, the M21 matrix has a better shock resistance than the 914 epoxy resin because of the presence of thermoplastic nodules, as seen before. Consequently, it could have an influence on the small ply part ejection. These results are thus consistent with the previous observations and also highlight that the difference of behavior between CFRP also occurs at the dynamic response early stages.

Properties	IM7	T300
Tensile strength	5.5 Mpa	3.5 Mpa
Tensile modulus	276 Gpa	230 Gpa
Ultimate elongation at failure	1.90%	1.50%

Table 3.12 IM7 and T300 carbon fibers mechanical properties [19-22]

4 Time resolved analysis of CFRP response to shock loading

The results given in the previous sections are all about the residual state of the composite material after laser shock. It is important because it helps to understand the induced damage growth. Considering the LASAT application, it also gives some elements about the diagnostics to use in order to characterize the laser shock induced damage. Especially for the bonded composite, it will enable a better understanding of the difference between damage inside a CFRP and damage inside a bond line. Nevertheless, no information of the dynamic response of CFRP materials to shock loading can be directly obtained by post-mortem analysis. That is why back face velocity measurements were performed by using VISAR. For composite materials, it is important time resolved experimental data which can be used to validate numerical models. This time resolved measurement provides information on shock propagation history, its effect on material, and velocity history. This last data is directly correlated to the stresses history evolution within the shocked material. The material behavior can be first validated without damage, by modeling, and then by taking into account damage propagation. Once validated, the models can then be used to evaluate the level of stresses generated by the shock wave propagation. Indeed, in case of these anisotropic materials, the stresses evaluation is not as easy as in isotropic material.

For the back face velocity measurements presented in the following sections, a progressive approach has been chosen. It is known from previous work [23-25] that the VISAR signals can be quite hard to analyze and to understand. Consequently, it has been chosen to simplify as much as possible the tested material. Naturally, unidirectional materials were chosen because they are orthotropic, and closest to the ply behavior. Indeed, it was not possible to investigate one ply, because it is too thin to enable a damage threshold framing. For that reason, 0.5 mm thick unidirectional T800/M21 composites were first investigated (section 4.1). Then, only the thickness was increased up to 3 mm, all other parameters remaining constant (section 4.2). This thickness has be chosen to be different from the first one tested, and also to be closer from the bonded composite thickness. The lay-up was not changed on purpose in order to still enable a correct understanding of the back face velocity signals. On these targets, the reproducibility of VISAR measurements has been checked (section 4.3). Finally, laser shocks were measured on crossed ply composites (section 4.4), in order to progressively reach the bonded composite material lay-up.

4.1 Time resolved measurements of thin unidirectional T800/M21 samples

Results obtained on 0.5 mm unidirectional T800/M21 targets are presented in this section. The recorded dynamic responses are what is the closest to the T800/M21 ply behavior. Indeed, the number of interfaces is limited as much as possible, and the material anisotropy is reduced to orthotropy. The samples have been hand polished to their use thickness from a 3 mm thick material. This induces some variation from one sample to another. Consequently the target thicknesses can vary from 0.5 to 0.7 mm. The number of ply is thus between 2 and 3. Aluminum painting was used as a sacrificial layer for interaction, and the laser shock were performed in water confinement configuration. For that, PPRIME 25 laser was used in Config-PPRIME-2. The laser shock parameters are given in Table 3.13. After the shock and the associated measurement, the samples were recovered from target holder to be analyzed by post-mortem analysis. The idea was to check that the post-mortem material state was consistent with the VISAR time resolved measurement. For that, both X-Ray radiographies and cross section observations were used. Two series of measurement are presented. The first one concerns the unharmed samples (see in Figure 3.40), and the second groups the samples for which spallation occurred (see in Figure 3.41).

Targets	Energy (J)	Pulse duration (ns)	Dfoc (mm)	Intensity (GW/cm²)	Verdi power (W)	Fringe factor
M4S1-1	14.06	23.15	4	4.84	5	329
M4S1-2	3.1	23.15	4	1.07	5	329
M4S1-3	3.05	24.83	4	0.98	1.35	843
M4S1-4	1.6	27.36	4	0.47	1.35	843
M4S1-6	0.64	25.19	4	0.20	2	542
M4S1-8	0.39	25.74	4	0.12	2	229.5
M4S1-9	0.39	24.48	4	0.13	2	229.5
M4S1-9	0.36	24.07	4	0.12	2	229.5
M4S1-10	1.34	25.34	4	0.42	2	229.5

Table 3.13 Laser shock parameters for 0.5 mm unidirectional T800/M21 time resolved experiments conducted in Config-PPRIME-2 – Associated VISAR parameters

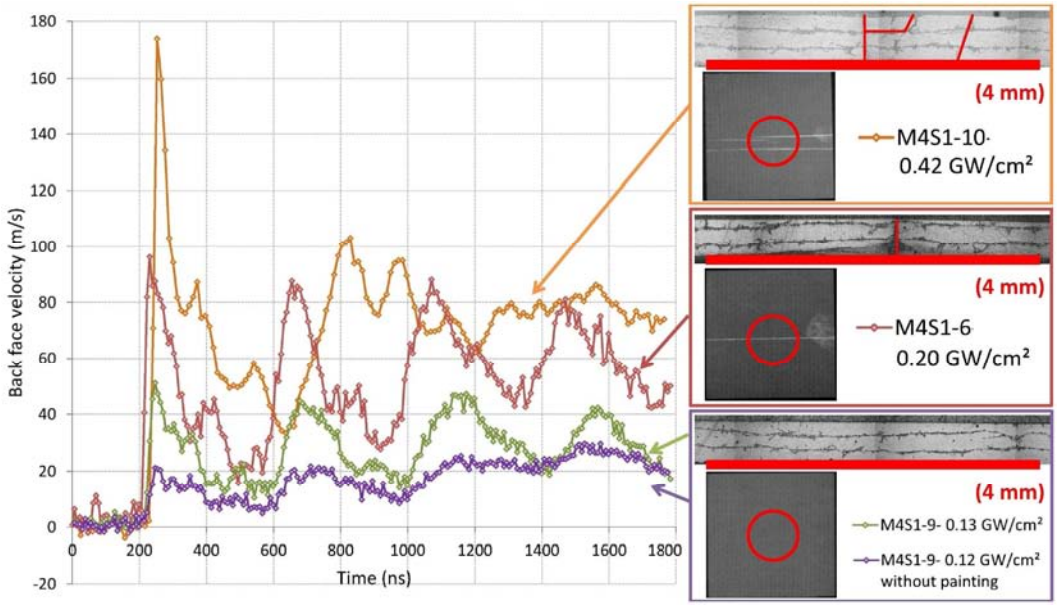

Figure 3.40, Back face velocity measurements in case of no damage and damage threshold obtained on 0.5mm unidirectional T800/M21 composite materials – Associated post-mortem analysis by X-Ray and micrographies

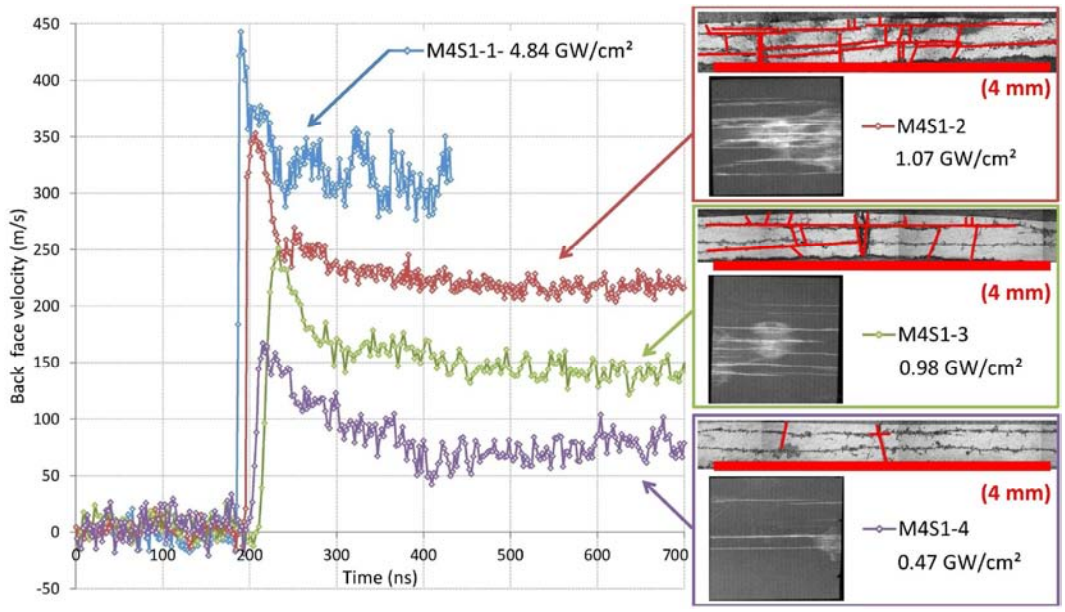

Figure 3.41, Back face velocity measurements in case of spallation obtained on 0.5mm unidirectional T800/M21 composite materials – Associated post-mortem analysis by X-Ray and micrographies

Considering first the measurements without any spallation presented in Figure 3.40, a lot of information can be obtained. The red signal and the green and purple signals respectively from M4S1-6 and M4S1-9 composite samples correspond to shock wave propagation without damage. This is proved by the observation of several shocks back and forth through the composite thickness. Indeed, four shock breaking-outs can be observed on the three signals. This means that the tensile stresses generated by the crossing of release wave inside the composite samples were not high enough to open it. Consequently, the wave can continue to propagate through the whole composite material. Another proof comes from M4S1-9 sample. Indeed, this sample has been shocked two times (see Table 3.13). The first shock corresponds to the green back face velocity presented in Figure 3.40. It has been performed in the configuration presented, and the back face velocity shows that no damage occurred. The second shock was performed right after the first one, without aluminum painting because it was removed by the first shock. The induced pressure was thus less important, which explains why the free surface velocity is smaller at the shock breaking out. Nevertheless, four shock breaking-outs are still visible on this second back face velocity measurement. This proves that the first shock did not break the composite, even after the observation time period.

From these three signals, the period of the shock back and forth can also be measured. For each sample, this period is approximately about 400 ns. Since the shocks were performed below 1 GW/cm², the material transverse response is still elastic (see Chapter 1, part 3). Consequently, the initial sound speed in the material can be evaluated. An approximation is enough because this velocity can vary from one sample to the other because of the thickness and also the ply architectures. Especially, the thermoplastic nodules can have an influence on this propagation velocity. By taking an average sample thickness of 600 µm, the sound velocity can be calculated by using equation (3.11). It is evaluated about 3000 m/s, which is consistent with the literature.

$$c_0 = \frac{2 \times thickness}{\Delta T} = \frac{1.2 \mu m}{400\ ns} = 3000\ m/s \tag{3.11}$$

Speaking of the back face velocity signal in itself now, some particular features can be observed. If looking to the red curve presented in Figure 3.40, an unusual bump can be observed after the first main peak. It is also visible on the green signal. The first shock breaking-out induces the free surface to accelerate up to a level which depends on the input pressure (meaning the laser intensity). Then, the velocity decreases, which is the sign of the release wave breaking-out. The first peak width is a bit under 100 ns, for a pressure input close to 50 ns if taking into account the water confinement (see in Table 3.13). The shift may be due to the release beam spreading through the composite thickness. About t = 400 ns on the red velocity, a sudden velocity increase can be observed during the release outcome. This “bump” is visible after each main peak and does not correspond to a regular shock pattern. One can say that this bump is due to the presence of an interface in the composite sample [23-25]. This is possible because the interplies could induce a change in shock impedance due to absence of fibers. Nevertheless, it is known from the literature that the shock behavior of CFRP in the transverse direction can be assimilated to the one of the resin. Since the resin in the interply is the same than the resin in the ply, the impedance mismatch should not be that important. It appears that there is room for another explanation to this phenomenon. The strong anisotropy of composite material could be an explanation for that. This will be investigated thanks to numerical modeling in Chapter 4.

The last back face velocity measurement presented in Figure 3.40 (M4S1-10, orange curve) could have been performed close to damage threshold of the CFRP material. Indeed, on this signal, no second shock breaking-out could be observed, which could be a sign for damage. Nevertheless, the signal is not as sharp as the following signals presented in Figure 3.41, which clearly shows a spallation process. The X-Ray radiography and cross section observation performed on this sample indicate that some damage did occur: only matrix cracks are visible, but no delamination (see in Figure 3.40). Being close to the damage threshold could have a role on the damage initiation. It is thus possible that the damage does not occur right after the crossing of release waves, but after a certain incubation time. When the laser intensity is increased (meaning the input pressure), the tensile stress level is also increased and is high enough to directly fracture the composite target (see in Figure 3.41).

Before switching to signals with spallation, a few comments should be added regarding to the post-mortem analysis of M4S1-6 and M4S1-9 samples. Indeed, the X-Ray radiography and the cross section observation of M4S1-9 sample are in agreement with the VISAR signal. No damage can be noticed through the composite thickness as well as in the composite plane. This is not the case of M4S1-6 sample, where the VISAR signal was indicating an absence of damage. A transverse crack in the 0° direction can be observed. It is located in the spot where the material is the thinnest. This crack is thus probably due to the bending component of the loading and should occur at long time after the shock initiation. It is also correlated to the size of the sample. This crack would probably not occur in case of a longer sample. Moreover, this kind of crack can not be detected by the VISAR measurements because it is in the propagation axis direction. In other words, this cracks do not disturbed the shock wave propagation in the transverse direction. It was probably fully developed after the VISAR recording time anyway. The shock wave propagation in the sample, meaning the generation of tensile stresses in the material is thus not responsible for that damage.

Finally, the signals with spallation can be commented. They are presented in Figure 3.41, with the associated post-mortem analysis. The X-Ray radiographies and the cross section observations confirmed for each sample that the spallation and/or delamination occurred. Note that the highest intensity shock completely destroyed the sample M4S1-1. That is why no post-mortem analysis was performed. The free surface velocity amplitude is consistent with the shock intensity level. Moreover, the spallation can be clearly identified on each composite target signals. The shock breaking-out accelerates the sample free surface up to a level depending on pressure. Then, it decelerates because of the release outcome. The tensile stresses generated by the crossing of release wave then break the sample. In case of composite, this spallation process is associated to delamination. The curve can be used to have a first approximation on the interlaminar tensile strength of the T800/M21 CFRP (transverse z direction). Of course, this value should be taken with care because the formula presented in Chapter 2 is valid for isotropic material. Anyhow this approach makes sense, since after a few nanoseconds the propagation under the shock area is the same at least in two directions on orthotropic CFRP targets. Anisotropy should have an influence, but if it has, it seems to be later if considering the previous analysis of the unharmed signal (about t = 400 ns). The velocity jump on the spall signals presented in Figure 3.41 is about 100 m/s. It is particularly visible on samples M4S1-1 and M4S1-2. Therefore, the interlaminar tensile strength (z direction) can be calculated by using equation (3.12). It is evaluated around 0.24 GPa. This value is between 2 and 4 time higher than what is given in the literature for quasi-static loading, depending on the sources (60 to 110 MPa, details given in Chapter 4). According to literature as well (see Chapter 1, part 3), this could be explained by the high strain rate resulting from the laser shock wave propagation. This value will be compared to the one found by numerical modeling in the Chapter 4.

$$\sigma_{ZZ} = \sigma_{T,m} = \frac{1}{2} \cdot \rho_0 \cdot c_0 \cdot \Delta U = 0.24\ GPa \quad with \quad \begin{cases} \rho 0 = 1580\ kg/m3 \\ c0 = 3000\ m/s \\ \Delta U = 100 m/s \end{cases} \tag{3.12}$$

4.2 Time resolved measurements of thick unidirectional T800/M21 samples

Time resolved measurements obtained on 3.0 mm thick unidirectional T800/M21 composite materials are presented in this section. This thickness was chosen in order to get closer to the end use thickness of bonded composite materials. Moreover, it gives complementary data on unidirectional sample. It will enable to check the observations made on the thinner CFRP. The experimental protocol is exactly the same. The samples were taken from a 3 mm monolithic material, and hand polished to get a correct surface light reflection. Therefore, the real thickness of these samples is about 2.9 mm which corresponds to 12 plies. The last one is a bit thinner than the others. The same laser configuration was used (Config-PPRIME-2). The laser shock parameters are presented in Table 3.14. It can be noticed that the same gradation in laser intensity was applied in order to obtain both signals from unharmed samples (Figure 3.42) and signals from spallation (Figure 3.43). For post-mortem analysis, only cross section observations were used. The delamination propagation is already well characterized, and the aim of the post-mortem analysis was only to check the agreement between the VISAR measurements and the actual damage in composite material.

Targets	Energy (J)	Pulse duration (ns)	Dfoc (mm)	Intensity (GW/cm²)	Verdi Power (W)	Fringe factor
M4S2-03	0,973	29,24	4	0,26	1	144.7
M4S2-04	1.49	30.39	4	0.39	2,5	229.5
M4S2-05	3.73	28.44	4	1.04	3,03	852
M4S2-06	9.23	28.64	4	2.57	3,03	852
M4S2-07	9.09	33.60	4	2.15	3,03	852
M4S2-08	4.17	27.34	4	1.21	3,03	852
M4S2-09	2.24	24.03	4	0.74	3,03	852

Table 3.14 Laser shock parameters for 3.0 mm unidirectional T800/M21 time resolved experiments conducted in Config-PPRIME-2 – Associated VISAR parameters

Results from unharmed samples are given in Figure 3.42. Indeed, the back face measurements obtained from sample M4S2-3 and M4S2-4 present two wide peaks separated by 1920 ns. This corresponds to the time of one shock back and forth. Indeed, the average thickness of the two targets is about 2.9 mm. Considering equation (3.11), this would mean that the sound velocity in the material is equal to 3021 m/s, which is really close to the velocity calculated thanks to the previous experiments if taking into account the thickness uncertainties. Therefore, the second peak observed on the VISAR signal around 2800 ns corresponds to a second shock breaking-out. Note that the shock attenuation is much stronger in this case, because of the sample thickness. The VISAR measurements thus demonstrate that the laser shock wave propagation did not break the sample. This is confirmed by the cross section observation also presented in Figure 3.42. Other features can be observed on the back face velocity signal. The second “bump” or second “peak” after the second shock breaking-out looks like the one observed on the 0.5 mm samples. Moreover, on the first release slope, other bumps traducing a back face velocity acceleration and deceleration can be observed. These features can be due to interfaces as well as anisotropy. This will be investigated by numerical modeling.

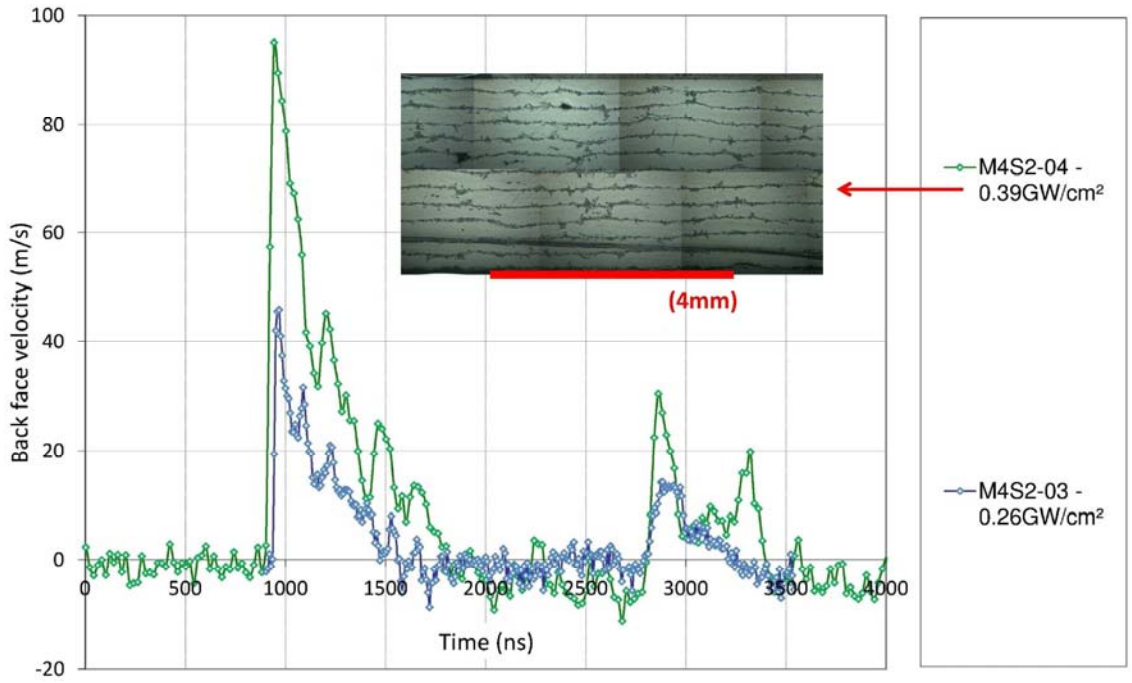

Figure 3.42, Back face velocity measurements in case of no damage obtained on 3 mm unidirectional T800/M21 composite materials – Associated micrography for example

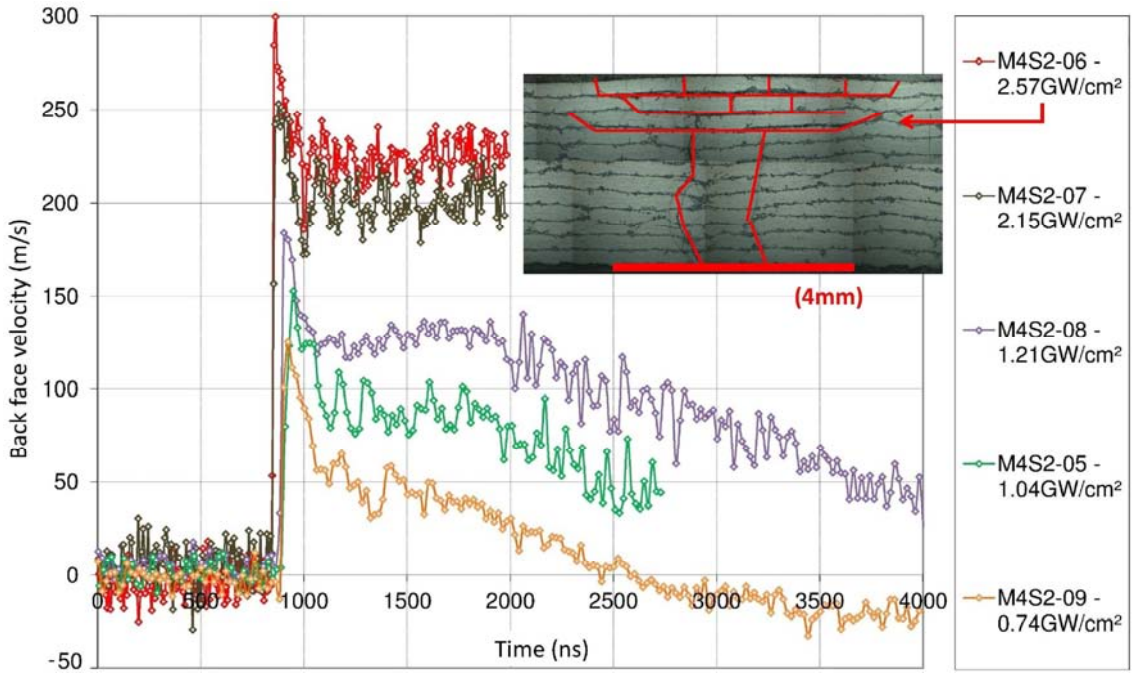

Figure 3.43, Back face velocity measurements in case of damage obtained on 3 mm unidirectional T800/M21 composite materials – Associated micrography for example

Finally, the signals with spallation can be described. They are presented in Figure 3.43. The free surface velocity amplitude is in good agreement with the progressive increase of laser intensity, meaning input pressure. Spallation is evidenced from each measurement, and damage has been observed on each sample by cross section observation. An example on sample M4S2-6 is given in Figure 3.43. For the four highest shocks, it is interesting to notice that the spall velocity remains more or less constant during about 2µs. After that, the measurements performed on sample M4S2-8 and M4S2-5 show a progressive deceleration of the detached composite part. This probably traduces the fact that the detached plies remained attached to the composite sample, outside from the shocked area. The tensile modulus of fiber may pull back the detached ply backward, which could explain this progressive deceleration. This phenomenon is also visible on sample M4S2-9, even if the constant velocity is less long. This could be due to the laser intensity which was lower, and gave less kinetic energy to the delaminated plies. The interlaminar tensile strength $\sigma_{T,i}$ (transverse z direction) can also be evaluated thanks to the signals. The velocity jump being not very sharp on M4S2-9 sample, the corresponding back face velocity measurement is not used to evaluate the velocity jump. The other signals give a $\Delta U = 73 \pm 7$ m/s. Thanks to equation (3.12), the T800/M21 interlaminar tensile strength in the transverse z direction is now evaluated around 0.18 ± 0.02 GPa. This is slightly different from the tensile strength measured on the 0.5 mm, and this could be explained by the strain rate. Indeed, in case of thicker material, the release beam spreads significantly compared to thin target. The tensile loading strain rate is thus reduced, which could explain this difference in the tensile strength.

4.3 Reproducibility

The results obtained during the reproducibility check campaign are presented in Figure 3.44. The sample preparation and shock configuration are exactly the same than the ones presented in the previous section. Note that in order to avoid a too wide uncertainty on the thickness of the samples, they were polished before being cut in three. The thickness of each sample is the same. Three shocks were produced on each different T800/M21 unidirectional composite samples. The laser parameters

were chosen to be under the damage threshold of the material, and identical for each sample. They are presented in Table 3.15. It can be noticed that laser intensities are really close one to another.

Targets	Energy (J)	Pulse duration (ns)	Dfoc (mm)	Intensity (GW/cm²)	Verdi power (W)	Fringe factor
T800M21-repro1	0,973	29,24	4	0,26	1	144.7
T800M21-repro2	0,982	32,08	4	0,24	1	144.7
T800M21-repro3	0,946	26,11	4	0,29	1	144.7

Table 3.15 Laser shock parameters for 3.0 mm unidirectional T800/M21 time resolved experiments conducted in Config-PPRIME-2 used for reproducibility check

The results are presented in Figure 3.44. It can be observed that the shapes of the three are really close from one sample to another. Especially, the timing of the first peak and the second peak respectively representing the first and the second shock breaking out is really close from one sample to another. This means that the material variations such as ply thickness, or thermoplastic nodule concentration do not really affect the material sound velocity. Speaking of velocity amplitude, the difference between the three signals is within 15 %. On the first peak, this could be due to the small laser intensities difference, but also on the laser interaction with Aluminum which slightly varies from one sample to another. The material variations have a small influence on the second peaks and phenomena. It can be deduced that the material state has more influence on the release behaviour and attenuation through the thickness than on the material velocity. The reproducibility is good regarding to the different possible uncertainty sources, but the variation of the back face velocity measurements will be taken into account in the analysis of bonded composite material experiments.

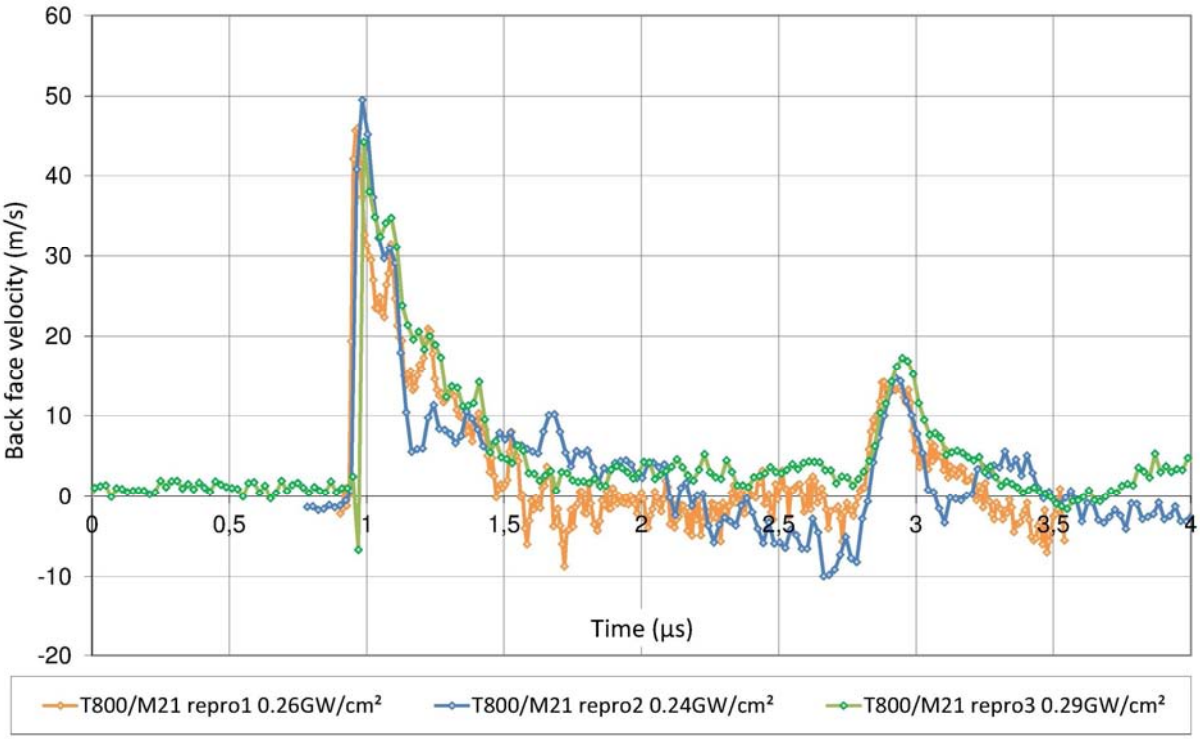

Figure 3.44, Back face velocity measurements below the damage threshold from three different 3 mm unidirectional T800/M21 composite materials, under same laser shock conditions – VISAR reproducibility

4.4 Time resolved measurement of crossed ply composite dynamic response

Finally, VISAR measurements were performed on crossed-ply composites. The material chosen is a T700/M21 CFRP, 1.5 mm thick, [0°,0°,90°,90°,0°,0°]. This choice has been made because this CFRP is the one used in the bonded composite samples investigated in the following chapters. Moreover, it is important to gather experimental data in order to prepare numerical modelling validation. The same experimental protocol than the one used in the previous investigations has been set up. Two identical shocks were performed on two different samples below the damage threshold in order to check the measurement reproducibility. The laser parameters are given in Table 3.16 and the VISAR results are given in Figure 3.45.

Targets	Energy (J)	Pulse duration (ns)	Dfoc (mm)	Intensity (GW/cm²)	Verdi Power (W)	Fringe factor
T700M21-05	0.92	28.65	4	0.26	1.0	144.7
T700M21-06	1.01	29.65	4	0.27	1.0	144.7

Table 3.16 Laser shock parameters for 1.5 mm T700/M21 crossed-ply laminate time resolved experiments conducted in Config-PPRIME-2 used for reproducibility check

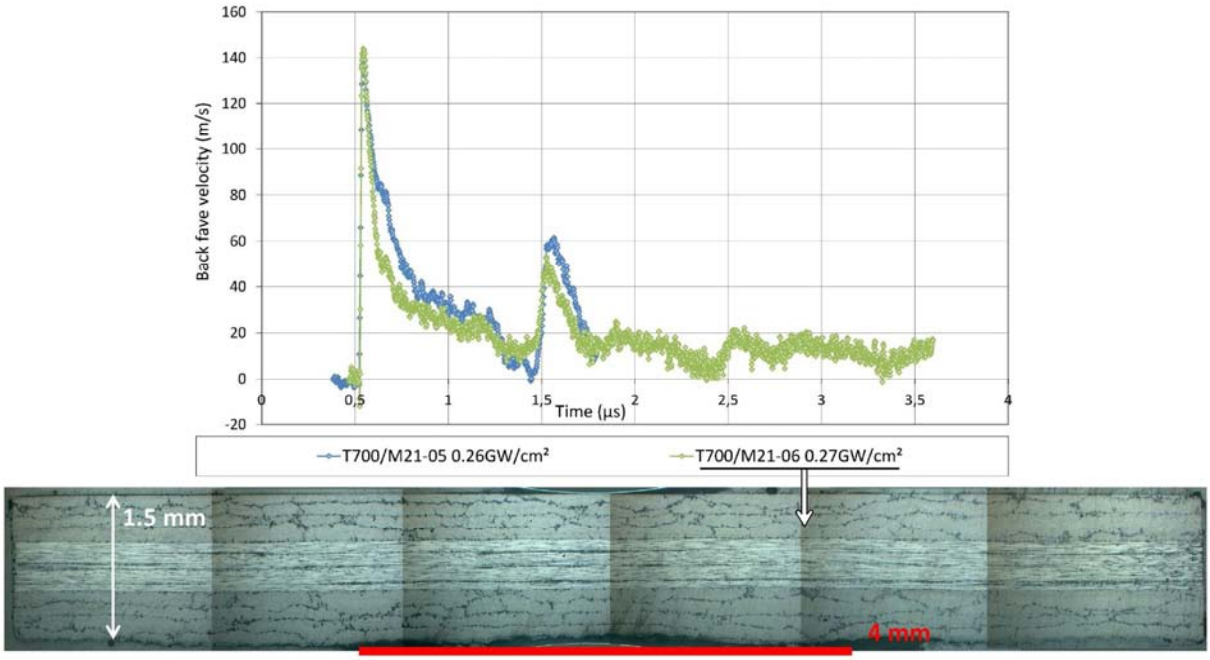

Figure 3.45, Back face velocity measurements below the damage threshold from two different 1.5 mm thick T700/M21 composite materials [0°,0°,90°,90°,0°,0°], under same laser shock conditions – VISAR reproducibility

On the green signal presented in Figure 3.45, three shock breaking-outs can be observed. This is the proof that the shock wave propagation did not fracture the CFRP, and that the damage threshold has thus not been exceeded. This has been confirmed by the cross section observation performed on the same sample also presented in Figure 3.45. The period between the two first shock breaking-outs can be evaluated close to 1 µs for both signals. Considering the 1.5 mm of the targets thickness, the sound speed in this material can be evaluated around 3000 m/s which is consistent with the previous measurements. It can also be observed that the shape of the signals slightly changed. The main peaks and the attenuation of the shock wave through the thickness remain consistent with the previous measurements, but all the second order accelerations and decelerations seem to have disappeared, especially on the release slopes. This phenomenon could come from the fact that 90° plies are

present in these materials. The anisotropy properties changed with the material lay-up which could have an influence on these second order features. By the way, this observation seems to indicate that the second order phenomena are more correlated to anisotropy than to interfaces, because interfaces are the same than in the previous samples. Finally, it can be observed that the signals are well reproduced from one sample to another, within 15% of uncertainty.

Part 3: Material property modifications under laser shock loading: mechanical, thermal and chemical modifications

In this last part, efforts are made to evaluate the possible modifications induced by laser shock on the composite and epoxy materials. It concerns two main investigation fields: i. The mechanical property modification induced by shock wave propagation in the material, meanwhile being below the material damage threshold; ii. The chemical or microstructural modifications under laser shock loading, especially of polymer material. The first point is discussed on unidirectional CFRP in section 1. The second point is detailed in the following sections on both CFRP and epoxy material using DSC and DMA analyses. Speaking of the LASAT industrial application, these two points are in fact related to industrial key issues. In case of an industrial testing, one wants to know if performing the test would be really non-destructive. It can also be wondered how many LASAT tests can be performed on the same part without any fatigue effect. From another point of view, it has been discussed in the 1st chapter the possibility of an increase of temperature behind the shock wave in epoxy targets. Epoxy resins properties being quite sensitive to heat, some microstructural modification under laser shock could happen.

1 Mechanical modification under repeated laser shocks under damage threshold

In this section, a study on the fatigue effects induced by repeated laser shock loading is reported. The idea was to understand what would happen if several shocks are produced on the same spot of a given target, in case of a stress level below the interlaminar tensile strength $\sigma_{T,i}$ (z direction) of the material. This investigation has been conducted on the T800/M21 unidirectional material, 3 mm thick, on which experimental data have already been gathered in Part 2. The choice of unidirectional samples has been made for two reasons. Firstly, it would one more time simplify the shock propagation and enable an easier understanding of the back face velocity signals. Secondly, it is known that unidirectional materials have a good resistance to bending only in the fibers direction, but is weak in the other directions. Repeating laser shock on a unidirectional CFRP could have the same effect than folding up many times a paper sheet. In other words, the weak bending resistance enables to expect fatigue effects on this material. Therefore, a 3 mm thick unidirectional T800/M21 composite sample was prepared from a plate. 6 laser shocks were performed on this sample, on the same spot, by using Config-PPRIME-2. The laser shock parameters were chosen to be below the laser shock damage threshold, according to the previous measurements presented in section 4.2, part 2 (see in Table 3.17). Water confinement and aluminum sacrificial layer are also used like in the previous experiment. This means that the front face of the sample is re-painted between each laser shock.

Targets	**Energy (J)**	**Pulse duration (ns)**	**Dfoc (mm)**	**Intensity (GW/cm²)**	**Verdi Power (W)**	**Fringe factor**
T800M21-repro2-01	0.98	32.08	4	0.24	1	144.7
T800M21-repro2-02	0.97	29.51	4	0.26	1	144.7
T800M21-repro2-03	0.89	29.00	4	0.24	0.75	144.7
T800M21-repro2-04	0.93	28.46	4	0.26	0.75	106.1
T800M21-repro2-05	0.88	25.88	4	0.27	1	106.1
T800M21-repro2-06	0.84	25.68	4	0.26	1	106.1

Table 3.17 Laser shock parameters for repeated shock investigation on T800/M21 unidirectional composite material conducted in Config-PPRIME-2

The time resolved free surface velocity measurements are given in Figure 3.46. The first shock is presented at the top, the following one is placed below and so one. The first shock repro2-01 is consistent with previous measurements for this laser intensity level. The shock breaking-out amplitude is about 50 m/s, and the period between this peak and the second breaking-out peak is consistent with a sound speed about 3000 m/s. A third shock breaking-out is even visible after t = 4.5 µs. This back face velocity signal is a clear signature of shock propagation without any damage for the reasons already given in Part 2. The second laser shock results in a slightly different back face velocity signal. The first peak is almost identical to the first one, uncertainties taken into account. That shows that after the first shock, the sample was unharmed at least under the laser spot area. The velocity amplitude is also close to the first one for a similar laser shock, which is another argument. The second peak corresponding to the second shock breaking-out is also visible with the same timing, but something happens in the following release slope. It looks like a spallation signature, even if it is not obvious. The absence of a third peak could indicate that damage has been initiated in the CFRP thickness. This damage should not be very important as proved by the third shock back face velocity measurement (repro2-03). The shock breaking-out is still clearly visible. The velocity amplitude is smaller though. It is indeed possible that the damage induces a small impedance mismatch which could distort the shock front amplitude. The second shock breaking-out is this time almost not visible. This shock propagation probably enhances the damage already created. Nevertheless, it is still possible to continue the measurement. Indeed, the fibers probably pull back the detached part toward the composite sample, as explained in Part 2. The plies should be in contact in spite of the probable matrix cracking. This is the reason why shock can still pass through the composite sample as proved by the three following measurements. The velocity amplitude is more modified because the damage is getting wider and wider. On the two last measurements, the same velocity signal shape is observed. As explained, the shock breaking-out is still visible, but right after, the frequency changes and looks like a spallation signal. It is in fact the shock back and forth in the detached ply which is visible once the tensile stresses have forced the broken part to separate. Each additional shock should continue to damage the sample.

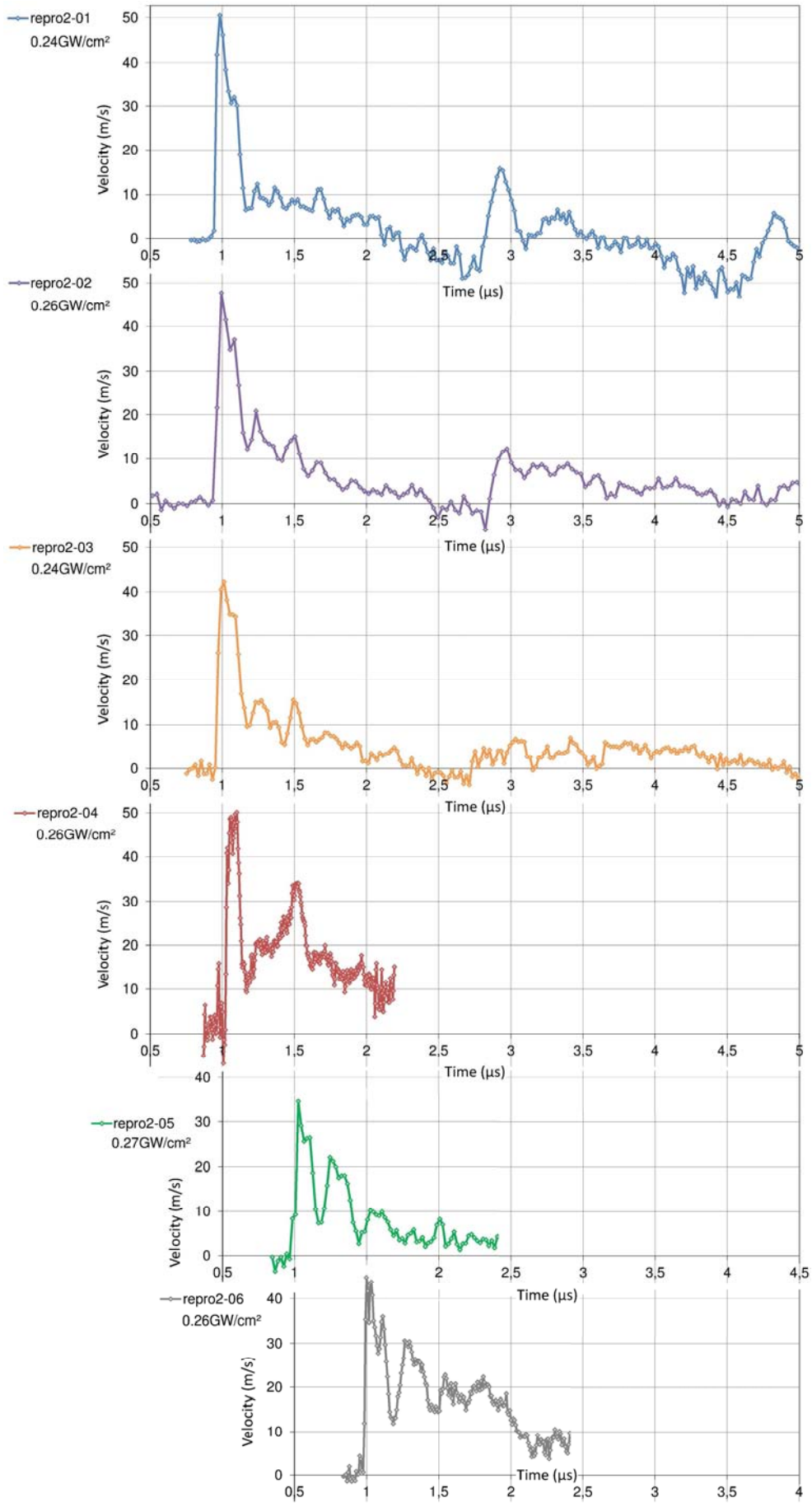

Figure 3.46, VISAR back face velocity measurements from the fatigue investigation on unidirectional T800/M21

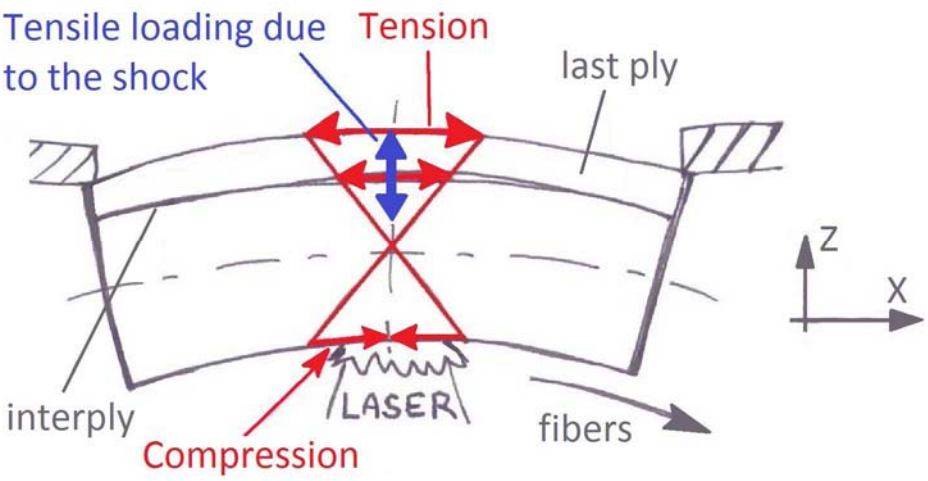

Figure 3.47, Sketch to explain the loading of the cracked area

After the 6 shocks, a cross section of the sample has been performed: a crack has been observed, located in the interply, before the composite last ply and close to a small void which probably concentrated the stresses. The crack is not really large, which is consistent with the explanation given. Hypotheses on its creation can be formulated. The damage location corresponds to the place where the maximum of σ_{ZZ} tensile stresses are generated by the laser shock propagation (250 µm deep). Moreover, at the early stages of the bending of the sample, this area is the more loaded in tension because it is located on the section edges. In addition to the stress concentration generated by the interply and the void, strong shear should be induced (see in Figure 3.47). This combination of loadings is repeated during the shock propagation time, and from one shock to the following. Shock after shock, the damage grows progressively. This result is quite important because it shows that CFRP can be degraded by repeated laser shocks, even if each shock is below the damage threshold of the material. Nevertheless, it has to be kept in mind that this result has been obtained on unidirectional CFRP, which is not really strong in bending, and on a target holder enhancing bending. Consequently, it could be interesting to continue this investigation by testing crossed-ply composites which should enable to avoid this problem. For the LASAT application, this study should be performed on the bonded sample in order to check if this phenomenon can also occur on these materials. This will be done in Chapter 5.

2 Residual stresses in shocked epoxy resins

In this section, the samples investigated on LULI2000 laser source have been analyzed by photoelasticimetry in order to observe the presence or not of residual stresses induced by the laser shock propagation and to evaluate them if need be. Note that no residual stresses were observed on the ELFIE shocked samples in spite the really high pressure induced by the laser irradiation (part 1, section 2). The photoelasticimetry setup mounted on the experimental chamber has enabled a direct observation on the samples residual state. Nevertheless, the pulse width was different in case of LULI experiments and the high pressure in stake could modify the material state. In order to investigate this phenomenon, and to evaluate the influence of the pressure on the residual state, two samples are compared in this section, namely Sep1-1 and Sep1-2. They have been recovered form the LULI experimental chamber after laser shock. The corresponding laser shock parameters are given in part 1, section 2, Table 3.2.

The sample presented in Figure 3.48 is sample Sep1-1. The laser shock wave propagation leaded to spallation as it is proved by the crater visible on the back face. In Figure 3.48-a, the residual stresses are revealed by the polarizers. The setup used to obtain these images is the one described in Chapter 2, section 3.1. Under the sample front face, it can be observed the material remains loaded within 2 mm depth. These residual stresses are located under the laser irradiation zone. On the contrary, the back face exhibits no residual stress, especially in the spallation area. This could be understood since the matter ejection probably relaxed the whole loading. To quantify the residual state, a first image is taken without the monochromatic filter in order to determine the first order fringe (see in Figure 3.48-a). Then, the filter is added and the fringe order can be identified for each fringe until the front face ablation point (see in Figure 3.48-b).

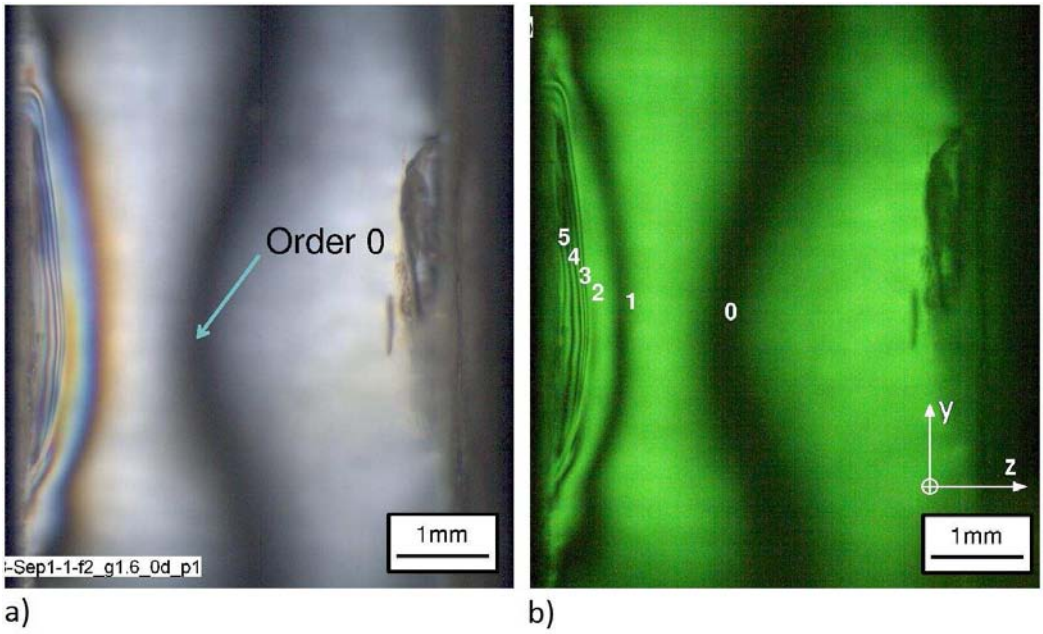

*Figure 3.48, **a)** White light source polarized image of epoxy Sep1-1 sample – Order 0 observed, **b)** 0.542 µm light source polarized image of Sep1-1 sample – Fringe orders observed*

Both Sep1-1 and Sep1-2 samples were observed using this technique (see the corresponding laser shock parameters in part 1, section 2, Table 3.2). Some hypotheses were made on the main stress directions. Indeed, z direction is assumed to be the main direction 1, since it is collinear with the laser loading axis. It is along this direction that the laser shock propagation induced tensile stresses. Moreover, y direction can be considered as the second main direction because the pressure loading is axisymmetrical (see axes in Figure 3.48). Regarding these assumptions, the quantity ($\sigma_z - \sigma_y$) corresponds to ($\sigma_1 - \sigma_2$) which can be calculated on each fringe by using the equation presented in Chapter 2, section 2.3, and recalled here as equation (3.13). The photoelastic constant has been chosen equal to 55.10^{-12} Pa^{-1}.The uncertainties on the depth measurement were evaluated by considering the image resolution as well as the fringe sharpness. Moreover, the errors on the residual stresses are due to the sample thickness variation and the spectral filter used. This residual stress state was plotted along the sample depth on the loading axis. Experimental points have been fitted to obtain a global trend of the residual stress evolution (see numerical values and graphic in Figure 3.49). Indeed, the matter was fully relaxed deep inside the sample, but the residual stresses increase exponentially in direction of the front face. Speaking of the front face, it is measured 240 µm deeper from the initial state because of the compression of the material resulting from the shock load. This compression could explain the origin of residual stresses.

$$\sigma_1 - \sigma_2 = \frac{k\lambda}{Ce} \quad with \quad \begin{cases} k : \text{fringe order} \\ \lambda : \text{filter wavelength} \\ C : \text{Photoelastic constant} \\ e : \text{thickness} \end{cases} \tag{3.13}$$

Fringe order k	Depth (mm)	Isochromatics σ1-σ2 (MPa)
0	2,11 ± 0.05	0.00
1	0.92 ± 0.05	0.99 ± 0.03
2	0.57 ± 0.05	1.97 ± 0.05
3	0.53 ± 0.05	2.96 ± 0.08
4	0.49 ± 0.05	3.94 ± 0.10
5	0.40 ± 0.05	4.93 ± 0.13
6	0.32 ± 0.05	5.91 ± 0.15
Front face after shock	0.24 ± 0.05	0.00

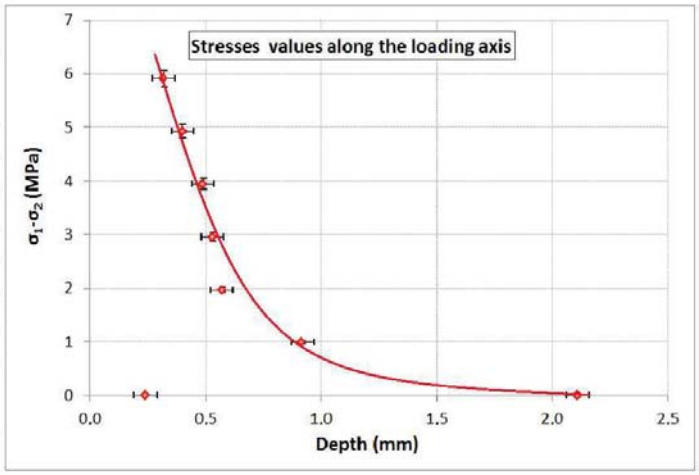

Figure 3.49, Measurement of the residual stresses observed by photoelasticimetry on epoxy sample Sep1-1

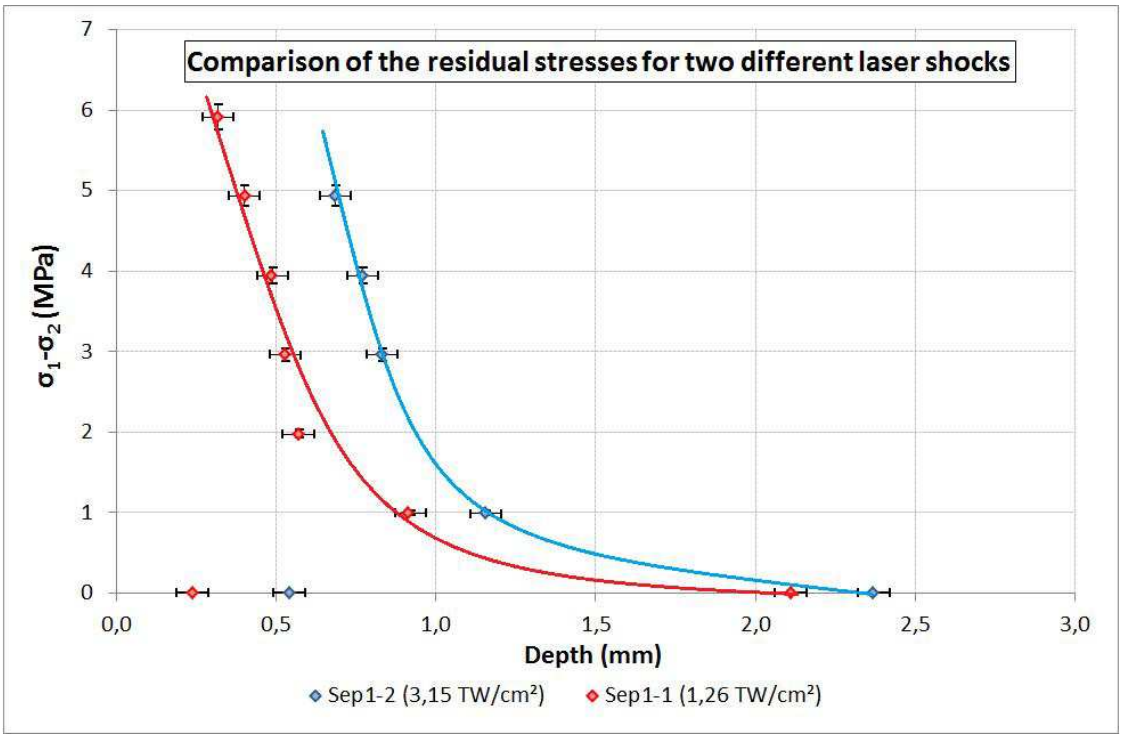

Figure 3.50, Comparison of the residual stresses for two different epoxy samples: Sep1-2 (3.15 TW/cm²) and Sep1-1 (1.26 TW/cm²)

On the second sample Sep1-2, the loading intensity was twice more than for Sep1.1 and therefore, it has created more damage in the material (see in Part 1, section 2, Table 3.2). Indeed, the spallation observed was wider and larger. The compressed front face is also twice deeper, about 500 µm (see the residual stress state of Sep1-2 in Figure 3.50). Nevertheless, the residual state evolution along the depth on the loading axis seems to be more or less the same than in case of Sep1-1. The residual

stresses are just shifted deeper into the material, and this translation corresponds to the difference in the front face position after compression. This could mean that the laser intensity level has no influence on the residual stress levels since the fringe distributions are really close from one sample to another, but plays on the residual stress spatial distributions.

Some comments can be added. In comparison with the laser shock induced pressure (50 – 100 GPa), it can be observed that the level of residual stresses is really low. This could be due to the laser pulse duration (about 3 ns in this case). The high compression state, if responsible for these residual stresses, does not last long enough to create higher residual stresses. This explanation is consistent with the fact that no residual stresses were observed from ELFIE experiments, for which the laser pulse was even shorter. In this case, even if the pressure was much more important, the loading time was not long enough to generate residual stresses. Nevertheless, these stresses could also result from a thermal loading coming with the laser irradiation. The difference in pulse duration also agrees with this second hypothesis. Indeed, the longer the thermal exposition, the deeper the residual stresses. More investigation should be performed in order to have a better understanding of the phenomenon.

3 Chemical or microstructural modification under laser shock loading

In this section, efforts are made to evaluate the chemical or microstructural modifications which could have occurred during the whole shock wave propagation. This includes the laser interaction and shock setting up, until the complete spallation of the target. Therefore, only post-shocked analyses were performed. The curing state of the epoxy resin before and after shock is the parameter of interest. Indeed, the literature has shown that the high pressure shocks are correlated with an important temperature increase. Above 20 GPa, the material can be modified if the compression state in long enough. In case of laser shock, the pressure can be much more important, but during shorter time. This is the case of the shock performed on LULI2000 and ELFIE laser sources. In these two cases, one can wonder if in spite of this shorter loading time, the high pressure only could be responsible for microstructural modifications. Two types of microstructural modifications can in fact be expected on the thermoset resin. On one hand, the molecules can be broken because of the high pressure, or overheating. As a consequence, the glass transition of the epoxy would be reduced. On the other hand, the shock and the associated temperature increase could enable molecular mobility and act like a post-curing process of the epoxy resin. This would be possible only if the epoxy was not well cured before the shock wave propagation. This phenomenon would lead to an increase of the glass transition of the material. Consequently, the best way to see a possible epoxy material modification after laser shock propagation is to use DSC (Differential Scanning Calorimetry), as done in the following sections. Speaking of the LASAT industrial application, it is also important to know if laser shock could have another effect than on the mechanical properties, especially on the epoxy resin content in CFRP.

3.1 DSC analysis

The first step is to analyze the samples recovered from ELFIE and LULI experiments (see part 1). Indeed, the highest pressure shocks have been produced on these materials. Moreover, they are well known resins, which could facilitate the analysis by DSC. In these analyses, and all the following ones by DSC, it has been chosen to treat separately the front face from the back face. The idea is to try to discriminate the effects resulting from the laser irradiation on one side (front face), and the ones

induced by the high strain rate tensile loading on the back face. For that, several small pieces were selected by post-mortem dissection from shocked samples by using diamond wire saw. As shown in Figure 3.51, it is possible to separate the Back Face (BF) from the Front Face (FF), in an impacted region (imp) or in a non-impacted region (himp). Global pieces (G) taking into account the whole sample thickness have also been taken from each region (G-imp and G-himp). All the samples analyzed by DSC refer to this denomination. Every piece can be measured by DSC, which enables the glass transition temperature evaluation, and then compared to a reference.

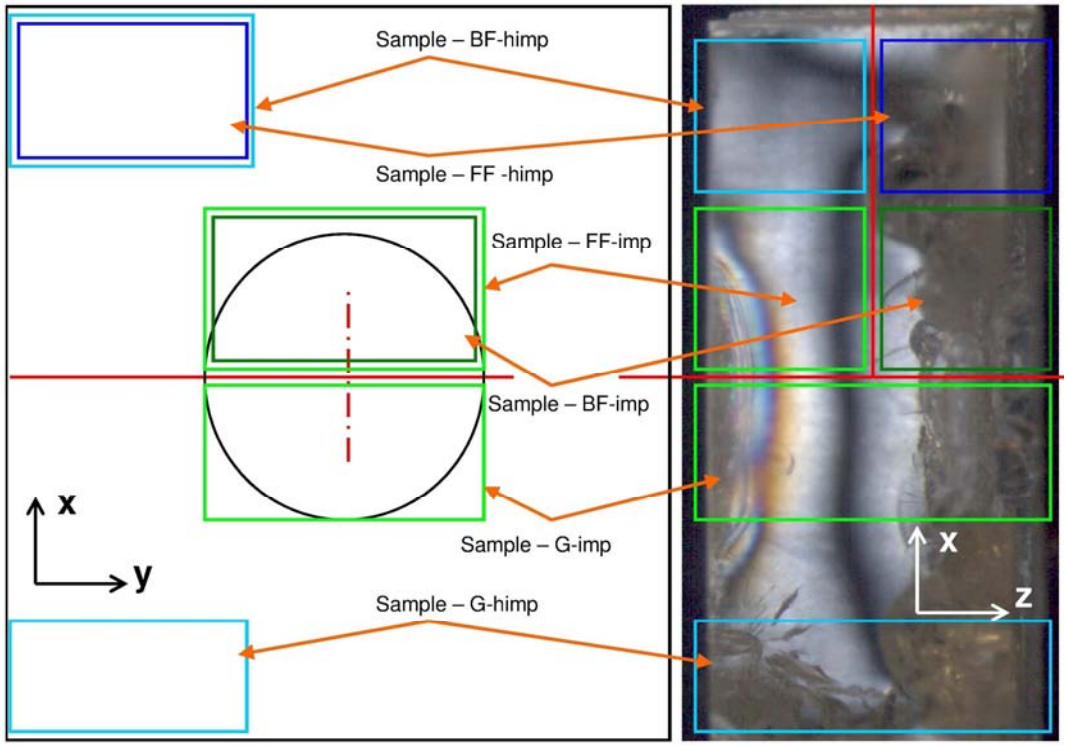

Figure 3.51, Selected zones on a shocked epoxy for DSC analysis

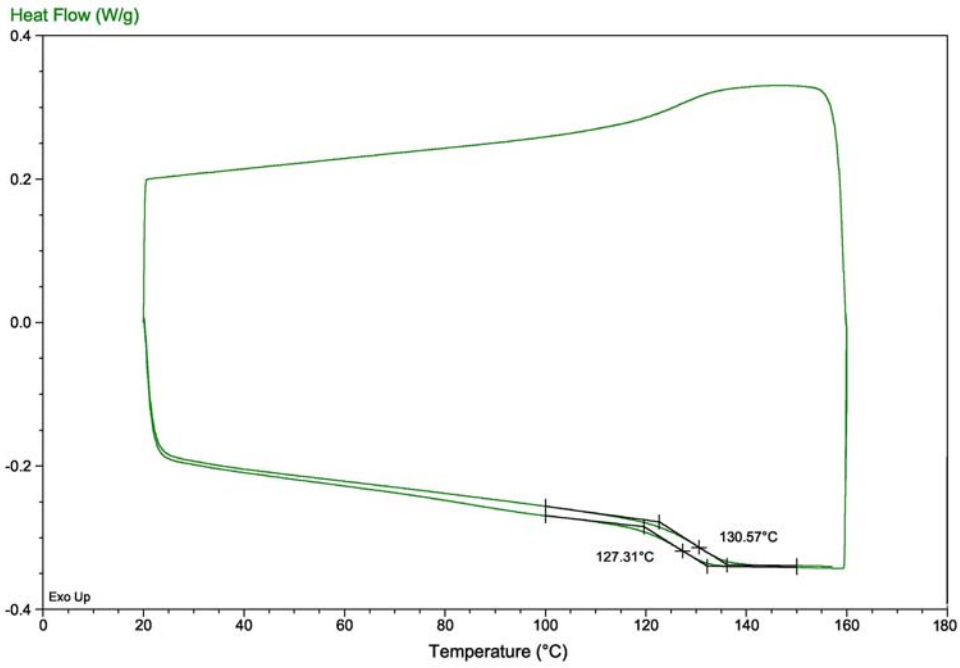

Figure 3.52, Reference cycle (1st heating, cooling, 2nd heating) of the epoxy resin in ELFIE and LULI experiments

The reference cycle of the epoxy resin before testing in ELFIE and LULI experiments is given in Figure 3.52. Its glass transition temperature can be evaluated from the calorific capacity jump on the first heating. It is about 127 °C. The first heating ended at 160°C, which enables a small post-curing to occur. Indeed, on the second heating the glass transition is evaluated close to 130°C. The small difference between the two glass transition temperatures indicates that the epoxy was already well cured, but also that a post-curing is possible.

From this starting point, DSC can now be performed on shocked epoxy in order to evaluate possible modification due to laser shock propagation. A first comparison is given in Figure 3.53. The 1st heating taken from the reference is compared with to the 1st heating of two different shocked sample front faces (Sep1-12 and Sep1-13, see Part 1, Table 3.3). To enable an easier reading of the figure, the three heat flows have been shifted. These two samples were shocked using ELFIE laser source, with laser intensity close to 0.6 PW/cm². It can be observed on the DSC analysis that almost no difference can be noticed. A small shift about less than 1°C can be seen, but this is probably in the DSC measurement uncertainties. It can be concluded that the high power laser irradiation, and associated pressure, did not modified the molecular arrangement of the front face, or at least not significantly.

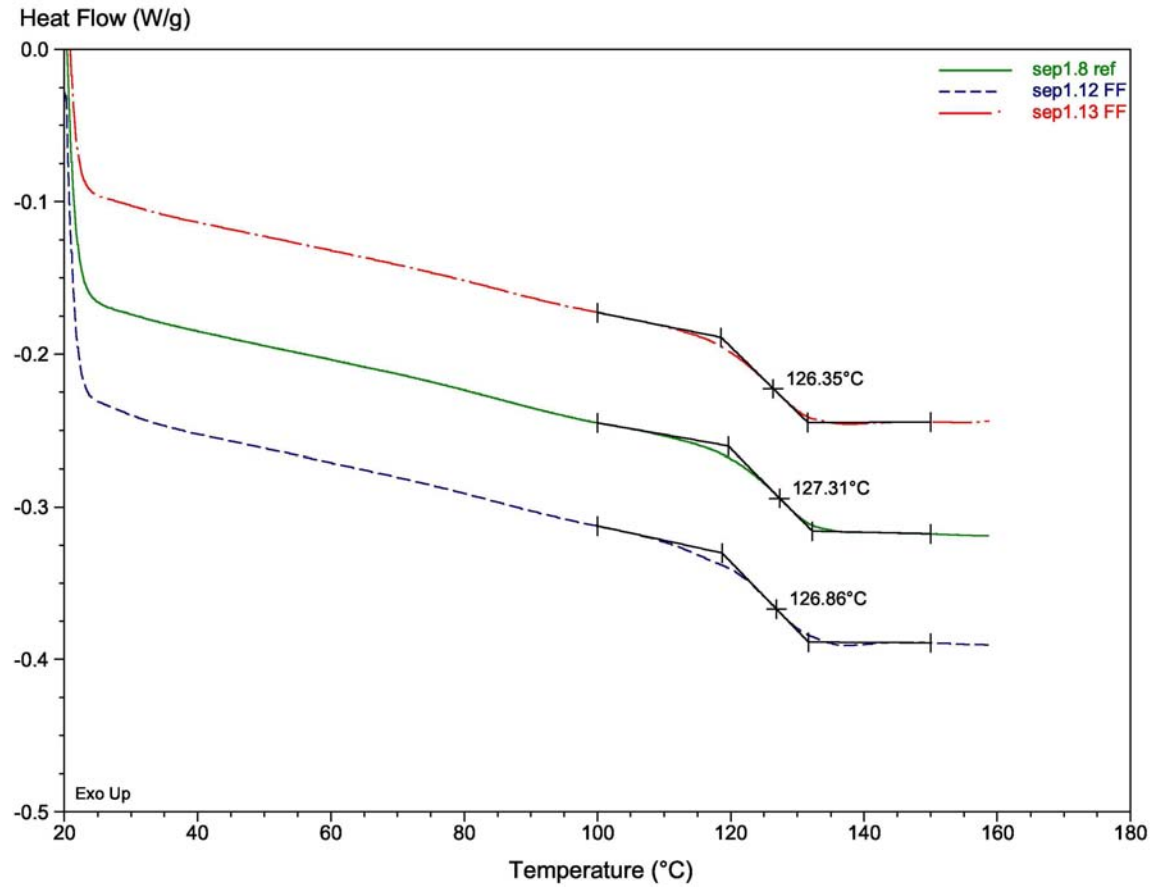

Figure 3.53, Comparison between the DSC 1st heating on the Reference and two DSC 1st heating thermograms from the front faces of two shocked epoxy resins (Sep1-12 and 1-13)

Same conclusion can be made on the sample back face. Indeed, 1st heating signals from the reference, Sep-13 front face, and Sep1-13 back face are compared in the Figure 3.54. This time, the signals have been shifted in order to be superposed. Thanks to that, no difference in the glass transition shape or temperature can be noticed. The same investigation has been performed on

Sep1-2, shocked using LULI2000. The idea was to verify that no effect can still be detected when changing the laser pulse parameters. In case of LULI2000 laser shocks, the pulse duration is longer, and the energy is higher. Pressures are still way above the 20 GPa limit found in the literature (see Chapter 1, Part 3). Nevertheless, no effect has been observed either (see Figure 3.55). Indeed, all the pieces described in Figure 3.51 have been extracted, analyzed by DSC and compared to the reference signal. No significant shift, out of the uncertainties, has been observed. Nevertheless, in case of sample Sep1-2, the damage was quite important. Thus, the small pieces were hard to extract, and their shape were not well adapted to DSC analysis. Nevertheless, all the signals are really clear, and the signal taken from the back face, in the impacted region could be significantly shifted from the reference.

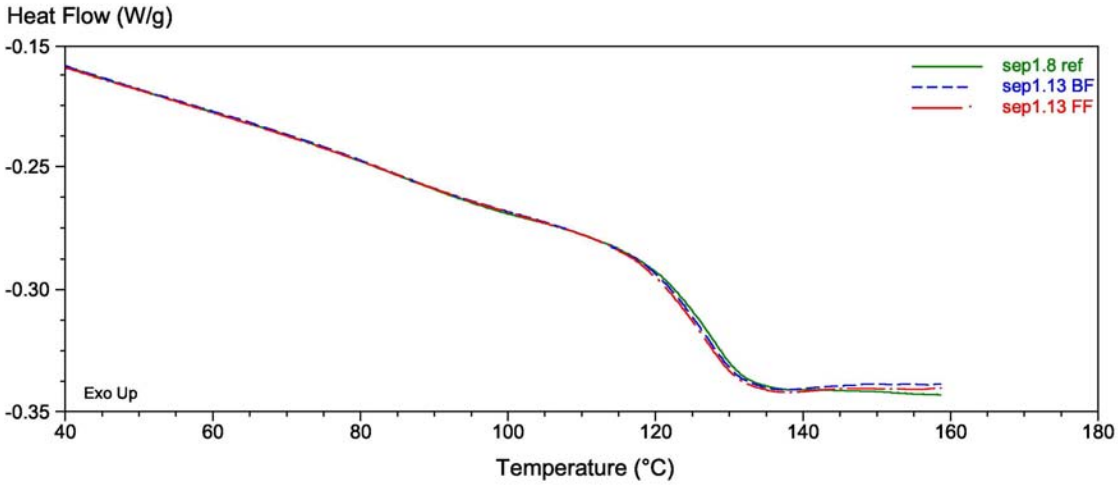

Figure 3.54, Comparison between the DSC 1st heating on the Reference and two DSC 1st heating thermograms from the front face and the back face of one shocked epoxy resin sample (Sep1-13)

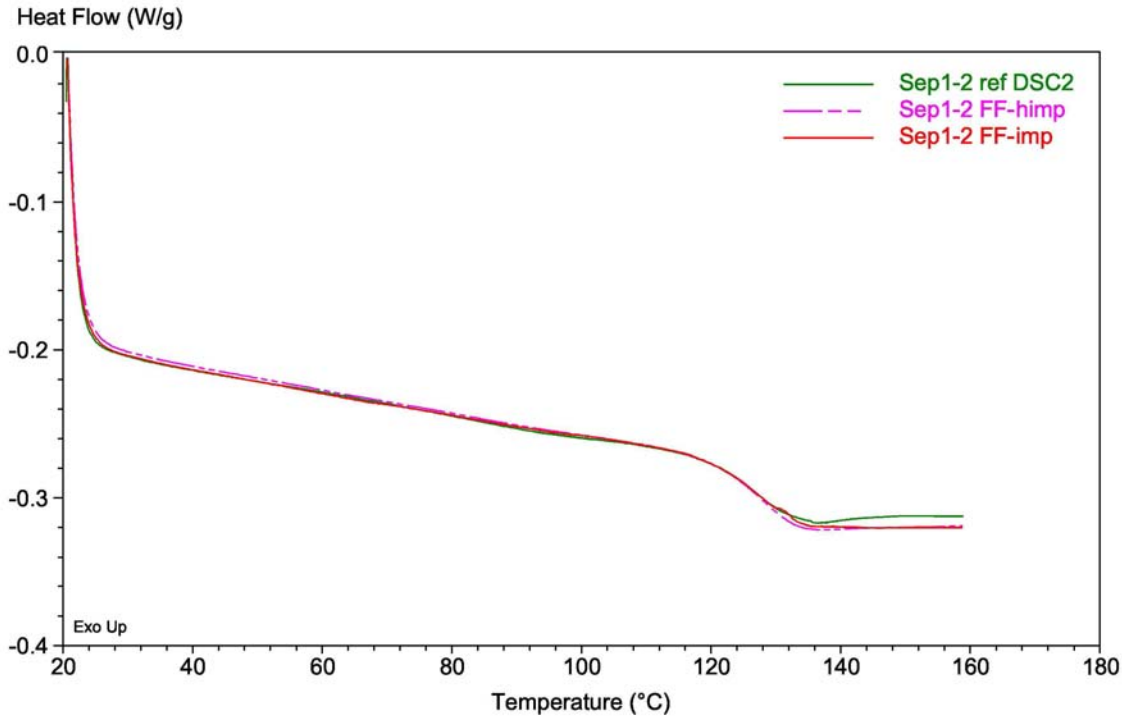

Figure 3.55, Comparison between the DSC 1st heating on the Reference and two DSC 1st heating from epoxy Sep1-2 sample taken from the front face in the impacted region and in the non-impacted region

There are three possible explanations to this absence of modification. The first one is to say that the laser pulse durations are too short in both cases for a chemical reaction to occur. The high compression state and/or the heat associated with the shock do give mobility to the molecule chains, but it is not long enough to enable the creation of bridges between molecules, sign of post-curing. The second explanation would be to consider that the epoxy tested was already very well cured. There was a gap, but not a huge one. Finally, it is also possible that the glass transition has been reduced because of chain breaking, but this phenomenon has been compensated by a post-curing resulting in an increase of the glass transition temperature. In fact, it is possible that the three explanations are correct and compete together. That is why the investigations presented in the next section deal with different epoxy materials, on a different laser source in order to try to see an effect.

3.2 Highlighting of a possible microstructural modification on epoxy resins

Regarding the previous observations, LY556 epoxy resin has been chosen for further investigation (see DSC reference cycle in Figure 3.56-a). This resin has not been post-cured before laser shock. Its glass transition was thus around 103 °C, which is relatively low. Indeed, on the first heating presented in Figure 3.56-a, a wide exothermic peak can be observed right after the glass transition. This is the sign of the epoxy post-curing. It is confirmed by the 2nd heating on which the glass transition can be estimated above 130°C. To sum up, the LY556 epoxy resin tested is not well cured and its glass transition temperature was close to one of the resin used in ELFIE and LULI experiments. On a 3mm thick LY556 sample, a laser shock was performed using Config-PPRIME-1. The shock parameters were in the range of the common parameters used with this laser. Especially, the pulse duration was close to 30 ns (60 ns with the confinement), and the laser intensity about 4.30 GW/cm² which corresponds to a pressure around 2 GPa (see calibration curve, Figure 4.11). This shock leads to the material spallation. After recovery, small pieces were cut as presented in Figure 3.51, and analyzed by DSC. The 1st heating signals are presented in Figure 3.56-b. As previously observed, the piece taken out from the sample front face shows no difference from the reference signal. Nevertheless, the signal recorded during the back face piece analysis is significantly different from the two others. Especially, the glass transition temperature identified on the 1st heating is higher of 4 °C. The post-curing exothermic peak also starts a bit later. This result is a bit surprising because a modification would have been more expected on the front face where the laser irradiation occurred. Moreover, the pressure induced by the laser shock is below the 20 GPa compression found in the literature. Consequently, it seems that high strain rate tensile stresses below 20 GPa could induce a small modification of the molecular arrangement of epoxy resin. It can be wondered how this modification occurs. An elevation of temperature is still possible, but that may not be the only effect. Indeed, high strain rate tension could bring enough molecular mobility to the material to enhance bridging. More investigations remain necessary before fully understanding the phenomenon. So far, it can be said that the shock provided a coupled phenomenon responsible of an energy equivalent to a temperature above 100°c during a few minutes. In order to check the reproducibility of these results, this experiment has been done in the exact same condition with another epoxy resin, and with the same laser parameters (see in Figure 3.57). The RTM6 sample chosen has a first glass transition about 200 °C (see in Figure 3.57-a). Post-curing was also possible as proved by the second heating glass transition temperature. The shocked RTM6 sample was analyzed exactly like in the case of LY556 sample. The first heating DSC signals are presented in Figure 3.57-b. The same shift between the reference and the back face piece has been observed, which confirmed that if there is an effect of laser shock, it is located where spallation occurred. It also shows that the energy brought by the shock wave propagation is at least equivalent to a temperature of 200°C during several minutes.

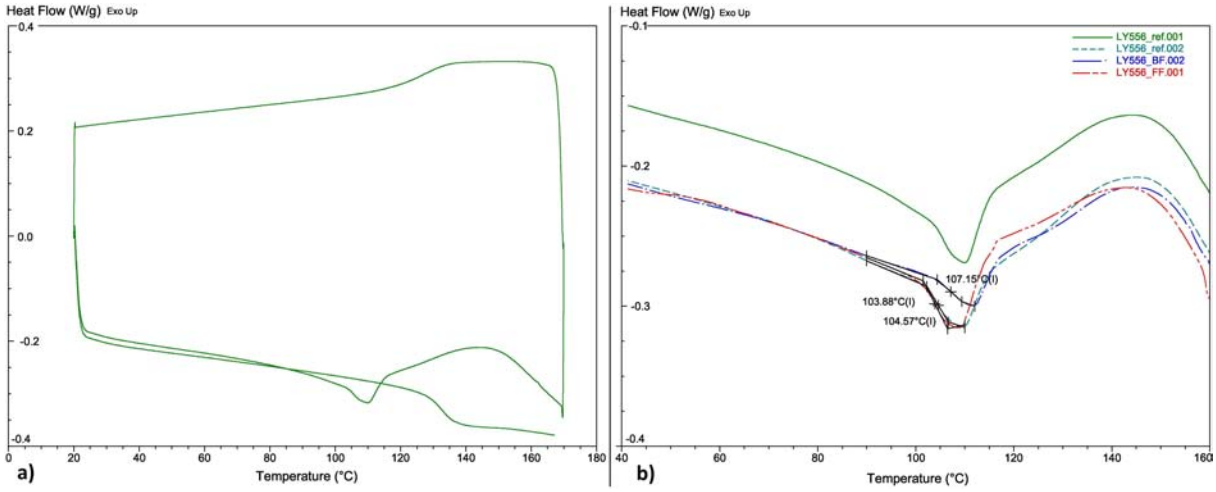

*Figure 3.56, **a)** Reference cycle of LY556 epoxy resin before testing (1st heating, cooling, 2nd heating) **b)** Comparison between the DSC 1st heating on the LY556 Reference and two DSC 1st heating from a shocked LY556 sample taken from the front face and the back face*

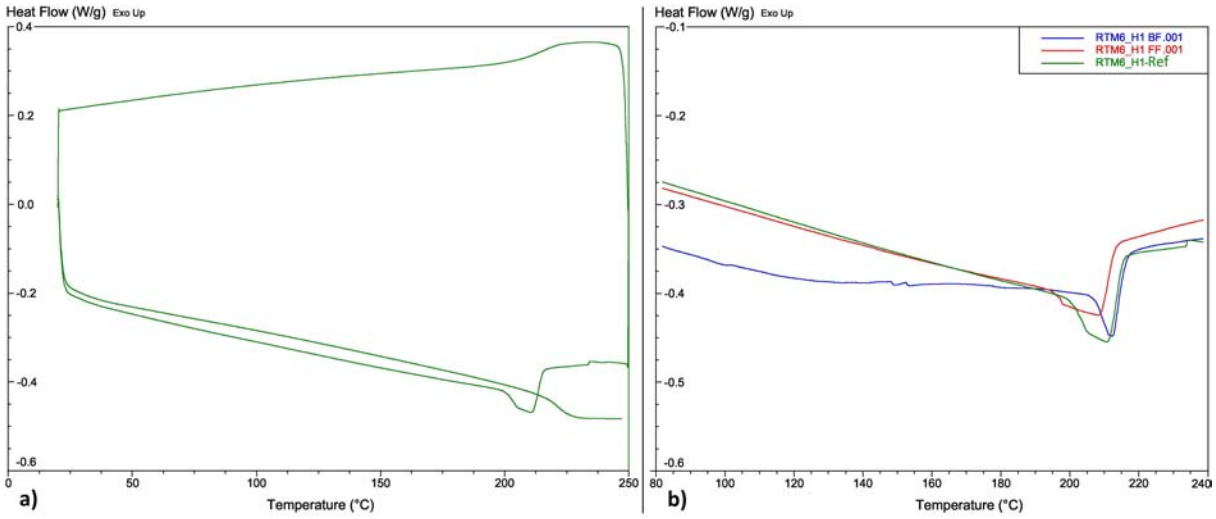

*Figure 3.57, **a)** Reference cycle of RTM6 epoxy resin (1st heating, cooling, 2nd heating) **b)** Comparison between the DSC 1st heating thermogram on the RTM6 Reference and two DSC 1st heating thermograms from a shocked RTM6 sample taken from the front face and the back face*

From this few data, it is hard to conclude, and caution should be taken. Contrary to what can be expected, the microstructural modification induced by laser shock wave propagation does not seem to occur on the front face of the shocked sample. This is consistent with the literature which indicates that no modification could occur below 20 GPa. Nevertheless, the spallation areas have shown in two different cases a slight increase of the glass transition. It seems to indicate that high strain rate tension below around 2 GPa (see calibration curve, Figure 4.11) could induce some small modifications of the epoxy resin molecular arrangement, considering this specific laser shock configuration. Especially, the pulse duration should be an important parameter to this matter. This investigation should be continued. For that, a material such as LY556 can be used on different laser installations providing different laser pulse widths. Then, DSC analysis can be systematically performed. Speaking of the LASAT application, it is not under too much trouble since the modification, if any, is not quite important and happened only on not well cured sample.

DMA (Dynamic Mechanical Analysis) have also been performed on shocked composite materials to provide complementary data on this investigation. The results are presented in Appendix B.

Conclusions and synthesis

In this chapter, epoxy resins under high pressure were studied from two points of view: time resolved observations of the shock wave propagation, and post-mortem residual state. Firstly, the observations of the shock wave propagation through epoxy targets have given quantitative information on the shock propagation. The shock front mean velocity was evaluated. Qualitative information on the shock patterns and repartition within the sample thickness were also obtained. The observation of the shock wave propagation through epoxy resins was also considerably enhanced by the use of time resolved photoelasticimetry. It highlighted the existence of a phenomenon probably correlated to the 2D effects phenomenon. These results provide new data, complementary to back face velocity measurement, to compare with numerical modeling.

In a second time, the shocked epoxy resins were analyzed thanks to post-mortem techniques to investigate the microstructural and mechanical residual states. In case of ultra-short laser pulse (300 fs, ELFIE experiments) no residual stresses were observed. No microstructural modification was evidenced as well. For short pulse (3ns, LULI2000 experiments), the same conclusions on the microstructure point of view can be made, but residual stresses were quantified on the sample front face about a few MPa. Finally, in case of a not well cured epoxy, a slight effect of the laser induced shock (25 ns, PPRIME) on the microstructure state was highlighted on the glass transition temperature. This result has been obtained in case of spallation only, and is reassuring for the industrial application.

Composite CFRP under laser shocks were then investigated. First, focus was made on studying the resulting damage from the shock wave propagation in cross-ply T800/M21, thin and thick laminates. The anisotropic damage parameters have been shown as well as the influence of the laser intensity level on the damage main dimensions. Damage scenario for the T800/M21 composite under high laser irradiation was formulated. In particular, the effect of thermoplastic nodules on the cracks propagation is clearly experimentally evidenced. These results were completed by experiments on two different unidirectional composites (T300/914, IM7/M21). Moreover, the laser shocks performed on thick cross-ply T800/M21 sample have enabled a better understanding of the damage growth behavior in the composite. More precisely, the resulting residual back face deformation was studied using Interferometric confocal microscopy. The elliptical characteristics of this deformation were determined by use of a statistical analysis of the data gathered. Analytical models were established to fit the experimental data and provided parameters allowing the correlation between the back face deformation and the laser shock intensity. Moreover, the gathered data can be used to plot charts which would enable the comparison of the damage tolerance of different composite materials.

Finally, VISAR time resolved experiments were performed on unidirectional model materials and applicative CFRP composites. The measurement reproducibility was checked. The data obtained respectively on thin and thick unidirectional T800/M21, cross-ply T700/M21 and FM300 adhesive bond material provide information on the dynamic response of these materials under laser shock loading. The shock propagation, without and with damage, is described by these signals which will consequently enable the numerical modeling of these material responses to laser shock. Speaking of application, VISAR measurements also highlighted a possible fatigue effect in case of repeated laser shock on unidirectional CFRP, probably because of bending. This point will have to be checked on bonded composite.

The results recalled and discussed in this conclusion were obtained thanks to several techniques, developed and adapted in this work to the diagnosis of shocked CFRP. The used techniques are quite efficient for the composite damage investigation, and will be used in the following chapters. As a synthesis, the main results associated to each technique are given in table 3.18.

Techniques	Associated main results
Post-mortem techniques	
Microscopy 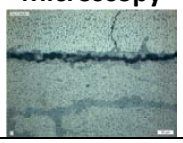	For cross-ply CFRP, thin and thick laminates, enabled the quantifications of the delamination width, depth, and the crack density resulting from the laser shock wave propagation.
X-Ray Radiography 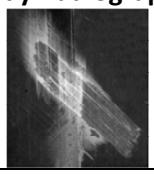	For cross-ply CFRP, thin laminates, completed the micrographies observations by enabling the quantification on the damage extent in the composite ply plane.
ICM 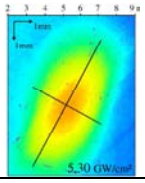	For thick cross-ply and unidirectional CFRP, enabled the quantification of the residual back face deformation resulting from the plies damage and buckling after the delamination induced by the laser shock wave propagation. Gave some elements on the possibilities to use an elliptical dimensionless ratio to characterize each CFRP sample.
Time resolved techniques	
Transverse Visualization (Shadowgraphy) 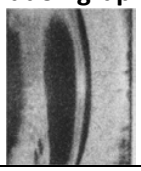	For thin unidirectional CFRP, enabled the observation of the behavior in the spallation induced damage difference, depending on the material characteristics. For classic epoxy material, enabled the shock wave observation through the target, giving quantitative information on the mean shock velocity, and qualitative information on the shock propagation pattern through the sample. It provided data, different from velocity measurement, to compare with numerical modeling.
Transverse Visualization with photoelasticimetry	For classic epoxy, highlighted the stress distribution occurring during the laser shock wave propagation. Data to compare with modeling. Post mortem photoelasticimetry enabled the observation of residual stresses for a specific pressure and pulse duration (LULI2000)
VISAR 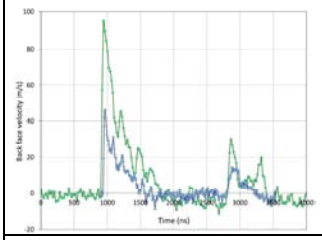	For FM300 Adhesive bond material, enabled the dynamic response analysis. For unidirectional CFRP, thin and thick laminates, enabled the dynamic response analysis, in cases of no damage and with spallation. For cross-ply CFRP, enabled the dynamic response analysis. For thick unidirectional CFRP, highlighted a possible fatigue effect of repeated laser shock loading. In all cases, data for modeling.
DSC 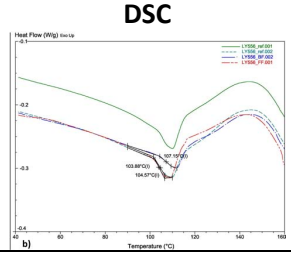	For classic epoxy, did not show any microstructure modification induced by laser shock in case of very high pressure, and really small pulse duration. Highlighted a possible small modification in case of lower pressure, but in case of longer pulses.

Table 3.18 Synthesis of the main results associated to each experimental technique used

References

[1] B. Gentilleau, M. Bertin, F. Touchard, J.-C. Grandidier, Stress analysis in specimens made of multi-layer polymer/composite used for hydrogen storage application: comparison with experimental results, Composite structures, Vol. 93, No. 11, 2011, pp. 2760-2767

[2] M. Bertin, F. Touchard, M-C. Lafarie-Frenot, Experimental study of the stacking sequence effect on polymer/composite multi-layers submitted to thermomechanical cyclic loadings, International Journal of Hydrogen Energy, Vol. 35, 2010, pp. 11397-11404.

[3] J. P. Colombier, P. Combis, F. Bonneau et al., Hydrodynamic simulations of metal ablation by femtosecond laser irradiation, Physical Review B Volume: 71 Issue: 16 Published: 2005 DOI: 165406 10.1103/PhysRevB.71.165406

[4] J. P. Cuq-Lelandais, M. Boustie, L. Berthe et al., Spallation generated by femtosecond laser driven shocks in thin metallic targets, Journal of physics D-Applied Physics Volume: 42, Issue: 6, Article Number: 065402 DOI: 10.1088/0022-3727/42/6/065402 Published: MAR 21 2009

[5] C.R. Phipps et al., J. Appl. Phys. 64 (3), p 1083 (1988)

[6] Grün et al., Appl. Phys. Lett. 39 (7), p 545 (1981)

[7] D. Laporte, F. Malaise, M. Boustie, J.M. Chevalier, E. Buzaud, C. Thessieux, Dynamic behaviour of two adhesive materials , DYMAT 19th Proceedings, Strasbourg, 245 (2010)

[8] M. Boustie, J.-P. Cuq-Lelandais, L. Berthe , C. Bolis., S. Barradas, M. Arrigoni, T. De Résseguier, M. Jeandin, Study of damage phenomena induced by edge effects into materials under laser driven shocks, J. Phys. D: Appl. Phys. 40 (22) , pp 7103–7108, (2007)

[9] J.-P. Cuq-Lelandais, M. Boustie, L. Berthe, P. Combis, A. Sollier, T. De Résseguier, E. Lescoute, E.Gay, L. Soulard et J. Bontaz-Carion, 2009, Two-dimensional investigation of laser shock induced spallation in subpicosecond regime, DYMAT 2009, Brussels, Belgium

[10] A. Ravasio et al., Hard x-ray radiography for density measurement in shock compressed matter, Phys. Plasmas 15, 060701 (2008); http://dx.doi.org/10.1063/1.2928156

[11] A. H. Zewail, Femtochemistry: Atomic Scale Dynamics of Chemical Bond using Ultrafast Lasers, Nobel lecture, Dec 10, 1999, and Biographical sketch. The Nobel Foundation – Stockholm (1999)

[12] J-P. Cuq-Lelandais, Etude du comportement dynamique de matériaux sous choc laser sub-picoseconde, Thèse de l'ENSMA (Ecole Nationale Supérieure de Mécanique et d'Aérotechnique), Ecole doctorale SIMMEA, 2010

[13] E. A. Abdallah, C. Bouvet, S. Rivallant, B. Broll, J-J Barrau, Experimental analysis of damage creation and permanent indentation on highly oriented plates, Composites Science and Technology, 2009, 69:1238-1245.

[14] F. Lachaud, C. Espinosa and L. Michel 2011, Impact damage of carbone-epoxy laminates" presented at the 17th JNC Conference (Journée Nationale des Composites), June 15-17th, 2011

[15] S. Petit, C. Bouvet, A. Bergerot, J-J Barrau, Impact and compression after impact experimental study of a composite laminate with a cork thermal shield, Composites science and Technology 67 (2007) 3286-3299

[16] N. Hongkarnjanakul, C. Bouvet, S. Rivallant, The effect of stacking sequence on the low-velocity impact response of composite laminates, presented to ECCM15, 15th European conference on composite materials, Venice, Italy, 24th-28th June 2012

[17] El-Hajjar, R. F., Petersen, D. R., Gaussian Function Characterization of Unnotched Tension Behavior in a Carbon/Epoxy Composite Containing localized fiber waviness, Composite structures (2011), doi: 10.1016/j.compstruct.2011.03.09.

[18] E. Gay, L. Berthe, M. Boustie, M. Arrigoni, P. Mercier, J. Bénier, Experimental study of composite damage under laser shock, presented at the 17ème Journée Nationale des Composites (JNC 17), June, 2011, Poitiers, France.

[19] http://www.comparts.co.il/files/T300DataSheet.58973619.pdf

[20] http://composites.ides.com/datasheet.aspx?ANON=OK&E=129203&FMT=PDF

[21] http://www.hexcel.com/Resources/DataSheets/Prepreg-Data-Sheets/M21_global.pdf

[22] http://www.matweb.com/search/GetMatlsByManufacturer.aspx?manID=81

[23] M. Perton, A. Blouin, J-P. Monchalin, Adhesive bond testing of carbon–epoxy composites by laser shockwave, J. Phys. D: Appl. Phys. 44 034012, 2010.

[24] E. Gay, Comportement de composites sous choc induit par laser: Développement de l'essai d'adhérence par choc des assemblages de composites collés, Thèse de l'Ecole Nationale Supérieure d'Arts et Métiers, Université Paris Tech, Ecole doctorale Sciences des Métiers de l'Ingénieur, 2011

[25] E. Gay, L. Berthe, E. Buzaud, M. Boustie, M. Arrigoni, Shock adhesion test for composite bonded assembly using a high pulsed power generator, published in Journal of Applied Physics 114, 013502 (2013)

CHAPTER 4: NUMERICAL MODELING AND EXPERIMENTAL VALIDATION

Introduction **160**

Part 1: Literature overview and presentation of the numerical tools **160**

1 Different finite element codes **160**

2 2. Shock and damage modeling on composite materials (literature overview) **161**

2.1 Quasi static loading and interlaminar strength 161
2.2 Low velocity impacts 162
2.3 A few words about buckling 164
2.4 Modeling High Velocity Impacts on composites 165
2.5 Epoxy resins modeling 167
2.6 What to keep in mind for laser shocks 167

3 Numerical tools selected and developed **168**

4 Preliminary step: Calibration of the pressure profiles **169**

Part 2: Modeling of the epoxy behavior under laser shocks **171**

1 Simulation of the shock wave propagation into an epoxy **171**

1.1 Model and parameters 171
1.2 Mapping of the shock wave propagation by simulation 172
1.3 Mapping of the shear stresses 174

2 Modeling FM300 behavior **176**

2.1 Modeling choice 176
2.2 Comparison experiment/simulation 176

Part 3: Composites: understanding the model to obtain a correct description of the dynamic behavior **177**

1 Composite model presentation **177**

2 Parametric studies on the composite models **181**

2.1 Pressure load parametric study 182
2.2 Influence of the interface stiffness 183
2.3 Anisotropic effect on the back face velocity 184
2.4 Analysis of the shock propagation along X, Y and Z directions 187
2.5 Parametric study on the material elastic parameters 189
2.6 Parametric study on sample thickness 192
2.7 A few words about thick composite model 192

3 From experiments to numerical modeling validation, results and discussions **195**

3.1 Numerical simulations validation procedure on thin unidirectional T800/M21 composite 195
3.2 Validation on other thin unidirectional T800/M21 experiments 200
3.3 Numerical simulation of 3 mm thick T800/M21 experiments 202
3.4 Numerical simulation of T700/M21 cross-ply composite 204

Conclusions & Synthesis **206**

References **209**

Introduction

This chapter deals with numerical modeling of laser shock on epoxy resins and CFRP composites. Indeed, numerical modeling is a key point in the development of the laser shock wave adhesion test. As previously explained, the laser shock propagation in CFRP knowledge should be improved by numerical modeling. Especially, the back face velocity and the corresponding waves, the stresses inside the material can be extracted from numerical modeling. From the previous results, numerical models are expected to give information about the anisotropy effects, as well as on the interface effects. Different parametric studies can also complete the data and enable a wider understanding of the laser shock phenomenon on composite material such as the effect of pressure or pulse duration. This knowledge will be quite useful in a second time for the optimization of the laser shock test (Chapter 5 and 6).

The first part will be dedicated to a literature review on what can be done to model shock in composite materials. The different codes available are first briefly described. Then, the different shock modeling possibilities found in the literature are presented. The works are sorted out by strain rate, as in the first chapter.

The second part of this chapter focuses on the numerical modeling of epoxy resins. Especially, the observations realized in the third chapter on the LULI laser shock experiment are simulated to confirm the conclusions made. In a second time, numerical modeling of the FM300 material (the adhesive in bonded samples) is presented. In particular, the method used to fit the FM300 samples VISAR signals is described in order to obtain a correct behavior modeling of this material. The correct simulation of the FM300 behavior under laser shock is an important point for the correct modeling of laser shock on bonded composite targets.

In the last part, the numerical simulations of the laser shock on composite material are presented. The modeling choices, general modeling considerations, and material model are first described. Then, different parametric studies are presented. They aim to understand the effect of each parameter on shock waves propagation: target geometry parameters, material model parameters, as well as laser parameters. The conclusions made thanks to these parametric studies are finally used to propose a numerical modeling leading to the best agreement with our experimental data, from thin and thick unidirectional CFRP to cross-ply composites.

Part 1: Literature overview and presentation of the numerical tools

1 Different finite element codes

In this work, focus is made on finite element codes and models already available. Indeed, using commercially available codes would facilitate the transfer of the developed numerical tools to industry. Indeed, the model should generally be 3D, or at least 2D, to take into account respectively anisotropy and orthotropy. Different commercial codes such as ABAQUS, ANSIS, RADIOSS, LS-DYNA,… can be adapted to the problem resolution. Historically, ABAQUS was considered as an implicit code, therefore more adapted to quasi-static loading modeling. On the other hand, RADIOSS or LS-DYNA are both initially explicit codes, more adapted to dynamics resolution. Indeed, in explicit codes the parameters at a given time step are calculated on the basis of the parameter value at the previous time step. Therefore, the calculation time only depends on the time step of the resolution, often linked to the mesh size. The frontier between implicit and explicit codes is not so clear any more

since each quoted code has been enhanced with respectively explicit and implicit modules. They are becoming full complex codes, enable to solve multi-physics coupled problems taking into account temperature, fluids, magnetism, etc… Speaking of RADIOSS and LS-DYNA, hydrodynamic models are also available. With time, the number of models and element formulation available has grown to enable a wide range of modeling of various problems. It can be used to model crash as well as explosions thanks to the different element formulations (namely ALE for Arbitrary Lagrangian - Eulerian and SPH for Smoothed Particle Hydrodynamics), and taking into account all the thermo-mechanical aspects. The computing time has also been reduced over the years by combination of more efficient codes, parallel calculations and improvement of computers rechnology. Composite models are rather recent, especially in case of shock applications. Therefore, modeling composite under shock still requires model validation/development as well as parameters identifications. Currently, many works address to these two issues, and are discussed in the following section.

2 2. Shock and damage modeling on composite materials (literature overview)

2.1 Quasi static loading and interlaminar strength

The laser shock loading on composite materials raises the question of interlaminar strength. Indeed, the high tensile stresses generated by the laser shock propagation load the material in z direction tension, also mentioned as transverse direction in this work. It is in fact the spallation phenomenon, which seems to be directly correlated to the interlaminar strength. Thus, it could be interesting to see how this interlaminar strength tests are modeled in the literature.

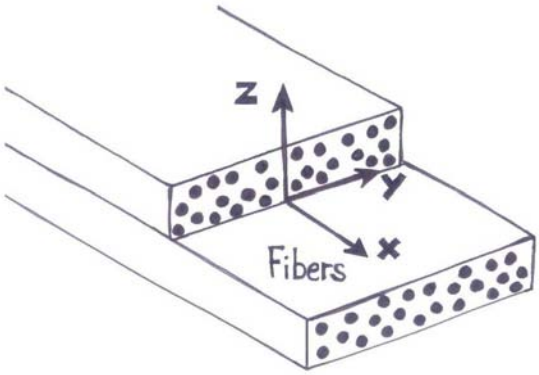

Figure 4.1 Coordinates system used in this chapter

It concerns both the normal strength, meaning the tension σ_{zz}, and the shear strength σ_{xz}, considering the coordinates presented in Figure 4.1. The normal strength corresponds to a loading in “mode I”. As previously presented, the interlaminar normal strength of a laminate is classically evaluated by GIC testing. A pre-crack is inserted during the curing process in the laminate itself. Then, the two unattached edges can be pulled in the opposite directions (see Figure 4.2-a). The shear strength corresponds to a loading in “mode II”. Experimentally, this kind of loading is generally performed by bending, three points bending or simple bending (see in Figure 4.2-b). Ylias et al. used cohesive law to describe these experiments, and the corresponding damage propagation [1-2]. They highlight the necessity of using a damage criterion coupling mode I and mode II. This has been done by including a cohesive law in LS-DYNA software, elastic linear in compression, and elastic non-linear in tension (see Figure 4.3). This description is classic for cohesive elements, and is already available in DYNA, but the research team wants to push forward this law development by including strain rate

effects in the years to come. Indeed, one part of their work consists in comparing experimental results between a quasi-static loading (2mm/min) and a "dynamic" loading (30m/min) on a T800/M21 laminate. The force/displacement curves recorded during the tests are consequently different, but almost no differences have been observed in the maximum displacement before failure, or release failure energy. This is consistent with the results presented in the first chapter, which showed that strain rate effects are observable at higher strain rate. Nevertheless, this approach is interesting and should pushed forward at higher strain rates.

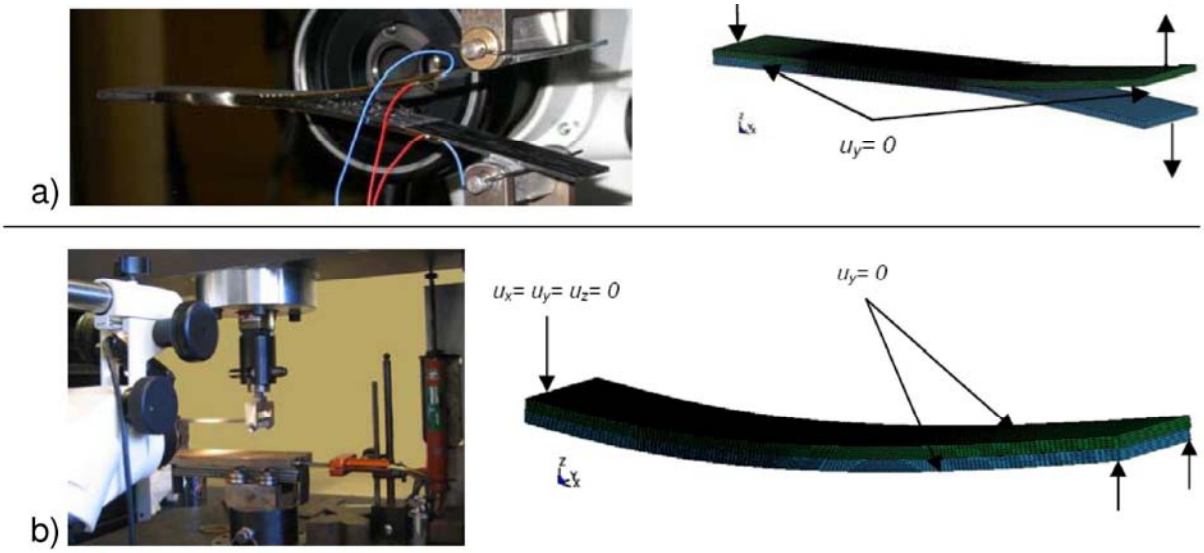

*Figure 4.2, **a)** Test of an unidirectional T800/M21 composite material in mode I, GIC testing and associated numerical modeling (from M. Ylias [1-2]), **b)** Test of the same unidirectional T800/M21 laminate in mode II, bending test and associated numerical modeling, M. Ylias [1-2]*

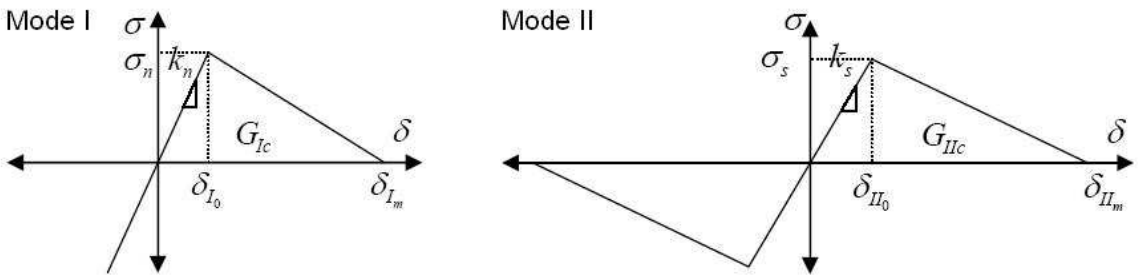

Figure 4.3, Cohesive law used by M. Ylias et al. [1-2] to model the interlaminar damage

Using a specific experimental set-up, M. Ylias et al. have succeeded to test a T700/M21 unidirectional laminate with a coupled mode I and mode II loading (50 % each), in quasi-static. They obtained release energies in mode I and mode II respectively equal to 545 J/m² and 13887 J/m². This experiment has been modeled, especially the damage propagation which corresponds to the negative slope curve after the maximum displacement. It shows that the damage propagation description using the coupled cohesive low correctly fits the quasi-static experiments.

2.2 Low velocity impacts

M. Ylias et al. validated their interlaminar damage propagation presented in the previous section by simulating low velocity impacts (LVI) [1-2]. It has been realized with a 16 mm diameter impactor, at 2.95 m/s, on a $[45,-45,0,0,90]_S$ T800/M21 composite material. The comparisons between experiments and simulation were performed using displacement against time curves, and C-scan

measurements. This last data has been compared to failed elements. Good fittings were obtained, which enable afterward to use the model to study stresses evolution during the impact. The used model parameters are interested to notice. Indeed, to obtain these good fittings, the cohesive element stiffness factors (corresponding to the linear compressive slope in Figure 4.3) were both set to 100 N/mm^3 in mode I and mode II. Similary, the maximum tensile strength, or interlaminar normal strength (σ_{ZZ}) has been chosen equal to the maximum shear strength, or interlaminar shear strength (σ_{XZ}). The value chosen corresponding to the T800/M21 is about 60 MPa. Note that this value is averagely what is used in all other works dealing with interlaminar strength on CFRP and GFRP [7-10], [14-18]. Nevertheless, GIC and GIIC energy releases have been set with two different values, respectively 765 J/m² and 1250 J/m². These values are chosen here as a rough estimate of these damage parameters, but the composite model used in this impact case is not fully described.

S. Heimbs et al. from EADS Innovation Works also investigated low velocity impact numerical modelling. In particular, they studied the difference in low velocity impact behaviour between preloaded and non preloaded CFRP using LS DYNA code [3]. The idea was to show that preloading CFRP plate enables to reduce the damage propagation. The material tested is a conventional CFRP (Cytec 977-2-35-12K HTS-134), with a quasi-isotropic lay-up $[-45°/0°/45°/90°]_{3s}$. In order to model the problem, LS-DYNA material model was used. There are mainly two material models which enable to describe damage propagation in composite material, mat_022 and mat_054 respectively named COMPOSITE_DAMAGE and ENHANCED_COMPOSTIE_DAMAGE [4-5]. The first one can be used with SOLID elements, when the second one only deals with SHELL. In S. Heimbs study, shell was used to model the problem, because the plate was quite sizable as well as the number of CFRP layers. Moreover, they were interested in the global plate behaviour and delaminations, for which shell are accurate enough. These two models are both elastic and include the same damage criteria based on Chang/Chang definition [6]. Note that MAT55, MAT58 and MAT59 can also be used for shell modelling, but have different damage criteria. The interfaces are modelled using a CONTACT_TIEBREAK, with a specific cohesive formulation which corresponds to the one described by M. Ylias (see Figure 4.3) [4-5]. Thanks to these choices, the comparisons on the displacement versus time curve between experiments and modelling are quite good. In a second time, S. Heimbs et al. used the numerical model to study the sensitivity of numerical results to modelling choice. Especially, they showed a result dependency on mesh size, contact penalty stiffness and the number of shell elements in the laminate thickness. Important differences were observed, in particular in the release behaviour after displacement due to compression. This can explain the contact stiffness importance. Mesh density and number of shells in the thickness deal with the propagation through thickness. The more refined the mesh, the better the stresses propagation. That is one of the reasons why other works prefer using SOLID elements, like in the work of B. S. Thatte et al. [7]. Indeed, the use of SOLID elements enables to look at the stress level within the laminate thickness. Nevertheless, the comparisons given on the displacement versus time curve are not very good. It shows that even if solid elements are used, it does not prevent from using an enough refined mesh even if it is probably not the only problem in this case. Indeed, B.S Thatte's work also raises the question of material properties, and material parameters from the numerical point of view. Indeed, the parameters used in this study have been theoretically calculated from fiber and resin parameters. No experimental validation is presented. These parameters can also lead to differences on the numerical model response if used as calculated. Other works avoid the question by taking the model results on their own, with no comparison with experiments [8].

To sum up with low velocity impacts, two other works can be quoted from A. Faggiani et al. and C.S. Lopes et al. [9-10]. Both works present the development of an intralaminar damage model based on different approaches. The number of damage parameters taken into account are also more numerous, but the coupled cohesive model between mode I and mode II remains as a basis. The damage model has been implemented in ABAQUS thanks to user laws. Once again, good fitting in the displacement versus time curves have been obtained. It helps to conclude that cohesive models are well adapted to low velocity impact modelling, especially to define the interlaminar tensile and shear strengths.

2.3 A few words about buckling

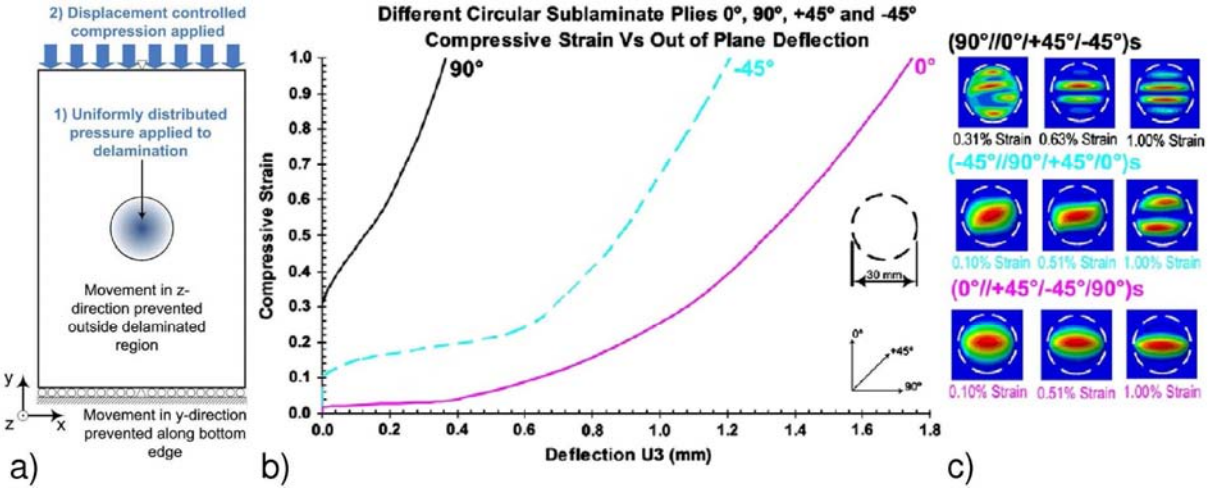

Figure 4.4, Work from R. Craven on buckling study [12] ***a)*** *Boundary conditions for FE models developed by R. Craven,* ***b)*** *Compressive strain versus out-of-plane deflection for circular thin film delaminations with different sublimate fibre orientations* ***c)*** *Corresponding 2D out-of-plane deformation for the different lay-ups.*

Before switching to high velocity impacts, works on composite laminate buckling modeling can be mentioned. Indeed, buckling induced by laser shock has been observed on the thick CFRP material (see Chapter 3, part 2, section 2). It is thus interesting to see if numerical model can described this phenomenon. Z. Zhang et al. provided a numerical analysis of CFRP beams buckling induced by impacts [11]. They used LS-DYNA models to simulate the buckling of a CFRP beam. Nevertheless, the impact initiating the buckling has been produced on the beam tip, parallel to the fiber direction. Modeling buckling is thus possible, but the studied case is slightly different. The numerical investigation published by R. Craven et al. and performed on ABAQUS are closer to the work conducted here [12]. They investigated the buckling of a quasi isotropic CFRP (IM7/8551-7) in two different cases: single delamination (only one initially delaminated ply) and multiple delaminations (all the plies are initially delaminated). Different lay-ups were investigated in each case. Since they were only interested in buckling, no particular damage propagation has been used. In fact, a delaminated region has been created on purpose between the plies by untying the nodes on purpose (see in Figure 4.4-a). The studied delamination shapes were chosen circular and elliptical. Out from these delaminated regions, the element nodes were tied to avoid propagation. Finally, the buckling is initiated by a compressive strain imposed on the sample edge (see in Figure 4.4-a). Then, the out-of-plane deformation can be observed. Results from numerical simulations in case of a circular initial delamination are given in Figure 4.4-b and c. First, the out-of-plane deflection versus compressive strain result can be commented. Indeed, it can be observed that buckling is much faster in case of a 0° delaminated ply compared to -45° and 90°. This result is in good agreement with the observation made in Chapter 3. Indeed, it can be considered that the laser shock tensile stresses initiate a circular

delamination due to the circular focus diameter. The damage propagation is then due to material lay-up and ply buckling (see in Chapter 3). It could explain why the delamination associated with ply buckling in case of laser shock more propagates in case of 0° plies than in cross-ply.

In a second time, the shape of the buckling out-of-plane delamination observed in case of a -45° initially delaminated ply can be commented. Indeed, the shape observed in case of a small initial compressive strain is really close to the one measured by ICM on shocked composite back face (see in Chapter 3). In R. Craven study, the deformation remains in the delaminated region, but it can be assumed that this blister would propagate without the numerical constrained condition. This good agreement partially confirms the analysis made of the laser shock phenomenon on thick CFRP target in Chapter 3. It also shows that laser shock on composite can provide interesting experimental data to compare numerical modeling with.

2.4 Modeling High Velocity Impacts on composites

In this section, works dealing with high velocity impacts (HVI) are presented. Indeed, on one hand the damage resulting from laser shock propagation in CFRP is closer to low velocity impact because laser shocks do not lead to perforation as high velocity impacts do. But on the other hand, low velocity impacts do not deal with shock propagation through the material thickness, when it is more commonly done in case of high velocity impact. As a proof of that, it has been shown in the previous section that low velocity impact can be modeled using shell elements with a good agreement to experimental results. In the works presented in this section, solid elements are used because they enable the evaluation of the stresses through the material thickness [13-22]. Reducing the error on these stresses is important because they are assuring the shock propagation in terms of calculation. Numerical modeling of high velocity impact is important to predict the composite response and associated damage growth in many cases. Hailstone impacts on composite part are an example [13]. Of course, this is also the case of military applications or space impact investigations. In fact, all cases deal with impact above 1 km/s. In 2000, H. D. Espinosa et al. worked on the modeling of plate impact experiments (3 km/s) found in the literature [14]. They developed a 3D anisotropic viscoplastic model to represent GFRP samples, and used different cohesive laws for interface modeling. Experimental data coming from manganin gauges and VISAR measurements have been used to compare with numerical results. Experimental parameters have been used for the material model parameters, and the interlaminar normal strength has been taken equal to 50 MPa. Several conclusions have been drawn. First, the exactitude of the numerical calculation depends on the mesh size, as it was the case for low velocity impact (LVI). The roughness of the interfaces has no influence on the interlaminar normal strength, but a small one on the interlaminar shear stresses. Shear stresses have been evaluated about 10 % of the tensile stresses in the worst case. Finally, the interface laws seem to have no influence on the velocity signals, but play on the numerical tension value leading to delamination.

Other works focus on the development and validation of a more complex damage propagation model [15-18]. Indeed, the Chang/Chang [6] damage model can trustfully be used for damage initiation, but has some limitation if a realistic description of damage propagation is sought. Once the failure criterion satisfied, the model parameters are set to zero, and no propagation law is directly implemented. More complex models try to take more damage parameter into account. This is the case of the model implemented in RADIOSS by EADS Innovation Works and based on the LMT model (Laboratoire de Mecanique et Technologie, ENS Cachan) [15]. In another model, including a progressive softening of material properties could enable a damage progressive opening. This

progressive failure is taken into account by the COMPOSITE_DMG_MSC model, developed by MSC (Materials Sciences Corporation) and implemented in LS-DYNA software (requires a specific additional license) [16]. The damage model efficiency has been demonstrated on two ballistic experiments, for which the damage extent were correctly described [16]. It has also been used to model ballistic impact on balsa composite and GFRP [17]. In this last case, the MSC model was particularly interesting because it enables to predict the residual behavior after impact, which is generally expected in this kind of modeling. Note that on this point, this is different from laser modeling, for which the early µs only are usually important. In addition to a cohesive law for the interface modeling, this model has also been used to test the impact response of BMS8-212 (CFRP) different lay-ups [18]. Good agreements have also been obtained. To sum up, this model well describing the composite progressive failure is interesting when the damage extent, the residual strength, or the resistance response are point of interest. This is a common trend in numerical modeling of composite under impact, as proved by other code developments, this time with ABAQUS software [19]. Another Cohesive models, progressive damage model, etc… enable to predict the material residual characteristics. It seems that the point of interest is really to describe as accurately as possible the final state of the target. Nevertheless, it is not given a better description of the shock wave propagation into the material, which has though its importance at these pressure levels.

In order to do that, several works address to the development of material models including equation of state dedicated to composite materials [20-23]. In these studies, the question of strain rate effects on the material mechanical properties is also raised [22-23]. This point was not so obvious in the previous work quoted. R. Vignjevic et al. propose a thermo-elastic damage model for CFRP [23]. The idea is to include a Mie Gruneisen equation of state (EOS) to the material model by decomposing the stress tensor. Mie Gruneisen EOS is generally used to describe hydrodynamic behavior of material at high pressure state. In their work, the damage is taken into account by a specific tensor. Note that due to the brittle properties of composite, especially at high strain rate, plastic deformations are generally neglected. This idea of adding an EOS to the classic composite model description is used in several works. M. Wicklein et al. also describe the composite behavior under high velocity impact by modeling the elastic deformations thanks to a linear relationship between stresses and strains by introducing nine elastic constants. The EOS is added for the hydrodynamic relation, linking pressure and density [22]. Using more complex model also raise the question of model parameters. As shown by M. Wicklein, all the parameters are important in case of HVI, and should be identified carefully for each different material. It can be done experimentally (see in Figure 4.5) or using theory [23]. Concerning this last point, a procedure has been formulated by S. Ryan to generalize the use of materials properties [23]. In this work, the errors on each parameter have been evaluated, and the strain rate problem outlined. From the laser shock point of view, The extreme strain rate involved by laser shocks brings materials into an unvestigated regime for which the materials properties values have to be determined, in the continuity of what is known.

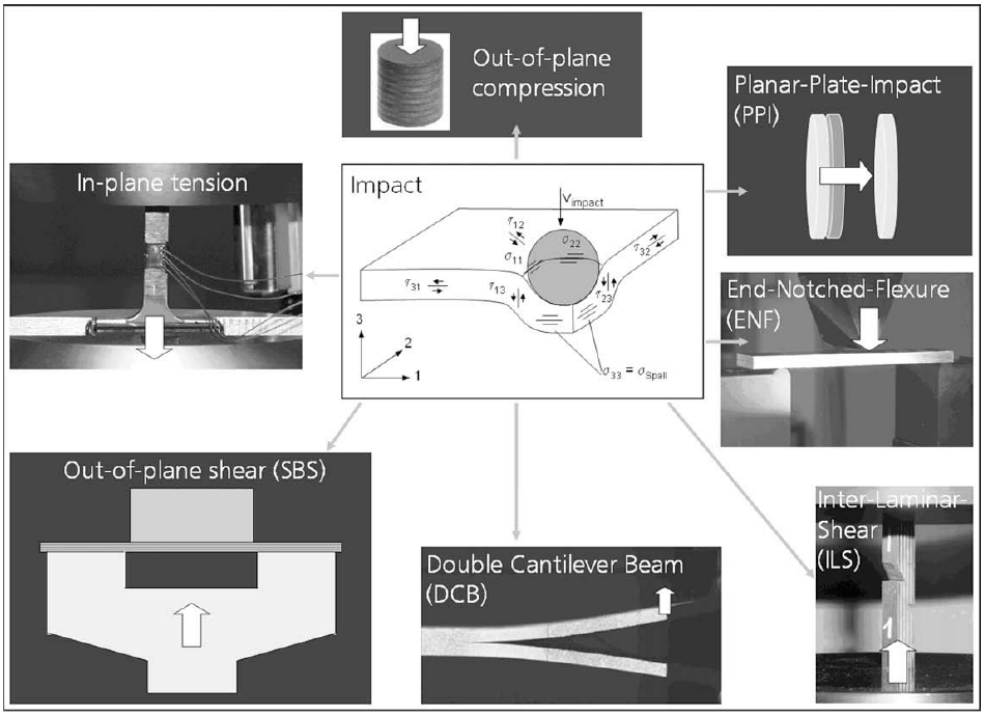

Figure 4.5, Different loading states in case of a High Velocity Impact on CFRP and associated characterization experimental tests [21]

2.5 Epoxy resins modeling

Concerning epoxy resins, their modeling under shock was an important part of D. Laporte PhD work [24-25]. What is important to recall here is that several models are already available for high pressure. D. Laporte demonstrated that the hydrodynamic state of the epoxy can be modeled, in a first approach, by using Mie-Grüneisen equation or polynomial laws. Moreover, on the contrary to the composite material, literature can provide parameters to feed the material's model. These parameters are easier to find since epoxy resins are isotropic. Of course, this is only the first approach. D. Laporte showed that visco-elastic characteristics should be taken into account for a better description thanks to different models. Significant differences can be observed on VISAR velocity signals in case of plate impact expereriments. Here again, the main differences are in the damage propagation modeling. D. Laporte has tested different model and different damage parameters and demonstrated the sensitivity of numerical spallation to these two points [25]. The most efficient numerical model to use has been shown but it appears that a first elastic hydrodynamic model can be used as a first step with enough accuracy.

2.6 What to keep in mind for laser shocks

The first point is to say that anisotropic model should be considered, especially for shock propagation. From commercial and available models, it is possible to use elastic model, or hydrodynamic models. This last case is still through developments in several investigations, and not yet available. Moreover, it requires material properties and parameters, specific to each composite modeled, and generally not yet available or hard to obtained. This difficulty is even higher in case of high strain rate problems. For that reason, it seems safer to use elastic models in case of laser shock modeling. The low pressure used, generally under 1 GPa, also allows this description regarding the 1st chapter overview. For higher pressure, the error induced by this modeling choice will be considered. Speaking of damage, many works address to the use of cohesive law to describe the interlaminar

damage propagation or progressive failure in composite laminate. These descriptions are quite important if the point of interest is the damage extent investigation or the material residual properties after shock. In case of damage initiation, all the criteria are more or less the same because of the brittle behavior of composite material. The important point is to have criterion for each typical damage feature: fiber breakage, matrix cracking in tension, in shear… Therefore, the Chang/Chang criterion can efficiently be used to model the damage initiation [3], [6]. Here again, the question of failure parameters in case of high strain rate could be raised. From the literature overview presented in the previous section, it is not fully clear whereas the used material parameters are taking into account strain rate or not. Regarding the overview presented in the 1st chapter, strain rate effect should be taken into account, at least in case of laser shock and ballistic impacts.

3 Numerical tools selected and developed

In this work, LS-DYNA software has been used to model laser shocks on epoxy resins, composites and bonded composites. This choice has been principally motivated by the literature overview, and the different tools available to model CFRP laminates (LS-PREPOST software) [4-5]. In addition, in this PhD study, a numerical tool has been developed to first enhance the numerical results by plotting X-T diagrams. These diagrams give the shock wave propagation in time for a given direction, generally the loading axis through the sample thickness (not always "X"). The pressure level is added thanks to a color code. In a second time, a code has been developed to track the maximum of stresses within the material thickness and along the shock propagation. It is done by working on the stresses versus time curves for each element, with a local research of maximum on specifically defined windows. This requires some parameters adjustments in order to adapt the calculation method to different levels of pressure (see in Figure 4.6). So the maximum of stresses, especially in tension, are tracked and recorded. This enables to plot the maximum tensile stress region on the X-T diagram given by the Matlab code. It is useful to understand the influence of laser parameters on the tensile stresses position, especially in case of bonded composite materials. This numerical tool, presented in Figure 4.6, can also be used for the technique optimization.

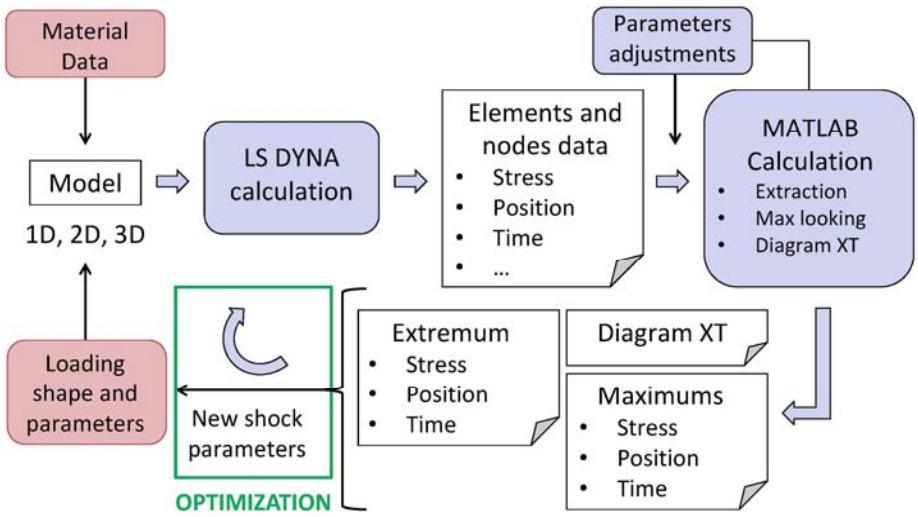

Figure 4.6, Principle of the calculation loop developed as a numerical tool for shock on composite analysis and optimization of LASAT technique on bonded CFRP

Note that this tool has been developed to work with 1D, 2D and 3D models. Depending of the studied case, each kind of model has been used (see in Figure 4.7). As explained in the previous section, only solid quadratic elements were used to model composite. Due to its anisotropy,

composite material should be studied by using 3D models. Nevertheless, it is not always possible. Indeed, modeling laser shocks requires using a really small mesh, from 5 µm to 10 µm depending on the pulse duration. Therefore, it was not possible to use 3D models for thick composite samples. For example, a 500 µm thick T800/M21 model, using symmetries, already represents 2 millions elements. Consequently, 3D models were only used in some cases to demonstrate the anisotropic effects on the shock propagation, especially on unidirectional CFRP. By several preliminary studies, it has been shown that unidirectional composite can also be modeled using 2D models, if the fibers are contained in the meshed plane, without significant error on the usual calculation time (< 10µs). Therefore, 2D models were used also to model thick unidirectional CFRP (see in Figure 4.7). For the reason given, cross-ply composites and bonded composites will also have to be modeled thanks to 2D mesh. The error due to the non modeling of one fiber direction should be kept in mind. Finally, 1D models can also be used for easy and well-known material, especially if the laser spot size is much more important than target thickness. In this work, 1D models have been used for calibration, described in the next section.

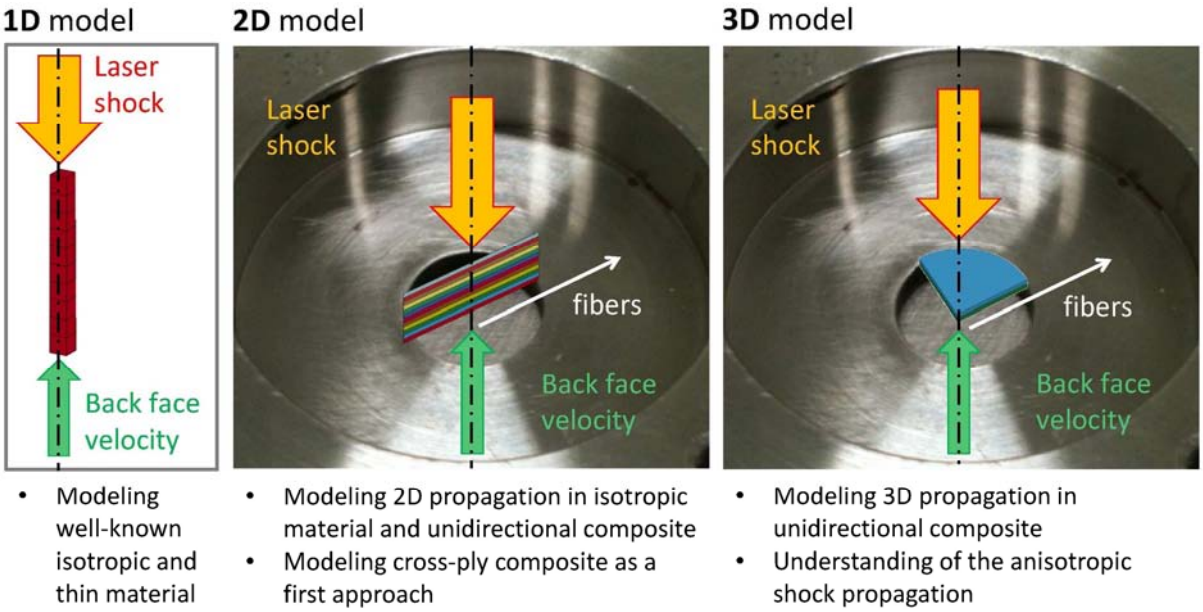

Figure 4.7, Different models to be used in the numerical investigation presented in this work

4 Preliminary step: Calibration of the pressure profiles

Before entering into deep modeling, the first step is to be sure of the pressure profile used to represent the laser loading. Indeed, the laser parameters are the key ones to tune for the LASAT technique optimization, and should be clearly modeled. Since LS-DYNA does not have a laser/matter interaction module yet, the pressure induced by the laser shock interaction has to be directly modeled. Technically, this is done by entering in the model a pressure temporal profile, on a spatial repartition. In order to avoid strong un-physical shear on the pressure area edges, smoothing has been introduced as presented in Figure 4.8. This choice is not too far from the real spatial distribution shown in Chapter 2. This has been used for both 2D and 3D models.

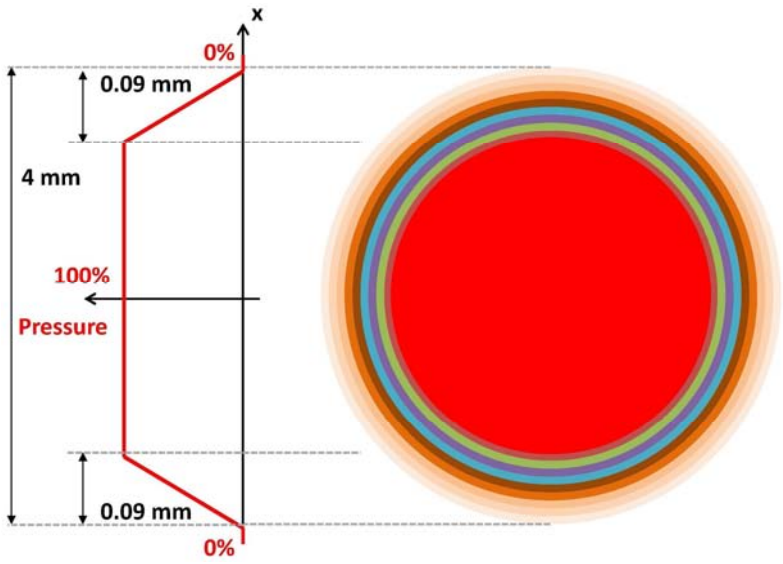

Figure 4.8, Numerical spatial distribution of the pressure representing the laser shock

The temporal profile has also to be determined by calibration. This step is quite important for a correct modeling, and the experimental procedure applied, using VISAR measurements, is described in Appendix C. Note that since the laser shock on composite are performed by using an aluminum sacrificial layer, the average pressure profile has been obtained thanks to a calibration on aluminum sample. This profile is presented in Figure 4.9. At mid-height, the pulse duration is about 50 ns, which corresponds to the 25 ns laser pulse in water confinement configuration. A long release shape can also be observed after the Gaussian peak. It is also well known for water confinement configuration. Once the average pressure pulse validated, it has been used to calibrate the correlation between laser intensity and induced peak pressure, still by using laser shocks on aluminum target (see in Appendix C). The resulting calibration curve is given in Figure 4.10 and also agrees with previous investigations commonly evidencing the root square law between intensity in GW/cm² and pressure in GPa (see in Figure 4.10) [26-27].

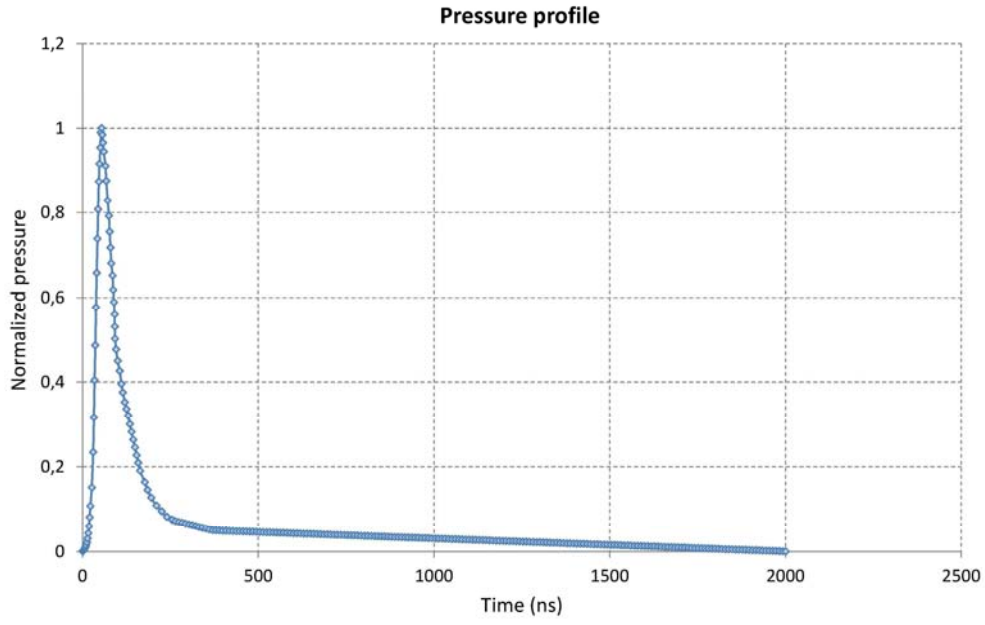

Figure 4.9, Average pressure temporal profile for PPRIME 25 (l=1.053µm, t=25ns) laser source obtained after laser shock calibration on aluminum samples (see Appendix C)

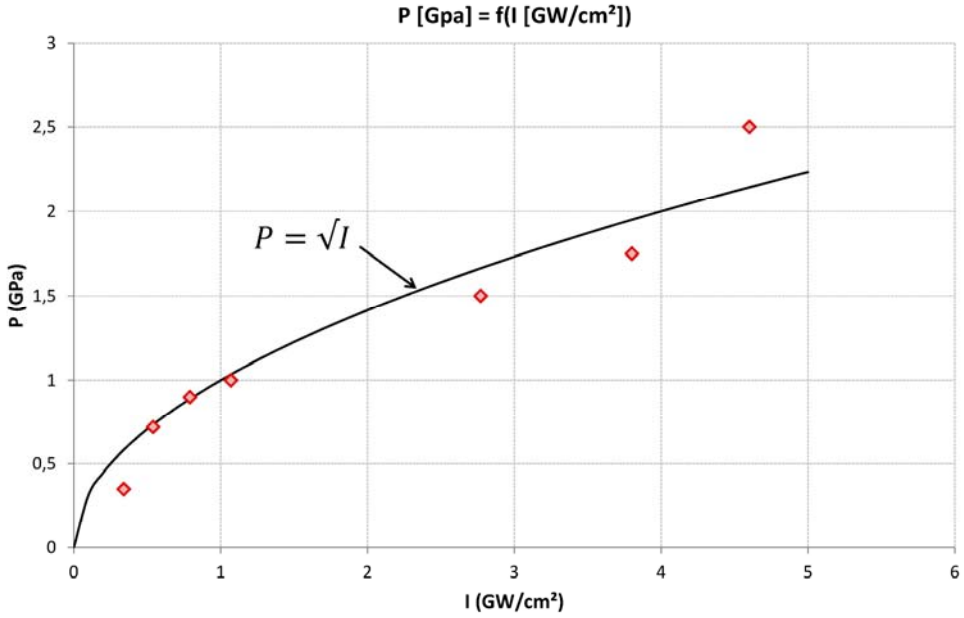

Figure 4.10, Calibration curve correlating pressure to laser PPRIME25 intensity based on aluminum calibration and using the average pressure profile given in Figure 4.9 (see Appendix C)

Part 2: Modeling of the epoxy behavior under laser shocks

In this part, two main numerical investigations dealing with epoxy resins are presented. The first one concerns a first modeling approach of the phenomenon observed during LULI2000 experiments. The idea is to reproduce the shape of the waves observed to validate the experimental observations. Moreover, it would help to select a material model for epoxy. Note that it would have been interesting to model ELFIE experiments, especially to obtain some elements on the equilibrium phenomenon observed by photoelasticimetry. Nevertheless, this modeling is quite complex, especially because of the really short pulse duration, and the models to use at this dynamic scale. For that reason, dynamic molecular simulation should be used, and these tools were not used in this work. The second investigation deals with the modeling of FM300 material, based on the previous modeling and the time resolved experiments presented in Chapter 3. A good description of the phenomenon by the model is expected for the following modeling steps, especially bonded composite modeling.

1 Simulation of the shock wave propagation into an epoxy

1.1 Model and parameters

For this modeling, and only for this one, the pressure pulse temporal profile has to be numerically calculated. Indeed, the experimental configuration is different, since a vacuum chamber is used, and no confinement layer is applied. Pressure profile has been obtained from ESTHER software, the same software than the one which has been used to calculate the laser irradiation corresponding pressure. The spatial repartition is as described Figure 4.8. The epoxy resin has been modeled using a 2D mesh, identical to the experiment visualization plane to enable comparisons. The modeling of 3 ns laser pulse requires really small mesh size. In this case, 5 µm has been chosen, and the correct transmission of the pressure pulse from one mesh to the following has been checked. The material

modeled has been chosen to be elastic hydrodynamic. This can be justified by the high pressure level. Technically, a linear polynomial law, linking pressure to density, has been used. It needs few parameters to work correctly, and these are given in Table 4.1. Note that the initial sound speed c_0 has been taken from a similar resin to the one studied in D. Laporte work [25]. The exact description of this law can be found in LS-DYNA manuals [4-5]. Their coefficients are calculated from the parameters given in Table 4.1. Nevertheless, no damage model has been added so far. Indeed, it would require viscoplastic models, and damage propagation models not investigated in this work. No spallation will be modeled.

ρ (g/cm^3)	c_0 (cm/µs)	s	Γ_0
1.14	0.2	1.493	1.13

Table 4.1, Epoxy material properties used for polynomial law coefficient calculation with ρ, the density, c0, the initial sound speed, and Γ_0, Mie Gruineisen's coefficient

1.2 Mapping of the shock wave propagation by simulation

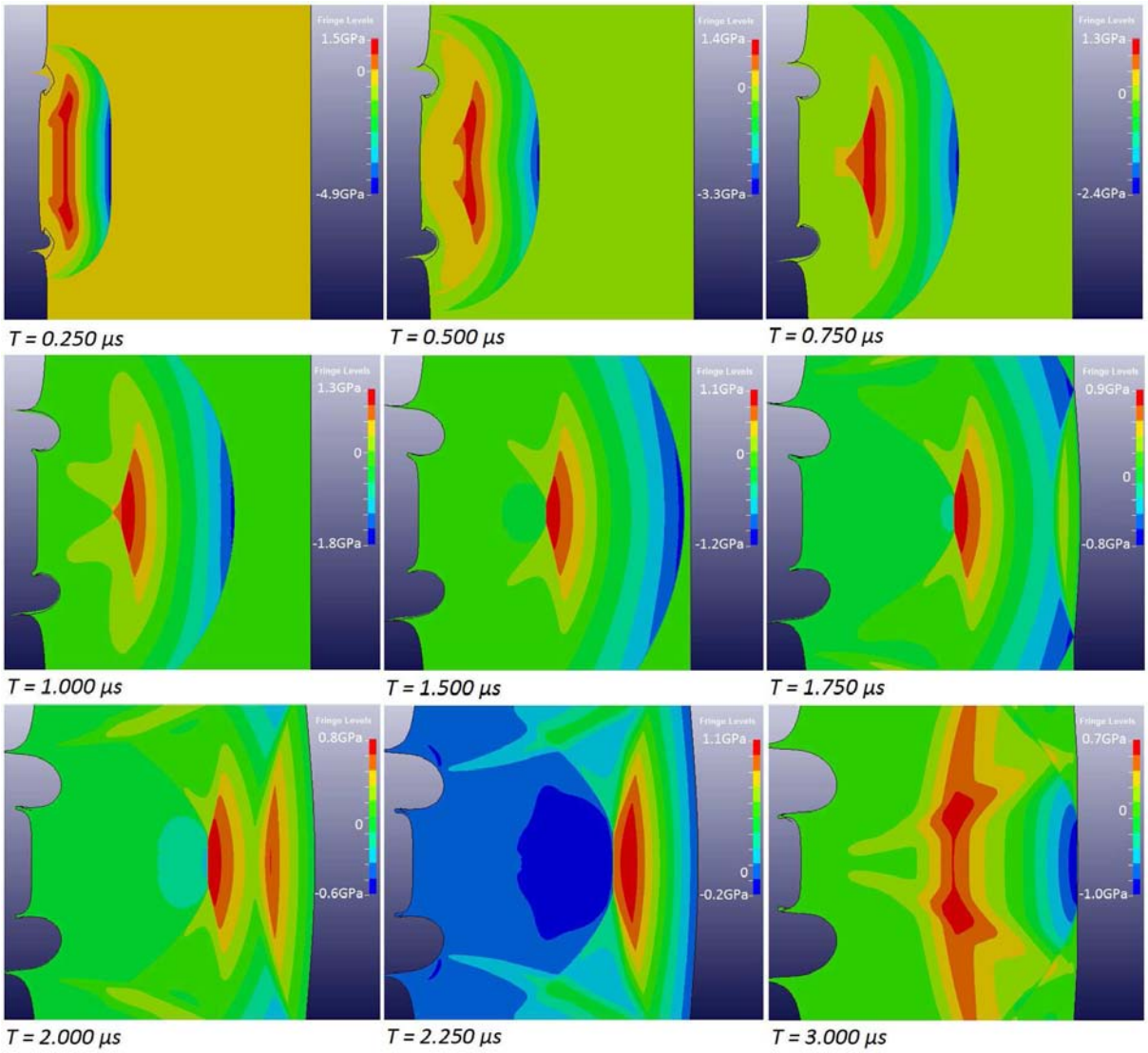

Figure 4.11 Snapshots of the LS-DYNA numerical simulation of the shock wave propagation into an epoxy target induced by intense laser irradiation (94 GPa, 3 ns) – Representation of σ_{zz} stress (LS-PREPOST, dynamic stress color code)

Figure 4.11 shows snapshots of the simulation corresponding to experiments presented in Chapter 3. The stresses σ_{zz} are represented thanks to a color scale, from red to blue which respectively traduce the compression and the tension, and changing from one image to the following (see in Figure 4.11). As explained in the previous section, the initial pressure is 94 GPa for the numerical modeling to be simulated in the exact same pressure condition.

Snapshots of the numerical simulation are presented at different times, and can be directly compared to the images presented in Chapter 3. At time 0.250 µs and 0.500 µs, the first propagation steps can thus be observed. The blue and green lines correspond to the shock and the edges effects already inducing tension behind the main shock wave propagation as proved by the red blur. This tension zone is then following the shock wave in its propagation through the epoxy thickness. This description is in agreement with experiment showing clearly the front of shock wave and tension produced by edge effects. Note that at 0.500 µs, the shock front and the edge effect are still really close to each other. Back to experiments, it could explain why only one main black shape can be observed on the snapshot taken at t = 0.500 µs. On the following propagation numerical images, the shock front separates from the 2D effect induced tension area. The numerical images taken at 1.0 µs particularly looks like to the experimental one, taken at the same time. The position of the shock front through the epoxy sample thickness is identical to the one experimentally measured. This is also true for the 1.5 µs image. The numerical shock front has reached the epoxy sample back face at the same time than the experimental one did. Therefore, the chosen numerical model well describes at least the shock propagation through the thickness. The model is reliable on that point. It shows that the shock is also strongly attenuated. It decays from 94 GPa at the initial time to 5 GPa compression in 250 ns. Until 1.5 µs, the shock amplitude continues decreasing but less drastically. It can also be noticed that the tension created by 2D effects (about 1GPa) is significant, and more constant than the shock front as attenuation is concerned.

The numerical snapshots taken at t = 1.75 µs and t = 2.0 µs show the shock front reflection on the back free surfaces. The timing also well corresponds to the experimental snapshot taken at 1.8 µs. This reflection leads to tensile loading visible on the numerical snapshot taken at 2.0 µs. The spatial repartition can be observed, and the maximum of stresses is located on the loading axis (about 0.8 GPa). These two snapshots are also the one for which the reflected wave coming back from the upper and lower edges (out from the snapshot windows) can be observed. They come back as tension, because the edges are free and also enable a shock reflection into release wave, which also cross the release wave following the shock. At 2.250 µs (numerically), the tension area propagating backward after the crossing of release meets the 2D effect induced tension area. Consequently, the whole area contained in the last 2 mm of the epoxy thickness is loaded in tension. This corresponds to the observation made at 2.2 µs, where a black blur has spread in the same region. The 2D effects induced tension also results in increasing the tension propagating backward. The tension level jumps from 0.8 GPa to 1.1 GPa.

Nevertheless, some phenomena are missing. Especially, the front face damage and the back face spallation are missing since no damage model has been implemented. The absence of spallation is thus not surprising. The front face damage is particularly non-physic. Indeed, EROSION has to be added to avoid high numerical gradients which create strong mesh deformation and thus lead to calculation crash. EROSION is the name of the additional card to use in order to delete the meshes reaching a certain level of stress or strain. In this case, the “cut off” strain value has been set to 200%. This modeling choice leads to the formation of artificial geometries created by the mesh suppression. The pressure profile spatial repartition could be a reason for strong gradients on the

loaded zone edges, but it is surely not the only problem. Since no damage in compression has been implemented, it is impossible to obtain a realistic front face deformation. Moreover, the residual stresses cannot be estimated because of the model used, which has no plasticity. The damage mechanisms in epoxy under dynamic behavior are still complicated to model with current simulation and there is still room to have a better numerical description of the phenomenon.

1.3 Mapping of the shear stresses

From the previous section, it is possible to conclude that the numerical model chosen is at least well describing the shock propagation and geometries. Therefore, some other data can be taken out from the model. This is the case of the shear stress σ_{ZX}, presented in Figure 4.12, and which could partially explain the phenomenon observed on the ELFIE experiment. It is not the same pressure, the same pulse duration, and the pressure profile, but it is the same material. Moreover, J.-P. Cuq-Lelandais has shown that it was possible to go from one scale to another, the phenomena being homothetic for some aspects [28]. Finally, due to the strong attenuation in both cases (LULI and ELFIE experiments) it is quite possible that the pressure level, after 1 µs, is more or less the same. No quantitative comparison can be made, but at least qualitative. It has been shown thanks to different laser shock experiments using different focus diameters that the equilibrium phenomenon observed by photoelasticimetry was correlated to 2D effects. Indeed, they were located in the shape formed by 2D release wave crossing. If looking to Figure 4.12 first three images, it can be observed that σ_{ZX} initiated at the pressure pulse edges (upper and lower). Their propagation kinematic is quite different from the shock front propagation (visible for example in the snapshot taken at t = 0.750 µs). This fact corresponds to the experimental observation made by time resolved photoelasticimetry. Note also that this shear loading is axi-symmetrical. Indeed, the color inversion from bottom to top is only due to the normal of elements which are changing of direction from one loading axis side to the other. Moreover, the diamond shape can also be observed, beginning with the images respectively taken at time 1.0 µs, 1.25 µs and 1.5 µs. By the way, it is corresponding to the time for which the diamond shape starts to grow on the ELFIE experimental observations. On these three images, a diamond shape under the loaded area can be identified. From t = 1.750 µs, the loaded area in shear continues growing, but another phenomenon seems to force the shear development in this particular shape. It becomes visible on the t = 1.75 µs image, but it is more obvious in t = 2.0 µs and 2.25 µs images. It is the shear induced by the wave reflection on the lateral free edges of the samples, upper and lowers (see in Figure 4.12). It can also be noticed that the level of shear stresses is about a few MPa, which also corresponds to the level of stresses evaluated by photoelasticimetry in case of residual stresses. A comparison between experiment and numerical modeling is given in Figure 4.13. The difference of timing can be explained by the different scales (pulse duration, pressure) as well as the difference in focus diameter. This last parameter can also explain the difference in the shape observed, as non-physic spot edges deformations do.

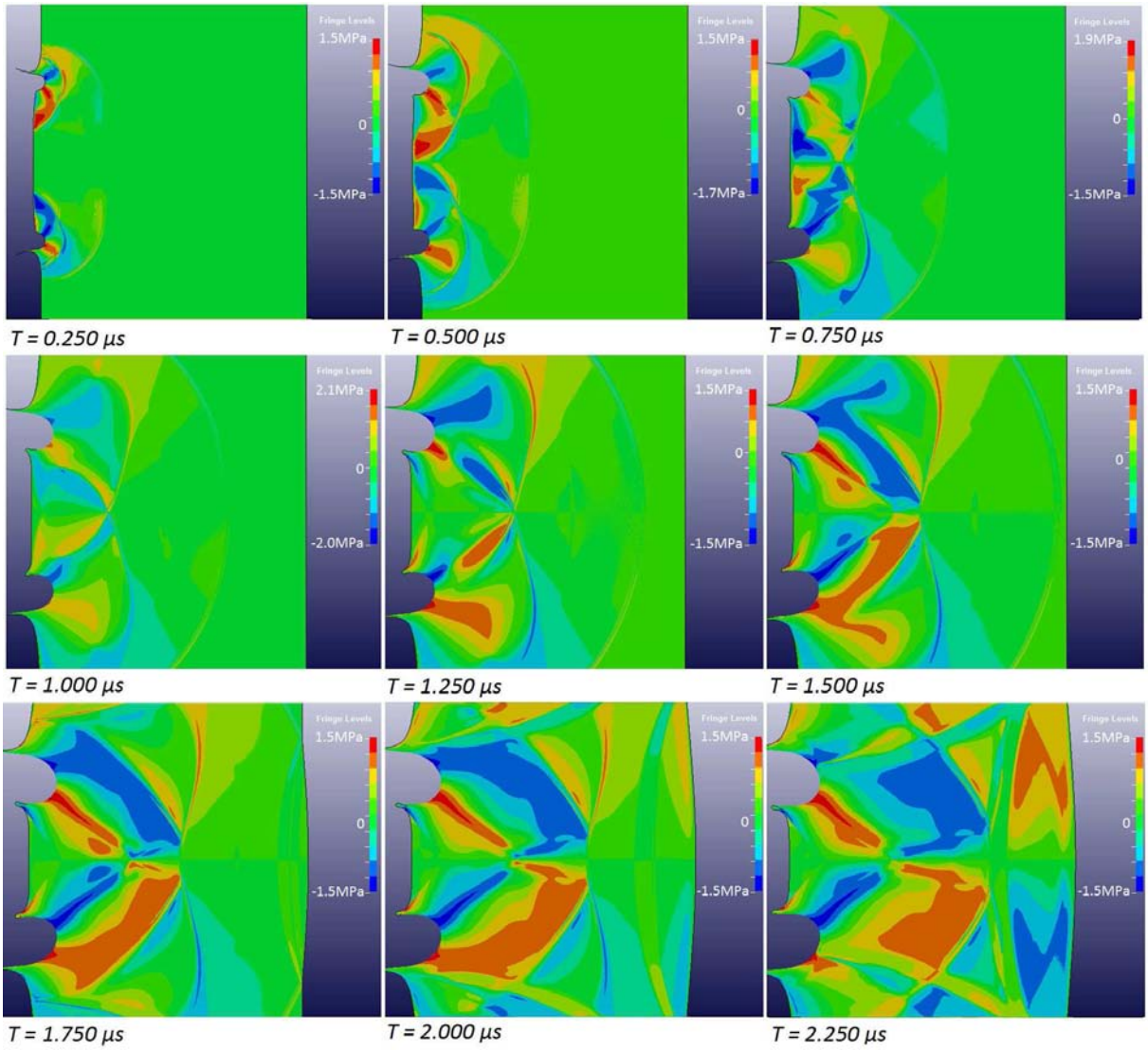

Figure 4.12, Snapshots of the LS-DYNA numerical simulation of the shock wave propagation into an epoxy target 5mm thick induced by intense laser irradiation (94 GPa, 3 ns) – Representation of σ_{ZX} stress (LS-PREPOST, dynamic stress color code)

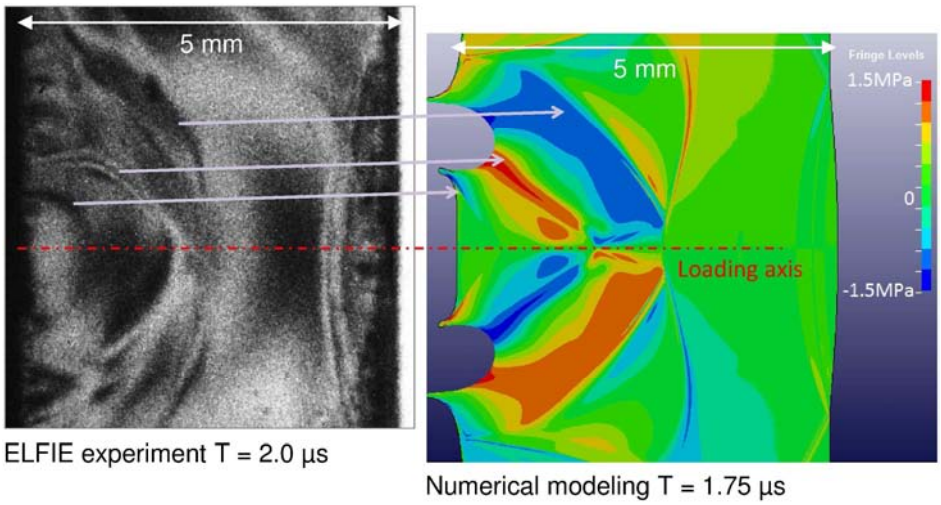

Figure 4.13, Comparison between a ELFIE experiment snapshot and a numerical simulation snapshot showing the σ_{ZX} shear stress

Back to experiments, the photoeleasticimetry setup enables the observation of the difference between the two main stresses σ_1- σ_2 as presented in the 2nd chapter. In this case, and with the axes used, it can be assumed that σ_1 corresponds to σ_{ZZ} and that σ_2 corresponds to σ_{XX}. Depending on the loading, the quantity σ_{ZZ} - σ_{XX} can be used to express the σ_{Zx} stresses. It is thus possible that photoelasticimetry enables the observation of shear stresses in this configuration.

To summarize, the used elastic hydrodynamic model enables a correct description of the shock wave propagation timing and extent pattern within the epoxy sample. Therefore, it can be considered that the model used is reliable enough for the shock phenomenon in epoxy. Cured epoxy resins having more or less the same material properties and sensitivity to strain rate, it can thus be assumed that this elastic hydrodynamic model can be also used for FM300 modeling.

2 Modeling FM300 behavior

In this section, results concerning the modeling of FM300 materials, the adhesive in bonded composite, are given. The idea is to use this model in the bonded composite models developed for numerical optimization investigation. Before that, FM300 model should be validated first by comparing the simulation results to the time resolved experiments obtained thanks to VISAR and presented in Chapter 3, part 2.

2.1 Modeling choice

It has been shown in chapter 3 that the FM300 material tested has an isotropic behavior under laser shock. Therefore, it is not a problem to use a 2D model in this case. It also enables to model the real geometry of the sample (thickness, and width), which is better for a more realistic results on the back face velocity signal. The previous results on epoxy material have shown that it was possible to use elastic hydrodynamic isotropic model to simulate epoxy behavior. In the FM300 case, it should also provide a correct description of the shock wave propagation. Therefore, the same polynomial law used in the previous section has been implemented in the FM300 model. Elastic properties are set to usual values in order to fit the experimental signal, only the initial sound speed has been changed. Indeed, density ρ, "s" parameter and Γ_0 do not change much from an epoxy resin to another. The material properties used for the polynomial law coefficient calculation are given in Table 4.2. In a second time, the maximum pressure of the input pressure curve has been adjusted to fit the velocity amplitude. Indeed, some small variation from the calibration curve has to be taken into account, because of the use of aluminum painting instead of real aluminum coating. This point is detailed in Appendix C. Note that the FM300 sample has been made on purpose by superposing several adhesive films, which can have an effect on the shock wave propagation not reproduced by the model.

ρ (g/cm^3)	c_0 (cm/µs)	s	Γ_0
1.14	0.223	1.493	1.13

Table 4.2, FM300 material properties used for polynomial law coefficient calculation

2.2 Comparison experiment/simulation

The comparison between the experimental back face velocity extracted from VISAR measurements and the numerical back face velocity is given in Figure 4.14. It can be observed that the choice of the initial sound speed enables to obtain a good agreement on the back and forth period. On the

numerical signal (red curve), three different shock breaking-outs can also be observed like in the experiment. The first peak is particularly well described, but the following peaks amplitudes do not match so well the experimental ones. Indeed, the experimental signal is much more attenuated through the FM300 sample thickness than numerical one is. This could be explained by the presence of the polyester fabric. Indeed, this "mesh" is present in each FM300 film constituting the sample. They should act like a filter, breaking the shock front into multiple transmission/reflection phenomena. This is possible that the polyester fabrics considerably attenuate the shock wave. Yet, these fabrics are not included in the FM300 model, so the string attenuation could not be represented. For the bonded application, this is not a so big issue since the LASAT approach often considers the first shock as the one responsible for tension, but that should be kept in mind for the analysis of several shock back and forth. Finally, the 2D effects shape can also be commented. The difference observed in each peak is probably due to the modeling choice of the pressure spatial repartition. In the model, the pressure area edges are sharper than the real ones.

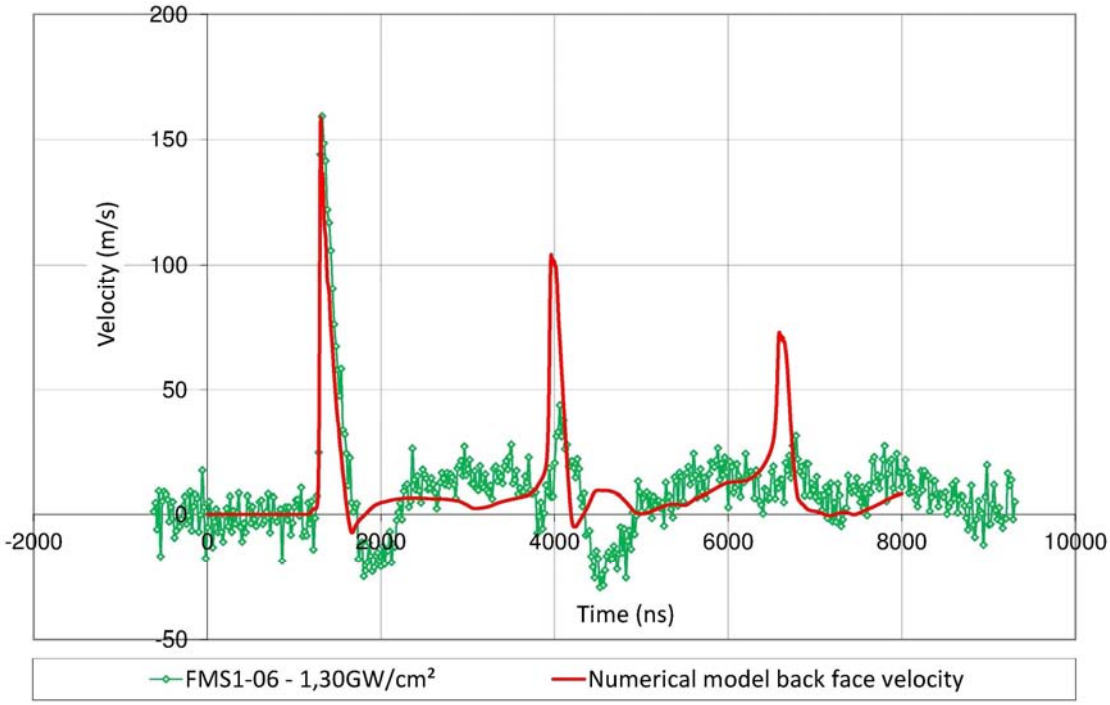

Figure 4.14, Comparison between the back face experimental velocity and the one given by numerical modeling (LS-DYNA)

Part 3: Composites: understanding the model to obtain a correct description of the dynamic behavior

1 Composite model presentation

All the composite models have been built on MAT_022_COMPOSITE_DAMAGE. This includes 2D and 3D models. This material model available in LS-DYNA (LS-PREPOST) has an orthotropic elastic behavior [4-5]. It is thus well adapted to the modeling of one composite ply. This model can be used on quadratic solid elements, well adapted to the shock wave propagation modeling. Note that this material model has its own orientation system. In the model presented, the material repair will always be initially collinear to the global axes system, taking x direction for fiber, y direction for the transverse direction, and z direction for the second transverse direction thus corresponding to the

loading axis. Therefore, the tensile stresses generated by the laser shock wave propagation will always be denominated as σ_{ZZ}. As shown by the literature overview, one of the key point in modeling composite material is to use the correct material parameters, and to understand the meaning of each of these parameters. Concerning, MAT_022, these parameters are given in Table 4.3. For each parameter, two names are given: the one used by LS-PREPOST software in the material card, and the name corresponding to the abbreviations used in this work.

LS-DYNA	Abb.	Parameters	Values	Source
Elastic properties				
RO	ρ	Density	1.58 g/cm^3	(a)
EA	E_{XX}	Tensile modulus in fiber direction x	165 GPa	(a)
EB	E_{YY}	Tensile modulus in the transverse direction y	8.5 GPa	(b)
EC	E_{ZZ}	Tensile modulus in the transverse direction z	8.5 GPa	(b)
PRBA	ν_{YX}	Poisson coefficient yx	0.02	(c)
PRCA	ν_{ZX}	Poisson coefficient zx	0.03	(c)
PRCB	ν_{ZY}	Poisson coefficient zy	0.035	(c)
GAB	G_{XY}	Shear modulus in xy plane	4.2 GPa	(b)
GBC	G_{YZ}	Shear modulus in yz plane	2.7 GPa	(b)
GCA	G_{ZX}	Shear modulus in zx plane	4.2 GPa	(b)
Damage parameters				
SC	σ_S	Interlaminar shear strength (0°)	110 MPa	(a)
XT	$\sigma_{T,f}$	Tensile strength in the fiber direction (0°)	2800 MPa	(a)
YT	$\sigma_{T,m}$	Tensile strength in the transverse direction (matrix)	110 MPa	(b)
YC	$\sigma_{C,m}$	Compressive strength in the transverse direction (matrix)	200 MPa	(b)
SN	$\sigma_{T,i}$	Tensile strength in the direction normal to elements/ Interlaminar tensile strength	110 MPa	(b)
SYZ	$\sigma_{S,YZ}$	Shear strength in the YZ plane	110 MPa	(b)
SZX	$\sigma_{S,ZX}$	Shear strength in the ZX plane	110 MPa	(b)

Table 4.3, T800/M21 orthotropic ply quasi-static properties (elastic and damage parameters) from different sources; Airbus data sheet (a), literature [2-3] (b) and calculated from literature (c)

The values used in first step are given in the table, as well as the source from which they are coming from. It is important to notice that these parameters are quasi-static, and taken at room temperature. The strain rate effect will be discussed in section 3. Note also that due to the modeling choice, some damage parameters are redundant. These damage parameters are used to initiate damage in the composite model thanks to four different criteria as described by Chang/Chang [3-6]. These criteria are given from equation (4.1) to equation (4.4). As explained before, no damage propagation model is particularly implemented. When one the criterion is met, the corresponding elastic property is set to 0. The “propagation” goes from an integration point to another due to average stress increase in one element. Note that in case of laser shock, the most important criterion is $e_{T,m}$, described in equation (4.3). Indeed, contrary to ballistic impact for which perforation is often observed, the damage induced by laser shock is generally matrix cracking, due to spallation. This is especially true on the first microsecond after impact. The other criteria also play a role, but later in the damage propagation, and close to time generally not simulated.

Tensile failure, fiber direction:
$$e^2{}_{T,f} = \left(\frac{\sigma_{XX}}{XT}\right)^2 + \left(\frac{\tau_{XY}}{SC}\right)^2 - 1 \quad \begin{cases} \geq 0 \ failure \\ < 0 \ elastic \end{cases} \tag{4.1}$$

Compressive failure, fiber direction:
$$e^2{}_{C,f} = \left(\frac{\sigma_{XX}}{XC}\right)^2 - 1 \quad \begin{cases} \geq 0 \ failure \\ < 0 \ elastic \end{cases} \tag{4.2}$$

Tensile failure, matrix direction:
$$e^2{}_{T,m} = \left(\frac{\sigma_{ZZ}}{YT}\right)^2 + \left(\frac{\tau_{XY}}{SC}\right)^2 - 1 \quad \begin{cases} \geq 0 \ failure \\ < 0 \ elastic \end{cases} \tag{4.3}$$

Compressive failure, matrix direction:
$$e^2{}_{C,m} = \left(\frac{\sigma_{ZZ}}{2SC}\right)^2 + \frac{\sigma_{ZZ}}{YC}\left(\frac{YC^2}{4SC^2} - 1\right) + \left(\frac{\tau_{XY}}{SC}\right)^2 - 1 \quad \begin{cases} \geq 0 \ failure \\ < 0 \ elastic \end{cases} \tag{4.4}$$

Interfaces have also been modeled by using a specific LS-DYNA law, well adapted to composite material (AUTOMATIC_SURFACE_TO_SURFACE_TIEBREAK). This interface law, noted TIEBREAK in the following sections, enables to initially put the ply in contact, and includes damage parameters. In fact, there are several available damage laws, several being cohesive. Nevertheless, these laws have not been used because some problems were met by adapting these laws to dynamics in this work. Especially, the compressive response of cohesive laws, or cohesive elements, was introducing too much perturbation in the shock propagation, and leads to non-physic attenuation or shock diffusion. As explained in the literature overview section, the main point is to initiate damage. The damage propagation is not numerically deeply investigated in this work. Nevertheless, the closest law to cohesive behavior has been chosen (OPTION 6). This law uses a unique failure criterion, taking into account two damage parameters respectively in tension and shear. The directions are defined regarding the normal to the interface. The parameters are given in Table 4.4, and the damage criterion is described in equation 4.5. Once the criterion is reached, the interface strength is progressively decreased. A parameter, called PARAM, provides the slope of this progressive interface damage (see in Figure 4.15). Physically, it should correspond to the interlaminar crack maximum size for which the interface is considered to be fully opened.

LS-DYNA	Abb.	Parameters
FS	fs	Static friction coefficient
FD	fd	Dynamic friction coefficient
SFS	K_s	Contact stiffness, slave part
SFM	K_m	Contact stiffness, master part
NFLS	σ_N	Interlaminar tensile strength
SFLS	σ_S	Interlaminar shear strength
PARAM		Maximum distance between the two surfaces, quantifying the full opening of the interface

Table 4.4, Main parameters of the contact card used to model interply (AUTOMATIC_SURFACE_TO_SURFACE_TIEBREAK, option 6)

$$\left(\frac{|\sigma_n|}{NFLS}\right)^2+\left(\frac{|\sigma_s|}{SFLS}\right)^2\geq 1 \qquad \begin{cases}\sigma_n : \text{Tensile stress}\\ \sigma_s : \text{Shear stress}\end{cases} \tag{4.5}$$

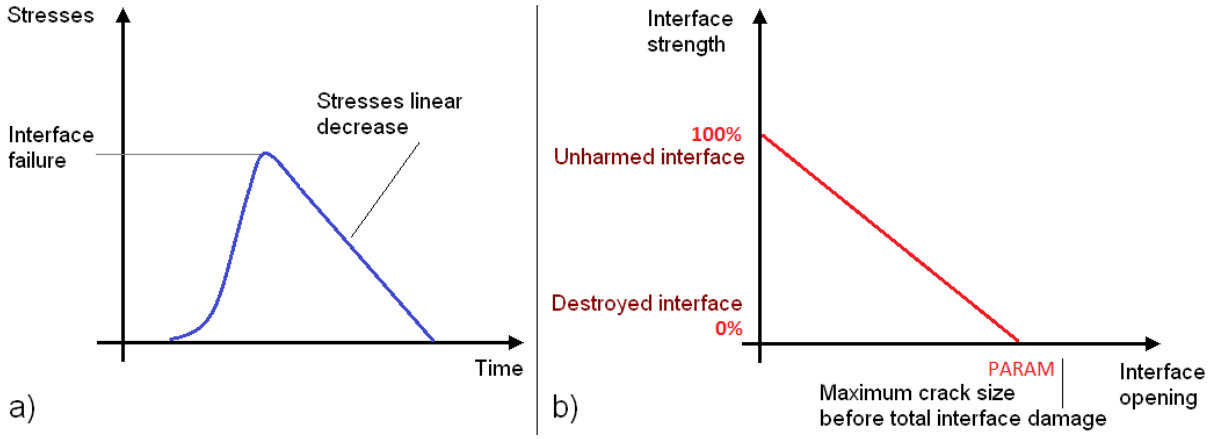

Figure 4.15, Principle of the damage propagation in the interfaces

Finally, it should be mentioned that the contact interface is a penalty contact law, as described by equation 4.6. Therefore, it presents contact stiffness, named Kc, for both interface sizes. These parameters are important because it will enable to numerically play on the interface smoothing, in order to highlight the interface influence in shocks propagation especially on the transmission/reflection of the shock.

$$f_s = K_c.\delta \qquad \begin{cases} fs : \text{Contact force}\\ Kc : \text{Contact stiffness}\\ \delta : \text{Penetration}\end{cases} \tag{4.6}$$

To sum up, a view of the axi-symmetric 3D model used in case of a two plies thick unidirectional composite is given in Figure 4.16.

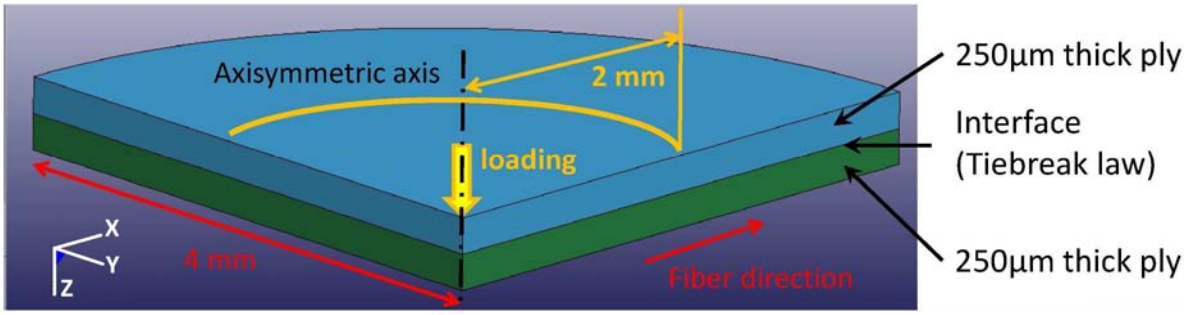

Figure 4.16, 3D model

2 Parametric studies on the composite models

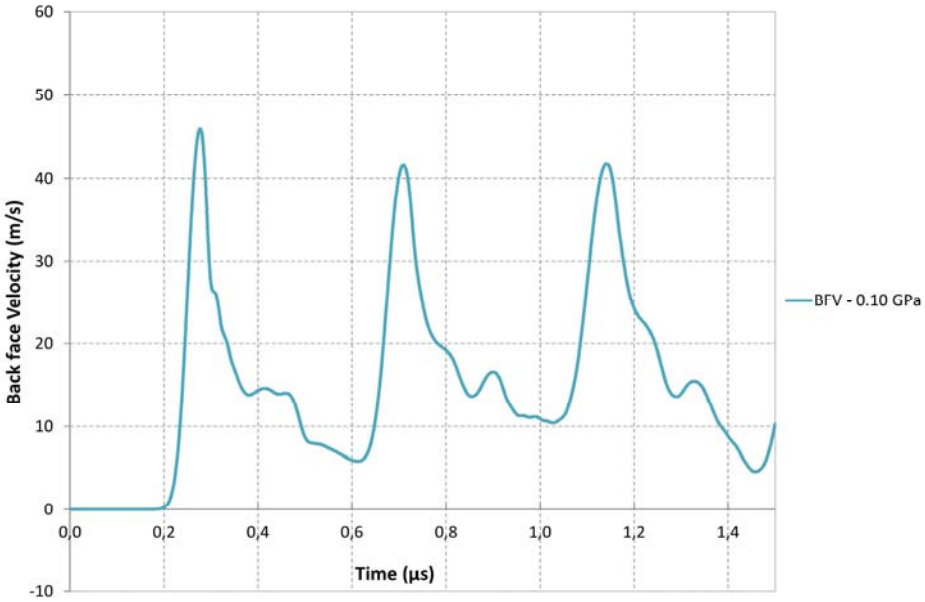

Figure 4.17, Typical back face velocity signal obtained from LS-DYNA numerical calculation, in case of a 3D model of a unidirectional T800/M21 composite CFRP (2 plies, 500 µm thick)

The numerical model presented in Figure 4.16 has been used in several parametric studies in order to understand the influence of each parameter on the composite shock response. Especially, damage behavior, interface influence, anisotropy effects, change in elastic properties and sample thickness influence on dynamic response are investigated. For these reasons, a 3D model has been developed. As shown in Figure 4.16, only one quarter has been modeled thanks to the symmetrical planes which can be defined in case of unidirectional CFRP. Nevertheless, it has to be kept in mind that this choice could induce few changes on 2D effects influence. Note also that this model is a two plies model. This choice has been made to model only one interface and thus enables a clear separation between interface effect, and anisotropic effects. Contrary to previous works, the interface thickness in itself is not modeled. There are two main reasons for that. Firstly, the interply thickness is not constant through the sample width, especially in presence of thermoplastic nodules. This has an influence on the composite response which could not be easily modeled anyway. Secondly, the literature overview in the 1st chapter evidenced that the shock response of CFRP in the transverse direction was more or less the same than the epoxy content. Therefore, the interplies should not induce strong impedance mismatch. If there is some, it is only due to the absence of fibers, and the concentration of thermoplastic nodules (which is also not homogeneous by the way). The elasticity brought by the thermoplastic nodules can be numerically represented by the contact stiffness. The other parameters, especially concerning the pressure profile are as described in the first section of this part, except that the spatial smoothing on the edge is more important here due to meshing choice. The linear decrease is made on 0.2 mm instead of 0.09 mm. The calculated back face velocity is recorded thanks to a time history set on the axisymmetric propagation axis. The back face velocity signals presented in this section always comes from the numerical sample back face, like a VISAR. An example is given in Figure 4.17 for a shock pressure of 0.1 GPa. The shock pressure corresponds to the pressure maximum value reached by the pressure profile. On this velocity profile, 3 shock breaking-outs can be observed. The same “bump” on the release path than the one experimentally observed is visible. The signal is explained in the following sections.

2.1 Pressure load parametric study

The first parametric study is the one describing the pressure influence on the numerical model response. Especially, the damage criteria activation is studied, for both composite material model and interface model. For that, the interface interlaminar strength has been reduced on purpose 10% lower than the composite strength (meaning 100 MPa in tension and shear). It could physically represent the weakening effect induced by the curing process, the absence of fibers, or the stress concentration generated by thermoplastic nodules. On this model, several calculations have been performed, each time by increasing the pressure. The corresponding calculated back face velocities (BFV) are presented in Figure 4.18, where the lowest pressure signal corresponds to the one shown in Figure 4.17.

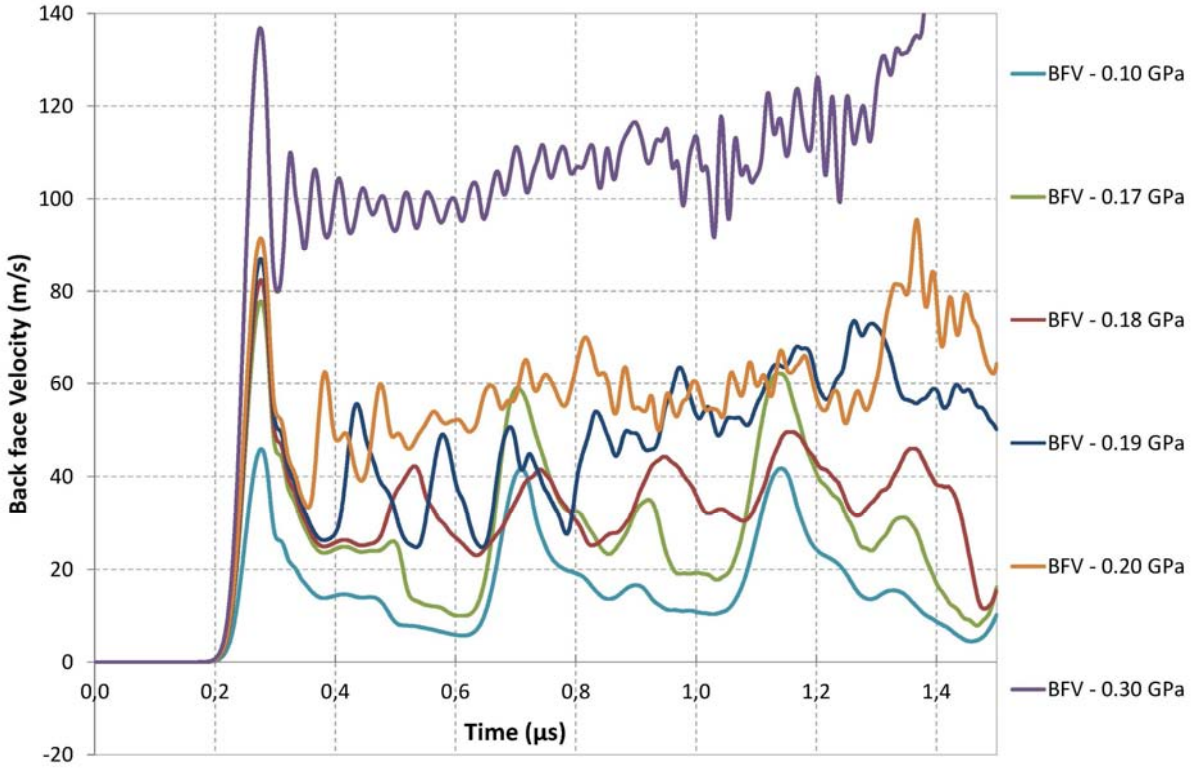

Figure 4.18, parametric study on the maximum pressure influence on the back face velocity signals simulated with a 3D model of a unidirectional T800/M21 composite CFRP (2 plies, 500 µm thick) – Observation of a progressive damage with the pressure increase

Logically, the maximum free surface velocity amplitude is directly correlated to the pressure level by a linear law. This is due to the elastic behavior of the model. The initiation of numerical damage is the point of interest. In Figure 4.18, in spite of some differences on the second order phenomena, the signals BFV-0.10 GPa and BFV-0.17 GPa are a clear sign of an absence of damage, on the observed time period. The three successive shock breaking-outs are visible. The back face velocity signal becomes significantly different starting with the numerical calculation run at 0.18 GPa. Indeed, after the first release slope, the frequency of the signal is clearly changing. In this case, a failure of the interface under the impacted region has been observed. This is traduced by the free surface velocity curve. Indeed, the new frequency corresponds to the shock back and forth period in the last composite ply. This damage has been numerically possible because of the difference in strength value between the interface and the composite. The tensile stresses generated by the reflection of the shock front on the free surface were not high enough to damage the composite, but not low

enough to let the interface unharmed. This observation is consistent with the shock wave theory, but has not been experimentally evidenced. This is clearly due to the experimental uncertainties on both laser intensity induced pressure and material variations. In numerical simulations, when increasing the pressure (0.19, 0.20, 0.30 GPa), the composite part of the model is progressively more and more destroyed. It can be observed thanks to the time separating the release slope to the following velocity bouncing back on the spallation signal. The higher the pressure, the sooner the spallation as the composite depth from the back face is concerned. The first damage criterion to be activated in all the cases is the tension in matrix one, which corresponds to shock theory, and the experimental observations made. This initiation progressively leads to delamination, even if its characteristics could not be really deduced from the model for the previously given reasons. The other criteria are also activated, after the initiation in matrix, and also propagate. The corresponding damage growth is statistically much less numerous than the one corresponding to the damage cracking. Finally, it can be noticed that in spite the modeling choice made on the damage propagation, the spallation signals are consistent with theory during 1 µs. Indeed, a constant ejection velocity can be observed. After this delay, the back face velocity starts do increase again which is probably due to the absence of elastic properties in the broken meshes. The broken material does not resist to ejection as it has been experimentally evidenced.

2.2 Influence of the interface stiffness

In a second time, the influence of the contact stiffness is investigated. Elasticity of the interface can be modified by changing the contact stiffness. Practically, it changes the transmission/reflection induced by the interface between the two composite plies. In this study, the input pressure has been kept constant and below the numerical damage threshold of both composite and interface for all the calculations performed. Only the contact stiffness of both interface planes has been varied. It is classically used between 0 and 1, 0 defining a perfectly smooth interface, and 1 defining a stiff interface. Here, it has been varied from 0.2 to 3.0, and a perfectly tied interface has also been modeled for comparison. The results are presented in Figure 4.19. The influence of the interface modeling is located in the velocity bump observed after the release slope of the main peak. Indeed, no difference has been noticed in the main peak itself. It appears that this velocity bump (see in Figure 4.19) is in fact composed of two bumps. The interface model seems to play on the second. A smooth interface results in a strong bouncing phenomenon, when a stiff interface almost removes this bouncing. This last observation has been confirmed by the tied interface calculation for which no bouncing can be observed. From one point of view, this result is consistent with the previous work since the interface does influence the velocity bouncing after the release slope. To sum up, if 2 identical materials are perfectly TIED, the interface behaves perfectly, and no impedance mismatch thus influences the shock propagation. If adding smoothing to the interface by changing the stiffness values, numerical impedance mismatch is added. This numerical phenomenon can be used if necessary to represent the effect of thermoplastic nodules. The interface effects are not the only phenomena in stake since a perfect interface also presents a bouncing. This could be explained by the composite anisotropy, as shown in the following section.

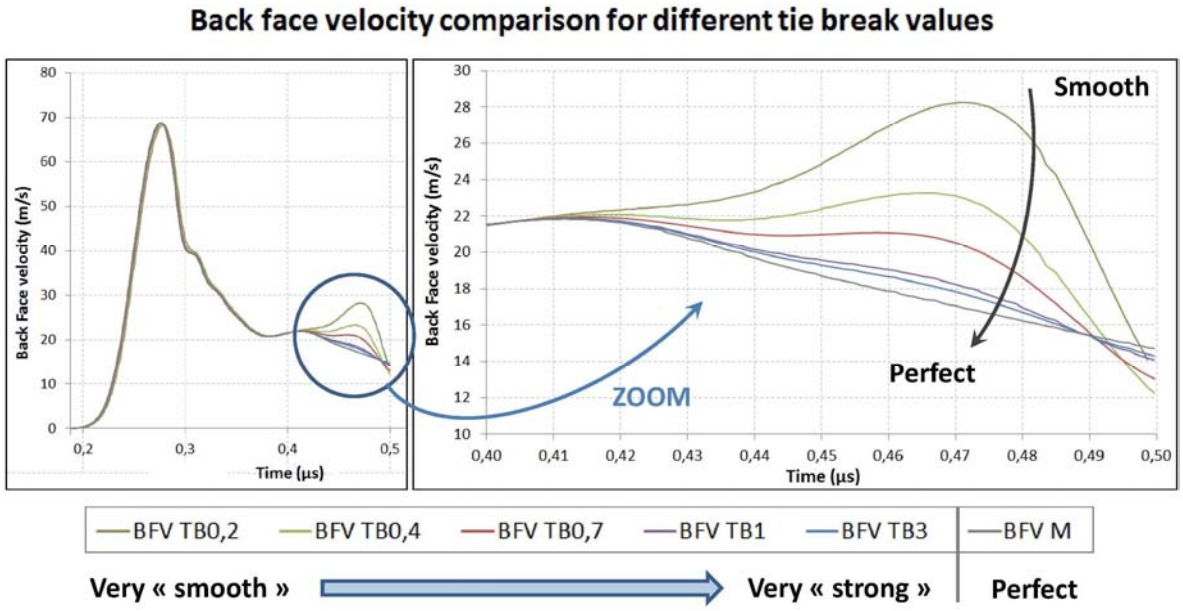

Figure 4.19, Influence of the contact numerical stiffness values on the calculated back face velocity signal, from very smooth to perfect contact at interply – Evidence of an interface bouncing – Unidirectional of two T800/M21 2 plies

2.3 Anisotropic effect on the back face velocity

The velocity seems to be made of two components, one being due to the interface, as previously explained. These two bouncing are shown in Figure 4.20, where the calculated back face velocity has been obtained with a stiffness value of 0.7.

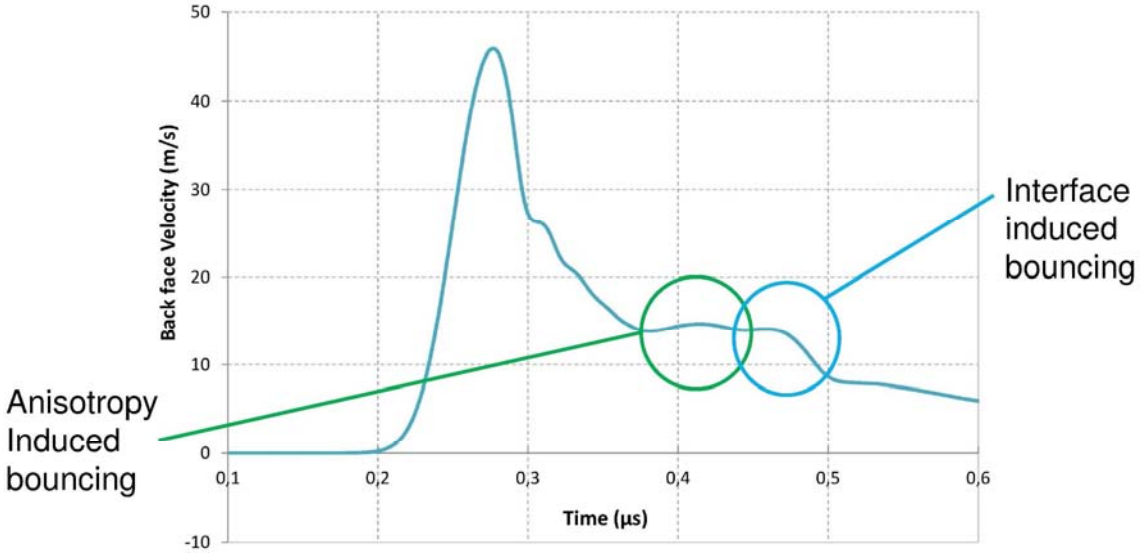

Figure 4.20, Back face velocity signal main peak, with the separation of the anisotropic bouncing and the interface bouncing for a two unidirectional plies of T800/M21 calculation

In order to analyze the anisotropy effect, the σ_{XX} stresses have been observed on both front and back face, because they represent the bending elastic response of the fibers (see in Figure 4.21). The bending response is in fact also correlated to 2D effects. Indeed, between the loaded and unloaded zones, a phenomenon of compression/tension is induced by the local character of the loading. It is visible on the front face snapshot, at t = 0.2 µs, in which compression is in blue and tension in red. This separation traducing a mechanical equilibrium can be justified by the loading geometry, as

shown by the sketch in Figure 4.21. The two loaded regions are propagating, toward the loading axis and the sample edges for compression and tension respectively. Due to anisotropy, this phenomenon mainly propagates in the X direction, but also through the thickness. Indeed, after a while, the symmetric loading can be observed on the sample back face. Once there, the information propagates also in the X direction, tension toward the loading axis and compression toward the edges because of the symmetry (see the sketch and the back face snapshots in Figure 4.21). The high fiber direction modulus Ex has two consequences. The first one is that the elastic propagation of the 2D bending effect is fast. The maximum of tension reaches the loading axis at about 0.4 µs. The second is stresses concentration effect. Indeed, the red area observed on the last back face snapshot is about 0.2 GPa in tension, when the initial pressure load was about 0.1 GPa. These two effects are responsible for the velocity bouncing on the free surface velocity release slope. Indeed, it can be observed in Figure 4.20 that change in curvature occurs a bit before 0.4 µs, which corresponds to the timing for which the tension induced by the 2D bending effects reaches the loading axis.

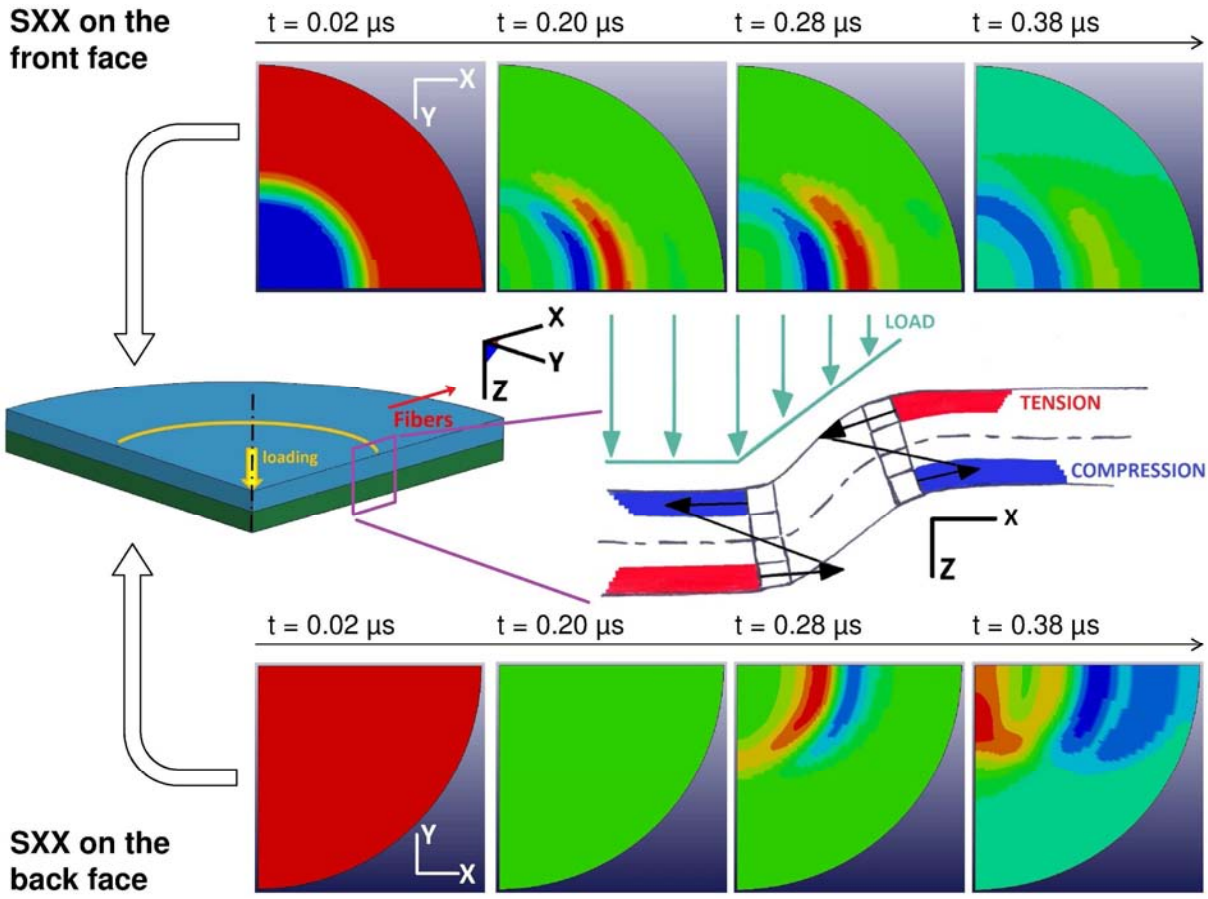

Figure 4.21, Evidence of the existing correlation between the bending elastic response of the composite fibers and the anisotropic bouncing observed on back face velocity - two unidirectional plies of T800/M21 calculation

It should be understood that this 2D effects is not only due to strong anisotropy. Indeed, in case of a low Ex (taken equal to Ez), the phenomenon is also visible in Figure 4.22. Nevertheless, it can be observed in this case that the timing is not the same at all. The tension and compression area do not propagate as fast as the previous case, and for that reason, the tension is far from the loading axis at t = 0.4 µs. It will be reached much later. Consequently, it is not creating stress concentration, and does not lead to a modification of the back face velocity signal, at least with the same timing.

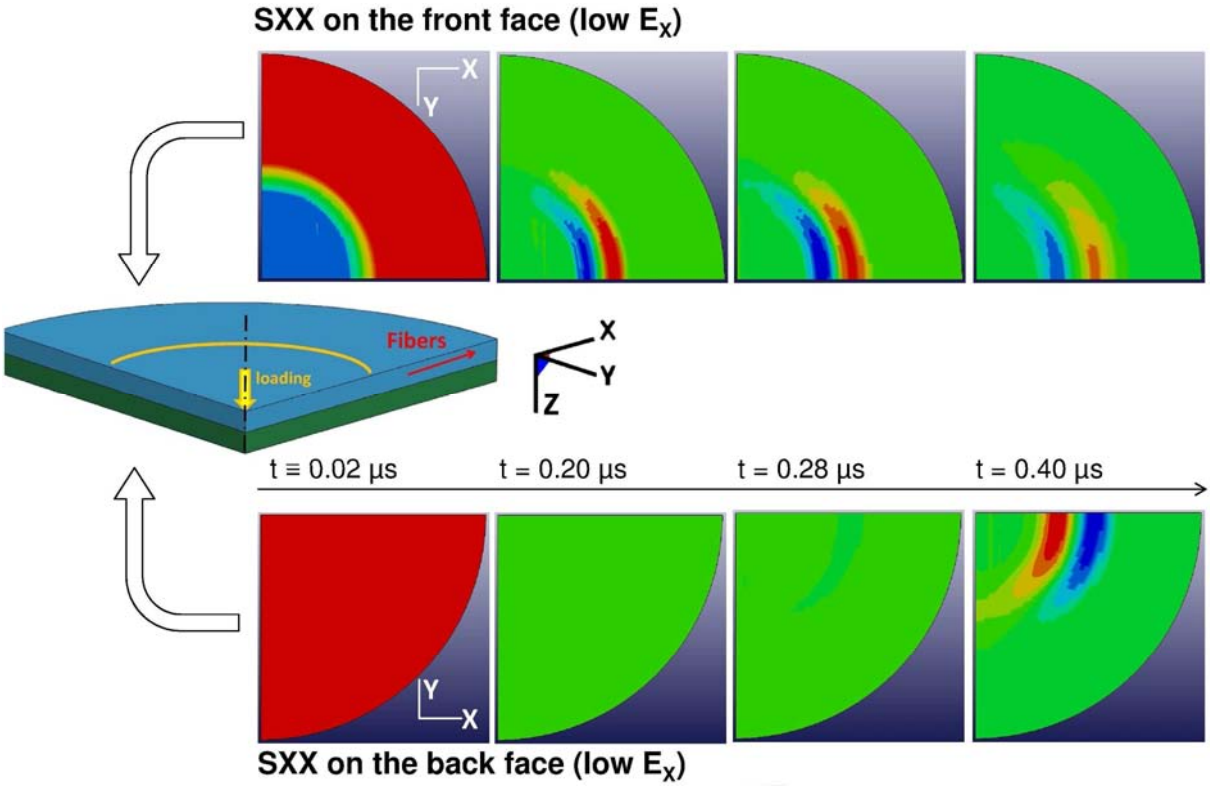

Figure 4.22, Same observation than the one presented in Figure 4.21 in case of a degraded fiber direction modulus showing the timing mismatch with the bending response - two unidirectional plies of T800/M21 calculation

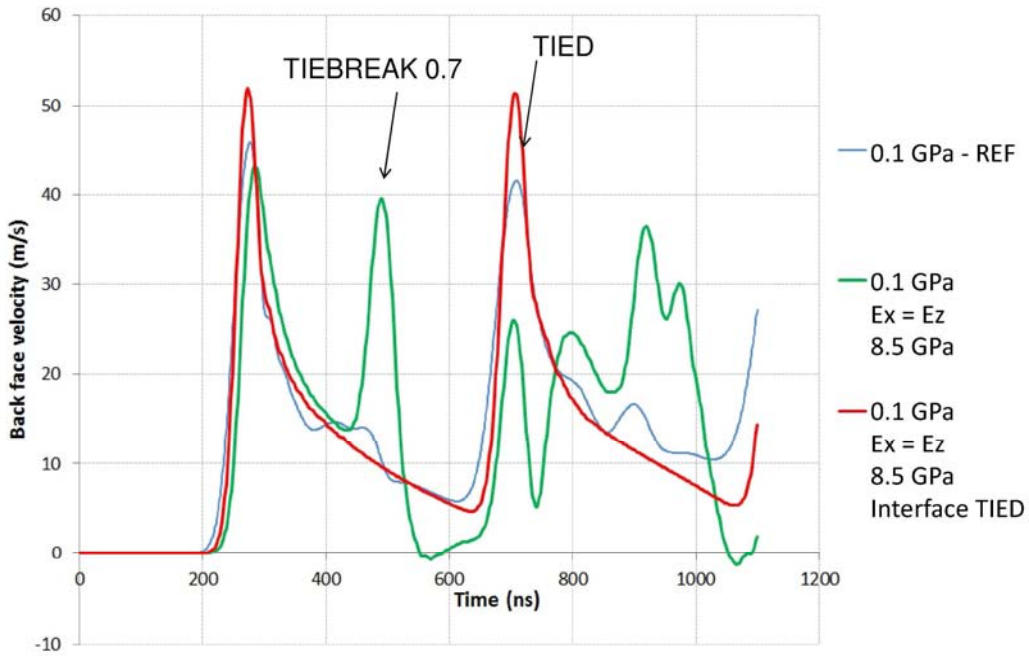

Figure 4.23, Comparison of the calculated back face velocity signals in case of degraded fiber direction modulus, in two different interface conditions - two unidirectional plies of T800/M21 calculation

The final proof concerning this investigation is given in Figure 4.23. If looking first to the blue and red curves, the difference on the back face velocity signal is shown. The red curve has been calculated in case of a perfect interface to remove the interface effect on the velocity signal. It represents the velocity obtained in the case of a degraded fiber modulus, at the same level of transverse modulus. The strong anisotropy is thus removed, and no bouncing can be observed anymore. The comparison

with the first initial modeling shows that the strong anisotropy is responsible for this bouncing. The green curve is resulting from the same modeling (low fiber modulus), but with a tiebreak interface set at 0.7. It shows this time a strong bouncing, therefore clearly attributed to the interface, and not physic at all. It can be deduced that strong anisotropy has in fact two main effects, one being physic and the other numerical. Firstly, it is responsible for a velocity bouncing due to a tensile stress concentration in the fiber direction and initiated by a 2D effects bending phenomenon. Secondly, it attenuates the interface effects on the back face velocity, avoiding a too important bouncing in case of TIEBREAK interfaces.

2.4 Analysis of the shock propagation along X, Y and Z directions

In this section, the first use of the developed Matlab code as a shock wave propagation observation tool is presented. It has been used to track the stresses propagation through several directions, depending on the point of interest. Indeed, the code relies on the data gathered thanks to two time history sets, one grouping the nodes and therefore giving information such as position, or velocity and the second one grouping the elements, and thus recording stresses. Of course, there is a link between the set of nodes and the set of elements because each node is associated to its corresponding element. The sets can be chosen depending on the direction of interest. A first example is given in Figure 4.24. In this example, the chosen direction is z direction, meaning the 0.5 mm numerical sample thickness. The Time/Position diagram obtained thus represents the shock wave propagation through the sample thickness, along the axisymmetric propagation axis more precisely. Position is reported on the horizontal axis, and time is referred on the vertical axis. The stress level is given thanks to a color code indicated to the diagram right. In the example presented in Figure 4.24, the represented stresses are σ_{ZZ}, going from compression (in blue) to tension (in red). The shock waves back and forth are visible. Moreover, the stresses can be quantified. Especially, in this case it can be observed that the attenuation is not really important. This is due to the small sample thickness.

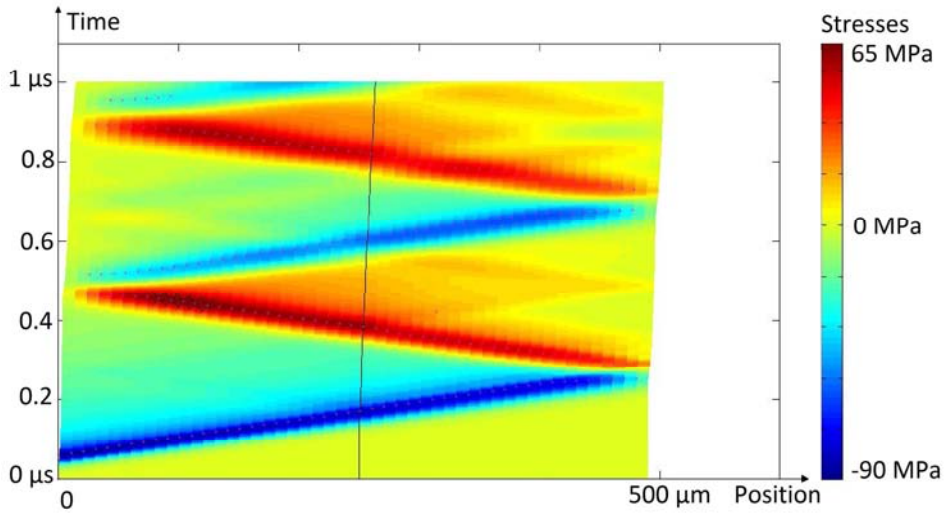

Figure 4.24, Time/position diagram along the z direction (composite thickness), in case of a 0.1 GPa laser shock – Representation of σ_{ZZ}, compression in blue, tension in red - two unidirectional plies of T800/M21 calculation

In a second time, the σ_{ZZ} stresses propagation in the two x and y directions can be represented. It is shown in Figure 4.25, for two different depth values (z = 130 µm and z = 380 µm). It can be observed that the propagation diagrams in x and in y are quite close for the two depths. Especially, the σ_{ZZ} stresses do not really propagate in the fibers and transverse direction, but remain concentrated

under the loading. This indicates that the propagation of σ_{zz} is in fact mainly isotropic under the loading area on the first µs propagation. This is consistent with the hypothesis of an isotropic damage initiation, based on σ_{zz} tension, under the loading area. Note that the small mismatches in the wave pattern visible in Figure 4.25 (and 4.26), are only due to mesh size variation because of modeling choice.

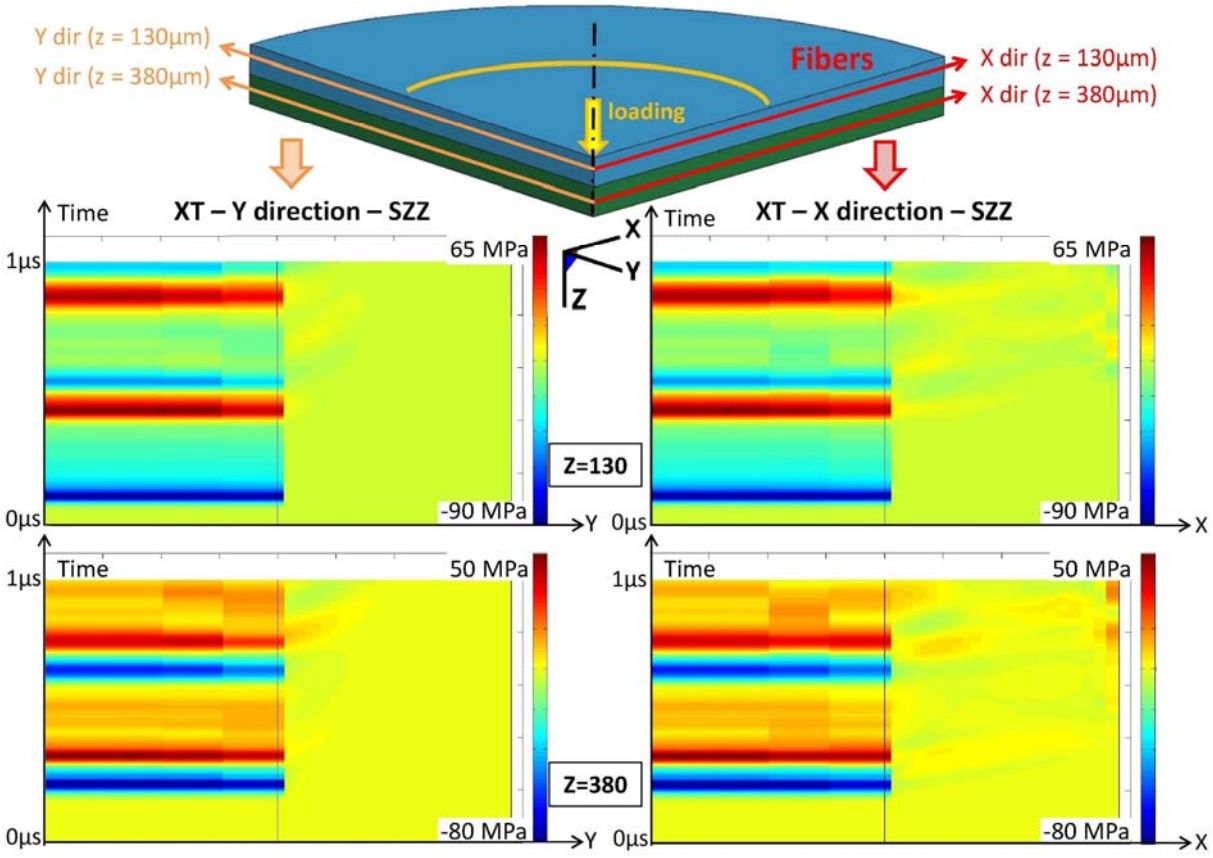

Figure 4.25, Time/position diagrams at two different sample depths (130 µm, 380 µm) along the x and the y directions (respectively fiber direction, and transverse direction), in case of a 0.1 GPa laser shock on two unidirectional plies T800/M21 material – Representation of σ_{zz}, compression in blue, tension in red

If keeping the same axes but now plotting the σ_{xx} stresses, the material anisotropy effects are visible as shown in Figure 4.26. Indeed, these stresses do not propagate in the y direction, when they do in the x direction. This observation is in good agreement with all the previous observations and conclusions.

Same kind of diagram has been plotted with σ_{yy} stresses. No clear difference between one direction and the other has been observed, and the level of these stresses was significantly lower outside of the loading zone. The three different shear directions have been plotted and the stresses quantified. The level of shear in the sample is below 10% of the main stresses in the whole sample thickness. It thus could be neglected in a first approach.

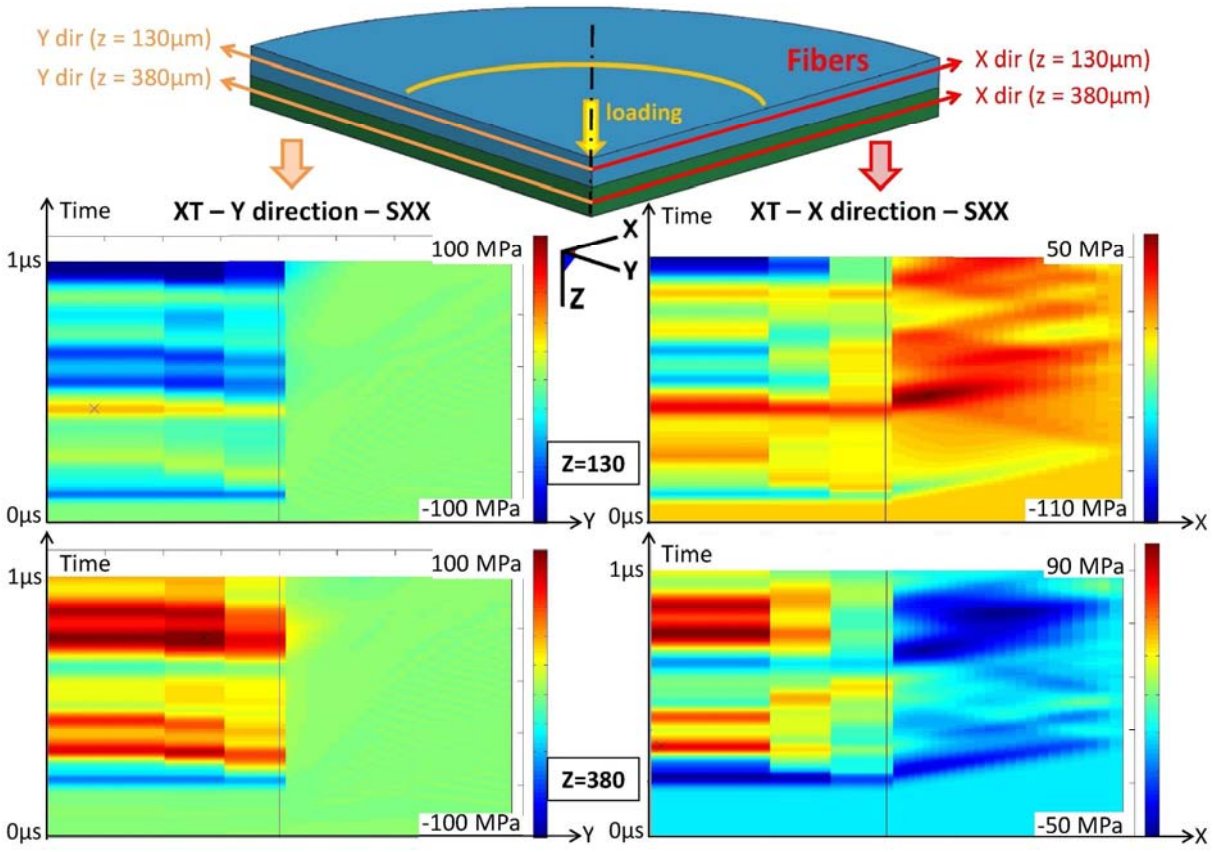

Figure 4.26, Time/position diagrams at two different sample depths (130 µm, 380 µm) along the x and the y directions (respectively fiber direction, and transverse direction), in case of a 0.1 GPa laser shock on two unidirectional T800/M21 plies material – Representation of σ_{xx}, compression in blue, tension in red

2.5 Parametric study on the material elastic parameters

In order to see the influence of the material elastic properties on the back face velocity signal, several calculations have been run. It is an important preliminary step to the correct fitting of experimental signal by the numerical modeling. For each simulation, only one parameter has been moved, and the pressure is kept constant during the whole investigation. Only the Young modulus influence has been investigated. Indeed, it is known from the literature overview that these parameters could have a strong influence on the shock response, and therefore on the free surface velocity. Moreover, the previous studies have shown that shear was not really important, at least on the phenomenon early stages. Therefore, it is not really necessary to investigate the shear modulus influence.

The first parametric study concerns the influence of the fibers modulus, Ex. The results for three different fibers modulus values are presented in Figure 4.27. It can be observed that this modulus does not have a strong influence on the back face velocity signal, but has some anyway. It is normal that this parameter does not influence the first order peaks timing since the waves mainly propagate in the transverse direction. Nevertheless, the fibers modulus plays on the anisotropy bouncing timing. This could have been expected regarding the results presented in the previous sections. Indeed, the higher the fiber modulus is, the faster the x stresses would be back on the shock propagation axis (see previous section). The fibers modulus variation also modifies the free surface velocity amplitude correlated to the first shock breaking-out. The higher the fibers modulus, the lower the velocity amplitude. Note that the Ex modulus should be quite high to induce significant changes. In figure 4.27, the difference are really visible for a modulus 10 times higher than the initial

value (green curve), when a modulus only twice greater than the initial value slightly changes the global shape of the signal.

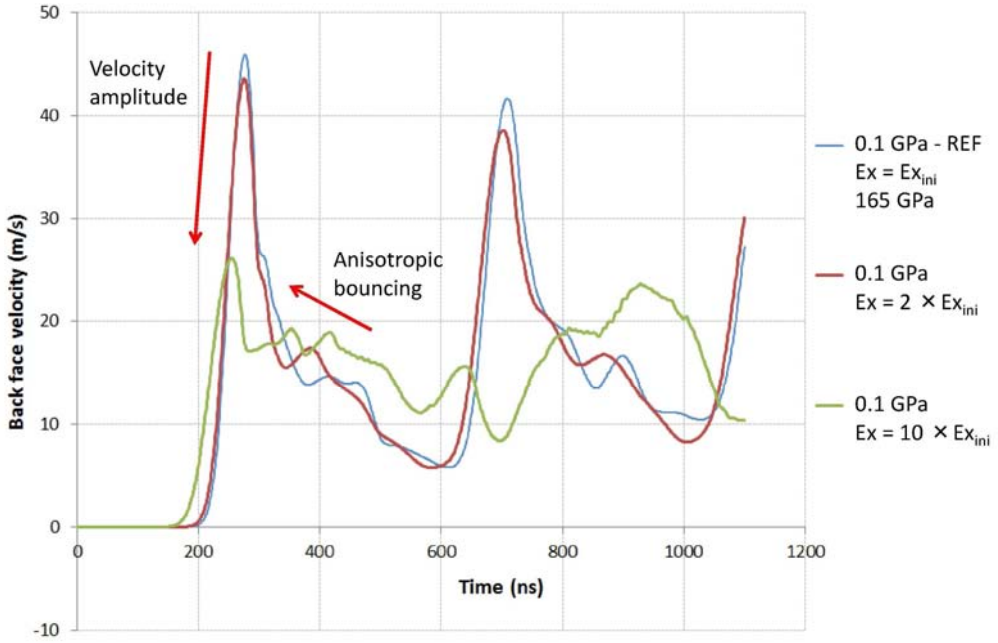

Figure 4.27, Comparison of the calculated back face velocity in case of different fiber direction modulus values (Ex) – Influence on the signal for a two unidirectional T800/M21 plies material

Next step is to analyze the effect of the transverse modulus on the back face velocity signal. The same variations on the transverse modulus Ez than the ones used for Ex have been applied to the material model, and the results are presented in Figure 4.28. Note that Ey has been moved identically to Ez, for more consistency. At a first look, it can be observed that this elastic parameter has much more influence on the back face velocity than the Ex modulus. Indeed, a multiplication by 2 of the Ez modulus already induces sizeable modification on the shock response. Especially, the shock back and forth period is shorter as well as the back face velocity amplitude. It is not surprising that this parameter has more influence than the Ex modulus. It is directly correlated to the transverse sound speed considering an acoustic approach giving the sound speed as the square root of ratio modulus over density. When the transverse modulus value is increased, the material sound speed is increased, and the shock waves are faster to go from one sample side to the other. Concerning the free surface velocity amplitude, the increase in the material stiffness is a possible explanation. This transverse modulus parameter seems to be the key one to modify in order to adapt the numerical model to the laser shock experiments. It is also possible to modify both parameters to obtain a more comparable shape to the experimental signals. This is presented in Figure 4.29. The numerical back face velocity presented there presents a modification of both Ex and Ez values of two times there initial value. The idea is to compare the global free surface velocity shape to the experimental one. For that, the two signals (numerical and experimental) have been plotted against dimensionless parameters. The time is replaced by the time divided by the shock back and forth period variable, and the free surface velocity is divided by the maximum velocity amplitude. It can be observed that the numerical calculation is really close, as the shape is concerned, from the experimental composite response. It leads to double conclusions. Firstly, the composite material model provides a correct description of the composite laser shock response. Secondly, changing the elastic parameters enables to get a better agreement between the numerical calculations and the experimental measurements, in case of a dimensionless representation. These parameters are the one to change

to obtain a good fitting between calculation and experiments, which agree with the strain rate effect on elastic properties reported in the literature.

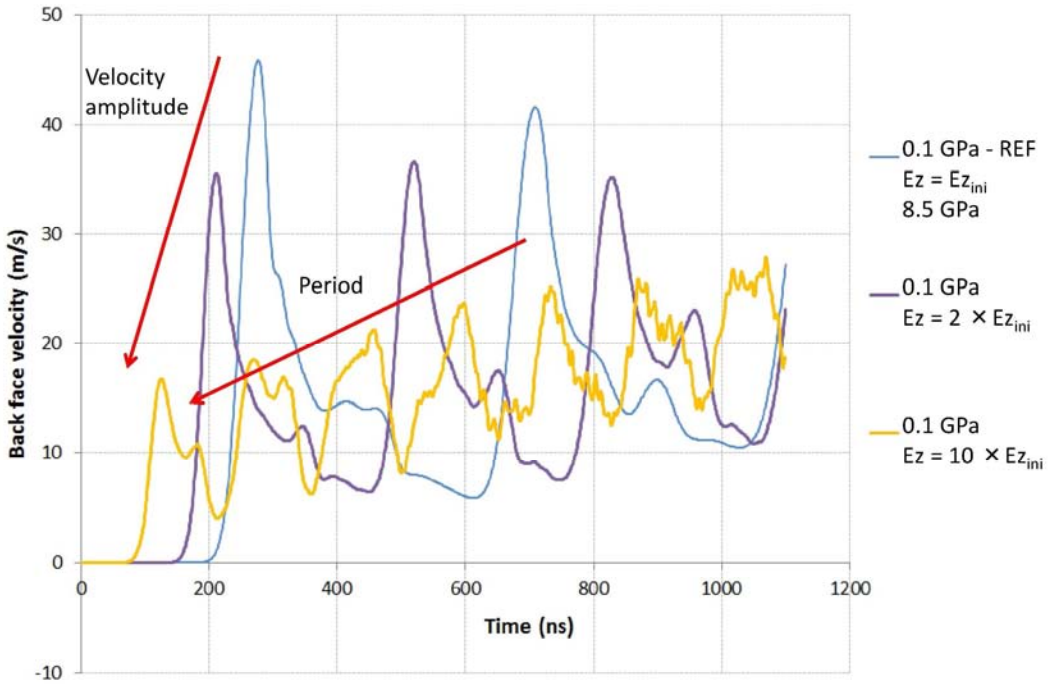

Figure 4.28, Comparison of the calculated back face velocity in case of different transverse direction modulus values (Ez) – Influence on the signal for a two unidirectional T800/M21 plies material

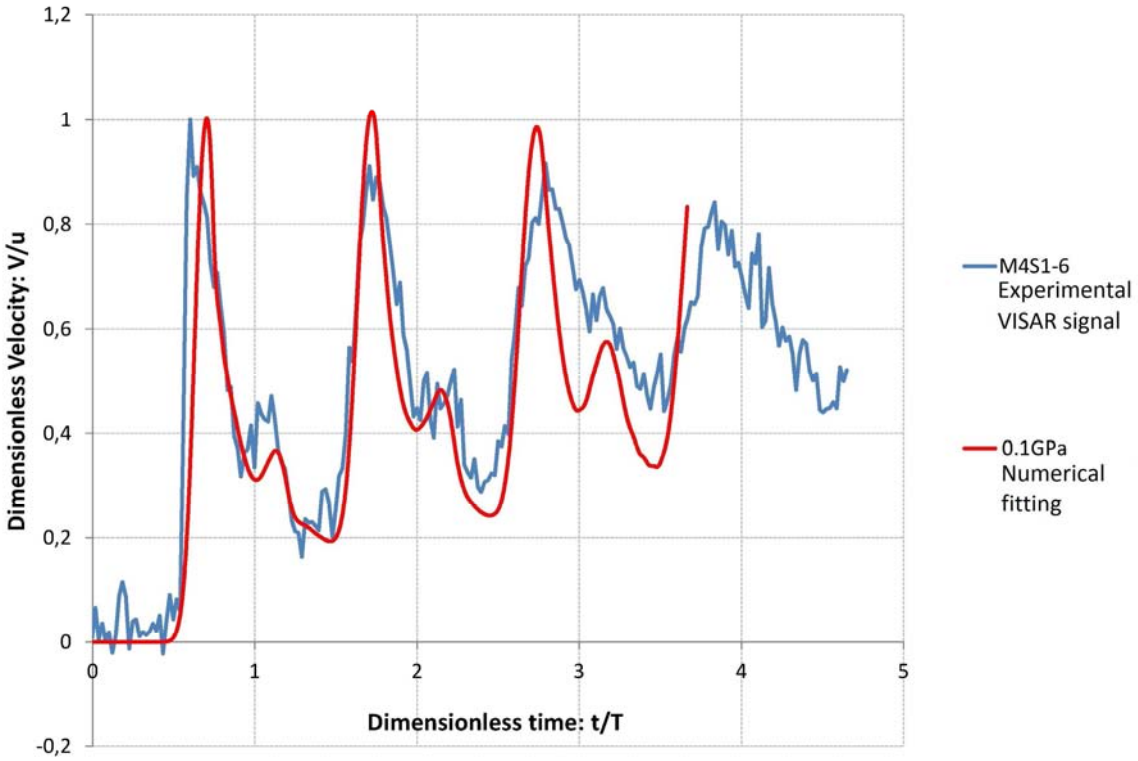

Figure 4.29, Dimensionless comparison of the calculated back face velocity in case of Ex and Ez moduli two times increased compared to the initial values, and an experimental VISAR signal for a two unidirectional T800/M21 plies material

2.6 Parametric study on sample thickness

In Chapter 3, it has been explained that due to experimental preparation protocol, the material thickness could significantly vary from one sample to another. This variation could induce differences on the back face velocity signal. In this section, it is numerically evidenced. The reference back face velocity is still the one presented from the beginning, with an interface tiebreak stiffness set at 0.7, and a maximum pressure load fixed at 0.1 GPa. Four additional calculations have been performed, using the same parameters, except that the model thickness has respectively changed to -10 µm, -50 µm (Figure 4.30-a) and + 10 µm, + 50 µm (Figure 4.30-b). Several comments can be made. Firstly, it can be noticed that the sample thickness influence on the free surface first peak amplitude is not really important. Indeed, changing the thickness is just slightly changing the attenuation through the composite sample. It becomes more important in case of a thicker sample, resulting in lower velocity amplitude, and less important in case of a thinner sample which leads to higher velocity amplitude. The sample thickness has also an influence on the second order peaks such as the one generated by 2D effects bending. In case of thinner sample, the bouncing is sharper but more important in terms of amplitude. In case of thicker sample, the bouncing is wider but lower. These observations are consistent with the 2D effects origin of the phenomenon, since their influence depends on the sample thickness in well known cases. The change which could be the more risky for fitting experimental results is the change in the back and forth period. This is perfectly normal because of the evident correlation between this period and the sample thickness. The differences start to become significant in case of a difference about 50 µm, as shown in Figure 4.30. Consequently, it should be kept in mind that the real thickness should be modeled for the numerical fitting to be consistent with the experimental data.

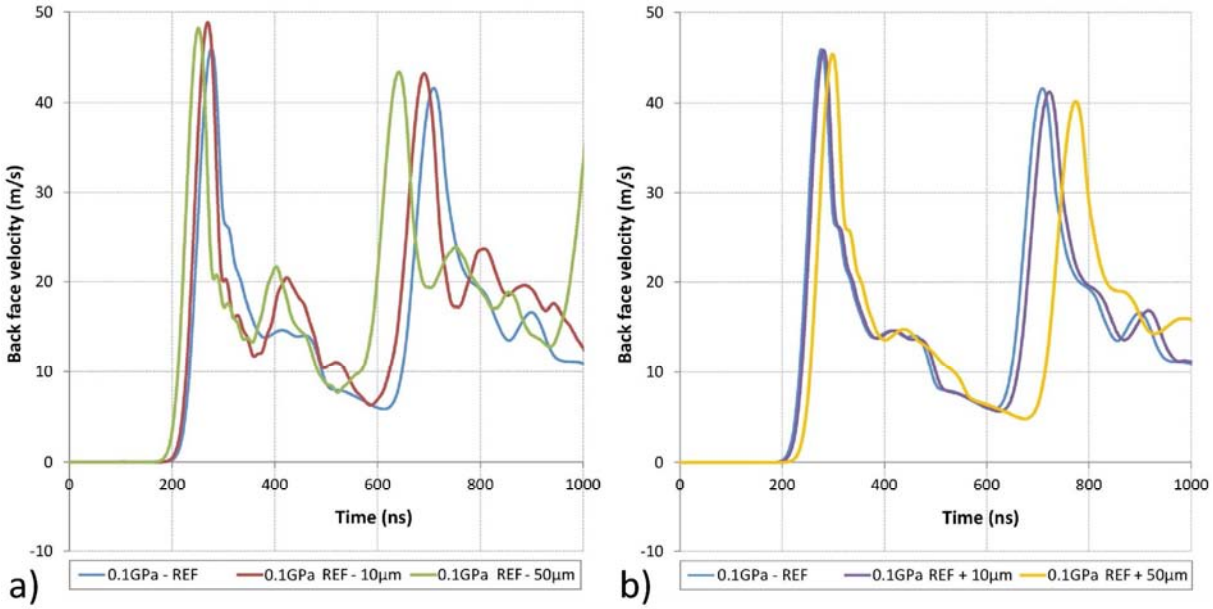

Figure 4.30, Comparison of the calculated back face velocity in case of different model thicknesses, thinner (a) and thicker (b) signal for a two unidirectional T800/M21 plies material – Influence on the BFV signals

2.7 A few words about thick composite model

In this section, a few results are given on thick unidirectional T800/M21 modeling to complete and confirm the previous observations. The model used is presented in Figure 4.31. It is 2D, since it was not possible to model the whole thickness in 3D. Based on the previous section analyses, it would not have brought strong differences anyway. Nevertheless, the complete width is modeled in order to

have a better description of the 2D effects. The material parameters are unchanged compared to Table 4.3, and the interface law is still TIEBREAK, with a 0.7 stiffness.

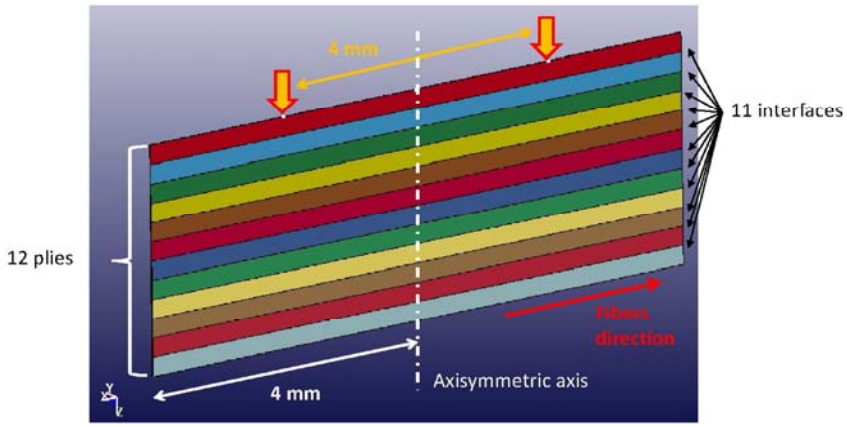

Figure 4.31, Unidirectional T800/M21 thick model (3mm), developed thanks to LS-PREPOST software

Time/position diagrams through the composite thickness (z direction) are presented in Figure 4.32 and 4.34. These diagrams are plotted along the axisymmetric axis presented in Figure 4.31. Starting with Figure 4.32, the shock propagation is shown below and above the numerical damage threshold. Another capacity of the developed Matlab numerical tool is shown in this Figure. Indeed, crosses indicate the maximum of tensile stresses achieved in the whole shock propagation. Moreover, a white area is added. It represents the tensile stresses being above 95% (in this case) of the maximum valued recorded. It gives an idea of the most loaded zone. In case of the propagation under the damage threshold, this zone is between 500 µm and 1200 µm deep from the sample back face. It is deeper that the actual crossing of release waves occurring about 250 µm deep, because of the presence of 2D effects which enhance the tension. Their influence becomes visible about 1 mm deep (from the front face), at 1.5 µs after the shock. It is the orange area visible in Figure 4.32-a. 2D effects are thus moving the position of maximum tensile stresses by enhancing the tension propagating backward after the release wave crossing. Nevertheless, in case of the propagation above the damage threshold, this effect in not visible anymore. Indeed, in the case of a pressure load about 0.5 GPa, the tensile stresses generated from the composite back face rapidly reach the tensile strength limit. The mesh is damaged, and the maximum of tensile stresses is of course reached before the damage occurrence. In this case, multi spallation can be observed. It could correspond to a physical phenomenon. Indeed, the tension has time to continue propagating backward through the sample due to incubation time. When the mesh is broken, the setting to 0 of the elastic parameters creates a numerical release propagating backward and thus enhancing the tension also propagating backward. For this reason, a second maximum region is obtained deeper from the first damage. It creates damage once again (see in Figure 4.32-b). The numerical model behaves as expected compared to theory.

The anisotropy effects can also be observed in case of thick T800/M21 samples. For that, the σ_{XX} stresses are plotted instead of σ_{ZZ} stresses. This Time/position diagram is given in Figure 4.33. It shows that the maximum of tension in the x direction is located on the sample back face (see red area in Figure 4.33). This zone in fact corresponds to the tensile stresses concentration induced by 2D effects bending and evidenced in the previous sections. It shows how this phenomenon propagates in case of a thick sample toward the back face. Note that it is almost synchronized with the corresponding compressive stresses concentration on the front face (see dark blue area around 1.2 µs on the front face in Figure 4.33).

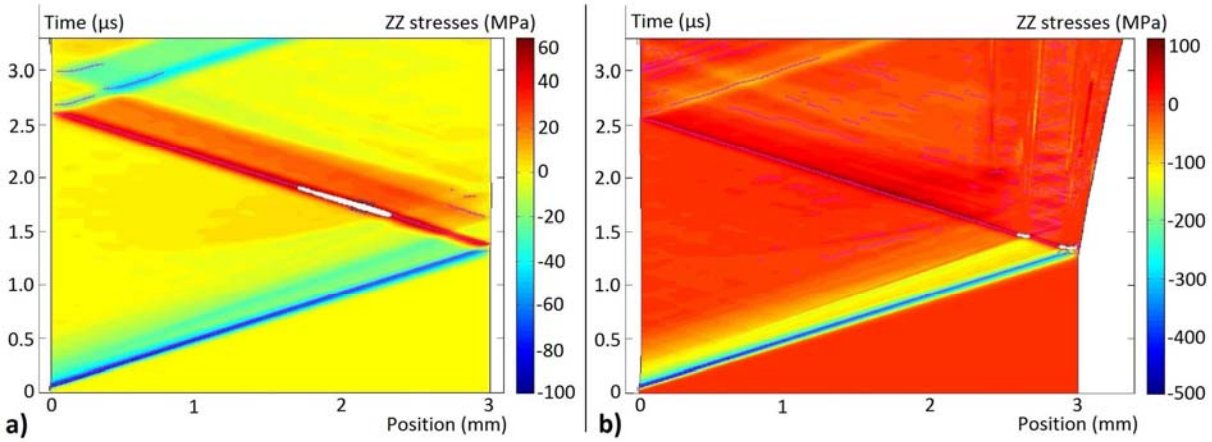

Figure 4.32, Shock propagation through the T800/M21 CFRP (3mm) thickness in case of two different pressure load values: 0.1 GPa (a) and 0.5 GPa (b) – Observation of the maximum of tension (white dots)

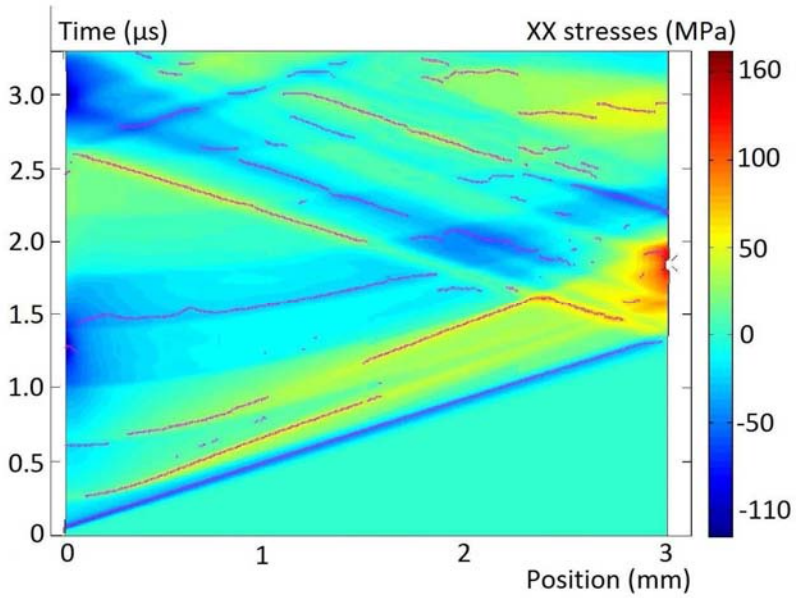

Figure 4.33, Shock propagation through the unidirectional T800/M21 (3mm) thickness in case of a 0.1 GPa pressure load – Observation of the σ_{XX} stresses propagation and concentration

Finally, the effect of the tensile modulus in the fiber direction has been evaluated. Two calculations have been performed, one with the reference parameters, the other one using a degraded fibers modulus to the level of the transverse one. The calculated back face velocities are presented in Figure 4.34.The purple curve corresponds to the reference case of a strong anisotropy. On this curve, the velocity bouncing occurs as expected from the previous investigations, meaning on the release slope. The timing of this bouncing corresponds to the one of the tensile stresses concentration on the sample back face identified in the Figure 4.32. In case of the degraded elastic properties, it has been assumed in the previous sections that this bouncing should occur, but later because of the lower sound speed in the x direction. This is confirmed in this thick CFRP case, where a late bouncing can be observed on the green curve. It has been confirmed by the corresponding time/position diagram that the phenomenon origin was the same, just delayed in time.

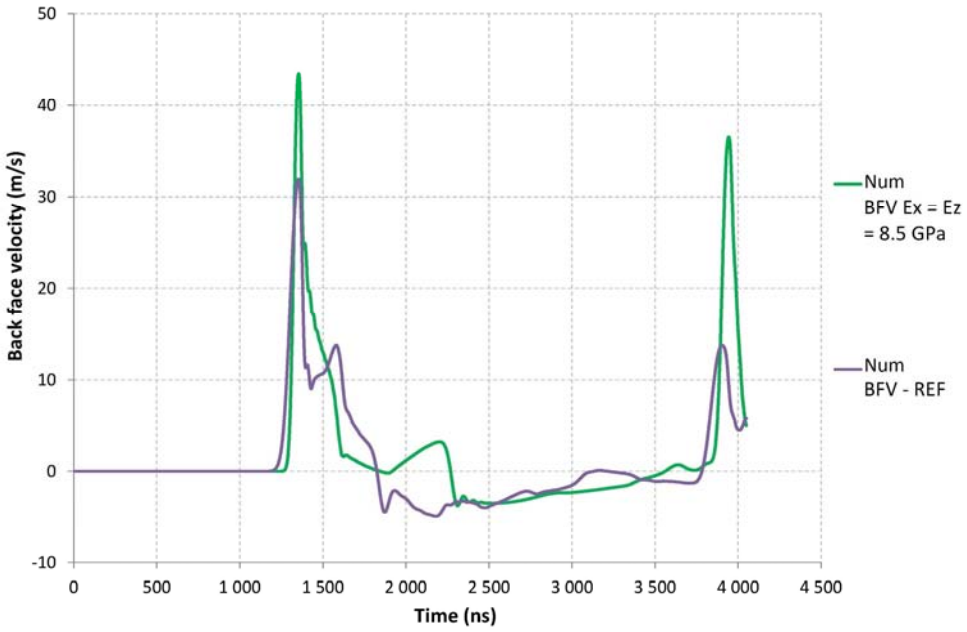

Figure 4.34, Comparison of the BFV velocity in case of thick T800/M21 numerical models, one using the standard parameters, the other one using a degraded elastic modulus in the fiber direction

3 From experiments to numerical modeling validation, results and discussions

3.1 Numerical simulations validation procedure on thin unidirectional T800/M21 composite

The parametric studies presented in the previous sections have given some elements on the model behavior under high strain rate laser shock, and parameters influence on the CFRP response. Especially, the elastic properties variations on the shocked composite back face velocity were quantified. Starting from the lessons learnt, the numerical modeling calculation can now be validated thanks to the experimental results. Note that the pressure profile is the starting point. As previously explained, it has been validated using a careful calibration on aluminum samples. It is consistent here because of the aluminum sacrificial layer used on composite samples. So, the pressure profile is untouched during the numerical fitting of composite VISAR experimental signals. It is an important point because it can explain some differences from one signal to another due to the laser/matter interaction uncertainties. The fitting has been realized on thin composite results, and then validated on thick composite samples. It is made of three main steps: 1. The fitting between calculated free surface velocity and experimentally measured velocity on only one signal without damage, 2. The extension of the resulting model to all the measurements performed for validation, without damage, 3. Based on the modeling of each experiments, especially of spallation signals, the dynamic interlaminar strength is adjusted as well as all the other damage parameters.

The chosen experimental signal to start with comes from M4S1-6 sample (see Table 3.13), presented in chapter 3 and recalled in Figure 4.35. For that, the real sample thickness has been modeled using a 2D model similar to the one previously presented. Note that this modeling choice will induce some small errors on the calculated back face velocity, especially on the 2D effects amplitude which are better reproduced using 3D. The fitting is realized by calculation iteration and using the following procedure:

- The first step is to adapt the elastic parameters. According to literature, it is known that the young moduli increase with the strain rate. Nevertheless, the modulus values in case of high strain laser shock loading are not known. Consequently, theses values are increased until obtaining a correct fitting between numerical calculation and the experimental signal. The first parameter to be varied is the one which influences the most the back face velocity signal, namely the transverse modulus. As shown in the previous sections, the back and forth shock period is directly correlated to the transverse modulus. A small change on this parameter induces sizeable modifications of the back face velocity signal. The idea is to get a numerical period as close as possible to the experimental one. In a second time, it seems quite possible that the transverse modulus and the fiber modulus would increase about the same range with strain rate. Consequently the fiber modulus is chosen thanks to a multiplicative factor in the same range than the one used for the transverse modulus. Moreover, the modulus giving the bigger anisotropic bouncing, and with the correct timing is selected. It is also increased to be in good agreement with literature.
- Once one of these two parameters is moved, the free surface velocity is calculated and compared to the experimental measurements. The following variations to apply can be deduced from the comparison. Especially, the periods can be compared, as well as the free surface velocity amplitude of the first peak. As shown in the previous section, this amplitude depends on pressure but also on the two moved parameters. Once the timing correctly fitted, the material properties are considered to be the good one, even if the maximum free surface velocity maximum is not exactly the good one.
- Consequently, the pressure level is adjusted in a second time, after the elastic properties modifications. The back face velocity is calculated and compared to the experimental signal. This step also enable to take into account the painting effect on the laser/matter interaction, as detailed in Appendix C. Note that pressure modification can also slightly modify the previous period fitting. In this case, elastic parameters should be adapted.
- These operations are repeated as often as necessary in order to get as close as possible to the reference experimental signal. This could represent about 20 calculations, shown in Figure 4.36 for illustration.

After this fitting procedure, a new set of elastic numerical properties is obtained, and the correct pressure amplitude can be evaluated. Then, the other experimental results are simulated using the same material model properties. Indeed, there is no reason why the elastic parameters should significantly change from one sample to another. Note that each sample has been modeled with its experimental actual thickness. A correct fitting of the other experiments with the numerical model thus gives reliability to the set of parameters calculated on the first experimental signal. Of course, the peak pressure has to be adjusted to fit the corresponding laser intensity. Only the first peak velocity amplitude is fitted during this step. Meanwhile, the points (Intensity, Pressure) are recorded to be compared to the initial calibration afterward (see Appendix C). The third step consists in adjusting the damage parameters. Once all the experimental data correctly modeled, the signals without damage and with spallation are discriminated. The damage parameters are averagely adjusted by enabling a correct modeling of the last non broken sample, and the first signal traducing spallation (in terms of pressure).

At the end, a set of material parameters is established, including elastic and damage parameters. It is adapted to the high strain rate loading induced by laser shock wave, and correctly describes the

studied CFRP behavior and damage under laser shock. Moreover, a curve correlating intensity to pressure is also obtained, and can be compared to the initial calibration.

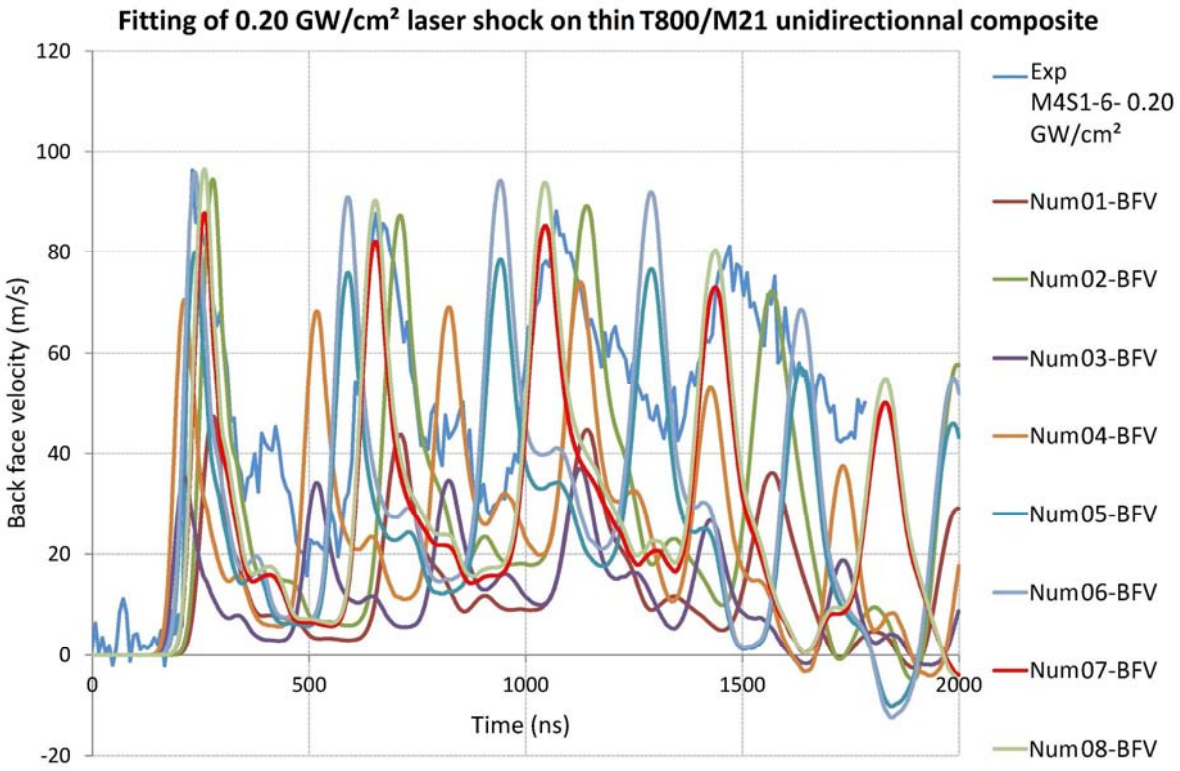

Figure 4.35, Illustration of the fitting procedure used for composite modeling by showing the different calculated signals with different elastic properties

The fitting results on the thin T800/M21 unidirectional CFRP experiments are presented in Figure 4.36 and Figure 4.37 for signal without damage and with spallation respectively. The first experiment to be modeled and fitted is the one obtained on M4S1-6 sample, 0.2 GW/cm² (see Table 3.13). It is presented in Figure 4.36 with its associated modeling results. The agreement between the experimental signal and the calculated one is relatively good. Indeed, the back and forth period and the first three peaks amplitude are well described by the numerical calculation. On the other hand, some elements are less correctly described: the peaks sharpness, the release end velocity missing and the anisotropic bouncing. The first peak sharpness is correct. This is due to the fact that this peak width is mainly driven by the pressure pulse width. Indeed, thanks to the low thickness, the attenuation is not really important, and does not too much modify the loading. The difference between calculation and experiment on the peaks width then increases for the second peak and even more on the third one. This is a clear effect of an attenuation modeling absence. Experimentally, the peaks progressively enlarge because of the release spreading through the material thickness. This is well known in shock theory, but can not be modeled by using an elastic model not coupled with a hydrodynamic description. The 2D model could also play a role here, since the shock energy could not be numerically dissipated in the y direction. Concerning the release tail residual velocity, a difference can also be noticed. This difference increases after each release, from 10 m/s to 20 m/s to 30 m/s (see in Figure 4.36). The model release behavior explanation can also be used here, but this is probably not the only reason. Indeed, these residual velocities define the material response on another scale length, which is generally the one of bending. The pressure pulse progressively pushes the sample, and leads to this progressive main slope which can be observed on the experimental signal. This phenomenon is mainly correlated to the release shape and amplitude

of the temporal pressure profile. Here, an average profile is used for modeling but it is possible that the experimental profile was slightly different (in this case, with a more important release amplitude) which could explain this difference. Finally, the anisotropic bouncing is more complex to explain. It has been shown that this feature is quite complex, and correlated to a lot of different parameters. The timing is correct, but not the amplitude. The use of a 2D model instead of a 3D model should clearly play a role on that, because it artificially reduces the fiber bending response. The pressure spatial repartition could also explain these differences. Anyway, these elements can be considered as second order phenomena, the main peaks, period and amplitude, being the most important features to fit for a correct model behavior. In this way, the model is now correctly describing the T800/M21 behavior. For that, the transverse moduli have been set to 14.45 GPa instead of 8.5 GPa, the quasi-static value, which correspond to a 1.7 multiplicative factor, and the fiber modulus has been increased to 330 GPa, instead 165 GPa in quasi-static, which correspond to a 2 multiplicative factor. So far, the other model parameters remain unchanged. Finally, the pressure maximum amplitude has been set at 0.26 GPa (see in Figure 4.36), in order to correctly model the signal amplitude.

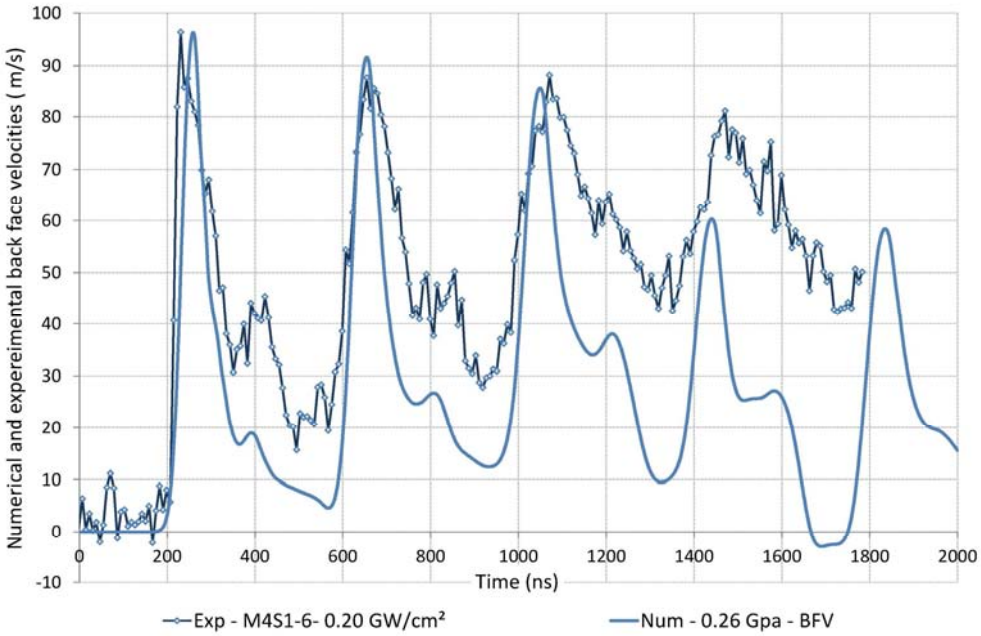

Figure 4.36, Comparison between numerical and experimental free surface velocities, in case of laser shock on M4S1-6 thin T800/M21 unidirectional sample, without damage for model validation

The last step is finally the fit of the experimental signal with spallation. For that, the damage parameters have to be adjusted to enable the spallation on the corresponding experimental signal. Before that, they were increased to prevent from damage in case M4S1-6 modeling. The numerical fit is presented in Figure 4.37 in case of spallation on sample M4S1-4. The set of parameters is unchanged, only the pressure in increased to fit the signal maximum amplitude. The fitting is quite good, except that with the increase of pressure, the shock breaking-out slope is getting stiffer, which is not modeled by the elastic model. For the damage to occur as experimentally evidenced, the interlaminar strength especially has to be increased to take into account strain rate effect. The previous studies have shown that this parameter was the key one to drive damage in the laser shock modeling, which is consistent with the literature. The interlaminar strength parameters, in tension and shear, for both composite and interface have been set to 275 MPa, which corresponds to the initial value increased by 2.5 times. Note that all the parameters have thus been increased with the same coefficient. This value is consistent with the literature. D. Laporte has found the same kind of

value in case of epoxy resin [25]. It is also close from the value experimentally established in Chapter 3, close to 240 MPa. Note that the velocity jump used to calculate this value was about 100 m/s, which is also described by the numerical modeling. The difference in the values thus comes from differences in the damage criteria hypothesis. Nevertheless, the model and the set of parameters are consistent with the literature and the experimental results obtained on thin T800/M21 unidirectional CFRP.

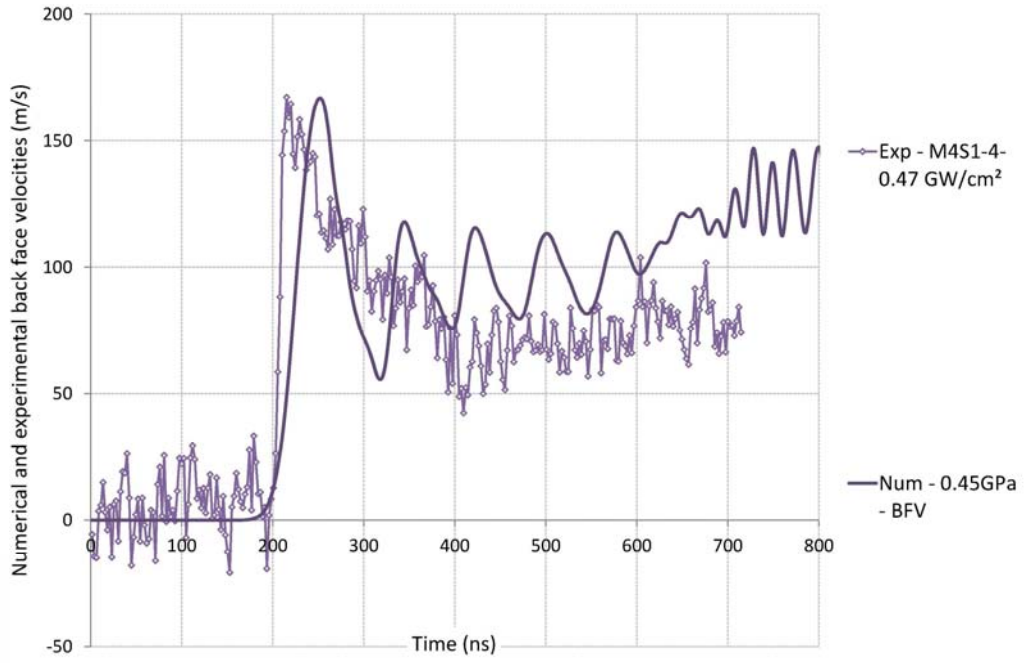

Figure 4.37, Comparison between numerical and experimental free surface velocities, in case of laser shock on M4S1-4 thin T800/M21 unidirectional sample, with spallation for model validation

To sum up, the corrections to apply to the elastic parameters in case of high strain rate laser shock are given in equation (4.7), with QS meaning quasi-static, and D for dynamic.

$$\begin{cases} Ez_D = 1.7 \times Ez_{QS} \\ Ex_D = 2 \times Ex_{QS} \\ \left(damage\ parameters\right)_D = 2.5 \times \left(damage\ parameters\right)_{QS} \end{cases} \tag{4.7}$$

A representation of the shock propagation through the material thickness can now be given with the correct material parameters. Two time/position diagrams are presented in Figure 4.38. The first one (a) corresponds to the modeling of M4S1-6 experiment (0.20 GW/cm²) and the second one to the calculation made for M4S1-4 (0.47 GW/cm²). In the first diagram, the shock back and forth can be observed. The attenuation can be quantified and the tensile stresses measured. They are about 110 MPa. The second time/position diagram perfectly agrees with literature, and enables the thickness measurement of the first spall. It highlights a second spall deeper in the material, in agreement with multi-spallation phenomenon previously explained. The maximum of stresses in this case corresponds to the interlaminar strength (275 MPa).

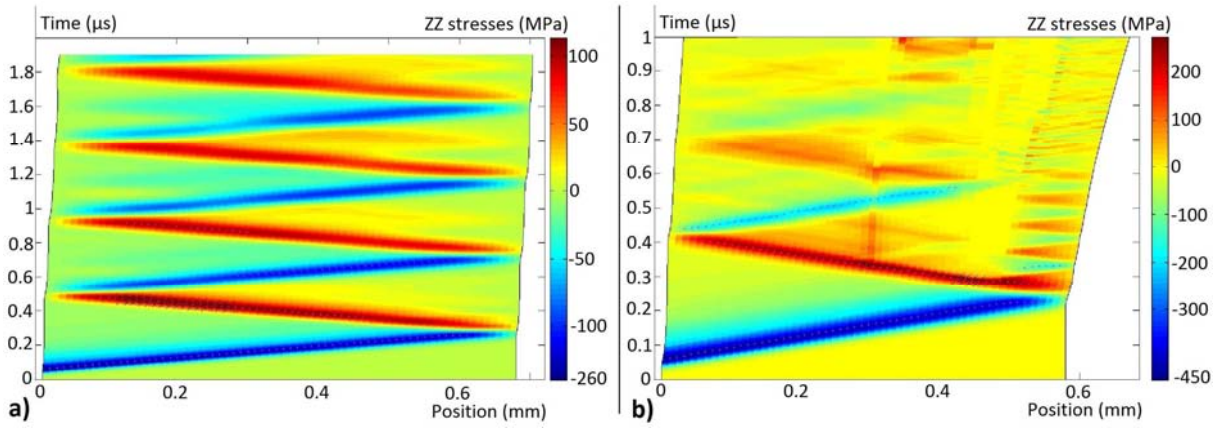

Figure 4.38, Time/position diagrams for a two plies T800/M21 unidirectional composite obtained with the material new set of parameters, without damage - 0.24 GPa (a) and with spallation – 0.45 GPa (b)

It is important to notice that the fitting is not perfect, but it could be better if each laser shock were modeled differently, by using different pressure pulse for each shock for example. All the uncertainties taken into account, the numerical calculations remain relatively close form the experimental results. Moreover, what is even more important for the LASAT application is to get a model which can be used to represent a whole experimental campaign. A good agreement in average, over several laser shocks is particularly sought. This point is discussed in the following section.

3.2 Validation on other thin unidirectional T800/M21 experiments

The reliability of the new set of parameters should be checked on other experimental signals. This is done on M4S1-9 sample (first shock, see Table 3.13) as presented in green in Figure 4.39, in case with out damage. The real thickness of the sample has been modeled. In order to fit this VISAR measurement, nothing has been changed, except the pressure level to adapt the modeling to the laser intensity. It has been reduced to 0.14 GPa, as shown in Figure 4.39. It can be observed that the peak amplitude fit is as good as on the previous experimental signal. Nevertheless, the period is not perfectly fitting the experimental signal. It could be due by material variation, which could have a small influence on the elastic properties. As explained, considering the uncertainties, this calculation is acceptable. Other experimental signals with spallation have also been calculated. The comparison between numerical calculation and experimental signal is given in Figure 4.40 Once again, the set of parameters is unchanged, only the pressure in increased to fit the signal maximum amplitude. The fitting is quite good, except that with the increase of pressure, the shock breaking-out slope is getting stiffer, which is not modeled by the elastic model. Indeed, this is a hydrodynamic behavior, getting more obvious above 1 GPa, which can not be elastically described.

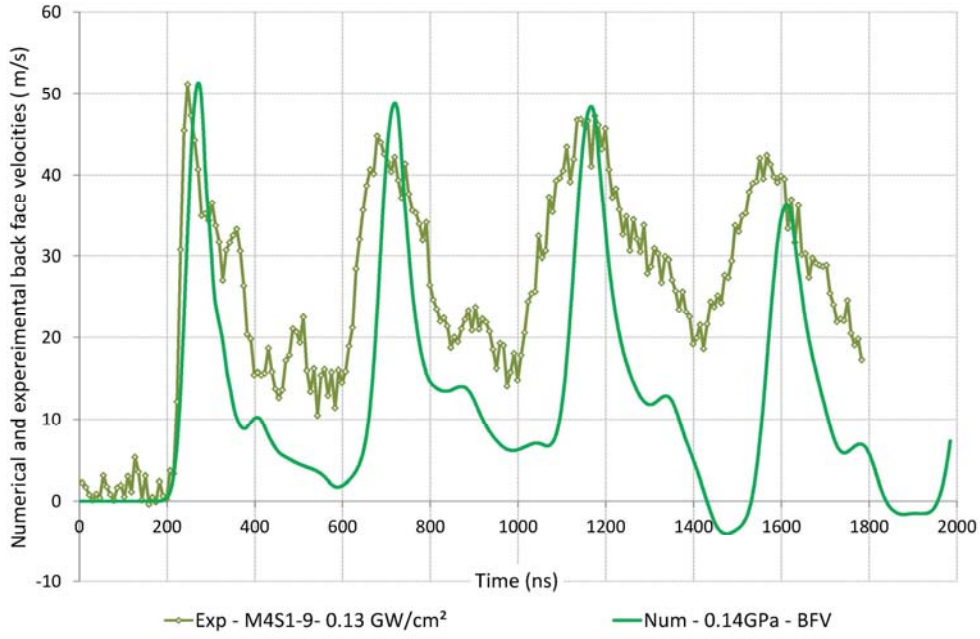

Figure 4.39, Comparison between numerical and experimental free surface velocities, in case of laser shock on M4S1-9 thin T800/M21 unidirectional sample, without damage

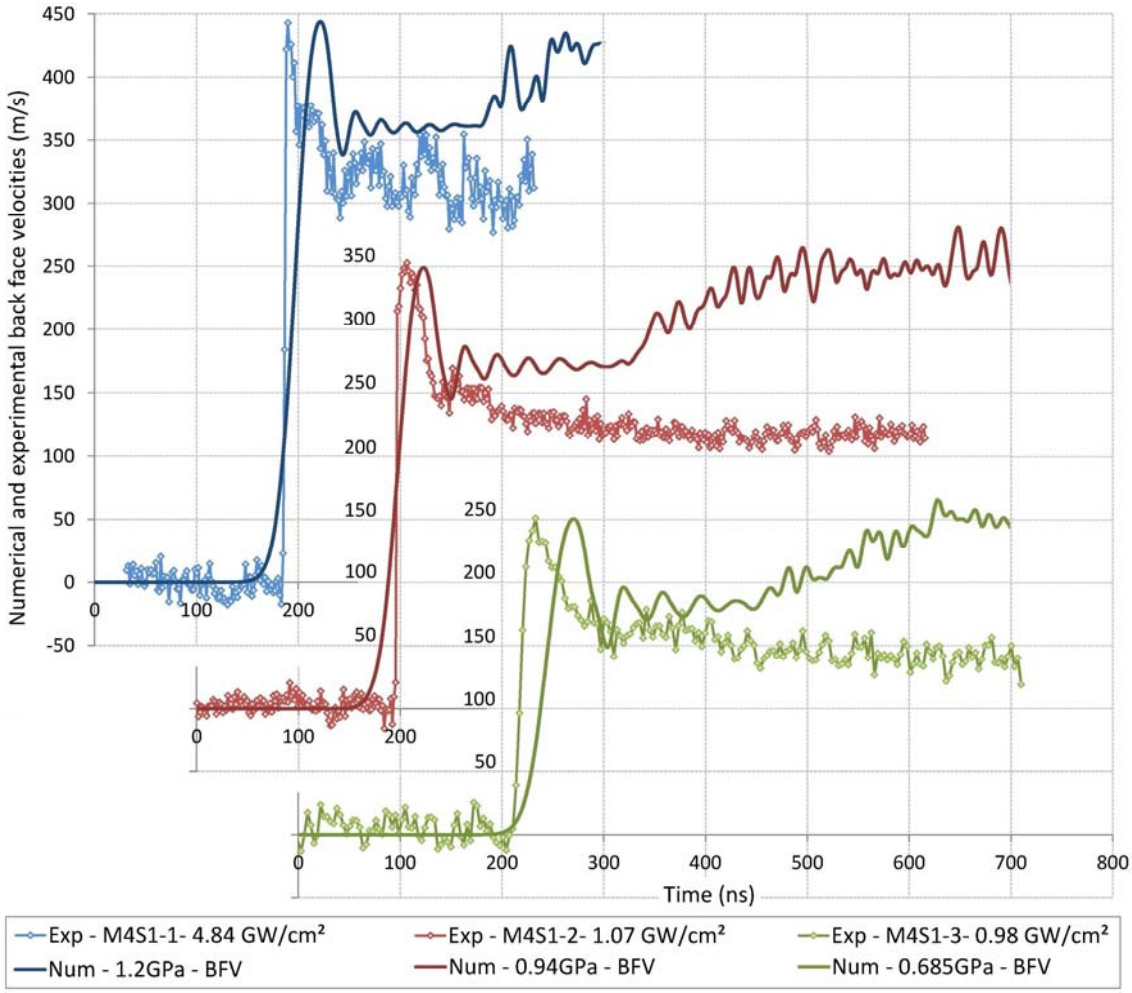

Figure 4.40, Comparison between numerical and experimental free surface velocities, in case of laser shocks on thin T800/M21 unidirectional sample, with spallation

3.3 Numerical simulation of 3 mm thick T800/M21 experiments

The model and its corresponding set of parameters have been validated on 0.5 mm thin composite targets. It can now be used to describe the behavior of 3 mm thick unidirectional composite samples, measured by VISAR in Chapter 3. The idea is also to check the model and its parameters on another data set, to validate its global consistency. First, two signals with no damage is modeled. The comparison between the experimental VISAR measurements (with dots) and the numerical calculations (solid lines) is given in Figure 4.41. Nothing has been changed from the previous material model. Of course, the correct sample thickness has been used (see in Figure 4.31), and the pressure adjusted in order to fit the shock breaking-out velocity amplitude (see Appendix C). It can be observed in Figure 4.41 that the fitting is quite good between experiments and simulations. The back and forth period matches, as the first peak description does. Some of the second order phenomena are also correctly represented and with the correct timing. Like in the case of thin CFRP, the attenuation correlated to the release spreading through the sample thickness is not modeled. That is why the numerical calculated first release slope is below the experimental one, and also why the anisotropic bouncing of the second shock breaking-out is closer to the shock breaking-out peak than the experimental one is. Thanks to this rather good agreement between calculation and experimental result, it can be considered that the developed numerical modeling provides sufficient robustness for dealing with the laser shock waves propagation and associated effects into CFRP.

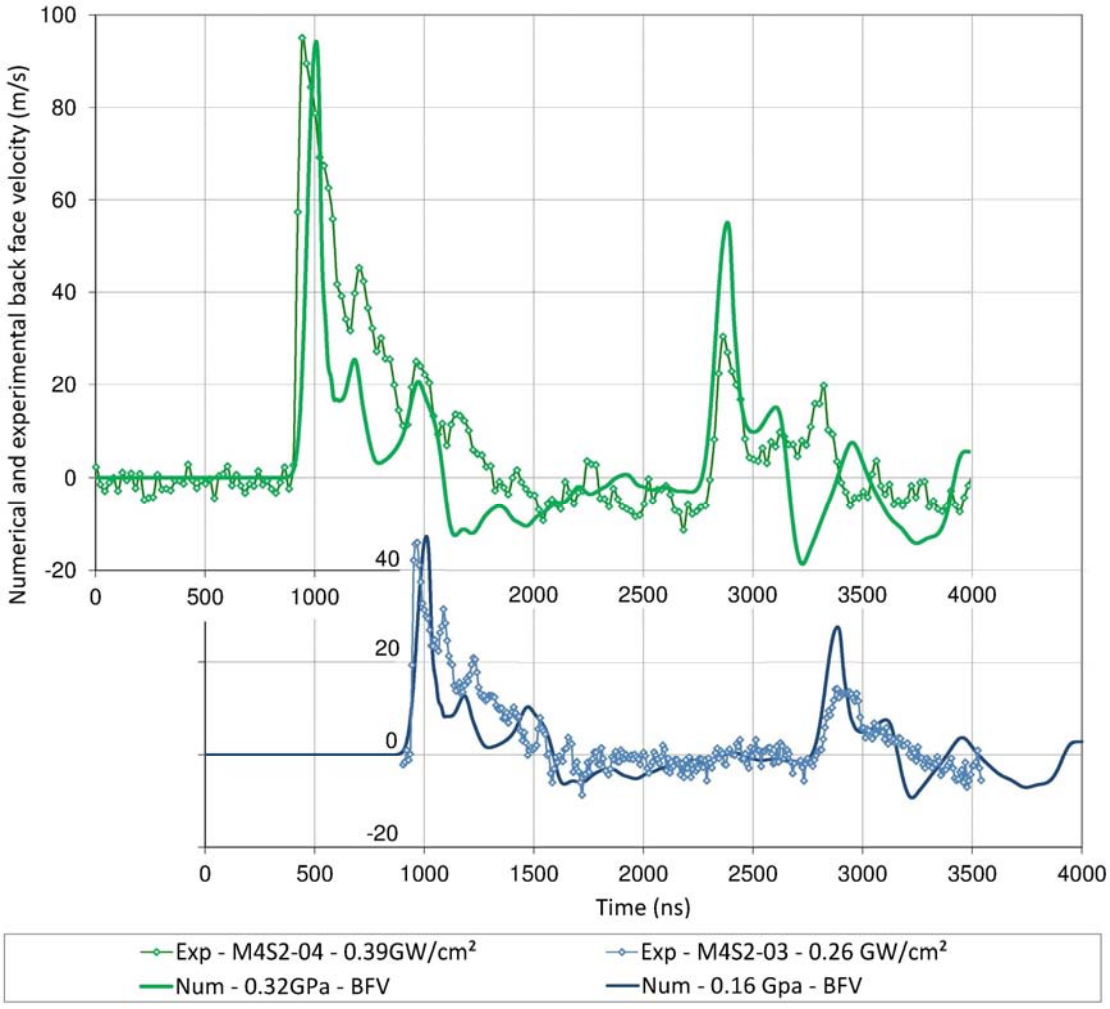

Figure 4.41, Comparison between numerical and experimental free surface velocities, in case of laser shock on 3 mm thick T800/M21 unidirectional sample, without damage

Speaking of damage now, the calculations are also in good agreement with experimental results as shown in Figure 4.42. The damage parameters have not been moved, as it could have been regarding the experimental results, because the chosen values already enable a numerical discrimination of the spallation signals from the unharmed signal. The same problem on the shock breaking-out stiffness can be observed, especially for the shock values above 1.21 GW/cm². Like in the previous calculation, the shock front does not become stiff, as it should be the case according to theory. This is due to the elastic model used. Note that the damage propagation in the composite is not physical at all for the highest pressure. This is consistent with the parametric studies done in the previous section.

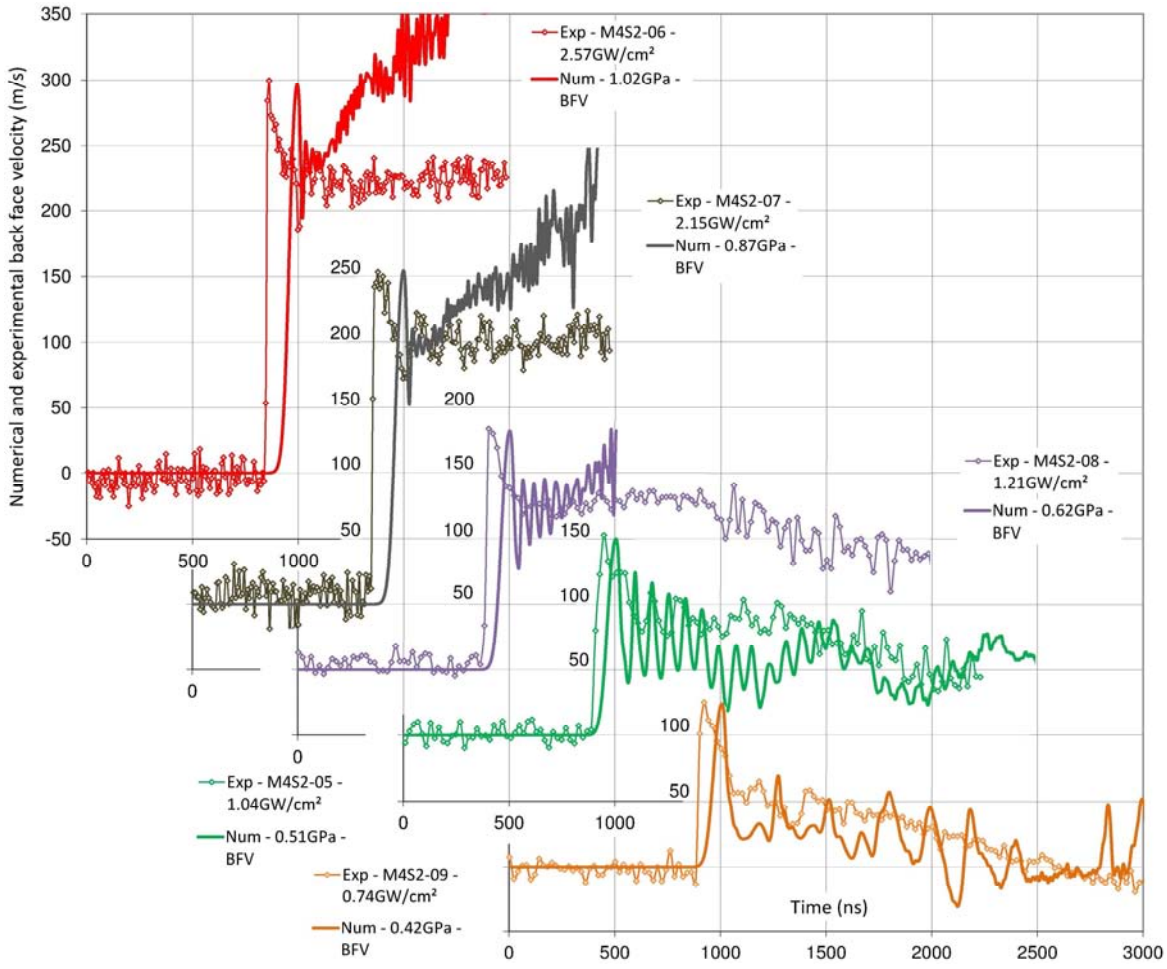

Figure 4.42, Comparison between numerical and experimental free surface velocities, in case of laser shock on 3 mm thick T800/M21 unidirectional sample, with spallation

In order to represent the shock propagation inside the T800/M21 thick samples, time/position diagrams are presented in Figure 4.43. The first one corresponds to sample M4S2-04, in a case for which the laser shock did not lead to damage (see Figure 4.43-a). The maximum of tensile stresses is also represented in this diagram. The white area corresponds to the location of the stresses which are above 90 % of the maximum value. Two zones can be observed. The closest one to the back face is generated by the crossing of release waves. Its depth from the sample back face corresponds to the shock theory for this kind of laser pulse. The second zone, wider and deeper in the material, is resulting from the crossing of the tensile loading, propagating backward, and the 2D effects induced tension. According this result, the damage should occur first in the closest area to the back face, where the maximum of tensile stresses is located. It has been confirmed by the second time/position diagram, presented in Figure 4.43-b, and corresponding to M4S2-09 sample (0.42 GPa). It shows that spallation did occur in the place where the maximum was located. The second high tension region is

considerably reduced, because of the weakening of the tension propagating backward after the first damage occurrence. It corresponds to experimental observations of damage in these materials (see Chapter 3, part 2, section 3 & 4). This diagram is also the demonstration that the damage changes the location of the tensile stresses maximum. It has to be kept in mind for bonded composite investigations.

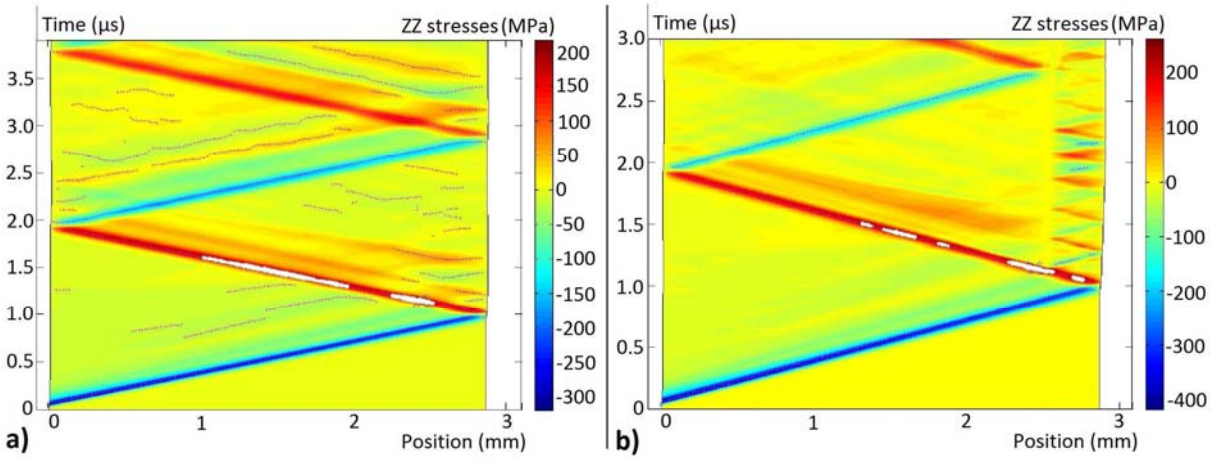

Figure 4.43, Time/position diagrams obtained in case of 3 mm thick unidirectional T800/M21 sample, without damage - 0.32 GPa (a) and with spallation – 0.42 GPa (b) – observation of the maximum loaded region through the sample thickness in each case

3.4 Numerical simulation of T700/M21 cross-ply composite

Finally, the cross-ply composite corresponding to ENCOMB sample can be modeled. It corresponds to the used material for the application. As explained in Chapter 3, it is made of 6 plies, each ply being 0.25 mm thick, and with the following stacking sequence [0°,0°,90°,90°,0°,0°]. It is made from T700S/M21 pre-impregnated plies, which has mechanical properties similar but slightly different from T800/M21 according to literature [1]. Note that it was not possible to test directly T700/M21 unidirectional material because of sample availability. Nevertheless, previous results are used. In the material model, some parameters have been modified according to literature to correspond to T700/M21, and then the multiplicative factors identified in the previous section (equation 4.7) have been applied on both fiber modulus and transverse modulus. The resulting set of parameters is given in Table 4.5. It can be noticed that the damage parameters have to be increased up to 350 MPa for a correct modeling of the unharmed sample. Indeed, due to sample thickness, the model has to be performed in 2D. Therefore, the fibers in the 90° are less correctly described than the fiber in the 0° direction. It is not an important issue for the σ_{zz} stresses propagation through the sample thickness, because it has been shown that it was mainly isotropic under the loaded area. But it becomes problematic for the bending response of the material, because the numerical model has less strength in the 90° direction. For this reason, the damage parameters have been increased to correspond to experiments. The fitting is shown in Figure 4.44. The experimental signals are globally well described by the numerical model. Some differences, similar to the previously observed ones on T800/M21, can be identified. In addition to the release behavior, the model choice could this time also induce more divergence than in the previous case because of the 90° fibers modeling. Same argument can be used for the attenuation.

LS-DYNA	Abb.	Parameters	Modified Values	Source
Elastic properties				
RO	ρ	density	1.58 g/cm^3	(a)
EA	E_{XX}	Tensile modulus in fiber direction x	**197.24 GPa**	(a)
EB	E_{YY}	Tensile modulus in the transverse direction y	**13.07 GPa**	(b)
EC	E_{ZZ}	Tensile modulus in the transverse direction z	**13.07 GPa**	(b)
PRBA	ν_{YX}	Poisson coefficient yx	0.02	(c)
PRCA	ν_{ZX}	Poisson coefficient zx	0.03	(c)
PRCB	ν_{ZY}	Poisson coefficient zy	0.035	(c)
GAB	G_{XY}	Shear modulus in xy plane	4.75 GPa	(b)
GBC	G_{YZ}	Shear modulus in yz plane	2.75 GPa	(b)
GCA	G_{ZX}	Shear modulus in zx plane	4.75 GPa	(b)
Damage parameters				
SC	σ_S	Interlaminar shear strength (0°)	350 MPa	(a)
XT	$\sigma_{T,f}$	Tensile strength in the fiber direction (0°)	7000 MPa	(a)
YT	$\sigma_{T,m}$	Tensile strength in the transverse direction (matrix)	350 MPa	(b)
YC	$\sigma_{C,m}$	Compressive strength in the transverse direction (matrix)	400 MPa	(b)
SN	$\sigma_{T,i}$	Tensile strength in the direction normal to elements/ Interlaminar tensile strength	350 MPa	(b)
SYZ	$\sigma_{S,YZ}$	Shear strength in the YZ plane	350MPa	(b)
SZX	$\sigma_{S,ZX}$	Shear strength in the ZX plane	350 MPa	(b)

Table 4.5, T700/M21 orthotropic ply modified properties (elastic and damage parameters) from different sources; Airbus data sheet (a), literature [2-3] (b) and calculated from literature (c) – The elastic parameters modified according equation 4.7 are written in bold.

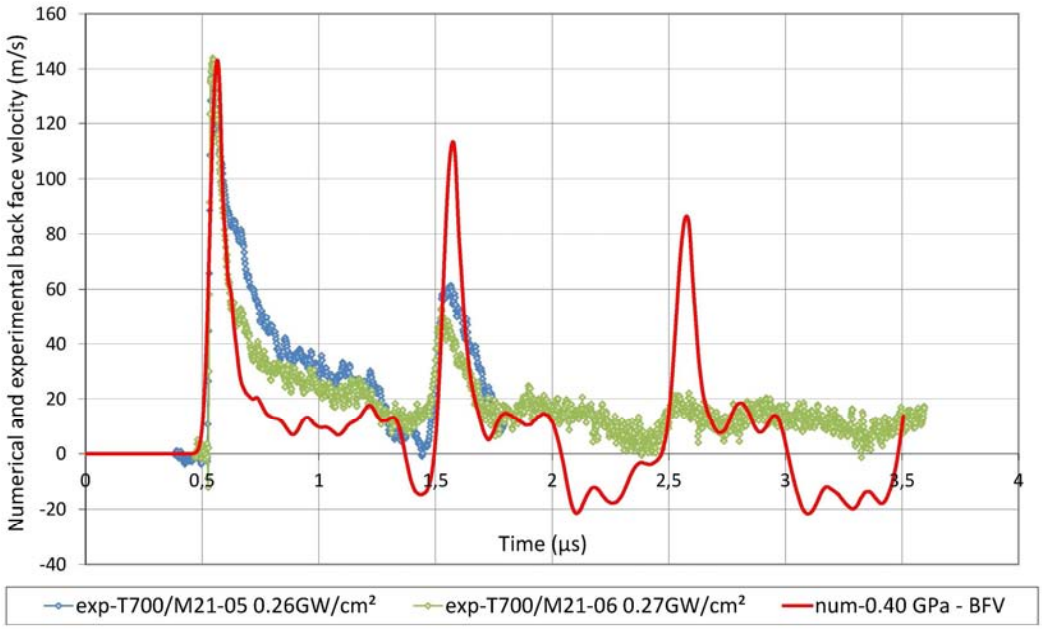

Figure 4.44, Comparison between numerical and experimental free surface velocities, in case of laser shock on a 1.5 mm thick T700/M21 cross-ply sample [0°,0°,90°,90°,0°,0°]

In Figure 4.45, three time/position diagrams are presented, one for each main stresses. It can be observed that the stresses propagation is consistent with the ply orientation. σ_{XX} stresses are significant only in the x direction ply (see in Figure 4.45-a), and the σ_{YY} stresses are visible in the y direction (see in Figure 4.45-b). The propagation of the σ_{ZZ} stresses is not disturbed by the change of orientation (see in Figure 4.45-c). This is consistent with the observations made on the 3D model in the previous section.

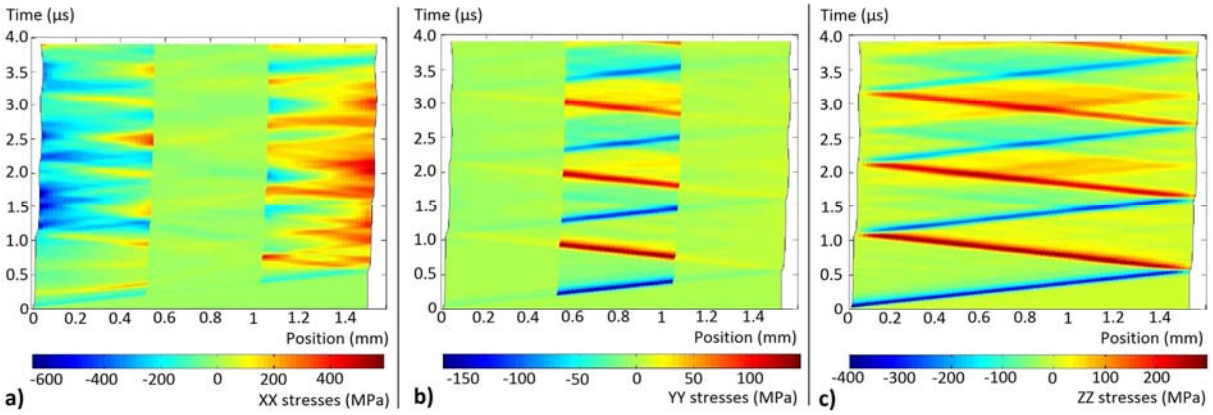

Figure 4.45, Time/position diagrams obtained in case of a 1.5 mm thick T700/M21 cross-ply sample [0°,0°,90°,90°,0°,0°], without damage – observation of σ_{XX} stresses (a), observation of σ_{YY} stresses (b) and observation of σ_{ZZ} stresses (c)

Conclusions & Synthesis

In this chapter, a literature overview on the existing models to describe shocks propagation and induced damage in composite materials has first been presented. It showed that various models were available, although few works address to high strain rate loadings. From this state-of-art review, it appears that the key issue is the model parameters identification, for behavior description as well as for damage propagation modeling. Choices were made for the laser shock modeling. An elastic hydrodynamic model has been chosen for epoxy resin modeling, and an elastic orthotropic model was implemented to describe the shock propagation in composite laminates. The Chang/Chang criterion was chosen to model the damage initiation in the composite, knowing that the key point for laser shock modeling is the damage initiation.

Numerical modeling of laser shocks in epoxy targets has been first performed. The aim of this investigation was to find a realistic and simple model to describe the FM300 adhesive bond material. Numerical simulations of LULI2000 experiments, presented in chapter 3, were used to validate the model choice. It showed a good description of the shock wave propagation and associated phenomena into an epoxy resin, with the correct chronology of waves events. It also enabled to identify the phenomenon observed by photoelasticimetry during ELFIE experiments as shear stresses propagation in the 2D effects zone. From this reliable modeling, a set of parameters has been established for FM300 bond material modeling, and validated by the good agreement of simulations with VISAR measurements.

Composite modeling was then deeply investigated. As a first step, parametric studies were performed on a 3D model of a thin (0.5 mm) unidirectional T800/M21 composite, made of two plies and using quasi-static parameters. Effects of pressure loading were shown, for numerical simulations until the spallation threshold. Interfaces and anisotropic 2D effects (σ_{XX} stresses) were evidenced and their signature on the back face velocity signals clearly identified. The anisotropic propagation has been shown by plotting the stresses distribution against time in the model different directions.

Nevertheless, it showed that the σ_{zz} stresses propagation mainly remains isotropic under the loaded area, so the damage initiation is. Moreover, the influence of the elastic material parameters on the model dynamic response has been shown. Especially, the transverse modulus has a strong influence on the waves time history and amplitude. The conclusions enabled to jump to the 2nd step, which was dedicated to the progressive model validation on several composite materials, using VISAR results. First, two signals were used, without and with damage, in order to adjust the material parameters to high strain rate laser loading. This set of parameters and the corresponding model is then validated on thin (0.5 mm) and thick (3 mm) unidirectional composite materials. Finally, the application on cross-ply T700/M21 composite has been correctly modeled. The simulations performed enable studies of the shock propagation in these materials, leading to a better understanding of their dynamic behavior. The main steps of the numerical validation and investigations are summed up in Table 4.6.

The developed numerical model is based on several assumptions. Nevertheless, considering the experimental uncertainties particularly on the pressure profile, the overall agreement with the whole experimental data is rather good, at least for the first back and forth into the targets with thicknesses up to 3mm. Therefore, the developed models in this chapter are correct enough to be used in a second time for bonded composite modeling investigations (chapter 5). It can also be used to test other shock configurations for the technique optimization studies (chapter 6).

Table 4.6, Main steps of the numerical investigations on composite samples performed in this chapter

Models	Back Face velocity comparisons	Time/position diagrams
Thin (0.5 mm) unidirectional T800/M21 composite material model validation		
2D unidirectional 0.5 mm model, dynamic T800/M21 parameters, TIEBREAK interfaces – **No damage**	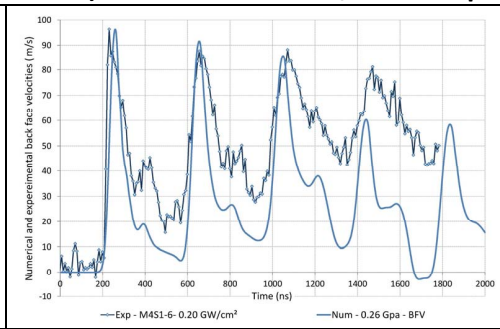	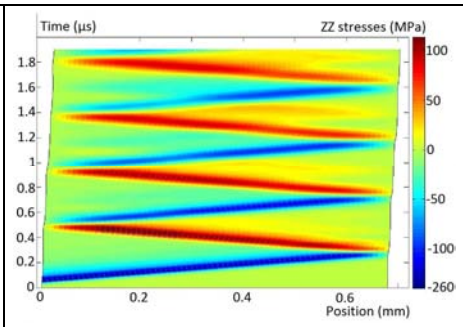
2D unidirectional 0.5 mm model, dynamic T800/M21 parameters, TIEBREAK interfaces – **With damage**	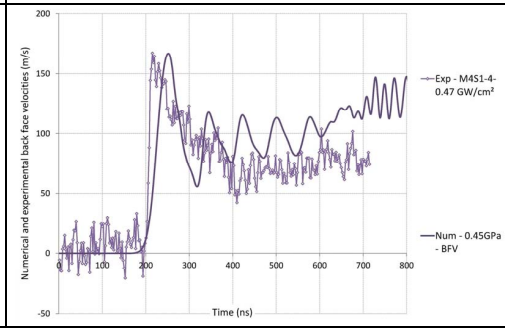	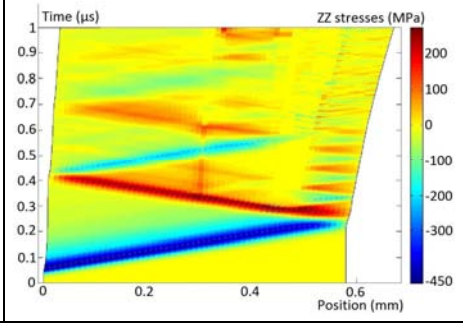
Thick (3.0 mm) unidirectional T800/M21 composite material model validation		
2D unidirectional 3.0 mm model, dynamic T800/M21 parameters, TIEBREAK interfaces – **No damage**	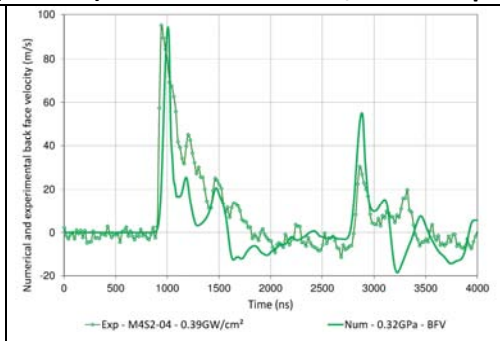	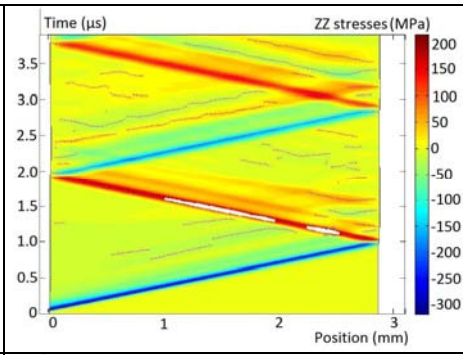
2D unidirectional 3.0 mm model, dynamic T800/M21 parameters, TIEBREAK interfaces – **With damage**	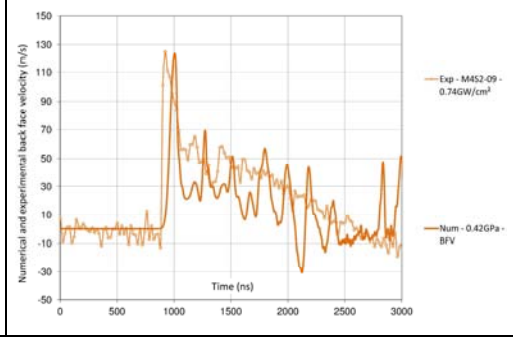	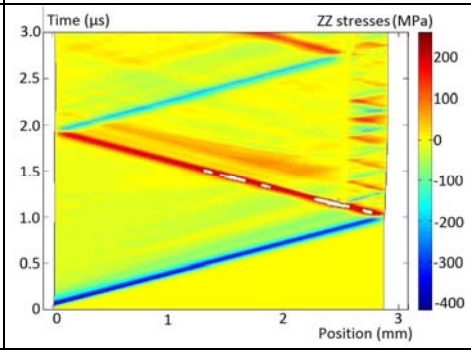
Thick (1.5 mm) cross-ply T700/M21 composite material model validation		
2D unidirectional 3.0 mm model, dynamic T800/M21 parameters, TIEBREAK interfaces – **No damage**	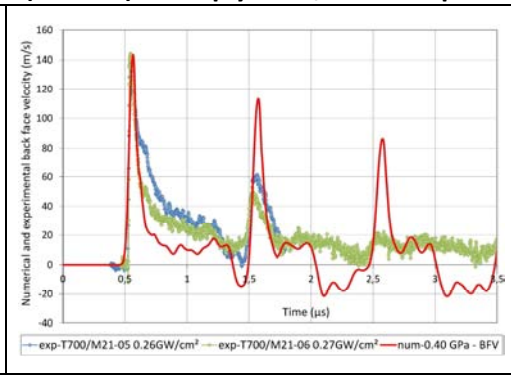	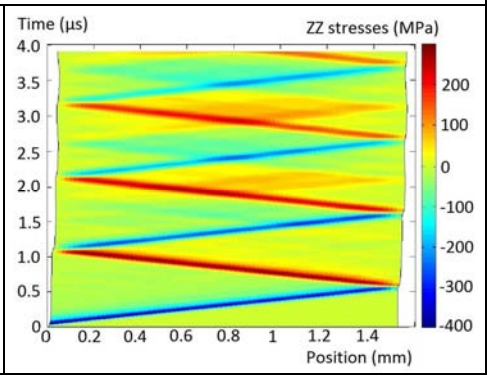

References

[1] M. Illyas, C. Espinosa, F. Lachaud, M.Salaün, *Simulation of Dynamic delamination and Mode I energy dissipation*, presented at the 7th international LS-DYNA Users Conference, Salzburg, Austria, 2009, http://www.dynalook.com/

[2] M. Ilyas, F. Lachaud, C. Espinosa, L. Michel, M. Salaün, *Dynamic delamination modeling of unidirectional composites by cohesive finite elements*, presented at the 16th Journée Nationales sur les Composites (JNC16), Toulouse, France, 10th - 12 th June, 2009

[3] S. Heimbs, S. Heller, P. Middendorf, *Simulation of Low Velocity Impact on Composite Plates with compressive Preload*, LS-DYNA Anwenderforum, Bamberg 2008, http://www.dynalook.com/

[4] LS-DYNA Keyword user's manual, Volumes I and II, Version 971, May 2007

[5] LS-DYNA Theory manual, compiled by John O. Hallquist, March 2006

[6] F. K. Chang, K. Y. Chang, *A progressive damage model for laminated composites containing stress concentrations*, Journal of Composite Materials, Vol. 21, 1987, pp. 834-855.

[7] B. S. Thatte, G. S. Chandekar, A. D. Kelkar, P. Chaphalkar, *Studies on Behavior of Carbon and Fiberglass Epoxy Composite Laminates under low velocity Impact Loading using LS-DYNA*, presented at the 10th International LS-DYNA Users' Conference, Detroit, USA, 2008, http://www.dynalook.com/

[8] R. Haynes, X. Tan, E. Armanios, *Effects of Barely Impact Damage on Bend-Twist coupling*, presented at the 26th Annual Technical Conference of ASC, September 26th – 28th, 2011, Montreal, Quebec, Canada.

[9] A. Faggiani, B. G. Falzon, *Predicting low-velocity impact damage on a stiffened composite panel*, published in Composites: Part A 41 (2010) 737–749, 2010

[10] C.S. Lopes, P.P. Camanho, Z. Gürdal, P. Maimí, E.V. González, *Low-velocity impact damage on dispersed stacking sequence laminates. Part II: Numerical simulations*, published in Composites Science and Technology 69 (2009) 937–947, 2009

[11] Z. Zhang, F. Taheri, *Dynamic pulsebulking analysis of FRP Composite laminated Beams Using LS-DYNA*, presented at the 7th international LS-DYNA Users Conference, Salzburg, Austria, 2009, http://www.dynalook.com/

[12] R. Craven, L. Iannucci, R. Olsson, *Delamination buckling: A finite element study with realistic delamination shapes, multiple delaminations and fibre fracture cracks*, published in Composites: Part A 41 (2010) 684–692, 2010

[13] M. Anghileri, L.-M. Castelletti, A. Milanese, A. Semboloni, *Modeling Hailstone Impact onto Composite Material Panel Under a Multi-axial State of Stress*, presented at the 6th European LS-DYNA Users' Conference, Gothenburg, Sweden, 2007, http://www.dynalook.com/

[14] H.D. Espinosa, S. Dwivedi, H.-C. Lu, *Modeling impact induced delamination of woven fiber reinforced composites with contact/cohesive laws*, published in Comput. Methods Appl. Mech. Engrg. 183 (2000) 259-290, 2000

[15] O. Allix, M. Dommanget, M. Gratton, P-L Héreil, A multi-scale approach for the response of a 3D carbon/carbon composite under shock loading, published in Composites Science and Technology 61 (2001) 409-415

[16] C.-F. Yen, *Ballistic impact modeling of composite materials*, presented at the 7th international LS-DYNA Users Conference, Salzburg, Austria, 2009, http://www.dynalook.com/

[17] L. J. Deka, U. K. Vaidya, *LS-DYNA Impact Simulation of Composite Sandwich Structures with Balsa Wood Core*, presented at the 10th International LS-DYNA Users' Conference, Detroit, USA, 2008, http://www.dynalook.com/

[18] M. Loikkanen, G. Praveen, D. Powell, *Simulation of Ballistic Impact on Composite Panels*, presented at the 10th International LS-DYNA Users' Conference, Detroit, USA, 2008, http://www.dynalook.com/

[19] A. Yoshimura, K. Nagakura, T. Okabe, H. Kusano, M. Yamada, Y. Tanabe, T. Ogasawara, H. Nakatani, S. Ogihara, *3D simulation of high-velocity impact damage progress in the CFRP laminates*, presented at the 15th European Conference on Composite Materials (ECCM15), June 24th – 28th, 2012, Venice, Italy

[20] A. A. Lukyanov, *An equation of state of a carbon-fibre epoxy composite under shock loading*, published in Eur. Phys. J. B 74, 35–45 (2010) DOI: 10.1140/epjb/e2010-00043-4, 2010

[21] R. Vignjevic, N. Djordjevic, T. De Vuyst, Progressive damage in woven CFRP in presence of shock wave, presented at the 15th European Conference on Composite Materials (ECCM15), June 24th – 28th, 2012, Venice, Italy

[22] M. Wicklein, S. Ryan, D.M. White, R.A. Clegg, *Hypervelocity impact on CFRP: Testing, material modelling, and numerical simulation*, published in International Journal of Impact Engineering 35 (2008) 1861–1869

[23] S. Ryan, M. Wicklein, A. Mouritz, W. Riedel, F. Schäfer, K. Thoma, *Theoretical prediction of dynamic composite material properties for hypervelocity impact simulations*, published in International Journal of Impact Engineering 36 (2009) 899–912, 2009

[24] D. Laporte, F. Malaise, M. Boustie, J.M. Chevalier, E. Buzaud, C. Thessieux, *Dynamic behaviour of two adhesive materials* , DYMAT 19th Proceedings, Strasbourg, 245 (2010)

[25] D. Laporte, Analyse de la réponse d'assemblages collés sous des solicitations en dynamique rapide. Essais et modélisations, Thèse de l'ENSMA (Ecole Nationale Supérieure de Mécanique et d'Aérotechnique), Ecole doctorale SIMMEA, 2011

[26] R. Fabbro, J. Fournier, P. Ballard, D. Devaux, J. Virmont, Physical study of laser produced plasma in confined geometry, Journal of Applied Physics, Vol. 68, n°2,775-784 (1990).

[27] L. Berthe, R. Fabbro, P. Peyre, L. Tollier, E. Bartnicki, Shock waves from a water confined laser-generated plasma, Journal of Applied Physics, Vol. 82, n°6, 2826-2832, 1997

[28] J-P. Cuq-Lelandais, *Etude du comportement dynamique de matériaux sous choc laser sub-picoseconde*, Thèse de l'ENSMA (Ecole Nationale Supérieure de Mécanique et d'Aérotechnique), Ecole doctorale SIMMEA, 2010

CHAPTER 5: CHARACTERIZATION OF THE BONDED COMPOSITE DYNAMIC BEHAVIOR UNDER LASER SHOCK - DEVELOPMENT OF THE LASER SHOCK WAVE ADHESION TEST

Introduction **212**

Part 1: Description of the bonded samples and experimental procedure **212**

1 Bonded samples and weak bonds **212**

2 Experimental procedure **217**

Part 2: Laser shock on symmetrical bonded composite: damage investigations, discrimination of weak bonds, and optimization issue **218**

1 Laser shocks **218**

2 Laser shock induced damage investigations on reference bonded samples **219**

3 Laser shock induced damage investigations on weak bonds **222**

4 Synthesis and discussion about LASAT discrimination potential **227**

4.1 Discrimination of weak bonds 227
4.2 Synthesis 229

Part 3: Laser shock on ENCOMB scenarios to qualify the mechanical adhesion of the bond under different contamination degrees **231**

1 Laser shocks **231**

2 About laser induced damage in non-symmetrical bonded composite **232**

2.1 Laser shock induced damage in Reference sample 232
2.2 Laser shock induced damage in release agent contaminated samples 233
2.3 Laser shock induced damage in moisture contaminated samples 233
2.4 Comparison between release agent contaminant and moisture contamination 235

3 Determination of the debonding and damage thresholds by use of post-mortem analysis **236**

3.1 Composite damage threshold for the reference sample 236
3.2 Damage thresholds for the release agent contaminated sample 239
3.3 Damage thresholds for the moisture contaminated samples 245

Part 4: Bonded composite modeling **249**

1 Time resolved experimental measurements **249**

2 Bonded composite modeling, and low intensity validation **251**

3 Numerical simulation at low intensity and results discussion **251**

4 Numerical simulation at mid intensity and in case of spallation **256**

Conclusions & synthesis **258**

References **259**

Introduction

The two previous chapters have set the basis of the bonded composite analysis under laser shock loading. So far, the damage resulting from laser shock propagation into CFRP composite is understood and quantified. The laser shock induced damage into bonded composite should not be very different from the one occurring in CFRP, and its description would need the elements given in Chapter 3. Moreover, the laser shock dynamic response of CFRP is now correctly modeled thanks to the investigation conducted in Chapter 4. These preliminary studies to bonded composite modeling have thus been performed, and can directly be used for deeper investigations.

For these reasons, this chapter is organized in two main steps: the first one concerns the experimental results obtained on different bonded CFRP, when the second one deals with numerical modeling. The first part gives some recalls and some complementary elements on the bonded material tested, divided in two categories namely symmetrical bonds and non-symmetrical bonds. Each category has its own reference sample, and different contaminated samples. Experimental results obtained on these two types of material are respectively given in Part 2 and Part 3. The laser shock induced damage is investigated thanks to the techniques presented in the chapter 3, and ultrasound method presented in Chapter 2. For all the samples, the damage thresholds are particularly studied in comparison with the classic mechanical testing. The correlation with the contamination degree is aimed. These investigations rely on post-mortem analyses, but time resolved measurements are also presented for the study of bonded composite dynamic response. Finally, the laser shock phenomenon on bonded composite is numerically investigated, on the basis of previous models.

Speaking of LASAT application, it has to be kept in mind that the technique could be used as a proof test method. The idea is to enable the discrimination of a reference bond from a weak bond, but nothing prevents from investigating deeper the threshold of the different weak bonds. In the industrial application, the reference bond should not be broken for the test to be reliable. Nevertheless, in the development phase currently running, every sample should be broken to determine the damage threshold of each material. To be sure that a given material will not break for a given shock, it is first necessary to know the shock parameters which induce damage in this material. For these reasons, all the samples tested in this chapter have been progressively loaded in order to determine their damage threshold. The NDT aspect of the test is yet not forgotten.

Part 1: Description of the bonded samples and experimental procedure

1 Bonded samples and weak bonds

Bonded composite samples investigated in this work have been briefly presented in Chapter 1, part 3. In this part, all the tested samples are presented. They are divided in two main categories: symmetrical bonds, and non-symmetrical bonds. The symmetry is defined relatively to the bond line. In symmetrical bonded composite sample, the composite thickness and lay-ups are the same on the two bond sides (see in Table 5.1). The symmetrical bonded CFRP category contains 5 different bonded samples, corresponding to 5 different bonding qualities. Two of them were produced and distributed in the frame of ENCOMB project (IFAM for contamination, EADS Cassidian for production

and characterization, University of Patras for mechanical testing). The three other samples are coming from our Airbus partner, who took in charge the contamination, production, characterization and mechanical testing. The different bonding strengths have been obtained thanks to different contaminations, always realized on one composite part. A short description is given below, and summarized in Table 5.1.

- ES1: Reference sample from ENCOMB project. It is a bonded composite made of two 1.5 mm thick cross-ply T700/M21 laminates, [0°,0°,90°,90°,0°,0°]. The composite surface was untreated, meaning that no contamination was applied. Nevertheless, composite parts were cleaned and prepared according to Airbus standards, which enabled to get a reference sample. The correct bond mechanical strength was checked by GIC testing in University of Patras (see Table 5.1).

- ES2: First ENCOMB contaminated sample. It is a bonded composite made of two 1.5 mm thick cross-ply T700/M21 laminates, [0°,0°,90°,90°,0°,0°]. One of the two composite parts was treated with a release agent (Frekote) solution in order to pollute one of its surfaces. The amount of Si remaining on the surface after the contamination process has been characterized by IFAM thanks to XPS analysis about 4 at%. Consequently, the mechanical strength is reduced (see Table 5.1).

- LA: reference from Airbus set of samples. It is a bonded composite made of two 1.5 mm thick cross-ply T800/M21 laminates, [0°,0°,90°,90°,0°,0°]. The composite surface was untreated, meaning that no contamination was applied. Nevertheless, the mechanical strength measured by GIC testing is much lower than the one measured on ENCOMB reference sample. The curing cycles were really close from one sample to another, and the slight difference in the pre-impregnated laminates could not explain this significant difference. According to Airbus, the composite laminates were reaching their lifetime end date, which could be a reason for this low value. The validity of GIC results can also be questioned.

- LE: SRB Peel-ply contaminated Airbus sample. It is a bonded composite made of two 1.5 mm thick cross-ply T800/M21 laminates, [0°,0°,90°,90°,0°,0°]. One of the two composite parts was treated by use of a contaminated peel-ply, similarly to what can be done with the release agent solution. It creates a coating of Si and F on one of the composite part surface. This contamination is responsible for low adhesion, as shown by the GIC values. It has been characterized by XPS about 3 at% of Si and 28.7 at% of F, which are both considered as responsible for low adhesion.

- LB: Release agent contaminated Airbus sample. It is a bonded composite made of two 1.5 mm thick cross-ply T800/M21 laminates, [0°,0°,90°,90°,0°,0°]. One of the two composite parts was treated by use of release agent solution, as it was the case for ES2. Nevertheless, the solution is less diluted for this LB sample, which leads to a high Si content on the composite part surface (18 at% of Si). Consequently, the bonding strength characterized by GIC mechanical testing is really low.

The GIC values of this first set of samples are given with their uncertainties in Figure 5.1. They were obtained thanks to the work of University of Patras as ENCOMB is concerned, and Airbus measurements for the other samples [1]. This graphic representation enables to show the progressive degradation of the bonding mechanical quality from one sample to another.

Ref	Geometry sketch	Contaminations	GIC [J/m²]	Source
Symmetrical bonds				
ES1	T700/M21 laminates FM300 bond 130 µm 2 × 0° 2 × 90° 2 × 0° 1.5 mm	Untreated (reference)	1234	ENCOMB – set1
ES2	2 × 0° 2 × 90° 2 × 0° 1.5 mm	Release agent (Frekote, 4 at% of Si)	373	ENCOMB – Set1
LA	T800/M21 laminates FM300 bond 130 µm 2 × 0° 2 × 90° 2 × 0° 1.5 mm	Untreated (Airbus reference)	298	Airbus
LE	2 × 0° 2 × 90° 2 × 0° 1.5 mm	Hydraulic fluid (SRB, 3 at% of Si, 28.7 at% of F)	66	Airbus
LB		Release Agent (Frekote, 18.3 at% of Si)	21	Airbus
Non – symmetrical bonds				
UT		Untreated (reference)	1073	ENCOMB – set2
RE	T700/M21 laminates FM300 bond 130 µm 2 × 0° 2 × 90° 2 × 0° 1.5 mm 2 × 0° 2 × 90° 2 × 0° 2 × 90° 2 × 0° 2.5 mm	**Release agent**		ENCOMB – set2
		RE1: 2.2 at% of Si	1063	
		RE2: 6.7 at% of Si	439	
		RE3: 8.4 at% of Si	61	
		RE4: 10.5 at% of Si	40.4	
MO		**Moisture**		ENCOMB – set2
		MO1: 0.46 wt%	1130	
		MO2: 0.84 wt%	914	
		MO3: 1.19 wt%	795	
		MO4: 1.29 wt%	885	

Table 5.1, Summary of all the bonded samples used in this work

The second set of samples corresponds to ENCOMB set 2, and contains non-symmetrical samples. They were produced and distributed in the frame of ENCOMB project (IFAM for contamination, EADS Cassidian for production and characterization, University of Patras for mechanical testing). One CFRP part is thicker than the other one. Note that for this set of samples, the contaminated composite, if any, is always the thinnest. This second set of sample has benefited from the first set of sample investigations. Especially, the knowledge obtained on the release agent solution has enabled to better control the contamination degree on the composite samples. The different bonding strengths have been obtained thanks to different contaminations, namely release agent (RE) and moisture (MO), and different degrees of each contamination. A short description is given below, and summarized in Table 5.1.

- UT: Reference sample for ENCOMB set 2. It is a bonded composite made of two cross-ply T700/M21 laminates, [0°,0°,90°,90°,0°,0°] (1.5 mm) for the thin composite, and [0°,0°,90°,90°,0°,0°, 90°, 90°,0°,0°] (2.5 mm) for the thick composite. This sample as been produced using Airbus standards, and can be thus considered as a reference. The bond mechanical strength was checked by GIC testing in University of Patras (see Table 5.1).

- Release agent samples (RE). These samples were produced using the exact same architecture and lay-ups than the previous sample UT. Four different contamination degrees were realized, in four different samples respectively named from RE1 to RE4 in order to follow the contamination degree increase. These contaminations have been performed by using different concentrated release agent solution. The amount of Si present on the composite part after contamination process is given in Table 5.1. The GIC tests realized on these samples gave results in good agreement with the contamination degree as shown in Figure 5.2 [2]. Note that only the first contamination degree cannot be discriminated from the reference sample.

- Moisture samples (MO). These samples were produced using the exact same architecture and lay-ups than the previous sample UT. Four different contamination degrees were also produced, in four different samples respectively named from MO1 to MO4 in order to follow the contamination degree increase. As explained in the first chapter, the contamination is done using water diffusion in the composite panel. Different salt saturated solutions using water at 70°C are used. The mass uptake is used to discriminate the different levels of contamination. The GIC test results obtained by University of Patras are summarized in Figure 5.3 [2]. It can be observed from this Figure that the correlation between the contamination degree (linked to the moisture amount), and the mechanical strength of the bonded sample is not obvious. The lowest contamination degree does not seem to modify the bonding quality, when the three following degrees do, but not with a trend corresponding to these degrees. No clear explanation has been found so far in the ENCOMB consortium.

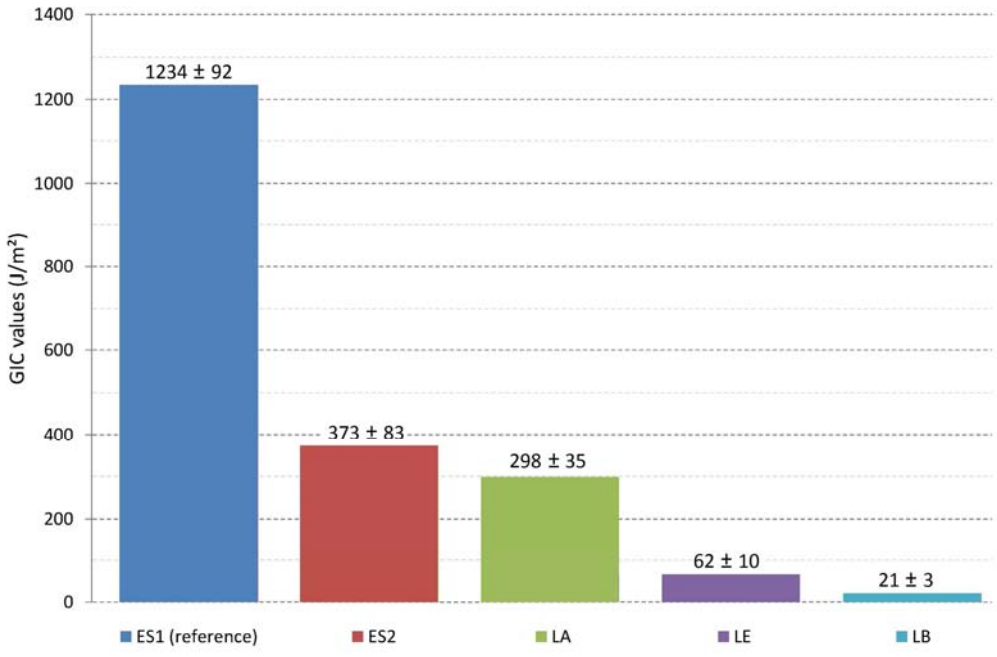

Figure 5.1, GIC mechanical testing results in case of symmetrical bonded CFRP [1]

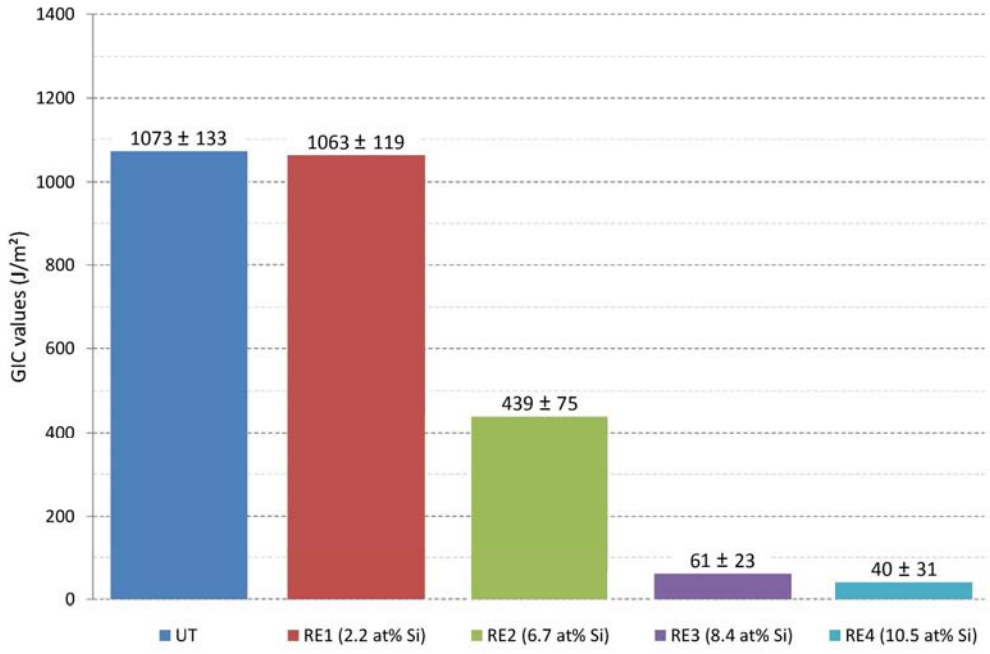

Figure 5.2, GIC mechanical testing results in case of non-symmetrical bonded CFRP – Release Agent [2]

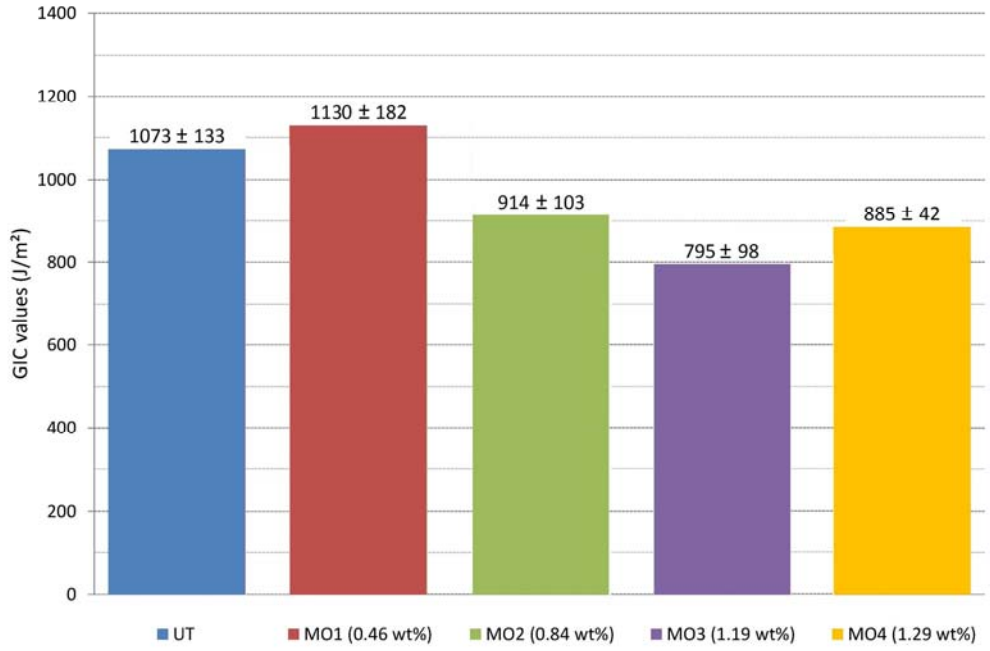

Figure 5.3, GIC mechanical testing results in case of non-symmetrical bonded CFRP – Moisture [2]

All the samples have been characterized using conventional ultrasounds before dissemination to ENCOMB partners. These measurements have shown no obvious defect such as detectable voids or delamination which could have occurred during the sample production [1-2]. Conventional ultrasounds were also not able to detect the different contaminations. Recalling Chapter 1, this was one of the conditions to consider the bonded samples as weak bonds. It is assumed that nothing happened to the samples during transportation. Microtomography was also used especially for evaluating the bond porosity of ENCOMB samples. On the first set of sample, porosity has been measured to a low level, and non-uniformly disseminated in the sample [1]. This problem was corrected for the second set of sample. Indeed, reference and release agent samples microtomographies showed no pores at all, except for the highest contamination degree [1-2].

Measurements on moisture samples have shown interesting results. The degree of porosity has been evaluated on two different regions of interest (ROI). One was taken close to the sample edge (Inboard), where the porosity could be higher due to curing process in vacuum bag. The second one was taken 15 mm far from the edges, in the middle of the measured sample (Outboard). Results are given in Table 5.2.

Samples	ROI	Pore content
MO1 (0.46 wt%)	Inboard	3.7 %
	Outboard	9.0 %
MO2 (0.84 wt%)	Inboard	3.4 %
	Outboard	38.9 %
MO3 (1.19 wt%)	Inboard	6.2%
	Outboard	11.6%
MO4 (1.29 wt%)	Inboard	5.4 %
	Outboard	22.4 %

Table 5.2, Summary of the porosity Microtomography measurements for Moisture bonded samples [2]

These results obviously not follow any particular trend, even if porosity content is quite significant compared to the other bonded samples. It could be assumed that this porosity could come from the moisture contaminant in the CFRP. Indeed, moisture is present inside the composite before curing. During the curing, the temperature increase can lead to phase transition, increasing the volume of water and leading to vapor formation. These bubbles can be trapped in the bond line, and finally create porosity. For this reason, porosity is not considered as resulting from a manufacturing problem in case of moisture sample, but as a direct effect of contamination. It could have an influence on the bonding strength, but this influence is also considered to be an effect of contamination.

2 Experimental procedure

The same experimental approach has been used on the two different sets of samples. It is made of three main steps (see in Figure 5.4). These investigation goals were to determine for each contamination scenario the damage threshold of the bond. The laser shocks were performed in a water confinement configuration, using Config-PPRIME-1. An aluminum painting sacrificial layer was also used on the sample front face (irradiated face) in order to produce more reliable pressure loads as previously explained. Note that no time resolved measurements have been performed to save time, because investigating 8 different samples is already a long task and VISAR requires time costing adjustments. Nevertheless, post shock analyses were performed to determine the damage and debonding thresholds. After the laser shock experiment, samples are recovered from the experimental room to be controlled. For that, three post-mortem techniques were used, selected on the basis of results previously obtained on composite materials: interferometric confocal microscopy (ICM), ultrasound or laser ultrasound inspection, and cross section observation. All the data gathered thanks to these techniques have been finally analysed to quantify the damage induced by laser shock on bonded composite and to determine the interesting thresholds. X-Rays have been performed, but it can only be used to have a global idea of the inside damage resulting from laser shock. Indeed, some problems were met to determine the depth of the induced damage. It was thus hard to know if a debonding or a delamination was observed for a given sample, both being usually observed.

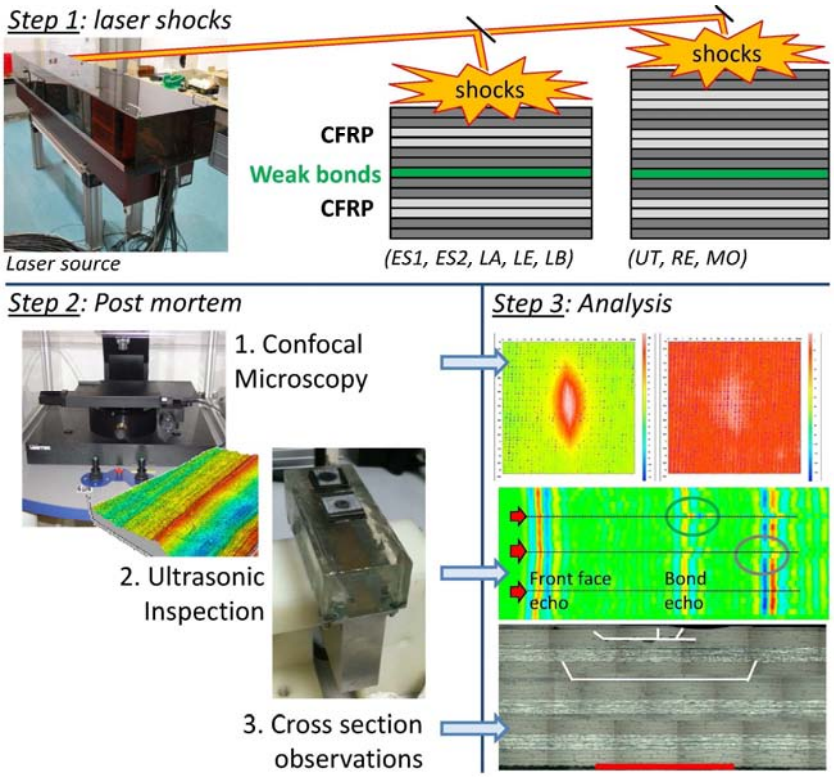

Figure 5.4, Three-step experimental procedure to investigate the damage threshold of bonded composite: Laser shocks, Post-mortem control, Analysis of the measurements

Part 2: Laser shock on symmetrical bonded composite: damage investigations, discrimination of weak bonds, and optimization issue

1 Laser shocks

Samples	Laser energy (J)	Pulse duration (ns)	Impact diameter (mm)	Intensity (GW/cm²)
ES1-4	7.60 ± 0.1	27.20 ± 0.2	4 ± 0.1	2.22 ± 0.20
ES1-5	5.66 ± 0.1	29.07 ± 0.2	4 ± 0.1	1.55 ± 0.15
LA-1	7.75 ± 0.1	26.66 ± 0.2	4 ± 0.1	2.31 ± 0.10
LA-2	5.36 ± 0.1	25.41 ± 0.2	4 ± 0.1	1.78 ± 0.17
LA-3	3.73 ± 0.1	27.85 ± 0.2	4 ± 0.1	1.06 ± 0.10
ES2-1	14.10 ± 0.1	26.31± 0.2	4 ± 0.1	4.51 ± 0.45
ES2-2	6.56 ± 0.1	23.91 ± 0.2	4 ± 0.1	2.18 ± 0.22
ES2-3	5.81 ± 0.1	26.09 ± 0.2	4 ± 0.1	1.77 ± 0.17
LB-1	7.90 ± 0.1	24.67 ± 0.2	4 ± 0.1	2.55 ± 0.20
LB-2	3.28 ± 0.1	26.66 ± 0.2	4 ± 0.1	0.98 ± 0.10
LB-3	0.70 ± 0.1	25.97 ± 0.2	4 ± 0.1	0.21 ± 0.02
LE-1	7.60 ± 0.1	26.98 ± 0.2	4 ± 0.1	2,24 ± 0.20
LE-2	3.28 ± 0.1	24.17 ± 0.2	4 ± 0.1	1.08 ± 0.10
LE-3	1.64 ± 0.1	27.33 ± 0.2	4 ± 0.1	0.48 ± 0.05

Table 5.3, Laser shock parameters used for the symmetrical bonded samples investigations

In this section, the results obtained on the first set of symmetrical bonded samples are presented. Between 5 (LA, LB, LE) and 7 (ES1 and ES2) various energy laser pulses were produced on the different samples, which represents about 30 shocks. Before testing, samples are extracted from bonded plates by diamond saw cuts. Their use size was about 1 cm². The back face was slightly

polished just to remove the surface roughness and enable better measurements by confocal microscopy. After the laser shocks, each sample is analyzed using the three different post-mortem techniques described in Figure 5.4. It represents a lot of data that is why a selection has been made for the results presented in the following sections. The laser shock parameters are given in Table 5.3. In the following section, the samples are referring to this table by their name, and the corresponding laser intensity used to test it.

2 Laser shock induced damage investigations on reference bonded samples

In this section, the two bonded sample references are thus investigated in order to determine their damage threshold to laser shocks. A representative overview of damage resulting from laser shock on a correctly bonded composite is given in Figure 5.5. An example of ICM measurement is given in Figure 5.6. Note that in this work, micrographies and ICM measurements are presented according to the following codes. The cross sections were performed perpendicularly to the 0° direction. The damage observed was enhanced using white lines. The ICM measurement gives an image of the sample out-of-plane residual back face deformation. The z deformation height is represented by the colour scale, where purple is referring to non-measured points (due to roughness or out of range height). The samples presented in Figure 5.5 and 5.6 are extracted from the ES1 reference series. Three different observations can be made:

i) *Delamination between the plies:* they are initiated by the high tensile stresses generated by the propagation of the laser induced shock wave inside the composite. Indeed, with the laser source used, the crossing of release waves responsible for the high tensile loading occurs close to the sample back face. On the micrography (see in Figure 5.5), it can be observed that the delaminations occurred between the 0° plies, and also between 90° and 0° plies. The delamination width in the y direction more or less corresponds to the focused diameter of the laser spot. Thanks to the residual back face deformation measurement by ICM, it has been evidenced that these delaminations mainly propagated in the 0° direction (x direction). Indeed, this delamination initiated by the laser loading leads to an elliptical blister oriented in the 0° direction (see ICM measurement in Figure5.6). In these experiments, the laser irradiation did not yield to spallation of the sample because the stresses were not high enough. That is why an elliptical blister can be observed by ICM at the back face.

ii) *Transverse matrix cracks, through the ply thicknesses*: they can be observed on the micrography (Figure 5.5). These cracks are due to the combination bending/buckling initiated by the laser loading, and associated with the main delaminations. As explained before, the experimental conditions also enhance a bending loading which is different from the shock wave loading, but also damaging for the bonded composite.

iii) *No debonding of the bonded interface*: It can be noticed that no debonding has occurred because of the laser shock wave propagation through the bonded composite target. Nevertheless, it is hard to have an idea of the stresses level when reaching the bond. Indeed, damage has occurred in the composite part as explained in i). As it has been explained in Chapter 3 and 4, the incubation time necessary to spallation enables the tensile stresses to continue propagating backward through the sample. Consequently, the bond is loaded in tension, but the tensile stresses would depend from too many parameters: material, damage initiation and propagation, initial pressure… Same kind of damage has been observed on all the ES1 shock samples. The highest intensity shock has been performed about 4 GW/cm². No debonding has been observed. This is good news, since these samples are references, and should represent correct bonds. These bonds can be qualified as strong bonds.

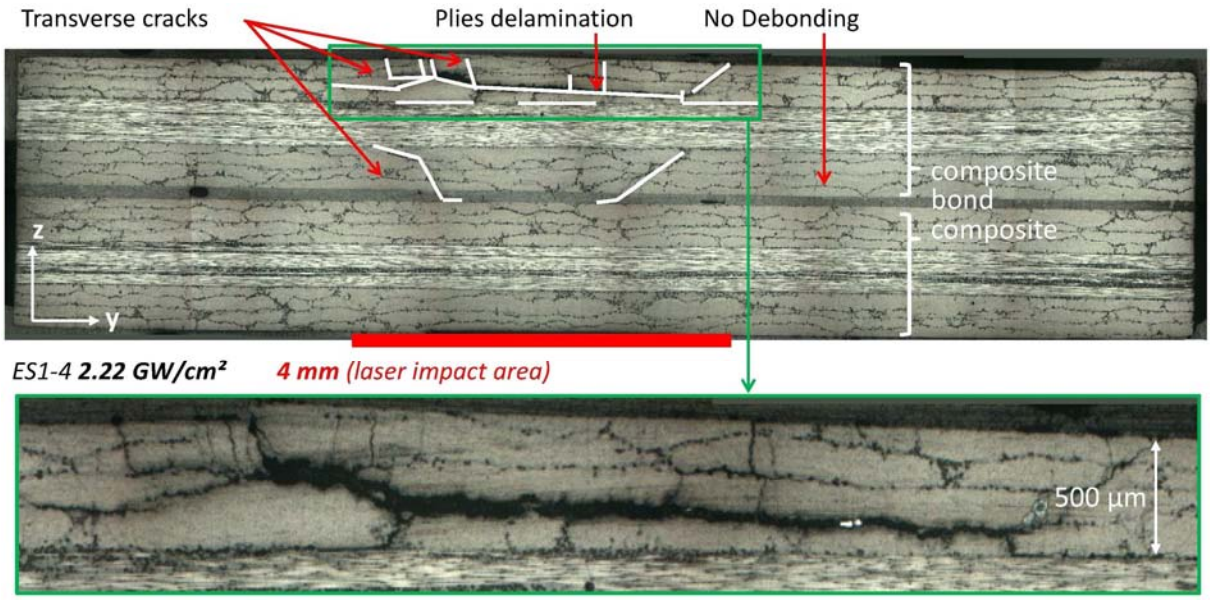

Figure 5.5, Damage resulting from the laser shock wave propagation into a correctly bonded T700/M21 composite observed by cross section microscopy (I = 2.22 GW/cm², water confinement)

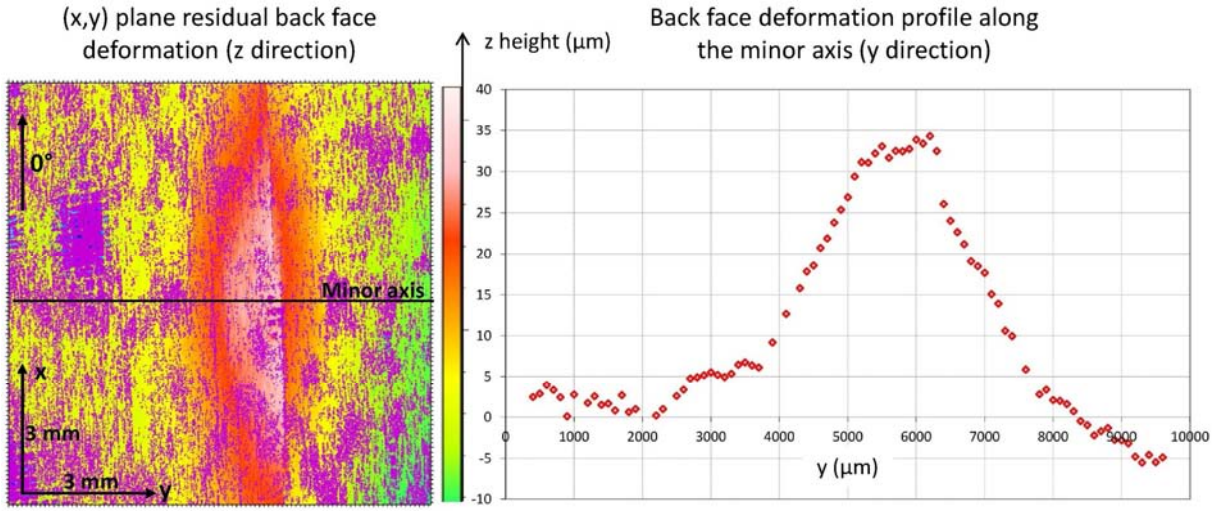

Figure 5.6, Damage resulting from the laser shock wave propagation into a correctly bonded T700/M21 composite observed by ICM (I = 1.55 GW/cm², water confinement)

It can be noticed that the damage resulting from laser shock wave in the bonded CFRP is not really different from what has been observed on thick CFRP in chapter 3 so far. For bonded sample reference, the bond behaves as a composite ply, at least as the damage is concerned. ICM measurements only show the presence of the damage in the back face composite part, and it is hard to get an idea of the bond state by this technique. In order to complete these data, ultrasounds were also used. This technique is closer to an industrial NDT method, and enables to evaluate the bond without cutting and destroying the sample. Two different A-scans are given in Figure 5.7. Looking at the reference signal taken from an unharmed ES1 sample (Figure 5.7-b), three main features can be observed: the front face (FF) echo, the bond echo, and the back face (BF) echo. The front face in ultrasounds corresponds to the location of the probe, but also to the front face as understood in terms of laser shock. These three main features are characteristic of an unharmed sample in terms of amplitude (A) and Time Of Flight (TOF). Note that the gates (blue, green and red in Figure 5.7) enable the analysis of these two parameters, respectively for the front face (blue gate), for the bond (green gate) and for the back face composite (red gate). The bond and composite gates are synchronized on

the front face gate. This will always be the case in this work. A Distance Amplitude Correction (DAC) is also used here, and in this part. This correction is used to compensate the attenuation of the ultrasound wave through the sample thickness. That is why the back face echo amplitude is here close to the one of the front face echo. This reference signal from an unharmed ES1 sample (Figure 5.7-b) can be compared to the A-scan taken on ES1-4 shocked sample (see Figure 5.7-c). The Front face echo is similar to the one obtained on the reference, as it is the case for the bond line echo when compared to the front face echo. Its amplitude and position (corresponding to the TOF) show that nothing has changed compared to the reference case. Nevertheless, the back face echo is different. It is slightly closer to the front face echo (TOF), which traduces delamination. Its amplitude is also lower. This is probably due to transverse cracks, which can considerably reduce the wave amplitude. In this case, ultrasounds were used to show that the bond was not opened by the shock wave propagation, but also revealed the composite back face part damage.

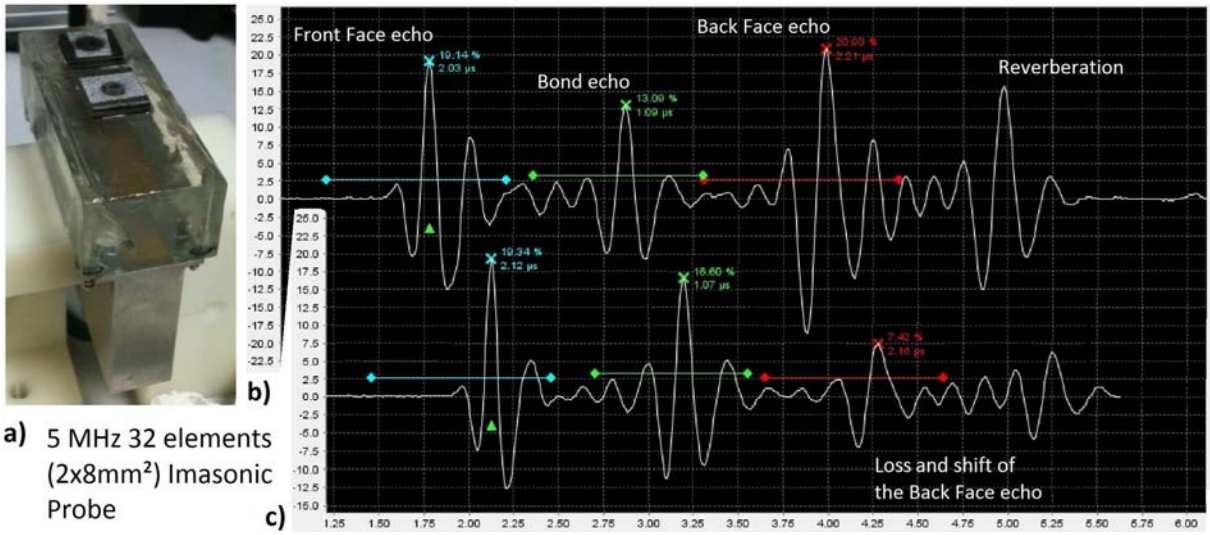

Figure 5.7, Ultrasound testing of ES1 bonded T700/M21 composite a) EADS IW probe used for measurements, b) A-scan signal from unharmed ES1 reference sample, c) A-scan from ES1-4 shocked composite sample (I = 2.22 GW/cm², water confinement)

Several laser shocks with different intensity levels have been performed on the two reference series. As an example, the results from LA samples are presented in Figure 5.8. When the laser intensity is way above the bonded sample damage threshold, the damage induced by the laser shock can be deeper than the bond itself as shown by observation on sample LA-1 and LA-2. In this last case, the slight delamination located in the 0° plies, below the bond, has also been observed by ultrasounds testing (see in Figure 5.8). This result proves that the bond is at least as strong as the composite. Indeed, since the bond is located before the delaminated ply, if considering the tension propagating backward, the level of tensile stresses induced in the bond should be higher than the one induced in the front face composite (using a first simple approach). The damage extents are well correlated to the laser shock intensity, in whatsoever form: delamination width, cracks density, residual back face deformation. Once again, these results are consistent with the previous analyses made of T800/M21 composite samples (back to chapter 3). It can also be noticed that the experimental data gathered by the three different post mortem techniques are fully consistent.

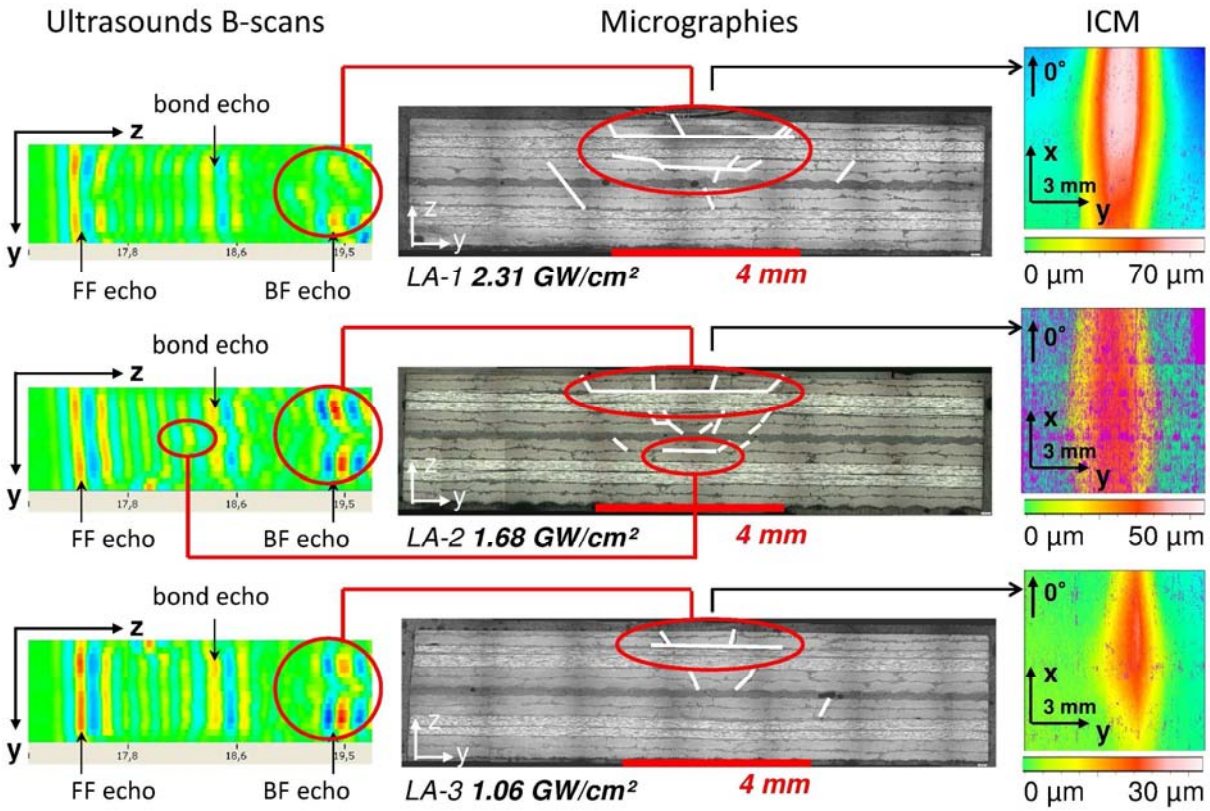

Figure 5.8, Correlation between the laser intensity and the LA reference samples induced damage quantified by ultrasounds, cross-section observation and confocal microscopy

Note that the same kind of damage has been observed in case of the ENCOMB reference ES1. According to GIC results, the bond strength of LA sample should be lower than the one of ES2 sample. Nevertheless, contrary to what can be expected from GIC testing, LA samples behave as ES1 samples, meaning without any bond damage.

3 Laser shock induced damage investigations on weak bonds

Results on the shocked weak symmetrical composite bonds are presented in this section. Following the discussion developed in the previous section, the main damage resulting from the laser shock wave propagation in the weak composite bonds is first described. Representative damage overviews are given in Figure 5.9 for micrography and in Figure 5.10 for confocal microscopy measurements. The sample presented in these Figures is extracted from the LB contaminated series, which means the weakest bond series. Three main types of damage can be observed:

i) *Delamination between the plies* and *ii) Transverse matrix cracks, through the ply thicknesses*: These two damage types are identical to the one described on the reference samples and presented in Figure 5.5 and have the same origin. The measurement of out-of-plane residual deformation by confocal microscopy presented in Figure 5.10 also confirms the delamination propagation in the 0° direction. The profile extracted from the 3D measurements and given in Figure 5.10 completely describes the blister shape along the y axis

iii) *Debonding of the bonded interface*: this debonding was possible thanks to the tensile loading propagating from the back face to the front face after the crossing of release waves. Even if some fracture energy was dissipated inside the composite, enough energy remained to initiate the debonding. This was not the case for the reference samples. For this sample, the adherence was low enough to conduct to a full debonding as shown by Figure 5.9. In the case

of debonding, no clue of a favourite propagation direction was found. Note that the sample being symmetrical, the contaminated composite side was hard to get for all the samples. Nevertheless, based on the previous results obtained on reference, it can be assumed that only the weak interface can be opened by the tensile stresses propagated backward.

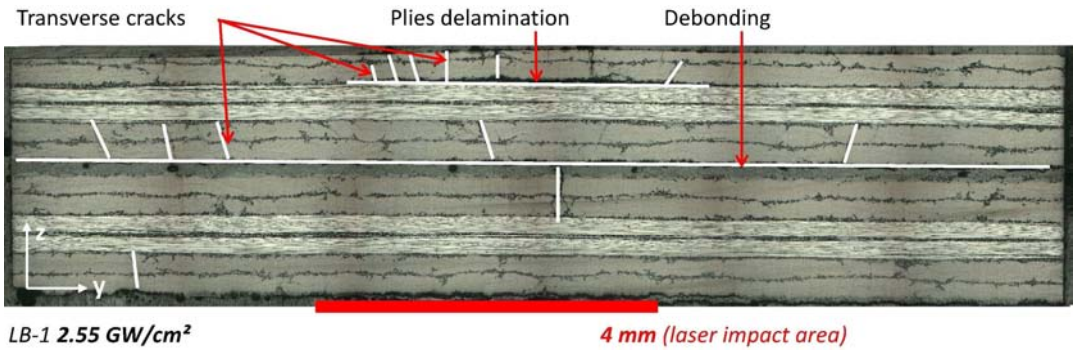

Figure 5.9, Damage resulting from the laser shock wave propagation into a weak T800/M21 cross-ply bonded composite observed by cross section microscopy (I = 2.55 GW/cm², water confinement)

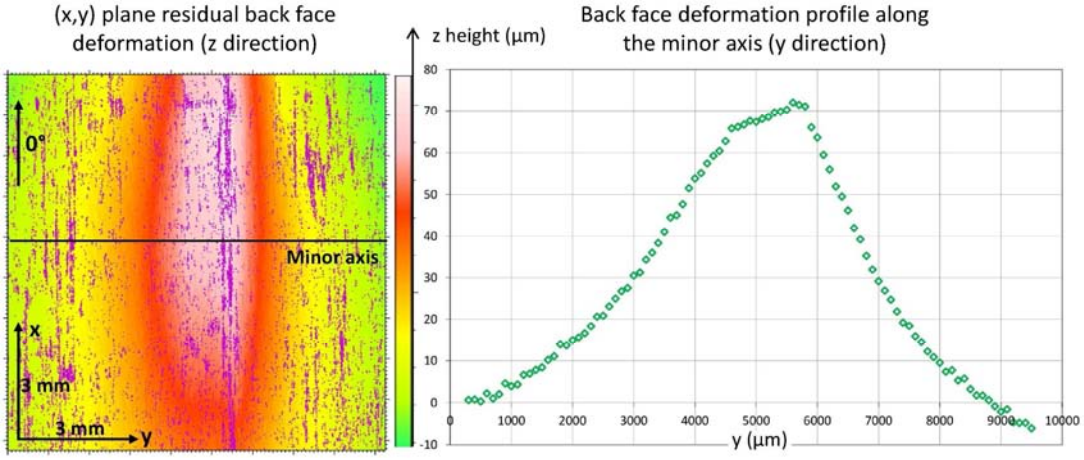

Figure 5.10, Damage resulting from the laser shock wave propagation into a weak T800/M21 cross-ply bonded composite observed by ICM (I = 2.55 GW/cm², water confinement)

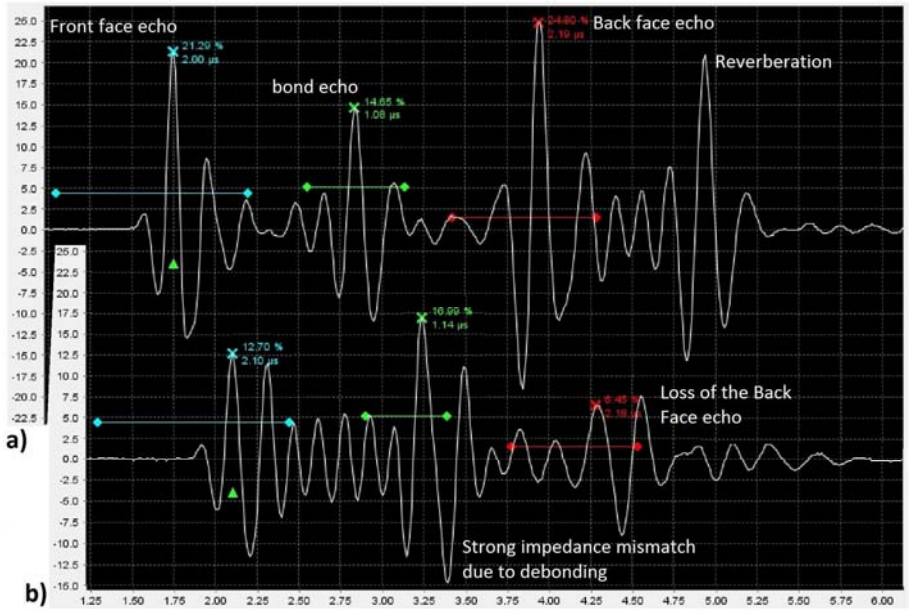

Figure 5.11, Ultrasound testing of LB bonded T800/M21 composite (EADS IW probe), a) A-scan signal from unharmed reference sample, b) A-scan from LB-1 shocked composite sample (I = 2.55 GW/cm²)

It is also interesting to see if the ultrasounds can be used to detect a debonding in this case. Keeping in mind the industrial application, ultrasounds could be used as an easy post mortem technique to characterize the damage resulting from the laser shock propagation. Results on LB-1 sample are given in Figure 5.11. Note that the A-scan reference signal is the same than the one presented in Figure 5.7. If looking to the bond echo of the shocked sample, a small shift in position as well as an increase in amplitude can be observed in comparison with the front face echo in Figure 5.11-b. This is traducing a stronger impedance mismatch than the one created by the presence of the bond, therefore highlighting a debonding. The second element which shows the debonding is the partial loss of the back face echo. This is due to the fact that the ultrasonic waves cannot easily reach the second composite part once the bond is opened. It is thus complicated to get information on the composite back face state in case of debonding.

Like for the reference samples, the damage extent can also be correlated to the laser intensities, for all the contaminated samples (cf Fig. 5.13 to 5.14). The micrographies and confocal microscopy measurements speak for themselves. The ultrasounds are also interesting to discuss. Indeed, ES2-3 and ES2-2 samples both present a debonding, but these two debondings are traduced differently on the B-scan. It can be observed that the bond echo is shifted in case of ES2-3 sample, only along the debonding length. The two non-debonded edges are a step closer to the front face. This is due to the fact that for this sample, the debonding occurred between the bond and the back face composite (second interface from the front face). It changes the impedance mismatch, shifting the maximum amplitude echo deeper in the direction of the back face. This is confirmed by the B-scan obtained in case of sample ES2-2. Indeed, the micrography performed for this sample indicates that the debonding occurred between the bond and the front face composite part. This time, no strong shift can be observed on the corresponding B-scan (see Figure 5.12). The debonding is evidenced by a shift in the amplitude of the bond echo, and the loss of the back face echo. Therefore, the ultrasounds can be used to identify which interface has been opened by the laser shock wave propagation. It also corresponds to the contaminated interface. Finally, in case of the highest laser shock, the damage is more important as shown by the cross section observation. In addition to a strong damage in the back face composite part and the debonding, the front face composite presents also several matrix cracks. This cracks network and the debonding, strongly attenuate the ultrasonic wave. Almost no signal propagates backward to the ultrasound sensor. That is why the B-scan presented in Figure 5.12 shows almost no reflected signal.

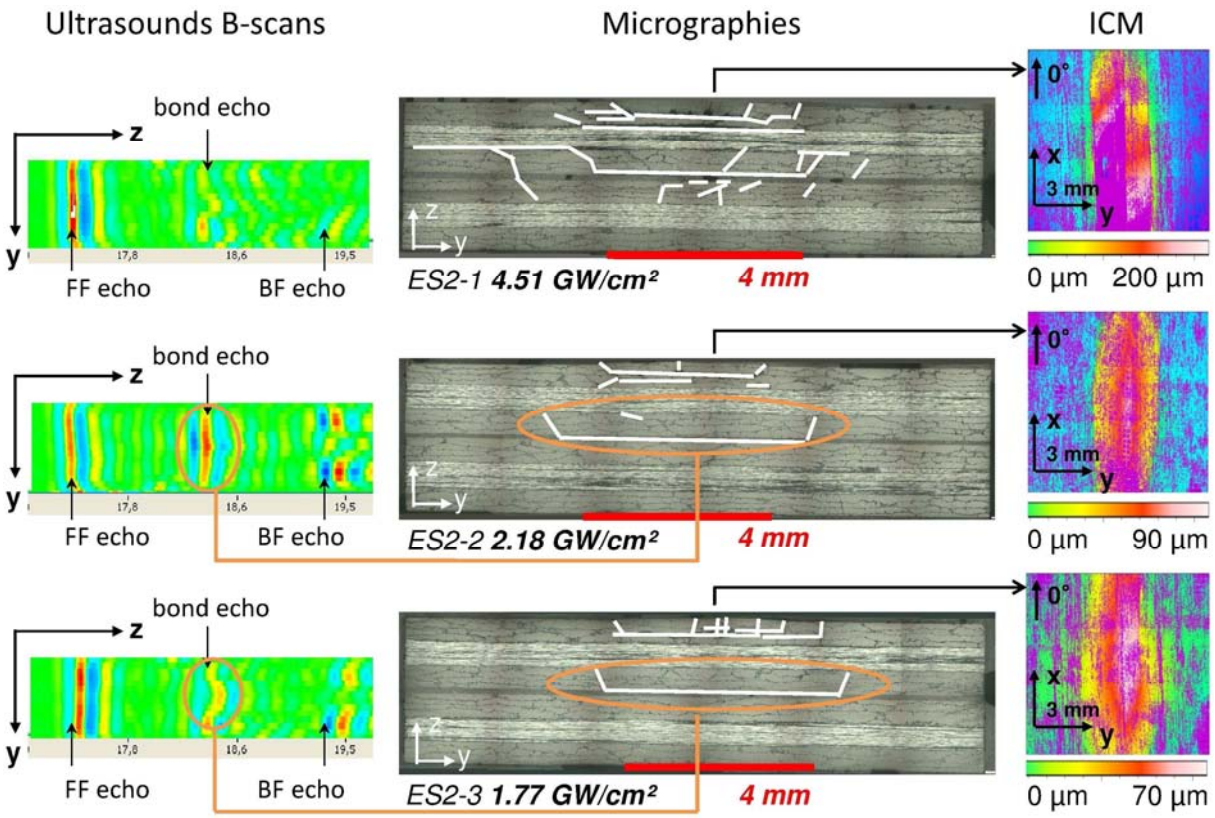

Figure 5.12, Correlation between the laser intensity and the ES2 samples induced damage quantified by cross-section observation, ultrasounds and confocal microscopy

Results obtained in case of LE contamination are summarized in Figure 5.13 with three micrographies and two of the corresponding ICM measurements. These three shocks enable to frame the bonded sample damage thresholds. The correlation between the laser intensity and the inside damage extent has been evidenced thanks to the micrographies (see in Figure 5.13). Indeed, the lowest intense laser shock (LE-3) did not lead to any observable damage, when the highest shocks (LE-1 & LE-2) progressively lead to damage, as previously described in Figure 5.11 and 5.12. The out-of-plane back face deformations captured by ICM also agree with the damage extent observed in the micrographies. As it is shown in Figure 5.13, the lowest shock did not modify the LE-3 samples back face. The sample back face deformation measurement reflects absence of delamination inside the composite thickness. A small blister can be observed on the sample LE-2, which is consistent with the inside delamination revealed by the corresponding micrography. This sample is the most interesting one of this series. Indeed, the composite part of the assembly remained almost unharmed after the laser shock wave propagation (20 µm high for the residual blister measured by ICM). This is due to the fact that the laser intensity used (~1 GW/cm²) was low enough for the induced tensile stresses to be close to the damage threshold of the CFRP composite. Nevertheless, these tensile stresses were high enough to open the bond line of the sample, whose damage threshold was even lower. With the three shock results presented in Figure 5.13, it can be concluded that the damage threshold of the LE bond line tested is between 0.48 GW/cm² and 1.08 GW/cm² and the composite one is probably close to 1.08 GW/cm².

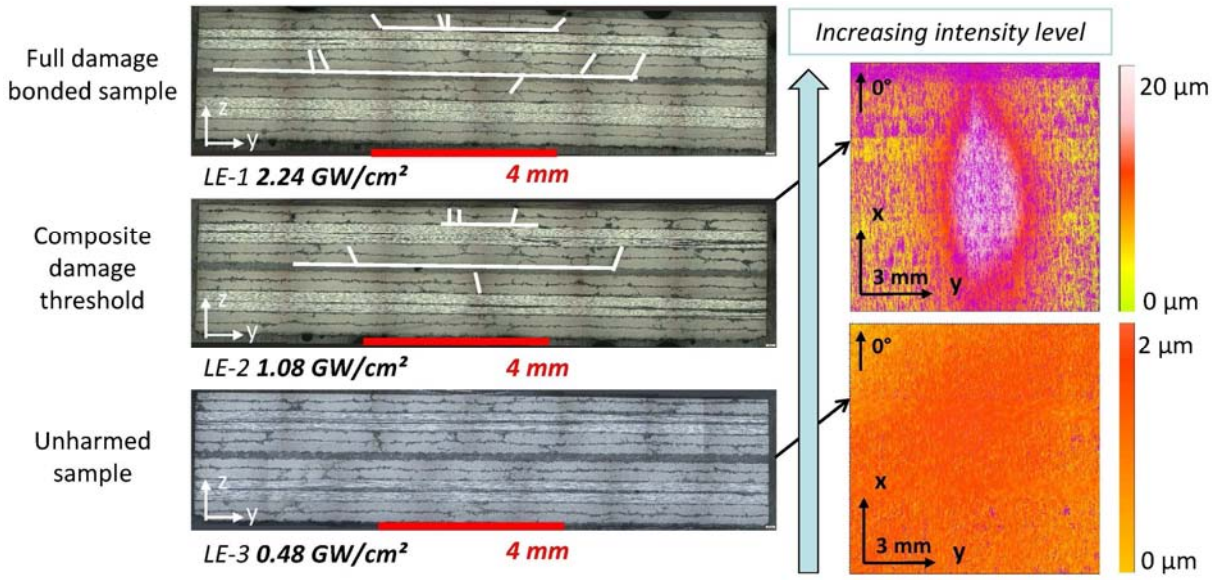

Figure 5.13, Correlation between the laser intensity and the LE samples induced damage quantified by cross-section observation, confocal microscopy – Damage threshold framing

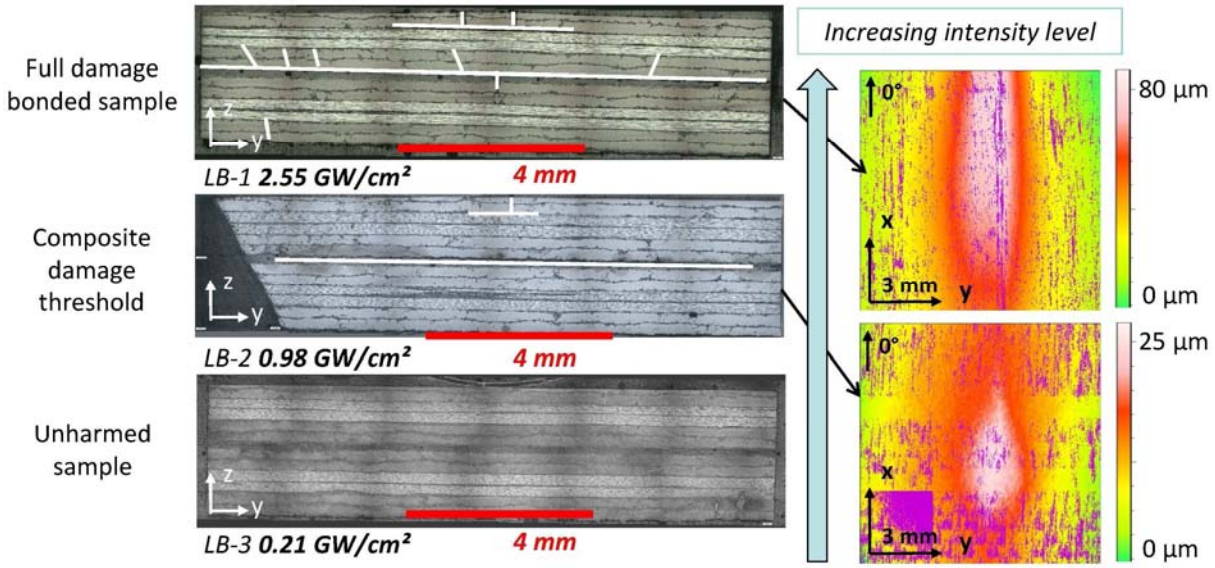

Figure 5.14, Correlation between the laser intensity and the LB samples induced damage quantified by cross-section observation, confocal microscopy – Damage threshold framing

The results obtained in case of LB contamination are summarized in Figure 5.14, and agree with the observations made on samples LE and ES2. The correlation between the laser intensity and the damage extent has also been evidenced in the case of the LB contamination. ICM measurement and micrographies are still consistent (see samples LB-1 and LB-2 in Figure 5.14). The results obtained on the LB samples are really similar from the ones coming from LE samples. Indeed, the LB bond line should have been opened by similar laser shock intensity than in the case of LE sample. According to the results presented in Figure 5.14, the LB bond line damage threshold is in the range [0.21 – 0.98 GW/cm²] which is really close to what has been observed on LE samples. This could be explained by the small difference on the adherence level induced by the contamination. Indeed, even if the contamination process is very different from LB to LE samples, their consequences on the adhesion level have been identified by the G_{IC} testing to be close to each other (see G_{IC} tests in Figure 5.1). Considering the uncertainties on the contamination process as well as the uncertainties on the laser shock produced, and the material properties, it would be difficult so far to distinguish these two

contamination levels. Moreover, the composite damage extent is also really close from LE series to LB series. Indeed, the out-of-plane small blister (about 25 µm high) observed by ICM on the LB-2 sample back face proves that the composite damage threshold is one more time close to 1 GW/cm². This similarity makes sense since the applied contaminations on both LE and LB series have no reason to affect the composite part of the assembly. The laminates being the same (T800/M21), it is logical that the induced laser shock damage is also the same for a given intensity in the different samples. This last point has been clearly evidenced by extracting back face deformation profiles from the ICM measurement, in order to compare the composite part damage extent in both case of LE and LB contamination. The ICM profiles taken at the middle of each blister along the y axis as shown in the previous Figures (5.6, 5.10), are presented in Figure 5.15. The LB-3 and LE-3 samples received the lowest shock in each series, which did not lead to any observable damage. Their back face surfaces are thus completely flat. Regarding the laser uncertainties, it can be considered that LB-1 and LE-1, as well as LB-2 and LE-2 have respectively received the same laser loading (see In Table 5.3). The back face deformations measured are similar in both cases as shown in Figure 5.15. The small differences observed can also be attributed to the experimental dispersion and material inhomogeneities. The reproducibility of the laser technique used is also proved by this result.

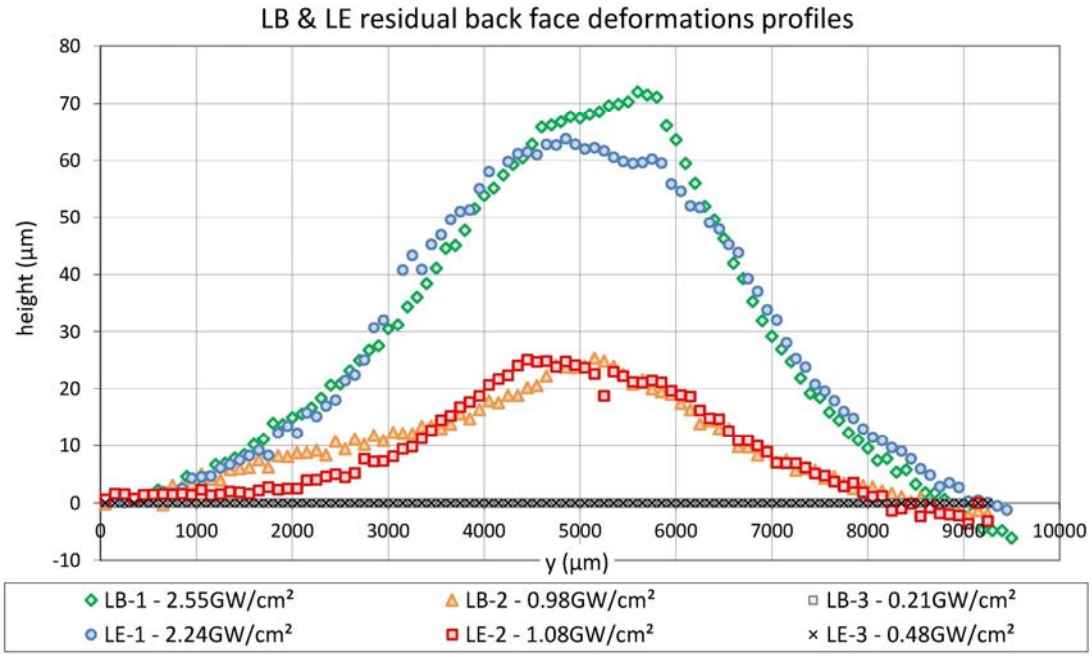

Figure 5.15, Comparison between the residual back face z deformations measured by ICM in case of LE and LB series for three different laser intensities.

4 Synthesis and discussion about LASAT discrimination potential

4.1 Discrimination of weak bonds

Firstly, Airbus samples can be discussed. In Figure 5.16, the shocked reference sample LA-1 is presented as well as the shocked weak bond samples LB-1 and LE-1. Considering the experimental dispersion, it can be considered that the same laser shocks were performed on each sample (at about 2.3 GW/cm²). In the case of the reference bond, the laser shock propagation did not lead to a debonding whereas the same shock induces the damage in the weak bonds presented. The potential of the laser technique to discriminate weak bonds from correct bonds is proved by this result. Nevertheless, in each case, the composite part of the assembly on the back side was delaminated by

the high tensile stresses. This observation is confirmed by the ICM measurements also presented in Figure 5.16. Indeed, the back face z deformations measured on the three samples are really close to each other since the composite damage are also close to each other. The laser parameters are in this case not adapted to the material tested. Indeed, the composite damage is due to the fact that the maximum of tensile stress is generated close to the sample back face. These results thus indicate that the development of the laser adhesion test requires optimisation of the laser parameters. Once the laser parameters will be optimized, ICM may provide an evidence of debonding by significantly different back face z deformation profiles which is not the case so far. It also raised the question of debonding detection which is an important aspect of the laser shock adhesion test. The back face measurements by ICM only reveal the composite damage. Therefore, another diagnostic should be used to detect the debonding. Ultrasounds could be this solution, as shown in Figure 5.17.

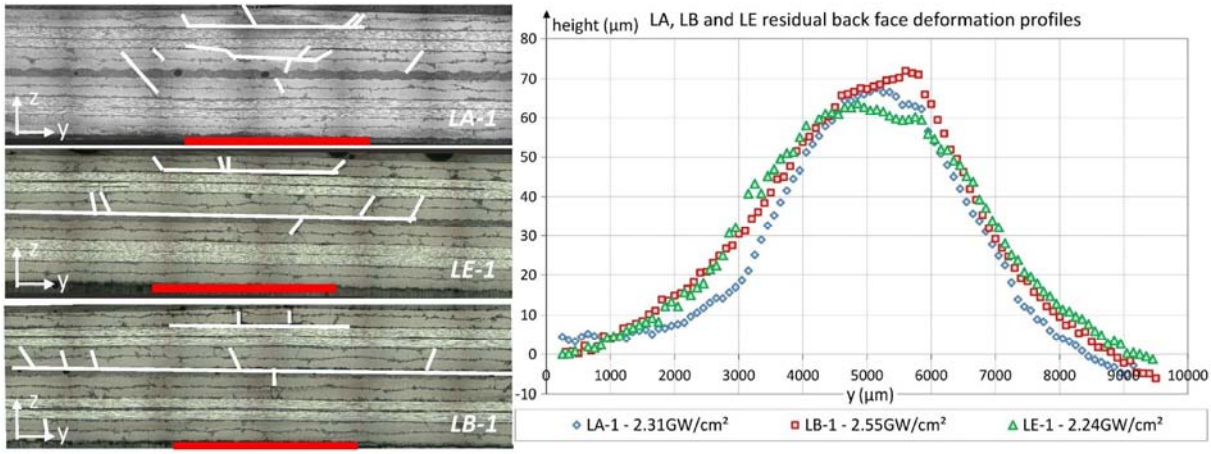

Figure 5.16, Comparison between a correctly bonded assembly (LA, T800/M21) and two weak bond samples (LB and LE) by use of cross section observations and ICM measurements

In Figure 5.17, results from ES2 series are compared. Each presented sample is described by a cross section observation and its corresponding B-scan measurement. Note that axes are turning by 90° from micrographies observation to B-scan representation. The first sample to be presented is a ES2 reference sample, meaning that this sample has not been shocked. It is used to get a reference B-scan to compare with the measurement performed on shock samples. The two following samples are respectively a weak ES2 bond, and a strong ES1 bond. Regarding the laser shock uncertainties, it can be considered that the same laser shocks were performed on the two samples. The cross section observations highlight that the bond has been opened in case of ES2 weak bond, but not in case of ES1 reference bond, the composite part damage being similar from one sample to the other. These observations are fully consistent with the one made on the Airbus samples (LA, LE, LB). The ultrasounds measurements presented in Figure 5.17 also enable to discriminate an opened bond from an unharmed bond. Indeed, if first looking to the ES2-2 B-scan in comparison to the reference B-scan, it appears that the bond echo presents a significant shift in amplitude. As previously explained, this traduces a sharp debonding. On the other hand, the ES1-4 B-scan presented in Figure 5.17 presents a bond line echo similar to the bond line echo reference (differences on the front face echoes taken into account). Therefore, ultrasound testing enables in this case to discriminate a debonded sample from an unharmed bond, in a non destructive way. This approach is thus really interesting for the industrial application, and should be coupled with the LASAT technique. In the current development phase, it can be kept in mind that confocal microscopy is efficient to determine the composite part damage threshold, when ultrasounds can be used for the determination of the bond damage threshold. Cross section observation can do both, but is destructive.

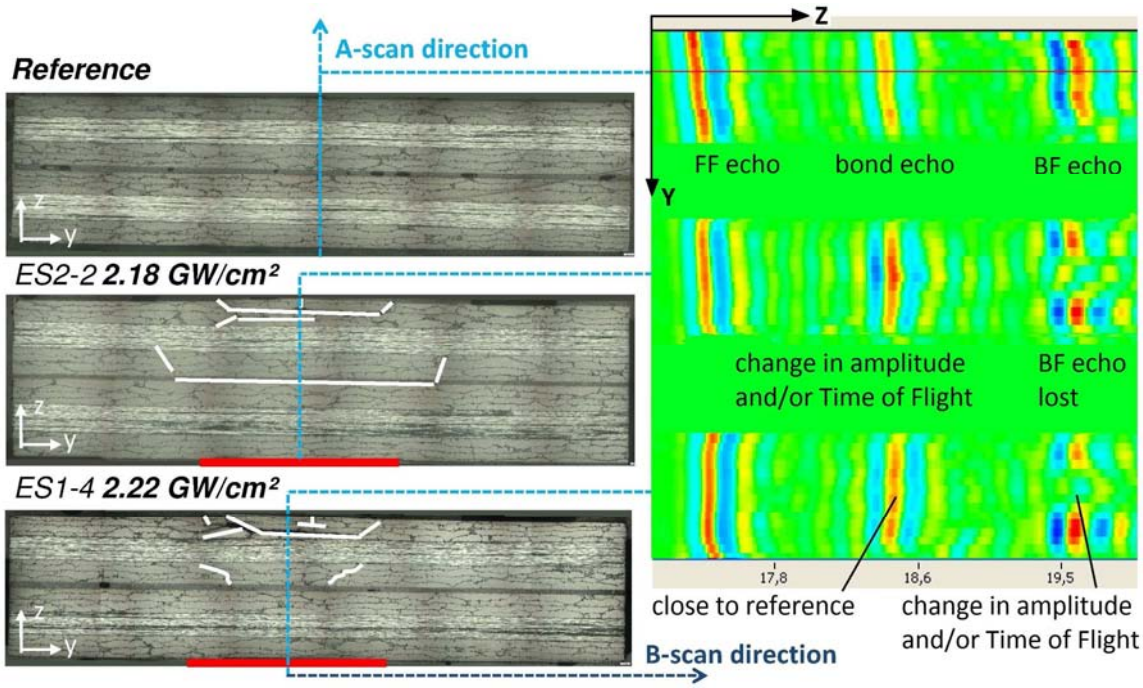

Figure 5.17, Comparison between a reference bonded assembly untouched, a shocked reference bonded assembly (ES1-4) and a shocked weak bond sample (ES2-2) by use of cross section observations and ultrasounds

4.2 Synthesis

The approach used to synthesize the laser shock results in this section is also used in the whole chapter. It is important to keep in mind the laser shock parameters seem not well adapted to the bonded composite samples. For this reason, the laser shock induced damage has always been observed in two different parts: the back face composite, and the bond. The maximum of tensile stresses resulting from the wave propagations occurred in the back face composite, which generally induced damage in this composite. In some cases, the remaining tension propagating backward was high enough to open the bond interface. For the highest intensity cases, the back face composite is often broken. Thus, a mixed damage is generally observed, at the bond interface and in the back face composite. For this set of samples, 30 laser shocks were performed, controlled and analysed using each post mortem technique previously described. The results are synthesized in Figure 5.18. For that, the GIC results are plotted as a first mapping of the sample bond strength (taken from Figure 5.1). The GIC failure energies determined by University of Patras and Airbus are represented using plain colour strips and are referred by the left axis. The two references and the three weak bonds are plotted. On these colour strips, two thinner strips are added. The grey one always corresponds to the assembly composite part (back face). The green always refers to the bond interface. These strips are used to show the damage threshold of the laser loading, and are quantified by the right axis. For both colours, the hashed strips represent the laser shocks which induced damage in the composite and/or the bond interface respectively. Note that the laser shocks above the lower intensity leading to damage are considered to result in damage. The plain strips correspond to the laser shock which let the samples unharmed, in the composite and/or in the bond respectively. Note that the laser shocks performed below the highest intensity shock letting the sample unharmed are also considered to let the sample unharmed. The space in between the plain and hashed strips therefore represents the range in which the damage threshold is included. It does not represent the uncertainties, because only 5 or 7 levels of energy were tested per samples. Nevertheless, the uncertainty on the laser intensity has been evaluated around 15%.

In Figure 5.18 results, it clearly appears that some data are missing to conclude properly. Indeed, too few shocks were performed between 0 and 2 GW/cm², range in which all the damage thresholds seem to be located. Moreover, unharmed sample after laser shock results were not obtained for the ES1 and ES2, which prevents from determining correctly the composite part damage threshold of this assembly. It is only possible to say that it is below 1 GW/cm². This point has to be kept in mind for the following experiments. Nevertheless, the graph shown in Figure 5.18 confirms the discrimination capability of the LASAT technique, associated with the correct diagnostics. If looking to the green strips, it shows that only the weak bonds have been opened by the laser shock propagation. In other words, ES1 reference and LA reference have been observed as strong. This is in good agreement with GIC testing in case of ES1, but not for LA. Indeed, the GIC value measurement indicated a value below the one of ES2 contaminated sample. This sample presents a bond damage threshold in the range [0.90 – 1.77 GW/cm²]. Therefore, it could have also been expected for LA samples. Back to part 1, the problems mentioned about this sample seem to be confirmed by these results. The GIC value can be questioned regarding this LASAT results.

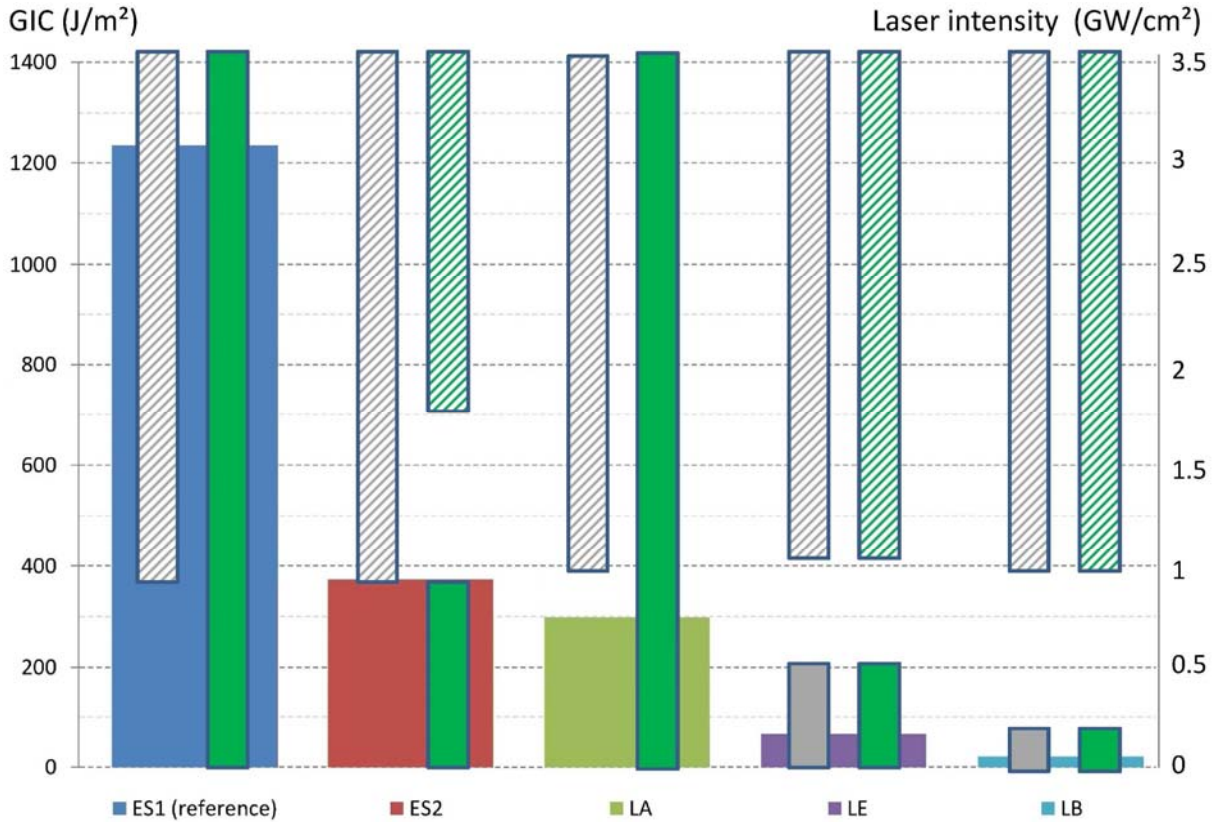

Figure 5.18, Synthesis graph of the shocked symmetrical bonded composite (from ENCOMB and Airbus) – Superposition of the GIC values obtained by mechanical testing and damage thresholds of the bond and the composite part obtained by LASAT

These results show that the weak bonds can be discriminated from their respective references by the LASAT technique. The composite part damage threshold in case of T800/M21 bonded samples can also be framed. Indeed, there is no reason why this threshold would be different from the LA reference to the LE and LB contaminated samples. Therefore, the sharper range can be used to frame this composite part damage threshold. It is reported in Figure 5.19 with its uncertainties, with the damage threshold frames of each weak bonds. Back to Table 5.3, the laser shock uncertainties are generally between 10 and 15 %. Here, it has been taken equal to 15 % in all the cases to maximize

the error, and thus also take into account material variability. This representation enables two conclusions:

- Firstly, it appears that the damage threshold frame of the composite part is identical to the bond damage threshold frame of LE sample. Therefore, these damage thresholds may be close to each other, which indicate that fine optimization would be necessary to locate the maximum of stresses only in the bond line.
- On the other hand, the composite damage threshold frame is different from the bond damage threshold frame of LB sample (see in Figure 5.19). In particular, the lower value is quite interesting. In the worst case, the uncertainties say that the composite part of the assembly would not be broken below 0.4 GW/cm². The LB sample bond could still be opened with intensity above 0.25 GW/cm². Consequently, a shock about 0.3 GW/cm² on the LB bonded composite should open the bond, but let unharmed the composite part. So far, it can be said that only this sample can be tested without any optimization of the laser shock parameters, because composite part damage threshold and debonding threshold are different enough. For the other bonded samples, optimization should be performed.

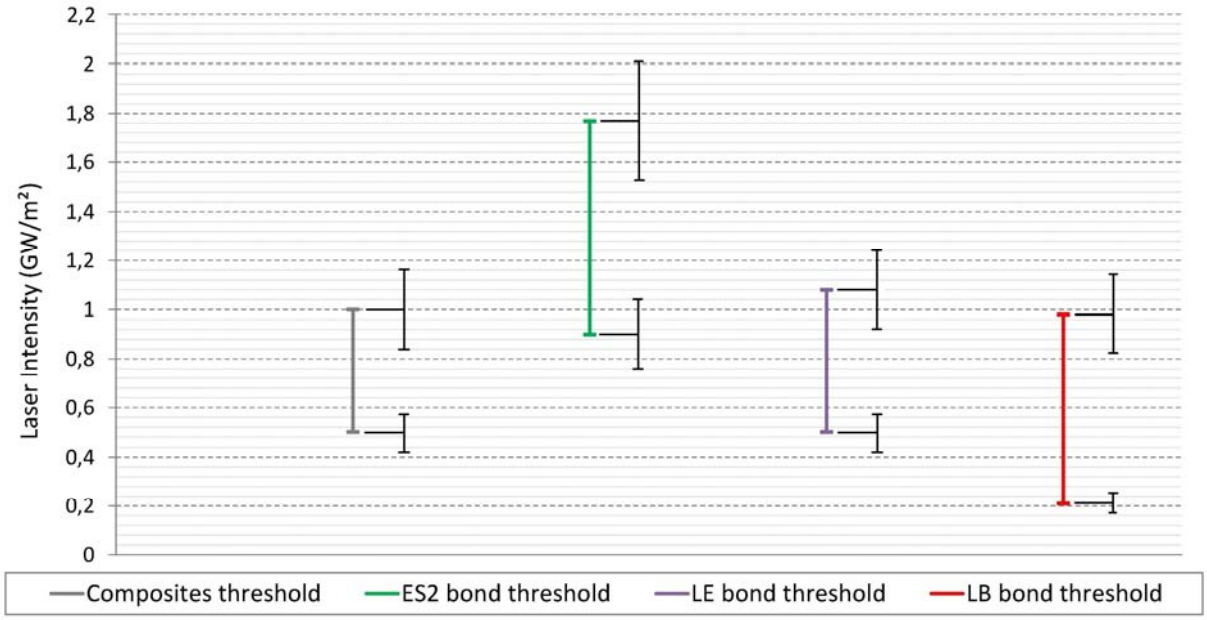

Figure 5.19, LASAT damage threshold of the T800/M21 bonded composite and the different weak bonds reported with their uncertainties

Part 3: Laser shock on ENCOMB scenarios to qualify the mechanical adhesion of the bond under different contamination degrees

1 Laser shocks

In this section, the results obtained on the second set of non-symmetrical bonded samples are presented. It contains the reference plate UT, the release agent contaminated plate RE and the moisture contaminated plate MO. The same experimental protocol has been used for these damage thresholds investigations than the one applied in case of symmetrical bonds. Moreover, thanks to the previous results, the number of shocks has been increased and better distributed in the intensity range, especially to low levels. Therefore, 9 shocks were produced for each contamination degree of each bonded samples, plus the reference. It represents 81 laser shocks, using Config-PPRIME-1, with

aluminum painting and water confinement. The shock parameters are reported in Appendix D. Before testing, samples are extracted from bonded plates by diamond saw cuts.

For the release agent contaminated samples (RE) and reference ones (UT), plate strips were used to save time during the preparation phase and shock procedure. Each strip has been shocked in three different locations. The sample strips length was taken in the 90° direction, since the composite damage mainly propagates in the 0° direction as previously shown. Therefore, composite damage resulting from one shock does not influence the following shock propagation and induced damage. The back face was slightly polished just to remove the surface roughness and enable better measurements by confocal microscopy. After the laser shocks, each strip is cut to isolate the shocked regions and these samples are analyzed using the three different post-mortem techniques already described. It represents a lot of data; that is why a selection has been made on the results presented in the following sections. The laser shock parameters are given in Appendix D. In the following section, the samples are referring to this table by their name, and the corresponding laser intensity used to test it.

For the moisture contaminated sample (MO), the procedure slightly changes. The shocks are directly performed on the different contaminated plates. After the laser shocks, each plate are cut to isolate the shocked regions and these samples are analyzed using the different post-mortem techniques described. Note that confocal microscopy was not used for this series considering that the results would not be really different from the results obtained on release agent samples. Post mortem investigations were focused on ultrasounds techniques and cross section observations, which proved their efficiency.

2 About laser induced damage in non-symmetrical bonded composite

2.1 Laser shock induced damage in Reference sample

An overview of the damage resulting from the laser shock wave propagation is given in Figure 5.20 thanks to a representative micrography and the corresponding ICM measurement. The observations are consistent with the damage previously revealed in symmetrical bonded samples. Indeed, no debonding is observed, at least until 4.32 GW/cm², which proves the high bond strength. Due to the used laser parameters, the maximum of tensile stresses is generated in the back face composite, and leads to delamination and matrix cracking in this composite part. ICM measurements also indicate that delamination mainly propagated in the 0° direction, which is consistent with the depth of delamination located in the 0° plies. The delamination width is more or less the same in the 90° direction than the one observed on symmetrical bonds. It is located under the impacted region, which is also consistent with previous experiments and modeling. The only difference could come from the residual back face deformation (see in Figure 5.20, ICM measurements). Especially, the deformation maximum height is less important in case of non symmetrical sample, compared to symmetrical samples for the same energy level. This is due to the sample thickness which is more important in the non-symmetrical case, leading to more important shock attenuation. For equivalent laser intensities, the tensile stress level is thus lower in non-symmetrical samples.

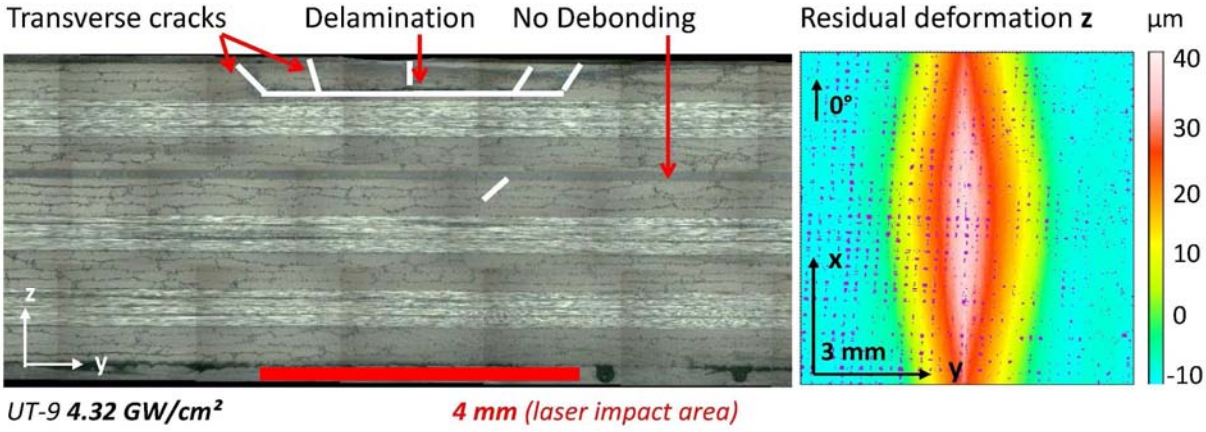

Figure 5.20, Damage resulting from the laser shock wave propagation into a non-symmetrical T700/M21 cross-ply composite assembly correctly bonded (reference UT) observed by cross section microscopy and confocal microscopy (I = 4.32 GW/cm², water confinement)

2.2 Laser shock induced damage in release agent contaminated samples

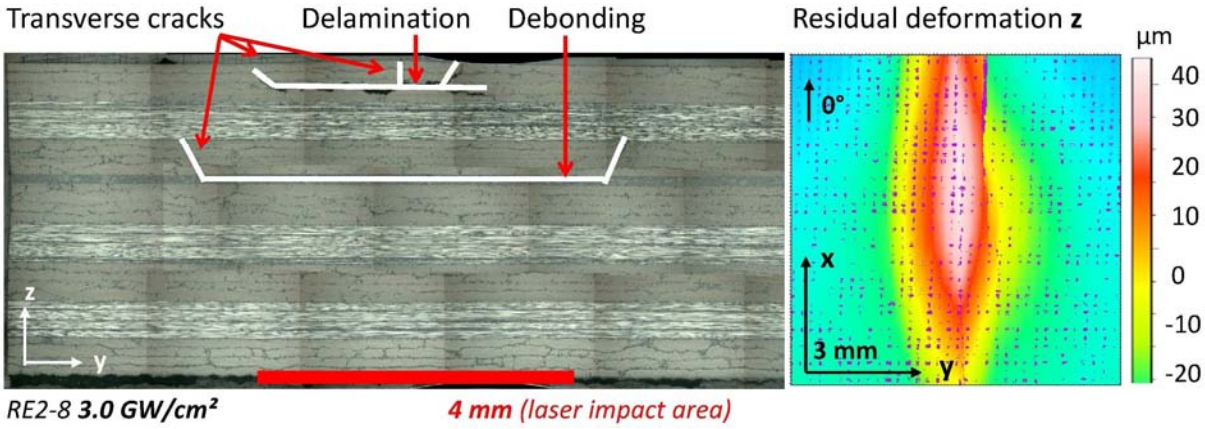

Figure 5.21, Damage resulting from the laser shock wave propagation into a weak non-symmetrical T700/M21 cross-ply composite assembly (Release agent contamination, RE2 – 6.7 at% of Si) observed by cross section microscopy and confocal microscopy (I = 3.0 GW/cm², water confinement)

In case of weak bond generated by a release agent contamination, the laser shock induced damage is presented in Figure 5.21. Once again, it really looks like the damage observed in case of contaminated symmetrical bonds. Delamination, matrix cracking and debonding can be observed. The delamination also propagated in the 0° direction, as shown by the ICM measurement. If comparing the two figures 5.20 and 5.21, it can be noticed that the damage extents are really similar from the reference sample to the release agent contaminated one. The only difference is the debonding, which occurred for the contaminated sample and not for the reference one.

2.3 Laser shock induced damage in moisture contaminated samples

Finally, the damage induced by laser shock on moisture contaminated sample is presented in Figure 5.22. The presented micrography comes from the MO3 (1.19 wt%) series. The same damage is visible: delamination, matrix cracking and debonding. The damage extent corresponds to what has been seen on the previous samples (release agent and reference). The contaminated composite corresponds to the one located on the back face as explained in Part 1. In case of the shocked sample presented in Figure 5.22, the damage in the bond line is quite important. It was thus possible to detect this damage thanks to ultrasounds, as shown in Figure 5.23. Note that a Distance Amplitude

Correction (DAC) has also been used in this case to enhance the bond and the back face echoes. If comparing the A-scan taken from the shock sample to the one taken from an unharmed sample, the shift in the bond echo amplitude traduces a high impedance mismatch, which can be linked to bond damage. It can also be noticed that the back face echo has completely disappeared on the shocked sample A-scan, which is also proof of bond line damage. These results are consistent with the previous observations made on the release agent and reference samples, as well as the results obtained on symmetrical samples.

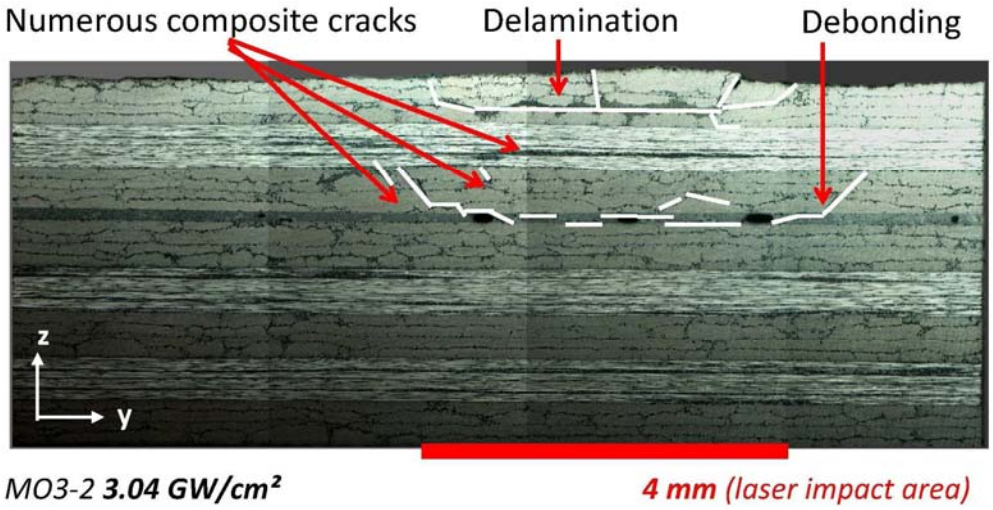

Figure 5.22, Damage resulting from the laser shock wave propagation into a weak T700/M21 cross-ply composite assembly (Moisture contamination, MO3 – 1.19 wt%) observed by cross section microscopy (I = 3.04 GW/cm², water confinement)

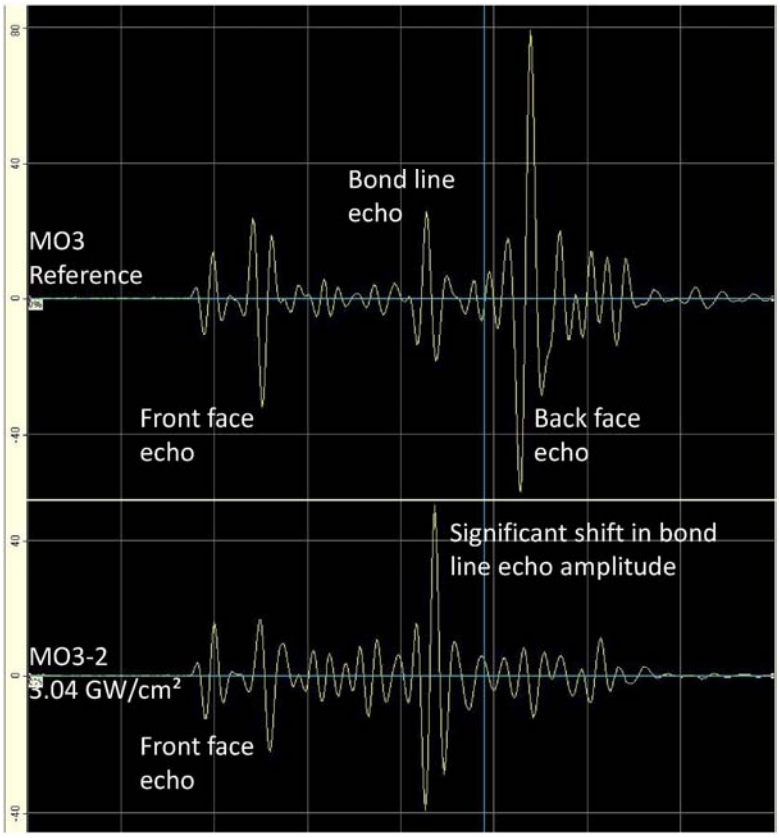

Figure 5.23, Evidence of the laser shock resulting damage into a weak T700/M21 cross-ply composite assembly (Moisture contamination, MO3 – 1.19 wt%) observed by ultrasonic inspection (I = 3.04 GW/cm²)

2.4 Comparison between release agent contaminant and moisture contamination

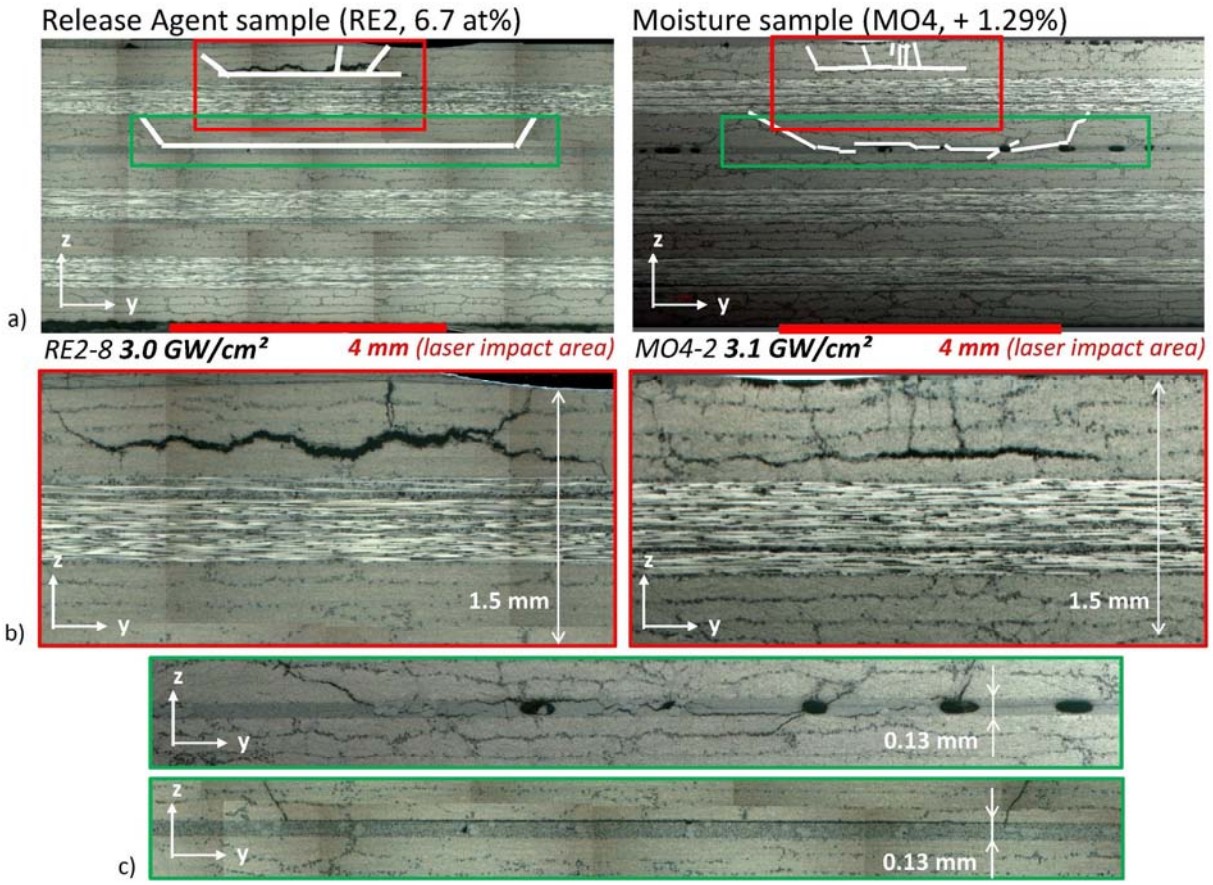

Figure 5.24, Comparison of the damage resulting from a laser shock on release agent contaminated sample, and moisture contaminated sample in case of equivalent laser shock intensity observed by microscopy (MO3, 1.19 wt%, I = 3.04 GW/cm², and RE2, 6/7 at% of Si, I = 3.0 GW/cm², water confinement) – Macroscopic comparison (a), close view on the composite damage (b), close view on the debonding (c)

In this section, let's focus on the difference between release agent and moisture contamination as damage resulting from laser shock is concerned. In Figure 5.24-a, two micrographic cross sections are presented. The first one on the left side is a micrography of release agent sample (RE2, 6.7 at% of Si) after a laser shock produced in water confinement (3.0 GW/cm²), already presented in Figure 5.21. The second one on the right side is a micrography of moisture sample (MO4, + 1.29%) after the same laser shock in terms of configuration and parameters (3.1 GW/cm²). At the bonded composite thickness scale, the damage induced by the laser shock looks really similar. A close view of these damage is given in Figure 5.24-b. It thus demonstrates that contamination does not affect the damage induced by laser shock wave propagation in the composite back part. The same observations on the debonding extent can be made on the damage located at the bond interface. Especially, the damage extent is close from one scenario to another. Nevertheless, if a closer look is given to the bond line state, differences in the bond region damage can be observed (see in Figure 5.24-c). Indeed, the debonding in case of a release agent contamination is really sharp. The debonded side of the assembly is systematically the contaminated side. Very few matrix cracking are observed, generally located on the debonding edges and due to bending. In case of moisture contamination, the failure scheme is different especially for the highest contaminations. Matrix cracks in the composite are more numerous close to the bond, and in both composite parts. The debonding jumps from one bond side to another. When pores are present, they often connect the cracks in the bond together. Therefore, it seems that release agent contamination and moisture contamination do not

have the same weakening effect on bond strength. When release agent has a really localized effect, moisture has an influence on the whole bond thickness plus the adjacent plies. In that last case, the whole bond is weaker. As explained, porosity may enhance this weakness if considered as a direct consequence of the contamination. It can also modify the shock response of the assembly, by creating many local impedance mismatches under the loaded region. Thus, the shock propagation and attenuation is not the same from moisture to release agent samples. Only the interface is weak in case of release agent contamination. These observations can have consequences on the damage threshold determination.

3 Determination of the debonding and damage thresholds by use of post-mortem analysis

This section describes the damage threshold framings of each bonded composite UT, RE, and MO. It is based on the analysis of each sample contamination degree by the three different post mortem techniques. Micrographies are used to visualize and quantify the damage resulting from the laser shock wave propagation. ICM is efficient to detect the smallest composite damage, and can therefore be used for composite damage threshold framing. Keeping in mind the industrial application, ultrasounds can be used to detect the first debonding, and thus enable the debonding threshold framing.

3.1 Composite damage threshold for the reference sample

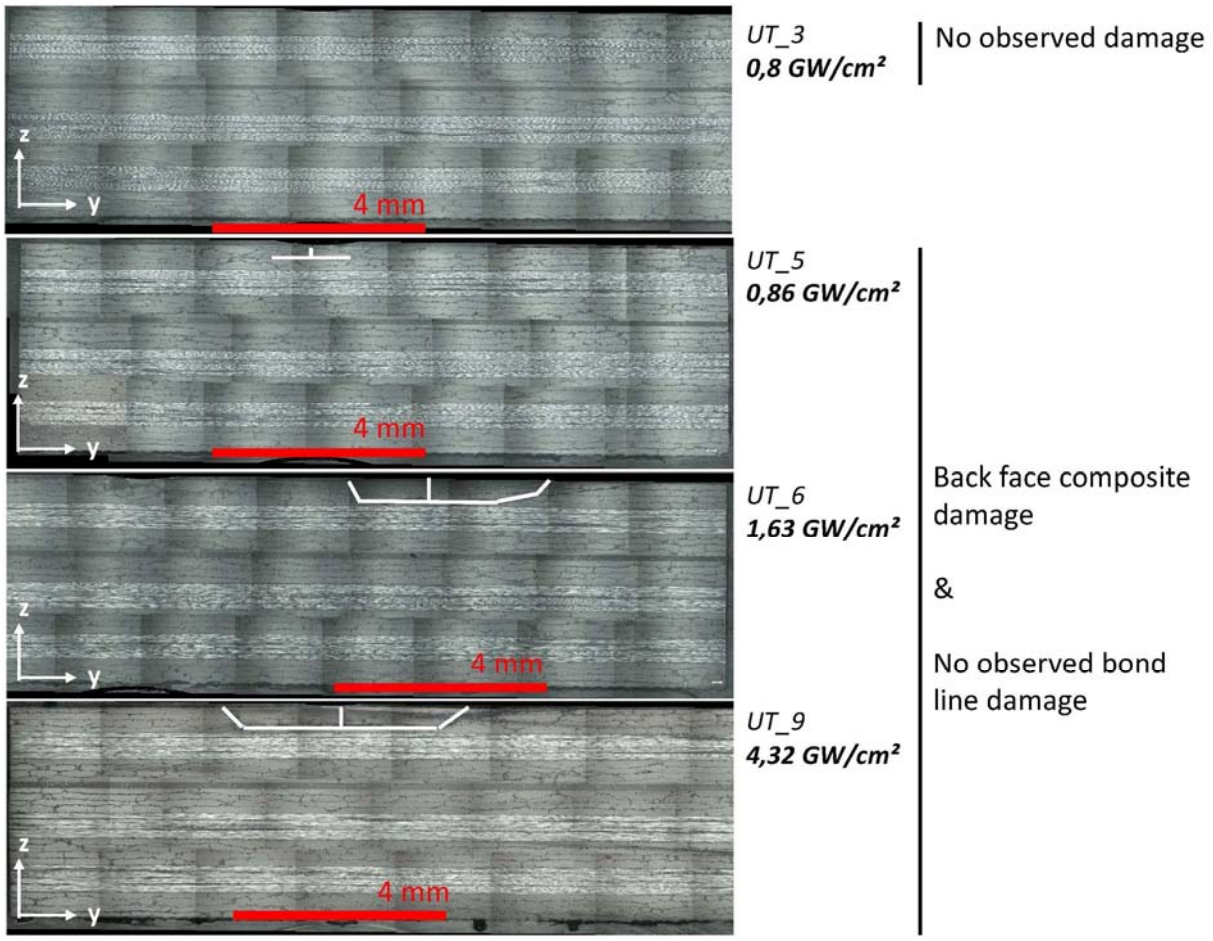

Figure 5.25, Correlation between the laser intensity and the damage extent in the reference non-symmetrical composite assembly sample (UT) evidenced by cross section observation

Starting with the cross section observation realized on reference (UT) samples, the correlation between the laser intensity and the inside damage extent is shown (see in Figure 5.25). The highest the energy, the largest the 90° direction delamination width. As previously explained, no debonding has been observed in case of the reference sample at least until 4.32 GW/cm², which is consistent with the expected strength of the bond line (see in Figure 5.2 for GIC values). The first two micrographies presented in Figure 5.25 also enable to frame the composite part damage threshold. The first broken sample is UT-5, shocked with a laser intensity of about 0.86 GW/cm². The cross section performed on sample UT-3 has revealed no damage resulting from laser shock propagation. Therefore, the composite part damage threshold for the reference bonded CFRP is in the range [0.8 – 0.86 GW/cm²].

This conclusion can be confirmed by the ICM measurements performed on the 9 UT reference samples, partially presented in Figure 5.26. The 8 measurements presented in this figure also evidence the direct correlation between the laser intensity and the residual back face deformation height, as well as the 90° direction delamination width. Note that the 0° direction can not be discussed because damage is leaving the sample in this direction. Only one residual deformation profile does not fit with this evolution. Indeed, UT-7 shows a weird profile, and a too important maximum height compared to the following one. For this sample, micrographies have revealed an important thermoplastic nodules concentration right in the loaded zone. The 0° top ply of the composite back face has broken along the 0° direction (vertical line on the ICM measurement presented in Figure 5.26). This damage, probably due to material microstructure, almost led to ply ejection. That is why the ply is very deformed.

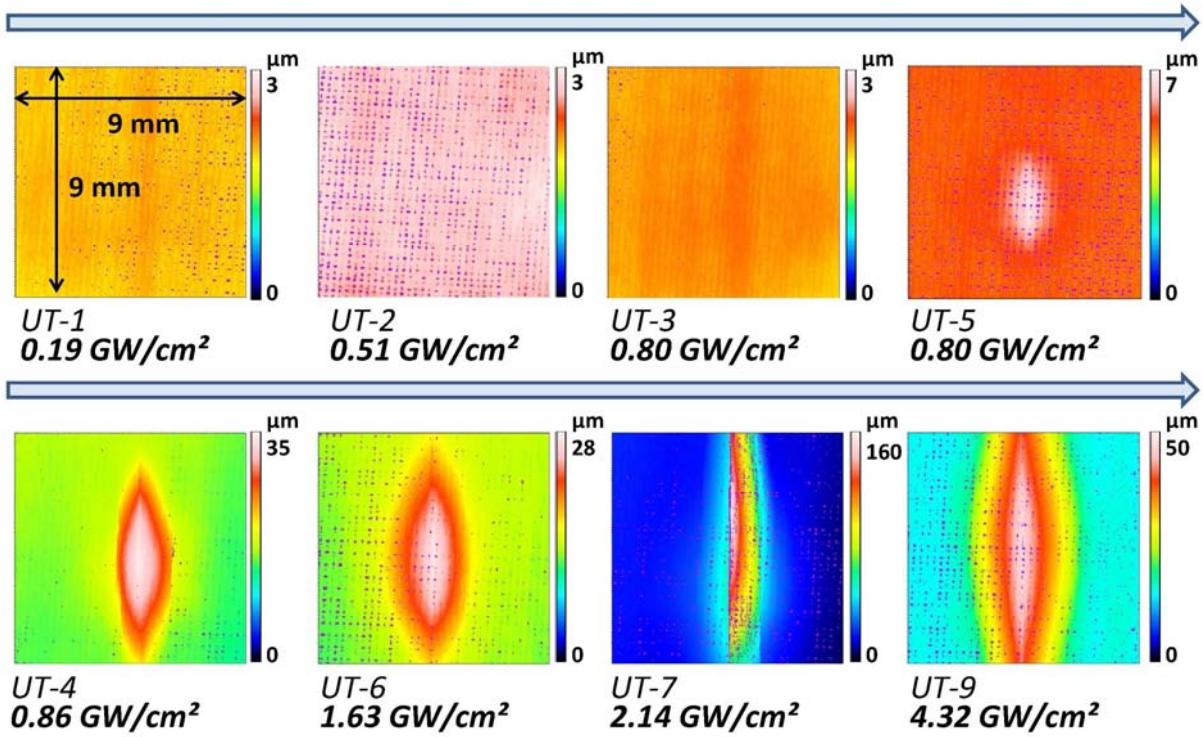

Figure 5.26, Correlation between the laser intensity and the residual back face deformation in case of the reference non-symmetrical composite assembly sample (UT) evidenced by ICM – Composite damage threshold

The ICM measurements realized on UT-3 sample show a complete flat surface, which is consistent with the micrography presented in Figure 5.25. On the other hand, the ICM data taken from UT-5 sample reveals a small composite blister, corresponding to the back face composite damage (matrix cracking and delamination) evidenced on the micrography presented in Figure 5.25. These measurements are consistent with the previous experimental results, and also enable the same framing on the composite damage threshold.

Finally, ultrasound results can be discussed. The multi-element pulse echo probe was used to excite the shocked composites with a 5MHz frequency, like in the previous investigations. The probe was placed on the sample front face, as usual. The data is represented as B-scan to investigate the target thicknesses. The probe width enabled the measurement of a sample plate containing three different shocks plus a reference sample which was used to get the reference A-scan and B-scan. B-scans from two UT bonded composite plates, each plate containing three shocks, are presented in Figure 5.27 with a reference signal. Note that the samples are the same than the ones presented in Figure 5.26. For the 6 shocks presented, the bond line echo almost does not change compared to the reference bond echo. Concerning the back face echo, the same observation can be made for the three lowest shocks (UT-1, UT-2 and UT-3). In the second plate (bottom of Figure 5.27), back face echo shows three amplitude high attenuations (“holes”), corresponding to the back face composite damage created by the three laser shocks respectively. For example, one A-scan taken from the reference sample is given in comparison to the A-scan recorded under the UT-6 laser shock. This last A-scan presents a change in back face echo TOF and amplitude compared to the reference A-scan, which traduces damage as previously explained. No strong difference can be observed in the bond line echo, which proves that the bond has not been opened.

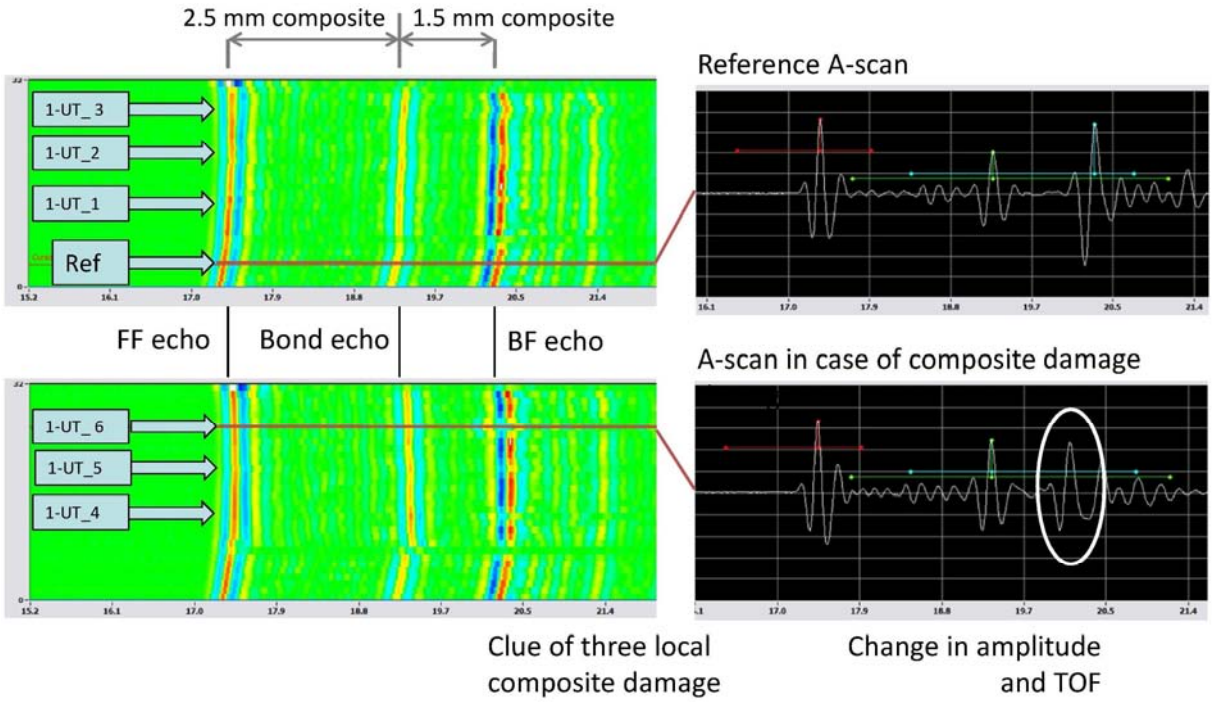

Figure 5.27, Correlation between the laser intensity and the inside damage in case of the reference non-symmetrical composite assembly sample (UT) evidenced by ultrasounds – Composite damage threshold

3.2 Damage thresholds for the release agent contaminated sample

In this section, the results on the RE2 contamination (6.7 at% of Si) are presented. Note that all the different contamination degrees have been investigated identically. Eight over the nine results of ICM measurements realized on RE2 samples are presented in Figure 5.28. The residual back face deformation in z direction after the laser shock wave propagation is quantified for this weak bond. The correlation between the laser intensity and the damage extent (width and height) is consistent with the trend previously observed on composite samples and the different bonded samples. As previously explained, the delamination initiated by the laser shock wave propagation in the composite part has mainly propagated in the 0° direction. That is why the back face deformation of the bonded composite looks like elliptical shape whose major axes are much longer than minor axes. Thanks to these ICM measurements, the damage threshold of the composite part of the assembly can also be determined. It can be identified as the lowest intensity for which a blister is observed like for UT samples. In the case of RE2, this threshold upper boundary is measured at **0.49 GW/cm²**. It corresponds to the first occurrence of a back face blister (see in Figure 5.28).

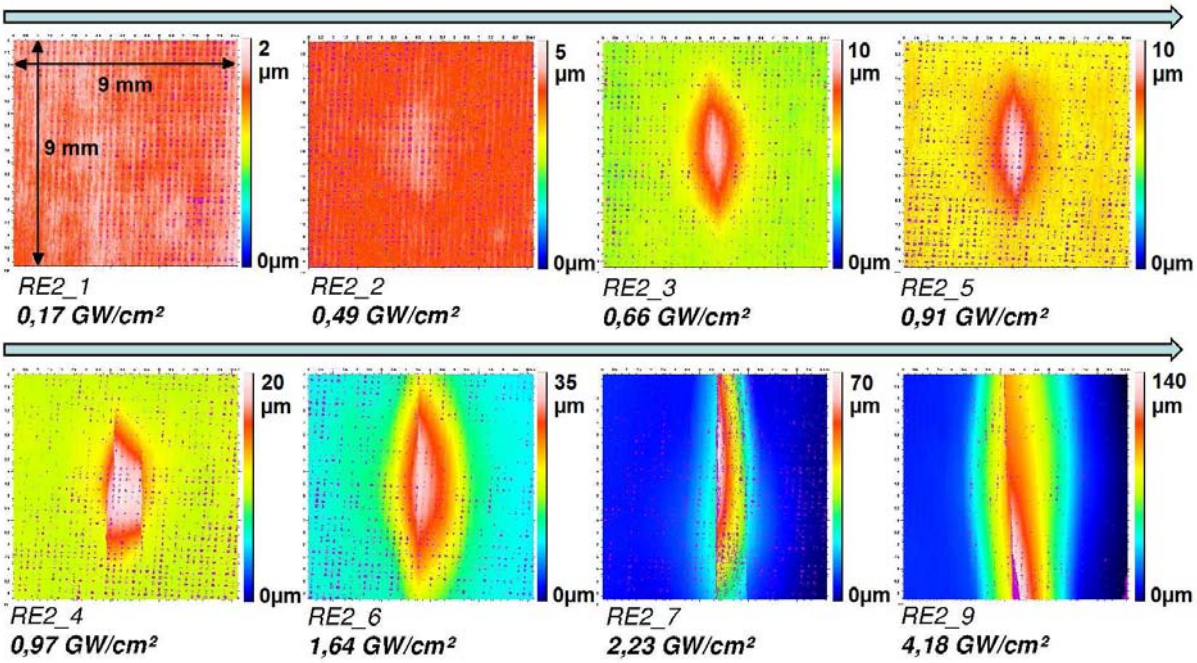

Figure 5.28, Correlation between the laser intensity and the residual back face deformation in case of the release agent contaminated composite assembly sample (RE2, 6.7 at%) evidenced by ICM – Composite damage threshold

In order to determine the bond line damage threshold, the ultrasounds technique has been used. Some results extracted from these measurements are presented in Figure 5.29. The presented B-scan enables to identify the three usual echoes useful to evaluate the inside damage: the front face echo, the bond line echo and the back face echo (see Figure 5.29). The loss of the back face echo reveals damage inside the composite part, and a shift in the bond line echo is representative of a local debonding. Thanks to these considerations, the composite damage threshold has been evaluated close to **0.49 GW/cm²** when the bond line damage threshold has been evidenced close to **0.66 GW/cm²**. These values are both upper boundaries.

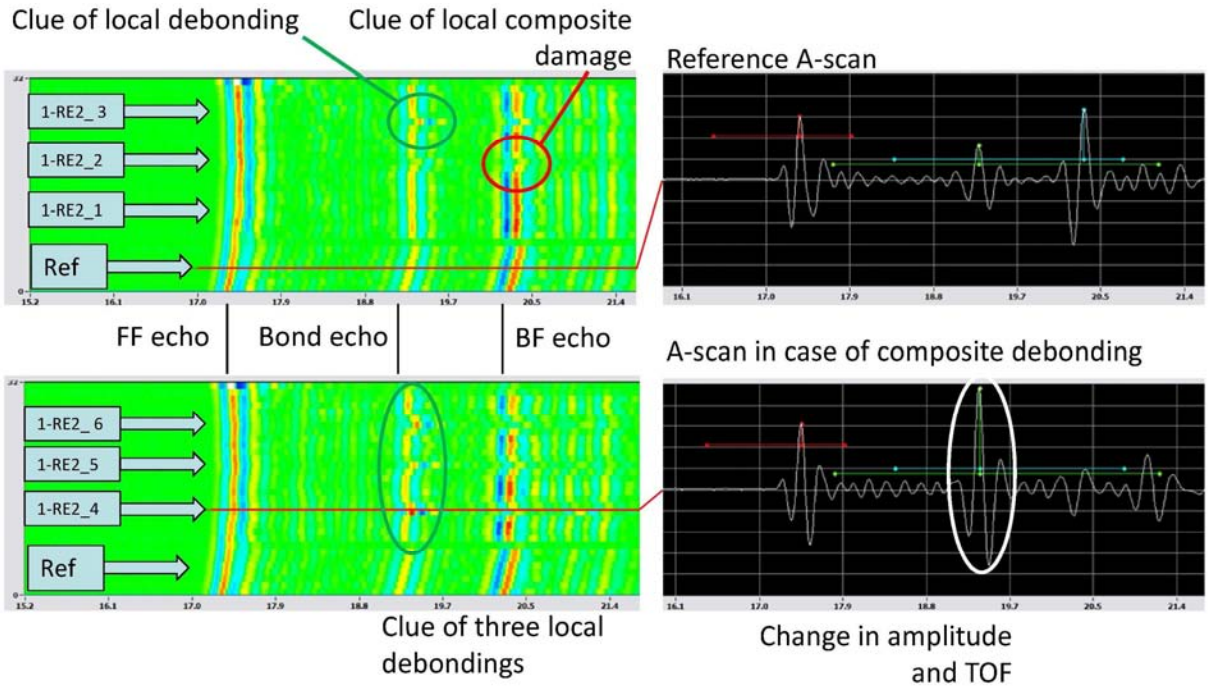

Figure 5.29, Correlation between the laser intensity and the inside damage in case of the release agent contaminated composite assembly sample (RE2, 6.7 at%) evidenced by ultrasounds – Debonding threshold

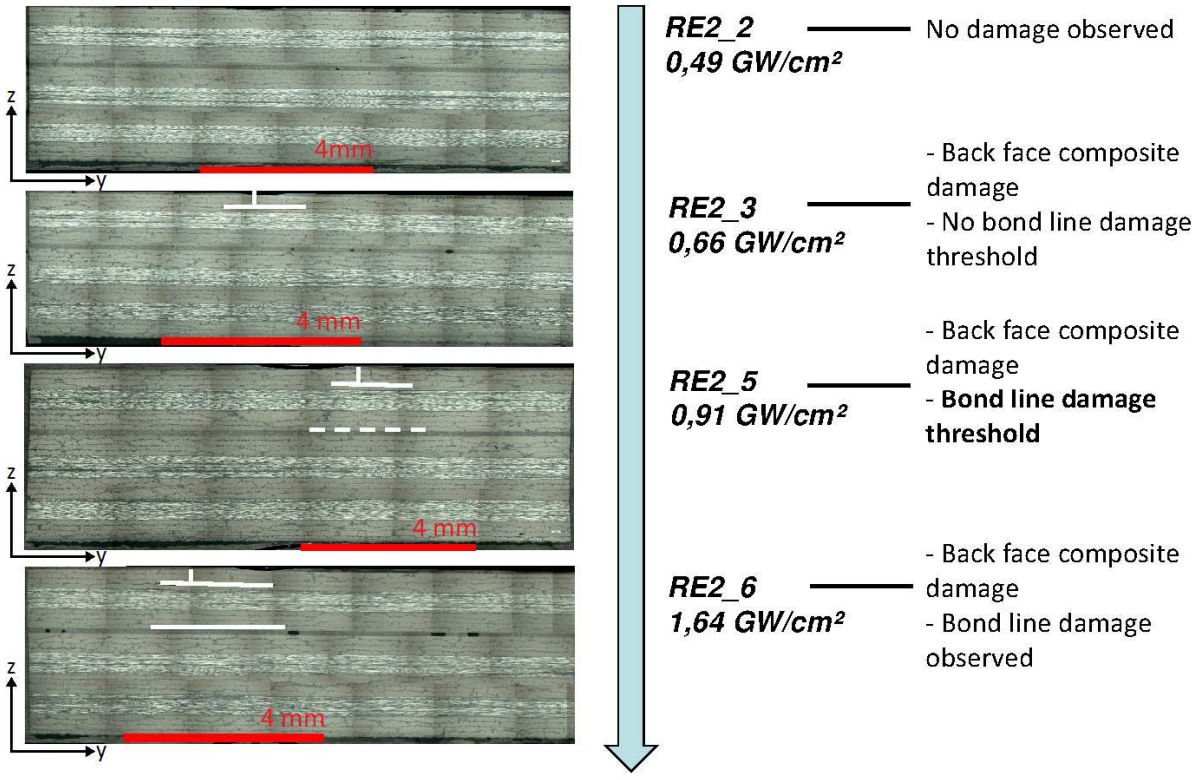

Figure 5.30, Correlation between the laser intensity and the damage extent in the release agent contaminated composite assembly sample (RE) evidenced by cross section observation

Cross section observations of the RE2 samples have been finally performed to confirm the conclusions made thanks to the two previous post-mortem techniques. Four micrographies are presented in Figure 5.30. The red line at the bottom of each image represents the 4 mm diameter impact area and the inside damage are enhanced by white lines as usual. Some differences with the threshold values previously determined can be noticed. Indeed, composite damage threshold upper

boundary is observed from **0.66 GW/cm²** and the bond line damage threshold one is identified at **0.91 GW/cm²**. Nevertheless, the correlation between the laser intensity and the inside damage remains unchanged. The small shift in the threshold values can be attributed to experimental uncertainties during the preparing process of cross section observations. Indeed, the delamination and cracks resulting from the laser shock wave propagation are concentrated in a really small region for the lowest intensity values. This is particularly visible on the ICM measurement realized on sample RE2-2 and presented in Figure 5.28. Consequently, the cutting needed for the cross section observation may miss the interesting region. Since the ultrasounds measurements agree with the confocal microscopy, the threshold determined with these two techniques are kept in the following analyses.

These measurements have been performed for each contamination degree. One of the most powerful ways for representing the whole data generated by these investigations is probably to use the laser ultrasound results. The LUIS laser ultrasounds set-up, developed by EADS IW (Technocampus EC2M, Nantes), has been used to scan the different shocked samples. This technology enables the inspection of large parts by moving the generation laser and the detection laser from spot to spot in a (x, y) plane (Chapter 2). Therefore, A-scans are directly recorded in the (x,y) scanning plane, and can then be displayed separately, grouped as B-scans or by C-scans. This last display is efficient to get in a glance the location of the main defects. As the current investigations are concerned, each shock sample is respectively associated to reference plate untouched from the reception. The chosen positioning of the samples is schematically shown in Figure 5.31, and is the same for the 4 contaminated RE samples and the reference UT. The reference plate of each contamination degree is placed on the shocked sample left. The three pre-cut plates are then placed in the increasing laser intensity order, from left to right, the lowest energy level being at the bottom (see in Figure 5.31). Speaking of the ultrasound data treatment, three gates are also used as shown on a reference A-scan in Figures 5.32, 5.33, 5.34. The first one is used to detect the front face echo, which corresponds to the face presented to the laser ultrasound irradiation, and also to the front face as understood in laser shock. The second gate (green one) is placed to track amplitude or Time Of Flight (TOF) changes in the bond line echo. Finally, the third gate (red one) is used to detect modification of the back face echo. Using specific software developed by EADS IW and named NDT Kit, calculation are performed to map C-scans. They can be plotted according the two different gates, in TOF or Amplitude.

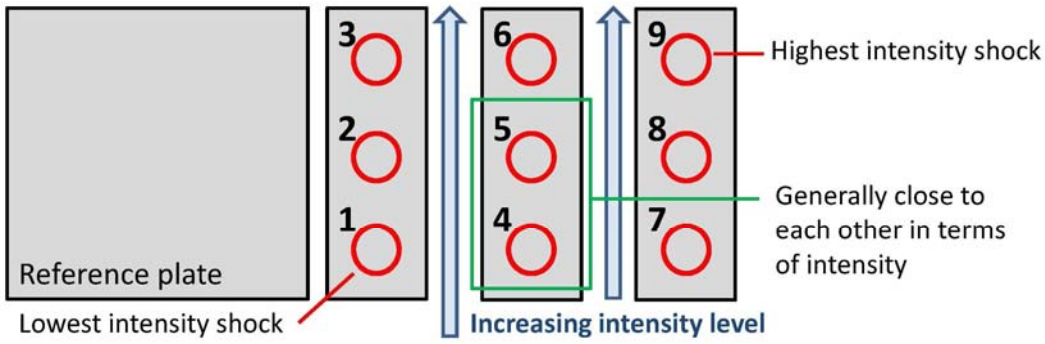

Figure 5.31, Position of the samples and of the shock spot references for each contamination degree of release agent samples in the following C-scans presented in Figures 5.32, 5.33 and 5.34

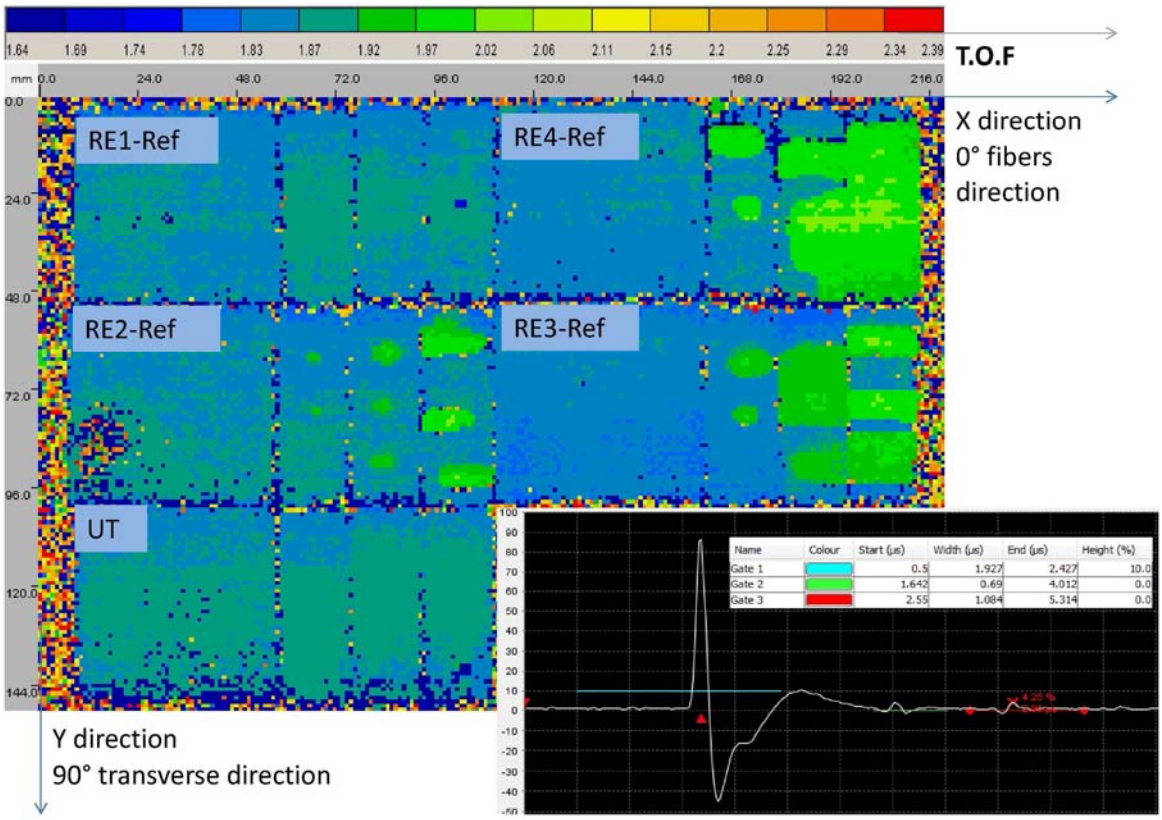

Figure 5.32, C-scan of the shocked release agent (RE) and reference (UT) samples, based on the bond line gate and displayed using the Time Of Flight (TOF) parameter, according the positioning presented in Figure 5.31 – Typical reference A-scan obtained thanks to LUIS laser ultrasounds set-up, with the gates positioning

A first C-scan of all the shocked release agent samples (RE1 to RE4) and shocked reference sample is given in Figure 5.32. It has been calculated using NDT Kit on the bond line gate (gate 2), and the time of flight is displayed. Note the TOF is a direct representation of z depth since the sound speed in the T700/M21 sample is known. It has been shown in part 2 that the time of flight changes in case of debonding. This was particularly the case for symmetrical T800/M21 bonded samples contaminated with release agent. More precisely, the bond line echo has been measured deeper in case of a second interface debonding, because of the change in impedance mismatch. In case of the release agent (RE) contaminated non-symmetrical sample, it is known from sample production and micrographic observation that the broken interface is the second one. Indeed, the contamination has been realized on the thinnest composite part. Therefore, the debonding should be traduced by a shift in TOF. This is observed in Figure 5.32. Indeed, it can be deducted from the reference plate measurements that the blue color corresponds to an unharmed bond. Consequently, the green areas correspond to the debonding regions. Several comments can be made. First, the observations made by laser ultrasound are generally consistent with the cross section observations and multi element probe measurements. It is confirmed that the reference bonds has not been opened, and the debonding thresholds identified thanks to laser ultrasounds correspond to the one find thanks to other techniques. The only dark point is the bond damage threshold of RE1 (2.2 at% of Si), which has not been detected. The spatial resolution of the laser ultrasound device, which is a bit lower than the multi element probe resolution, could be a reason for that. In a second time, the correlation between the laser intensity and the debonding extent is shown. It is particularly visible on sample RE2 (2.2 at% of Si). The debonding more easily propagates with higher energy values. It can also be observed that there is a direct correlation between the debonding extent, and the contamination degree. For similar laser intensities, the debondings are more and more sizeable for the highest contamination.

Still looking to the bond line echo, amplitude modifications due to laser shock can also be investigated. The C-scan mapping of the bond echo amplitude in the (x,y) plane is given in Figure 5.33. In the previous part, conventional ultrasounds on debonded samples have also shown that a shift in the bond echo amplitude can occur in case of strong debonding. This is also the case for non symmetrical bonded samples, as shown in Figure 5.33. Due to strong impedance mismatch in case of strong debonding, the bond echo is amplified. It is particularly visible on the last two contaminated samples, for which the debonding are the most obvious. Nevertheless, this C-scan display is a bit less efficient for the debonding thresholds determination. Indeed, the RE1 sample (2.2 at% of Si) hardly shows some amplitude changes compared to its reference plate. This is also the case of the first 6 shocks produced on RE2 (6.7 at% of Si), even if it is getting better for the last 3.

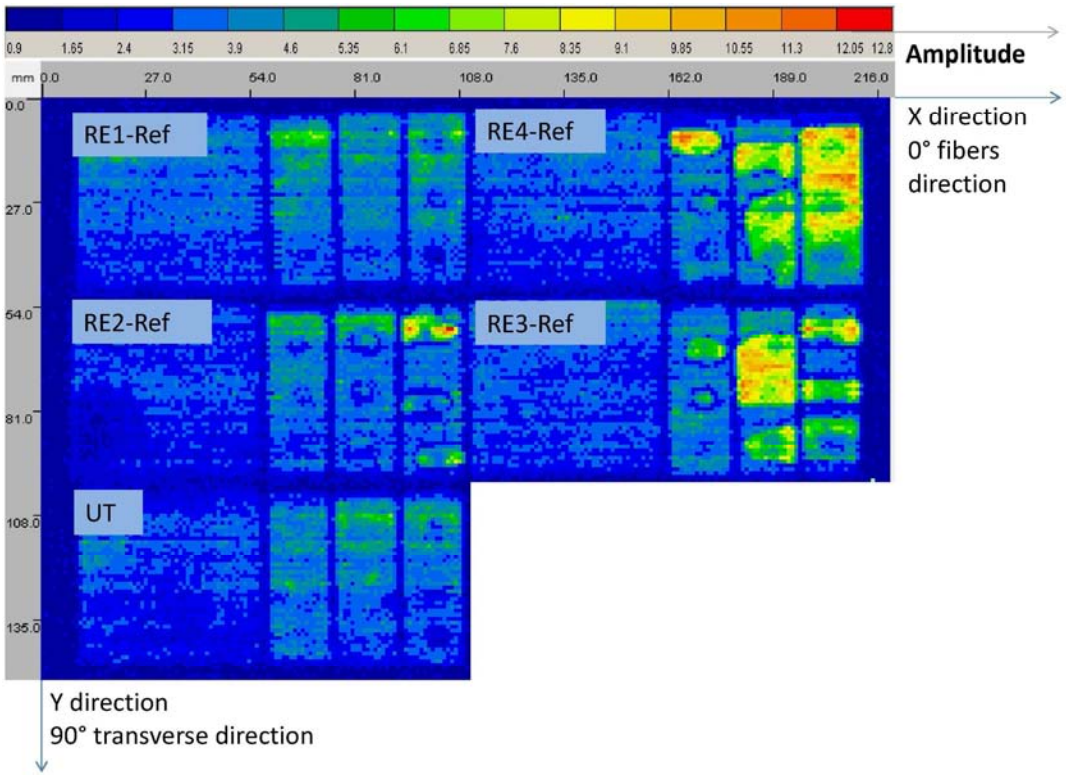

Figure 5.33, C-scan of the shocked release agent (RE) and reference (UT) samples, based on the bond line gate and displayed using the amplitude parameter, according the positioning presented in Figure 5.31

Finally, C-scan amplitude display can be used on the composite gate (gate 3) in order to evidence some of the composite damage. In the previous investigations, it has been shown that a composite damage could be traduced by a change in TOF, in case of obvious delamination, and in amplitude, in case of delamination and matrix cracks. On the shocked release agent sample, and shocked reference sample (UT), this C-scan display is given in Figure 5.34. Note that no information can be obtained from the RE3 (8.4 at% of Si) and RE4 (10.5 at% of Si) as the composite damage is concerned. Indeed, in these tow cases, the debonding are so important that the ultrasound cannot pass through the bond and reach the second composite part. For proof, no echo at all is observed on the gate under the debonding region for these two samples (see in Figure 5.34, RE3 and RE4). Moreover, the extent of these regions exactly corresponds to the debonded regions detected thanks to the previous C-scan presented in Figure 5.32. This is different for the other samples. Indeed, the UT sample and RE1 sample presented almost no debonding. Therefore, the composite part can be reached, and the composite damage highlighted. From these signals observations, the thresholds seem to be confirmed, as well as the correlation between damage and laser intensity.

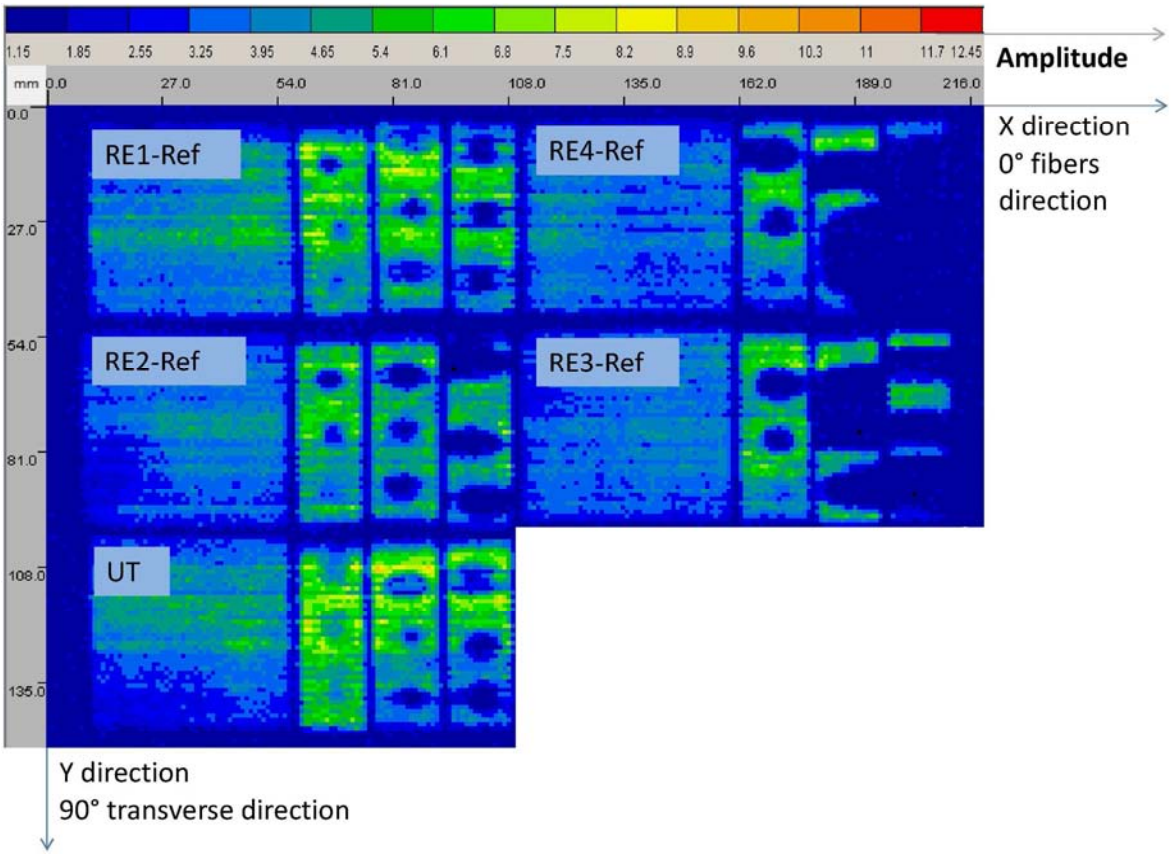

Figure 5.34, C-scan of the shocked release agent (RE) and reference (UT) samples, based on the composite gate and displayed using the amplitude parameter, according the positioning presented in Figure 5.31

Finally, all the presented data, and not presented data, can be summarized and compared to GIC value or contamination degree. This is done in Figure 5.33 by using the same representation than the one used in Figure 5.18. Considering first the bond interface damage threshold (green strips), a correlation can be found between the GIC mechanical testing and the laser shocks. Indeed, the damage thresholds evaluated thanks to the laser shock follow the decreasing trend shown by the GIC testing. In other word, the damage thresholds found thanks to LASAT are correlated to the Si concentration present on the CFRP panel prior to bonding. The first contamination degree (RE1, 2.2 at% of Si) has been discriminated from the reference case. Indeed, the laser shocks performed on the reference until 4 GW/cm² did not create a debonding, but the bond interface in case of 2.2 at% contamination was opened around 2 GW/cm². In this case, the LASAT technique gives different results from GIC testing, since the mechanical test did not enable to discriminate the reference from the contaminated case. A strain rate effect could be a reason for this difference. It can also be noticed that the damage threshold of both RE3 (8.4 at%) and RE4 (10.5 at%) contamination degree are equal. Indeed, the adhesion strengths evaluated by GIC are close. It is normal that the results are also close by LASAT evaluation. More shots could have been necessary to discriminate these two levels, but the difference in the threshold damage could be in the uncertainty range. This was also the case for LE and LB samples in part 2. Speaking of the composite damage threshold (grey strips), it can be noticed that failure in composite occurred in each case. This damage in the composite part is the consequence of a non-optimized test and should be avoided for the industrial application. In fact, there is no real difference compared to the symmetrical bonds in terms of geometry. The bond is still at the same depth from the composite back face surface. Only the shock attenuation is stronger in case of the non-symmetrical thicker samples. The laser shock parameters are thus still not adapted to the tested material. The composite thresholds are close to each other, averagely around 0.25

GW/cm² for the lower boundary, and close to 0.5 GW/cm² for the upper one. Only the reference seems to be higher, but there is no particular reason for that. This framing is quite low compared to the one obtained on the T800/M21 composite materials. The use of a different laminate (T700/M21 in this case) could be a reason for that. Moreover, it is a key problem for the LASAT test application. From the synthesis graph shown in Figure 5.35, and by considering the uncertainties on the laser parameters, it appears that the composite damage threshold and the debonding threshold are in the same ranges even for the highest contamination degrees. This observation prevents from using a non optimized laser configuration to test the samples. As a conclusion, even if the bond strength can be successfully linked to the contamination level in case of release agent samples, optimization should be performed to avoid composite damage.

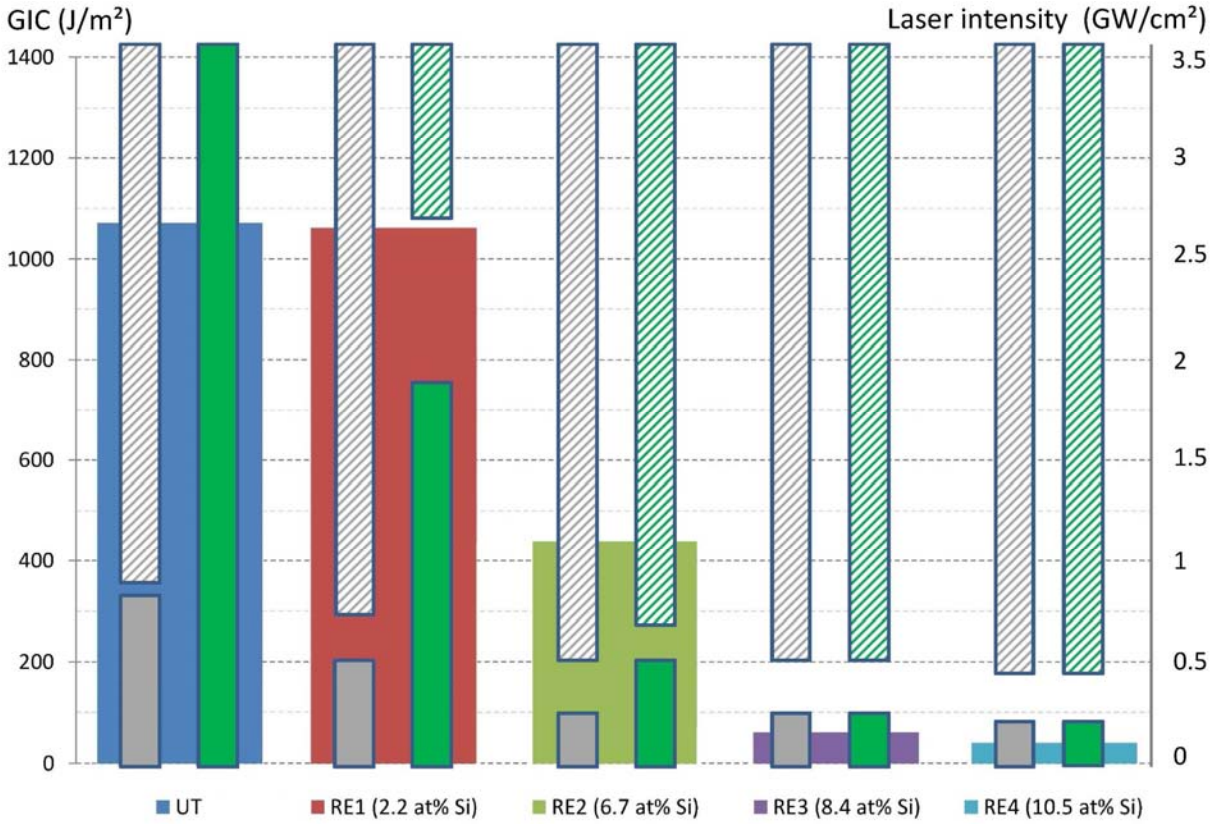

Figure 5.35, Synthesis graph of the shocked release agent contaminated bonded composite (from ENCOMB) – Superposition of the GIC values obtained by mechanical testing [2] and damage thresholds of the bond and the composite part obtained by LASAT

3.3 Damage thresholds for the moisture contaminated samples

In this last section, experimental results enabling the damage thresholds determination in case of moisture contaminated samples are presented. It has to be kept in mind that this contamination scenario is different from the previous one, and that porosity could influence the test results. A series of 5 micrographies extracted from the MO4 results are presented in Figure 5.36. It can be observed that the porosity in the bondline is not the same from one sample to another, which shows that the porosity is not homogeneously distributed in the bonded composite. This is consistent with the Microtomography results discussed in Part 1.

Speaking first of the composite damage threshold, the first damage occurrence in the T700/M21 laminates has been observed for a laser intensity about 0.78 GW/cm² in case of MO4 sample (1.29 wt%). The previous laser shock at about 0.62 GW/cm² did not lead to any observable damage. This

framing is a bit above all the other threshold values obtained on the other contamination degrees (closer to 0.5 GW/cm²), but remains consistent with the previous results. In a second time, the debonding threshold can now be discussed. In case of MO4 series, the first damage occurrence in the bondline has been observed in MO4-6 sample. The cracks is hardly visible, and it is therefore complicated to considered this crack as a "debonding" and even as a bond damage. Therefore, the upper threshold framing boundary is here shown as equal to 0.86 GW/cm², observed in sample MO4-5 (see in Figure 5.36). Bond damage is clearly more visible, and more sizeable, but it is not the fully debonded length which could have been observed in case of release agent contamination. As explained, the cracks jump from one interface to another, crossing porosity if any. This particular damage profile is confirmed by the observation of the following micrographies (see in Figure 5.36). The damage extent evolution, whatsoever in the bond or in the composite laminate, is consistent with the laser intensity increase.

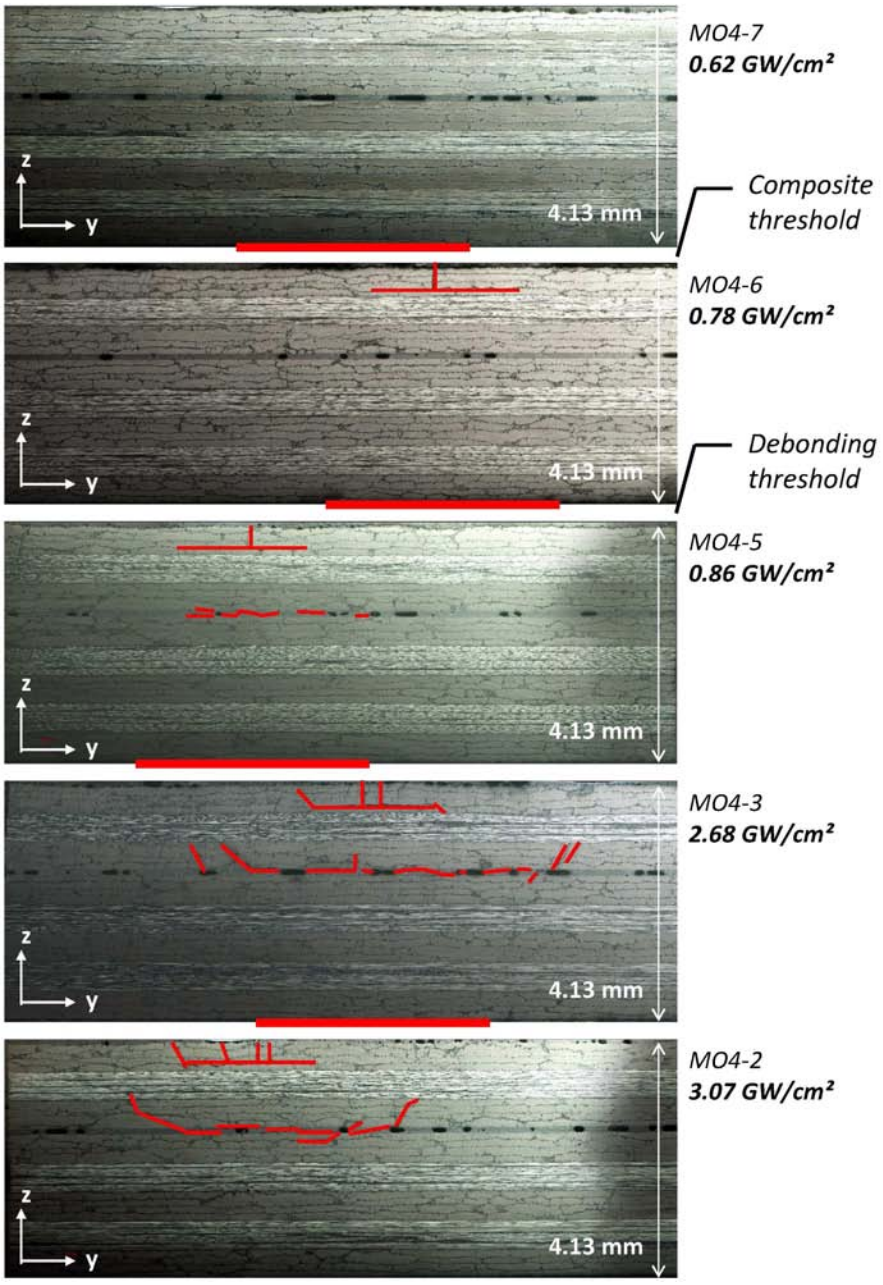

Figure 5.36, Correlation between the laser intensity and the damage extent in the moisture contaminated composite assembly sample (MO) evidenced by cross section observation

In spite the numerous ultrasound tests performed on moisture contaminated samples, using equally multi-element probe or laser ultrasounds, the damage in the bond was quite hard to indentify. This is particularly true for the highest contamination degree. The presence of irregular porosity could induce mistake in the A-scan interpretation between a pore and/or a debonding. The damage profile is also quite diffusive because of numerous cracks in the composite and in the bond. Finally, the hypothetic presence of water could also have an effect on the ultrasounds propagation, and thus hide some impedance mismatch. Nevertheless, the absence of damage observation in the bondline enables to use laser ultrasounds results to quantify the composite damage. This has been done with both LUIS and LUCIE lasers, and the results are similar. The sample positioning, with the shock references is shown in Figure 5.37. Note that shot 1 on sample MO1 failed. For each shocked sample, a reference plate is added on the left or on the right (see in Figure 5.38). The reference UT is placed on the left in Figure 5.38. The LUIS results are displayed using a TOF representation on gate 3, corresponding to the composite back wall echo. It can be first observed that the composite part damage is globally more or less the same from one contamination degree to the others, which is consistent with the release agent results. The moisture contamination amount does not seem to influence the composite strength to laser shock loading. Nevertheless, ultrasounds have some difficulties to represent the smallest defects, especially in case of MO3 sample.

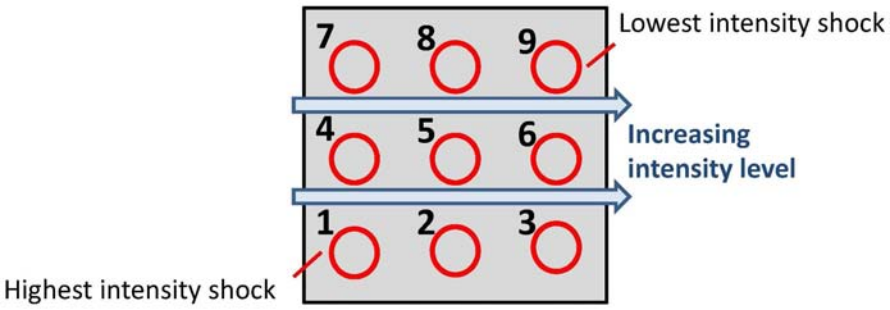

Figure 5.37, Position of the shock spot references for each moisture contamination level samples in the following C-scans presented in Figure 5.38

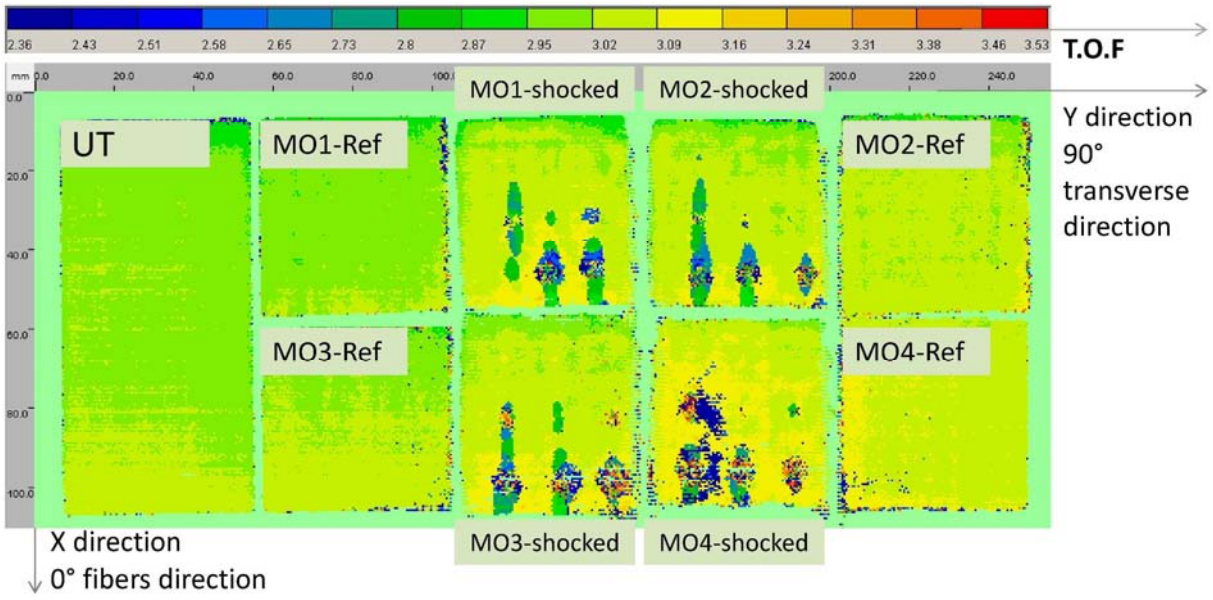

Figure 5.38, C-scan of the shocked (MO) and reference (UT) samples, based on the composite back face gate and displayed using the TOF parameter, according the positioning presented in Figure 5.37

Finally, these results can be used to identify the merged damage zone. From the LUIS measurements, it can be observed that only the damage resulting from shock 1 and shock 4 are merged in case of sample MO2, MO3 and MO4. Consequently, and according to the shooting sequence, the damage created during shock 1 could have influenced the damage created in shock 4 by changing the shock reflection. Therefore, shock 4 for these three samples can not be used for bond line damage threshold framing. This has a strong consequence only for MO1 results, for which shock 4 could have provided an unharmed point at about 2.0 GW/cm², thus enabling a sharper damage threshold framing (see in Figure 5.39). It is not a problem for the composite damage threshold since the shock 5 always broke the composite laminate.

Finally the thresholds values can be summarized using the same representation than the one used for release agent results. The synthesis chart is given in Figure 5.39, and the presented thresholds are only based on cross section observations. If just looking to the discrimination efficiency between the reference and the contaminated samples, it has been found that LASAT can detect each moisture contamination. The reference, unchanged from the release agent tests, has a much higher bond interface damage threshold than the moisture contamination samples. Nevertheless, the correlation between the mass increase and the LASAT damage threshold is not obvious. The first contamination degree (+ 0.46%) has been detected when GIC testing gave an adhesion level close to the reference. For this contamination degree, laser shocks with various intensities could give a better idea of the damage threshold. Nevertheless, it is possible that the three contamination degrees + 0.46%, + 0.84% and + 1.19% have similar bond interface strength (in the uncertainty level). Only the + 1.29% contamination has been clearly discriminated from the three others. In that case, the really high level of porosity could have had an influence on the bond strength. Note also that the shock value highlighted in red could be the threshold value as explained before (Figure 5.36), because a small crack initiation has been observed.

The composite damage threshold of each contamination degree framing is better defined, thanks to the choice in the used intensities values. Considering the laser parameter uncertainties and material variation, it can be concluded that this threshold is close to 0.5 GW/cm² (for this given laser loading). It has been particularly evidenced thanks to MO3 results, for which two identical shocks gave respectively a composite and no composite damage. The results on the other contamination degrees are also in good agreement with this observation. This threshold is not very different from the damage threshold obtained with the release agent samples. The moisture contamination seems to have no effect on the composite strength.

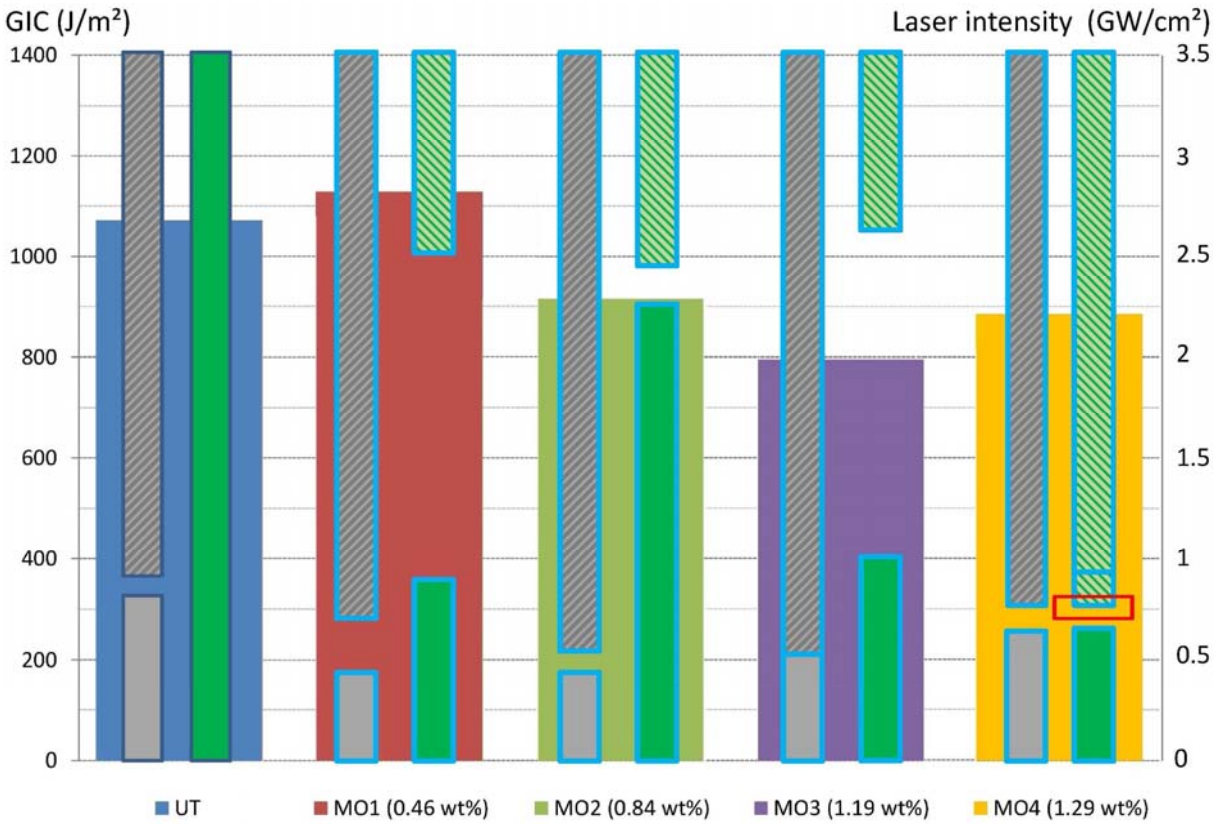

Figure 5.39, Synthesis graph of the shocked moisture contaminated bonded composite (from ENCOMB) – Superposition of the GIC values obtained by mechanical testing [2] and damage thresholds of the bond and the composite part obtained by LASAT

Part 4: Bonded composite modeling

In this part, the numerical models developed for the non-symmetrical bonded T700/M21 composites are validated on experimental results obtained thanks to VISAR. Firstly, the time resolved experiments performed on UT samples are given and discussed. In a second time, the model developed on the basis of previous numerical results is presented, and validated for low intensity shock signals. The model is used to identify each feature contained in the back face velocity signal. Finally, the model is used for higher intensity shocks, and the numerical results are discussed in comparison with experimental signals.

1 Time resolved experimental measurements

The first step for a reliable modeling is to obtained time resolved data on bonded composite to validate the model with. For that, the UT samples were selected. Indeed, in order to have a better understanding of the back face velocity signals, it is easier to start by being sure of the interface quality, and by testing a non-symmetrical bonded composite to separate phenomenon which could be superposed because of the symmetry. 1 cm² samples were cut from the UT plate, painted with aluminum painting for the laser interaction, and shocked using Config-PPRIME-2. The shocks were doubled in order to check the reproducibility. The laser shock parameters used are given in Table 5.4 and the VISAR results are presented in Figure 5.40. Note that cross section observations have been performed after the laser shocks to confirm the conclusions made in the following paragraph.

Targets	Energy (J)	Pulse duration (ns)	Dfoc (mm)	Intensity (GW/cm²)	Verdi power (W)	Fringe factor (km/s)
ES1-01	0.92	27.31	4	0.27	0.75	0.1447
ES1-02	0.95	25.72	4	0.30	1	0.1447
ES1-03	3.65	26.67	4	1.09	1	0.1447
ES1-04	1.99	29.67	4	0.54	1	0.1447
ES1-05	3.83	26.62	4	1.14	1	0.1447

Table 5.4 Laser shock parameters for bonded cross-ply T700/M21 (UT lay-up) time resolved experiments conducted in Config-PPRIME-2 – Associated VISAR parameters

The two samples UT-01 and UT-02 were shocked with an average intensity of about 0.28 GW/cm². The resulting back face velocity measurements show no spallation on the observed period. Indeed, the peak observed after 4 µs corresponds to the second shock breaking-out after one shock back and forth in the bonded composite if considering an average sound speed about 3000 m/s. It can be observed that the attenuation between the first shock breaking out and the second one is quite strong, probably because of the sample sizeable thickness and the bonded composite cross ply lay-up. Second order phenomena are observed on the signal, whose origins are complex to explain without numerical modelling. Note also the good reproducibility between the two shocks. In case of sample UT-3, the laser intensity has been increased up to 0.54 GW/cm². Consequently, the free surface velocity at the shock breaking-out is more important. The other features are quite close to the two previous signals. It shows that this sample did not break as well during the shock wave propagation. The last two shocks performed about 1.1 GW/cm² have led to spallation, as it is shown by the absence of velocity bouncing at about 4 µs. Despite a good reproducibility between the two shocks on the main peak, the following slopes, traducing the damage initiation, slightly change from one sample to another. This is probably due to differences in material characteristics, especially the M21 resin heterogeneities. These five signals can enable the numerical model validation in case of no damage, and spallation.

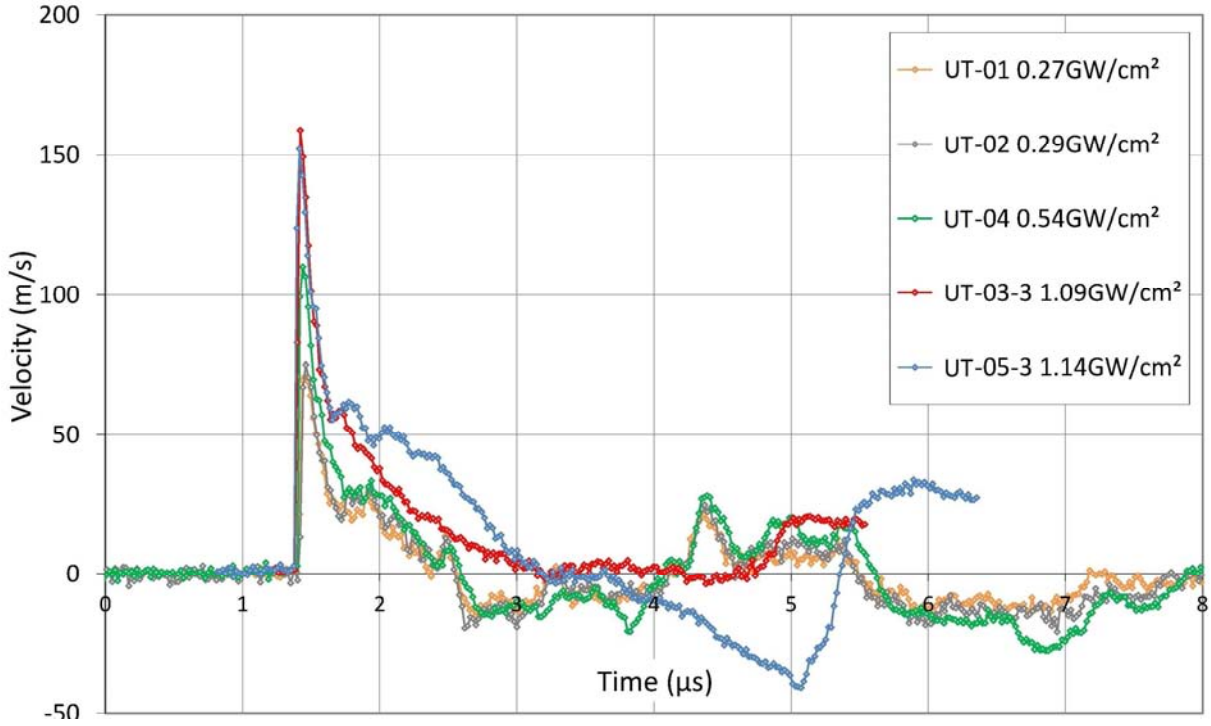

Figure 5.40, Back face velocity measurements from no damage to spallation obtained on 4.13 mm bonded cross-ply composite T700/M21 materials, referred as UT (Reference sample)

2 Bonded composite modeling, and low intensity validation

The used model for bonded composite calculation is presented in Figure 5.41. It is made on the basis of the results presented in Chapter 4. The material model for the laminates is exactly the same than the one developed for the 1.5 mm thick cross-ply T700/M21 material (see chapter 4, part 3, section 3.4). The two composite parts are modeled using this material card. The interfaces are made by using TIEBREAK contact previously presented. The damage parameters have been set equal to the composite damage parameters, also identical to what has been used in the previous T700/M21 modeling. The FM300 bond adhesive material has also already been modeled in chapter 4. The used material card in this bonded model is thus the same than the one used and validated in chapter 4 (part 2, section 2). The interfaces between the two composite parts and the bond have been perfectly TIED. Indeed, the developed model should represent the reference samples. Since these interfaces have never been experimentally broken, it is logical to prevent a numerical debonding. Note that a 2D model has to be used for the same reason than the one given for T800/M21 thick unidirectional sample modeling. Therefore, differences with the experiments on the bonded composite back face velocity could be observed because of this choice. To sum up, nothing has been changed from previous modeling, except the pressure level in order to calculate the correct free surface velocity like in the case of unidirectional composites (see Appendix C).

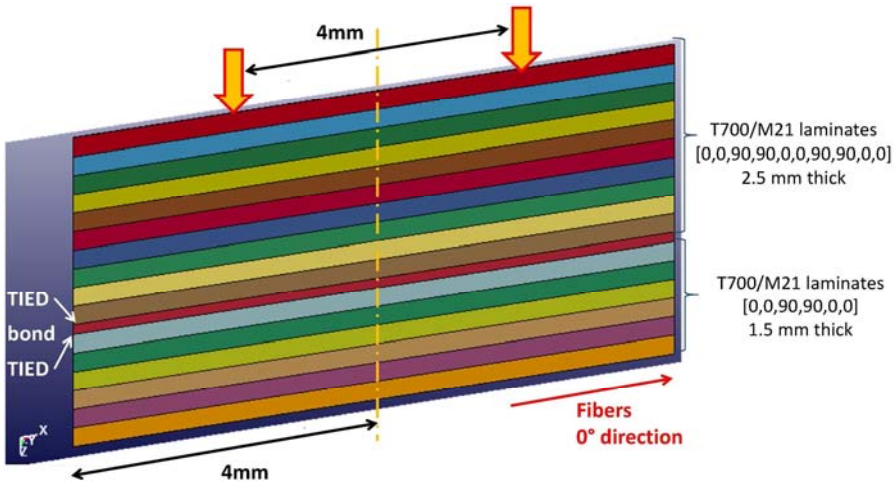

Figure 5.41, Bonded cross ply T700/M21 model, representing UT reference sample, developed thanks to LS-PREPOST software on the basis of previous numerical results.

3 Numerical simulation at low intensity and results discussion

A first comparison between numerical calculation and VISAR experimental signal is given in Figure 5.42. This result shows the good agreement between the experimental data and the simulation. Thus it validates once again the numerical model and the chosen material parameters, as nothing has been modified from the previous modeling. The biggest difference between the numerical calculation and the two experimental signals is observed on the main release wave, after the main peak. This difference is explained with Figure 5.44. For all the other main peaks and second order peaks, the agreement is pretty good. The second order peaks between t = 2.5 µs and t = 4µs are all reproduced by the numerical calculation. This is also the case of the second main peak occurring after t = 4 µs, and traducing the absence of spallation process during the observed period. Slight differences on the peaks amplitude can be observed. The large thickness, added to the different ply orientations, should be a reason for that.

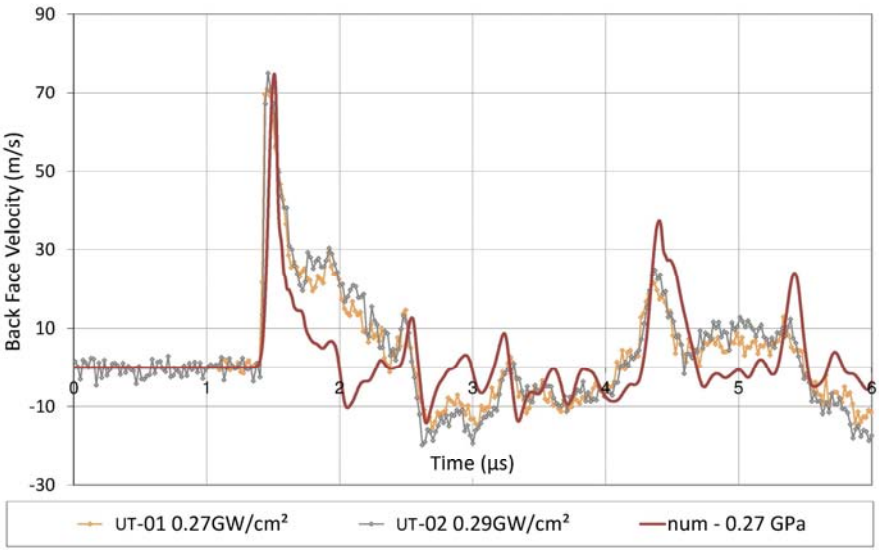

Figure 5.42, Comparison between numerical and experimental free surface velocities, in case of a laser shock on a bonded composite T700/M21 sample (UT reference), without damage (0.27 GPa)

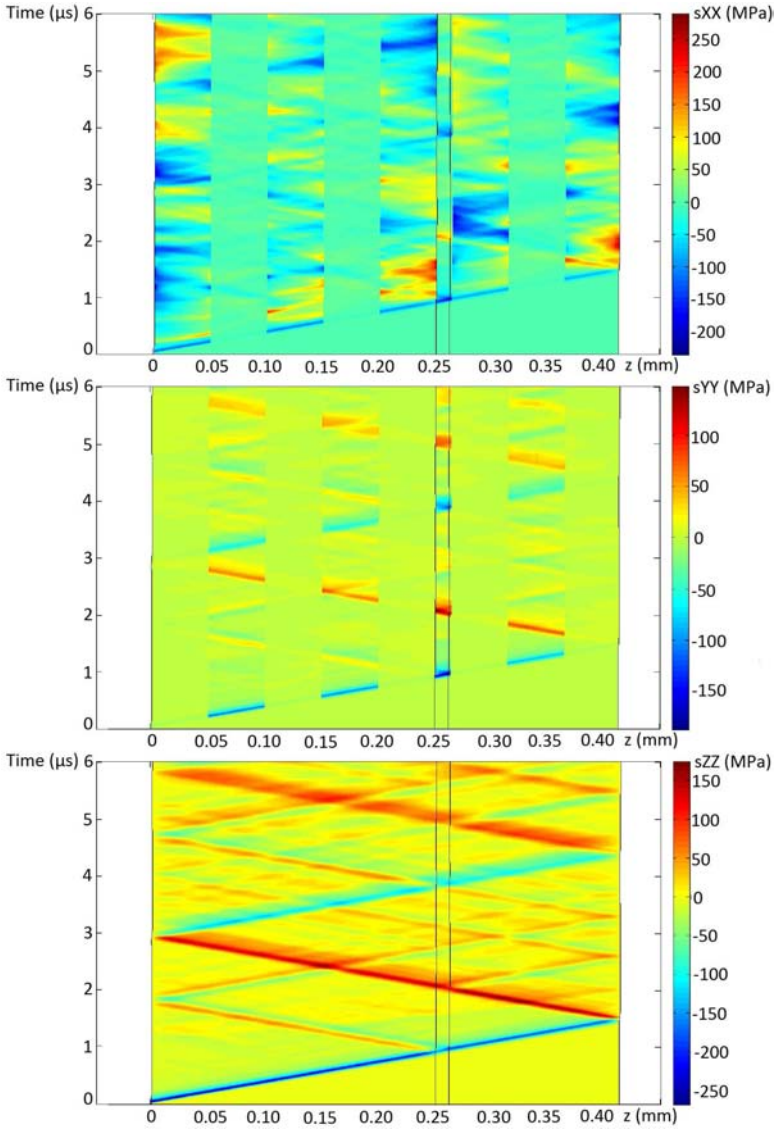

Figure 5.43, Time/position diagrams calculated in the z direction for a bonded composite T700/M21 sample (UT reference), for the three main stresses – 0.27 GPa

Since the model has been experimentally validated, it can be used to map the stresses propagation through the T700/M21 bonded composite. Three time/position diagrams along the sample thickness (z direction) are thus given in Figure 5.43, for the three main stresses directions. It enables to check that the stresses are correctly transferred from 0° plies to 90° plies (see the first two diagrams in Figure 5.43), and that the σ_{zz} propagation through the sample is correct since the z transverse direction has the same characteristics for 0° plies and 90° plies. The F300 adhesive bond also correctly behaves according to its isotropic characteristics. Indeed, the three main stresses are more or less the same in the bond, and at all time.

The T700/M21 bonded composite model can be used to identify the origin of each peak observed on the back face velocity signal. This is quite important because the understanding of the back face velocity signal is a key point for the LASAT technique and for its optimization. A small change in one of the velocity pattern could indicate an induced damage. In Figure 5.44, a time/position diagram mapping the propagation of σ_{zz} stresses within the bonded composite is first given. Note that it has been rotated 90° compared to the usual representation position. The time axis is thus horizontal, and enables to plot the calculated back face velocity signal below the time/position diagram. Finally, the experimental free surface velocity signals are added below the calculated velocity. The time axis scale is the same for the three plots, which enables direct comparisons from the time/position diagram to the back face velocity signals. Thanks to this representation, almost each peak of the velocity signals can be explained in terms of shock wave transmissions and reflections through the bonded composite based on the Time/position diagram. In Figure 5.44, arrows have been added to go from the time position diagram, to the different back face velocities. Note that the color code is important. The blue arrows correspond to the phenomena linked to a compression on the time/position diagram, also represented in blue there. It is linked to a free surface acceleration, traduced by a bouncing jump in the velocity signal. The red arrows correspond to the phenomena linked to tension on time/position diagram, where strong tension is also represented in red. It is correlated to a free surface negative acceleration, traduced by a fast velocity decrease. These two patterns form a velocity peak. Finally, green arrows are used to differentiate the other phenomena from the ones just presented, especially for the several 2D effects.

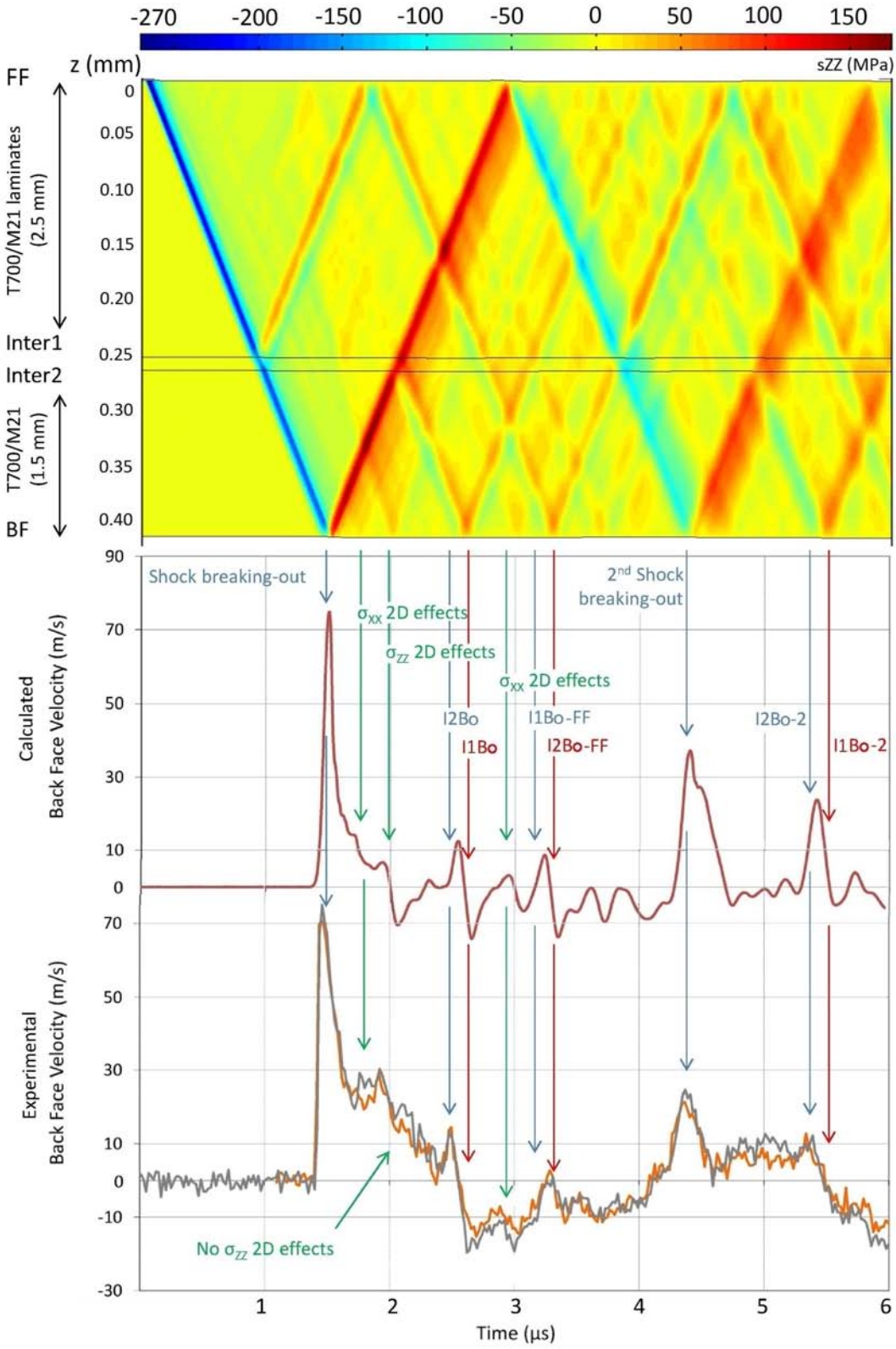

Figure 5.44, Time/position diagram in the z direction for a bonded composite T700/M21 sample (UT reference), associated with the back face velocity measurement and calculation in case of a no damage shock (0.27 GPa) – Identification of the different peak origins helped by the numerical modelling

In Figure 5.44, velocity peaks can be explained based on the time/position diagram. The two main peaks are the easiest to identify, and fit to theory. Indeed, it can be observed that the shock wave breaking-out does correspond to the fast increase of the free surface velocity. The reflection into release wave, and then tension wave leads to the fast decrease, both phenomena forming the first

peak. The second shock breaking-out does correspond to the velocity peak observed after t = 4 µs, as previously explained. In the time/position diagram presented in Figure 5.44, it corresponds to the main W shape. All the other peaks are explained in Table 5.5, where the first column gives the references to Figure 5.44 arrows, and the second one contains the explanation on the corresponding peak origin. Peaks are sorted out according to time.

References	Origin explanation
1st shock Breaking-out	This back face velocity peak corresponds to the shock wave breaking-out and reflection on the free surface.
σ_{XX} 2D effects	It corresponds to the 2D anisotropic effects evidenced in Chapter 4. Indeed, the small bouncing evidenced on the main release slope does not have a shock origin, but is generated by a σ_{XX} stress concentration at the free surface. This stress concentration is visible with the correct timing in Figure 5.43, first diagram.
σ_{ZZ} 2D effects	It corresponds to the conventional 2D effects on the main σ_{ZZ} stresses and leads to an important decrease in the back face velocity. This has not been evidenced experimentally, or in a much less importance at least. This is probably due to the absence of 3D modelling.
I2Bo	**I**nterface **2 Bo**uncing – This velocity bouncing is induced by the compression wave coming from the reflection of the main tension wave propagating backward on the second bond interface.
I1Bo	**I**nterface **1 Bo**uncing – This velocity decrease immediately following I2Bo is induced by the tension wave coming from the reflection of the main tension wave propagating backward on the first bond interface.
Note that these two transmission/reflection phenomena are consistent with the shock theory in terms of impedance mismatch	
σ_{XX} 2D effects	This bouncing does not seem to be due to a transmission/reflection phenomenon. Therefore, it could be attributed to anisotropy.
I1Bo-FF	**I**nterface **1 Bo**uncing – from **F**ront **F**ace. It is induced by the compression wave coming back from the front face after a first reflection of the shock wave at the 1st bond interface. Indeed, the shock is reflected into a tension wave propagating backward at the first bond interface. This wave is itself reflected into a compression wave after reaching the front face.
I2Bo-FF	**I**nterface **2 Bo**uncing – from **F**ront **F**ace. It is induced by the tension wave coming back from the front face after a first reflection of the shock wave at the 2nd bond interface. Indeed, the shock is reflected into a compression wave propagating backward at the second bond interface. This wave is itself reflected into a tension wave after reaching the front face.
Note that these two transmission/reflection phenomena are consistent with the shock theory in terms of impedance mismatch	
Not referred small peaks	The small peaks observable between t = 3.2 µs and t = 4 µs are partially due to the I2Bo and I1Bo, because each wave has been reflected toward the bond, where it has been reflected again toward the back face.
2nd shock breaking-out	This back face velocity peak corresponds to the shock wave breaking-out after a back and forth.
I2Bo-2	**I**nterface **2 Bo**uncing – 2nd release. This phenomenon is similar to I2Bo. It is induced by the compression wave coming from the reflection of the second main tension wave propagating backward on the second bond interface.
I1Bo-2	**I**nterface **1 Bo**uncing – 2nd release. This phenomenon is similar to I1Bo. It is induced by the tension wave coming from the reflection of the second main tension wave propagating backward on the first bond interface.

Table 5.5 Back face velocity peaks origins according their timing position

These results show that laser shock numerical modeling enables a complete understanding of the experimental back face signals. Thanks to this analysis, it is now possible to associate each experimental peak to the corresponding shock phenomenon. This had never been done yet for such complex bonded composite samples and it will be very useful for the LASAT optimization and its industrial development.

4 Numerical simulation at mid intensity and in case of spallation

The model has been used for higher pressure, and compared with the experiments. In Figure 5.45, the laser shock performed on the reference T700/M21 bonded material (0.54 GW/cm²) is correctly modeled as shown by the averagely good comparison between the experimental signal and the calculated one. Moreover, these results show that with the damage parameter determined in chapter 3, the numerical model predicted the integrity of the assembly for this shock intensity, in agreement with the experiment.

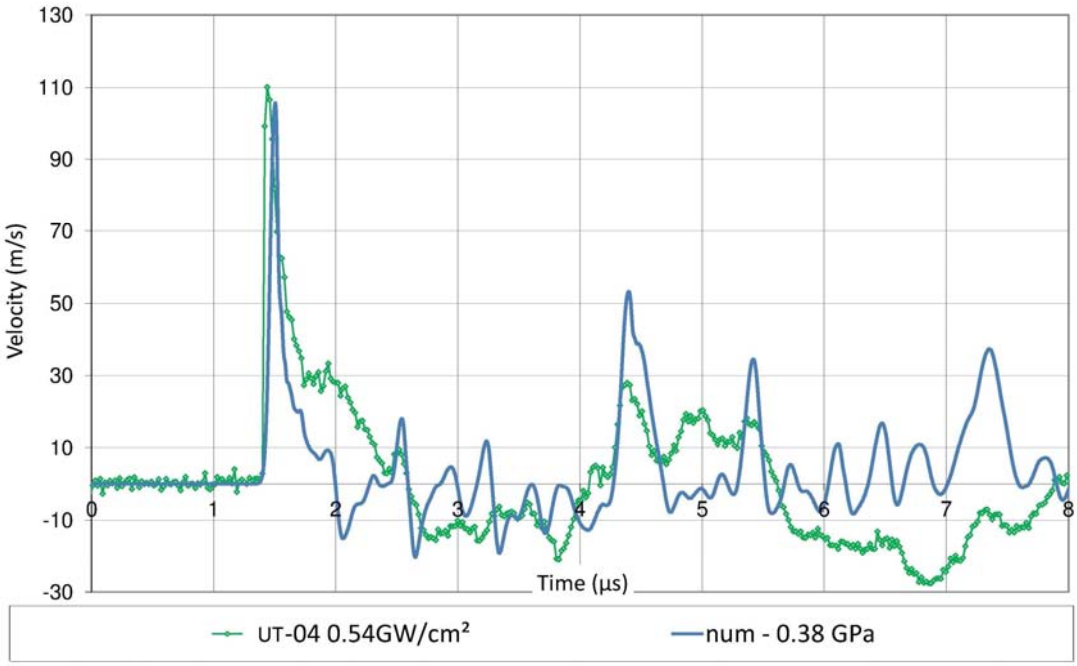

Figure 5.45, Comparison between numerical and experimental free surface velocities, for a bonded composite T700/M21 sample (UT reference), in a second non-breaking case (0.38 GPa)

The last calculation to be performed is the one presented in Figure 5.46 using both a time/position diagram and the different back face velocity signals comparison chart. In this case, the experiments performed on the T700/M21 bonded material have shown a damage characterized by the absence of the second shock breaking-out. The numerical model also provides this information, still using the same damage parameters as those determined in Chapter 4 (see in Figure 5.46). Thanks to the time/position diagram presented, the depth of the damage can be identified. It seems that the two 0° plies first break from the 90° plies, and after 0.5 µs separate one from another. This is traduced by two different shock propagation frequencies in the broken parts, visible on the Time/position diagram, and on the back face velocity signal. Since these frequencies are clearly visible until 3 µs, it seems that only the interplies (TIEBREAK interface) break in a first time, and then the composite breaks in a second time. The damage criterion of the interplies is probably more easily reached than the one of the composite. Comparing the broken calculated signal to the experimental one, it can be observed that the oscillations are much more visible in case of the calculation. This can be due to the

chosen damage modeling assumptions, but also to behavior modeling which is elastic. Adding viscosity could help to reduce these oscillations. Nevertheless, these results demonstrate that the model can also be used as a tool to produce lasers shock induced damage signals. Thus, it constitutes and efficient tool for the LASAT optimization

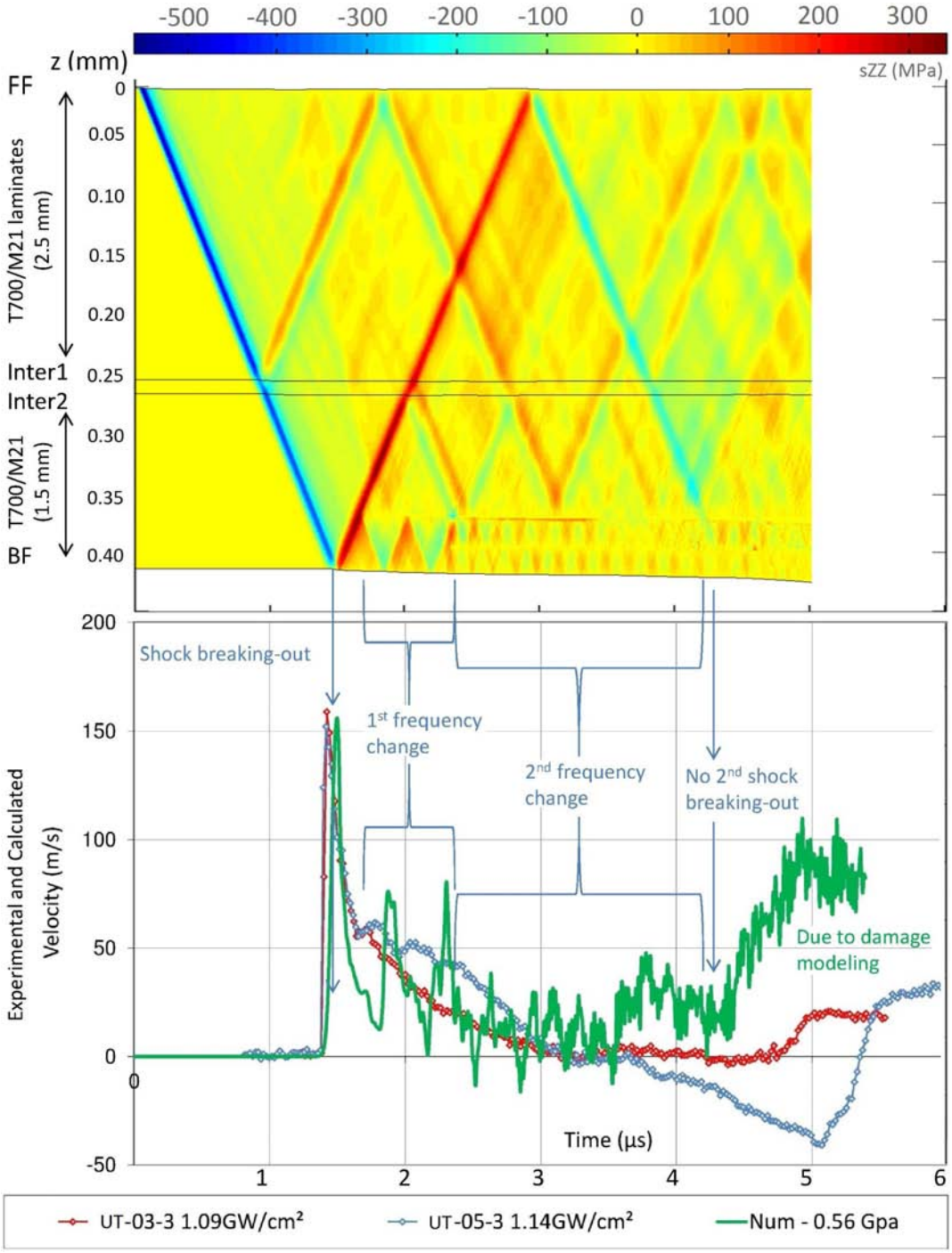

Figure 5.46, Time/position diagram in the z direction for a bonded composite T700/M21 sample (UT reference), associated with the back face velocity measurement and calculation in case of spallation (0.56 GPa) – Identification of the different peak origins helped by the numerical modelling

Conclusions & synthesis

In this chapter, experimental and numerical results obtained on bonded composites were presented. Two sets of samples have been tested, the first one containing symmetrical samples (two composite plates of the same thickness), and the second one grouping non-symmetrical samples (one thick plate bonded with a thin one). Samples have different origins: ENCOMB samples (EADS Cassidian) for some of them (ES1, ES2, UT, RE, MO) and Airbus for the other ones (LA, LE, LB). Each set contains references and contaminated samples. GIC results from University of Patras and Airbus have been used to compared with LASAT results.

Laser shocks were performed on each type of samples, and every shock was analyzed using several post-mortem techniques. Between five and nine shocks were produced on each contamination degree in order to determine the damage thresholds of the bonded assemblies. The performed analysis after the shocks enabled a deep investigation of the laser shock induced damage in these bonded CFRP, all the results forming a consistent data. In particular, it can be noticed that ICM had been efficient to measure the residual back face deformation. The small elliptical blisters measured are a clear indicator of an internal damage in the composite (see chapter 3). Thus, the confocal microscopy is useful to determine the damage threshold of the composite. Concerning debonding threshold, the ultrasounds (conventional or laser) were used and shown to be quite efficient in some cases. The interface opening creates voids inside the material which leads to a strong impedance mismatch clearly influencing the ultrasound wave propagation. Finally, cross section observations enable the damage quantification in both composite and bond interface. Details on the failure mechanisms can thus be obtained, and enable comparison between the different scenarios of contamination.

Focusing on symmetrical samples, the experimental results enabled the discrimination between the references and the different contaminated samples. It also shows that the laser parameters used were not correctly adapted to the bonded system testing. Optimization would be necessary to avoid breaking the composite part while testing the interface. According to the determined threshold, only LB scenario provided a bond weak enough to be tested without optimization.
For non-symmetrical samples, same adaptation problem was observed. The different laser energy level tested enabled a sharp framing of damage thresholds, especially in case of release agent contamination. In this case, the debonding threshold evolution is in quite good agreement with the contamination degree provided by ENCOMB partners and GIC results. For moisture samples, results should be carefully considered, because porosity could influence the shock propagation and complicates the ultrasounds results interpretation. Nevertheless, if taking only the upper debonding threshold framing boundary, results are also in good agreement with the contamination degrees. For both types of contamination, the damage threshold of the T700/M21 laminate is quite low compared to the debonding threshold. Therefore, a more optimized shock configuration is necessary for these scenarios.

Finally, numerical modeling calculations obtained on bonded composites, and the corresponding experimental validations were presented. Results show good agreement between numerical simulations and experimental back face velocities. Therefore, the model and the corresponding time/position diagram representation were used to identify the main back face velocity patterns. It led to a better understanding of the velocity signals, ie of the behavior of bonded CFRP. This

knowledge can then be used to clarify the current possibilities of the LASAT technique, and to forecast its optimization solutions.

References

[1] ENCOMB (266226) Deliverable D2.1: *Set of samples and sample characterization (by reference methods for adherent surface and adhesive bond characterization and mechanical testing) for screening of ENDT methods*, 20th December, 2011

[2] ENCOMB (266226) Deliverable D2.2: *Set of samples and report on sample characterization (by reference methods for adherent surface and adhesive bond characterization and mechanical testing) for testing of ENDT methods*, 2nd May, 2012

CHAPTER 6: LASAT CURRENT CAPABILITIES, NUMERICAL OPTIMIZATION AND ASSOCIATED EXPERIMENTAL DEMONSTRATION

Introduction **262**

Part 1: Current LASAT possibilities **262**

1 Repeated loading on bonded targets **262**

2 Current LASAT possibilities for the considered assemblies **265**

Part 2: Tunable focus diameter **268**

1 Principle of the optimization by tunable focus diameter **269**

2 Non-symmetrical bonded assembly: loading on the thick composite face **271**

3 Non-symmetrical bonded assembly: loading on the thin composite face **274**

Part 3: Tunable pulse duration **276**

1 Principle of the optimization by tunable pulse duration **276**

2 Numerical optimization by tunable pulse duration **278**

2.1 On non-symmetrical bonded assembly 278
2.2 On symmetrical bonded composite assembly 282

3 Experimental validation of the numerical optimization by plate impacts experiments **285**

3.1 Plate impacts and VH measurements 286
3.2 On really weak bonds (LE) 288
3.3 On reference ES1 289

Part 4: Double shock approach **290**

1 Double shock on the assembly front face solution **290**

1.1 Principle of the optimization by the front face double shock 290
1.2 Double shock on the front face, numerical approach 291

2 The symmetrical laser shock **293**

2.1 Principle of the optimization by symmetrical laser shock 294
2.2 Symmetrical laser shock on bonded composite, numerical optimization and experimental validation 295
2.2.1 Non-symmetrical T700/M21 bonded samples *295*
2.2.2 Symmetrical T800/M21 bonded samples *296*
2.3 Experimental validation of symmetrical laser shock on bonded composite 297
2.3.1 On ENCOMB ES1 & ES2 ..... *298*
2.3.2 On weak bonds *299*

Conclusions & synthesis **300**

Introduction

This chapter deals with the LASAT current capabilities and the different optimization solutions which are developed in this work to make the technique more efficient. Considering the current laser configurations, the interfaces which can already be tested are first discussed in part 1. For optimization, the key point is to enable a dynamic loading as close as possible from the bond line, and therefore avoiding breaking the composite during the test. In this work, four different optimization solutions have been investigated and compared: tunable focus diameter, tunable pulse duration, front face double shocks and symmetrical laser shock. They are respectively discussed in part 2, part 3 and part 4.

Part 1: Current LASAT possibilities

1 Repeated loading on bonded targets

In this first part, the tests which can already be performed in the current configuration are discussed. First, the non-destructive characteristic of the test method has to be checked. Indeed, when a laser shock is produced below the damage threshold of the reference bonded assembly, it should not induce any modification. In other words, the question is to know if the laser shock test can induce some fatigue effect on the bonded composite, by modifying its mechanical properties. This study is linked to the one conducted on unidirectional T800/M21 sample in Chapter 3. In case of bonded assembly, 10 shocks, in the same intensity range and below the reference damage threshold, were produced on the same UT sample. The used laser configuration was Config-PPRIME-2, in order to monitor the sample dynamic responses by VISAR measurements. Between each laser shock, aluminum painting is put back on the sample front face so the laser/matter interaction is realized in the same conditions. The laser shock parameters are given in Table 6.1.

Laser shock reference on UT-repro1	Energy (J)	Pulse duration (ns)	Dfoc (mm)	Intensity (GW/cm²)	Verdi power (W)	Fringe factor (km/s)
ES1-repro1-01	0.82	28.68	4	0.23	0.75	0.1061
ES1-repro1-02	0.92	29.09	4	0.25	0.75	0.1061
ES1-repro1-03	0.91	27.29	4	0.26	0.75	0.1061
ES1-repro1-04	0.85	27.05	4	0.25	1	0.1061
ES1-repro1-05	0.79	23.08	4	0.27	0.75	0.1061
ES1-repro1-06	0.81	26.05	4	0.25	0.75	0.1061
ES1-repro1-07	0.88	24.01	4	0.29	0.75	0.1061
ES1-repro1-08	0.83	25.66	4	0.26	0.75	0.1061
ES1-repro1-09	0.87	30.41	4	0.23	0.75	0.1061
ES1-repro1-10	0.92	24.48	4	0.30	0.75	0.1061
ES1-repro1-11	1.71	27.13	4	0.50	0.75	0.1447
ES1-repro1-12	2.66	27.63	4	0.77	0.75	0.1447
ES1-repro1-13	3.56	24.25	4	1.17	1	0.1447

Table 6.1 Laser shock parameters for bonded cross-ply T700/M21 (UT-repro1 sample) time resolved experiments conducted in Config-PPRIME-2 – Associated VISAR parameters

The 10 successive VISAR measurements are presented in Figure 6.1, in which the time and velocity origins have been shifted to enable an easy reading of the signals. It can be observed that all the signal patterns, identified in the previous chapter, can be seen on each presented signal. Especially,

the first peak is well reproduced with the shock breaking-out, anisotropic bouncing, and bond interface reflection bouncing. The second shock breaking-out, occurring 4 µs after the laser deposition and traducing the absence of damage in the bonded structure, is also visible on the 10 signals with more or less amplitude. The slight differences are within 20% variation which corresponds to the different uncertainties already evidenced. This good reproducibility of the bonded composite dynamic response, from one shock to the following, is even more evidenced in Figure 6.2, in which all the signals are superposed. Since the signals are identical, within the uncertainty range, it confirms that the sample dynamic response is the same for the 10 shocks. Consequently, it proves that no mechanical modification detectable by this technique has been induced by the laser shocks performed below the bonded composite damage threshold.

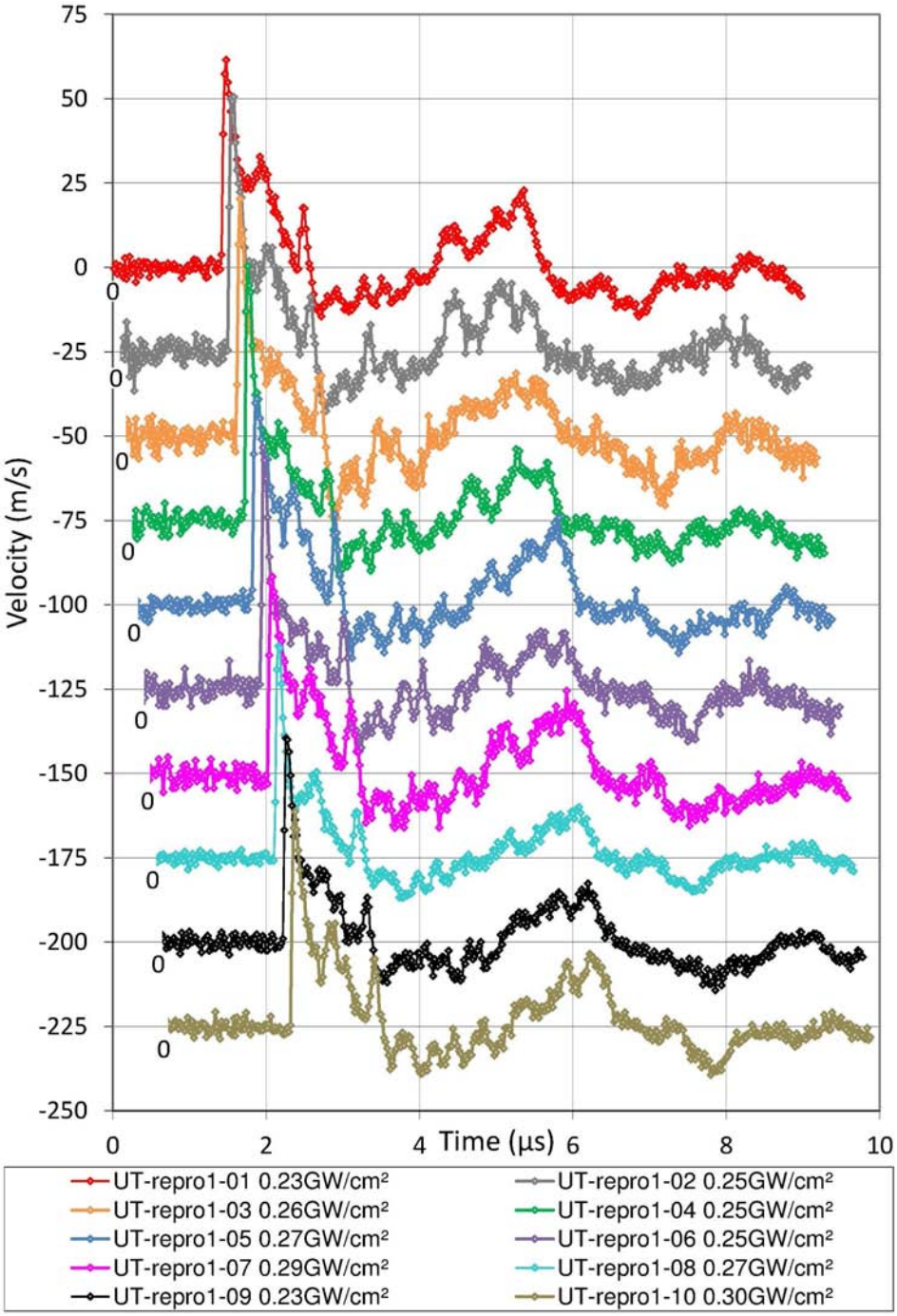

Figure 6.1, 10 successive VISAR measurements of the laser shocks performed on the same UT sample shifted in time and velocity amplitude to enable pattern recognition

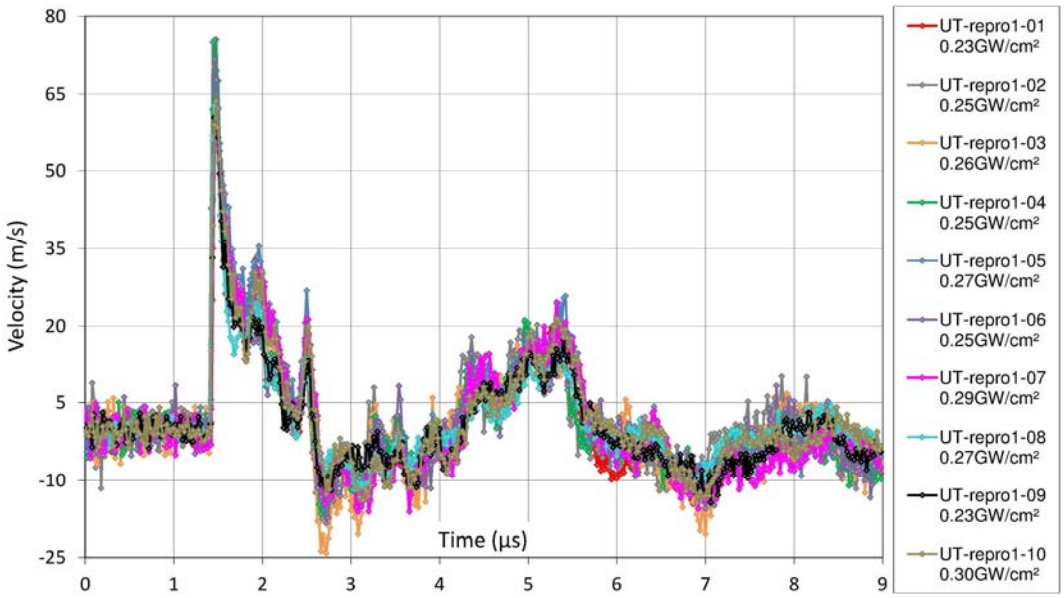

Figure 6.2, 10 successive VISAR measurements of the laser shocks performed on the same UT superposed to show the good reproducibility from one shock to the following

In a second time, on the same UT sample, pressure has been progressively increased by changing the laser energy in order to check that the damage threshold of the bonded sample has not been moved by the 10 previous repeated laser shocks. The laser parameters are given in Table 6.1 and the corresponding measurements are presented in Figure 6.3. The green/brown curve corresponds to the 10th laser shock produced on UT-repro1 sample, and presented in the two previous figures. The laser intensity was about 0.3 GW/cm² in this case, like for the shocks performed before. Then, the blue curve corresponds to the VISAR measurement performed during the following shock. In this case, the laser intensity was increased up to 0.5 GW/cm². Consequently, the shock breaking-out back face velocity amplitude is higher in this case (see in Figure 6.3). Despite this increase of pressure, this higher shock did not lead to damage inside the bonded target. Indeed, the second shock breaking out is still visible after t = 4µs. Its amplitude is a bit higher because of the higher input pressure. Back to chapter 5, a VISAR measurement realized during a shock performed about 0.54 GW/cm² also evidenced an absence of damage for this pressure level, but without any repeated shock before. It can be thus concluded that the damage threshold of this given bonded target has not been decreased. Then, in both cases the following intensity level did show a damage initiation in the bonded target. In case of sample presented in chapter 5, this intensity level was about 1 GW/cm². In case of sample UT-repro1, it was about 0.8 GW/cm², which is close from the other energy level. The VISAR measurement realized in this last case is presented in Figure 6.3 (orange curve). The damage initiation is evidenced thanks to the absence of the second shock breaking-out induced velocity bouncing, usually observed at about 4 µs. For this shock, the bouncing is shifted almost 1 µs later, which is a clear sign of a mechanical modification of the bonded sample such as damage initiation. As final proof, a last shock has been produced on the UT-repro1 sample, with laser intensity of about 1 GW/cm². The first shock breaking-out corresponds to the previous one, probably because the initiated damage during the previous shock was small enough not to modify the first wave passing through. Then, the second higher frequency visible on the red curve indicates the presence of a noticeable damage, such as a delaminated zone.

These experimental results show that the damage threshold has not been modified after 10 repeated shocks and for this particular bonded structure. It is a clear indication showing no fatigue effect, until, induced by repeated loading on the same spot. This is encouraging regarding the laser shock adhesion test industrial application, for which only one or two shocks per spot can be considered enough to test the bonded interface. It is also in good agreement with the conclusions made on the absence of significant microstructural modifications under laser shock discussed in Chapter 3.

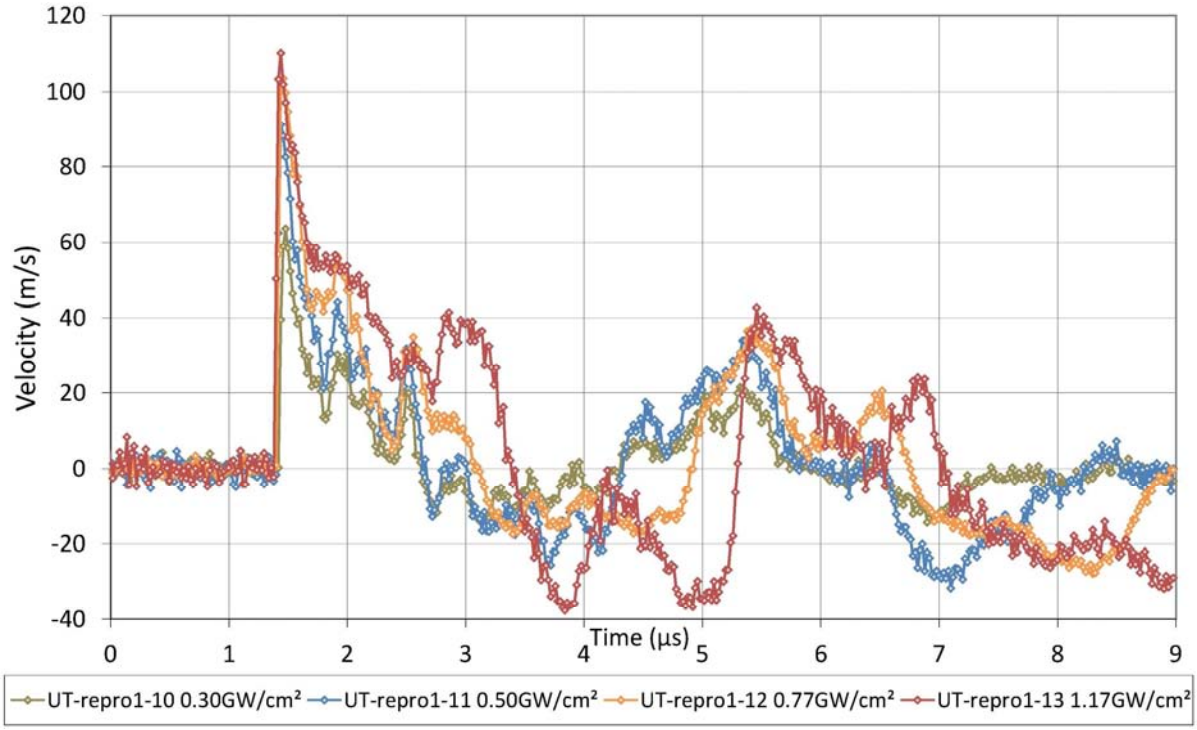

Figure 6.3, VISAR signals measured on UT-repro1 sample, corresponding to the produced shocks progressive increase of the laser intensity until the damage initiation in this bonded composite

2 Current LASAT possibilities for the considered assemblies

In this section, the developed and validated numerical model of bonded composite is used in order to evaluate the current possibilities of the laser shock adhesion test technique, if no optimization is performed. Therefore, the test is considered to rely on the current laser configuration, such as the one available in PPRIME. This study is presented here in case of the non-symmetrical T700/M21 bonded composite (meaning UT lay-up) with a loading on the thick composite face, but could also have been performed on the symmetrical T800/M21 bonded composite by using the same approach. Several calculations are run, using the same input pressure amplitude on the bonded composite. The highest pressure level which did not induce any experimentally observable damage and no numerical damage initiation has been chosen. It corresponds to 0.38 GPa, as explained in Chapter 5. According to previous results, this pressure level corresponds to the maximum of energy which can be given to the target, without breaking the composite part of the assembly. This energy level being fixed, the idea is now to see what kind of interface strength can be tested in this configuration. For that, the TIEBREAK damage criteria of the bonded model second interface are progressively weakened from the composite interlaminar strength $\sigma_{T,i}$ to a lower percentage of this strength. For each calculation, the back face velocity is calculated, as well as the time/position diagram showing the waves propagation within the bonded composite target. Calculations start with an interface strength equal to the composite strength. Two examples of the obtained results are given in Figure 6.4.

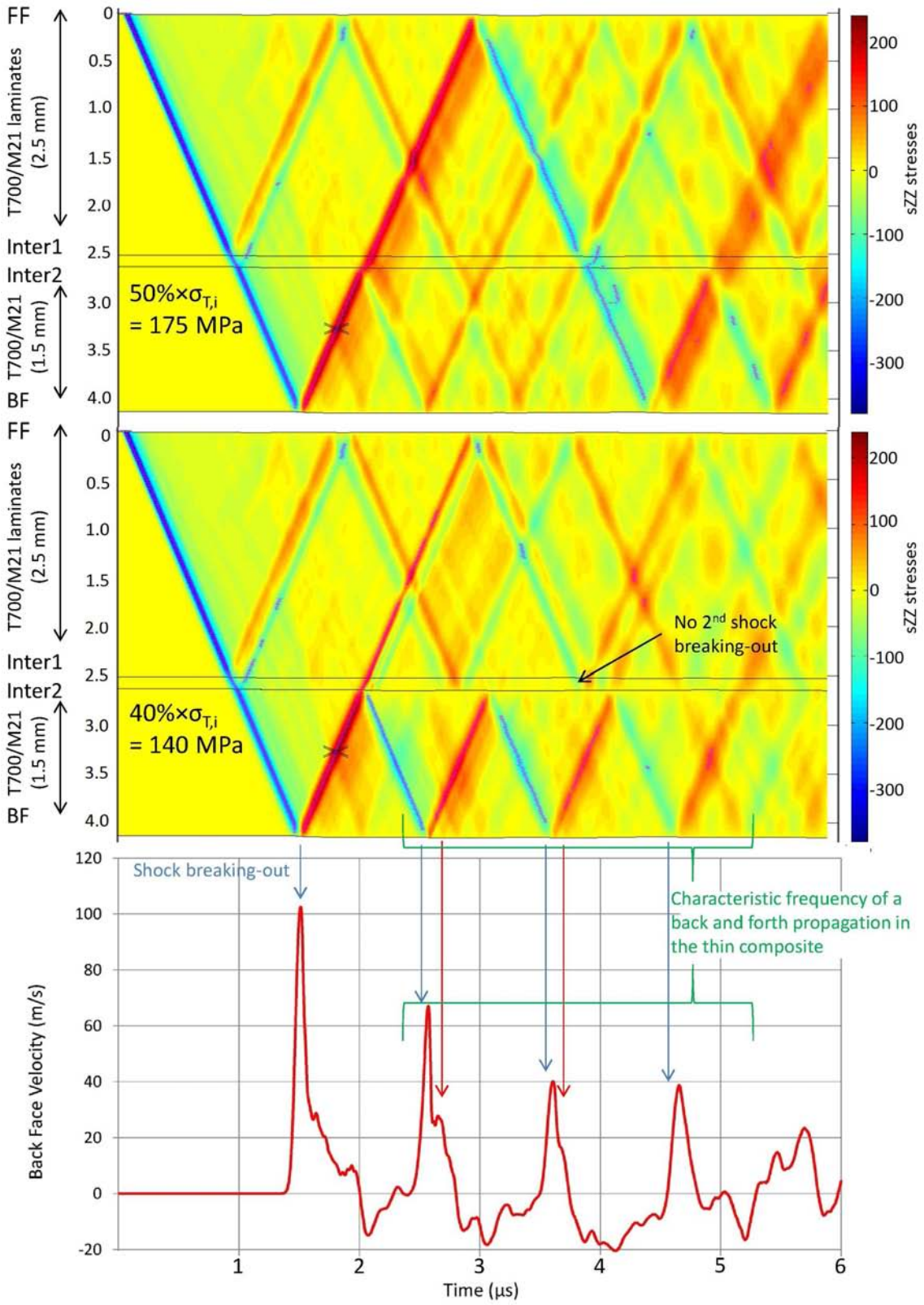

Figure 6.4, Numerical investigation of the current LASAT capabilities: Time/position diagram with a degraded interface about 50% of the composite interlaminar strength (175 MPa), time/position diagram with a degraded interface about 40% of the composite interlaminar strength (140 MPa), associated calculated back face velocity characterizing the debonding

Figure 6.4 is divided in three main parts, two time/position diagrams and one calculated back face velocity signal. The first given time/position diagram corresponds to a calculation performed by using an interface damage criteri reduce to 50% of the composite interlaminar strength, for both tensile

and shear criteria. No difference from the diagram given in chapter 5 can be noticed, except in the stress levels because the input pressure was not the same. Especially, the absence of bond interface damage is evidenced by the main W shape traducing the shock back and forth propagation through the whole bonded composite target. The tensile stresses propagating backward from the back face were not high enough to activate the damage criteria. The second time/position diagram results from the same simulation, except that the 2nd bond interface damage criteria have been reduced by 10 % from the previous calculation. Until t = 2 µs, the shock wave propagation in the bonded composite target is logically identical to the previous one. When the tension propagating backward from the composite back face, the tensile stresses are high enough this time to activate the damage criteria, and lead to the interface breaking. It occurred after a short numerical incubation time, which is due to the stress level progressive increase until the damage criterion is met. The incubation time is also representing a physical phenomenon, which enables a part of the main tension to propagate back in the thick composite before the damage initiation. The main tension wave is thus divided in two. A small part can pass through the bond into the thick composite, and a second part is strongly reflected at the interface into a shock wave propagating afterward in the thin composite part. The waves remain trapped in the thin composite, as shown by the back and forth propagation visible in the thin composite (see in Figure 6.4). Indeed, the waves cannot go through the bond anymore because of the impedance mismatch created by the interface opening. For the same reason, second main shock breaking-out cannot occur in the propagation pattern. This specific wave propagation into the thin composite part is clearly identified thanks to the corresponding back face velocity signal presented at the Figure 6.4 bottom. The back and forth frequency is characteristic of the wave propagation in this 1.5 mm T700/M21 laminate. This is shown by using blue and red arrows in Figure 6.4. The absence of a second shock breaking-out is also evidenced by this free surface velocity signal. It can be compared to the signal obtained thanks to the first calculation (see in Figure 6.5). Two main differences can be observed. The most obvious one is probably the change in frequency observed between the two interface strength models. In particular, the third peak in case of red curve does not exist on the blue one. Moreover, the fourth peak of the red curve is delayed from the second peak of the blue curve, corresponding to the second shock breaking-out. This difference can prevent from confusing a propagation leading to debonding, and a propagation which does not. The amplitude of the shock breaking-out velocity peaks is also different from one case to the other. This is due to the interface opening which creates a higher impedance mismatch than the one created by the bond only. Therefore, the second peak in case of red curve is higher than the small bouncing induced by impedance mismatch on blue curve.

Considering LASAT application, these signals could be used to monitor the debonding, and enable an easy identification. Indeed, it can be assumed that the blue curve is the signature of the highest shock which can be performed on this bonded composite, below the damage threshold. Thus, it can be used as a reference signature. When a difference is experimentally observed from this curve, out from the uncertainty range, it can be inferred that the monitored shock did open the interface. Numerically, the difference between the reference curve (blue one) and the monitored curve (red one in this case) can be plotted. It is done using a green curve Figure 6.5. In this case, the uncertainties on the back face velocity should be considered within ± 20% of the maximum velocity amplitude. Therefore, if the green curve goes out from the [-20, 20 m/s] range, the differences between the signals can be considered to be high enough to evidence a mechanical modification of the target, such as debonding in this case. This representation enables to take into account both changes in frequency and amplitude. Going further, each type of damage in this given target should induce a different back face velocity signal, which can now be understood thanks to modeling. In

other words, a delamination 50 µm deep from the back face would not have the same signature than a delamination 200 µm deep, and even than a debonding. For each specific damage occurrence, the difference curve from the reference will change. Thanks to numerical calculations, this curve can be predicted and used to identify the difference experimental patterns. Experimentally, this representation would enable a fast identification of the damage depth, type and dimensions.

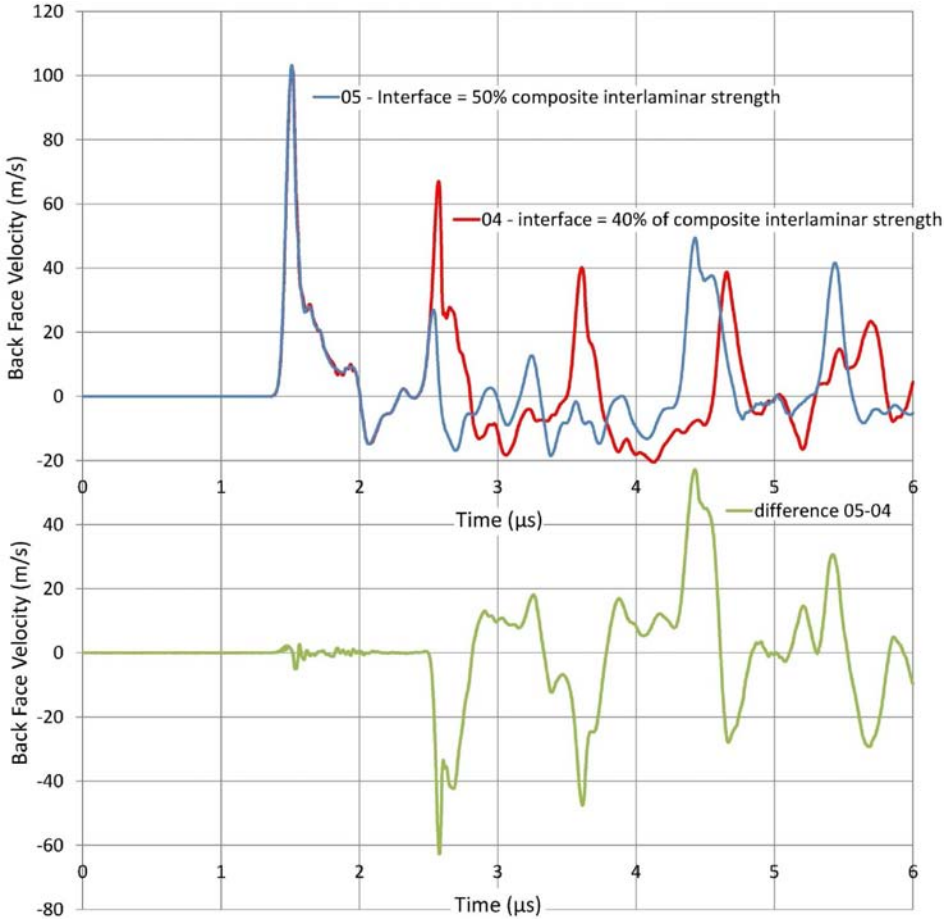

Figure 6.5, Calculated back face velocity (BFV) signal from the previous modeling (see Figure 6.4): BFV in case of a degraded interface about 50% of the composite interlaminar strength (175 MPa) in blue, BFV in case of a degraded interface about 40% of the composite interlaminar strength (140 MPa) in red, difference between the two previous curves plotted in green

In this part, it has been shown that it should be possible to test an interface whose strength is inferior or equal to 40% of the composite interlaminar strength. This value relies on numerical modelling. But, experimentally, it should be shifted to lower values if taking into account the laser parameters uncertainties. In the following parts, focus is made on the numerical results, assuming a perfect laser source. Nevertheless, the experimental uncertainties have to be kept in mind.

Part 2: Tunable focus diameter

In this part, LASAT optimization by use of tunable focus diameter is discussed. The main idea is to play on the 2D effects additional tensile stresses timing by changing the loading zone dimension. In the first section, the optimization technique principle is shown by using numerical modeling on 3 mm thick unidirectional T800/M21 samples (presented in Chapter 4). Then, it is applied to T700/M21 non-symmetrical bonded composites, using first the laser loading on the face of the thick plate, and then on the face of the thin composite plate.

1 Principle of the optimization by tunable focus diameter

In Figure 6.6, two different Time/position diagrams are presented. They have both been obtained thanks to the developed Matlab tool, after LS-DYNA numerical calculation of a laser shock on a 3 mm thick unidirectional T800/M21 composite. All the modeling parameters are the same from one calculation to another, especially the pressure set to be below the damage threshold of the composite model (see parameters in Chapter 4, Table 4.3). The only difference is the focus diameter which varies from 2 mm to 4 mm, respectively in Figure 6.6-a and 6.6-b. On the 2mm time/position diagrams, the σ_{zz} 2D effects are clearly visible. It is represented by the yellow/orange zone, above the main shock propagation, starting about 0.7µs. This 2D tensile stress pattern appearing time in the shock propagation is quite early, which is consistent with the focus size. Indeed, when the focus is small, the release waves generated from the loaded area edges rapidly cross the axi-symmetrical axis of the loading, along which the diagram is plotted, creating thus a tensile loading on the axis. It can be observed that this additional tensile zone meets the main tension area generated by the crossing of release waves at the sample back face (about 2.5 mm deep from the front face). The 2D effects resulting tension and the main tension generated by the crossing of release waves are thus combined to create higher tensile stresses. Therefore, the maximum of tensile stresses is detected in this back face region as shown by the small black cross visible in the Time/position diagram. The white area represents the location of the stresses in the range [95%max – max]. If switching to the 4 mm case, it can be observed that the highest stresses are distributed differently. Indeed, the exact maximum remains located close to 2.5 mm deep from the front face because of the crossing of main release waves, but the 95% maximum loading zone is more spread. Especially, a sizable zone, centered around 1.5 mm deep, can be observed. For a wider focus diameter, the 2D effect additional stresses appear later and deeper in the composite material. Consequently, it crosses the main tension wave, propagating backward after the crossing of release waves, later in the propagation pattern. 2D effects thus enhance a different region of tensile stresses.

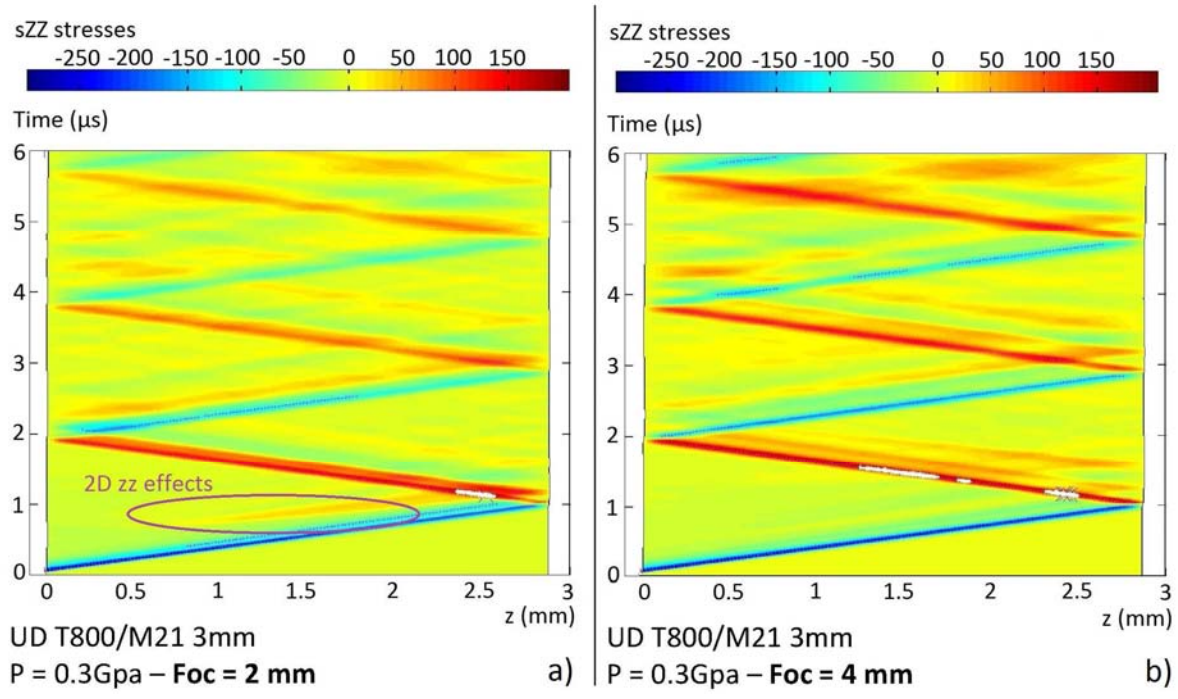

Figure 6.6, Time/position diagrams from laser shocks on 3 mm thick unidirectional T800/M21 composite materials in case of two different focus diameters: 2 mm (left diagram), 4 mm (right diagram)

The change of focus diameter has logically a noticeable effect on the back face velocity signals. As an example, three different calculated back face velocity signals are given in Figure 6.7 in case of three different focus diameters. In case of 2mm, it can be observed that the 2D effects have an attenuation effect on shock amplitude, stronger than in the two other cases. This is logical because 2D effects influence the shock propagation sooner in case of small spots. The focus diameter also influences the 2nd order phenomena such as anisotropy effects, which is consistent with the discussion developed in Chapter 4.

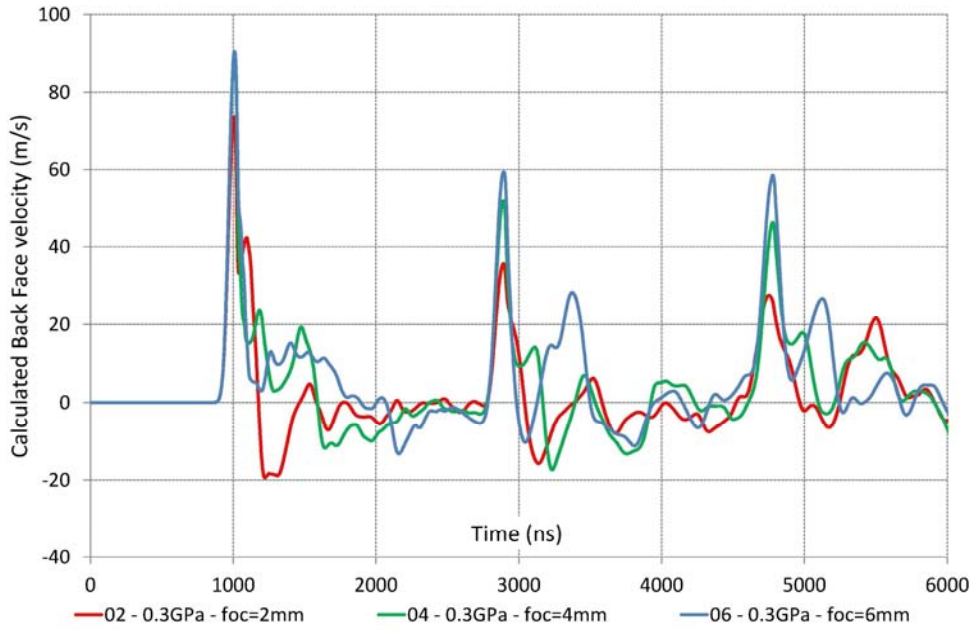

Figure 6.7, calculated free surface velocities from laser shocks on 3 mm thick unidirectional T800/M21 composite materials in case of three different focus diameters: 2 mm (red), 4 mm (green), 6 mm (blue)

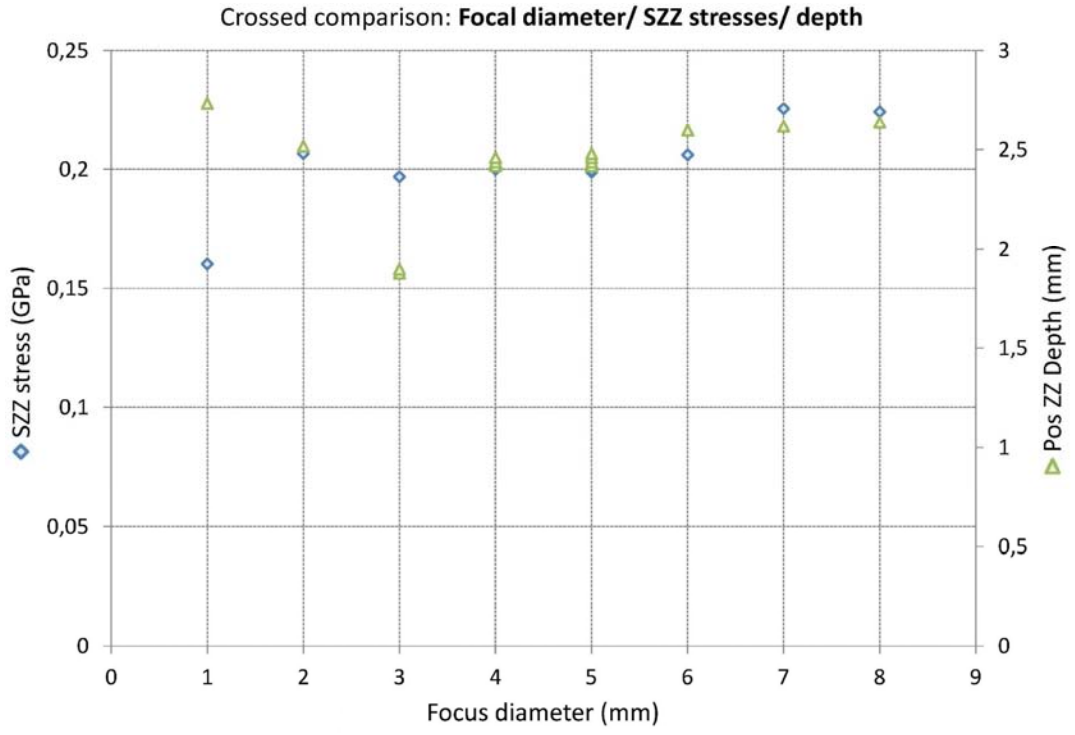

Figure 6.8, Synthesis chart of the stresses maximum value and their corresponding depth in case of laser shock on 3 mm thick unidirectional T800/M21 composite material, for different focus diameters

Finally, the influence of the focus spot dimension can be summarized using a crossed comparison diagram, such as the one presented in Figure 6.8. The different focus diameters simulated are placed on the horizontal axis. The maximum of tensile stresses detected by the developed Matlab tool is plotted as a function of focus diameter in diamond shape blue dots, and referred by the left axis. For each diameter values, the depth location of the tensile stresses maximum in the sample thickness is added using green triangular dots, and referred by the right axis. Thanks to this representation, several conclusions can be made. For locating the maximum of tensile stresses as deep as possible, the 2D effects are more efficient in the case of a 3mm diameter. Nevertheless, if looking the extended 95% maximum zone, it is not that obvious and a 4 mm diameter can also be used. After 4mm diameter, the 2D effects almost have no more influence on the tensile stresses maximum level, as well as on their position.

2 Non-symmetrical bonded assembly: loading on the thick composite face

This optimization principle has been used on non-symmetrical bonded composite (2.5mm/ bond/ 1.5mm). For that, numerical modeling of the bonded composite is used. It is identical to the one presented in Chapter 5. Like in the previous section, the pressure is kept constant about 0.3 GPa, and the focus diameter is changed from one calculation to the other. Three Time/position diagrams are presented in Figure 6.9 for three different focus diameters: 2 mm, 4 mm, and 6 mm. Once again, the location of the tensile stresses maximum through the composite thickness is marked by a cross, and the stresses above 95% of the maximum are represented using white areas. The 2 mm diameter case is similar to the calculation presented in case of unidirectional T800/M21 (see in Figure 6.6). The 2D effects occur quite early after the main shock propagation, and thus enhance a maximum of tensile stresses close from the thin composite back face. In case of a 4 mm diameter, the 2D effects are delayed, and cross the tension wave propagating backward after a while, deeper from the back face than in the 2 mm case. Typically, a 4mm diameter should be more adapted than a 2 mm diameter for testing the bond strength. Finally, a calculation using a 6 mm diameter is presented at the bottom of Figure 6.9. In this case, the 2D effects are late enough to enhance tensile stresses in the thicker composite plate, meaning the front face. In fact, the maximum detected is due to three tension sources in this case. The first one is logically the main tension propagating backward from the back face, after the crossing of release waves. The second one is the tension created by 2D effects. And the third one is due to the shock and release reflection on the two bond interfaces, then reflecting on the front face to finally cross the main tension propagating backward. This explains the maximum region geometry.

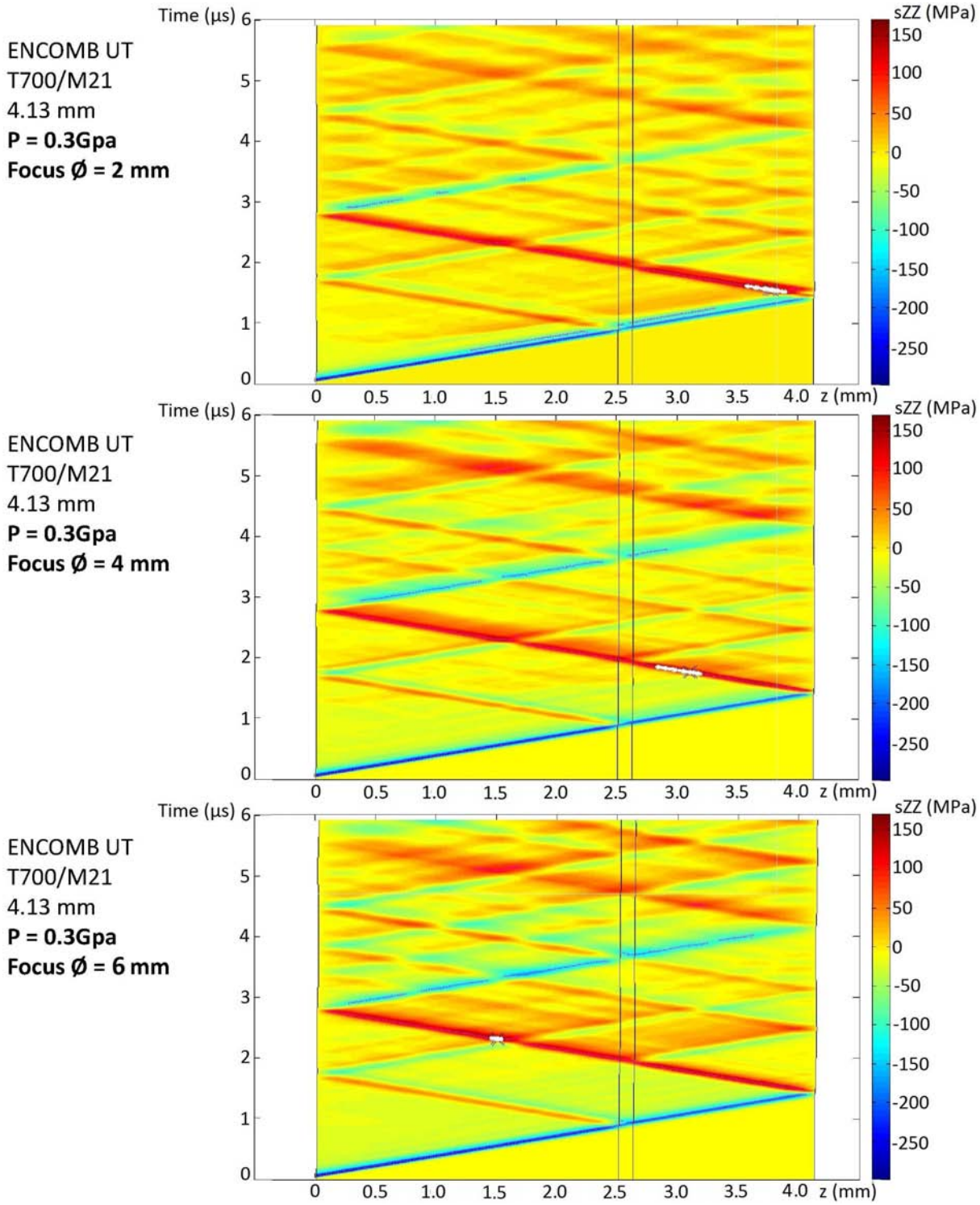

Figure 6.9, Time/position diagrams from laser shocks on the thick plates of cross-ply T700/M21 composite bonded assemblies (2.5mm/ bond/ 1.5mm) in case of three different focus diameters: 2 mm, 4 mm and 6 mm

Like in the case of unidirectional T800/M21 composite, the back face velocity signal obtained on bonded composite simulation also changes depending on the focus diameters. The signals coming form the modeling discussed in Figure 6.9 are presented in Figure 6.10. Same observations can be made on the attenuation, the anisotropic bouncing, and the conventional 2D effects influences on the velocity signals, than the one discussed in the previous section.

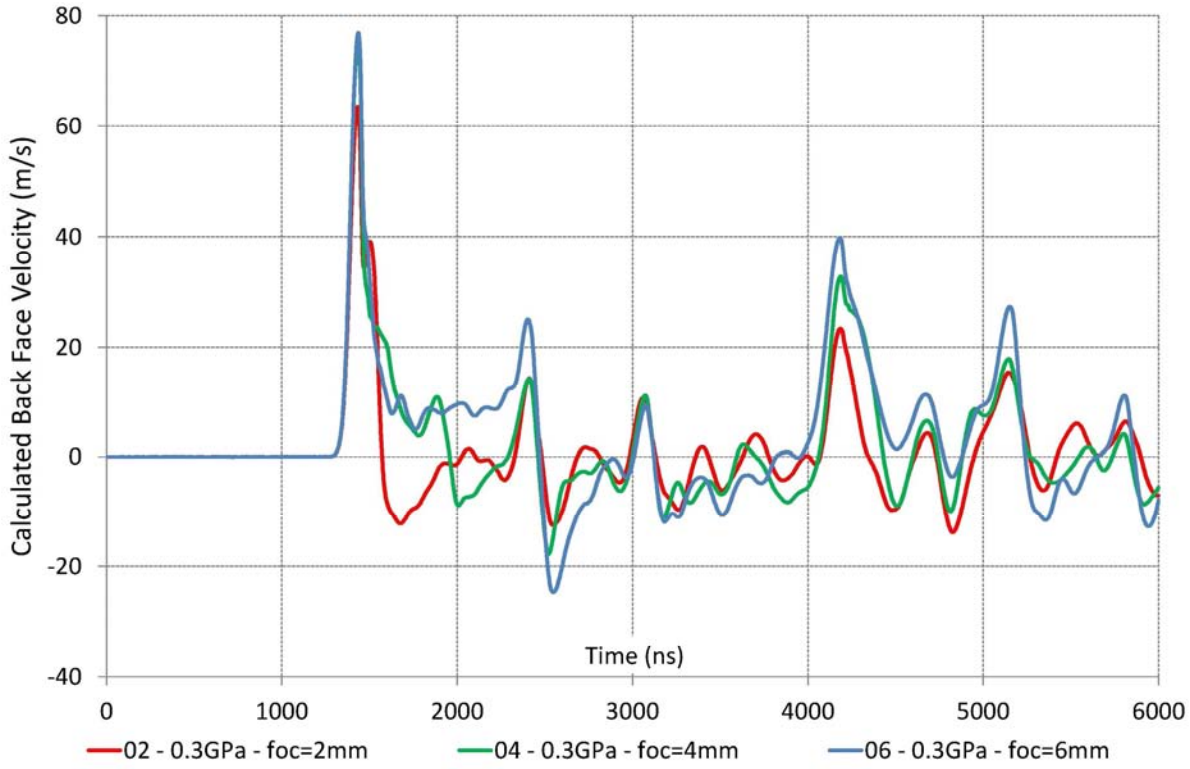

Figure 6.10, calculated free surface velocities from laser shocks on the thick plates of cross-ply T700/M21 composite bonded assemblies in case of three different focus diameters: 2 mm (red), 4 mm (green), 6 mm (blue) – Corresponding to the time/position diagrams presented in Figure 6.9

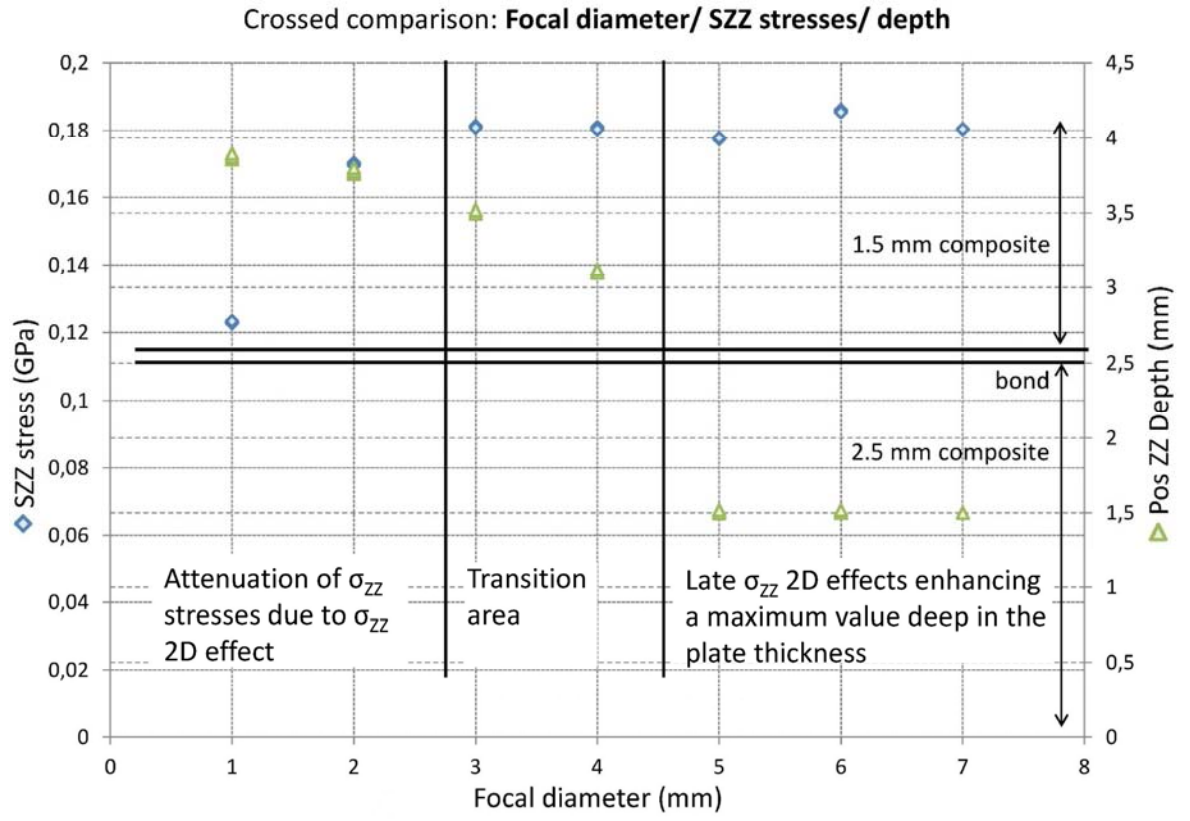

Figure 6.11, Synthesis chart of the stresses maximum value and their corresponding depth in case of laser shock on the thick plates of cross-ply T700/M21 composite bonded assemblies, for different focus diameters

Finally, the focus diameter parametric investigations can be summarized by using the graph presented in Figure 6.11. Considering only the LASAT application to the composite bond testing, it can be concluded that the 2D effects can efficiently be used to locate nearer the bond line the maximum of tensile stresses in the case of 4 mm diameter. This is the diameter value that we have used for testing bonding composite. Nevertheless, it is not well optimized yet, because the maximum is still not right on the interface. Moreover, the thin composite plate is loaded with 90% of the maximum value, which is still important. Figure 6.6 shows that for 1 and 2 mm diameters, the 2D effects soften the σ_{zz} tensile stresses. Between 2mm and 4mm diameters, the 2D effects enable to enhance a maximum stress zone deeper in the back face composite, and the maximum stress level is reached. For wider diameters, the 2D effects are late enough to reinforce the late tensile stresses coming from the reflection at the bond line, as previously explained. It locates the maximum of tensile stresses in the thick CFRP plate, near the front face.

3 Non-symmetrical bonded assembly: loading on the thin composite face

On non-symmetrical bonded composite, the same approach can be used with the laser loading being performed on the other composite plate, meaning on the thin composite face. Indeed, it has been shown in the previous section that the shock reflection on the bond line could induce modifications in the maximum of tensile stresses position. Therefore, changing the position of the bond compared to the loaded side could also induce some modification of the maximum position, depending on the diameter size. This is presented in Figure 6.12. The three same diameter dimensions were numerically tested: 2 mm, 4 mm, 6 mm. This time, laser shock was produced on thin composite plate, as it is visible in Figure 6.12. The maximum position dependency on the focus diameter is shown by these three Time/position diagrams. Results from this second parametric investigation are summarized in Figure 6.13. If only considering the LASAT application case, it can be concluded that, from this composite side, the 2D effects are more efficient to locate nearer the bond line the maximum of tensile stresses also in case of a 4mm diameter. Once again and even if this parameter value is better, this solution is not a full optimization. Before 4mm diameter, the 2D effects soften the σ_{zz} tensile stresses as it is shown by the decrease of tensile stresses maximum with the diameter reduction. For diameters wider than 4 mm, the 2D effects have no more influence on the position on the maximum of tensile stresses, as well as on the maximum value. Wide diameters should be preferred. Finally, no strong differences with the opposite case have been noticed, which means that both tests (from the two sides) can be performed to load near the bond line.

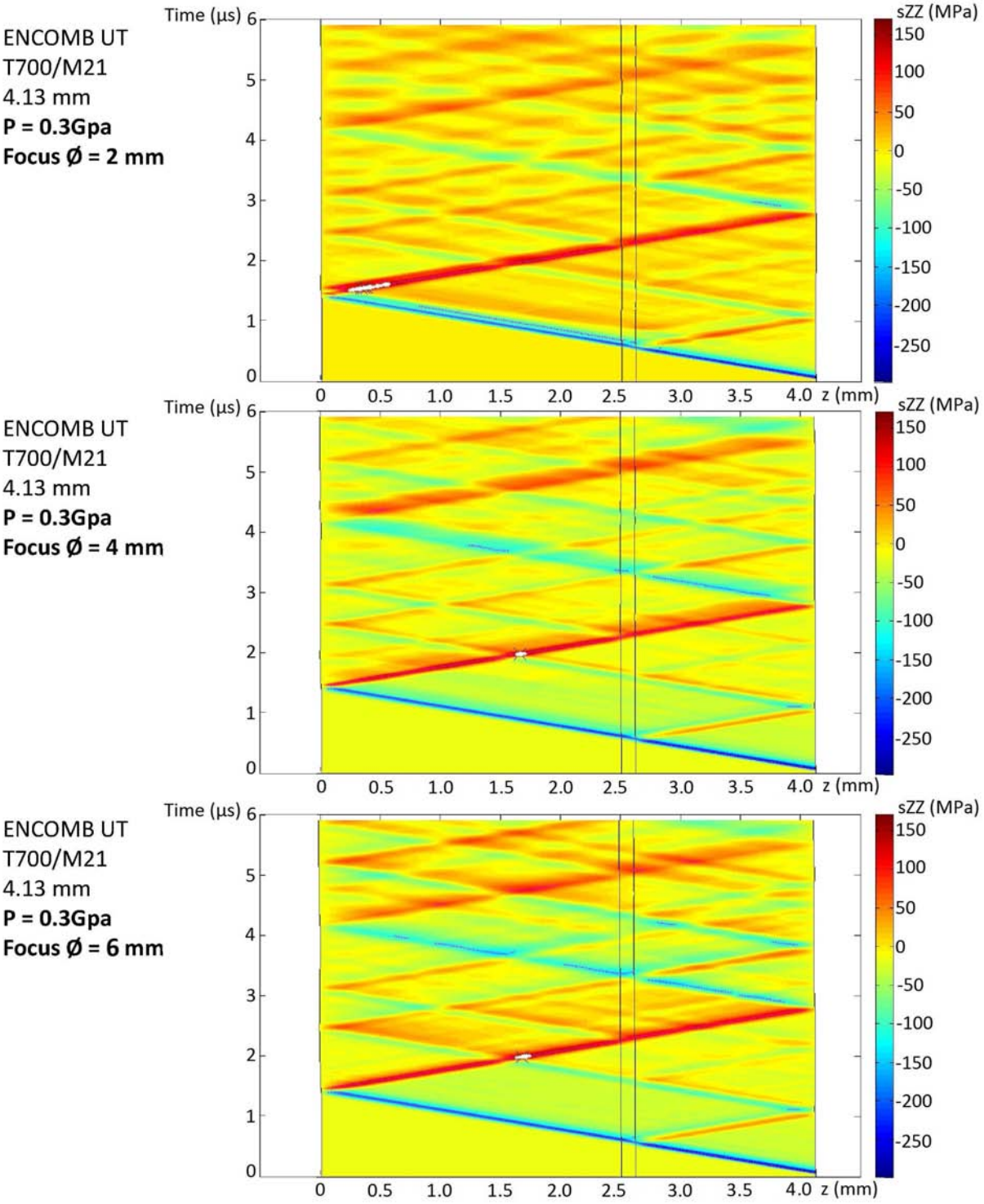

Figure 6.12, Time/position diagrams from laser shocks on the thin plates of cross-ply T700/M21 composite bonded assemblies in case of three different focus diameters: 2 mm, 4 mm and 6 mm

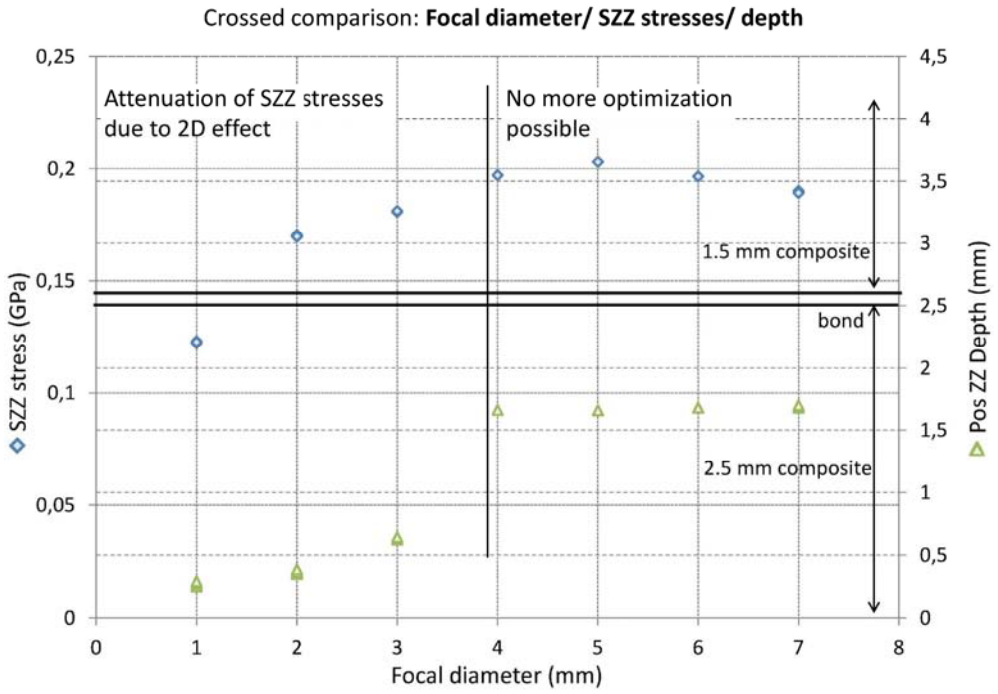

Figure 6.13, Synthesis chart of the stresses maximum value and their corresponding depth in case of laser shock on the thin plates of cross-ply T700/M21 composite bonded assemblies, for different focus diameters

In conclusion, it has been shown in this part that changing the focus diameter of the laser could induce sensitive modification in the maximum stresses distribution in the (time, position) plane. Especially, the σ_{ZZ} 2D effects timing is directly linked to the focus size, and have an enhancing effect on the tension wave propagating backward from the back face. In either shocks on the thick composite face or on thin composite face configurations, the first reflection on the bond is also an important source of tensile stresses, more visible in case of large spots. In this large spot configuration, the superposition of tension from the back face, 2D σ_{ZZ} effect induced tension, and tension coming from this reflection is responsible for high stress levels. It seems that from a given diameter, it is not possible anymore to move the maximum of tensile stresses within the target thickness. If looking for an optimal configuration for the non-symmetrical T700/M21 bonded composite, it seems that a 4 mm diameter shock on the thick composite face enables to generate high tensile stresses near to the bond line. Nevertheless, this configuration is not fully optimized because the maximum is not located right on the bond. Going further, it could be interesting to determine general rules, based only on the target thickness, and the different sound speed in the material.

Part 3: Tunable pulse duration

The next optimization technique to be tested in this work is the tunable pulse duration. The principle of this optimization solution is given based on aluminum simulations in the first section. In a second time, the tunable pulse duration optimization is numerically investigated on both non-symmetrical T700/M21 bonded composite and symmetrical T800/M21 bonded composite. An experimental validation using plate impacts on these last samples is finally presented in the third section.

1 Principle of the optimization by tunable pulse duration

The principle of the LASAT optimization by use of tunable pulse duration is presented in Figure 6.14.

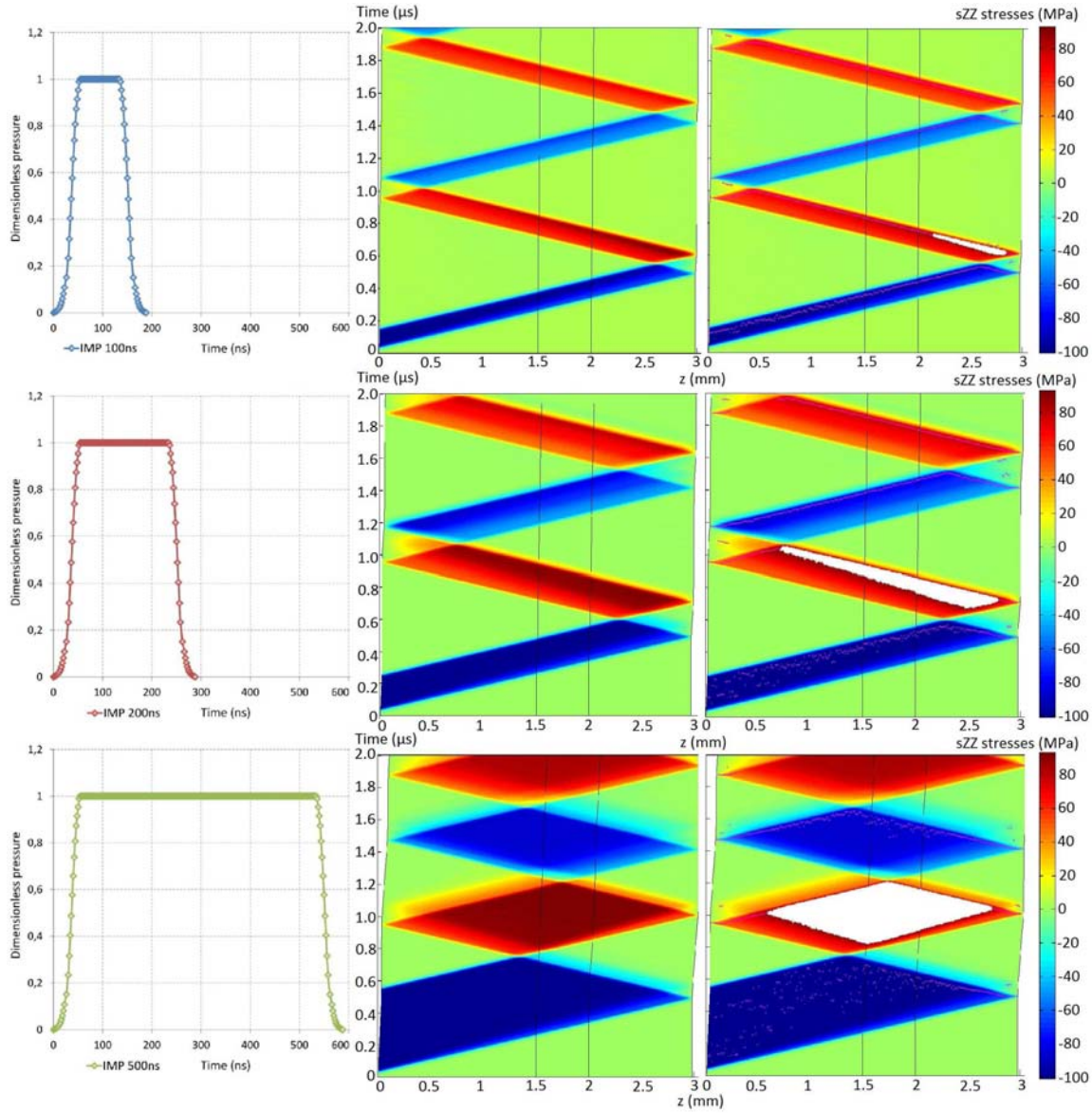

Figure 6.14, Effect of a tunable pulse duration in case of a three-aluminum-target presented thanks to time/position diagrams, with and without maximum tensile loading zones (white zones).

A simple aluminum numerical model is used in order to demonstrate the optimization principle. It is modeled in 1D, to enable fast calculation, and it used a classic aluminum elastic hydrodynamic material model. The 1D model is made of three layers, each layer being perfectly tied. The three layers are made of aluminum, still to enable an easier approach by avoiding the transmission/reflection phenomena at the interfaces. On this model, three different pressure profiles have been tested. They are square-shaped, all admitting 0.1 GPa as the maximum of pressure, but each of them presents a different pulse duration: 100 ns, 200 ns, 500 ns. The three profiles are given on the left of Figure 6.14, using the same scales for comparison. Two time/position diagrams are associated with each pressure profile. The first one represents the σZZ propagation through the three-aluminum-layer material. As usual, blue corresponds to compression and red to tension. By the way, it can be noticed that it is easier to differentiate release wave from tension wave on this kind of sharp loading than in case of Gaussian pulses. Indeed, until the crossing of the two release waves within the sample thickness, no tension can be generated. This is particularly visible in the 500 ns pulse case. The second time/position diagram is the same than the first one, but presents in addition the area loaded above 95% of the detected maximum values. From Figure 6.14, two interests of the

optimization by use of tunable pulse duration are shown. Firstly, changing the pulse duration enables to move the position of the tensile stresses maximum. Especially in this case, if longer pulses are used, the tensile stresses maximum will be moved deeper in the material thickness from the target back face. Secondly, the shape of the most loaded area (represented in white in Figure 6.14) changes in the time/position plane with the pulse duration. It enables for example to create longer stresses in an interface. In the aluminum case presented in Figure 6.14, this is particularly visible in case once again of the 500 ns pulse calculation. In that case, the first stresses are also created in the middle on the sample, which is also interesting for the LASAT application.

2 Numerical optimization by tunable pulse duration

This optimization principle has been numerically used on non-symmetrical bonded composite (section 2.1), and symmetrical bonded composite (section 2.2). Shocks are always performed on the thick plate face. The pressure profiles used in the following section were defined as presented in Figure 6.14. The optimization principle has been experimentally demonstrated using plate impacts. It is presented in the third section.

2.1 On non-symmetrical bonded assembly

A numerical parametric investigation on the non-symmetrical T700/M21 assembly (2.5mm/ bond/ 1.5mm) has first been performed. The numerical model has not changed from the previous investigation and still represents the UT reference assembly. The focus diameter is kept constant at 4 mm and the maximum pressure is set below the damage threshold about 0.15 GPa. The pressure profile width at mid-height has been varied from 50 ns to 500 ns, square-shaped as shown in Figure 6.14. For each calculation, the maximum of tensile stresses is recorded by the developed Matlab tool, in terms of level, timing and position. This numerical data can then be used to compare the differences in pulse characteristic efficiency to test the bond interface. This is done in the synthesis chart presented in Figure 6.15, where the σ_{ZZ} stress levels (in blue dots) and their position in the sample thickness (green dots) are plotted for each pulse width, given in the horizontal axis.

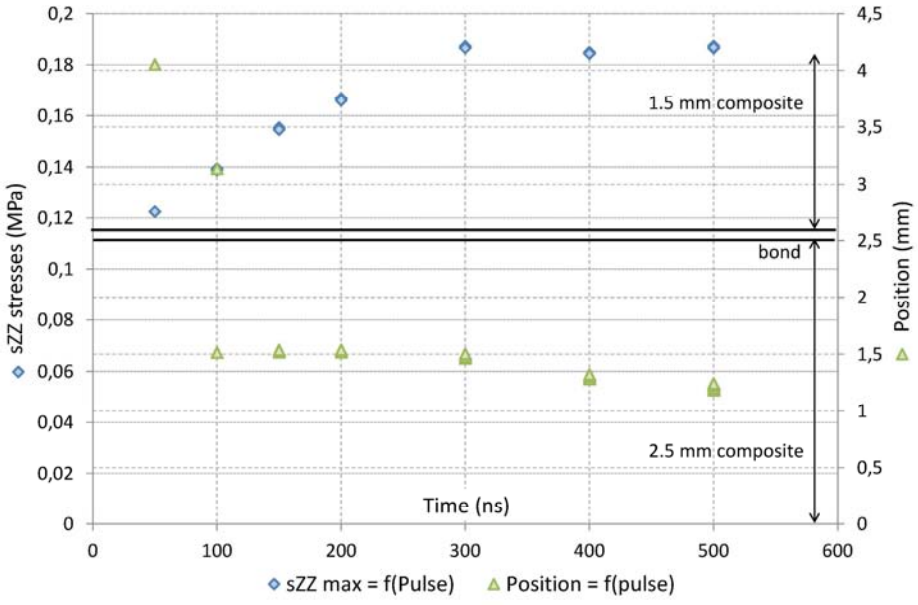

Figure 6.15, Synthesis chart of the stress maximum values and their corresponding depth in case of laser shock on cross-ply non-symmetrical T700/M21 bonded composites, for different pulse durations

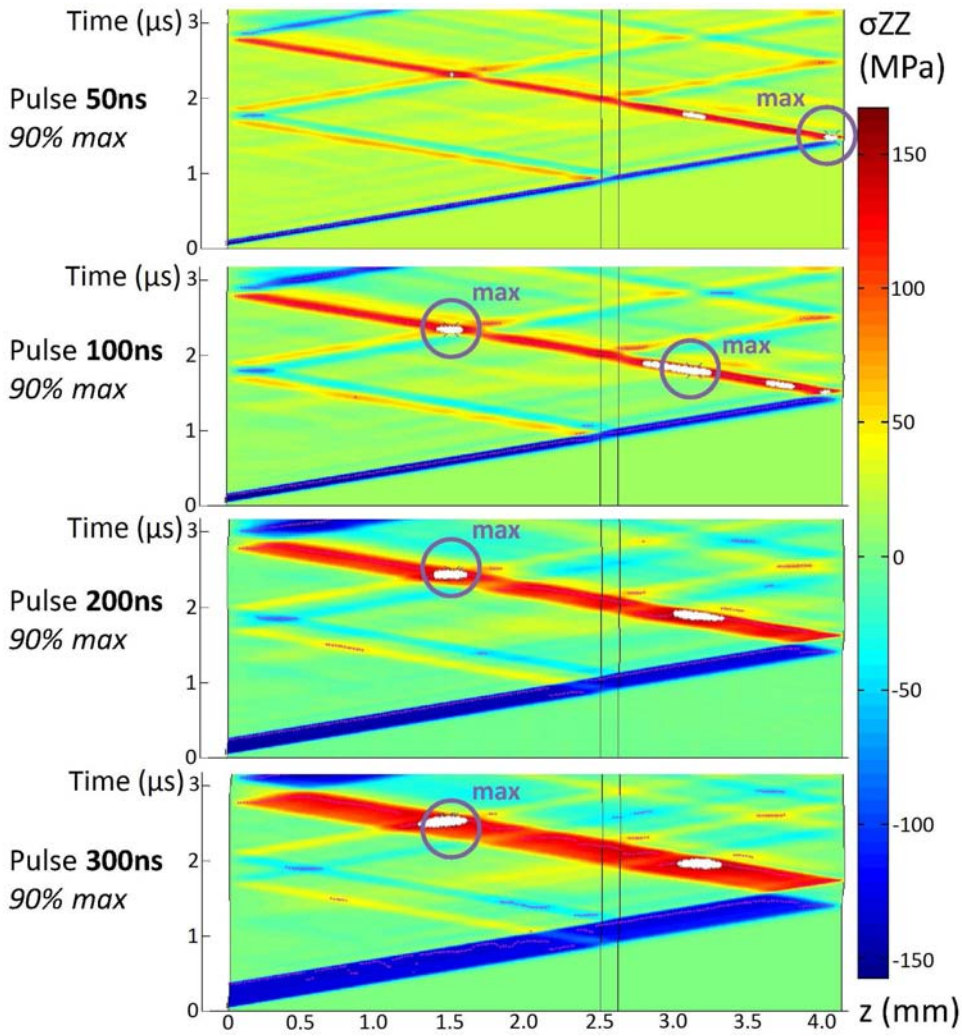

Figure 6.16, Effect of tunable pulse duration in case of a non-symmetrical T700/M21 bonded composite assembly, presented thanks to time/position diagrams, and enhanced with maximum tensile loading zone at 90%, in white color

If looking first to the σ_{zz} stress levels (blue dots in Figure 6.15), it can be observed that from 300 ns long pulses, they remain constant about 0.18 GPa, even with the pulse duration increase. Before that, the shorter pulses induce attenuation of the main tensile stresses which is consistent with theory. The position of the exact tensile stresses maximum can also be looked at as a function of pressure pulse width. In Figure 6.15, the presented results show that the maximum stress level rapidly falls in the thick composite plate. Note that the calculation performed by using a 100 ns pulse reaches a maximum in two different locations. As previously explained in the focus diameter investigation, this maximum loaded zone is mainly due to the reflection of the main shock on the bond interface, and then reflected again on the front face. This pattern is also visible in Figure 6.16, where time/position diagrams are presented. These diagrams allow a better understanding of the maximum stresses distribution in the bonded composite sample. In Figure 6.16, the added white areas on the time/position diagrams represent the maximum of tensile stresses in a 10% range below the exact maximum value recorded by the Matlab code. Therefore, it can be observed that from 100 ns to 300 ns pulse duration width, the positions of the maximum zone are thus not really changing. Moreover, none of this region is actually located on the interface to test (the one on the thin composite side). Nevertheless, the calculation performed by using pulse duration about 500 ns is interesting. It is presented thanks to the corresponding time/position diagram in Figure 6.17. In this Figure, the maximum stresses have been added by using a purple color scale gradation. These zones

are calculated from the exact maximum detected by the developed Matlab program, and then represented with different color level. The clearest zone enhances the stresses calculated in the range [70%max – max]. The following gradation color levels represents the stresses in the range [80%max – max], and so on. This representation gives an idea of the maximum stresses distribution in the (time, position) plane.

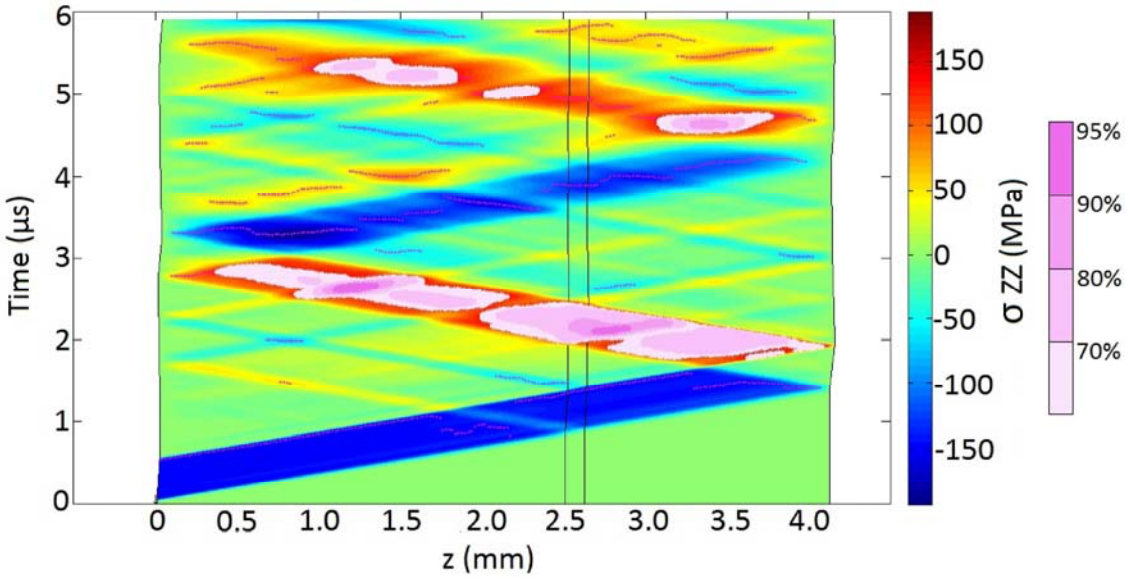

Figure 6.17, Numerical modeling of a laser shock about 500 ns long on a non-symmetrical T700/M21 bonded assembly - time/position diagram enhanced with colored maximum tensile loading zones at 70, 80, 90 and 95%

In Figure 6.17, the maximum of tensile stresses is once again located in the thick composite plate, because of the reflection of the release wave on the first bond interface, like in the previous cases. This time, a maximum loading zone is also visible right at the bond interface to test in the range [95%max, max]. Consequently, it should be possible with an accurate laser source to test a bond interface strength inferior or equal to 95% on the composite interlaminar strength with this loading. Moreover, these high stresses are the first one to occur if looking to the shock wave propagation timing. Therefore, if the bond is opened by the tensile stresses, the tension will not propagate backward in the thick composite plate, or at least not with the same level. The tension in this area should be considerably reduced, and the damage in the composite thus avoided. This results demonstrates that there is an optimization possibility for testing the second bond interface in a non-symmetrical T700/M21 bonded assembly (2.5mm/ bond/ 1.5mm) by use of relatively long pressure pulse (500 ns).

Another possibility is to use a pulse duration allowing the first tensile stresses created by the shock wave propagation to be located where expected (on the second interface), even if they do not correspond to the highest stresses. In order to do that, the first release wave coming from the front face unloading should intersect release wave propagating backward from the back face, meaning on the bond. Since the two layers are the same in terms of shock impedance, the pulse width of interest directly corresponds to the back and forth period in the back face composite plate. Indeed, in case of elastic propagation the release wave is parallel to the shock wave, only geometry rules the propagation. This is shown in Figure 6.18, where the time/position diagram in case of a 1000 ns laser pulse calculation is given. It can be observed that the crossing of release waves initiating tension occurs slightly before 2 µs right on the second bond interface. If the generated stresses are high enough compared to the interface tensile strength, then the bond can be opened.

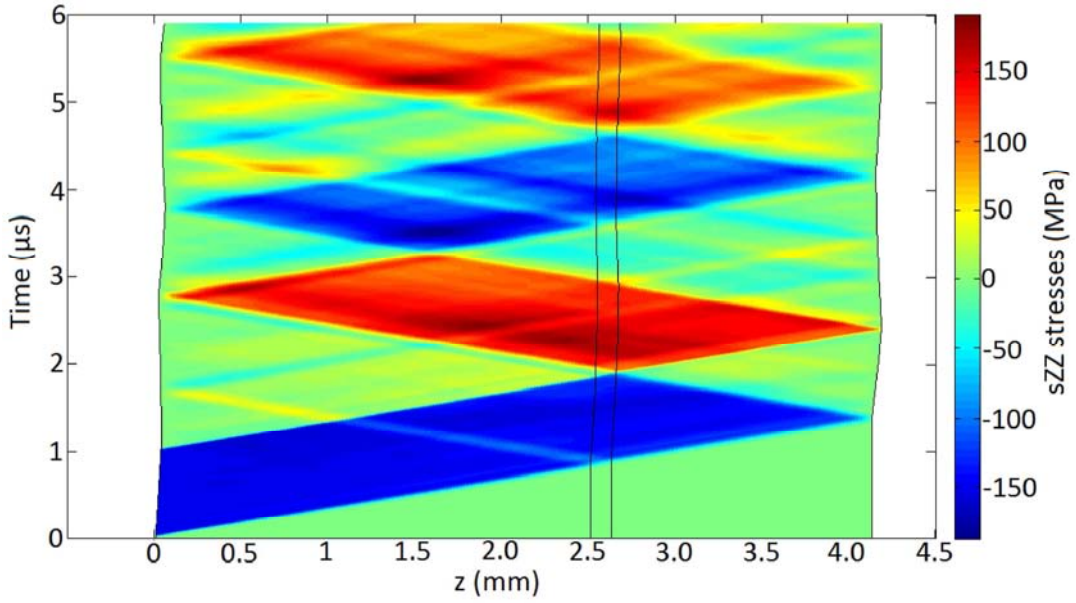

Figure 6.18, Numerical modeling of a laser shock about 1000 ns long on a non-symmetrical T700/M21 bonded composite assembly, forcing the first tensile stresses to be on the 2nd bond interface - time/position diagram without maximum tensile stress representation.

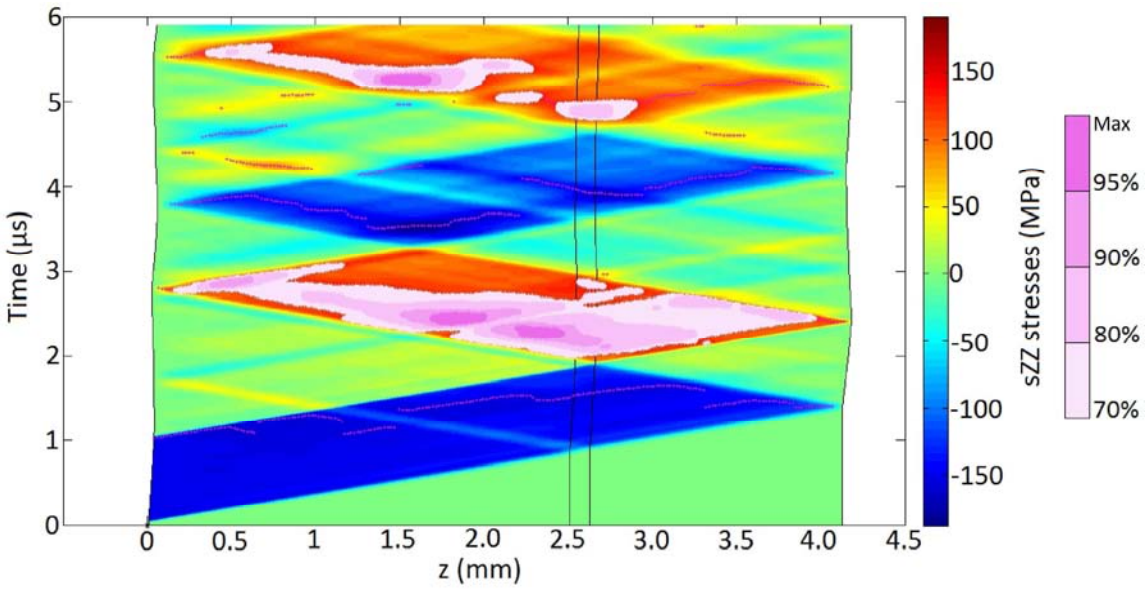

Figure 6.19, Numerical modeling of a laser shock about 1000 ns long on a non-symmetrical T700/M21 bonded composite assembly, forcing the first tensile stresses to be on the 2nd bond interface - time/position diagram enhanced with colored maximum tensile loading zones at 70, 80, 90 and 95%.

It is important that the first tensile stresses generated in the bonded sample open the bond, because the maximum of tensile stresses are not located in the bond as shown in Figure 6.19. In this Figure, the same maximum stress distribution representation than the one presented in Figure 6.17 is used. Therefore, it can be observed that the maximum stresses region is mainly located in the range [1.5 – 2.5 mm], and appears after t = 2µs. This area will probably be modified by the bond damage, still assuming that the first stresses are high enough to open it. If they are not, then the composite can be broken because of the highest tensile stresses. Keeping in mind that the shock adhesion test should not be destructive for the correct bonds, an interface inferior or equal to 70 % of the composite interlaminar strength can be tested with these shock parameters according to the calculated stress distribution.

2.2 On symmetrical bonded composite assembly

Results obtained on symmetrical bonded samples are given in Figure 6.20. Like for non-symmetrical bonded sample, the numerical optimization data is given by using time/position diagrams. The numerical model used to obtain these results has been developed on the basis of the one presented in Chapter 4. The loaded zone is kept constant on about 4 mm, and the maximum pressure is set to 0.15 GPa to be below all the damage thresholds. The tested pressure profiles are the same ones than in the previous section.

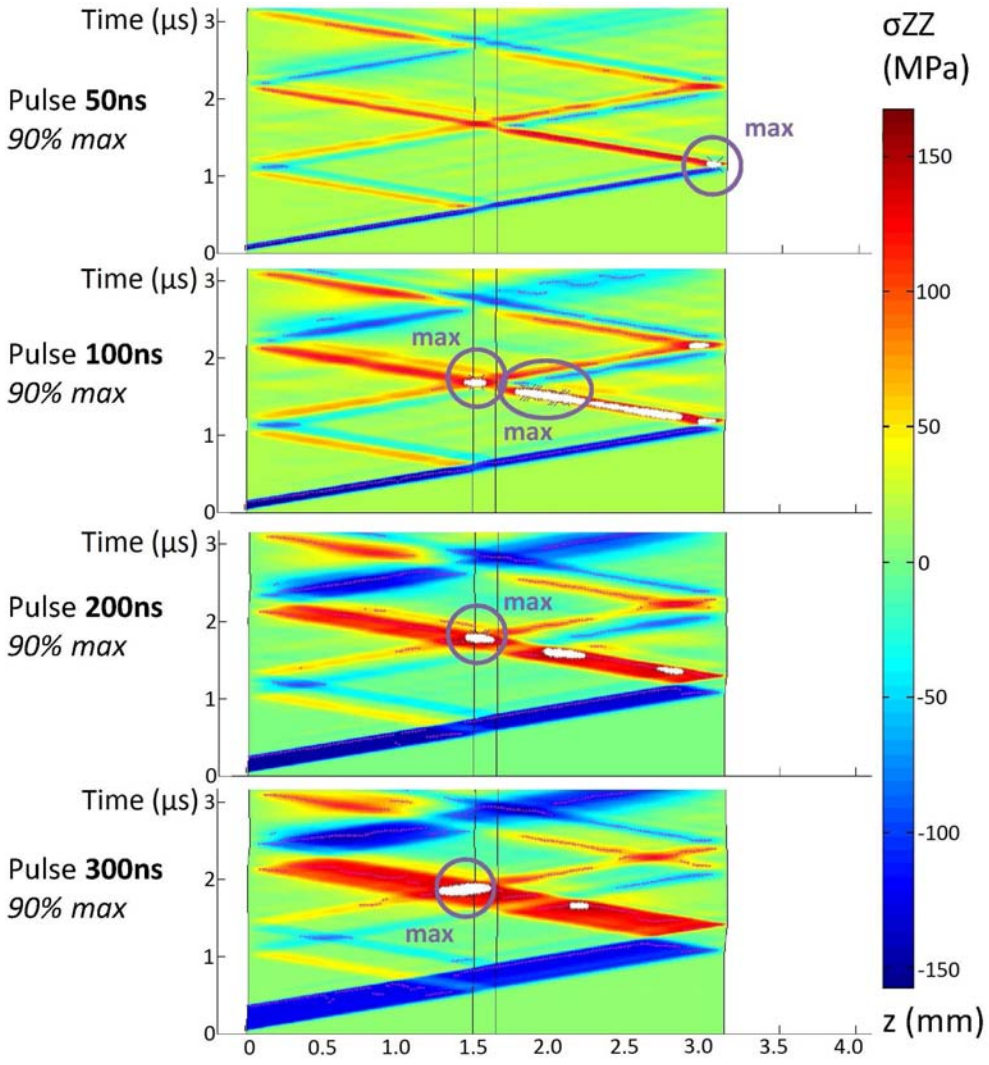

Figure 6.20, Effect of tunable pulse duration in case of a symmetrical T800/M21 bonded composite target, presented thanks to time/position diagrams, and enhanced with maximum tensile loading zone at 90% in white color

In Figure 6.20, the first diagram has been calculated with 50ns pressure profile. This pressure pulse corresponds in a first approach to the one of PPRIME25 laser apparatus, meaning that the obtained numerical result is close to what should have happened during the LASAT experiments on this assembly. As it has been observed on non-symmetrical bonds, the maximum of tensile stresses is located close to the assembly back face. In case of this sharp pressure temporal profile, this is even more pronounced. It confirms that the carried out experiments were not performed in an optimized case. When the pulse duration is increased, the tensile stress maximum zone is moved deeper in the bonded composite as it is shown by the 100 ns pulse duration calculation (see in Figure 6.20). Several exact maximum values are detected close to the second bond interface. Almost all the back face

composite is loaded with the same high stresses level. From this pulse duration, the first bond interface starts to be loaded with the highest tensile stresses. Indeed, the symmetrical bonded composite assemblies present a quite interesting geometry. On non-symmetrical samples, it has been shown that the first release reflection on the bond interface was responsible for a high tensile loading in the thick composite plate. This maximum loaded zone is possible thanks to the tension propagating backward after the crossing of release waves at the composite back face. It enhances the tension created by the front face reflection of the first described phenomenon. Therefore, both tensions are important to generate the maximum loading. In case of symmetrical bond, the sample geometry enables the two tension waves, the one propagating backward from the composite back face and the one coming on ward from the front face, to intersect in the middle of the sample, i.e. in the bond. Consequently, shots in the range [100-300ns] present an interesting configuration to optimize the LASAT test for the given geometry. For that, the best configuration seems to be obtained in case of 400 ns pulse duration. The time/position diagram corresponding to this laser pulse duration is given in Figure 6.21. Compared to the previous ones, it is enhanced by the use of graduated colors for the maximum loaded zones. This specific representation highlights two important elements.

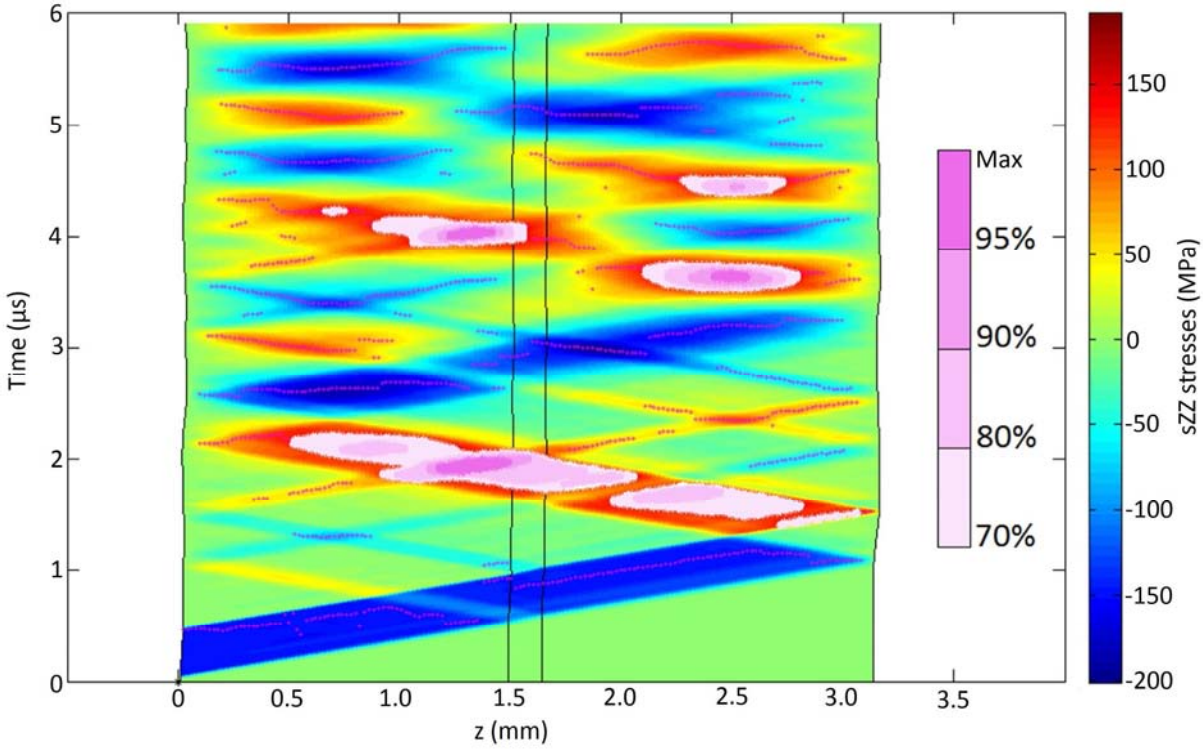

Figure 6.21, Numerical modeling of a laser shock about 400 ns duration on a symmetrical T800/M21 bonded composite assembly - time/position diagram enhanced with graduated colors for maximum tensile loading zones at 70, 80, 90 and 95%.

- Firstly, the maximum of tensile stresses (5% range) is located at the bond first interface (see in Figure 6.21). This loaded zone is relatively concentrated on this specific area, and is not deeply distributed through the composite sample.

- Secondly, and that is the key point, the back face composite is not loaded with more than 90% of the tensile stresses maximum during the first tension propagation (stresses in the range [80%max, 90%max]. Therefore, it can be assumed that there would be a gap between the load level at the bond interface, and in the composite which would enable an optimized

test. Moreover, it can be observed that the composite is loaded after 3µs on the second tension propagation through the assembly. According to the model, the stresses level seems to be still quite high, but it has to be remembered that the numerical model is not correctly describing the stress attenuation through the composite. Therefore, it is possible that these high stress regions would not exist in case of real laser shocks.

Consequently, for these shock parameters and this bonded assembly geometry, the maximum stress distribution should enable to test a bond interface whose strength is inferior or equal to 105% of the composite interlaminar strength.

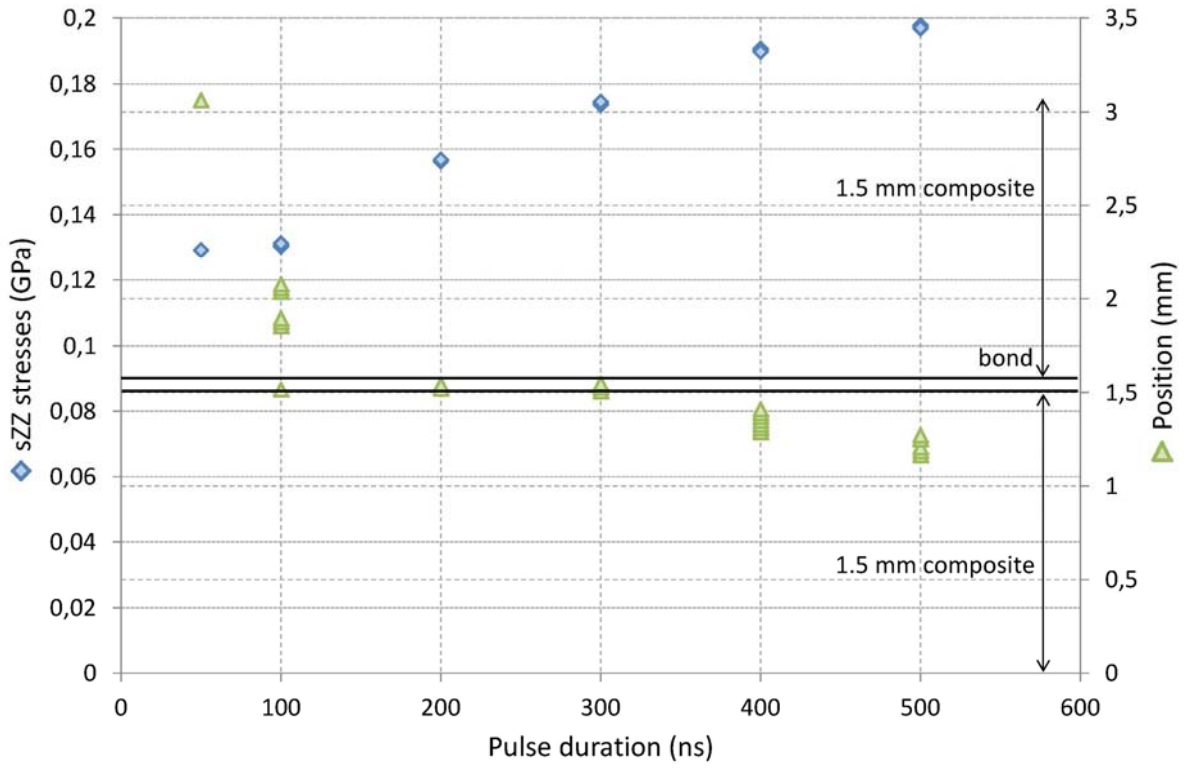

Figure 6.22, Synthesis chart of the stress maximum values and their corresponding depth in case of laser shock on cross-ply T800/M21 composite bonded assemblies, for different pulse durations

If longer pulses are used, the zone of maximum of tensile stresses starts to be shifted toward the composite front face as shown by the synthesis chart presented in Figure 6.22. In case of the 500 ns pulse width calculation, the maximum values of tensile stresses are detected 200 µm deep in the front face assembly from the bond. This is logical since the reflection of the release wave coming from the loading occurs later in case of longer pulses. Consequently, the crossing between the two tension waves also occurs later, meaning closer to the front face in this case. This can be understood by looking to the transmission/reflection phenomena in Figure 6.21. Thanks to this parametric investigation, a first optimization possibility for this specific sample geometry by use of relatively long pulse (400 ns) is shown.

As for non-symmetrical bonded assemblies, another possibility of optimization is the use of a pulse duration corresponding to the back and forth period in the back face composite plate. Here again, the optimized configuration will be efficient only if the first stresses generated in the material are high enough to immediately open the bond interface (see in Figure 6.23, left). This is important because the numerical modeling revealed that the maximum of tensile stresses is located in the front

face composite, with a difference about 80% with what is produced in the bond thickness (see in Figure 6.23, right). Consequently, it will not be possible to test a bond interface exceeding 80% of the composite interlaminar tensile strength.

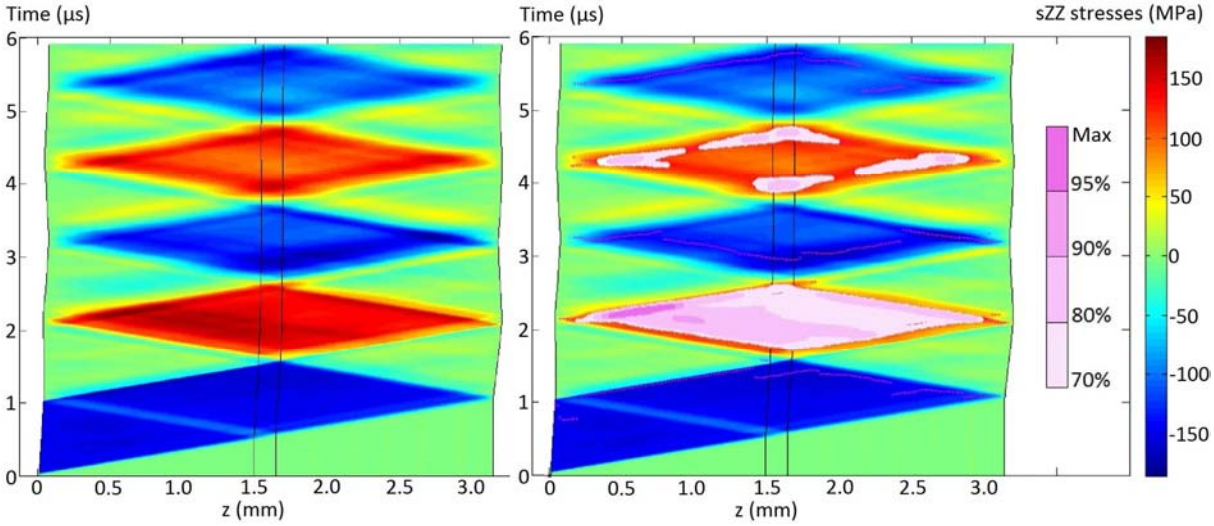

Figure 6.23, Numerical modeling of a laser shock about 1000 ns duration on a symmetrical T800/M21 bonded composite assembly - time/position diagram without any maximum zones superposition (left) and enhanced with graduated colors for maximum tensile loading zone at 70, 80, 90 and 95% (right).

Finally, this numerical study on the laser pulse duration shows that the shock wave adhesion test on non-symmetrical and symmetrical bonded assembly specific geometries could be optimized by two different ways:

- By creating a maximum tension zone on the bond interface to be tested: with a 500 ns pressure pulse for non-symmetrical samples and with a 400 ns laser duration for symmetrical target. In the first case, it should be possible to test an interface whose strength is inferior or equal to 95% of the composite interlaminar strength. This value goes up to 105% of the composite interlaminar strength in the second case. The composite damage would be avoided if the bond is actually opened and if the shock source is accurate enough.

- By generating the first tensile stresses at the bond interface. The back and forth period in the back face composite being the same in case of non-symmetrical samples and symmetrical samples, the pressure pulse duration should set in both cases up to 1000 ns. The energy level has also to be adjusted for the first stresses to exceed the bond interface tensile strength. The solution is less demanding than the previous one, but requires more power because longer pulses. In case of the shock adhesion test, interfaces stronger than 70% and 80% of the composite interlaminar strength could not be tested without breaking the composite parts. Nevertheless, if the bond is opened, composite damage may be avoided.

3 Experimental validation of the numerical optimization by plate impacts experiments

In this section, the use of the first tensile stresses optimization solution is experimentally validated. The idea is to produce a pressure load duration in the range of what has been numerically calculated in the two previous sections. Problem is that 1000 ns square-shaped pressure pulse is not something which can be produced today thanks to available laser sources. Therefore, this optimization solution

is validated by using plate impact experiments on symmetrical bonded composite assembly. Indeed, plate impacts are a good means to artificially tune the pulse duration width as shown in Figure 6.24. In a first approach, the pressure load duration is directly correlated to the projectile thickness. It can be defined as the back and forth duration. The unloading release wave, required to create tension when crossing the release wave reflected from the target back face, comes from the reflection of the shock created in the projectile on its back free face. Consequently, if the plate impact is too thin, or if the sound velocity in the projectile is too high, then the unloading wave is back on the target quite early. In this case, the crossing of release waves can occur in the composite part (see in Figure 6.24-a). On the other hand, if the plate thickness and the sound speed velocity in the projectile are correctly adapted to the tested target, then the crossing of release waves generating the first tensile stresses can be correctly located (see in Figure 6.24-b).

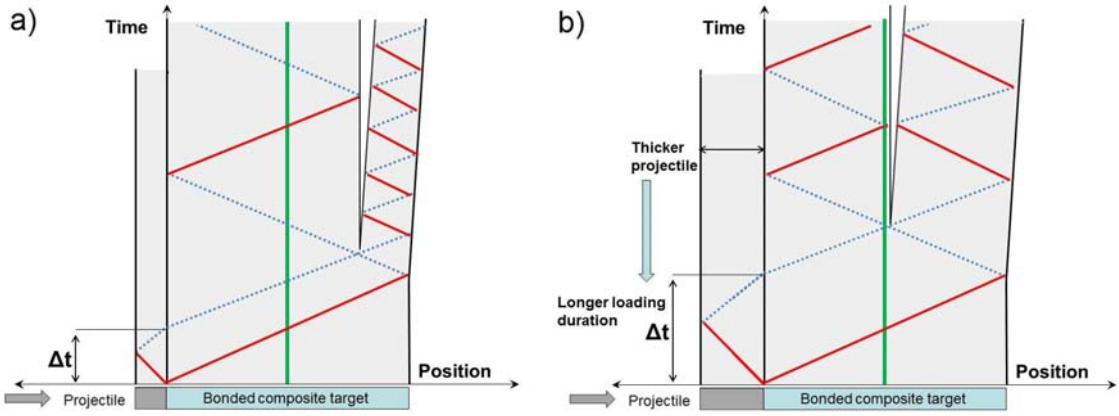

Figure 6.24, Principle of the shock wave adhesion test optimization by use of plate impacts: non-optimized test (a) and optimized test by use of the adapted plate thickness (b)

3.1 Plate impacts and VH measurements

The plate impact experiments have been realized at ENSTA-Bretagne, using the two experimental configurations described in Chapter 2, Table 2.2. Aluminum projectile have been used to create sizable pressure loads, which can be compared to the level used in laser shocks. This point has been first checked by using back face velocity measurements on shocked unidirectional T800/M21 composite materials (3 mm thick). For that, Config-ENSTA-2 has been used, meaning that a PDV probe has been used to measure the free surface velocity. In a second time, plate impacts were produced on weak and strong bond (config-ENSTA-1) to show the optimization capability in case of a correct positioning of the first tensile stresses generated in the bonded composite targets. The shock parameters of the presented results are given in Table 6.2.

Samples	Plate thickness (mm)	Material projectile	Projectile mass (g)	Carry-projectile mass (g)	Photodiode Speed (m/s)
T800-P-1	1	Aluminium	3.29	16.64	84
T800-P-2	1	Aluminium	3.29	16.11	47
LE-E-1	1	Aluminium	3.29	16.35	53
LE-E-3	3	Aluminium	10.09	16.55	51
LE-P-2	3	Aluminium	10.09	16.31	30
LE-P1	3	Aluminium	10.09	16.11	85
ES1-Can3	3	Aluminium	10.22	16.58	90

Table 6.2, Plate impact shock experimental parameters for the presented results

Results from PDV measurements and post-treatments (see in Figure 6.25) have been obtained on 3 mm thick unidirectional T800/M21 composite samples, in the specific plate impact experimental configuration presented in Chapter 2. In particular, it has to be remembered that the composite samples are held in an epoxy carrier to fit the experimental cell. Two different projectile velocities were produced, at 84 m/s and 47 m/s, yielding to two different shock pressures. Indeed, the two first velocity peak amplitudes are about 90 m/s in the first case, and 33 m/s in the second one. Since it is the same type of target in both cases, the pressure induced by the two different impacts is really different. The velocity first jump differs from one shock to another only because of the triggering mode on the photodiode. Therefore, the difference in the shock breaking-out is due to the difference in the projectile velocities, and not in the shock propagation. On the green signal, the back and forth period characterizing the 3 mm thick unidirectional T800/M21 composite material can be observed. The period is about 2 µs, which corresponds to what has been observed in case of laser shocks. In addition, it can be noticed that the pressure level is in the same range than the one resulting from laser loading, since the free surface velocity amplitude is also in the same range. According to previous measurement in case of laser shock, and the back and forth period observation, it appears that the composite samples did not break in these cases. Finally, it can be observed that the signal global shapes change from what is known in case of laser shocks. Especially, the free surface velocity remains relatively high after the first shock reflection and backward propagation. This is probably due to the complex structure of the target epoxy holder, which can slightly move in the cell under impact. To sum up, the important point is that it is possible with this kind of loading to create different pressure levels on the composite target, below the local damage threshold of the composite for this kind of loading.

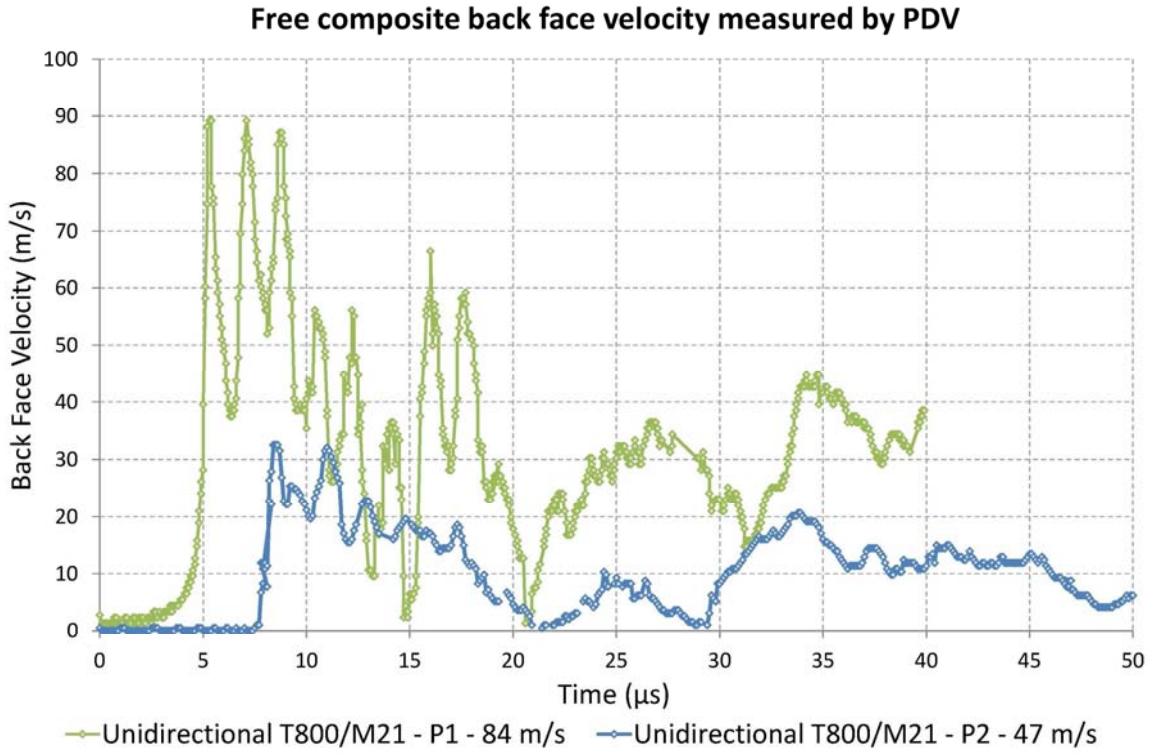

Figure 6.25, Measurement of free surface velocities in case of aluminum plate impacts on 3 mm thick unidirectional T800/M21 composite samples, for two different projectile velocities: 84 m/s (green), 47 m/s (blue)

3.2 On really weak bonds (LE)

Plate impacts were performed on the LE weak bond samples to confirm the optimization capability. Two different plate impact shocks were performed, at a given impact velocity, meaning constant pressure, but with two different plate thicknesses. The resulting damage on LE weak bond composite sample is shown in Figure 6.26-a. In the first cross section, the aluminum plate thickness was of about 1mm and no damage can be observed in the bonded composite. The maximum tensile stresses were located in the composite and were not high enough compared to the local damage threshold of the composite part to produce cracks or delamination. The second plate impact was produced at the same velocity, but with a plate thickness about 3 mm. In this case, a full debonding has been observed, with almost no damage in the composite part (see in Figure 6.26-a). Indeed, the shock velocity in aluminum at this pressure level is close to 5500 m/s, when the shock velocity in composite can be considered close to 3000 m/s depending on the material quality, resin contents… Using a 1D acoustic approach, it appears that a 3 mm plate thickness enables to generate maximum of tensile stresses close to the bondline, which is located 1.5 mm deep in the bonded composite sample. This is due to the factor 2 on the shock velocity. Finally, the pressure was not really different than the one generated during the first impact presented. This time, the first tensile stresses were better located and the damage threshold of the bondline was low enough for debonding. This result demonstrates that tuning the shock duration has an influence on the tensile stresses distribution. It prevents from breaking the composite material.

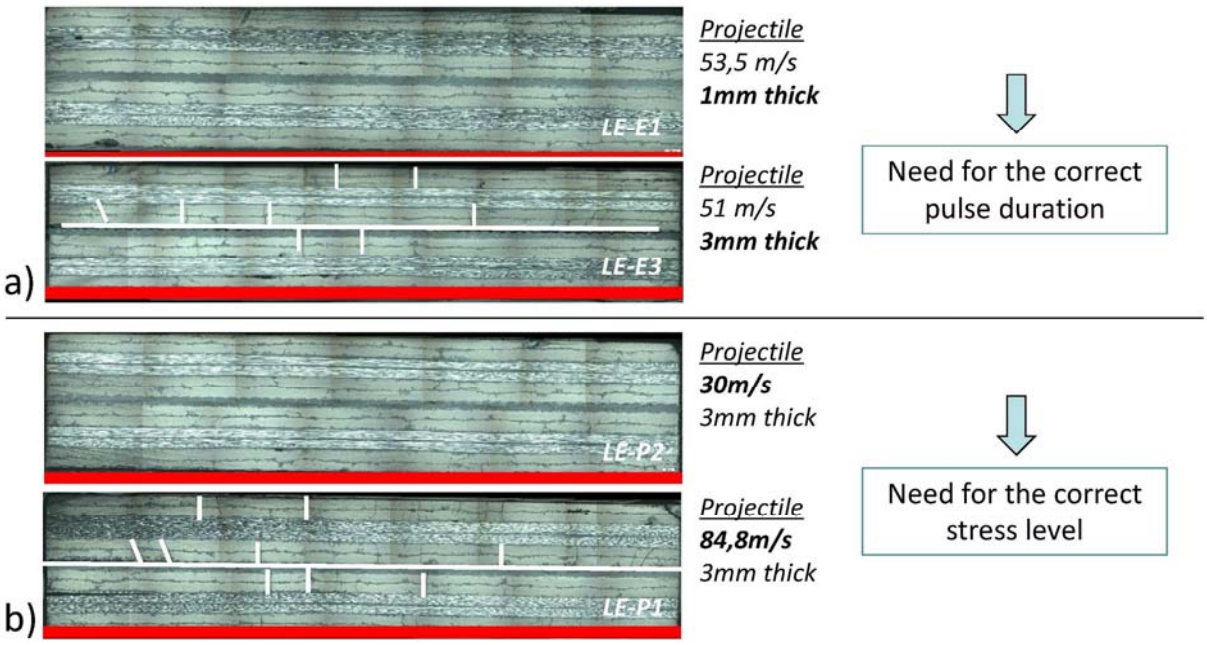

Figure 6.26, a) Parametric study results on the influence of the plate thickness in case of plate impact shock on bonded composite samples, at constant induced pressure. b) Parametric study result of the pressure loading influence on the debonding of weak composite bond, using constant plate thickness.

The pressure is also an important parameter, because the first generated tensile stresses have to be high enough for the bondline damage threshold to be exceeded. This is shown by the results presented in Figure 6.26-b. Indeed, the two plate impacts presented were performed with the same projectile thickness. The thickness was chosen to be equal to 3 mm, which corresponds to the optimized case for the bonded composite tested. Two different projectile velocities were used to produce two different pressure loads (see in Figure 6.25 and in Table 6.2 for shock parameters). The first sample was shocked with a projectile velocity measured close to 30 m/s, which generated

corresponding pressure and tensile stresses below the damage threshold of both composite and bondline. Indeed, no damage was identified on the cross section observation (see first micrography, Figure 6.26-b). The second shock was performed with a plate flying at 85 m/s. This time, the induced pressure was high enough to crack the bondl ine, as it can be observed in Figure 6.26-b, second micrography. These results show that the pressure level and the pulse duration are two key parameters.

3.3 On reference ES1

The last experimental results presented in this section concern a plate impact performed on ES1 ENCOMB reference. This test has been performed in the optimized configuration as defined in the previous section, meaning by using a 3 mm thick aluminum projectile. According to the numerical simulation performed in this configuration, it is known that the first stresses will be located in the bond line, with a level about 80 % of the tensile stresses maximum detected during the whole propagation. The post-mortem state of the material has been analyzed by using cross section observation. The micrography is presented in Figure 6.27. Numerous cracks and strong delamination can be observed, the composite parts have been severely harmed. Nevertheless, the bond does not present any damage. In this case, the pressure state induced by the plate impact was high enough to break the composite but not the bond. This is consistent with the laser shock results obtained on this sample. In addition to numerical modeling, it can also be concluded that the bond interfacial strength is at least equal to 80% of the interlaminar tensile strength of the T800/M21 composite material, in this specific assembly.

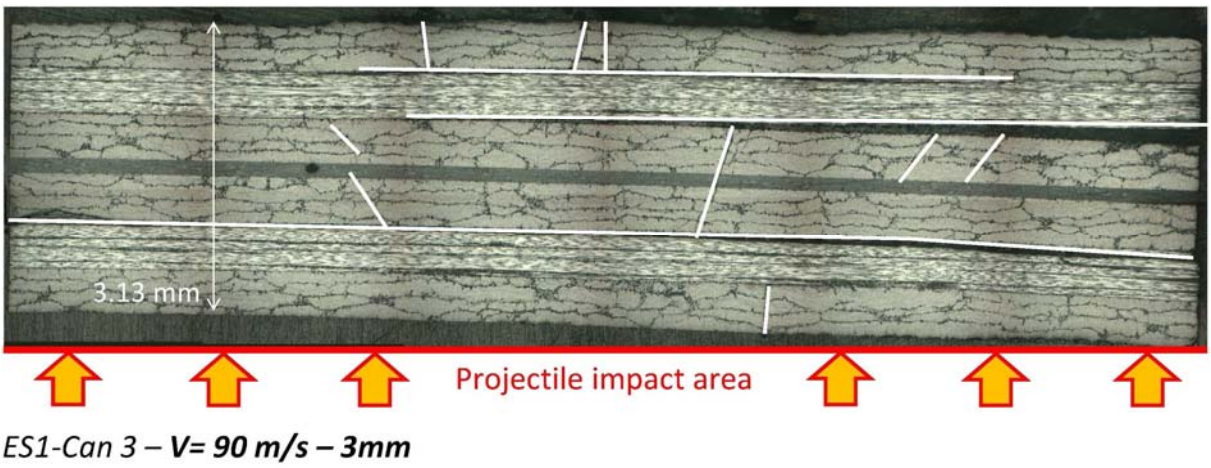

Figure 6.27, Plate impact using a 3 mm thick aluminum projectile (90 m/s) on a ES1 bonded sample

In this part, the optimization solution by use of tunable pulse duration has been first numerically investigated on both non-symmetrical and symmetrical bonded assembly. It showed that it is possible to generate the maximum of tensile stress or to produce the first tensile stresses at the interface to test by using specific pressure pulse durations. The experimental results presented in this last section evidenced the optimization capacities by using the first tensile stresses generation at the bond interface. For that, aluminum plate impacts were realized on symmetrical T800/M21 bonded assembly samples, in the best configuration for this sample geometry. Weak bonds have been opened, when reference ones did not, which is consistent with previous results but with an absence of strong composite damage in addition. This plate impact investigation demonstrates that the pressure level and the pulse duration are two key parameters for the shock wave adhesion test optimization.

Part 4: Double shock approach

In this part, two optimization solutions are discussed. The first one deals with double shock, produced on the same sample face. The second still use two shocks, but on the two different target faces, and is named synchronized symmetrical shocks.

1 Double shock on the assembly front face solution

1.1 Principle of the optimization by the front face double shock

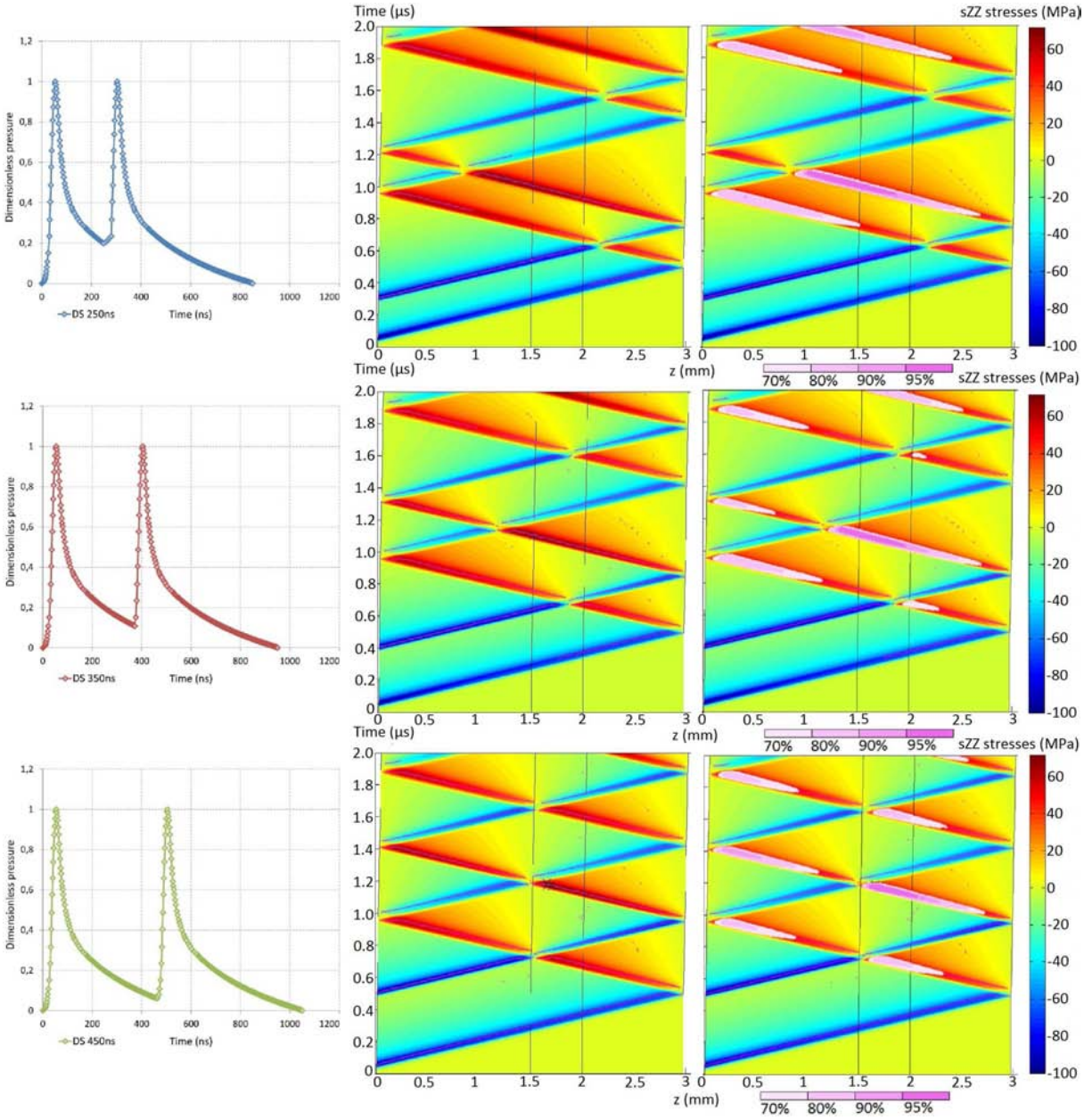

Figure 6.28, Effect of a double laser shock on a three-aluminum-target front face presented thanks to time/position diagrams, with and without maximum tensile loading zones in graduated colors

The principle of the double shock on sample front face optimization is shown in Figure 6.28. For that, the 1D three-layer aluminum model has been used to obtain time/position diagrams which demonstrate the optimization technique. The idea is to enhance the main tension generated by a

first laser pulse induced shock reflection on the back face, by the one created by a second pulse, synchronized with the first one. For that, Gaussian laser with release tail have been used to tailor future optimized experimental configurations to be tested on the forthcoming new PIMM laser facility, HEPHAISTOS. Three different pressure profiles have been tested, as shown in Figure 6.28. The second pulse is synchronized with the first one, using three different delays: 250 ns, 350 ns, 450 ns respectively in blue, red and green. It is assumed here that this pulses generation is possible in water confinement configuration, which has not been experimentally evidenced yet. Moreover, the confinement layer should be able to sustain two shocks. Another problem is the issue of sacrificial layer. Using double shock requires the use of a calibrated sacrificial layer to be sure that the first shock will not remove the whole layer. Otherwise, the laser/matter interaction will change. Nevertheless, these particular loadings enable to move the position of the tensile maximum stresses within the target thickness (see time/position diagrams in Figure 6.28). The exact maximum values (black crosses), as well as the maximum loaded zones, can be moved. This is due to the fact that the second tension wave enhances the tension state generated by the first tension wave, when propagating backward. This is visible on the time/position diagrams presented in Figure 6.28. Consequently, the timing with which this second tension wave is back in the target is important to increase tension in a specific region. Moreover, this timing is directly connected with the second shock initiation on the target front face, in regards with the first shock initiation. In other words, the delay between the two pressure pulses is the one to control the maximum tension zone (see in Figure 6.28). Nevertheless, the time/position diagrams enhanced with maximum regions in graduated colors shown in Figure 6.28 enable the observation of 80% loading zones, especially in the first thick layer. This is logical since the first tension wave to be produced by release crossing on the first pattern is fully developed and remains high. It has to be kept in mind for composite application.

1.2 Double shock on the front face, numerical approach

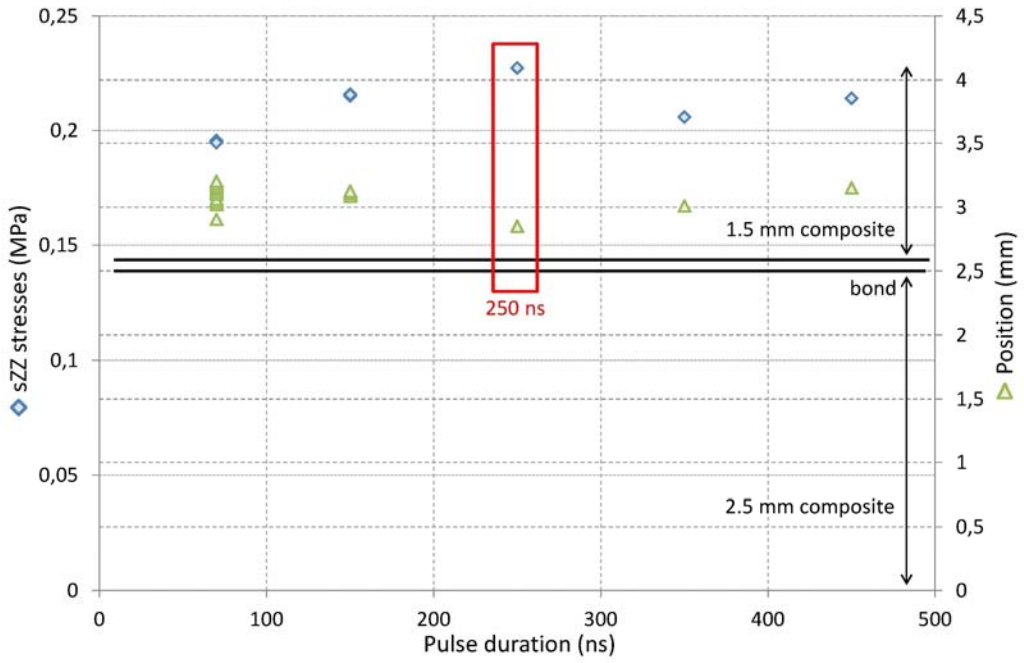

Figure 6.29, Synthesis chart of the stress maximum values and their corresponding depth in case of double laser shock on cross-ply T700/M21 composite bonded assemblies, gap between the two pulses – Best adjustment for Δt = 250 ns

This double shock solution has been numerically investigated on non-symmetrical T700/M21 bonded composite assembly. The model used is unchanged from previous investigations; focus diameter is set to 4 mm, and the maximum pressure amplitude to 0.3 GPa. Several delays have been tested from 70 ns, to 450 ns (see in Figure 6.29). If looking first to the exact maximum position and level, it seems that a delay of 250 ns offers the best configuration. Indeed, the tension maximum is located close to the second bond interface in this case. Its level is also maximized.

The analysis of time/position diagrams provides complementary information. In Figure 6.30, three time/position diagrams are given in different configurations, using a 90% enhanced white zone. In each case, it can be observed that impedance mismatch created by the bond is once again important for the position of maximum stresses. The first reflection of the two main shocks, then reflected again on the front face, enhances the main tension in the 150 ns delay case. Moreover, it is the reflection of the main tension wave on the bond interfaces which enables the positioning of a maximum zone close to the bond. This is particularly visible in Figure 6.30 for 250 ns and 350 ns. These three diagrams also confirm that the best case is the 250 ns delay case. Nevertheless, if looking to this configuration only, it can be seen that the 90% maximum loading zone is not reaching the bond interface. In order to have an idea of the maximum stresses distribution through the composite thickness, additional loaded regions have been plotted in Figure 6.31.

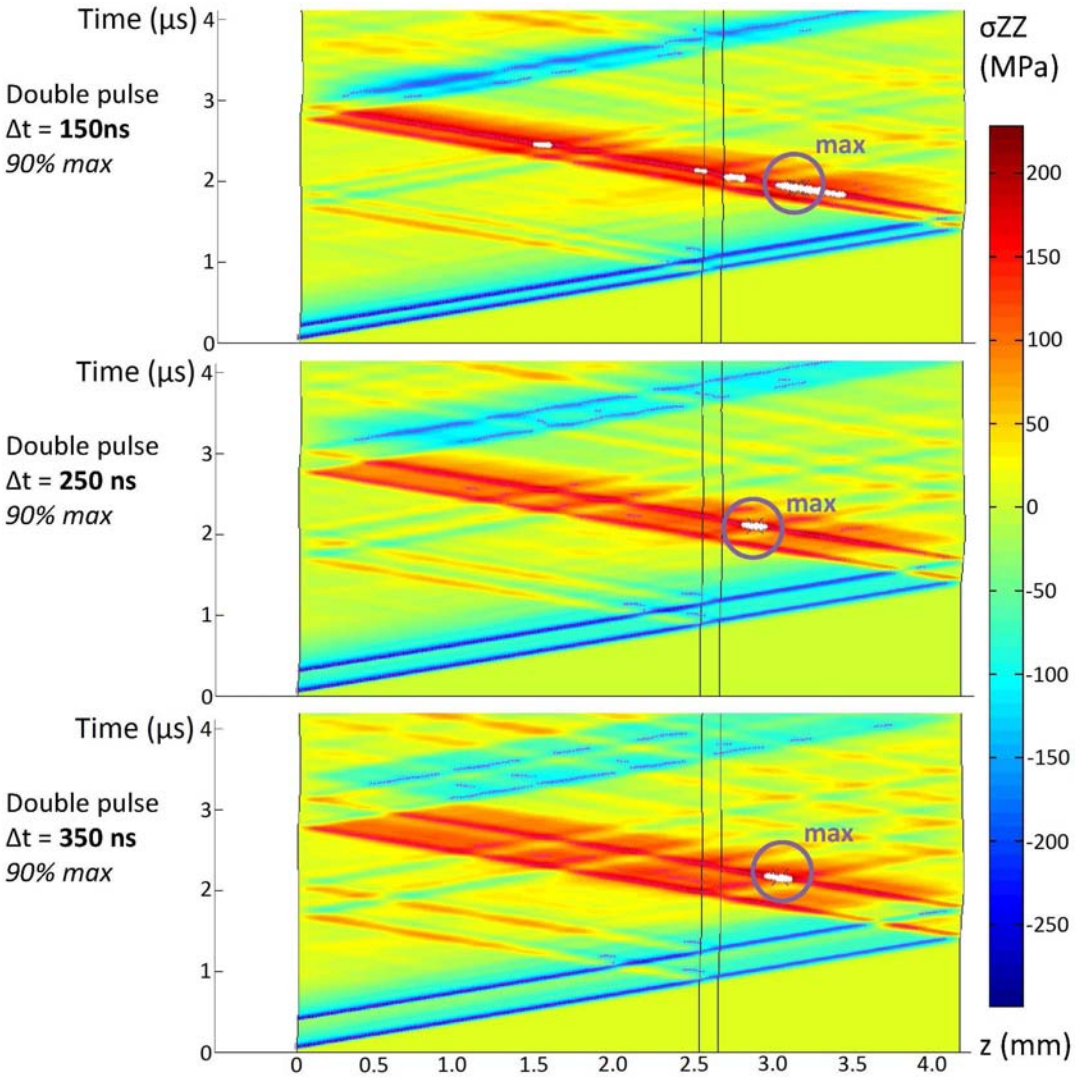

Figure 6.30, Effect of double front face laser pulse in case of a non -symmetrical T700/M21 bonded composite target, presented thanks to time/position diagrams, and enhanced with maximum tensile loading zone at 90% in white color.

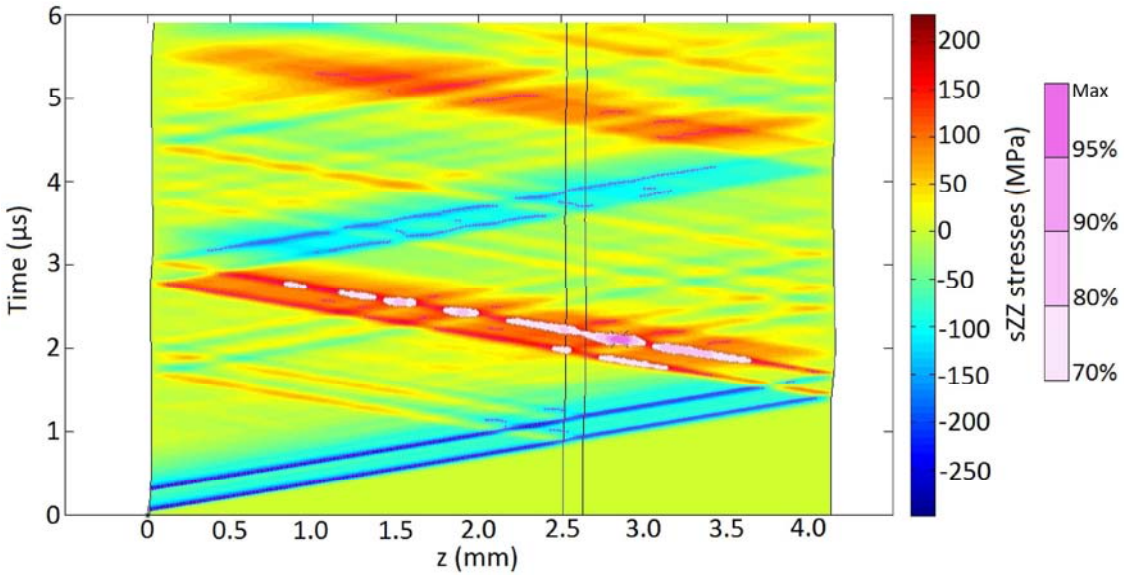

Figure 6.31, Numerical modeling of a double front face laser shock, separated of about Δt = 250 ns, on a non-symmetrical T700/M21 bonded composite target - time/position diagram enhanced with maximum tensile loading zones at 70, 80, 90 and 95% in graduated colors

The stress level on the bond interface is in the range [70%max, 80%max] and the maximum value is calculated in the back face composite part. It means that the composite is loaded with higher stresses than the bond, especially in the closest region from the back face enhanced in purple, where stresses 20% below the maximum level are detected. Several other regions, like the first one in time on the first main tension wave or the last ones in the thick composite plate, also present stresses in the range [70%max, 80%max]. Consequently, this optimization solution would work only if the interface to test is at least 30% weaker than the composite laminates, as the tensile interlaminar strength is concerned. In other words, a bond interface whose strength is inferior or equal to 70% of the composite interlaminar strength could be tested in an optimized configuration. Else, the composite would be broken before the tension can reach the bond interface. Nevertheless, this solution could present an alternative to long pulse, because it requires less power. It can also be better adapted to other geometries. Same stress distribution has been noticed on symmetrical bonds.

2 The symmetrical laser shock

At first, the symmetrical laser shock principle is demonstrated on a three-aluminum-layer target by numerical calculation. Then, this optimization solution has been numerically investigated in case of non-symmetrical T700/M21 bonded samples, and then symmetrical T800/M21 bonded samples. An experimental validation is finally given in the last section in case of symmetrical bonded samples. The experimental validation on non-symmetrical bonded samples should be possible by using Hephaistos laser source.

2.1 Principle of the optimization by symmetrical laser shock

The principle of LASAT optimization by use of symmetrical laser shock is shown in Figure 6.32. These numerical simulations have been obtained for a three-aluminum-layer target. Instead of performing the two laser shocks on the same surface, they are produced by using both sides. In this case, the crossing of the two tension waves, respectively generated after the shock reflection into release wave on each surface, can create higher tensile stresses.

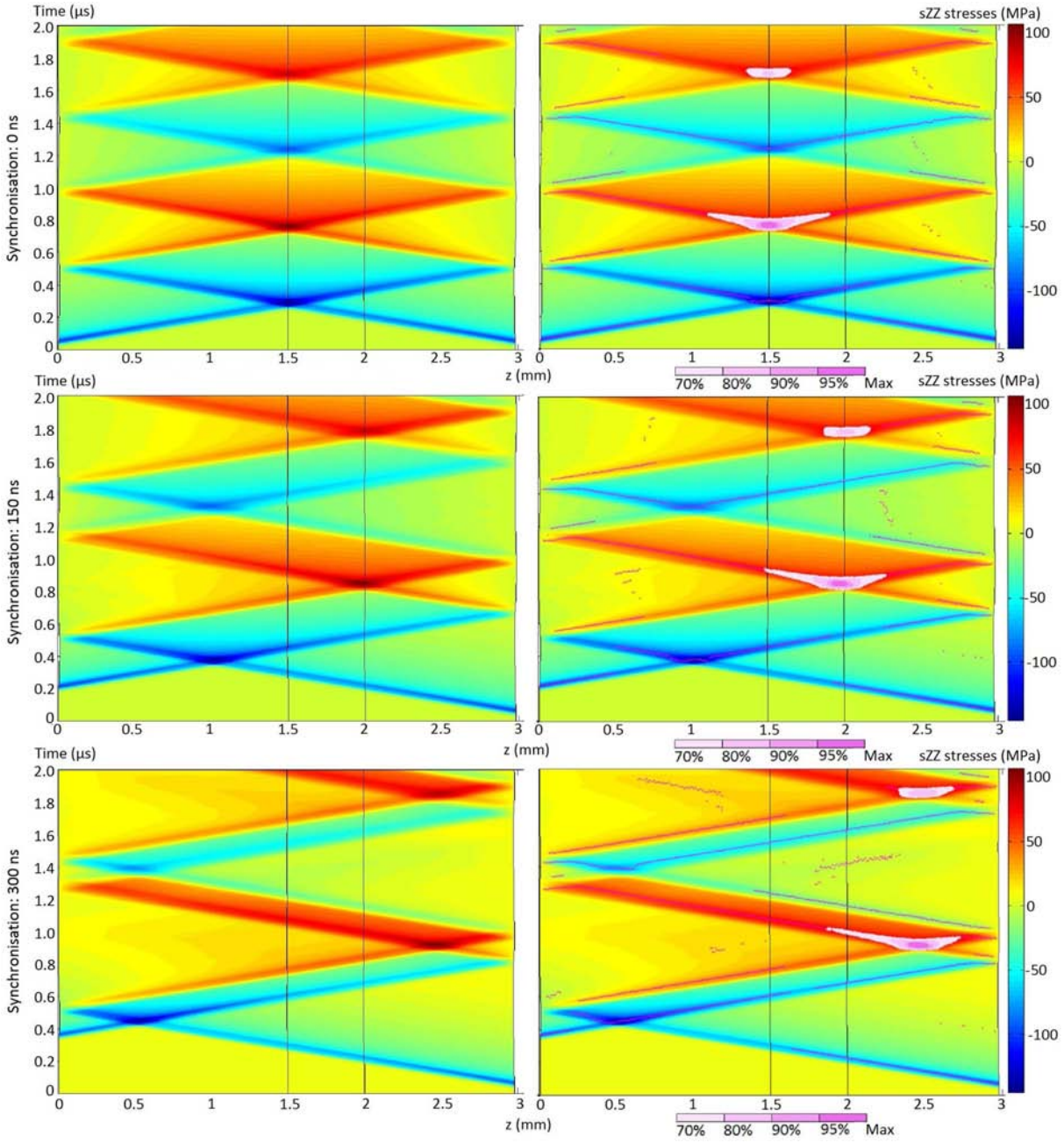

Figure 6.32, Effect of symmetrical laser shocks on a three-aluminum-target front face presented thanks to time/position diagrams, with and without maximum tensile loading zones in white color

In a first approach, the symmetrical shock can be produced simultaneously, and considering no impedance mismatch, then this higher tension is produced exactly in the middle of the sample, as shown in Figure 6.32, first two diagrams. If assuming no attenuation, the tension generated by one pulse on each face is equal to – P for an initial loading equal to P. Therefore, the maximum tension

generated by the crossing of these two tension states should be equal to -2P, still assuming no attenuation. This solution thus presents a real interest. Moreover, the position of the two states crossing can be adjusted by playing on the two shock synchronization as shown by the following four time/position diagrams in Figure 6.32. In elastic regime, the positioning is geometric. If delaying the shock produced on the sample left side, the tension states will intersect closer to the right face. It is shown in case of 150 ns and 300 ns delay configurations in Figure 6.32. The opposite is also true. This optimization technique presents another interest, especially useful for the LASAT application to the bonded composite. It is shown by the three diagrams presented in the right column, where the maximum loaded regions have been enhanced by a purple color scale. Indeed, this representation evidences that the highest stresses, in the 30% range below the maximum, is quite concentrated in space and in time. This characteristic would enable to target the point of interest to test, and prevent from creating too important tensile loads in the rest of the sample. For the bonded composite, where the similarity of composite and bond strengths is an issue, this point is really interesting.

2.2 Symmetrical laser shock on bonded composite, numerical optimization and experimental validation

2.2.1 Non-symmetrical T700/M21 bonded samples

The numerical investigation has been performed with the models already presented. Focus diameter is set to 4 mm, and each pulse pressure amplitude is equal to 0.15 GPa. The time/position diagrams presented in Figure 6.33 come from this numerical modeling. The first one (a) presents a symmetrical loading perfectly synchronized. In this case, the two tension states resulting from each shock reflection intersect in the middle of the sample, as it was the case on the three-aluminum-layer model. The impedance mismatch does not affect the positioning of the maximum tensile stresses. The 90% zone is also located in the middle of the sample, and quite concentrated. Nevertheless, in the non-symmetrical bonded case, the interface to test is not in the middle of the sample. For the highest tensile stresses to be generated on the interface to test, the shock produced on the thick composite plate has to be delayed about 400 ns, as shown in the second time/position diagram using a stress distribution representation (see in Figure 6.33, b). The maximum of tensile stress, represented by black cross, is located on the interface thanks to the synchronization. Unfortunately, a small loaded zone also appears in the thick composite plate, and before the interface loading in the range [90%max, 95%max]. This high tensile state is due to the reflection of the thick composite plate shock on the bond line. It means that the thick composite part is loaded with the same level of stresses than the bond interface. It reduces the maximum interface strength which can be potentially tested to a value close to the composite interlaminar strength. Within this limitation, this optimization seems to be possible if using a reliable laser source, like Hephaistos, which would reduce the uncertainties on the laser parameters.

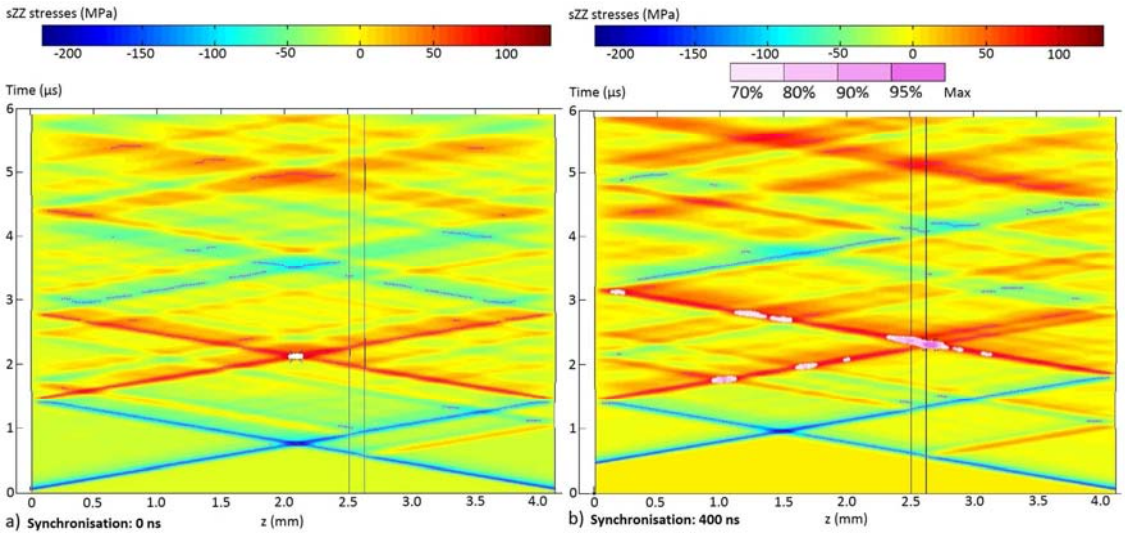

Figure 6.33, Effect of symmetrical laser pulses in case of a non -symmetrical T700/M21 bonded composite target, presented thanks to time/position diagrams, and enhanced with maximum tensile loading zones at 90% colored in white: perfect synchronization (a) and 400 ns delay on thick composite (b)

2.2.2 Symmetrical T800/M21 bonded samples

In case of symmetrical bonded composites, the geometry is more favorable for two main reasons. Firstly, the interface to test is, almost, in the middle of the sample. Thus no synchronization has to be used and the shocks can be produced at the same time. Secondly, the impedance mismatch created by the presence of the bond is less problematic in this case. Indeed, the transmission/reflection phenomena should be superposed with the main shock patterns. The results of the numerical simulation are presented in Figure 6.34 thanks to two time/position diagrams, one being maximum representation less, and the second one showing the highest tensile stresses distribution. If taking the time as the reference for the phenomenon description, tensile stresses in the range [70%max, 80%max] can be first observed in the two composite parts. According to their time occurrence, these could be due to the crossing of the two 2D effects zones. Then, the two tension states intersect and create the most loaded region. The whole bond thickness is loaded with stresses in the range [95%max, max], which is adequate for the bond testing. This zone propagates through the interfaces to the composite plate, at a lower level (80% then 70% as shown in Figure 6.34). After t = 2 µs, the two tension waves reach their respective front face, where another high tensile stresses region is observed. The level is in the range [80%max, 90%max]. Moreover, these high tension regions would not exist if the bond breaks before. Consequently, optimization is possible in this case. Moreover, if a reliable laser source is used, it should be possible to test an interface 5% stronger than the composite itself, but not much more.

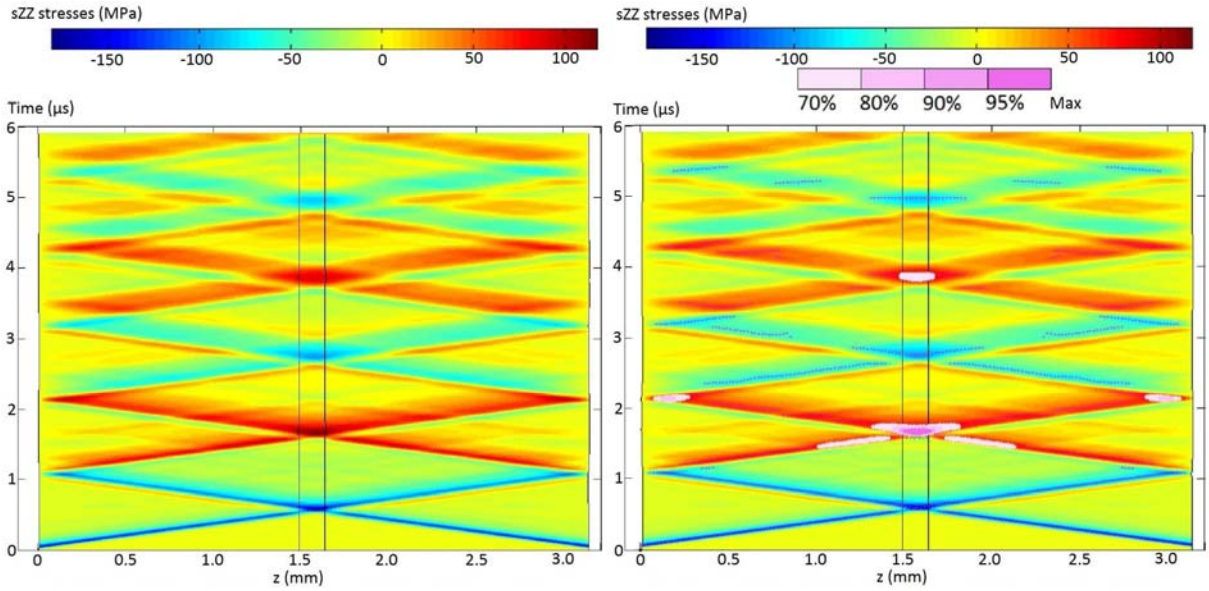

Figure 6.34, Effect of symmetrical laser pulses perfectly synchronized in case of a symmetrical T800/M21 bonded composite target, presented thanks to time/position diagrams with no maximum (left) and enhanced with maximum tensile loading zones at 70%, 80%, 90% and 95% in graduated colors (right)

2.3 Experimental validation of symmetrical laser shock on bonded composite

This optimization solution has been experimentally evidenced using in the laser source in Institute PPRIME, by using Config-PPRIME-SYM. In this configuration, it was complicated to use water confinement because the two sample sides should be irradiated. By the way, this point could also be an issue for industrial application. Instead, a transparent adhesive tape has been used as a transparent medium on both faces. Therefore, no accurate direct comparison can be made between the laser intensities presented in this section, and the ones used in the previous investigations. The experimental setup is shown in Figure 6.35. The laser beam has been divided in two by using a beamsplitter. The difference in the energy level of each beam is due to polarization issue and has been corrected by using optical densities. The two beams are sent on target by using two focusing lenses. One can notice that the beam paths dot not measure the same length. One of the path is less than one meter longer than the other one, which represents less than 3 ns delay between the two pulses. This is neglected. The laser shock parameters are given in Table 6.3, and the corresponding results are presented in the next two sections.

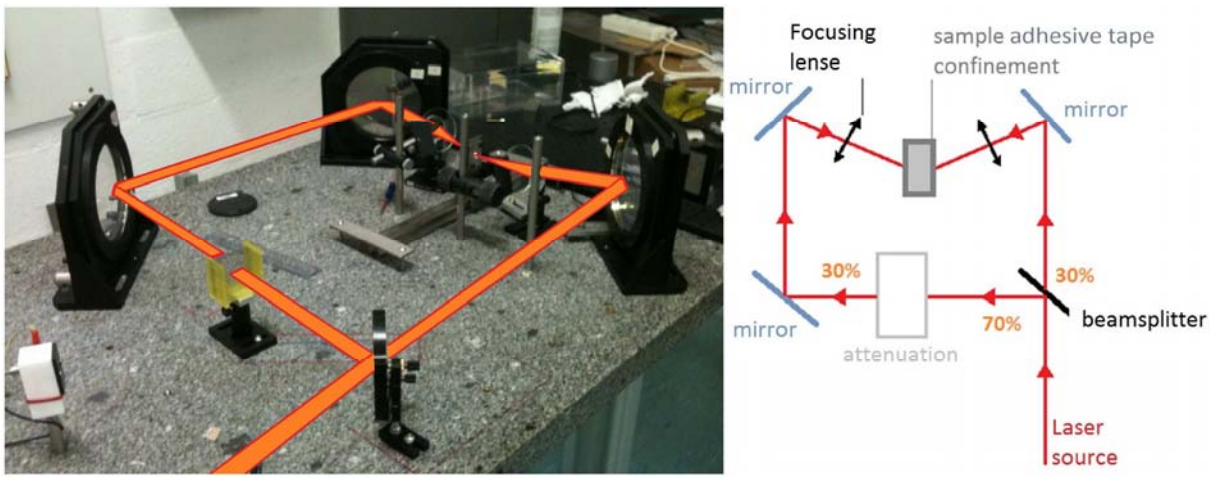

Figure 6.35, Experimental setup realized to validate the symmetrical laser shock optimization solution

Sample	Laser Energy (J)	Pulse duration (ns)	Focus diameter (mm)	Intensity (GW/cm²)
ES1-10	7.76	25.29	4	2.44
ES2-10	7.68	24.8	4	2.50
LB-7	5.30	25.16	4	1.68
LB-6	8.19	41.00	4	1.59
LB-8	3.94	36.11	4	0.87
LB-9	1.67	28.52	4	0.47

Table 6.3, Symmetrical laser shock parameters for optimization solution validation

2.3.1 On ENCOMB ES1 & ES2

The first two results to be presented are the one obtained on symmetrical ES1 and ES2 bonded composite assemblies. Cross sections have been performed to analyze their post-mortem state after a symmetrical laser irradiation. They are both presented in Figure 6.36. The intensity used here is the maximum which can be obtained from the experimental configuration. Starting with ES1 sample, it can be observed that the bond was not opened by the laser shock waves propagation. This is consistent with the conclusions made on the direct shock configuration data. Moreover, both composite parts present delamination and cracks. This observation is consistent with the numerical simulation because it has been shown than the composite part can be heavily loaded if the bond is not opened. Nevertheless, it is not possible to say which of the stresses, the first tensile stresses (about 1µs) or the second highest ones (about 2 µs), did break the composite parts. This uncertainty is the same in case of sample ES2, even if the bond has been opened by the symmetrical shock in this case. From the previous experimental results, it is known that the damage threshold of the bond and the composite laminates are probably close one from the other. Knowing that the bond has not been opened for lower intensity values, this result is logical.

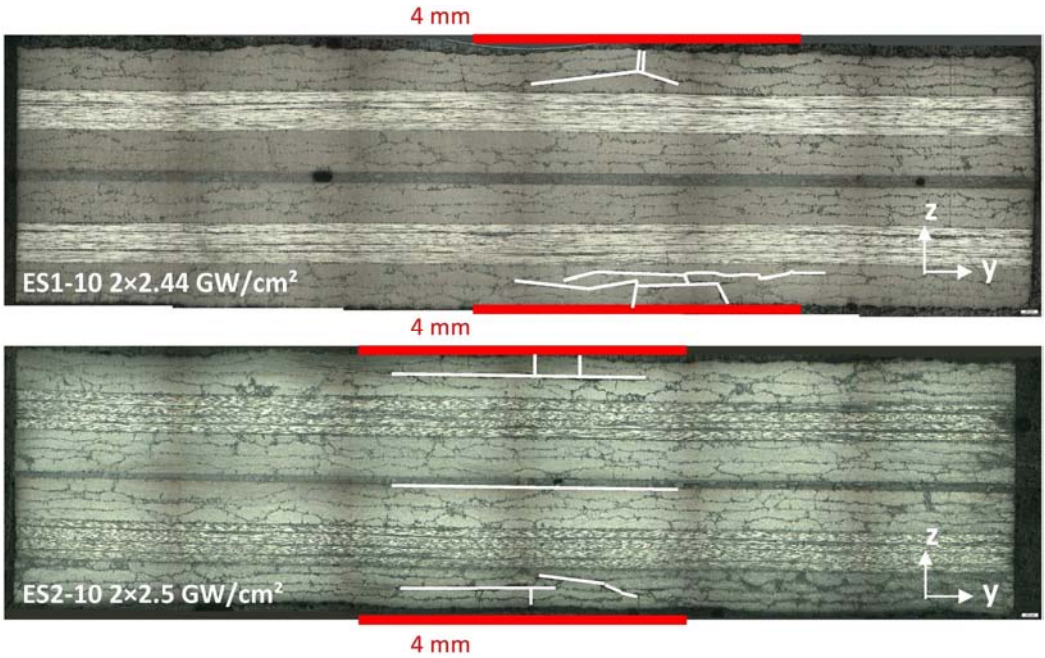

Figure 6.36, Post mortem state of ES1 and ES2 samples after a symmetrical laser shock, using setup shown in Figure 6.35, and adhesive tape confinement – observed by micrography

It can be concluded that even if this optimized solution enables to bring the highest stresses in the bond, the composite parts can still be broken if their damage threshold is too close from the bond one. This is different in case of really weak bonds, because the damage thresholds are further one from another

2.3.2 On weak bonds

Symmetrical laser shocks have been performed on both LE and LB series, and the results are quite close. As an example, four extracted shocks from the LB symmetrical shocks campaign are presented in Figure 6.37 by using cross section observations. From these results, it can be observed that it is possible to generate tensile stresses in the bond high enough to open it, without breaking the composite part. Indeed, the small cracks visible in case of sample LB-6 are not important, and did not lead to delamination. There are surely due to the sample size, added to the experimental configuration which could induce more bending than if the test would have been performed on a large plate. For LB series, the debonding threshold has been identified by ultrasounds, and confirmed by cross section observation, to be equal to about 0.90 GW/cm² on each beam. No damage in the T800/M21 laminates has been observed. It proves the efficiency of this optimized solution for this particular type of assembly.

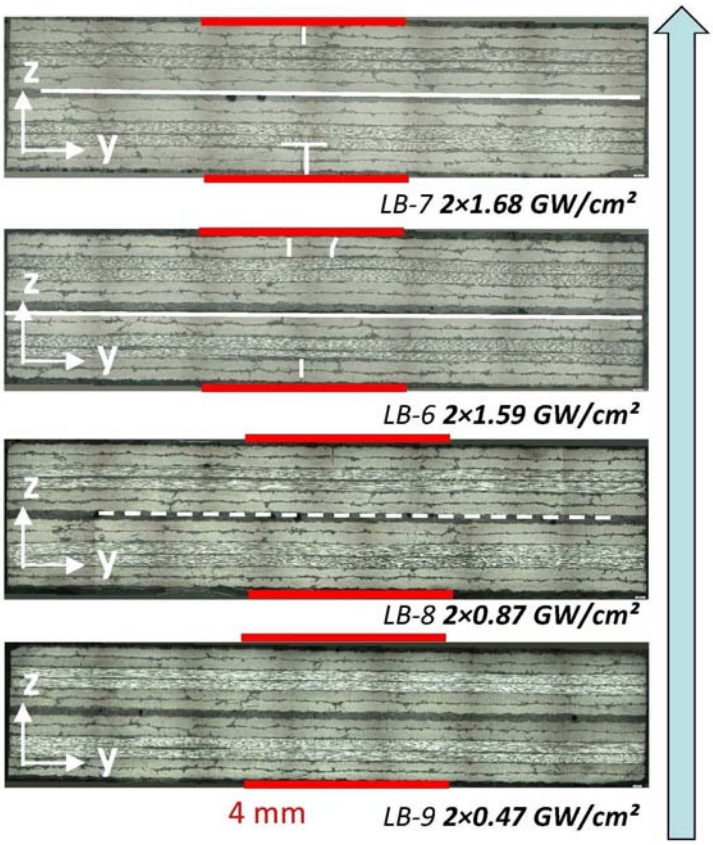

Figure 6.37, Post mortem state of LB samples after symmetrical laser shocks, using setup shown in Figure 6.35 – observed by micrography

Some concluding remarks can be formulated on this optimization technique. The most important is probably that it enables to create the maximum of tensile stresses wherever it could be used to test the irradiated sample, through its whole thickness. The range potentially tested will be even wider with shorter pulses. For long pulses, it could be difficult to test the material close to the two faces, but for that, direct shock solutions could be used. Therefore, it is theoretically possible to test any

kind of interface with a reliable laser source, in the limit of being no more than 5% stronger than the material constituting the different layers. This condition is specific to composite, and should be re-evaluated for other materials. In case of weak bonds, the solution is more efficient than the direct approach, because it creates the maximum of tensile stresses in the bond, and not in the composite part. It is thus easier to avoid breaking the composite parts during the test, which is a clear sign of optimization. Like for all the previous configurations tested, the weaker the bond will be, the easiest it will be to prevent from damage in composite.

Conclusions & synthesis

In the 1st part, the testing possibilities of the current laser configuration have been investigated. Firstly, the absence of fatigue effects due to repeated loadings under the damage threshold has been checked. Up to 10 repeated laser shocks, no detectable mechanical damage has been observed by VISAR measurements on a given bonded target. Moreover, it has been checked afterward that the damage threshold was not reduced because of these previous loadings. Numerical modeling was used to evaluate the current LASAT possibilities in PPRIME laser source configuration. The use of the back face velocity analysis as a mean of discrimination between a broken and unharmed bond has been shown by the numerical results. The results show that an interface whose strength is inferior or equal to 40% of the composite interlaminar strength could be tested without breaking the composite part. This value, like the following ones, should be carefully considered, because of the experimental uncertainties of the laser parameters.

If the interface is stronger than 40% of the composite interlaminar strength, then the technique should be optimized. Different solutions are proposed in the following parts. Firstly, the influence of the laser focus diameter on the position of the maximum tensile stresses has been investigated on the non-symmetrical T700/M21 bonded assembly. It showed that the 4 mm diameter case was the most interesting for the application in terms of tensile stress distribution. Nevertheless, changing the focus diameter is not enough to fully optimize the stress distribution, mainly because of the impedance mismatch at the bond level.

The optimization solution by tunable pulse duration presents interesting characteristics, and can be separated in two main possibilities:

- The first solution consists in locating the maximum of tensile stresses at the bond interface. It enables to test an interface whose maximum strength is in the range of the composite interlaminar strength $\sigma_{T,i}$. It requires an accurate pressure load. This stress distribution occurs in case of a 500 ns and 400 ns pressure pulses respectively on non-symmetrical T700/M21 bonded assembly, and symmetrical T800/M21 bonded samples.

- The second one relies on the first tensile stresses generation at the bond interface. It avoids loading in tension the composite parts before the bond. Therefore, it is less demanding in terms of energy accuracy, but it enables to test a lower maximum tensile strength, inferior or equal to 70% of $\sigma_{T,i}$ in case of non-symmetrical T700/M21 bonded assembly, and to 80% of $\sigma_{T,i}$ in case of symmetrical T800/M21 bonded samples. This solution has been experimentally validated by use of plate impact experiments on different symmetrical bonded samples.

The double shock on the front face solution has also been numerically studied. This laser configuration could present some difficulties for its technical implementation; the confinement medium should subtend two shocks, and the sacrificial layer should be correctly calibrated. Nevertheless, it is a good alternative to the previous solution because it requires less energy than long pulses for an equivalent interface strength tested (inferior or equal to 70% of $\sigma_{T,i}$).

Finally, the synchronized symmetrical laser shock configuration has been developed, as a surgical strike device. It enables to create a sharp tensile loading wherever wanted in the material thickness. Moreover, the interface strength which can be tested can reach the composite interlaminar strength (100% of $\sigma_{T,I}$ in case of non-symmetrical assembly and 105% in case of symmetrical assembly) according to the numerical results. It gives the possibility of easily test any kind of interface, like interplies for example, by changing the delay between the two pulses. This solution has been experimentally evidenced on symmetrical bonded assemblies, and results show that this solution is more efficient to avoid damage in composite parts. This solution is the object of a Patent deposit. All these results are summarized in Table 6.4

Current LASAT Technique possibilities			
Repeated laser shock loading on reference sample		Current testing possibilities	
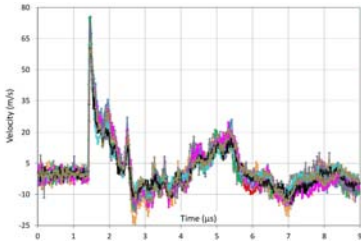	**10 shocks** without observable mechanical modifications	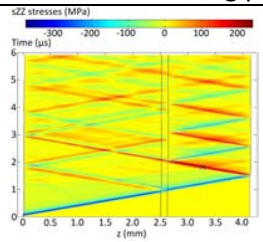	Bond interface strength ≤ **40%** of the composite interlaminar strength

LASAT optimization by tunable pulse duration				
	By using the highest tensile stresses		**By using the first tensile stresses**	
On non-symmetrical T700/M21 bonded assemblies	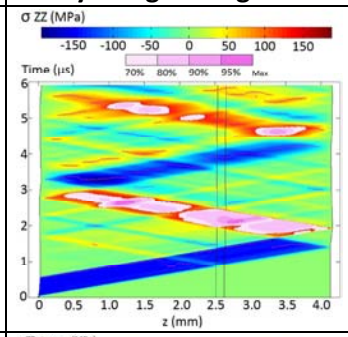	Bond interface strength ≤ **95%** of the composite interlaminar strength	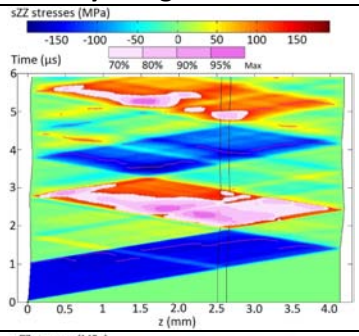	Bond interface strength ≤ **70%** of the composite interlaminar strength
On symmetrical T800/M21 bonded assemblies	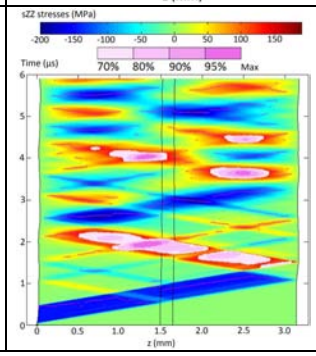	Bond interface strength ≤ **105%** of the composite interlaminar strength	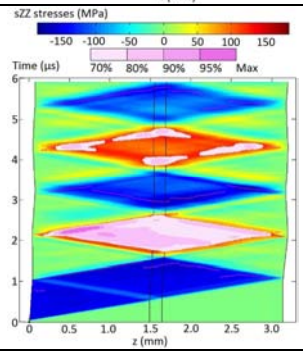	Bond interface strength ≤ **80%** of the composite interlaminar strength

LASAT optimization by double shock approaches				
	By using a symmetrical laser shock		**By using a double shock on the front face**	
On non-symmetrical T700/M21 bonded assemblies	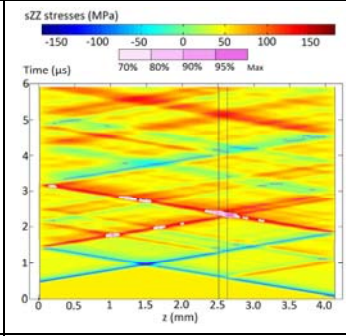	Bond interface strength ≤ **100%** of the composite interlaminar strength	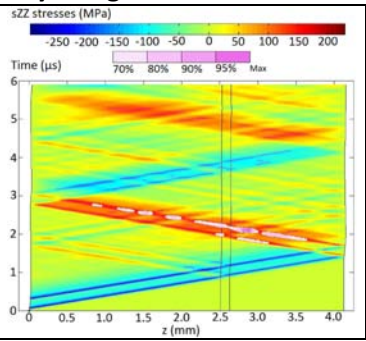	Bond interface strength ≤ **70%** of the composite interlaminar strength
On symmetrical T800/M21 bonded assemblies	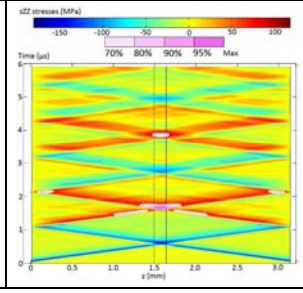	Bond interface strength ≤ **105%** of the composite interlaminar strength		

Table 6.4, Main results of the numerical optimization on composite samples performed in this chapter (laser shock at z = 0)

CONCLUSIONS AND PERSPECTIVES

Synthesis of this work

Studies have been conducted in order to develop a shock wave adhesion test for bonded CFRP composites. Despite the numerous NDT techniques available in the aeronautic industry, no technique can be clearly identified to deal with the weak bond issue and to enable a mechanical quantification of the bond strength. According to previous investigations, it appears that LASAT technique (LAser Shock Adhesion Test) could be a solution. It is well adapted to the industrial context, and can provide a non-destructive proof of the bonding quality. Nevertheless, few studies about the response of CFRP and bonded CFRP to high strain rate laser shock have been performed so far. The understanding of their behavior is though a key point for the technique development and optimization. The investigations conducted in this work aim to a better understanding of propagation and associated effects of laser shocks in composites and bonded composites. Especially, the developed technique has been tested on different industrial scenarios provided in the frame of ENCOMB European project, led by the Fraunhofer Institute IFAM, and in strong relationship with Airbus and EADS as application end users. In this work, both experimental and numerical investigations were performed in order to respectively provide original data on the CFRP laser shock response, and a better understanding of the bonded assemblies behavior in order to open the way to the LASAT technique optimization.

Several shock sources have been used in different configurations to investigate the dynamic behavior of thermoset materials, composite laminates and bonded composite assembly. It goes from the largest laser facility with high energy level and short pulses such as the one available in LULI laboratory (Polytechnique, Palaiseau), to smaller ones, closer to industrial sources, such as the one used in PPRIME (25J, 25ns) or in the PIMM (10J, 8ns). Plate impacts were also realized thanks to a gas gun available in ENSTA-Bretagne. In order to analyze all these shocks, two categories of techniques have been used. On one hand, time resolved systems were used to quantify the dynamic response of the material tested: the VISAR (Velocity Interferometer System for Any Reflector), the PDV (Photonic Doppler Velocimetry) and a specific transverse visualization system specially developed for this investigation. On the other hand, post-mortem techniques were used to analyze and quantify the resulting damage in the composite targets. It is the case of cross section observations, X-ray radiographies, Interferometric Confocal Microscopy, Differential Scanning Calorimetry and Dynamic Mechanical Analysis, as well as conventional and laser ultrasounds techniques in collaboration with EADS Innovation Works. Each used technique provides unique data which are complementary to the information gathered thanks to the other ones.

VISAR 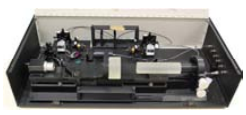	**PDV**	**Visualization**		
Micrographies	**X-Ray Radiography**	**ICM** 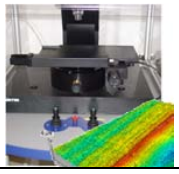	**Ultrasounds**	**DSC/DMA**

Epoxy resin behavior under high pressure was first studied through time resolved observations of the shock wave propagation, and post-mortem residual states. Quantitative data on the shock propagation as well as qualitative information on the distribution of shock patterns within the sample thickness was obtained, especially thanks to the use of time resolved photoelasticimetry. These results provide new data, complementary to back face velocity measurements, to compare with numerical modeling. The shocked epoxy resins were also analyzed to investigate the microstructure and mechanical residual states. No microstructural modification was observed in case of short laser pulses (ELFIE and LULI2000) and residual stresses were quantified on the sample front face to about a few MPa only in case of LULI2000 experiments. Finally, a slight effect of the laser induced shock (PPRIME25) on the microstructural state was highlighted in case of a not well cured epoxy. This result has been obtained in case of spallation only, and is reassuring for the industrial application.

Composite CFRP under laser shocks were then investigated. Focus was made on studying the resulting damage from the shock wave propagation in different T800/M21 lay-ups. The anisotropic damage extents have been quantified and correlated to the laser intensity level. Moreover, the laser shocks performed on thick cross-ply T800/M21 samples have enabled a better understanding of the residual deformation blister induced by damage growth at the composite back face. The elliptical characteristics of this deformation were determined by use of a statistical analysis of the data gathered. These results were completed by experiments on two different unidirectional composites (T300/914, IM7/M21). The whole experimental data has been used to establish charts which would enable the comparison of the damage tolerance of different composite materials. Finally, VISAR time resolved measurements were performed on unidirectional reference materials and applicative CFRP composites in order to obtain information on their dynamic response under laser shock. The measurement reproducibility was checked.

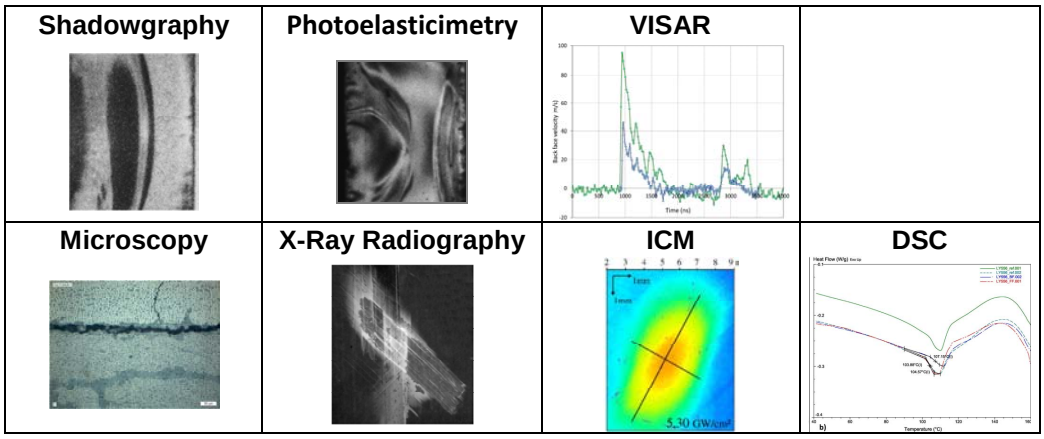

The time resolved experimental results were then used to validate the proposed numerical modeling of laser shock propagation in these materials. A literature overview first shows that various models were available to describe shock in composites, although few works address to high strain rate loadings. The key issue is the model parameters identification, for behavior description as well as for damage propagation modeling. Therefore, an elastic hydrodynamic model has been chosen for epoxy resin modeling, and an elastic orthotropic model was implemented to describe the shock propagation in composite laminates. The Chang/Chang criterion was chosen to model the damage initiation in the composite. The LS-DYNA code has been used to perform the simulations, and a specific Matlab program has been develop to enable the shock propagation pattern visualization and

the stress distribution identification. It can be seen as a computer aided Analysis tool for understanding all the relevant parameters effects on shock waves propagation into materials.
On epoxy targets, numerical simulations in good agreement with LULI2000 experiments in terms of shock propagation have been obtained and validate the model choice. A set of parameters has been found for FM300 bond material modeling, and validated by the good agreement between simulations and VISAR measurements.
Composite modeling was deeply investigated. Several parametric studies were performed on a 3D model of a thin (0.5 mm) unidirectional T800/M21 composite, made of two plies and using quasi-static parameters. Influences of pressure loading, interfaces and anisotropic 2D effects (σ_{XX} stresses), and elastic material parameters were evidenced. Their signatures on the back face velocity signals were clearly identified. Especially, the transverse modulus has a strong influence on the waves time history and amplitude. The anisotropic propagation patterns were shown and understood by plotting the stresses distribution versus time in the model different directions. A set of parameters for the studied composite materials adapted to high strain rate laser loading has been proposed. The model was then progressively validated in several thicknesses and lay-up cases, using VISAR results. Considering the experimental uncertainties, particularly on the pressure profile, the overall agreement with the whole experimental data set is rather good, at least for the first back and forth into the targets.

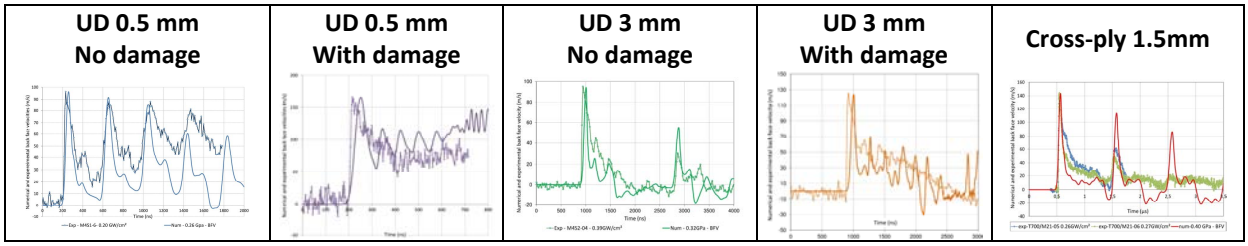

Thanks to these main steps, bonded composite assemblies were then investigated, experimentally and numerically. Two sets of samples were tested, the first one containing symmetrical bonded composites, and the second one, non-symmetrical ones. Each set contains references and contaminated samples. GIC results from University of Patras and Airbus have been used to compare with LASAT results.
Laser shocks were performed on each type of samples and analyzed in order to determine their damage thresholds. The post-mortem analysis enabled a deep investigation of the laser shock induced damage in these bonded CFRP, all the results providing consistent data. The confocal microscopy was useful to determine the damage threshold of the composite part, when the ultrasounds (conventional or laser) were efficient to evaluate the debonding thresholds. Details on the failure mechanisms were obtained by cross section observations, and enabled comparison between the different scenarios of contamination in terms of damage behavior. Focusing on symmetrical samples, the experimental results enabled the identification of contaminated samples, and highlighted the need for laser parameters optimization in order to avoid breaking the composite part while testing the interface. Same adaptation problem was observed for non-symmetrical samples. In this case, a sharp framing of damage thresholds were obtained, especially in case of release agent contamination. The debonding threshold evolution is in quite good agreement with the contamination degree provided by ENCOMB partners and GIC results. Moisture results should be carefully considered, because of random porosity in the bond, but they showed also a good agreement with the contamination degrees.

Numerical modeling of bonded assembly showed good agreement with experimental back face velocities. Therefore, the model and the corresponding time/position diagram representation were used to identify the main back face velocity patterns. It led to a better understanding of the velocity signals main patterns, connected to the dynamic behavior of bonded CFRP.

Finally, the testing possibilities of the current laser configuration and the optimization solutions have been investigated. The absence of fatigue effects due to repeated loading under the damage threshold has been checked, and the numerical modeling was used to evaluate the current LASAT possibilities in PPRIME laser source configuration. It showed that an interface whose strength is inferior or equal to 40% of the composite interlaminar strength could already be tested using reliable laser source, without breaking the composite part, according to modeling results. If the interface is stronger than that, then the technique should be optimized.

Changing the laser focus diameter can already be a solution for some bonded geometries to locate the maximum tensile stresses where wanted. In case of the non-symmetrical lay-up tested in this work, the 4 mm diameter case showed the most interesting tensile stress distribution.

The optimization solution by tunable pulse duration was numerically investigated. The maximum of tensile stresses can be generated at the bond interface. In case of lay-ups tested in this work, it enables to test an interface whose maximum strength is in the range of the composite interlaminar strength $\sigma_{T,i}$. The first tensile stresses can also be generated at the bond interface by using longer pulses. It avoids loading in tension the composite parts before the bond and it enables to test a maximum tensile strength, inferior or equal to 70% of $\sigma_{T,i}$. This solution has been experimentally validated by use of plate impact experiments on different symmetrical bonded samples.

The double shock on the front face solution presents a good alternative to the previous solution because it requires less energy than long pulses for an equivalent interface strength tested. Nevertheless, this laser configuration could present some problems dealing with the laser/matter interaction in confined regime.

At last, the synchronized symmetrical laser shock configuration is one of the most promising solutions, if a two side access is possible. It enables to create a sharp tensile loading wherever wanted in the material thickness. The interface strength which can be tested can reach the composite interlaminar strength according to the numerical results. It gives the possibility of easily testing any kind of interface, like interplies for example, by changing the delay between the two pulses. This solution has been experimentally evidenced on symmetrical bonded assemblies, and results show that even in case of very weak bonds, this solution is the most efficient to avoid damage in composite parts.

Current configuration	**Tunable pulse duration 1st sol.**	**Tunable pulse duration 2nd sol.**	**Double shock on front face**	**Synchronized symmetrical shock**
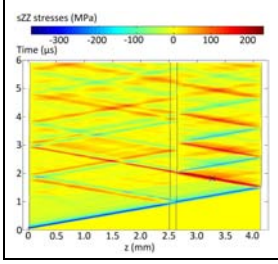	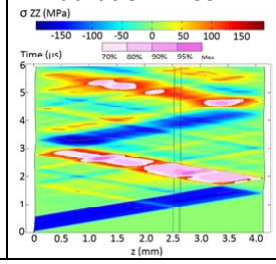	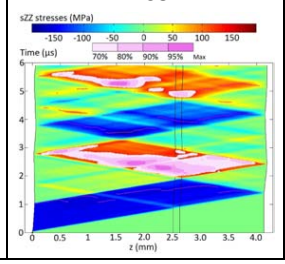	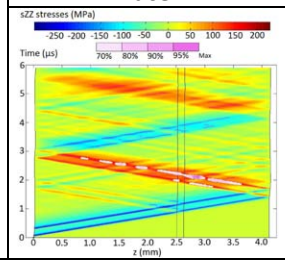	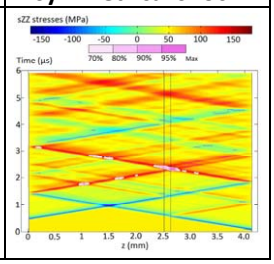

Perspectives

This work leads to interesting perspectives. Firstly, at the scale of the laser/matter interaction, some investigations can be carried out. In this work, first elements on the microstructural modification of thermoset material under laser have been given. So far, no strong modification seems to be observed, especially for short pulses, well cured material, and low energy level. Nevertheless, the laser/matter interaction in case of composite material is an open field for research investigation. About epoxy resins, the use of time resolved photoelasticimetry shadowgraphy has enhanced the understanding of the shock phenomenon. This setup could be used in other shock configuration to gather even more experimental data in order to reach a better phenomena understanding. More generally, other material could be tested such as glass materials. On this subject, collaborative studies have been recently started to investigate their response to shock. However, for CFRP material, time-resolved X-ray radiography could be performed to study shock wave propagation and damage dynamic.

Another point is to enhance the numerical model developed in this work, especially for composite material. It will allow obtaining an even more reliable shock description. Especially, switching to 3D models as a first step would enable a better shock attenuation description, and therefore more reliable stress values. This would enable a sharper optimization and the direct use of the stress values instead of comparing thresholds with the composite strength. A more accurate comparison with GIC results could also be reached. Indeed, an energy calculation could be performed based on the model to compare with the energy failure obtained by GIC testing. Another key point is to use a more accurate and reliable damage propagation model. Starting with already developed cohesive law could be a first step if it can be adapted to high pressure and high strain rate. Then, more complex model could be investigated, such as the one implemented in RADIOSS by EADS Innovation Works and based on the LMT model (Laboratoire de Mecanique et Technologie, ENS Cachan) [1]. Next step could also be the use of discrete elements to obtain a really fine description of the spallation phenomenon induced by laser. In this case, the fiber/matrix interaction could be taken into account. It may go through the development of adapted damage law, specific to composite under laser loading [2-3].

From the experimental point of view, some perspectives can also be discussed. Speaking of long pulses, some configurations are actually not possible by using laser. It is the case of 1000 ns pulse. Alternative shock generators for this range exist, but their readiness for industrial applications is not that obvious. Nevertheless, pulses in the range 100ns – 300ns could be tested with some specific equipment such as the GCLT (Générateur de Choc Laser Transportable, CEA-BIII). It should be used to demonstrate that it is possible to move the position of the damage within the sample thickness, using the highest or the first tensile stresses solutions. In this work, shock parameters for the test of symmetrical and non-symmetrical assemblies have been defined by numerical modeling in case of double shock approach. The HEPHAISTOS laser source, soon available in PIMM, could be used for the corresponding experimental validation. Indeed, this source produced by Thalès is made of two identical lasers, separable and with synchronization possibilities. These lasers match industrial requirements (high rate and quality of well controlled and reproducible laser irradiation conditions), and the parameters uncertainties will be considerably reduced. It should enable a more accurate test, and prove the efficiency of the symmetrical configuration. It should be possible to experimentally demonstrate that damage can be produced in each interply, and interface, simply by

changing the delay between the two pulses, as it has been numerically established in the present work.

The question of damage detection is also an important point. In this work, it has been shown that the measurement of an understood back face velocity gives a lot of credits to the technique. It enables a correct phenomenon description, and discrimination between damage and non damage occurrence. In this study, VISAR system has been used a lot, but it is quite complicated to adjust for composite material or different reasons. A few PDV results were shown in this work. This system presents a good alternative, as a front or back face measurement technique. It is compact, it requires less optical adjustment than the VISAR thanks to a full optical integration, and it is less damaging for the sample tested because of the used wavelength. Dreamed all-in-one solution could come from laser ultrasounds system. As shown in this work, ultrasounds can be efficient to detect debonding and damage resulting from laser shocks. The laser ultrasound device is made of two lasers, one being responsible for the sample excitation, and the second one being in charge of the analysis. Inspired from this technique, it should be technologically possible to use the first laser shock as a shock adhesion test by adjusting the energy level. Meanwhile, it also creates the excitation necessary for the ultrasounds scanning, the response being measured by the second laser. Different studies should be conducted on that aspect.

INDUSTRIAL READINESS CONCLUSIONS AND PERSPECTIVES

In this last conclusion section, some elements on the way we see a potential practical use of this work in an industrial context are given in regards to its future development and use. The protocol developed in this work for the technique adaptation to the bonded assemblies in stake can be discussed. In this work, the main steps to achieve in order to adapt the technique to different bonded assemblies have been established. As shown in Figure C.1, this method can be decomposed in five main steps which should be completed to adapt the LASAT technique on an “unknown” bonded material. “Unknown” should be understood in regards to the laser shock adhesion test technique, and not in a general consideration.

Let’s assume that a completely different material has to be tested, like for example two GFRP cross-ply laminates bonded together in a non-symmetrical assembly by an adhesive different than FM300. Then, the same method used to investigate the T700/M21 and T800/M21 bonded samples can be applied (see in the Figure C.1). The preliminary step is to correctly calibrate the pressure profile, and have clear measurement and understanding of it. This is necessary for the following steps. This step is necessary only if the laser/matter interaction is not well-known or different from documented cases. Then, the dynamic response under laser shock of the GFRP plies, the bond adhesive material, and GFRP cross-ply laminate should be quantified, using for example 10 shocks of different intensities to cover the whole experimental range, with time resolved measurements of back free surface. The gathered results during this phase can be used in a second time in order to validate the numerical models. These models can then be put together in order to simulate the dynamic response of the GFRP bonded assembly to test, the bonded model being validated by another experimental campaign conducted on a reference bonded assembly (steps 3 and 4). Based on the bonded assembly experimental and numerical results, the shock adhesion test can finally be better adapted to the material to test. It is not sure that an optimized configuration will be found for each assembly, but the best configuration can be highlighted in comparison to the known damage thresholds of the

material. If need be, the best shock configurations can be experimentally validated by performing a few shocks in order to check the damage location, the damage and debonding thresholds. In case of the assemblies presented in this work this last one remains to be investigated with a reliable laser source. At the end, the bond quality control can be performed by shock wave adhesion test, without running this five steps procedure each time.

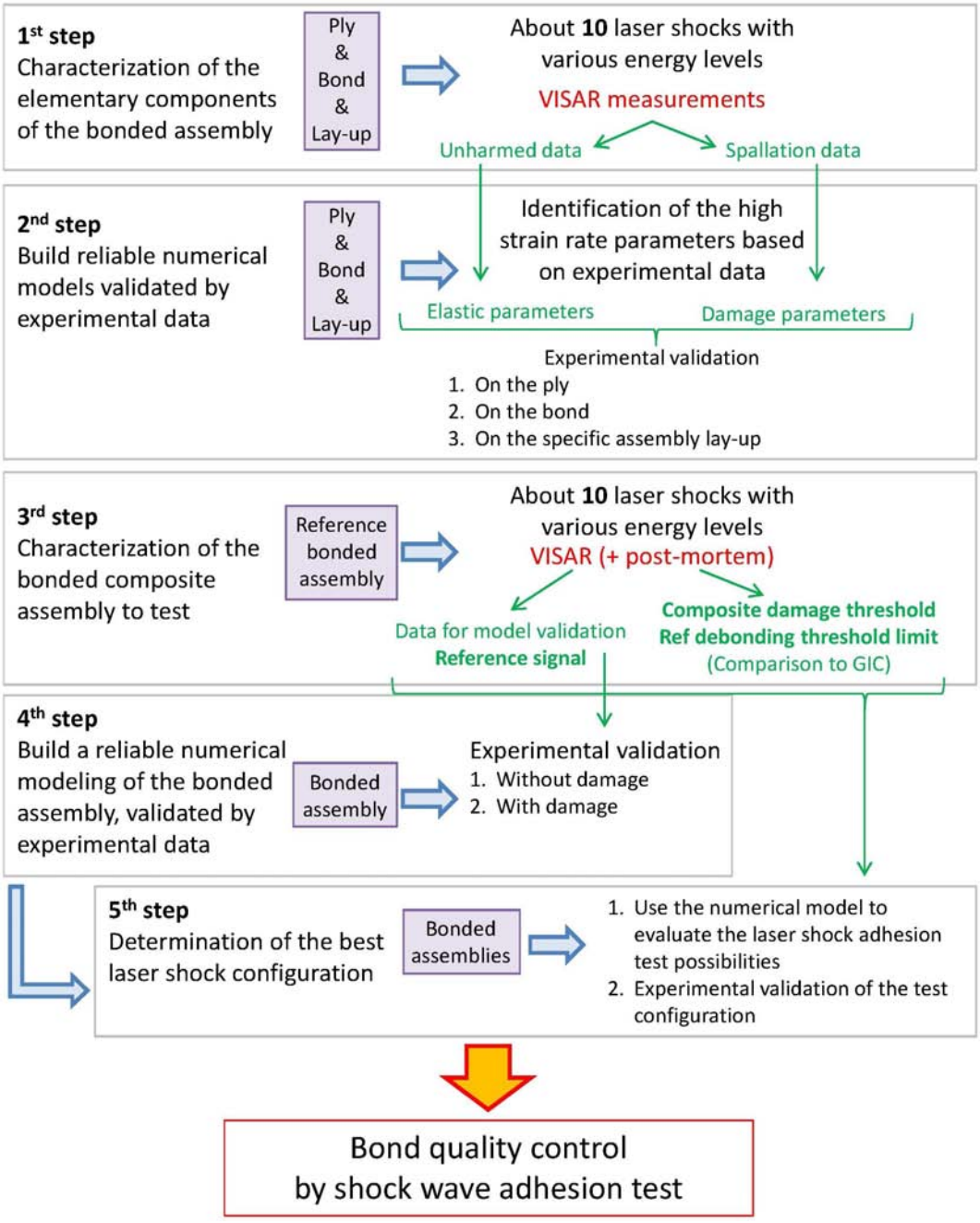

Figure C.1, The suggested protocol to adapt the LASAT technique for an “unknown” bonded assembly

All these steps are not necessary if the material is already well characterized under dynamic loading, or if it is close from the bonded assemblies already known. Depending on the information available, some steps can be skipped. For example, in this work, the T800/M21 and T700/M21 composite plies have been considered to be close enough to use some of the results obtained on one laminate for the other one. Moreover, some other geometries can already be tested with the results presented in

this work. Indeed, if just adding a few 0° or 90° plies to the bonded samples investigated in this work, then step 5 can directly be used. The whole approach has to be applied for very different assemblies only, to get the best shock configuration to use. By the way, it could be interesting to test different assemblies by changing the thickness or the lay-up to get another validation point of the technique (considering this work gives validation point on the tested assemblies). Moreover, the optimized configurations presented in this work can be interesting to revisit already tested samples such as metal coating, aluminum assemblies or thermal barriers. These new shock configurations may enhance the domain which can be tested by the shock adhesion test technique in terms of thickness, impedance mismatch configurations and specific sample geometries. Besides, it provides a Computer Aided Design of the shock parameters/configuration the best suitable to generate the very first tension states where and when desired for a given multi-layer assembly. This opens wide possibilities for either sensing the bond quality of selected interfaces, or the local strength of such structures.

Finally, a possible industrial implementation of the technique can be suggested (Figure C.2). For that, it is assumed that the optimized shock configuration has been selected. The correct bond performance should be known, as well as its signature to laser shock load whatever is the diagnostic. Moreover, the kind of weakness expected to be detected has to be specified in order to correctly dimension the security coefficient taken on the laser intensity to avoid breaking the correct bonds. The laser and associated diagnostic should be first adjusted on the spot to test. The laser shock can then be produced, taking into account the security coefficient. The analysis made, whatever time resolved or post-shock, are compared to the reference signature for an equivalent shock. If a difference is noticed out of the uncertainty range, it means that the bond has been opened, if not, it means that the bond corresponds to what was expected. Then, the laser can be moved to the next point to test.

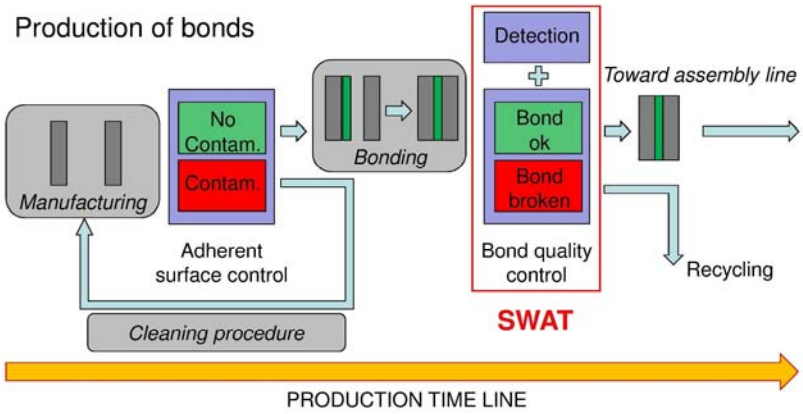

Figure C.2, Suggested industrial implementation technique

References

[1] O. Allix, M. Dommanget, M. Gratton, P-L Héreil, *A multi-scale approach for the response of a 3D carbon/carbon composite under shock loading*, published in Composites Science and Technology 61 (2001) 409-415

[2] D. Iliescu, D. Gehin, I. Iordanoff, F. Girot, M.E. Gutiérrez, *A discrete element method for the simulation of CFRP cutting*, published in Composites Science and Technology 70 (2010) 73–80

[3] M. Jebahi, J-L Charles, F. Dau, L. Illoul, I. Iordanoff, *3D coupling approach between discrete and continuum models for dynamic simulations (DEM–CNEM)*, published in Comput. Methods Appl. Mech. Engrg. 255 (2013) 196–209

APPENDIX A - ENCOMB PROJECT AND ENCOMB TECHNIQUES

A.1 ENCOMB project organization and partners

Figure A.1 European map representing the geographical organization of ENCOMB partners with the associated countries, institution and companies involved.

14 different European partners are involved in ENCOMB (www.encomb.eu), gathering industrial companies, academic institutes, and research laboratories. From the industrial point of view, the project is leaded by Airbus (Bremen, Germany), whereas the scientific coordination is steered by the Fraunhofer Institute IFAM (Bremen, Germany). An overview of the European collaboration is given in Figure A.1, with all the different partners and the associated countries. The project is structured in 6 main work packages, briefly described below. All the partners, their actions in the different work package, and their techniques are given in Table 1.1.

- **WP1**: Definition of the scenarios to investigate in the European project. This task is realized by Airbus (C. Bockenheimer, B. Ehrhart). The purpose is to link the research and the technical developments to the industrial issues. Typically, Airbus is defining the contamination which can occur prior to bonding process, and the related weak bonds to be tested by the investigated techniques.

- **WP2**: Sample preparation and characterization. In this work package, the bonded CFRP samples are prepared according to the recommendations of Airbus. The samples are produced for each partner, and characterized by conventional devices. EADS Cassidian is in charge of the production of the contaminated and bonded samples (E. Rau). They are

supported by Airbus (Nantes, France) which is providing the composite panels, and by IFAM which is working on the contamination procedure. Concerning the bonded samples, one half is reserved to the GIC mechanical testing which are realized by the University of Patras (Patras, Greece). These tests are essential because they give the bond strength of the sample produced, which can be used as a reference for the following technique development.

- **WP3**: Control of the adherent surfaces prior to bonding. This work package groups all the investigations of the techniques dedicated to the control of surface and the detection of contaminants as defined by Airbus.

- **WP4**: Control of the adhesively bonded CFRP properties. This work package is dedicated to the investigations of the methods developed to quantify the bonding mechanical quality. The idea is also to link the contamination to the effective cohesive strength of the adherent. Industrially speaking, the discrimination between a weak bond and a correct one should become possible thanks to the technique developed. The work presented here is part of this work package.

- **WP5**: Dissemination. This work package is leaded by EASN (Budingen, Belgium)

- **WP6**: Management task, realized by the Fraunhofer Institute IFAM. M. Hoffmann is in charge of the scientific coordination, and D. Stübing is responsible for the global coordination of the project.

Airbus	Bremen, Germany	WP1	Definition of the scenarios
Fraunhofer Institute IFAM	Bremen, Germany	WP2	Contamination of composite
		WP3	Laser induced Breakdown Spectroscopy (LIBS)
			X-Ray Fluorescence Spectroscopy (XRF)
			Infrared Spectroscopy (IR)
			Optically Stimulated Electron Emission (OSEE)
			Aerosol Wetting Test (AWT)
			Electromechanical Impedance Spectroscopy (EIS)
			Active Thermography (AT)
		WP6	Coordination of the project
EADS Cassidian	Munich, Germany	WP2	Production and diffusion of the samples
		WP4	Ultrasonic excited thermography
			Ultrasonic frequency analysis
EADS Innovation Works	Munich, Germany	WP2	Microtomography characterization of the bonded CFRP
University of Patras	Patras, Greece	WP2	Mechanical characterization of the bonded sample by GIC testing
Fraunhofer Institute IZFP	Zaarbrücker, Germany	WP3	Nuclear Magnetic Resonance (NMR)
		WP3 & WP4	Optical Exited Active Thermography (OEAT)
Italian National Agency for New technologies, Energy and Sustainable Economic Development (ENEA)	Portici, Italy	WP3	Artificial olfaction & E-nose

RECENDT	Linz, Austria	WP3	Infrared Spectroscopy (MID - NIR)
			Optical Coherence Tomography (OCT)
		WP4	Laser Ultrasounds (LU)
National Academy of Sciences of Ukraine	Kyyiv, Ukrain	WP3 & WP4	Thz Measurements
Polish Academy of Sciences (IMP PAN)	Gdansk, Poland	WP3 & WP4	Laser Scanning Vibrometry (Lamb waves) (LSV)
			Vibrothermography
		WP4	Electro-mechanical Impedance (EMI)
A2 Technologies (Agilent Technologies)	Glasgow, Scotland	WP3/WP2	Mid Infrared Spectroscopy (Exo Scan)
Ecole Polytechnique Fédérale de Lausanne (EPFL)	Lausanne, Switzerland	WP3 & WP4	Fiber Bragg Grating sensors
University of Bristol	Bristol, United Kingdom	WP4	Non Linear Ultrasounds
EADS Innovation Works	Nantes, France	WP4	Laser Ultrasounds (LU)
CNRS - Institute PPRIME & PIMM	Poitiers & Paris, France	WP4	Laser Shock Wave Adhesion Test (LASAT)

Table A.1 List of the ENCOMB partners with the associated countries, work package activities and developed techniques in the frame of the European project

A.2 ENCOMB Techniques developed for weak bonds detection

The synthesis presented in this section gives an overview of what is currently done to face the weak bond issue, in the frame of ENCOMB project. Instead of presenting the techniques per work package, the developed methods are sorted out by major families. Note that a selection has been made to describe only the techniques which are already giving some promising results. When a technique is used by several partners, the most advanced is presented.

A.2.1 Spectroscopy techniques

The techniques presented in this section are based on spectroscopy analysis. In the frame of the project, they are used to detect the presence of contaminants on the CFRP surfaces before bonding (WP3). The principle is the same for each technique: the molecules of the material surface are excited using an energy source, and then relaxed by emitting radiations or matter depending on the irradiation nature. The excitation can be made using laser (LIBS), X-Ray (XRF) or infrared irradiation.

The Laser Induced Breakdown Spectroscopy (LIBS) is one of the techniques developed by IFAM for the CFRP surface evaluation in the frame of ENCOMB [1]. A laser irradiation is produce on the surface to analyze. This powered irradiation creates a plasma made of the molecules composing the surface. Then, an atomic emission spectroscopy is performed on the plasma generated from the surface. According to the wavelength peaks observed on the signal, the elemental composition of the surface can be detected. The work carried out by IFAM has shown that LIBS is efficient to detect the presence of phosphor, and thus is well adapted to the Skydrol scenario. Some good results have also been obtained on release agent tests. Nevertheless, this technique is not well adapted to the detection of moisture, since the plasma can mix with the ambient air. Even if a similar diagnostic is

equipping the Mars rover Curiosity, the level of development of the technology is not high enough to go from the lab to industries yet.

X-Ray Fluorescence spectroscopy (XRF) is also developed by IFAM for the ENCOMB project. The principle is a bit different from the LIBS. A X-Ray source is used to excite the surface molecule electrons. The X-Ray source level is calibrated to remove some electrons from the smallest atomic orbital which leave a vacant space for highest atomic orbital electrons. These electrons fall into the vacant space to respect the atomic balance, meanwhile they emit X-Ray. This radiation is measured and then analyzed to identify the molecule responsible for this emission. The work conducted by IFAM on this technique has shown a good efficiency to detect the Skydrol contamination because of the phosphor content [2]. Nevertheless, no difference was found between the reference, the thermal degraded and moisture scenarios.

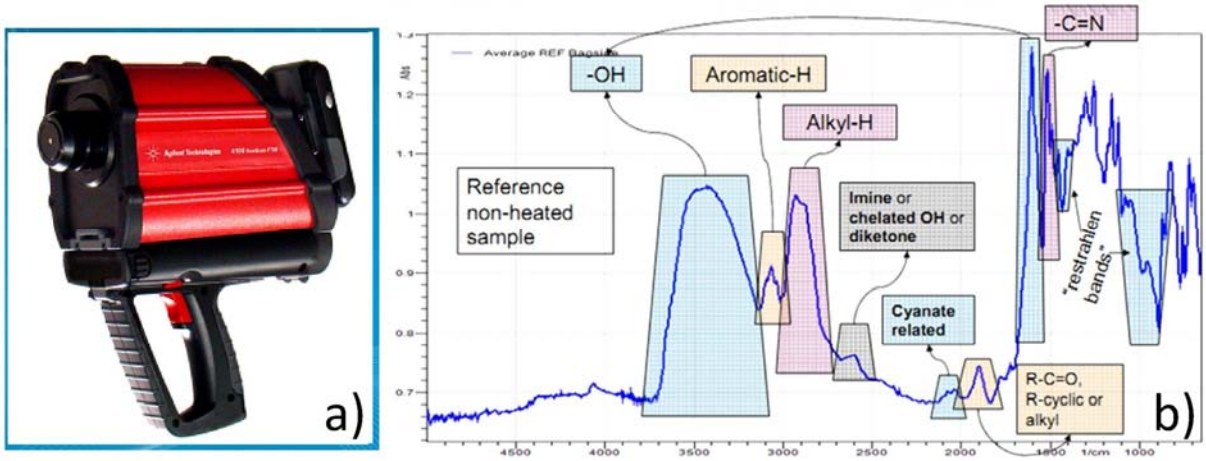

Figure A.2 a) Picture of the Exoscan FTIR developed by Agilent Technologies and used in the frame of ENCOMB project (Agilent and IFAM) – b) Absorbance measurement obtained using an Exoscan FTIR on an untreated CFRP composite considered as a reference, composition identification (from Agilent Technologies, L. Tang)

The last technique presented in this section is probably the most efficient for the contamination detection and concerns infrared spectroscopy [3]. Several partners are developing this technique (RECENDT, Agilent & IFAM), but the most advanced is the commercial FTIR Exoscan (see in Figure A.2, a). It has been developed by A2 Technologies, recently associated to Agilent Technologies. This device is already used in some aeronautical applications, and has been added to this project to be pushed forward in the contamination detection. Infrared irradiation of the target is used. By measuring the reflected radiations, the absorbance of the tested surface can be determined as a function of the wavelength. The absorbance is in fact the sign of a particular molecule movement, which can indicate the presence of the corresponding molecule. That way, the chemical composition of the surface can be evaluated precisely. The main difference between the FTIR Exoscan and the other IR methods is the fast calculation time which gives a result in a few seconds. In case of CFRP material, the spectrum measured is mainly the one of the epoxy content. Indeed, due to the manufacturing process of CFRP, a thin layer of epoxy generally remains on the CFRP surface. An example is given in Figure A.2, b. By using this technique, each contamination can be clearly identified by a shift in the absorbance recorded signal. The work of Agilent Technologies (L. Tang) and IFAM has shown that the shift of particular bandwidth peak can be correlated to the presence of different contaminants. In particular, release agent, Skydrol plus water mixture and moisture contaminations have been detected by identifying the particular shift in the absorbance signals. The case of thermal degradation is slightly different since chemical modification is induced by the heat. In

this case, Agilent Technologies has noticed clues of oxidation on the FTIR signal meanwhile a diminution of the epoxy content. These are proofs of thermal degradation. Thanks to these good results, the Exoscan has been moved from WP3 to WP2 during the project to help to the characterization of contamination.

A.2.2 Contactless surface control techniques

The three techniques presented in this section are also related to the detection of surface contaminants (WP3). They differ from the previous one by the choice made for the detection, which is not spectroscopy, but remain contactless methods. Aerosol Wetting Test (AWT) developed by IFAM, Artificial olfaction & E-nose investigated by ENEA and Optically Stimulated Electron Emission (OSEE) also elaborated by IFAM are presented in this section.

The AWT is close to the Water Break Test (WBT) previously introduced. It is based on the surface tension of CFRP in presence of contaminants. In case of WBT, a flow is generated by gravity on the composite surface to analyze. The contaminated areas are identified thanks to the flow curvature and breaking on the composite panels (hydrophobic or hydrophilic properties). In case of AWT, the panel to test remains horizontal and a nozzle is used to produce calibrated droplets which drop on the surface. The droplet size and shape on the CFRP surface depends on its surface tension, meaning its chemical composition. This property is well adapted to the detection of silicon-based release agent. Indeed, silicon is well known to be hydrophobic. The droplet size, shape and distribution change in presence of silicon [4]. Thus, the wetted surface can be monitored using a camera, and the analysis of the droplet could be enough to locate a contaminated area. The work conducted by IFAM has shown that a correlation can be drawn between the release agent contamination degree (meaning the amount of Si on the surface) and the droplet mean size [5]. Nevertheless, this technique is less adapted to the detection of other contaminations, especially the one based on water (moisture and Skydrol). Indeed, in these cases the water coming from the aerosol can mix with the water present from the contamination. Therefore, the results are much harder to interpret.

Artificial olfaction and E-nose developed by ENEA has also given good results in the contamination detection. The e-nose is designed to look like a mammalian olfactory system, and is aimed to “smell” chemical substances. The olfactory receptor (our nose) is replaced by an electrical sensor array, the olfactory bulb which is an interface between the receptor and the brain, is played by a preprocessor, and the interpretation of the brain is done by a pattern recognition algorithm [6]. The first layer is generally a solid state gas sensor, and each sensor has a different affinity with different elements of the gas mixture under analysis. During their investigations, the ENEA team had to select the appropriated sensors for the contaminated CFRP applications, and the most efficient pattern recognition algorithm. The sensors had to be changed to switch from one contamination to another. Therefore, a hybrid sensor array using both electromechanical sensor and Ion Mobility spectrometer could detect all the different aeronautic contaminants according to their work [7]. All the ENCOMB contaminants have been detected thanks to this method as shown in Figure A.3. E-nose and artificial olfaction seem to be a good candidate for the Airbus application scenarios, even if the contamination degrees are not clearly distinguished yet.

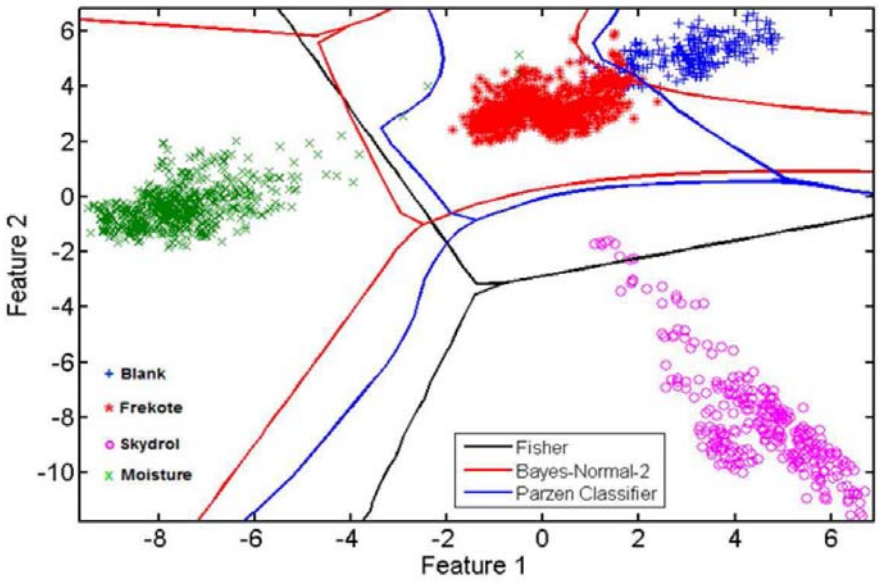

Figure A.3 Discrimination of the different composite surface contaminants as investigated in ENCOMB by the e-nose and artificial olfaction technology (from P. Di Palma and ENEA work [7])

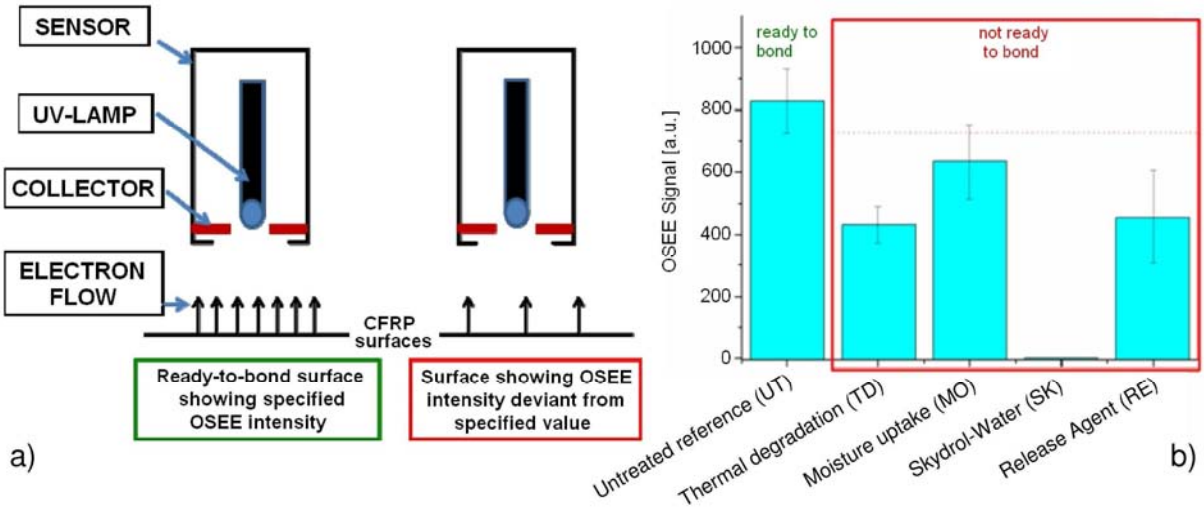

Figure A.4 a) Principle of the OSEE technique applied to contaminants detection on CFRP surfaces – b) Discrimination of the different contamination by OSEE analysis (from K. Brune and IFAM work [8])

The Optically Stimulated Electron Emission technique developed by IFAM is the last to be presented in this section. The principle of the technique is shown in Figure A.4, a. The material surface to analyze is irradiated using Ultra-violet light which induces an electron flow emission out of the surface. Depending on the surface state, meaning the presence or not of contaminants, the electron flow measured by the collector is more or less intense. The work conducted at IFAM aims to correlate this OSEE intensity signal to the contamination present on the composite panels [8]. One figure presented in their work is reported in Figure A.4, b. It shows that the OSEE technique enables the detection of all contaminants compared to a reference untreated sample. From the industrial point of view, the technique can discriminate a ready-to-bond surface from a not ready-to-bond surface (see in Figure A.4, b). Nevertheless, the scenarios thermal degradation, Moisture and release cannot be differentiated one from another so far. Latest investigations on this technique address this issue. It has also been experimentally demonstrated that the repetition of measurement on the

contaminated surface has a cleaning effect. Moreover, it has been possible to discriminate different levels of contamination in case of release agent scenario [9].

A.2.3 Thermography methods

Some thermography inspection methods are also investigated in the frame of ENCOMB project. The idea of all the methods is to measure the sample thermal response to a given excitation in order to detect a discontinuity revealing the presence of contaminants. The thermography methods are well adapted to the detection of cracking or debonding [10-11]. The purpose is here to estimate their efficiency to detect chemical contamination or weak bonds as defined in ENCOMB project. The technique can be equally used on contaminated composite surfaces or contaminated bonded composite.

An active thermography method is investigated by IFAM in order to detect the presence of moisture in CFRPs. They want to use the water content effect on the epoxy glass transition to observe any change in the CFRP thermal response to a progressive heat up. So far, they have some problems in demonstrating the feasibility of this test by using DSC (Differential Scanning Calorimeter) analysis. The same kind of technique is developed by the other Fraunhofer institute involved in the ENCOMB project (IZFP). Optical Excited Active Thermography (OEAT) is based on powered flash lamps used to irradiate during some milliseconds a material to evaluate. The IR camera is recording the IR radiations coming from the cooling plate. The infrared range observed is a combination between the mid infrared range (4.4 – 5.2 µm) and the low infrared range (7.8 – 8.8 µm). One more time, the presence of contaminant should be traduced by a thermal discontinuity in the plate cooling down. So far, no result was found on contaminated composite panels, but the technique seems to be more sensitive in case of bonded panels. This is due to the fact that the thermal inertia is more important in this last case. Differences in IR emission intensity have been noticed in case of the release agent scenario, between the contamination degrees. Nevertheless, none of these measurements can be correlated to bond strength so far.

Vibrothermography is developed by IMP PAN. Instead of using a lamp for the thermal loading, a thermal excitation is applied to the material to test. The high frequencies (kHz) generate a self-heating of the samples, which is recorded using an infrared camera. This technique could work for both contaminated CFRP and contaminated bonded CFRP. So far, some differences between the references and the contaminated composite and contaminated bonds respectively have been highlighted by the Polish Academy investigations (see in Figure A.5). Even if some differences can be noticed, no clear correlation between the thermal patterns and the contamination nature or degree has been found [12].

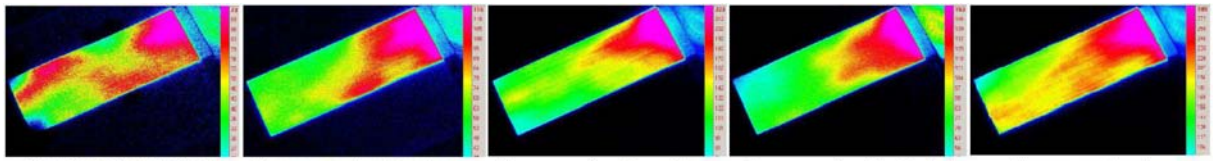

Figure A.5 Examples of Vibrothermography measurements on the different contaminated CFRP investigated in the frame of ENCOMB project (from P. Malinowski and IMP PAN work [12])

A.2.4 Intrusive nondestructive testing/ Health monitoring

The two techniques presented in this section are still related to the contamination detection, but are also linked to health monitoring. Indeed, it is interesting to couple the two approaches to develop even smarter materials. Especially, the fiber grating brag sensors are pushed to equip the next generation of aeronautical smart materials. In the frame of ENCOMB project, EPFL is working to detect contaminant inside the composite sample or bonded composite samples by using impregnated optical fibers. Especially, water could be detected because its presence affects the fiber refractive index. To this goal, the water absorption of CFRP and bonded CFRP should be understood. Experimental and numerical investigations are currently running to get more information on this behavior [13].

Electro Mechanical Impedance (EMI) technique is also from the world of smart materials [14]. IMP PAN is developing this method to investigate the bonded CFRP. The admittance (inverse of impedance) is measured thank to a piezoelectric transducer which is mounted at the middle of each sample to analyze. The bandwidth used for the measurements is between 4 Hz and 5 MHz. Then, the registered spectra are analyzed to identify the frequency peaks traducing a local decrease in conductance which characterized the tested sample. The presence of a contaminant in the bonded composite influences the material conductance. Therefore, discrimination between the different contaminations can be made by analyzing several frequency ranges (see in Figure A.6) [12]. More recently, the technique has been used to investigate the different contamination degrees of a given scenario. P. Malinowski et al. have shown that EMI enables to discriminate different levels of contamination in case of bonded composite release agent scenario. Since the frequency response is more or less the same (same contaminant), the Root Mean Square Deviation of each spectra was calculated to highlight the differences [14-15]. Then, the GIC tests can be used to correlate the EMI measurement to the mechanical strength of the bond. This characteristic cannot be directly obtained thanks to EMI measurements.

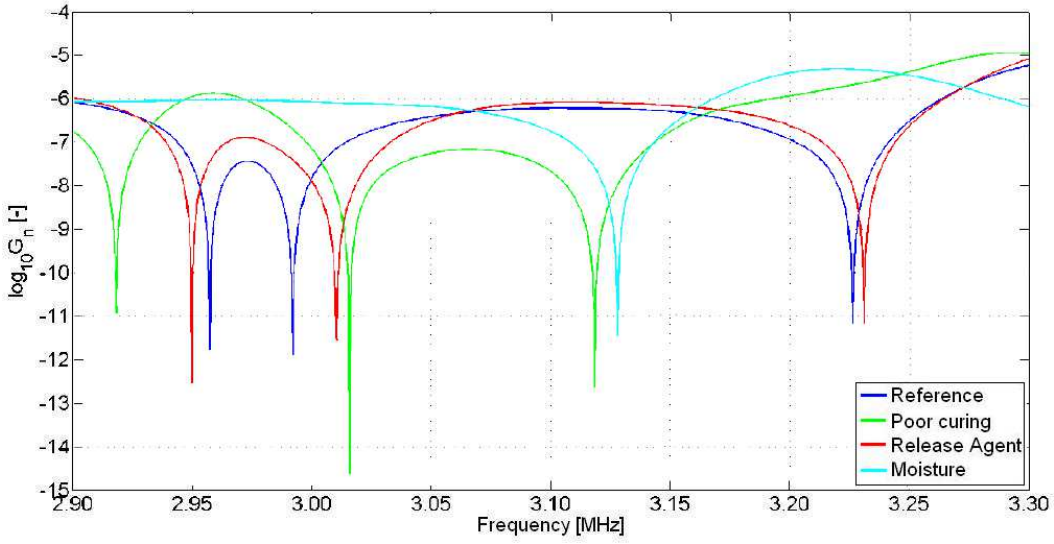

Figure A.6 EMI spectra measurements of the contaminated bonded CFRP – Logarithm of conductance in the bandwidth of 2.9 – 3.3 MHz (from P. Malinowski and IMP PAN work [14])

A.2.5 Wave propagation methods and Ultrasounds

In this last section, the methods based on the wave propagation are presented. Ultrasounds techniques are the more investigated, but work on lamb waves is also performed in the frame of ENCOMB by IMP PAN. The Laser Scanning Vibrometry technique is the only one from this family to be practical to both contamination detection in CFRP and in bonded CFRP (WP3 & WP4) [12], [17]. The idea is to measure the wave propagation induced by a piezoelectric excitation (200 kHz) along the composite sample to test. This measurement is done by a Laser Vibrometer which can register the wave field in the sample (see in Figure A.7, a). The presence of a contaminant, on the composite surface or in the composite bond, should theoretically delay or enhance the wave propagation by changing the material impedance. Therefore, a difference in the wave speed velocity means that a contaminant is present. The Polish Academy of Science has shown a significant increase of the wave velocity in case of moisture contamination of CFRP [12], [17]. The velocities have been measured with sufficient difference to discriminate the moisture scenario from the other cases which cannot be separated from the reference case (see Figure A.7, b)). The same kind of experiments has been conducted on bonded composite materials in the different scenario cases. Once again, the moisture sample have shown faster wave propagation even if the deviation is a bit more important for bonded CFRP (see in Figure A.7, c)) [15-16]. The other contamination scenarios, release agent and low curing, have not been discriminated from the reference sample due to deviation in the measurements. Nevertheless, this technique is interesting because it can enable the detection of water in both CFRP panels, and bonded composite. Very likely, the test would become harder to perform if only some areas were contaminated with water.

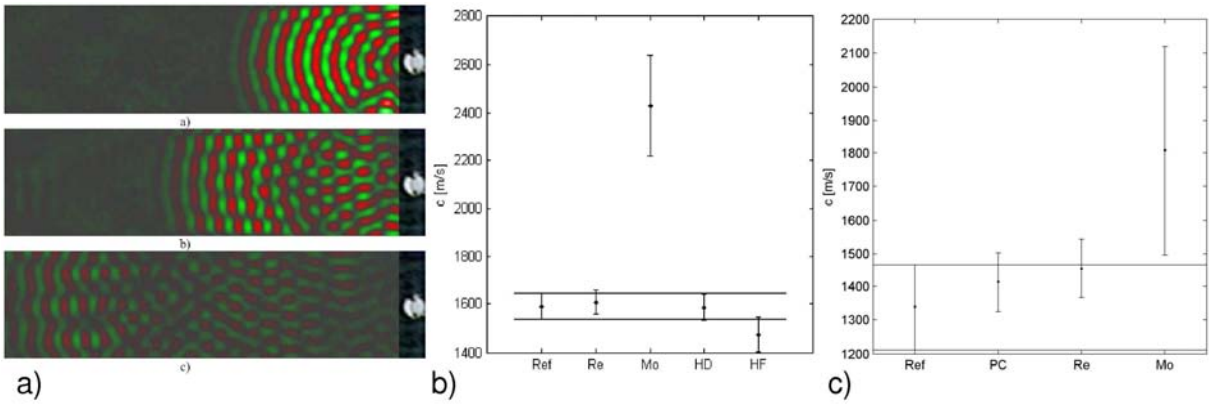

Figure A.7 a) Measurement of the wave propagation induced by piezoelectric excitation in a CFRP composite by laser scanning Vibrometry (from P. Malinowski work [17]) – b) Measured wave velocities for the different contaminated CFRP (from P. Malinowski work [17]) - c) Measured wave velocities for the different weakly bonded CFRP and reference (from P. Malinowski work [17])

Ultrasounds techniques are finally presented. Note that the use of ultrasounds for the detection of damage will be presented in detailed in Chapter 2. Contrary to laser scanning vibrometry, these techniques are investigated in the frame of ENCOMB only for the detection of weak bonds. The idea that ultrasounds can be used to control the adhesion is not new [18], but the analysis tools are more recent. Three different “kinds” of ultrasounds have been tested by the ENCOMB partners: Laser ultrasounds (EADS IW, RECENDT), conventional ultrasound probe with frequency analysis (EADS Cassidian), and Non Linear Ultrasounds (University of Bristol).

Laser ultrasounds technique has already been presented and will be detailed in the following chapters. It is really efficient to detect damage inside the composite materials, such as delamination or debonding. It has been tested on weak bonds to see if the presence of contaminant could influence the bonded material response to the ultrasounds propagation. So far, no clear trend has been observed by EADS IW for the three scenarios (moisture, release agent, poor curing). RECENDT is progressing in the development of its own laser ultrasound source, and recently succeed to detect a crack in a bonded composite [19]. The reason for this absence of detection is probably the really low change in the bonded material mechanical impedance induced by the contaminant presence. The solution could come from a deeper analysis of the ultrasounds signal as it is done by EADS Cassidian. Indeed, recent works have shown that regular ultrasounds probe (5MHz) could detect the presence of contaminants if a frequency analysis is done on the raw data (see in Figure A.8) [20].

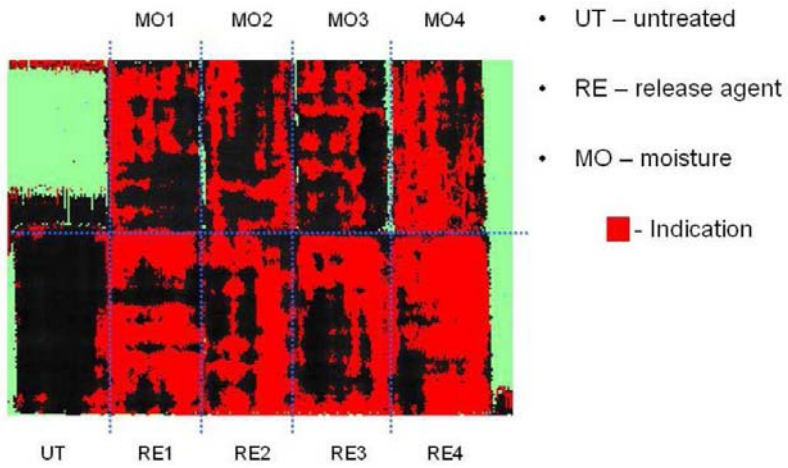

Figure A.8 Discrimination of contaminated bonds (release agent and moisture) by ultrasound frequency analysis (from G. Heichler work [20])

The contamination thin layer is considered as a layer which can modify the ultrasounds frequency. With the appropriate tool, and frequency analysis, this small difference can be detected and enables to discriminate contaminated sample from reference. In Figure A.8, this frequency difference is displayed using a post treatment software. Each bonded composite are displayed from the top, meaning in the composite plan. The red areas reveal the contamination. Further investigations address to the separation of the different contaminant degrees, which require more sensitivity in the frequency analysis.

This ultrasound frequency analysis can be considered as post treatment done on the data to enhance the detection. The Non Linear Ultrasounds technique developed by the University of Bristol is doing the opposite. Instead of enhancing the post-treatment, the measurement itself is done more precisely by using an algorithm which adapts the ultrasounds emission to the material to test. The ultrasounds are more focused, and can detect smaller defects or smaller changes in the material thickness [21]. So far, some differences have been observed between the reference and the contaminated bonds. The correlation is not completely clear though, but more work is needed.

References Appendix A

[1] Markus, S. et al., *Detection of Contaminants on Polymer Surfaces Using Laser Induced Breakdown Spectroscopy (LIBS)*, Polymer Surface Modification: Relevance to Adhesion, Mittal, K. L. (Ed.), (4), Utrecht: VSP, (2007)

[2] K. Albinsky, K. Brune, S. Dieckhoff, O. Hesebeck, U. Lommatzsch, S. Markus, *Advances in bonded repair of CFRP aircraft structures by surface inspection*, presented at the 2nd International Conference on Advanced Composite Materials and Technologies for Aerospace Applications, June 11-13, 2012, Wrexham, United Kingdom

[3] L. H. Pearson, *Diffuse reflectance IR spectroscopy for bonding surface contamination, Review of Progress*, published in Quantitative Nondestructive Evaluation Vol. 10A, New York, 1991

[4] R. Wilken, et al., EP 1893974 B1, *Method and Device for Testing a Surface Quality*, FhG zur Förderung der angewandten Forschung e.V. (date of publication: 2009-04-15)

[5] S. Markus, C. Tornow, S. Dieckhoff , M. Boustie, R. Ecault, L. Berthe, C. Bockenheimer *Extended Non-Destructive Testing of Composite Bonds*, presented at the SAE International Conference, 2011, Toulouse, France. Report No.: 2011-01-2514.

[6] F. Rock, N. Barsan, U. Weimar, *Electronic nose: Current status and future trends, Chemical Reviews*, Vol. 108, 705–725, 2008

[7] P. Di Palma, S. De Vito, M. Miglietta, E. Massera, G. Fattoruso, B. Mastroianni, G. Di Francia, *CFRP Surface Contamination Detection by an Electronic Nose Device for Quality Assessment of Adhesive Bonds in Lightweight Aircraft Structures*, presented at the 3rd International Conference of Engineering Against Failure (ICEAF III), 26th – 28th June 2013, Kos Island, Greece

[8] K. Brune, L. Lima, M. Noeske, K. Thiel, C. Tornow, S. Dieckhoff, M. Hoffmann, D. Stübing, Pre-bond Quality Assurance of CFRP Surfaces Using Optically Stimulated Electron Emission, presented at the 3rd International Conference of Engineering Against Failure (ICEAF III), 26th – 28th June 2013, Kos Island, Greece

[9] K.Brune, S. Dieckhoff, M. Hoffmann, L. Lima, D. Stübing, C. Tornow, Pre-bond Quality *Assurance of CFRP-surfaces by using Optically Stimulated Electron Emission*, presented at the Adhesion '13 Conference, September 4th – 6th, 2013, York, United Kingdom

[10] G. Walle, et al., *A thermal NDT technique for surface crack testing in conductive materials*, Materials Testing, 9, 2009

[11] H. Aglan, et al., *Cumulative fatigue disbond of adhesive joints and its detection using thermal wave imaging*, In Thompson, DO, Chimenti, DE, eds., Review of Progress in quantitative non-destructive evaluation, Vol. 14, 431-438, 1995

[12] P. Malinowski, T. Wandowski, L. Skarbek, W. Ostachowicz, *Non-destructive assessment of CFRP composites with elastic waves, vibrothermography and EMI technique*, presented at the 3rd International Conference of Engineering Against Failure (ICEAF III), 26th – 28th June 2013, Kos Island, Greece

[13] L. P. Canal, V. Michaud, *Microscopic mechanisms and modelling of water diffusivity in adhesive composite joints*, to be published in Composites Part A: Applied Science and Manufacturing journal

[14] P. Malinowski, K. I. Tserpes, T. Wandowski, L. Skarbek, W. Ostachowicz, *Composite bonds assessment using EMI technique*, presented at the 9th International Workshop on Structural Health Monitoring, September 10th – 12th, 2013, 2013

[15] P. Malinowski, L. Skarbek, T. Wandowski, W. Ostachowicz, *CFRP bonds evaluation using piezoelectric transducer*, presented at the 4th Symposium for NDT in Aerospace, November 13th – 15th, 2012, Augsburg, Germany

[16] P. Malinowski, T. Wandowski, W. Ostachowicz, *Assessment of CFRP Composites Using Laser Vibrometry*, presented at the ISEM-ACEM-SEM-7th ISEM '12, November 8th – 11th, 2012, Taipei, Taiwan

[17] P. Malinowski, T. Wandowski, W. Ostachowicz, *Characterization of CFRP using piezoelectric transducer and laser vibrometry*, presented at the 10th International Conference on Damage Assessment of Structures, July, 8th – 10th, 2013, Dublin, Ireland

[18] H. G. Tattersall, *The ultrasonic pulse-echo technique as applied to adhesion Testing*, J. Phys. D: Appl. Phys., Vol. 6, 1973

[19] R. Seyrkammer, R. Galos, B. Reitinger, J. Kasberger, P. Burgholzer, *NDT in Composite Bonding for Aeronautic Applications with Laser Ultrasound and Infrared Spectroscopy*, presented at the 3rd International Conference of Engineering Against Failure (ICEAF III), 26th – 28th June 2013, Kos Island, Greece

[20] G. Heichler, T. Grundner, E. Rau, *Ultrasonic Frequency Analysis*, presented at the 3rd International Conference of Engineering Against Failure (ICEAF III), 26th – 28th June 2013, Kos Island, Greece

[21] A. J. Croxford, J. Potter, K. Sapountzi, Ultrasonic Array Inspection of Weak Bonds, presented at the 3rd International Conference of Engineering Against Failure (ICEAF III), 26th – 28th June 2013, Kos Island, Greece

APPENDIX B - DMA ANALYSIS OF SHOCKED COMPOSITE

B.1 DMA technique

The DMA (Dynamic Mechanical Analysis) is a technique which can be used to characterize the microstructure of polymer materials. DMA or DTMA for Dynamic Thermo Mechanical Analysis can also provide an evaluation of the glass transition of epoxies, but the technique is different, and can not be directly compared with the DSC analysis. Indeed, mechanical properties are also evaluated against temperature by DMA such as the storage modulus. A schematic example of DMA response obtained on a thermoset resin is given in Figure B.1. The samples are mechanically loaded with sinusoidal stresses during the heating, generally by bending or three-points bending. The evolution of the storage modulus against temperature gives information on the elasticity modulus dependency on temperature. It shows the significant loss in mechanical properties in the rubber-like state. The other two parameters which are the loss modulus and Tangent Delta give information on the molecular arrangement and viscoplastic response of the material tested. For example, the loss modulus evolution with temperature gives information about two relaxation phenomena occurring at two different temperatures. The significations of these two relaxations are not really clear for the scientific community, but are clearly correlated to molecular rearrangements. Moreover, these two signals enable the observation of the glass transition in case of a thermoset resin. The evaluation of the glass transition temperature can slightly vary from one feature to the other. In this work, the Tg will always be evaluated from the loss modulus (see in Figure B.1).

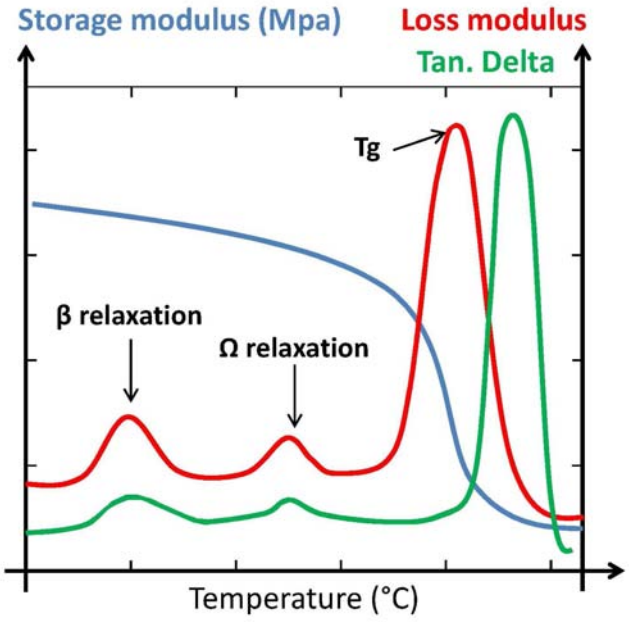

Figure B.1 Sketch of a typical result from DMA (Dynamic Mechanical Analysis)

B.2 Results on composite CFRP

The effects highlighted in the previous section have been investigated on CFRP composites in order to be closer from the application case. In this investigation, DMA was used on shocked T800/M21 samples. In fact, it was not possible to use DSC analyses for this material. Indeed, by taking small amount of the material, the thermoplastic nodule heterogeneity induces strong differences in the

DSC signals, just because the concentration changes from one small part from another. The thermoplastic melting peak thus hides the epoxy glass transition in some cases, which prevents from observing differences between the different sample regions. Moreover, DMA would give more sensitivity to the measurements. Four different samples were investigated by DMA (see in Figure B.2). They have been all taken from the initial T800/M21, 6 mm thick, CFRP. The first one to be measured is a reference sample whose geometrical characteristics are given in Figure B.2. This sample has been untouched after the sample preparation. The DMA results give a basis to compare other analyses with. They are given in Figure B.2, and are normal for such material. Indeed, the storage modulus progressively decreases until a drastic fall corresponding to the glass transition. On the loss modulus, the β and ω relaxations characterizing the epoxy resin are both visible. The final high peak enables the glass transition evaluation about 190 °C. The Tan delta signal is also in agreement with the two previous parameters. This data has been compared to shocked sample results. Firstly, a sample geometrically identical to the reference has been shocked (named DMA T800/M21 1.5 mm). Four laser shocks were produced in order to shock the whole use length of the sample, with a good covering rate (see in Figure B.2). Config-PPRIME-1 was used, and the confinement has been realized with transparent scotch. Indeed, it was not possible to use water due to the sample geometry, but the pressure under scotch confinement was high enough to enable damage. This has been checked afterward by cross section observation. Averages of each laser shock parameter are given in Table B.1. Note that the intensity has been reduced on purpose in order to not create too important damage which would have prevented from performing DMA analysis. A second sample has been shocked in the exact same conditions, but this one was thicker (named DMA T800/M21 3 mm). With this sample, the idea was to separate the front face from the back face after the shock. 3 mm was chosen to still enable spallation, and to obtain after sample cutting thicknesses close to the ones already analyzed by DMA. The laser intensity has to be increased in consequence to enable spallation (see averages of the laser shock parameters in Table B.1, and sketch of the sample geometry in Figure B.2).

	Average parameters			
Samples	**Energy (J)**	**Pulse duration (ns)**	**Focus diameter (mm)**	**Intensity (GW/cm²)**
DMA T800/M21 – 1.5 mm	13.9	29.64	5	2.39
DMA T800/M21 - 3 mm	14.6	26.37	4	4.41

Table B.1 Average of the laser shock parameters used on T800/M21 samples for DMA investigations conducted in Config-PPRIME-1

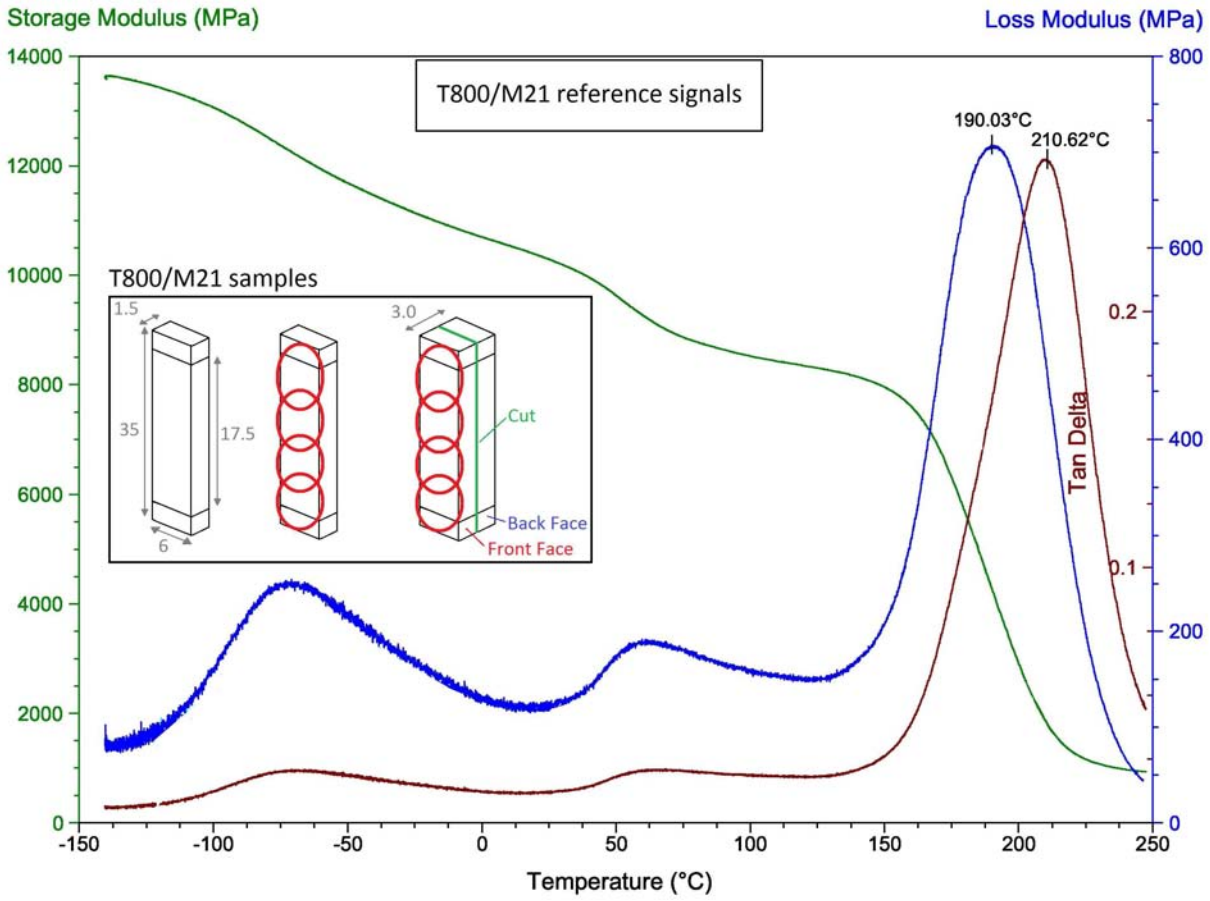

Figure B.2, Used samples for DMA investigation of shocked T800/M21 composite materials, reference, shocked full thickness (1.5 mm), shocked front face only (1.5 mm), shock back face only (1.5 mm) – DMA measurements (Storage, loss modulus and Tan Delta) for the reference sample

The different results obtained from each DMA analysis have been compared. As it could be expected, the storage moduli have been shifted to lower values because of the damage induced by the laser shock propagation. No other differences have been noticed. The comparison of the loss modulus signals is more interesting. It is presented in Figure B.3. Two main differences can be observed, in the ω relaxation and in the glass transition. Indeed, it can be noticed that the ω relaxation peak has almost disappeared on both DMA T800/M21 1.5 mm and T800/M21 3 mm back face signals. On the contrary, almost no difference can be seen between the front face and the reference relaxations. The nature of what happened is not clear, but something did happen. The fact this phenomenon only appeared on back face and full thickness seems to indicate that the modification is correlated to dynamic tension and resulting damage. This result is consistent with the previous one. Speaking of the glass transition temperature, same conclusions can be made. Indeed, the front face of T800/M21 3 mm sample shows a glass transition about 192 °C, which is quite close from the glass transition evaluated on the reference (190 °C). The glass transition of the back face sample has been evaluated about 200°C, meaning 5 % above the reference sample. In between, the glass transition of the full thickness sample is about 197 °C. This proves that the modification did occur on the back face, where damage has been created. If the shift is smaller on the full thickness sample, it should be because of an averaging effect of the whole sample thickness. In any case, these results evidence that the laser shock wave propagation does have an effect on the molecular state of the epoxy resin, probably because of spallation, and within the laser parameters used in this investigation.

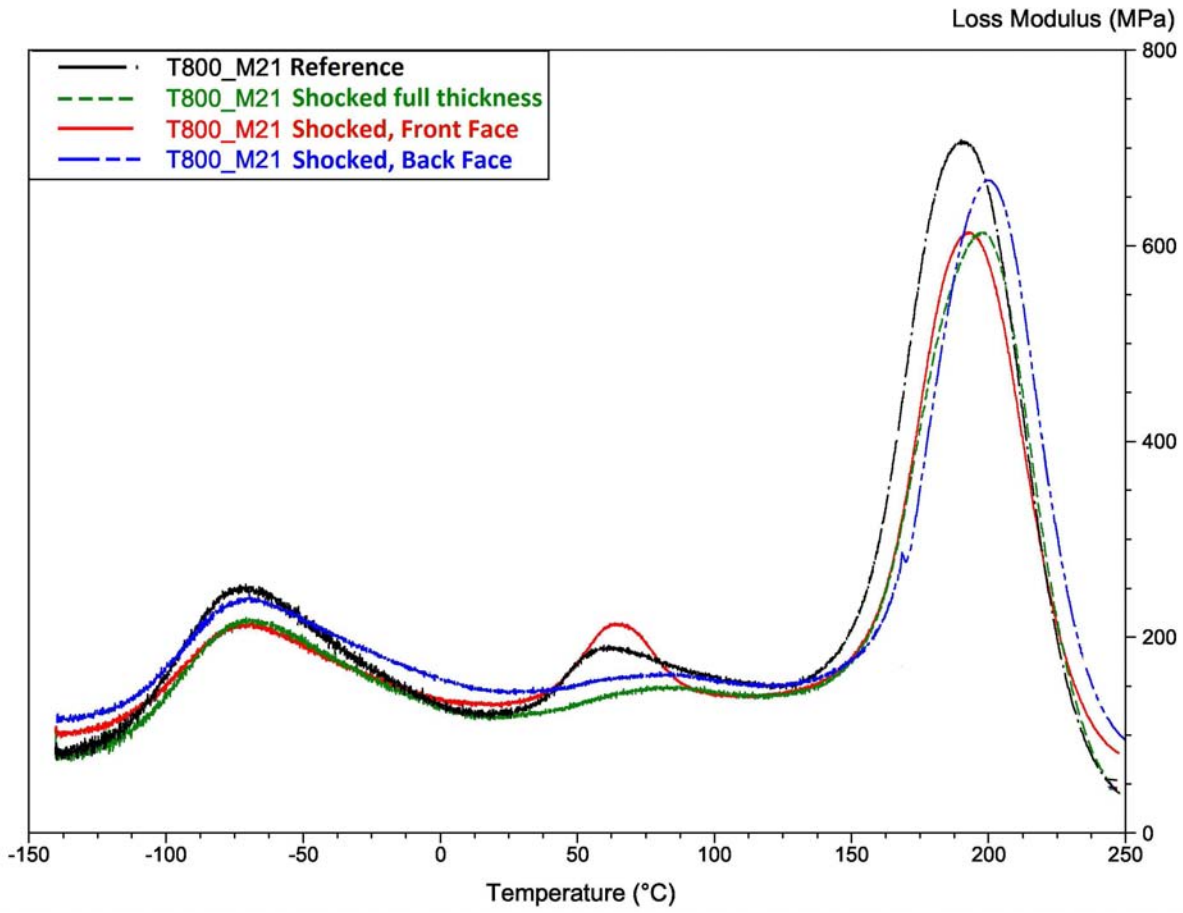

Figure B.3, Comparison of the loss modulus signals between the reference, the shocked sample and the shocked sample front face and back face – Results for T800/M21 composite material

Nevertheless, it is hard to conclude on the nature of this phenomenon. According to literature, the high compression only cannot explain this phenomenon since the shock performed here are way below 20 GPa. Added to the previous results on epoxy resin, this last observations made on composite seem to indicate that the high strain rate dynamic tension provides an energy equivalent to a post-curing of a few minutes above 200°C. The temperature increase associated with the shock propagation is probably not the only phenomenon responsible for these modifications. Pulse duration, high strain rate, and damage initiation should be considered. More investigations remain necessary to fully understand the phenomenon.

Speaking of the LASAT application, it is good news. The small difference observed between shocked and un-shocked composite is in the correct direction. In other words, the laser shock propagation has a post-curing effect, which is good for the material quality. Moreover, differences have only been noticed in case of spallation. It can be assumed that when no spallation is generated, these modifications would be even lower because the energy level is lower. This point remains to be checked by analyses below the damage threshold.

The same kind of investigation was conducted on FM300 sample, but no clear difference was observed. This was explained by the shock attenuation which is much stronger in this material than in the other, or because of different induced damage.

APPENDIX C – CALIBRATION OF THE PRESSURE PROFILE

In this appendix, the protocol to calibrate the pressure profile is first given. It is based on both experimental measurements by VISAR and numerical calculation of laser shock on aluminum target. In a second time, calibration curves linking laser intensity to induced pressure are given for aluminum targets and aluminum painted composite samples. These curves are valid for PPRIME25 laser source, and water confinement configuration.

C.1 VISAR experimental data for pressure profile calibration

Firstly, the experimental results used to calibrate the pressure profile are presented. These laser shock experiments have been realized on aluminum samples, for which the material properties are well-known. Moreover, the correlation between laser intensity and induced pressure is well documented in this case [1-2], which is giving a reference to compare with. Laser shocks were produced on 0.250 mm thick aluminum targets, in PPRIME25 laser shock configuration. Indeed, for the P = f(I) calibration curve definition to be possible, back face measurements have to be gathered for several shock pressure to compare with numerical modeling. Laser shock parameters for the signals used in this appendix are presented in Table c.1. Note that reproducibility has been checked, even if the results are not presented here.

Sample	Energy (J)	Pulse duration (ns)	Focus diameter (mm)	Intensity (GW/cm²)	Verdi Power (W)	Fringe factor(m/s)
Al01	20.26	35.04	4	4.60	1	229.5
Al04	14.90	31.20	4	3.80	1	229.5
Al06	10.73	30.80	4	2.77	1	229.5
Al08	4.47	33.15	4	1.07	1	229.5
Al10	3.58	36,06	4	0.79	0.71	229.5
Al12	2.38	35.00	4	0.54	0.71	229.5
Al14	1.49	34.51	4	0.34	0.71	229.5

Table c.1 Laser shock parameters for the aluminum samples used in this appendix

The VISAR measurements of the back face velocity are presented in Figure c.1. It shows a good correlation between the laser intensity level and shock breaking-out induced velocity amplitude. These experimental signals are used for two things.

- First, one of these measurements is used to define the temporal shape of the pressure profile to obtain the best agreement between numerical calculation and the experimental measurement chosen. The other experimental signals are then used in a second time in order to validate the selected pressure profile (section C.2)
- Once the pressure profile validated, it can be implemented in the numerical modeling in order to evaluate the pressure corresponding to laser shock experiments. For the aluminum targets in stake, it gives (I[GW/cm²], P[GPa]) points which can be plotted on the a (I,P) chart in order to define the calibration curve for aluminum targets, in the used laser configuration (section C.3).

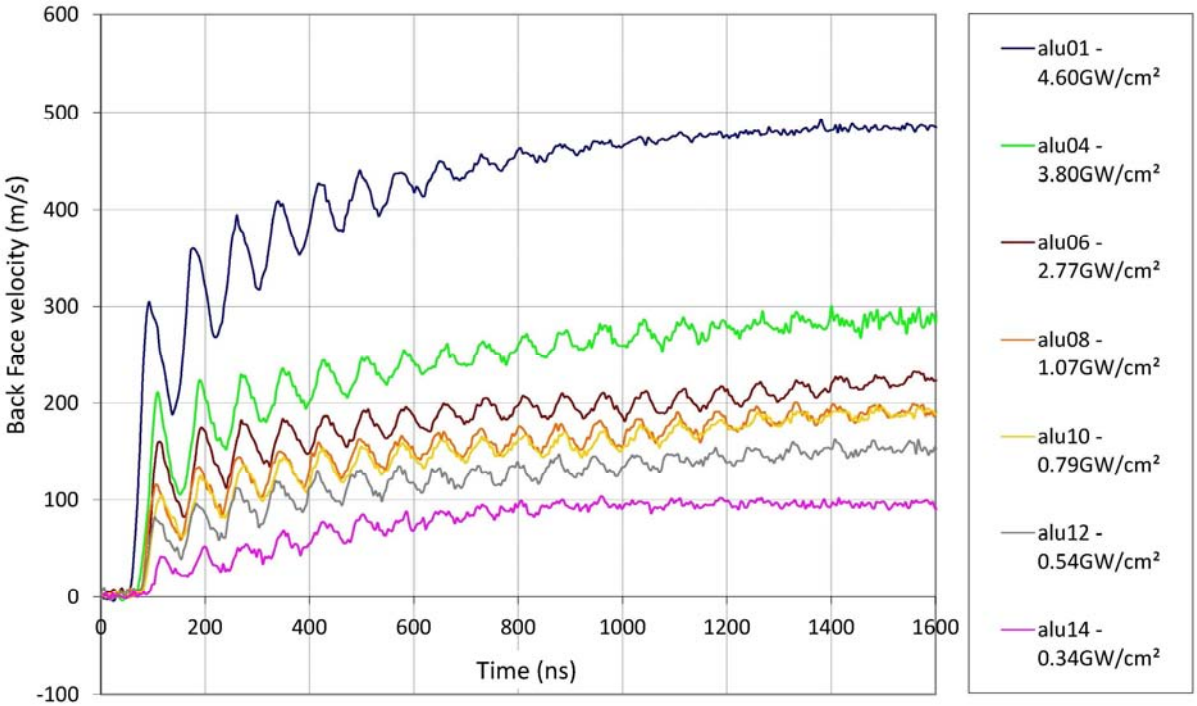

Figure c.1 Back face velocity measurement obtained by VISAR on 0.250 mm thick aluminum samples, irradiated by PPRIME25 laser source, in water confinement configuration

C.2 Pressure profile definition and validation

First, the pressure profile corresponding to the laser/aluminum interaction is defined, in case of PPRIME25 laser source and in water confinement configuration. For that, numerical modeling is used. Since the aluminum targets are about 0.250 mm thick for a 4 mm laser shock spot, a 1D model has been used. An elastic-plastic hydrodynamic law has been used for aluminum based on material parameters available in the literature [3]. The idea is to obtain a good agreement between the back face velocity measurement and the velocity calculated by using the defined pressure profile. When reached, it means that the pressure profile is correctly describing the laser/matter interaction in the experimental configuration. Here, the 1.07 GW/cm² laser shock experiment has been chosen for the pressure profile definition, because according to the literature laws, the pressure level is about 1 GPa in this case [1-2]. Therefore, pressure level has not to be adjusted first, and focus can be made on the velocity profile shape and frequency comparisons. The following steps are then followed in order to obtain a pressure temporal profile which enables a correct modeling of the laser shock on the aluminum target.

1. A pressure profile, based on the temporal laser pulse shape and taken into account the water confinement effect on the pressure pulse duration is drawn.

2. This pressure profile is implemented in the model, and the numerical back face velocity is calculated.

3. The calculated back face velocity is compared with the experimental ones, and differences are observed.

4. According to the comparison made, the pressure temporal profile is adjusted to get a better agreement between the calculated and experimental velocities. Especially, the

pressure profile mid-height duration plays on the back and forth period in the aluminum target. On the other hand, the tail shape of the pressure profile has an influence on the asymptotic back face velocity. Therefore, these two main features are to be adjusted in order to converge toward a better agreement.

5. The calculation is run another time with the new pressure profile, and a comparison is made with the experimental data.

6. Depending on the comparison, step 4 and 5 can be repeated as often as necessary. Figure c.2 is given as an illustration of this two-step looping. On the left, all the shapes of the temporal pressure profile implemented in the aluminum model are given. On the right, the corresponding back face velocities calculated are given, the red curve being the experimental signal.

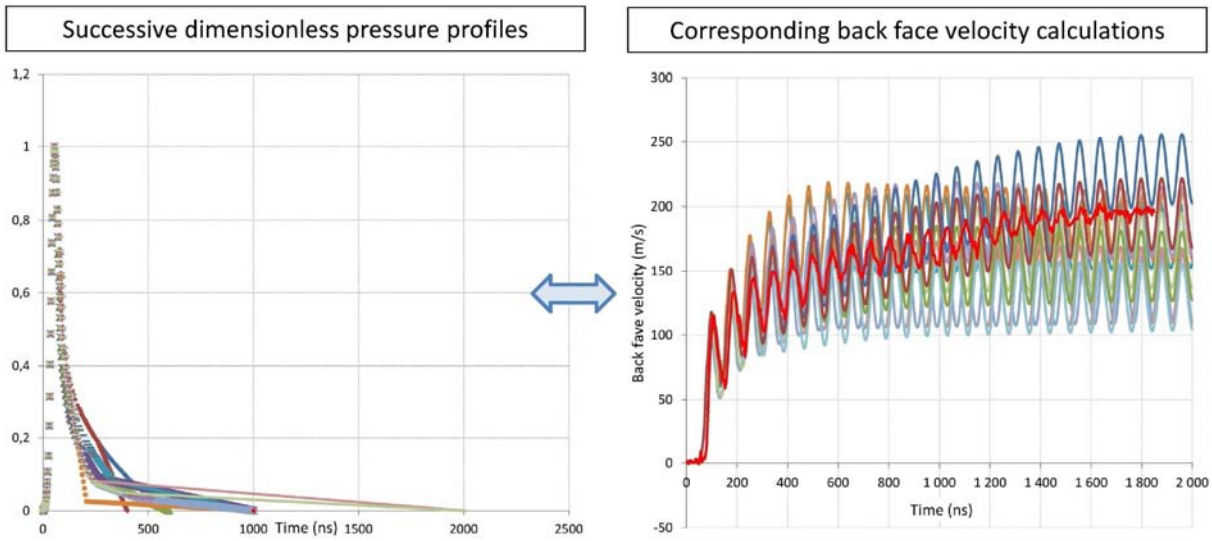

Figure c.2 Loop between pressure profile adjustment and laser shock on aluminum modeling in case of 1GW/cm² experimental data (in red)

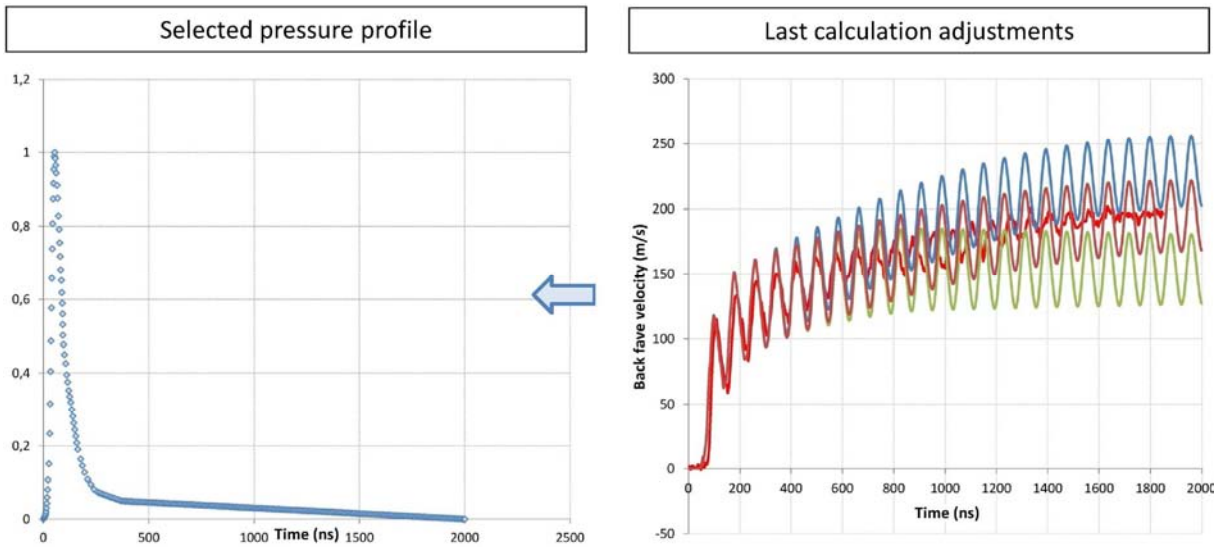

Figure c.3 Last pressure profile adjustment and aluminum model calculation to obtain a good agreement between experiment and numerical calculation

In Figure c.3, the last three calculations before obtaining a correct pressure profile are given in comparison with the experimental signal. In particular, the release tail of the pressure profile has been adjusted for these last calculations. They enabled to define the pressure profile presented in Figure c.3, left. Finally, the comparison between the numerical back face velocity, calculated using this selected profile, and the experimental signal (measured in case of 1.07 GW/cm² laser shock) is given in Figure c.4. It shows a good agreement between the calculated and experimental back face velocity.

The agreement is particularly good on the five first velocity peaks, meaning the five first back and forth shock propagation. After that, the signal is more attenuated in terms of velocity amplitude than the experimental signal. This is clearly due to the 1D model geometry choice, which prevents from correctly simulating the attenuation due to the 3D shock propagation. Nevertheless, the asymptotic velocity obtained from the model is correct in comparison to experiment, which shows that the release tail is correctly adjusted for this case. The pressure profile should now be validated on the other back face velocity signals.

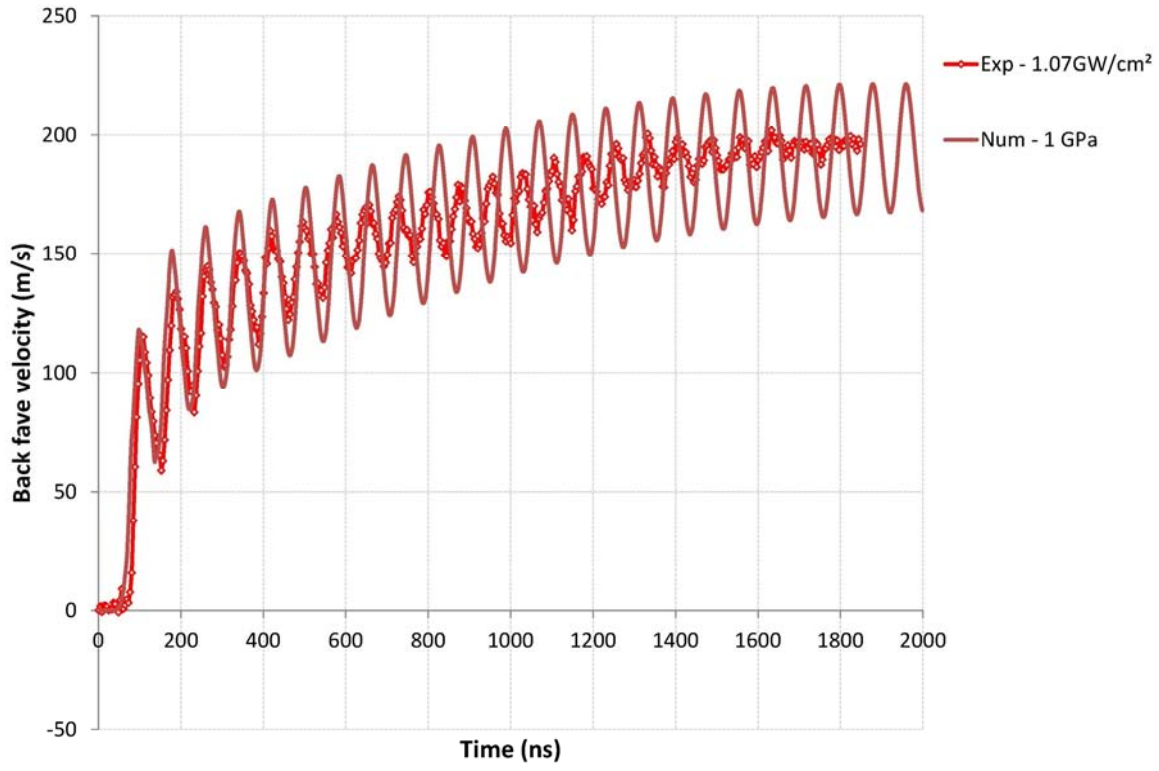

Figure c.4 Final agreement between the numerical calculation, using the selected pressure profile, and the experimental VISAR data in case of a laser shock about 1 GW/cm² on 0.250 mm aluminum target

C.3 Validation of the pressure profile

The validation of the pressure profile has two goals. First, it should show that the selected pressure profile can be used to model a whole experimental campaign. Then, it enables to obtain (I,P) points for each laser shock performed in order to plot calibration curve linking laser intensity to induced pressure. Therefore, calculations are performed in order to simulate each laser shock for which a back face velocity has been measured. For that, the maximum of pressure is increased or decreased in order to obtain a correct fit of the first peak of each velocity signal. Since the pressure profile is correct, fitting the first peak also should enable to fit the following ones. The results are shown in

Figure c.5. The noisy clear red signal corresponds to the experimental data, when the dark red signals correspond to the calculation. If speaking first of the global shape agreement between numerical calculation and experimental signal, it is correct in average. Over the whole data, the agreement is rather correct but the difference observed highlights some uncertainties, especially in the release tail of the pressure profile. It could come from the laser pulse itself, but also from the water confinement which cannot be exactly the same from one shock to another. It has to be kept in mind for composite modeling, because the same average distribution has been observed.

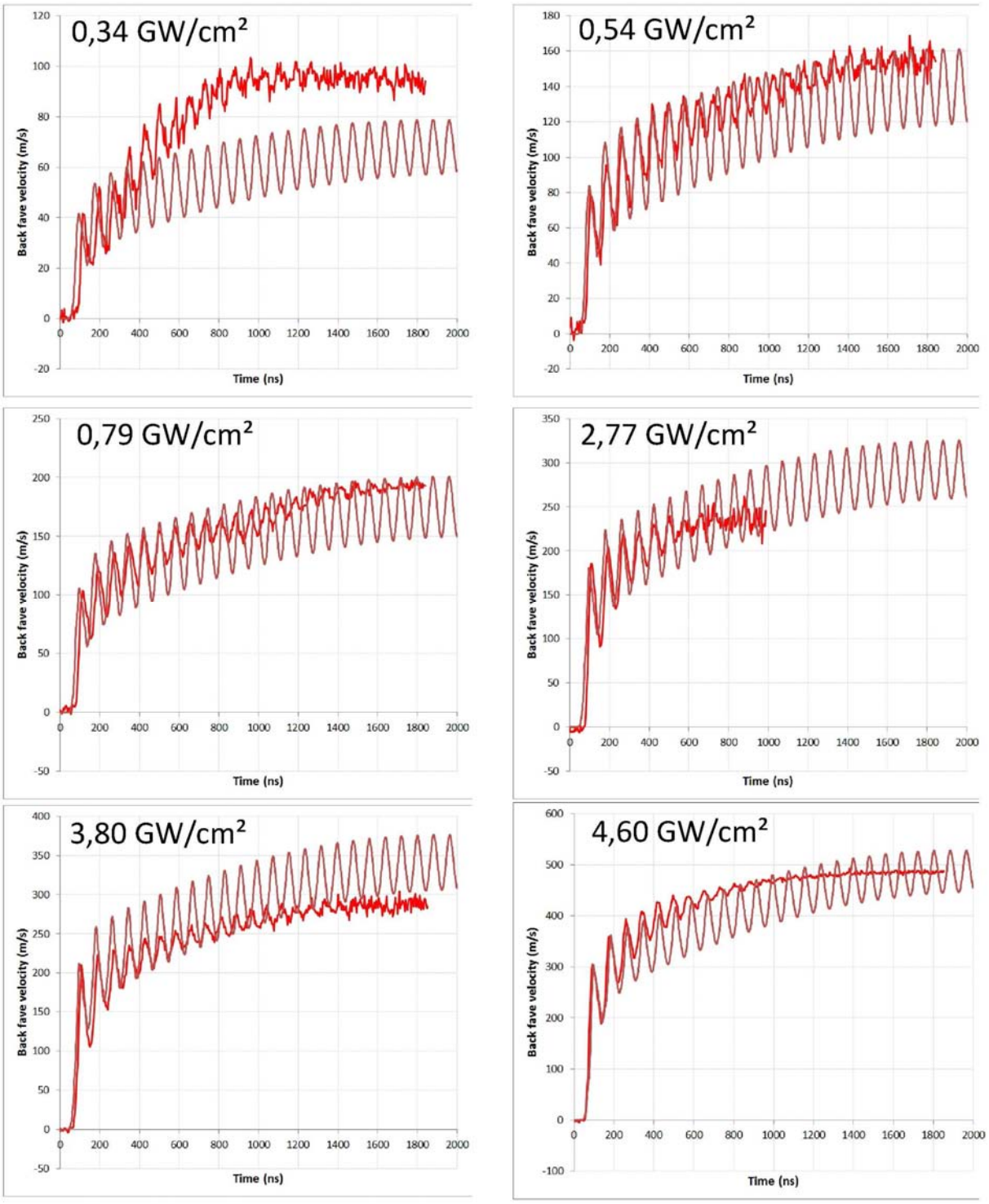

Figure c.5 Validation of the pressure profile by comparing calculated and experimental back face velocity signals from the experimental campaign on aluminum targets – Adjustment of the pressure level

In average thus, the pressure profile is validated, and these numerical simulations enable to get several (I,P) points, which can now be used to plot a calibration curve, linking pressure to laser intensity. This is done in the next section.

C.4 Calibration curves

C.4.1 Calibration curve for aluminum targets

The calculation presented in Figure c.5 enabled to calculate the pressure level corresponding to each different laser shocks. These (Intensity, Pressure) points have been reported in Figure c.6 in order to plot a calibration curve linking laser intensity to the corresponding induced pressure. This curve is valid only for PPRIME laser source, in water confinement configuration, and only for aluminum targets. On this chart, the curve $P = \sqrt{I}$ has been added. It corresponds to a well-known correlation between intensity and pressure for this kind of laser/matter interaction [1-2]. Consequently, the calibration found in case of PPRIME laser source is constituent with the literature.

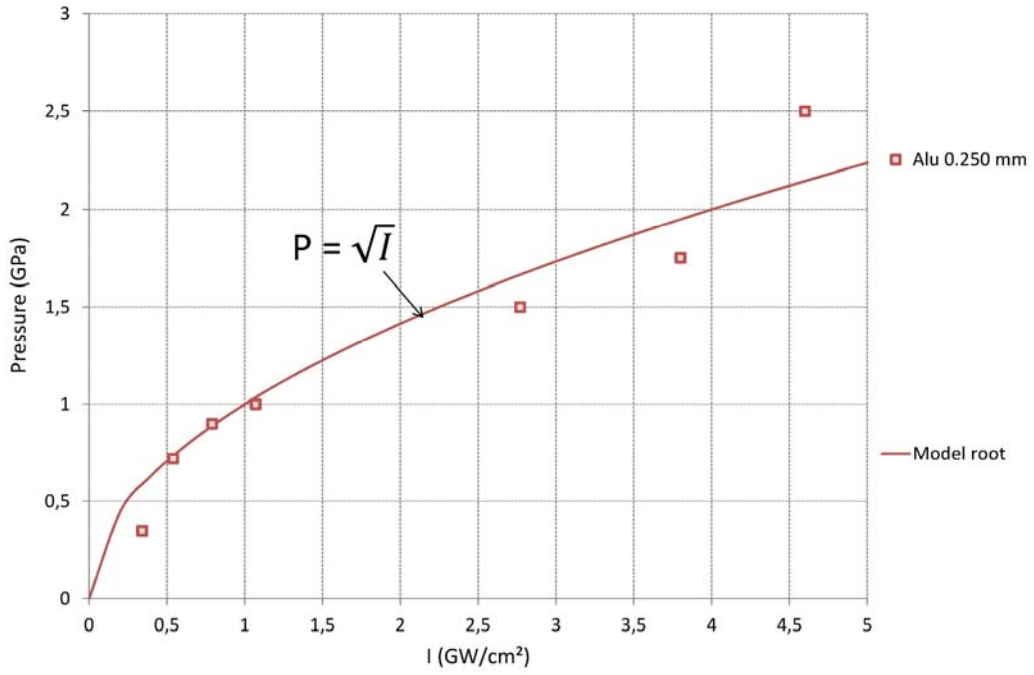

Figure c.6 Calibration curve in case of the PPRIME 25 laser shock, in water confinement configuration, for aluminum samples

C.4.2 Calibration curve for composite targets

Finally, the shocks performed by using aluminum painting as sacrificial layer can be used to plot a specific calibration curve. As explained in this document main body, each numerical modelling of shocks on the different CFRP materials required a pressure adjustment in comparison with the aluminum calibration curve. This can be explained by the experimental use of aluminum painting instead of real aluminum. This painting probably presents some organic additive. Hence, the deposited aluminum layer has probably a lower density compared to real aluminum. Thus, it could weaken the laser/matter interaction, and results in a lower pressure level. For all the performed calculations, the (intensity, pressure) points have been collected to be plotted on the same calibration curve than the one given on aluminum. The results are presented in Figure c.7. The

evolution of the induced pressure as a function of intensity corresponds to the one observed on aluminum, but the peak pressure is shifted to lower value as expected. Nevertheless, all the points are averagely on the same curve, defined as described by equation (C.1). This curve can be used for all the composite targets, which is consistent with the fact that all the composite experiments have been performed with aluminum painting. It will be kept in mind as a reference curve to go from intensity to pressure in case of laser shock on composite with aluminum painting as ablator, and in case of PPRIME25 laser source in water confinement configuration.

$$P(GPa) = 0.6 \times \sqrt{I(GW/cm^2)} \qquad \text{(C.1)}$$

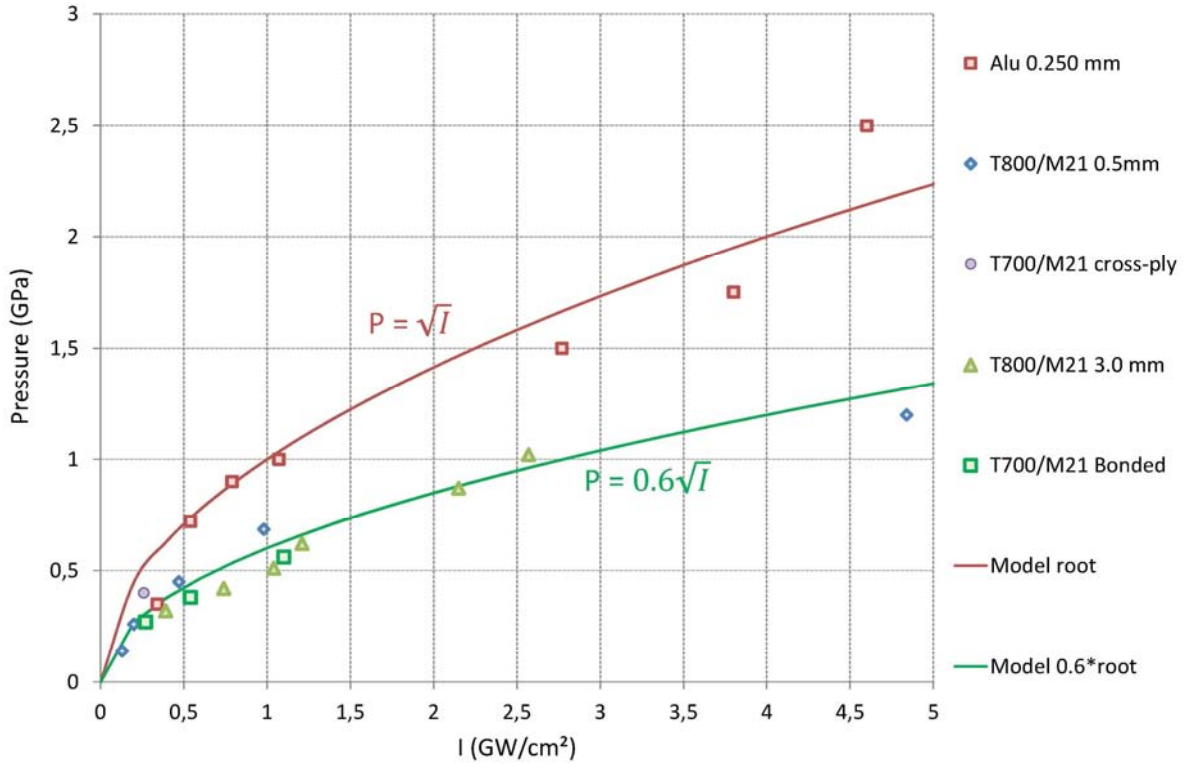

Figure c.7 Calibration curve in case of the PPRIME 25 laser shock, in water confinement configuration, for aluminum samples and all the composite targets with aluminum painting added ablator

[1] R. Fabbro, J. Fournier, P. Ballard, D. Devaux, J. Virmont, *Physical study of laser produced plasma in confined geometry*, Journal of Applied Physics, Vol. 68, n°2,775-784 (1990).

[2] L. Berthe, R. Fabbro, P. Peyre, L. Tollier, E. Bartnicki, *Shock waves from a water confined laser-generated plasma,* Journal of Applied Physics, Vol. 82, n°6, 2826-2832, 1997

[3] J-P. Cuq-Lelandais, *Etude du comportement dynamique de matériaux sous choc laser sub-picoseconde*, Thèse de l'ENSMA (Ecole Nationale Supérieure de Mécanique et d'Aérotechnique), Ecole doctorale SIMMEA, 2010

Appendix D - Sample Set 2 laser shock parameters

Samples/ shot	Laser Energy (J)	Pulse duration (ns)	Focus diameter (mm)	Intensity (GW/cm²)
Reference (UT)				
UT-1	0.92	44.30	4.2	0.19
UT-2	2.44	31.20	4.2	0.51
UT-3	3.82	25.18	4.2	0.80
UT-4	5.20	28.00	4.2	1.09
UT-5	4.13	27.87	4.2	0.86
UT-6	7.79	30.00	4.2	1.63
UT-7	10.24	32.00	4.2	2.14
UT-8	12.53	30.00	4.2	2.62
UT-9	20.63	30.50	4.2	4.32
Release Agent contamination (RE1 - 2.2 at% of Si)				
RE1-1	1.07	32.80	4.2	0.22
RE1-2	2.44	33.80	4.2	0.51
RE1-3	3.51	35.20	4.2	0.74
RE1-4	5.04	36.00	4.2	1.06
RE1-5	4.13	34.20	4.2	0.86
RE1-6	7.79	35.20	4.2	1.63
RE1-7	9.78	34.63	4.2	2.05
RE1-8	13.45	34.50	4.2	2.82
RE1-9	17.72	35.20	4.2	3.71
Release Agent contamination (RE2 - 6.7 at% of Si)				
RE2-1	0.83	32.17	4.2	0.17
RE2-2	2.37	35.40	4.2	0.50
RE2-3	3.16	38.13	4.2	0.66
RE2-4	4.37	40.40	4.2	0.97
RE2-5	4.14	44.70	4.2	0.91
RE2-6	7.49	41.30	4.2	1.64
RE2-7	10.39	36.40	4.2	2.23
RE2-8	14.06	41.60	4.2	2.99
RE2-9	19.71	38.10	4.2	4.18
Release Agent contamination (RE2 - 8.4 at% of Si)				
RE3-1	0.95	34.00	4.2	0.20
RE3-2	2.38	34.29	4.2	0.50
RE3-3	3.36	34.70	4.2	0.70
RE3-4	4.58	34.38	4.2	0.96
RE3-5	4.13	34.38	4.2	0.87
RE3-6	7.49	34.40	4.2	1.57
RE3-7	9.78	34.35	4.2	2.05
RE3-8	14.21	34.31	4.2	2.99
RE3-9	18.64	34.31	4.2	3.92
Release Agent contamination (RE2 - 10.5 at% of Si)				
RE4-1	0.89	34.19	4.2	0.19
RE4-2	2.19	34.14	4.2	0.46
RE4-3	3.27	34.28	4.2	0.69

RE4-4	4.28	34.11	4.2	0.91
RE4-5	4.13	34.18	4.2	0.87
RE4-6	7.03	34.13	4.2	1.49
RE4-7	10.39	34.01	4.2	2.21
RE4-8	13.29	34.00	4.2	2.82
RE4-9	20.17	33.83	4.2	4.30
Moisture contamination (MO1 - 0.46 wt%)				
MO1-1	17.582	22.93	4	6.10
MO1-2	12.516	37.4	4	2.66
MO1-3	11.026	34.53	4	2.54
MO1-4	9.238	36.76	4	2.00
MO1-5	3.725	33.53	4	0.88
MO1-6	3.129	35.21	4	0.71
MO1-7	3.1737	34.64	4	0.73
MO1-8	1.6837	34.43	4	0.39
MO1-9	1.0579	32.23	4	0.26
Moisture contamination (MO2 - 0.84 wt%)				
MO2-1	16.39	37.09	4	3.52
MO2-2	13.41	34.06	4	3.13
MO2-3	10.579	34.8	4	2.42
MO2-4	9.089	32.17	4	2.25
MO2-5	3.576	32.52	4	0.88
MO2-6	2.9651	35.42	4	0.67
MO2-7	2.3542	32.54	4	0.58
MO2-8	1.6688	32.54	4	0.41
MO2-9	1.0877	33.9	4	0.26
Moisture contamination (MO3 - 1.19 wt%)				
MO3-1	16.837	33.47	4	4.00
MO3-2	13.112	34.28	4	3.04
MO3-3	10.877	33.02	4	2.62
MO3-4	9.387	33.67	4	2.22
MO3-5	3.427	30.8	4	0.89
MO3-6	4.3806	34.53	4	1.01
MO3-7	2.8906	34.24	4	0.67
MO3-8	1.9966	33.84	4	0.47
MO3-9	1.9966	31.87	4	0.50
Moisture contamination (MO4 - 1.29 wt%)				
MO4-1	15.794	30.38	4	4.14
MO4-2	12.218	31.65	4	3.07
MO4-3	10.728	31.83	4	2.68
MO4-4	8.493	33.33	4	2.03
MO4-5	3.427	31.59	4	0.86
MO4-6	3.1439	32.09	4	0.78
MO4-7	2.4883	32.09	4	0.62
MO4-8	1.639	33.59	4	0.39
MO4-9	0.8195	32.39	4	0.20

RESUME – CHAPITRE 1

Le chapitre 1 de ce manuscrit de thèse présente le contexte de l'étude, et l'état de l'art associé. Il est articulé en trois parties complémentaires : la première partie présente les besoins industriels qui ont motivé cette étude. La deuxième partie est consacrée à l'état de l'art sur la technique développée dans cette étude, afin de montrer les voies d'amélioration possibles et de justifier les choix scientifiques faits pour ce travail. Enfin, la troisième partie présente une revue bibliographique des phénomènes de chocs sur les matériaux composites, car la compréhension de ces phénomènes constitue un point clé pour l'étude menée.

L'usage croissant des matériaux composites dans le secteur aéronautique démontre un besoin grandissant pour l'allégement des structures. Cet allégement est principalement motivé par la réduction de la consommation des appareils, logiquement associée à la masse de ces derniers. La prochaine étape passe par l'utilisation de nouvelles techniques d'assemblages, telle que le collage, qui permettrait de nombreux gains en terme de masse, de coût, et de temps de production. Cette technique est aujourd'hui maitrisée pour différents types de structures, mais son extension à certains domaines de l'avion nécessite encore la levée de quelques verrous technologiques. En particulier, aucune technique non destructive ne permet aujourd'hui de contrôler la qualité mécanique des joints collés. C'est dans ce contexte que le projet ENCOMB (Extented Non destructive testing for COMposite Bonds, www.encomb.eu) a été monté, sous la tutelle industrielle d'Airbus et d'EADS, et coordonné par le Fraunhofer Institute de Brême (IFAM). Dans ce cadre, plusieurs techniques sont développées afin de permettre le contrôle des assemblages collés de composites. Deux axes sont principalement développés : le contrôle des surfaces avant collage pour détecter la présence de contaminant pouvant affaiblir l'adhésion, et celui des assemblages collés, afin de quantifier leur qualité mécanique. La technique LASAT (Laser Adhesion Test), développée dans ce travail de thèse, permettrait de répondre à la 2ème problématique.

La technique LASAT s'appuie sur la propagation d'ondes de choc générées par l'interaction laser/matière pour créer un chargement de traction, bref et intense, au cœur du matériau à tester. Avec les paramètres de choc adéquats, c'est-à-dire les réglages optimisés du laser, le chargement en traction peut permettre le test d'une interface. Cette technique a été utilisée pour la première fois en 1978 par J. L. Vossen, puis brevetée dans le cas de systèmes métalliques par V. Gupta (1995). Ceci démontre l'intérêt industriel pour la technique, intérêt confirmé par les travaux menés dans les années 2000 sur différents types de systèmes tels que les barrières thermique, les couches minces, les coldsprays… Plus récemment, la technique a été utilisée pour le test de systèmes plus épais, aluminium/colle/aluminium dans le cadre de la thèse de D. Laporte. Les années 2010 voient également l'apparition des premiers travaux sur des assemblages composites, avec les études de R. Bossi pour Boeing, ainsi que de M. Perton et E. Gay dans le cadre du projet franco-canadien SATAC. Ces travaux montrent en particulier la faisabilité du test dans certaines configurations, mais mettent aussi en évidence le manque de compréhension du phénomène de choc laser sur matériaux composites, pourtant essentielle pour l'adaptation du test à ce type de systèmes complexes.

L'analyse des travaux antérieurs a permis de dégager une approche scientifique, basée sur plusieurs étapes, afin de développer et d'optimiser le test d'adhérence par choc laser aux assemblages composites collés utilisés dans l'aéronautique. La première étape doit permettre la compréhension des phénomènes de choc sur les composants élémentaires d'un assemblage collé typique, à savoir la

résine epoxy et les composites CFRP (Carbon Fiber Reinforced Polymer) unidirectionnels. Les données expérimentales collectées permettent dans un deuxième temps de modéliser ces phénomènes de choc, de manière fiable. Une fois ces études réalisées, le comportement des assemblages peut alors être analysé, d'abord expérimentalement, puis numériquement sur la base des résultats précédents. Le modèle numérique développé pourra permettre une meilleure compréhension du phénomène avant et sera également utilisé pour l'optimisation de la technique.

Ce chapitre se termine avec une étude bibliographique portant sur les phénomènes de choc sur matériaux composites, essentiellement CFRP. Il en ressort que de nombreuses études sont actuellement en cours, majoritairement pour des problématiques de tenue à l'impact des structures composites. Le cas des impacts basse et moyenne vitesses sert principalement a étudié la résistance mécanique résiduelle des structures choquées. Les impacts hyper véloces, du type balistique, se concentrent sur la résistance à la perforation des structures testées. Finalement, très peu d'études ont été publiées au sujet du choc laser sur matériaux composites. Ceci montre la nécessité d'une telle étude dans ce travail. De plus, les différentes techniques utilisées dans littérature pour analyser la réponse des assemblages collés sont répertoriées. La caractérisation des propriétés mécaniques du joint est généralement recherchée, par le biais de ces différentes techniques. Les assemblages testés dans le cadre du projet ENCOMB sont finalement présentés. L'accent est mis sur la réalisation de la contamination avant collage, en utilisant par exemple des solutions à base d'agent de démoulage (IFAM). La perte des performances quasi-statiques associée aux différentes contaminations est également présentée sur la base des travaux de l'Université de Patras.

RESUME – CHAPITRE 2

Dans le chapitre 2, les techniques expérimentales utilisées pendant cette thèse sont détaillées. Certains travaux expérimentaux ont fait l'objet de collaboration avec différents partenaires, qui sont également présentés. La première étape est de produire un choc. Pour cela, différentes sources de choc ont été utilisées, comme des sources laser, mais également des lanceurs à gaz comprimé. Dans le cadre de l'ILP (Institut Laser Plasma, http://www.ilp.u-bordeaux1.fr), plusieurs sources laser sont disponibles. Leur différentes caractéristiques, définies pour différents usages, sont détaillées dans ce chapitre. Les sources de chocs utilisées pendant cette thèse sont les suivantes:

- Les sources laser LULI2000 et ELFIE, développées par le laboratoire LULI (Laboratoire pour l'Utilisation des Laser Intenses, Polytechnique, Palaiseau), sont des installations de recherche à haute énergie (respectivement 1000J et 10J) et à faible durée d'impulsions (respectivement ns et fs), permettant d'atteindre des intensités laser très élevées. Dans ce travail, ces sources ont principalement été utilisées pour l'étude des phénomènes de choc sur epoxy.
- La source laser de l'institut PPRIME (25J, 25 ns), plus compacte que les installations précédentes. Cette source se rapproche d'une source à usage industriel, et a été la plus utilisée dans cette étude. Entre autre, elle a servi aux essais sur composite unidirectionnels et sur assemblages collés, avec et sans instrumentation.
- La source laser du PIMM (Laboratoire Procédés et Ingénierie en Mécanique et Matériaux, Art et Métiers, Paristech), permet d'utiliser des paramètres laser différents de ceux des autres sources.
- Le lanceur à gaz comprimé de l'ENSTA Bretagne, qui a permis de réaliser des impacts de plaque sur composite unidirectionnel et sur assemblages collés.

Afin d'instrumenter les expériences de choc, plusieurs diagnostics résolus en temps ont été utilisés. Ils sont présentés en détail dans le chapitre 2. Ils permettent une mesure directe de la réponse dynamique du matériau chargé, que ce soit en visualisant les ondes, ou en relevant la vitesse de surface libre, représentative de l'histoire de la propagation des ondes dans la cible.

- Le VISAR (Velocity Interferometer System for Any Reflector). Ce système basé sur le principe de l'interférométrie optique, permet une mesure très précise de la vitesse de surface libre pendant la propagation des ondes.
- La sonde VH (ou PDV, Photonic Doppler Velocimetry), développée par le CEA – BIII, ce dispositif voisin du dispositif VISAR,
- La visualisation transverse par ombroscopie, ici adaptée à l'étude de la propagation des chocs dans les epoxy, avec la collaboration du CEA-BIII.

Après le choc, les échantillons peuvent généralement être récupérés pour une analyse fine de leur état résiduel. Pour ce faire, plusieurs technique post-mortem ont été utilisées dans ce travail et sont présentées dans le chapitre 2. Elles permettent de quantifier l'endommagement résultant de la propagation des ondes de choc dans le matériau, à travers la mesure de différentes grandeurs, plus ou moins adaptées à chaque technique. En voici la liste:

- Coupes pour observations micrographiques, radiographies X, microscopie confocale, Differential Scanning Calorimetry (DSC) et Dynamic Mechanical Analysis (DMA). Ces dispositifs ont été utilisés à l'Institut PPRIME,

- Tests ultrasons conventionnels et laser, développés par EADS Innovation Works (Suresnes et Technocampus EMC2, Nantes), et utilisés dans le cadre de cette collaboration.

Toutes ces techniques ont été utilisées afin de quantifier le niveau d'endommagement résultant du choc laser. En particulier, la microscopie confocale s'est révélée très utile pour quantifier les déformations résiduelles à l'arrière des échantillons. Les données expérimentales ainsi obtenues fournissent des informations complémentaires, utiles pour corréler le niveau d'endommagement à l'intensité laser.

Techniques	Mesures		Avantages	Inconvénients
Techniques Post-mortem				
Micrographies	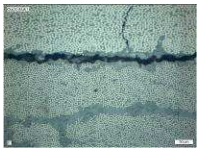	Observation et quantification de l'endommagement	. Observation directe de l'endo. . Identification de l'endo.	. Détruit les échantillons . Demande un long temps de préparation
Radiographie X	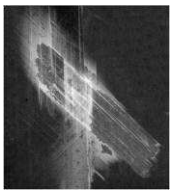	Observation de l'endommagement	. Complète les informations obtenues par microscopie . Visualisation des zones délaminées	. Pas d'information dans la profondeur . L'utilisation de l'iodure de zinc pollue les échantillons
Microscopie confocale 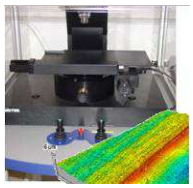	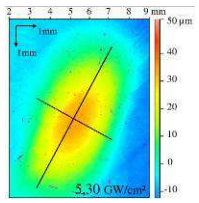	Quantification de la déformation résiduelle en face arrière	. Technique non destructive . Haute résolution . Données quantitatives sur la déformation résiduelle	. Nécessite des surfaces correctement polies avant analyse . Limité à la mesure de petites déformations
Test ultrasons	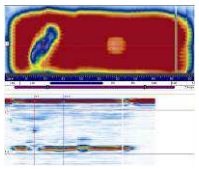	Analyse des délaminages et des décollements	. Usage rapide . Peut détecter les délaminages et les décollements . Usage industriel	. Ne peut pas détecter toutes les fissures . Ne peut pas détecter les petits défauts . Temps d'acquisition
Laser ultrasons	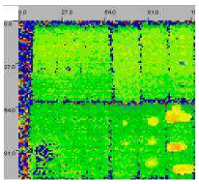	Analyse des délaminages et des décollements	. Usage rapide . Développé pour une application industrielle . Géométrie complexe	. Ne peut pas détecter toutes les fissures . Ne peut pas détecter les petits défauts . Résolution plus basse que les sondes
DSC/DMA	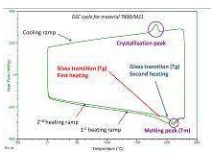	Propriétés thermomécaniques des cibles impactées	. Caractérise l'état chimique/moléculaire du matériau	. Nécessite de faible quantité de matière pour l'analyse (destruction cible)

Techniques	Mesures		Avantages	Inconvénients
Techniques résolues en temps				
VISAR 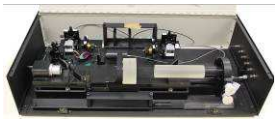	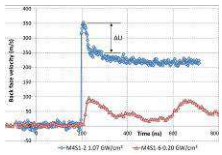	Mesure de surface libre	. Mesure de la réponse dynamique des CFRP . Sans contact . Bonne résolution	. Réglages de l'interferométrie assez complexes . Nécessite de préparer les échantillons
PDV	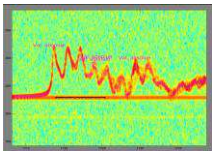	Mesure de surface libre	. Mesure de la réponse dynamique des CFRP . Facile à installer . multi vitesses	. Résolution temporelle plus faible que le VISAR, en particulier pour les cibles minces
Visualisation transverse	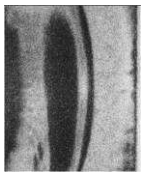	Visualisation du phénomène de choc	. Observation directe du phénomène . Identification des méchanismes de choc	. Information qualitative due à l'épaisseur de l'échantillon sondé.

RESUME – CHAPITRE 3

Le chapitre 3 décrit l'ensemble des résultats expérimentaux obtenus sur composites CFRP seuls, et sur la résine époxy, qui sont les constituants élémentaires des assemblages collés étudiés. Le but de ces études était de mieux appréhender les phénomènes complexes de propagation d'onde dans ces matériaux. En particulier, l'anisotropie du composite peut avoir une influence sur la propagation des ondes et sur celle de l'endommagement. Ce chapitre est divisé en trois parties. La première traite des résultats expérimentaux obtenus sur les résines époxy, incluant le matériau FM300 utilisé comme film adhésif dans les assemblages collés. La deuxième partie se consacre aux composites CFRP, minces, épais, unidirectionnels et croisés. Les mesures résolues en temps et les analyses post-mortem sont présentées. Enfin, la dernière partie s'interroge sur les modifications moléculaires, microstructuraux ou même thermiques pouvant intervenir sous chargement laser. Cette partie s'appuie en particulier sur des études post-mortem, incluant de la DSC.

Dans un premier temps, les observations de la propagation de l'onde de choc dans une résine époxy transparente ont donné des informations qualitatives sur la géométrie et la répartition de l'onde. Ces observations ont été considérablement améliorées en utilisant un système de photoélasticimétrie. Ce système a mis en avant la distribution des contraintes de cisaillement pendant la propagation de l'onde de choc. La vitesse moyenne du front de choc a également pu être évaluée. Ces résultats fournissent de nouvelles données, complémentaires d'une mesure de vitesse et utiles à la compréhension du phénomène de choc sur époxy. Elles sont aussi utilisables en comparaison des résultats numériques. Dans un second temps, l'état résiduel des résines choquées a été analysé grâce à des techniques post-mortem, afin d'étudier les effets induits sur la microstructure. Dans le cas des impacts laser ultra-brefs (300 fs, expériences ELFIE) aucune contrainte résiduelle ou modifications microstructurales résultant du choc n'ont été observées. Pour les impulsions courtes (3ns, expériences LULI2000), les conclusions sont les mêmes sur le plan microstructural, mais dans ce cas, des contraintes résiduelles de quelques MPa ont pu être quantifiées du côté de l'interaction laser/matière. Finalement, dans le cas d'une époxy relativement mal cuite, un léger effet du choc laser (25 ns, PPRIME) sur l'état de la microstructure a été mis en évidence grâce à l'étude de la transition vitreuse par DSC. Ce résultat a été obtenu dans le cas d'un écaillage marqué, ce qui est rassurant pour l'application industrielle, car sur-dimensionnant.

Les composites CFRP sous chargement laser ont ensuite été étudiés. La première étape consistait à étudier l'endommagement résultant de la propagation des ondes de choc dans des composites T800/M21 croisés, fins et épais. Le caractère anisotropique de l'endommagement a été analysé, ainsi que l'influence de l'intensité laser sur ses principales dimensions. Un scénario d'endommagement pour les composites T800/M21 a également été formulé. En particulier, l'effet des nodules thermoplastiques présents dans la résine M21 sur la propagation de l'endommagement a clairement été identifié expérimentalement. Ces résultat ont été complétés par des essais sur deux matériaux unidirectionnels différents (T300/914, IM7/M21). De plus, l'analyse des chocs laser effectué sur des composites T800/M21 croisés épais a permis une meilleure compréhension du comportement à l'endommagement dans le composite. Plus précisément, la déformation résiduelle de la face arrière, résultant du choc laser, a été étudiée et quantifiée par l'utilisation de la microscopie confocale. Les caractéristiques elliptiques de cette déformation ont été déterminées par l'analyse statistique des données collectées. Des modèles analytiques ont alors pu être établis pour représenter les mesures expérimentales, et ont fourni des paramètres utilisables pour corréler la déformation résiduelle à l'intensité laser. De plus, ces résultats ont finalement permis de tracer des

abaques pouvant être utilisés afin de comparer les seuils d'endommagement de différents matériaux composites, et donc, leur qualité.

Finalement, des expériences VISAR ont été réalisées sur des matériaux « modèles », ie des CFRP unidirectionnels, et « applicatifs », ie des plis croisés. La reproductibilité des mesures sur ces matériaux a été vérifiée et prouvée. Les données obtenues respectivement sur composites T800/M21 unidirectionnels, fins, épais, T700/M21 croisés et le matériau du joint FM300, ont fourni des informations sur la réponse dynamique de ces matériaux sous chargement laser. La propagation des ondes de choc, avec ou sans endommagement, est décrite par ces signaux, et sert également pour la validation des modèles numériques développés pour la description du phénomène. En terme d'application industrielle, les mesures VISAR effectuées sur composite unidirectionnel ont aussi mis en évidence un possible effet de fatigue dû au chargement laser répété, probablement à cause de la composante en flexion du chargement.

Le tableau ci-dessous associe les résultats obtenus avec les techniques expérimentales correspondantes. Il s'agit d'une synthèse illustrée.

Techniques	Principaux résultats associés
Techniques post-mortem	
Microscopie 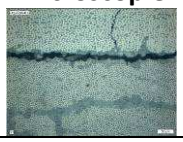	Pour les composites CFRP croisés, fins et épais, la microscopie a permis la quantification des délaminages (profondeur, largeur…), et l'évaluation de la densité de fissures résultant de la propagation des ondes de chocs dans le matériau.
Radiographie X 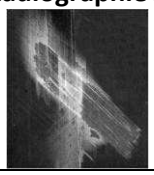	Pour les composites CFRP croisés, de faible épaisseur, la radiographie a complété l'observation micrographique en permettant la quantification de l'étendue de l'endommagement dans le plan du pli.
ICM 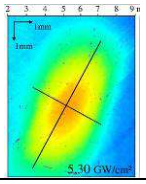	Pour les composites croisés épais, et les composites unidirectionnels, la microscopie confocale a permis de quantifier la déformation résiduelle de la face arrière des échantillons, résultant du flambement des plis délaminés par la propagation des ondes de choc.

Techniques	Principaux résultats associés
Techniques résolues en temps	
Visualisation transverse (Ombroscopie) 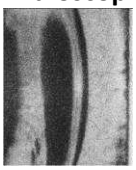	Pour les composites unidirectionnels minces, la visualisation transverse a permis d'observer des différences dans le comportement à l'écaillage de différents composites CFRP soumis à un choc laser. Pour les résines époxy transparentes, cette technique a permis l'observation directe de la propagation des ondes de choc au travers de la cible, donnant ainsi des informations quantitatives telle que la vitesse de choc moyenne, et qualitatives sur la géométrie de la propagation de l'onde dans le matériau. Ce diagnostic a fourni des informations différentes de la mesure de vitesse de surface libre, pouvant également être comparées aux résultats numériques.
Visualisation transverse avec photoélasticimétrie	Pour les résines époxy transparentes, ce dispositif a permis de mettre en évidence une distribution de contraintes spécifique pendant la propagation des ondes de choc. En particulier, il a permis l'identification des ondes de cisaillement. Ces données peuvent aussi être comparées aux résultats numériques. Les observations post-mortem par photoélasticimétrie ont permis de mettre en évidence des contraintes résiduelles dans le cas d'un chargement spécifique (LULI2000).
VISAR 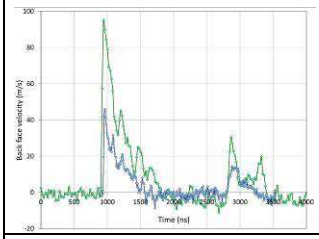	Pour le matériau FM300 (joint), le VISAR a permis l'analyse de sa réponse dynamique. Pour les CFRP unidirectionnels, laminas fins et épais, le VISAR a permis l'analyse de leurs réponses dynamiques, sans endommagement et avec écaillage. Pour les CFRP croisés, le VISAR a permis l'analyse de leurs réponses dynamiques. Pour les CFRP unidirectionnels épais, les mesures VISAR ont permis d'identifier un possible effet de fatigue dû à un chargement répété des choc laser. Dans tous les cas, ces données sont utilisables pour valider les modèles.
DSC 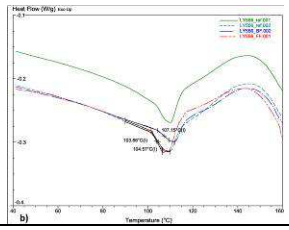	Pour les résines époxy, les mesures par DSC n'ont pas montré de modifications microstructurales induites par des chargements laser de très haute pression, et très faible durée d'impulsion. Elles ont mis en évidence une possible modification mineure, dans le cas d'une pression plus faible, avec des impulsions plus longues, et un écaillage marqué.

RESUME – CHAPITRE 4

Le chapitre 4 traite des aspects numériques de cette thèse, à la fois pour les résines époxy et pour les composites CFRP. En effet, la modélisation numérique est un point clé du développement du test d'adhérence par choc laser. Cette dernière peut considérablement améliorer la compréhension des phénomènes de propagation d'onde de choc dans ces matériaux. Plus spécifiquement, la vitesse matérielle de surface libre, les ondes correspondantes, et les contraintes au sein du matériau peuvent être obtenus par le biais de la simulation numérique. La compréhension qui découle de ces études est dans un second temps très utile à l'optimisation de la technique, abordée dans les chapitres 5 et 6. La première partie de ce chapitre est dédiée à un revue bibliographique faisant état des différents choix de modélisation possibles pour les problèmes traitant de dynamique rapide dans le cas des composites. La deuxième partie se concentre sur la modélisation des époxys, et s'appuie sur les résultats expérimentaux présentés au chapitre 3. Les époxys purs et le matériau constituant le joint de colle FM300 sont tous deux abordés. Enfin, la troisième et dernière partie de ce chapitre traite de la simulation des phénomènes de choc laser sur composite CFRP, en insistant particulièrement sur les choix de modélisation réalisés. Différentes étapes de validation du modèle ont été réalisées.

Dans la première partie de ce chapitre, la revue bibliographique se concentre sur les modèles numériques disponibles dans la littérature pour décrire les problèmes de choc sur composites, et sur l'endommagement induit par de telles sollicitations. En guise de bilan, il apparait que plusieurs modèles sont disponibles, via des codes commerciaux, pour décrire ces problématiques. Les travaux identifiés traitent majoritairement de la tenue à l'impact (tour de chute, impact hyper véloce,…) des structures composites, et l'évaluation prédictive de leur caractéristiques mécaniques résiduelles. Pour cela, le développement de modèles complexes d'endommagement est souvent visé, pour raffiner la description numérique des différents modes d'endommagement. Par contre, assez peu de travaux se consacrent à la modélisation de chargement, et de l'endommagement induit, à haut taux de déformation. De ce point de vue, l'un des points clés de ce travail est donc l'identification des paramètres élastiques et d'endommagement adaptés à la dynamique rapide. Les choix réalisés pour la modélisation du choc laser sur composite sont présentés et justifiés. En particulier, une loi élastique/ hydrodynamique a été choisie pour la modélisation de la résine sous choc laser. Le comportement du pli composite est lui modélisé par une loi élastique/ orthotrope, et l'endommagement est basé sur un critère de Chang/Chang. Ce modèle d'endommagement est relativement simple, et peu précis pour décrire la propagation de l'endommagement, mais permet une bonne description de l'initiation de l'endommagement, ce qui est l'objectif ici.

La modélisation des phénomènes de choc laser sur des cibles de résine époxy est présentée en premier. L'idée était de définir un modèle numérique, contenant des paramètres identifiés, pour décrire correctement le comportement du joint FM300 (fait d'époxy) dans l'assemblage collé. Pour cela, les expériences réalisées sur la source LULI2000 et présentées dans le chapitre 3 ont été utilisées pour valider le choix du modèle, et ses paramètres. La comparaison entre les visualisations par ombroscopie et les calculs numérique a montré la capacité du modèle à décrire correctement la propagation des ondes dans ce matériau, avec la bonne chronologie et la bonne répartition spatiale. De plus, la simulation numérique a également permis de reproduire la propagation des ondes de cisaillement observée par photoélasticimétrie durant la campagne d'essais sur la source laser ELFIE. Sur les bases de ces simulations, le modèle pour décrire le comportement du joint FM300 a été validé grâce à des mesures VISAR.

La modélisation du comportement des matériaux composites sous chargement laser a ensuite été étudiée. D'abord, plusieurs études paramétriques ont été conduites sur un modèle de composite mince (0,5 mm) unidirectionnel T800/M21, constitué de deux plis et utilisant des paramètres quasi-statiques. Les effets du niveau de pression sur la cible ont été montrés jusqu'au seuil d'écaillage. Les effets 2D d'anisotropie et d'interfaces ont aussi été identifiés, ainsi que leur signature sur les signaux de vitesse de face arrière. Le caractère anisotropique de la propagation de contrainte en fonction du temps a été montré en observant les différentes directions de propagation. Cette étude a également montré que la propagation des contraintes σ_{zz} (compression/ traction) restait globalement isotropique sous la zone chargée et sur les temps d'observation considérés (qq µs). L'initiation de l'endommagement par écaillage est donc également isotropique. De plus, l'influence des paramètres élastiques du modèle sur la réponse dynamique du matériau a été évaluée. En particulier, le module transverse du pli composite a une forte influence sur la fréquence des allers-retours des ondes, et sur leur amplitude. Ces conclusions ont permis de passer à la deuxième étape, dédiée à la validation progressive du modèle numérique grâce aux mesures VISAR. Dans un premier temps, deux signaux avec et sans endommagement ont été utilisés pour identifier les paramètres matériaux adaptés au taux de déformation du choc laser. Ce jeu de paramètres est ensuite validé sur des composites unidirectionnels minces (0,5 mm) et épais (3,0 mm). Finalement, le comportement d'un composite T700/M21 croisé a été correctement modélisé. Ces simulations ont permis l'étude de la propagation d'ondes de choc dans ces matériaux, conduisant à une meilleure compréhension de leur comportement dynamique. Les principales étapes de la validation numérique sont résumées dans la tableau ci-dessous.

Il est important de noter que les modèles développés sont basés sur plusieurs hypothèses assez restrictives. Cependant, au regard des incertitudes expérimentales sur le profil de pression en particulier, l'accord global entre simulations et expériences est plutôt bon sur la gamme d'épaisseur considérée et la base temporelle d'observation. En conséquence, les modèles développés dans ce chapitre peuvent directement être utilisés pour la modélisation des assemblages collés.

Modèles	Comparaison expérience/ calcul	Diagrammes temps/position
Composite T800/M21 unidirectionnel mince (0,5 mm) – Identification des paramètres du modèle		
Modèle 2D unidirectionnel 0.5 mm, Identification des paramètres élastiques – **Pas de rupture**	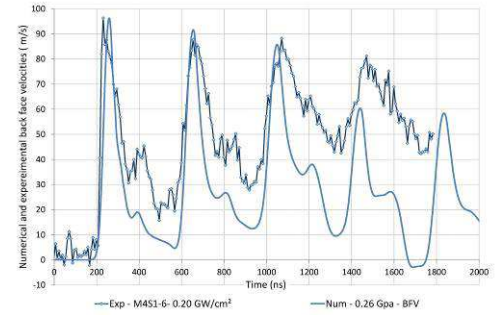	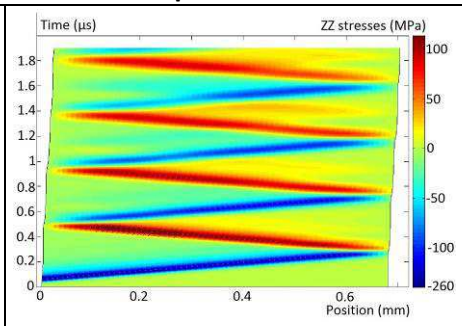
Modèle 2D unidirectionnel 0.5 mm, Identification des paramètres d'endommagement – **Ecaillage numérique**	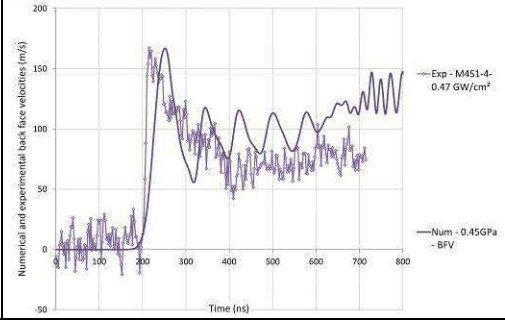	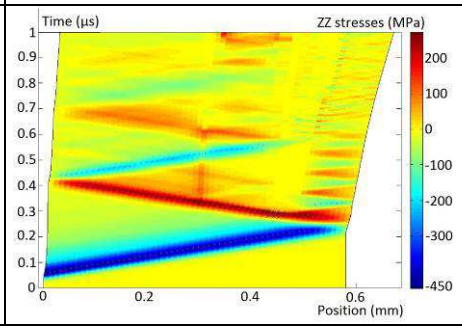
Composite T800/M21 unidirectionnel épais (3.0 mm) – Validation du modèle		
Modèle 2D unidirectionnel 3.0 mm, validation des paramètres élastiques – **Ecaillage numérique**	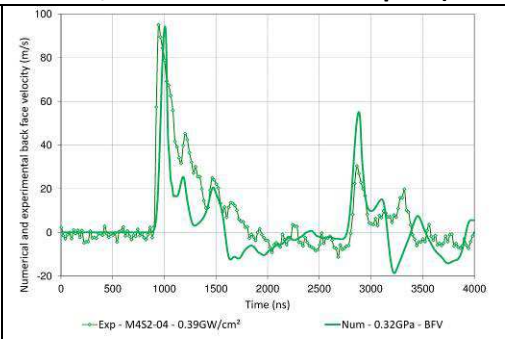	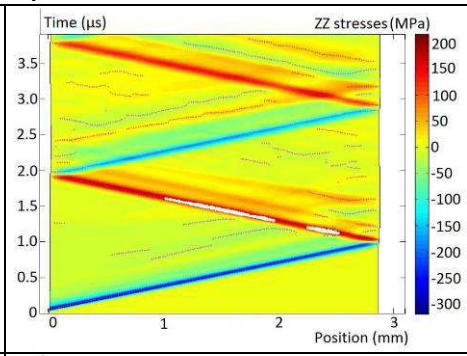
Modèle 2D unidirectionnel 3.0 mm, validation des paramètres d'endommagement – **Pas de rupture**	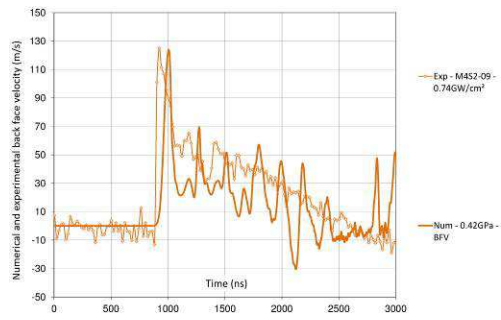	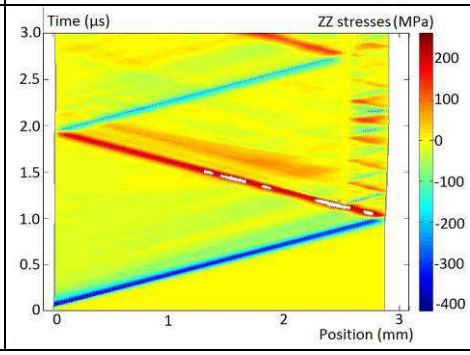
Composite T700/M21 croisé (0/90) épais (1.5 mm) – Validation du modèle		
Modèle 2D croisé 1.5 mm, validation des paramètres élastiques – **Pas de rupture**	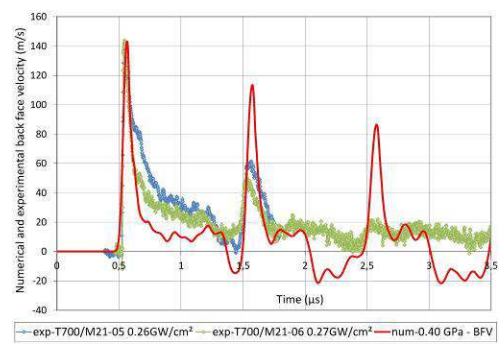	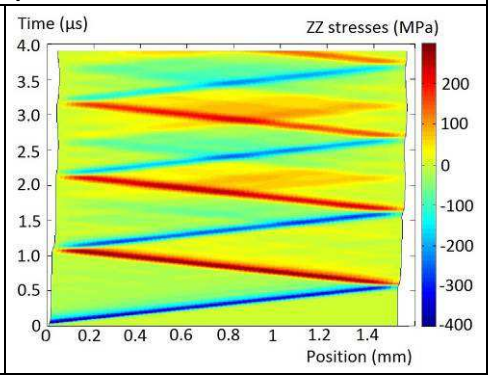

RESUME – CHAPITRE 5

Dans les chapitres précédents, le comportement dynamique des composites CFRP sous chargement laser a été analysé, et un modèle numérique a été développé et validé. En s'appuyant sur ces travaux préliminaires, les assemblages collés peuvent maintenant être étudiés.

Le chapitre 5 est organisé en deux blocs: le premier concerne les résultats expérimentaux obtenus sur les différents assemblages collés testés, le deuxième regroupe les résultats numériques. La première partie de ce chapitre donne quelques rappels sur les assemblages collés ainsi que des compléments d'information sur les matériaux testés, divisés en deux catégories : assemblages symétriques (deux plaques composites de même épaisseur) et non symétriques (une plaque épaisse collée à une plaque mince). Les échantillons symétriques proviennent d'Airbus (LA, LE, LB), et les échantillons non-symétriques ont été fournis dans le cadre du projet ENCOMB (UT, RE, MO), et ont été réalisés par EADS Cassidian. Chaque catégorie contient un matériau référence et plusieurs échantillons contaminés à différents degrés. Les résultats expérimentaux sur chacune de ces deux catégories sont présentés respectivement dans la partie 2 et la partie 3. Tous les échantillons testés ont été progressivement chargés par choc laser afin de déterminer leurs seuils d'endommagement. Les endommagements induits ont été analysés grâce aux techniques présentées dans le chapitre 2 et éprouvées lors de l'étude sur composites CFRP dans le chapitre 3. Les seuils d'endommagement ont été étudiés en comparaison avec les essais GIC réalisés par l'Université de Patras (Grèce), avec une attention particulière portée sur la corrélation de ces seuils avec les degrés de contamination. La dernière partie présente finalement les résultats numériques obtenus sur les assemblages collés.

Entre 5 et 9 chocs ont été réalisés pour chaque degré de contamination afin de déterminer les seuils d'endommagement. Chaque état résiduel résultant de chaque choc laser a été analysé à l'aide de diagnostics croisés, le tout formant un ensemble de données complémentaires. En particulier, la microscopie confocale s'est révélée très efficace pour quantifier la déformation résiduelle des assemblages en face arrière. Les petites cloques elliptiques mesurées sont des indicateurs clairs de l'endommagement interne de la partie composite de l'assemblage. Ainsi, la microscopie confocale a été utilisée pour déterminer les seuils d'endommagement composite. Pour ce qui est des seuils de décollement, ou d'endommagement du joint, les ultrasons (conventionnels ou laser) ont été utilisés et se sont montrés très efficaces pour certaines contaminations. L'ouverture des interfaces crée des vides dans le matériau qui conduisent à une forte désadaptation d'impédance influençant de manière significative la propagation des ultrasons. Finalement, des coupes micrographiques ont été réalisées afin de quantifier et d'identifier les modes d'endommagement. Ceci a permis de comparer les effets des différents contaminants sur ces derniers.

Pour ce qui des échantillons symétriques, les résultats expérimentaux obtenus ont permis de discriminer les assemblages contaminés des assemblages de référence. Ils ont également montré que les paramètres laser utilisés n'étaient pas correctement adaptés à l'architecture des échantillons testés. En conséquence, une optimisation des paramètres de choc est nécessaire pour éviter d'endommager la partie composite de l'assemblage pendant le test de l'interface collée. Au regard des différents seuils identifiés, seul le scénario LB a permis d'obtenir un joint suffisamment faible pour être testé sans optimisation. Dans le cas des échantillons non-symétriques, le même souci d'optimisation des paramètres de tirs a pu être constaté. Cependant, la discrétisation en énergie choisie pour la campagne d'essai a permis un encadrement fin des seuils d'endommagement, en particulier dans le cas du scénario à l'agent de démoulage. Dans ce cas, l'évaluation du seuil de décollement est en bon accord avec les degrés de contamination fournis par les partenaires du projet

ENCOMB, et les essais mécaniques réalisés par l'Université de Patras. Le cas de la contamination à l'eau est plus délicat à traiter, et les résultats doivent être considérés avec prudence car la porosité importante des échantillons peut influencer la propagation des ondes de chocs et l'interprétation des résultats ultrasons. Néanmoins, si on considère seulement la borne supérieure de l'encadrement des seuils d'endommagement, les résultats sont également en accord avec la gradation des degrés de contamination. Pour chacune des contaminations, le seuil d'endommagement de la partie composite de l'assemblage (T700/M21, face arrière) est très bas comparé aux seuils de décollement des joints. Une optimisation des paramètres de choc est indispensable pour ces assemblages.

Finalement, les simulations numériques réalisées sur les assemblages collés ont été présentées, et comparées aux résultats expérimentaux obtenus par VISAR. Les résultats obtenus montrent une très bonne corrélation entre données expérimentales et numériques, ce qui valide le modèle numérique développé. De plus, la représentation des diagrammes temps/positon couplée avec les signaux de vitesses a permis une meilleure compréhension du phénomène de choc laser sur ces assemblages. En particulier, chaque pic observé sur les signaux de vitesse a pu être identifié. Cette compréhension peut alors être utilisée pour mieux appréhender les capacités actuelles de la technique LASAT, puis permettre la définition de solutions d'optimisation.

RESUME – CHAPITRE 6

Le chapitre 6 traite des possibilités actuelles de la technique LASAT, c'est-à-dire sans changement de configuration, ainsi que des solutions d'optimisation développées dans ce travail afin de rendre la technique plus efficace. Les possibilités actuelles de la technique sont décrites dans la première partie du chapitre. Pour ce qui est de l'optimisation, le point clé est d'arriver à positionner le chargement de traction aussi proche que possible de l'interface collée à tester, et donc d'éviter d'endommager la partie composite de l'assemblage lors du test. Dans ce travail, quatre solutions d'optimisation ont été étudiées et comparées : l'ajustement du diamètre de la tache focale, la modification de la durée d'impulsion, l'utilisation d'un double choc en face avant, et l'utilisation du choc symétrique synchronisé. Ces solutions sont respectivement discutées en parties 2, 3 et 4.

Dans un premier temps, les capacités de test de la configuration actuelle (telle que disponible à PPRIME) ont été étudiées. D'abord, il a été vérifié l'absence d'effet de fatigue dû à des chargements laser répétés au même point sous le seuil d'endommagement. Jusqu'à 10 tirs, aucun endommagement mécanique n'a été détecté par mesure VISAR sur l'assemblage collé sollicité. De plus, le seuil d'endommagement du matériau n'a pas diminué après ces 10 tirs. Ce point est important pour la viabilité industrielle du test. Ensuite, la modélisation numérique a été utilisée pour déterminer les capacités de test de la technique LASAT avec les installations PPRIME utilisées. Pour cela, la vitesse de face arrière a été utilisée comme un moyen de discrimination entre un décollement et une absence de décollement. Les résultats montrent qu'une interface dont la résistance inter laminaire en traction serait égale au plus à 40% de la résistance en traction du pli composite (en transverse) peut être testée sans endommager le composite. Cette valeur, comme les suivantes, doit être considérée avec prudence à cause des incertitudes sur les paramètres laser.

Dans le cas où la résistance de l'interface est supérieure à 40% de celle du composite, alors la technique doit être optimisée. Pour cela, différentes solutions ont été proposées dans ce travail. D'abord, l'influence du diamètre de focalisation sur la position des contraintes maximales a été étudiées dans le cas des assemblages collés non-symétriques T700/M21. Cette étude montre qu'un diamètre de 4 mm est le plus intéressant pour l'application considérée en termes de répartition de contraintes dans l'épaisseur de l'assemblage. Cependant, se limiter à changer le diamètre de focalisation n'est pas suffisant pour complètement optimiser la distribution de contraintes, principalement à cause de la désadaptation d'impédance qui a lieu au niveau du joint de colle.

L'optimisation par ajustement de la durée d'impulsion du laser présente des caractéristiques intéressantes et peut être divisée en deux possibilités principales :

- La première solution consiste à localiser les contraintes maximales au niveau de l'interface collée. Cela permet de tester une interface dont la résistance est de l'ordre de grandeur de la résistance inter laminaire du composite $\sigma_{T,i}$. Cela demande un réglage assez fin des paramètres de choc, en particulier de la pression. Cette configuration de la répartition des contraintes a lieu pour d'une durée d'impulsion de 500 ns et de 400 ns dans les cas respectivement les assemblages non-symétriques T700/M21 et les symétriques T800/M21.

- La seconde solution est basée sur la localisation des premières contraintes générées dans le matériau au niveau de l'interface à tester. Cela évite de charger la partie composite de l'assemblage. En conséquence, cette solution est moins exigente par rapport à la précision en pression, mais permet un test d'une interface de résistance inférieure ou égale à 70% de $\sigma_{T,i}$

dans le cas d'un assemblage non-symétrique T700/M21, et à 80% de $\sigma_{T,i}$ dans le cas d'un assemblage symétrique de T800/M21. Cette solution a été validée expérimentalement grâce à des expériences d'impact de plaques sur les assemblages symétriques.

La solution utilisant un double choc en face avant a été étudiée de manière numérique, la source laser permettant sa validation expérimentale n'étant pas encore disponible. De plus, elle peut présenter quelques difficultés d'implémentation, en particulier à cause du confinement et de la couche sacrificielle qui doivent tenir deux chocs. Cela reste une bonne alternative à la solution précédente parce que cela demande moins d'énergie que les impulsions longues pour une gamme d'interfaces testées du même ordre (inférieure ou égale à 70% de la résistance du composite).

Finalement, la configuration par chocs symétriques synchronisés a été développée, comme un outil de « frappe chirurgicale ». Cette solution permet de créer un chargement étroit (temporellement et spatialement) de traction n'importe où dans l'épaisseur du matériau. De plus, la résistance de l'interface pouvant être testée peut atteindre la valeur du composite (100% de $\sigma_{T,I}$ dans le cas de l'assemblage non-symétrique, et 105% dans le cas de l'assemblage symétrique) d'après les résultats des simulations. Cette solution donne la possibilité de tester facilement n'importe quel type d'interface, comme par exemple des interplis, en changeant le délai entre les deux impulsions laser. La validation expérimentale a été effectuée sur les assemblages symétriques, et les résultats montrent que cette solution est très efficace pour éviter l'endommagement du composite dans l'assemblage. Cette solution a fait l'objet d'un dépôt de brevet. L'ensemble des solutions d'optimisation est résumé dans le tableau ci-dessous.

Possibilités actuelles de la technique LASAT			
Chocs répétés sur l'assemblage de référence		Possibilités de test actuelles	
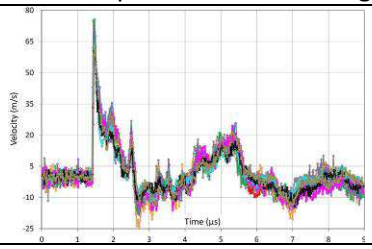	**10 chocs** sans modification mécanique observable	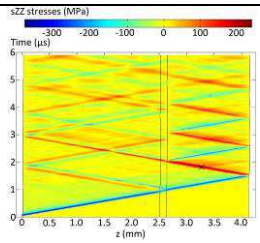	Résistance interface collée **≤ 40%** résistance interlaminaire composite

Optimisation de LASAT par ajustement de la durée d'impulsion				
	En utilisant les contraintes maximales		**En utilisant les premières contraintes**	
Sur assemblages collés non-symétriques T700/M21	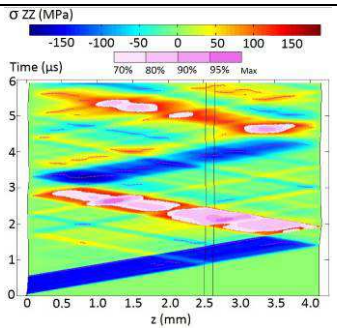	Résistance interface collée **≤ 95%** résistance interlaminaire composite	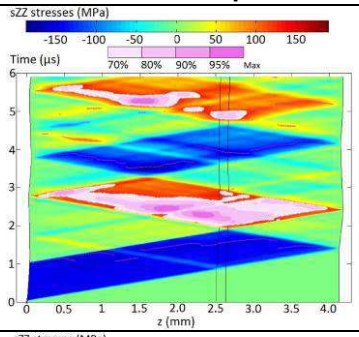	Résistance interface collée **≤ 70%** résistance interlaminaire composite
Sur assemblages collés symétriques T800/M21	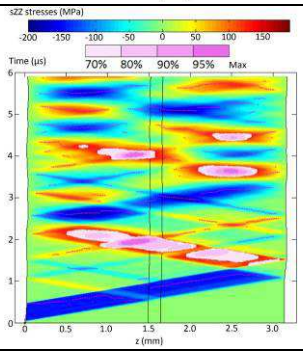	Résistance interface collée **≤ 105%** résistance interlaminaire composite	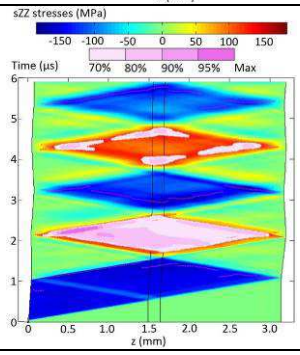	Résistance interface collée **≤ 80%** résistance interlaminaire composite

Optimisation de LASAT par double chocs				
	En utilisant les chocs symétriques		**En utilisant le double choc face avant**	
Sur assemblages collés non-symétriques T700/M21	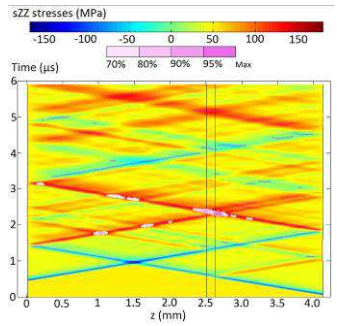	Résistance interface collée **≤ 100%** résistance interlaminaire composite	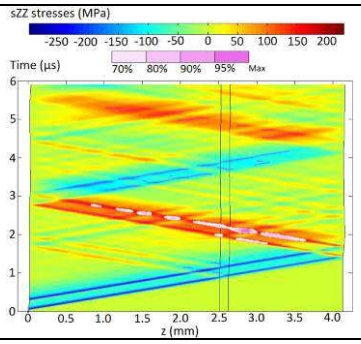	Résistance interface collée **≤ 70%** résistance interlaminaire composite
Sur assemblages collés symétriques T800/M21	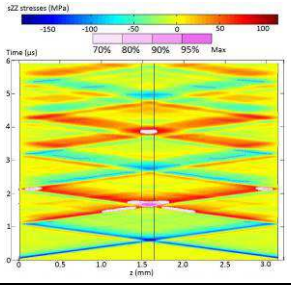	Résistance interface collée **≤ 105%** résistance interlaminaire composite		

Experimental and numerical investigations on the dynamic behaviour of aeronautic composites under laser shock - Optimization of a shock wave adhesion test for bonded composites

Ce travail vise le développement d'une méthode non destructive permettant de contrôler la qualité mécanique des joints collés aéronautiques, en utilisant les ondes de choc générées par impact laser (projet ENCOMB). Des chocs ont été réalisés à l'aide de dispositifs tels que des sources laser ou des canons à gaz. Différents diagnostiques ont été utilisés : le VISAR, la VH, la visualisation transverse, la microscopie optique et confocale, la radiographie X, le contrôle ultrasons...Des échantillons de résine et des composites stratifiés carbone/époxy ont d'abord été étudiés. Des chocs laser instrumentés, couplés à des analyses post-mortem, ont permis une meilleure compréhension des phénomènes de choc dans ces matériaux. Les résultats obtenus sur les assemblages composites collés montrent que la technique de choc laser permet de discriminer différents degrés d'adhérence. L'utilisation de modèles numériques, développés grâce aux données expérimentales, a permis d'analyser la propagation du choc dans ces assemblages complexes. Ces résultats ont démontré la nécessité d'optimiser la technique, afin de tester exclusivement l'adhérence du joint collé, sans endommager les composites de l'assemblage. Plusieurs solutions d'optimisation sont proposées tels que l'utilisation d'une impulsion variable, ou celle de double chocs. Ces solutions ont été validées expérimentalement et l'optimisation numérique a fourni les paramètres de choc pour de futurs tests. Finalement, ce travail fournit des résultats originaux sur le comportement dynamique de composites stratifiés et permet de progresser vers l'adaptation du test d'adhérence par choc laser à différents assemblages composites.

This work aims the development of a non-destructive technique to control the mechanical quality of aeronautics adhesive bonds (ENCOMB project). Shocks were realized by use of laser sources or gas gun, and different techniques were used to analyse the shocks such as: VISAR, PDV, Shadowgraphy, optical and confocal microscopy, X-ray radiography, ultrasound testing…Epoxy resins and carbon/epoxy composite laminates were first investigated. Monitored laser shocks, in addition to post-mortem analyses, enabled to better understand the shock phenomenon on these complex materials. The results obtained on bonded composite showed that the laser shock technique can be used to discriminate different adherence levels. The use of numerical models, developed thanks to the experimental data, enabled to analyze the shock propagation in these complex assemblies. They also evidenced the need for optimization, in order to test only the bond interface and not to break the composite parts on the assembly. Several optimization solutions are formulated such as the use of tuneable pulse duration, or double shock configurations. Some of these solutions have been experimentally validated, and the numerical optimization gives the shock parameters to use for the next experimental campaigns. Finally, this work provides original results on the dynamic behaviour of composite materials under laser shock and leads to the adaptation of the laser shock adhesion test to any kind of bonded composite assemblies.

Mots clés/ Key words:

- Composites à fibres de carbone/ Carbon composites
- Assemblages collés/ Adhesive joints
- Stratifiés/ Laminated materials
- Choc (mécanique)/ Shock (mechanics)
- Lasers/ Lasers
- Simulation par ordinateur/ Computer simulation
- Essais (technologie)/ Testing
- Contrôle Non Destructif/ Non-destructive testing
- Adhésion/ Adhesion
- LASAT/ Laser adhesion test
- Polymers/ Polymers
- Tolérance aux dommages/ Damage tolerance